ACS SYMPOSIUM SERIES 1077

NMR Spectroscopy of Polymers: Innovative Strategies for Complex Macromolecules

EDITED BY

H. N. Cheng, Tetsuo Asakura,
and Alan D. English

Downloaded by 89.163.35.42 on June 19, 2012 | http://pubs.acs.org
Publication Date (Web): October 14, 2011 | doi: 10.1021/bk-2011-1077.fw001

NMR Spectroscopy of Polymers: Innovative Strategies for Complex Macromolecules

In NMR Spectroscopy of Polymers: Innovative Strategies for Complex Macromolecules; Cheng, H., et al.;
ACS Symposium Series; American Chemical Society: Washington, DC, 2011.

Downloaded by 89.163.35.42 on June 19, 2012 | http://pubs.acs.org
Publication Date (Web): October 14, 2011 | doi: 10.1021/bk-2011-1077.fw001

Downloaded by 89.163.35.42 on June 19, 2012 | http://pubs.acs.org
Publication Date (Web): October 14, 2011 | doi: 10.1021/bk-2011-1077.fw001

ACS SYMPOSIUM SERIES **1077**

NMR Spectroscopy of Polymers: Innovative Strategies for Complex Macromolecules

H. N. Cheng, Editor
Southern Regional Research Center,
U.S. Department of Agriculture, Agricultural Research Service
New Orleans, Louisiana

Tetsuo Asakura, Editor
Tokyo University of Agriculture and Technology
Koganei, Tokyo

Alan D. English, Editor
DuPont Central Research and Development
Wilmington, Deleware

Sponsored by the
ACS Division of Polymer Chemistry, Inc.

American Chemical Society, Washington, DC

Distributed in print by Oxford University Press, Inc.

Downloaded by 89.163.35.42 on June 19, 2012 | http://pubs.acs.org
Publication Date (Web): October 14, 2011 | doi: 10.1021/bk-2011-1077.fw001

Library of Congress Cataloging-in-Publication Data

NMR spectroscopy of polymers : innovative strategies for complex macromolecules /
H. N. Cheng, Tetsuo Asakura, Alan D. English, editor[s].
p. cm. -- (ACS symposium series ; 1077)
"Sponsored by the ACS Division of Polymer Chemistry, Inc., American Chemical Society, Washington DC."
Includes bibliographical references and index.
ISBN 978-0-8412-2667-8
1. Polymers--Spectra--Congresses. 2. Nuclear magnetic resonance spectroscopy--Congresses. 3. Polymers--Analysis--Congresses. I. Cheng, H. N. II. Asakura, Tetsuo. III. English, Alan D., 1947- IV. American Chemical Society. Division of Polymer Chemistry.
QC463.P5N58 2011
547′.7046--dc23
2011036489

The paper used in this publication meets the minimum requirements of American National Standard for Information Sciences—Permanence of Paper for Printed Library Materials, ANSI Z39.48n1984.

Copyright © 2011 American Chemical Society

Distributed in print by Oxford University Press, Inc.

All Rights Reserved. Reprographic copying beyond that permitted by Sections 107 or 108 of the U.S. Copyright Act is allowed for internal use only, provided that a per-chapter fee of $40.25 plus $0.75 per page is paid to the Copyright Clearance Center, Inc., 222 Rosewood Drive, Danvers, MA 01923, USA. Republication or reproduction for sale of pages in this book is permitted only under license from ACS. Direct these and other permission requests to ACS Copyright Office, Publications Division, 1155 16th Street, N.W., Washington, DC 20036.

The citation of trade names and/or names of manufacturers in this publication is not to be construed as an endorsement or as approval by ACS of the commercial products or services referenced herein; nor should the mere reference herein to any drawing, specification, chemical process, or other data be regarded as a license or as a conveyance of any right or permission to the holder, reader, or any other person or corporation, to manufacture, reproduce, use, or sell any patented invention or copyrighted work that may in any way be related thereto. Registered names, trademarks, etc., used in this publication, even without specific indication thereof, are not to be considered unprotected by law.

PRINTED IN THE UNITED STATES OF AMERICA

Downloaded by 89.163.35.42 on June 19, 2012 | http://pubs.acs.org
Publication Date (Web): October 14, 2011 | doi: 10.1021/bk-2011-1077.fw001

Foreword

The ACS Symposium Series was first published in 1974 to provide a mechanism for publishing symposia quickly in book form. The purpose of the series is to publish timely, comprehensive books developed from the ACS sponsored symposia based on current scientific research. Occasionally, books are developed from symposia sponsored by other organizations when the topic is of keen interest to the chemistry audience.

Before agreeing to publish a book, the proposed table of contents is reviewed for appropriate and comprehensive coverage and for interest to the audience. Some papers may be excluded to better focus the book; others may be added to provide comprehensiveness. When appropriate, overview or introductory chapters are added. Drafts of chapters are peer-reviewed prior to final acceptance or rejection, and manuscripts are prepared in camera-ready format.

As a rule, only original research papers and original review papers are included in the volumes. Verbatim reproductions of previous published papers are not accepted.

ACS Books Department

Downloaded by 89.163.35.42 on June 19, 2012 | http://pubs.acs.org
Publication Date (Web): October 14, 2011 | doi: 10.1021/bk-2011-1077.pr001

Preface

Nuclear magnetic resonance (NMR) spectroscopy is a premiere technique for the studies of polymers. Since 1950s, the literature on this topic has grown rapidly. A large body of ingenious techniques has been developed that have enriched the field and provided NMR practitioners with many valuable tools to use in their work. The field now covers a broad spectrum of activities, from polymer identification, quality control, and reaction monitoring to structure determination, polymer morphology, compatibility, chain conformation, dynamics, diffusion, and imaging.

For many years we have organized successful symposia devoted to NMR Spectroscopy of Polymers at roughly every 3 years. The purpose is to provide an international forum for the presentation of recent advances in NMR techniques and characterization of natural and synthetic polymers, including agriculturally based materials. We strive to invite speakers who are acknowledged leaders in this field. Over the years, it has become the largest and the foremost symposia for the NMR studies of polymers.

This book is based on such a symposium held at the Pacifichem meeting on December 17-21, 2010 in Honolulu, Hawaii. At this meeting, there were 43 talks and 24 posters, representing the state-of-the-art research of polymer NMR in solids, liquids, and imaging. Many exciting new techniques and findings were reported.

In this symposium book, a total of 30 articles are included, covering the following topics:

Fundamental and applied research
New methodology development
Polymer structure determination
Polymer dynamics and diffusion
Nanostructures and nanocomposites
Supramolecular assemblies
Blends, miscibility, and heterogeneity
Polymers under confinements and on surfaces
Multidimensional NMR

In addition, we are thankful to Professor Hans Spiess for an overview of solid NMR and Professor Peter Rinaldi for a tutorial on solution NMR. It is our hope that this book provides a good representation of what is happening at the forefront of research in polymer NMR and also captures some of the excitements we saw at the Pacifichem symposium.

This book is targeted for chemists, physicists, biochemists, and chemical engineers as well as graduate students who are engaged in research and

In NMR Spectroscopy of Polymers: Innovative Strategies for Complex Macromolecules; Cheng, H., et al.;
ACS Symposium Series; American Chemical Society: Washington, DC, 2011.

applications of polymer NMR. It can also be a useful reference book for people who are interested in these topics.

We thank the authors for their timely contributions and their cooperation while the manuscripts were being reviewed and revised. Thanks are also due to the ACS Division of Polymer Chemistry, Inc. for sponsoring the 2010 symposium. We also acknowledge the generous funding from the ACS Division of Polymer Chemistry, Inc., Air Force Research Laboratories, Agilent Technologies, Bruker Corporation, Chlorella Industry Co., Ltd., Japan Medical Materials Co., JOEL, Ltd., MR Resources, National Science Foundation (NSF) Division of Materials Research, New Era Enterprises, and REC Materials, Inc.

H. N. Cheng
Southern Regional Research Center
USDA – Agricultural Research Service
1100 Robert E. Lee Blvd.
New Orleans, LA 70124, U.S.A.

Tetsuo Asakura
Department of Biotechnology
Tokyo University of Agriculture and Technology
2-24-16 Nakacho
Koganei, Tokyo 184-8588, JAPAN

Alan D. English
DuPont Central Research and Development Department
Experimental Station
Wilmington, DE 19880, U.S.A.

Downloaded by 89.163.35.42 on June 19, 2012 | http://pubs.acs.org
Publication Date (Web): October 14, 2011 | doi: 10.1021/bk-2011-1077.pr001

H. W. Spiess - An Appreciation

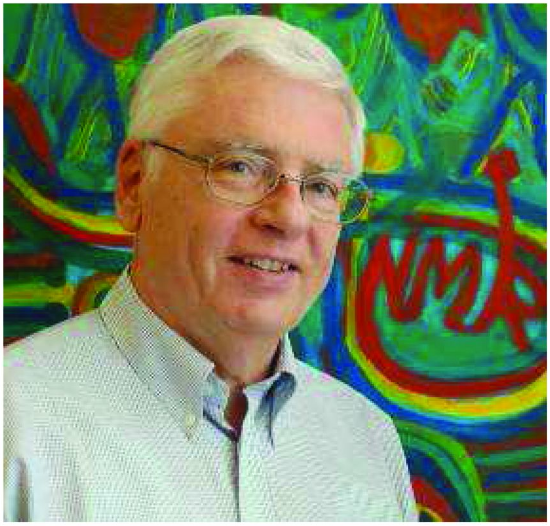

Downloaded by 89.163.35.42 on June 19, 2012 | http://pubs.acs.org
Publication Date (Web): October 14, 2011 | doi: 10.1021/bk-2011-1077.pr002

Hans Wolfgang Spiess studied at the University of Frankfurt and was awarded his Ph.D. there in 1968. He worked as a postdoctoral fellow with R. K. Sheline at Florida State University (1968–1970), K. H. Hausser at the MPI for Medical Research, Heidelberg (1970–1975), and H. Sillescu at the University of Mainz (1975–1983, including habilitation). He held professorships at the University of Münster and the University of Bayreuth (1981−1984). Since 1984, he has been one of the directors of the Max Planck Institute in Polymer Research in Mainz.

Professor Spiess is an acknowledged leader in polymer NMR. He has developed a large array of new NMR techniques for elucidating structure, dynamics, phase behavior and order in synthetic macromolecules and supramolecular systems. With brilliance and creativity, he applies these techniques to study new polymer materials in order to relate their microscopic and macroscopic behavior. His scientific depth and breadth can be illustrated by the following examples:

- Two-and three-dimensional NMR methods for studying molecular dynamics
- High-resolution multiple quantum NMR spectroscopy of solids for the investigation of molecular structure and organization

- Spin diffusion techniques for determining the phase behavior and compatibility in block copolymers, polymer blends, and core shell particles
- NMR imaging and hyperpolarization by laser polarization, dynamic nuclear polarization and parahydrogen induced polarization
- Investigation of polyelectrolytes and biomacromolecules in solution with a broad variety of EPR methods including nm distance measurements
- Chain motion and its relationship to mechanical properties in crystalline and amorphous polymers as well as dynamics at the glass transition

In addition to his prolific scientific work, Professor Spiess has served as chairman of the European Polymer Federation (1991–1992) and chairman of the Capital Investment Committee of the German Science Foundation (1994–1996). He was chairman of the Committee for Electronic Data Processing of the MPG (1997−2006), President of the Groupement AMPERE (2000−2006), and a Member of the Scientific Council of the Federal Republic of Germany (1999−2005). He is the current President of the International Society of Magnetic Resonance. He has also collaborated with the editors of this volume and others to organize many international meetings dealing with NMR Spectroscopy of Polymers to promote the development of this field.

He is the recipient of numerous awards and honorary lectureships. These include the Leibniz-Prize of the DFG (1987), NMR Award of the Eastern Analytical Symposium (2000), the AMPERE Prize (2002), the Liebig Medal of the German Chemical Society (2002), the Presidential Medal of Cornell University (2002), the Award of the Society of Polymer Science, Japan (2003), the Zavoisky Prize (2010), and the Paul J. Flory Prize for polymer science (2010). He holds honorary degrees (Dr. h.c.) of the Technical University of Cluj-Napoca, Romania (1997) and the Adam Mickiewicz University, Poznan, Poland (1998). Since 2011 he has been an Honorary Member of the Society of Polymer Science, Japan.

After a distinguished career, Professor Spiess is retiring from the Max Planck Institute. On behalf of all the authors in this symposium volume, we thank him for his splendid work over the years and wish him health, happiness, and continued vigor in years to come.

H. N. Cheng
Tetsuo Asakura
Alan D. English

Downloaded by 89.163.35.42 on June 19, 2012 | http://pubs.acs.org
Publication Date (Web): October 14, 2011 | doi: 10.1021/bk-2011-1077.pr002

Chapter 1

Innovative NMR Strategies for Complex Macromolecules

H. N. Cheng,*,[1] Tetsuo Asakura,[2] and Alan D. English[3]

[1]Southern Regional Research Center, USDA Agricultural Research Service,
1100 Robert E. Lee Blvd., New Orleans, LA 70124, U.S.A.
[2]Department of Biotechnology, Tokyo University of Agriculture and
Technology, 2-24-16 Nakacho, Koganei, Tokyo 184-8588, Japan
[3]DuPont Central Research and Development Department,
Experimental Station, Wilmington, DE 19880, U.S.A.
***E-mail: hncheng100@gmail.com**

Downloaded by 89.163.35.42 on June 19, 2012 | http://pubs.acs.org
Publication Date (Web): October 14, 2011 | doi: 10.1021/bk-2011-1077.ch001

In recent years there has been an increasing research emphasis on complex macromolecular systems. These include polymers with precise control of structures, multicomponent systems with higher degrees of organization, polymers involved in micelles, interfaces, and confined environments, nanochemistry and nanostructures, biopolymers and bio-inspired chemistry, and application-driven polymer designs, such as fuel cells, batteries, and ionic conductors; sensors and information processors; drug delivery, biomedical devices, and imaging; stimulus-responsive polymers, gels, and networks with defined function and control. Successful NMR studies of these polymers require judicious applications of existing techniques and development of new or improved strategies and methodologies. In this article the polymer/NMR literature in 2007-2011 is reviewed in view of the recent trends in polymer research, with selected examples taken from the literature and from the chapters included in this book.

Introduction

Nuclear Magnetic Resonance (NMR) is a premiere technique for polymer studies (*1*–*5*). The literature in the NMR of polymers continues to grow. Since

1990 there have been 3815 articles classified under NMR and polymer science, and 3463 articles under NMR and material science in the ISI Web of Knowledge (*6*). A summary with selected topics is shown in Table 1.

Table 1. Subject analysis of literature search for the category of "NMR" since 1990 in the ISI World of Knowledge

topic	*record count*				*total*	*%*
	1990-1994	*1995-2000*	*2001-2006*	*2007-2011*[a]		
chemistry	8284	10290	9681	6999	35254	50.0
instrumentation	120	139	122	88	469	0.7
polymer science	1122	1242	1000	451	3815	5.4
material science	647	1047	911	858	3463	4.9
biochemistry	3802	3940	3388	2294	13424	19.0
biophysics	1112	1262	1122	720	4216	6.0
food science	180	261	341	294	1076	1.5
plant sci. + agriculture	356	464	457	377	1654	2.3
total	18060	21013	18462	12960	70495	89.8

[a] Coverage in 2011 up to July 1, 2011 only.

Downloaded by 89.163.35.42 on June 19, 2012 | http://pubs.acs.org
Publication Date (Web): October 14, 2011 | doi: 10.1021/bk-2011-1077.ch001

A survey of these articles indicates several recurring research themes. In addition to the utility of the wide array of NMR techniques to determine polymer structures and solve polymeric problems, many researchers are concentrating on increasingly complex macromolecular systems and on the development of new or improved NMR strategies and methodologies. These trends are partly stimulated by improved instrumentation, more sophisticated characterization techniques, innovative synthetic methods, and application-driven polymer designs. The complex macromolecular systems (*7*) include the following (not mutually exclusive) areas: 1) polymers with precise control of structures, 2) multicomponent systems with higher degrees of organization, including blends, composites, organic-inorganic hybrids, and supramolecular assemblies, 3) polymers involved in micelles, interfaces, and confined environments, 4) nanochemistry and nanostructures, 5) heterogeneous materials, such as emulsions, foams, and microporous materials, 6) biopolymers and bio-inspired chemistry, and 7) application-driven polymer designs, such as polymers for fuel cells, batteries, and ionic conductors; sensors and information processors; drug delivery and biomedical devices, stimulus-responsive polymers, gels, and networks with defined function and control.

It may be noted that this book provides an excellent collection of examples of these complex macromolecular systems, together with the corresponding NMR strategies and methodologies designed to study them. The purpose of this article is to survey the NMR/polymer literature in the past 4-5 years in view of the various research themes and polymer types and to highlight these developments with selected examples taken from the recent literature and from appropriate chapters of this book.

NMR Strategies and Methodologies

As macromolecular systems become more complex, NMR has been keeping up with both established and novel strategies and methodologies. Several review articles in the past 5 years provide good summaries of the latest developments. The articles by Spiess (*8*) on solid state NMR and by Rinaldi (*9*) on solution NMR in this book are especially outstanding. They are also helpful overviews for people who are relatively new to the field.

Other recent reviews of NMR of solid polymers include the articles by Chen and Kurosu (*10*) on semicrystalline polymers, Paasch and Brunner (*11*) on methods and applications that pertain to bioanalysis, Bockmann (*12*) on strategies for structure determination of proteins, and Spiess (*13*) on the combined use of solid state NMR and other complementary techniques. In addition, solid state NMR of inorganic polymers has been reviewed by Borisov et al. (*14*), and liquid crystals by Domenici (*15*). As for solution NMR of polymers, there have been several recent reviews, particularly for biomacromolecules, e.g., Felli and Brutscher (*16*) and Foster et al. (*17*) on recently developed NMR methodologies, Mittermaier and Kay (*18*) on biomacromolecular dynamics, Tate (*19*) on anisotropic nuclear spin interactions for the morphological analysis of proteins, Loria et al. (*20*) on characterization of enzyme motions by relaxation dispersion, Markwick et al. (*21*) on molecular dynamics simulations for the analysis of NMR data, and Bouvignies et al. (*22*) on the utility of residual dipolar couplings for studies of proteins in solution.

Many specific NMR techniques and methodologies have been reviewed in the appropriate chapters in this book and are described in the next section under different research themes. In the following paragraphs, brief summaries are given of selected techniques and methodologies that either have general utility or are not adequately covered in the next section.

An important technique is NMR imaging. Two recent reviews by Britton (*23*) and Villaraza et al. (*24*) have appeared. NMR imaging studies have been reported of penetration of water into mesoporous matrices (*25*) and hydrogels (*26*), and of styrene in polyethylene in supercritical CO_2 (*27*). In this book Peng et al. (*28*) have reported a new class of ^{19}F polymeric imaging agents, which provide high contrast because the body does not contain a significant concentration of fluorine to give a background signal. Therien-Aubin et al. (*29*) have employed NMR imaging to monitor the release process of pharmaceutical tablets, and Baianu and Prisecaru (*30*) to study the hydration of wheat grains.

Another fruitful area of research is the use of NMR for diffusion measurements. In his chapter Macdonald (*31*) gives a good introduction to the pulsed field gradient experiment used for diffusion studies. Pulsed field gradient results are reported by Macdonald (*31*), Hou et al. (*32*), and Jespersen et al. (*33*)

Downloaded by 89.163.35.42 on June 19, 2012 | http://pubs.acs.org
Publication Date (Web): October 14, 2011 | doi: 10.1021/bk-2011-1077.ch001

in this book. Two recent reviews, by Walderhaug et al. (*34*) and Cozzolino et al. (*35*), have also provided helpful complementary information, particularly on different types of applications.

^{129}Xe NMR can be employed to measure pore size and volume in porous materials. In his article, Yoshimizu (*36*) has studied the microvoids in several glassy polymers and correlated the results with excess free volume in the polymers. Other examples in the recent literature include analysis of porosity in membranes and oligopeptides (*37*) and microporous polymer networks (*38*).

Latex state NMR is reviewed by Kawahara (*39*); high resolution NMR spectra for elastomers have been obtained through Brownian motion of the latex dispersion. Similar results on a polymer slurry are reported by Thakur et al. (*40*), except that ^{1}H and magic angle spinning have been used.

The combination of rheology and NMR is a relatively newer development. A recent review has described the basics of rheo-NMR and some applications (*41*). The article by Bohme and Scheler (*42*) in this book examines the relaxation behavior of polymer melts under shear. In the literature a paper has also reported shear deformation of polymer melts observed via ^{1}H NMR (*43*). The combination of electrophoresis and NMR is discussed by Hou et al. (*32*). Electrophoretic NMR has also been reported recently by Scheler (*44*, *45*).

A technique that has gained a fair amount of traction is field cycling (*46*). This is a good way to determine the frequency or field dependence of NMR relaxation times. There are two means of achieving field cycling. A sample can be moved mechanically to positions with different magnetic flux densities (called "sample shuttling"). Alternatively, special electronics and magnet design permit fast switching of magnetic fields between 0 and 0.5 T in a few milliseconds (commonly known as "fast field cycling"). Some examples in the recent literature include segmental reorientation dynamics in polybutadiene melts (*47*), dynamics of polybutadiene in nanoscopic confinement (*48*), diffusion (*49*) and dipole-dipole interactions (*50*) in polymer melts. More examples have been given in a recent NMR field cycling relaxometry conference in Turin (*51*).

In solution NMR, of course, the utility of multidimensional NMR is well known (*9*, *52*). Isotopic labeling can also be helpful, especially in biomacromolecules (*17*, *53*). Several techniques have been developed to speed up the time needed for NMR (*54–57*). An area that continues to show vitality is the combination of chromatography and NMR. In the literature several publications couple NMR with size exclusion chromatography (*58–60*), and NMR with liquid chromatography at critical conditions (*59*, *61–63*). A high temperature 10-mm cryoprobe has been found to give higher sensitivity for ^{13}C NMR of polyolefins at sample temperatures of 120-135°C (*64*). Other recent interesting articles include stop-flow NMR for fast reactions (*65*), high pressure NMR (*66*), and use of specially designed labeled chain transfer agents to facilitate analysis of polymers made with controlled free radical polymerization (*67*). Additional new developments are given in the reviews by Spiess (*8*) and Rinaldi (*9*).

Downloaded by 89.163.35.42 on June 19, 2012 | http://pubs.acs.org
Publication Date (Web): October 14, 2011 | doi: 10.1021/bk-2011-1077.ch001

Downloaded by 89.163.35.42 on June 19, 2012 | http://pubs.acs.org
Publication Date (Web): October 14, 2011 | doi: 10.1021/bk-2011-1077.ch001

Major Research Themes

Polymers in Solution and in the Melt

It is well known that solution NMR can be utilized to identify unknown polymers, to determine homopolymer tacticity, copolymer composition and sequence, branching and chain ends, and irregularities such as head-to-head and tail-to-tail structures (*2–5*). The number of papers published on microstructures of polymers is large and beyond the scope of this article. The tutorial chapter by Rinaldi (*9*) gives an excellent review of advanced solution techniques being used. In their article (*52*), Rinaldi et al. have applied advanced 2D solution methods to analyze fluoropolymers. Another way to carry out NMR analysis of microstructure is via statistical models; this is reviewed by Cheng and Miri (*68*). Acrylic latex copolymers have been studied by solution NMR and statistical analysis by Beshah and Antrim (*69*). Solution NMR has also been employed to study poly(ε-L-lysine) by Maeda et al. (*70*), carbohydrate-protein interactions by Baianu and Prisecaru (*30*), and silk fibroin in fluorinated solvents by Nagano et al. (*71*).

A different way to study polymer microstructure and dynamics is to observe them in the melt (*72–75*). In this book Hunt et al. (*76*) have included a molten inclusion compound in their studies. Hubner et al. (*77*) have implemented the analyses of molten polyolefins in an industrial R&D setting where sample high throughput is important. Bohme and Scheler (*42*) have studied molten polymers with rheo-NMR. Ries et al. (*78*) have investigated the NMR rescaling approximation and its application to the relaxation of polymer melts above their glass transition temperatures. The relaxation in polymer melts has also been reported by Chavez et al. in the literature (*79*).

Structure-Dynamics-Properties Relationships

This is a common theme that runs throughout many of the solid state NMR articles in this book. As Spiess pointed out in his review (*8*), NMR provides unique information on the local conformation of polymers as well as time scale and amplitude of rotational motions in bulk. In particular, the articles by Jespersen et al. (*33*), Asakawa et al. (*80*), Litvinov (*81*), Miyoshi (*82*), and Magusin et al. (*83*) illustrate the valuable information obtainable in different polymeric systems. In addition, the papers by White et al. (*84*) and Pramoda et al. (*85*) describe experimental methods that can be applied to probe the dynamics of polymer mixing and polymer-filler interactions, respectively.

There is a large body of literature on solid state NMR studies of the dynamics of different polymers. For example, Saalwachter (*86*) has provided a review of ^{1}H multiple quantum method for studies of chain dynamics and structural constraints in polymeric soft materials. The dynamics of elastomers has been studied by the multiple quantum method and computer simulations (*87*), time-domain NMR (*88*), and maximum entropy method (*89*).

In NMR Spectroscopy of Polymers: Innovative Strategies for Complex Macromolecules; Cheng, H., et al.;
ACS Symposium Series; American Chemical Society: Washington, DC, 2011.

Downloaded by 89.163.35.42 on June 19, 2012 | http://pubs.acs.org
Publication Date (Web): October 14, 2011 | doi: 10.1021/bk-2011-1077.ch001

Polymers with Precise Control of Structure

Recent advances in polymer synthesis permit more precise and well defined polymeric molecules to be prepared. NMR has been used for polymer characterization in many of these cases. Recent examples of polymers analyzed by NMR include those made with single-site catalysts (*90–93*), "precision" polymers made via acyclic diene metathesis/hydrogenation by Wagener et al. (*94–96*), polymers made with controlled or living polymerizations (*67*, *97–99*), and polymers made via enzyme catalysis (*100–102*). In this book Alam et al. (*103*) have studied poly(ethylene-co-acrylic acid) with precise distribution of pendant carboxylic acid group along the polymer backbone and its ionomer with partial neutralization of the carboxylic acid with Zn^{2+} and Li^{+}; the results have been compared with ionomers with random spacing of the carboxylic groups. Another example is the computer-assisted approach devised by Cheng and Miri (*68*) for the analysis of NMR spectral intensities for polyolefins made with single-site metallocene catalysts.

Blends, Composites, and Nanostructures

This category includes polyblends, composites, organic-inorganic hybrids, supramolecular assemblies, and nanostructures. Reviews have been reported of solid state NMR studies of multicomponent organic/inorganic materials by Geppi et al. (*104*), polymer/clay composites by Olejniczak et al. (*105*), and polymeric and supramolecular systems by Brown (*106*). Reviews have also been given by White and Wachowicz (*107*) on polyblends, and by White et al. (*84*) on experimental methods that have been developed to probe the dynamics and thermodynamics of mixing in amorphous blends. Examples of polyblends are given in this book by White et al. (*84*) and Asano (*108*). Yoshimizu (*36*) studied the free volume in a polymer blend with ^{129}Xe NMR. Examples of polyimide-graphite composites are shown by Pramoda et al. (*85*), and organic-inorganic hybrids by Jespersen et al. (*33*).

Nanochemistry is a hot topic today. Silica nanoparticles are reported in the papers by Jespersen et al. (*33*) and Thakur et al. (*40*). The former paper uses NMR relaxation and PFG to measure the dynamics of this nanoscale ionic material prepared from silica nanoparticles. The latter paper employs magic angle spinning (MAS) to identify organic moieties adsorbed or covalently bonded to silica nanoparticles. Asano (*108*) has studied poly(vinyl isobutyl ether)/poly(ε-L-lysine)/saponite-clay nanocomposites. In the recent literature, NMR studies have also been reported for several blends (*109*, *110*), nanocomposites (*111–114*), polyelectrolyte complexes (*115*), and polyelectrolyte multilayer systems (*116*).

Micelles, Interfaces, and Confined Environments

There is continued interest in polymer micelles, interfaces, and polymers in confined environments. A review has appeared on NMR studies of block copolymer micelles (*117*). In this book, Macdonald (*31*) introduces bicelles as

In NMR Spectroscopy of Polymers: Innovative Strategies for Complex Macromolecules; Cheng, H., et al.;
ACS Symposium Series; American Chemical Society: Washington, DC, 2011.

membrane mimetics and confinement media. He has studied the diffusion of poly(ethylene glycol) confined in bicelles, using the pulsed field gradient (PFG) NMR method. Hunt et al. (*76*) have observed the conformation and motions of a hydrocarbon model compound in α-cyclodextrin using chemical shifts and T_1 information. In the literature, NMR has been used to study interfacial polymers in carbon nanotube-based nanocomposites (*118*), surfactant layers in polymer-clay nanocomposites (*119*), and polymer adsorbed on silica (*120*) and inorganic membrane (*121*). Studies have also been made of ultra-thin polymer films on a substrate; NMR measurements permit information to be obtained on polymer dynamics (*122*) and polymer mixing (*123*) under confined environments.

Downloaded by 89.163.35.42 on June 19, 2012 | http://pubs.acs.org
Publication Date (Web): October 14, 2011 | doi: 10.1021/bk-2011-1077.ch001

Biopolymers, Biochemistry, and Bio-inspired Chemistry

As shown in Table 1, NMR has been utilized extensively for biochemistry and biophysics, and (to less extents) plant science, food, and agriculture. The natural polymers (such as proteins, polysaccharides, lipids, and related materials found in nature) have been increasingly exploited for industrial and health related applications. In this book microbial poly(ε-L-lysine) has been studied by Maeda et al. (*70*), and blends and composites of poly(ε-L-lysine) by Asano (*108*). Nagano et al. (*71*) have determined the structure of silk fibroin by NMR, and designed and produced recombinant proteins from transgenic silkworm for use as biomaterials. Nakazawa et al. (*124*) have conducted a detailed multinuclear NMR study of amyloid β-peptide (the major component of plaques in Alzheimer's disease), particularly its interaction with lipid bilayers and ganglioside. In the literature, there are many papers on biomimetic or bio-inspired polymers, most of which used NMR for characterization (e.g., refs. (*125–127*)). Several articles have reported the encapsulation of proteins with reverse micelles (*128–130*) and chaperonin (*131*) as a method to enhance biophysical studies of proteins.

NMR is a frequent tool to study polysaccharides. Recent articles on NMR of polysaccharides include chondroitin sulfate (*132*), alginate (*133*), chitin and chitosan (*134*), tamarind seed polysaccharide and larch arabinogalactan (*135*). In this book, Baianu and Prisecaru (*30*) have applied solution NMR and T_2 to investigate interactions of wheat gliadin with sucrose in aqueous solutions and wheat gluten-glucomannan interactions in hydrated gels.

Application-Driven Polymer Designs

Several topics are of current interest, such as polymers for energy applications, for sensors and information processors, for drug delivery and biomedical devices, and stimulus-responsive polymers, gels and networks with defined function and control. For fuel cells, batteries, and ionic transducers, ionomers are often involved. The benefit of NMR to characterize ionomers is illustrated by Hou et al. (*32*) (using ^{2}H and PFG NMR) and Alam et al.. (*103*) (using 1D and 2D ^{1}H MAS). In the literature, reviews have been reported of the different NMR techniques used for polyelectrolytes (*34*) and polymer electrolyte membranes for fuel cells (*136–138*). NMR has been employed to study polyelectrolyte systems containing poly(ethylene oxide) and alumina (*139*).

An example of π-conjugated polymers for possible electronic devices is given by Asakawa et al. (*80*). A solution NMR study of a conjugated polymer has been reported by Rahman et al. (*140*). A solid state NMR study of the structures of materials involved in organic light-emitting diodes has been reported by Kaji (*141*).

A study of coordination number of borate in poly(vinyl alcohol) gel is reported by Yamada (*142*), using 1D and 2D ^{11}B NMR. The utility of NMR to study phase transitions in aqueous polymer solutions and gels has been reviewed by Spevacek (*143*). $T_{1\rho}$ measurements have been engaged to investigate the phase structures of poly(vinylidene fluoride) gels (*144*). A novel NMR approach for the studies of gelation in flexible polymer systems has been devised by Saalwachter et al. (*145*).

Downloaded by 89.163.35.42 on June 19, 2012 | http://pubs.acs.org
Publication Date (Web): October 14, 2011 | doi: 10.1021/bk-2011-1077.ch001

Acknowledgments

Thanks are due to Suhad Wojkowski at USDA Southern Regional Research Center for her help on the literature search.

Mention of trade names or commercial products in this publication is solely for the purpose of providing specific information and does not imply recommendation or endorsement by the U.S. Department of Agriculture. USDA is an equal opportunity provider and employer. DuPont Company and Tokyo University of Agriculture and Technology are also equal opportunity providers and employers.

References

1. Recent books in the past 10 years include refs. 2-5. Recent reviews are cited in the appropriate sections in this article.
2. Cheng, H. N.; English, A. D. (Eds.) *NMR spectroscopy of polymers in solution and in the solid state*; ACS Symposium Series No. 834; American Chemical Society: Washington, DC, 2002.
3. Mirau, P. A. *A practical guide to understanding the NMR of polymers*; Wiley: Hoboken, NJ, 2004.
4. Kitayama, T.; Hatada, K. *NMR spectroscopy of polymers*; Springer: New York, 2004.
5. Cheng, H. N. *Structural studies of polymers by solution NMR*; RAPRA Review Reports, Vol. 11, Number 5, Rapra: Shewsbury, UK, 2001.
6. Thomson Reuters, New York, NY. http://www.webofknowledge.com/.
7. *Interdisciplinary Globally-Leading Polymer Science & Engineering*, NSF Workshop, 2007. www.nsf.gov/mps/dmr/NSF_Polymer_Workshop.pdf.
8. Spiess, H. W. ACS Symposium Series 1077; American Chemical Society: Washington, DC, 2011; Chapter 2.
9. Rinaldi, P. L. ACS Symposium Series 1077; American Chemical Society: Washington, DC, 2011; Chapter 3.
10. Chen, Q; Kurosu, H. *Ann. Rep. NMR Spectrosc.* **2007**, *61*, 61247–61281.
11. Paasch, S; Brunner, E. *Anal. Bioanal. Chem.* **2010**, *398*, 2351–2362.
12. Bockmann, A. *Magn. Reson. Chem.* **2007**, *45*, S24–S31.

Downloaded by 89.163.35.42 on June 19, 2012 | http://pubs.acs.org
Publication Date (Web): October 14, 2011 | doi: 10.1021/bk-2011-1077.ch001

13. Spiess, H. W. *Macromolecules* **2010**, *43*, 5479–5491.
14. Borisov, A. S.; Hazendonk, P.; Hayes, P. G. *J. Inorg. Organomet. Polym. Mater.* **2010**, *20*, 183–212.
15. Domenici, V. *Pure Appl. Chem.* **2011**, *83* (Special Issue), 67–94.
16. Felli, I. C.; Brutscher, B. *ChemPhysChem* **2009**, *10* (9-10), 1356–1368.
17. Foster, M. P.; McElroy, C. A.; Amero, C. D. *Biochemistry* **2007**, *46* (2), 331–340.
18. Mittermaier, A. K.; Kay, L. E. *Trends Biochem. Sci.* **2009**, *4* (12), 601–611.
19. Tate, S. I. *Anal. Sci.* **2008**, *24* (1), 39–50.
20. Loria, J. P.; Berlow, R. B.; Watt, E. D. *Acct. Chem. Res.* **2008**, *41* (2), 214–221.
21. Markwick, P. R. L.; Malliavin, T.; Nilges, M. *PLOS Comput. Biol.* **2008**, *4* (9): Art No. e1000168 2008
22. Bouvignies, G.; Markwick, P. R. L.; Blackledge, M. *ChemPhysChem* **2007**, *8*, 1901–1909.
23. Britton, M. M. *Chem. Soc. Rev.* **2010**, *39*, 4036–4043.
24. Villaraza, A. J. L.; Bumb, A.; Brechbiel, M. W. *Chem. Rev.* **2010**, *110*, 2921–2959.
25. Le Feunteun, S.; Diat, O.; Guillermo, A.; Poulesquen, A.; Podor, R. *Magn. Reson. Imaging* **2011**, *29* (3), 443–455.
26. Zainuddin; Strounina, E. V.; Hill, D. J. T.; Whittaker, A. K. *Polym. Int.* **2010**, *59* (11), (Special Issue), 1520-1525.
27. Thurecht, K. J.; Hill, D.; Whittaker, A. K. *Macromol. Chem. Phys.* **2006**, *207*, 1539–1545.
28. Peng, H.; Thurecht, K.; Hsu, S.; Blakey, I.; Squires, O.; Kurniawan, N.; Rose, S.; Whittaker, A. K. ACS Symposium Series 1077; American Chemical Society: Washington, DC, 2011; Chapter 28.
29. Therien-Aubin, H.; Wang, Y. J.; Zhu, X. X. ACS Symposium Series 1077; American Chemical Society: Washington, DC, 2011; Chapter 27.
30. Baianu, I. C.; Prisecaru, V. ACS Symposium Series 1077; American Chemical Society: Washington, DC, 2011; Chapter 20.
31. Macdonald, P. M. ACS Symposium Series 1077; American Chemical Society: Washington, DC, 2011; Chapter 14.
32. Hou, J.; Li, J.; Wilmsmeyer, K. G.; Zhang, Z.; Madsen, L. A. ACS Symposium Series 1077; American Chemical Society: Washington, DC, 2011; Chapter 15.
33. Jespersen, M. L.; Mirau, P. A.; von Meerwall, E.; Vaia, R. A.; Rodriguez, R.; Fernandes, N. J.; Giannelis, E. P. ACS Symposium Series 1077; American Chemical Society: Washington, DC, 2011; Chapter 9.
34. Walderhaug, H.; Soderman, O.; Topgaard, D. *Prog. Nucl. Magn. Reson. Spectrosc.* **2010**, *56* (4), 406–425.
35. Cozzolino, S.; Sanna, M. G.; Valentini, M. *Magnetic Resonance Chem.* **2008**, *46*, S16–S23.
36. Yoshimizu, H. ACS Symposium Series 1077; American Chemical Society: Washington, DC, 2011; Chapter 31.
37. Ripmeester, J.; Moudrakovski, I.; Soldatov, D.; Pawsey, S.; Anedda, R. *ACS Polym. Prepr.* **2008**, *49* (1), 653–654.

38. Weber, J.; Schmidt, J.; Thomas, A.; Bohlmann, W. *Langmuir* **2010**, *26* (19), 15650–15656.
39. Kawahara, S. ACS Symposium Series 1077; American Chemical Society: Washington, DC, 2011; Chapter 29.
40. Thakur, K. A. M.; McCormick, M.; Thompson, W. L.; Cao, C.; Schultz, W. J. ACS Symposium Series 1077; American Chemical Society: Washington, DC, 2011; Chapter 30.
41. Callaghan, P. T. *Rheol. Acta* **2008**, *47* (3), 243–255.
42. Böhme, U.; Scheler, U. ACS Symposium Series 1077; American Chemical Society: Washington, DC, 2011; Chapter 26.
43. Douglass, B. S.; Cormier, R. J.; Callaghan, P. T. *Phys. Rev. E* **2007**, *75*(4), Article No. 041802.
44. Bohme, U.; Scheler, U. *ACS Polym. Prepr.* **2008**, *49* (1), 670–671.
45. Scheler, U. *Curr. Opin. Colloid Interface Sci.* **2009**, *14* (3), 212–215.
46. For example, Kimmich, R.; Anoardo, E. *Prog. NMR Spectrosc.* 2004, *44*, 257-320.
47. Herrmann, A.; Novikov, V. N.; Rossler, E. A. *Macromolecules* **2009**, *42* (6), 2063–2068.
48. Hofmann, M.; Herrmann, A.; Ok, S.; Franz, C.; Kruk, D.; Saalwachter, K.; Steinhart, M.; Rossler, E. A. *Macromolecules* **2011**, *44* (11), 4017–4021.
49. Kehr, M.; Fatkullin, N.; Kimmich, R. *J. Chem. Phys.* **2007**, *126* (9), Article No. 094903.
50. Fatkullin, N.; Gubaidullin, A.; Stapf, S. *J. Chem. Phys.* **2010**, *132* (9), Article No. 094903.
51. *Seventh Conference on Field Cycling NMR Relaxometry*, June 2−4, 2011. www.ffcrelax.com/ffcrelax/home.php.
52. Rinaldi, P. L.; Baiagern, S.; Fox, P.; Howell, J. L.; Li, L.; Li, X.; Lyons, D. F.; McCord, E. F.; Sahoo, S. K.; Twum, E. B.; Wyzgoski, F. J. ACS Symposium Series 1077; American Chemical Society: Washington, DC, 2011; Chapter 21.
53. Liu, D. S.; Xu, R.; Cowburn, D. *Methods Enzymol.* **2009**, *162*, 151–175.
54. Schanda, P. *Prog. in NMR Spectrosc.* **2009**, *55* (3), 238–265.
55. Vitorge, B.; Bodenhausen, G.; Pelupessy, P. *J. Magnetic Resonance* **2010**, *207*, 149–152.
56. Springer F.; Steidle G.; Martirosian P.; Syha R.; Claussen C. D.; Schick F. *Invest. Radiol.* 2011, online, PMID: 21577126.
57. Deschamps, M.; Campbell, I. D. *J. Magnetic Resonance* **2006**, *178*, 206–211.
58. Cudaj, M.; Guthausen, G.; Hofe, T.; Wilhelm, M. *Macromol. Rapid Comm.* **2011**, *32* (8), 665–670.
59. Hiller, W.; Sinha, P.; Hehn, M.; Pasch, H.; Hofe, T. *Macromolecules* **2011**, *44* (6), 1311–1318.
60. Pasch, H.; Heinz, L. C.; Macko, T.; Hiller, W. *Pure Appl. Chem.* **2008**, *80* (8), 1747–1762.
61. Sinha, P.; Hiller, W.; Pasch, H. *J. Separation Sci.* 2010, *33*(22), Special Issue, 3494-3500.
62. Hiller, W.; Sinha, P.; Pasch, H. *Macromol. Chem. Phys.* **2009**, *210*, 605–613.

Downloaded by 89.163.35.42 on June 19, 2012 | http://pubs.acs.org
Publication Date (Web): October 14, 2011 | doi: 10.1021/bk-2011-1077.ch001

63. Hiller, W.; Sinha, P.; Pasch, H. *Macromol. Chem. Phys.* **2007**, *208* (18), 1965–1978.
64. Zhou, Z; Kummerle, R.; Stevens, J. C.; Redwine, D.; He, Y. Y.; Qiu, X. H.; Cong, R. J.; Klosin, J.; Montanez, N.; Roof, G. *J. Magnetic Resonance* **2009**, *200* (2), 328–333.
65. Christianson, M. D.; Landis, C. R. *Concept Magn. Reson., Part A* **2007**, *30A* (4), 165–183.
66. Whittaker, A.; Blakey, I.; Thurecht, K.; Squires, O., ; Varcoe, K. *ACS Polym. Prepr.* **2008**, *49* (1), 678–679.
67. Pach, M.; Zehm, D.; Lange, M.; Dambowsky, I.; Weiss, J.; Laschewsky, A. *J. Amer. Chem. Soc.* **2010**, *132* (25), 8757–8765.
68. Cheng, H. N.; Miri, M. J. ACS Symposium Series 1077; American Chemical Society: Washington, DC, 2011; Chapter 22.
69. Beshah, K.; Antrim, R. F. ACS Symposium Series 1077; American Chemical Society: Washington, DC, 2011; Chapter 23.
70. Maeda, S.; Sasaki, C.; Kunimoto, K.-K. ACS Symposium Series 1077; American Chemical Society: Washington, DC, 2011; Chapter 19.
71. Nagano, A.; Suzuki, Y.; Nakazawa, Y.; Gerig, J. T.; Asakura, T. ACS Symposium Series 1077; American Chemical Society: Washington, DC, 2011; Chapter 17.
72. Schaler, K.; Ostas, E.; Schroter, K.; Thurn-Albrecht, T.; Binder, W. H.; Saalwachter, K. *Macromolecules* **2011**, *44* (8), 2743–2754.
73. Castignolles, P.; Graf, R.; Parkinson, M.; Wilhelm, M.; Gaborieau, M. *Polymer* **2009**, *50* (11), 2373–2383.
74. Hu, W.; Hagihara, H.; Miyoshi, T. *Macromolecules* **2007**, *40*, 3505–3509.
75. Kimmich, R.; Fatkullin, N. *ACS Polym. Prepr.* **2008**, *49* (1), 689–690.
76. Hunt, M. A.; Villar-Rodil, S.; Gomez-Fatou, M. A.; Shin, I. D.; Schilling, F. C.; Tonelli, A. E. ACS Symposium Series 1077; American Chemical Society: Washington, DC, 2011; Chapter 16.
77. Hubner, G.; Fonseca, I.; Parkinson, M. ACS Symposium Series 1077; American Chemical Society: Washington, DC, 2011; Chapter 24.
78. Ries, M. E.; Bansal, A.; Brereton, M. G. ACS Symposium Series 1077; American Chemical Society: Washington, DC, 2011; Chapter 25.
79. Chavez, F. V.; Saalwachter, K. *Macromolecules* **2011**, *44* (6), 1560–1569.
80. Asakawa, N.; Inoue, Y.; Yamamoto, T.; Shimizu, R.; Tansho, M.; Yazawa, K. ACS Symposium Series 1077; American Chemical Society: Washington, DC, 2011; Chapter 10.
81. Litvinov, V. M. ACS Symposium Series 1077; American Chemical Society: Washington, DC, 2011; Chapter 11.
82. Miyoshi, T. ACS Symposium Series 1077; American Chemical Society: Washington, DC, 2011; Chapter 12.
83. Magusin, P. C. M. M.; Orza, R. A.; Litvinov, V. M.; van Duin, M.; Saalwächter, K. ACS Symposium Series 1077; American Chemical Society: Washington, DC, 2011; Chapter 13.
84. White, J. L.; Wachowicz, M.; Gill, L.; Damron, J.; Wolak-Dinsmore, J. ACS Symposium Series 1077; American Chemical Society: Washington, DC, 2011; Chapter 4.

Downloaded by 89.163.35.42 on June 19, 2012 | http://pubs.acs.org
Publication Date (Web): October 14, 2011 | doi: 10.1021/bk-2011-1077.ch001

85. Pramoda, K. P.; Mya, K. Y.; Lin, T. T.; Wang, J.; He, C. B. ACS Symposium Series 1077; American Chemical Society: Washington, DC, 2011; Chapter 6.
86. Saalwachter, K. *Prog. NMR Spectrosc.* **2007**, *51* (1), 1–35.
87. Saalwachter, K; Sommer, J. U. *Macromol. Rapid Comm.* **2007**, *28*, 1455–1465.
88. Chavez, F. V.; Saalwachter, K. *Macromolecules* **2011**, *44* (6), 1549–1559.
89. Aguilera-Mercado, B. M.; Cohen, C.; Escobedo, F. A. *Macromolecules* **2009**, *42* (22), 8889–8898.
90. Galland, G. B.; Da Silva, L. F.; Nicolini, A. *J. Polym. Sci., Part A: Polym.Chem.* **2005**, *43*, 4744–4753.
91. Landis, C. R.; Christianson, M. D. *Proc. Nat. Acad. Sci. U.S.A.* **2006**, *103*, 15349–15354.
92. Cherian, A. E.; Lobkovsky, E. B.; Coates, G. W. *Macromolecules* **2005**, *38*, 6259–6268.
93. Dijkstra, P. J.; Du, H.; Feijen, J. *Polym. Chem.* **2011**, *2*, 520–527.
94. Boz, E.; Nemeth, A. J.; Wagener, K. B.; Jeon, K.; Smith, R.; Nazirov, F.; Bockstaller, M. R.; Alamo, R. G. *Macromolecules* **2008**, *41*, 1647–1653.
95. Boz, E.; Nemeth, A. J.; Alamo, R. G.; Wagener, K. B. *Adv. Synth. Catal.* **2007**, *349*, 137–141.
96. Boz, E.; Nemeth, A. J.; Ghiviriga, I.; Jeon, K.; Alamo, R. G.; Wagener, K. B. *Macromolecules* **2007**, *40*, 6545–6551.
97. Moad, G.; Chong, Y. K.; Mulder, R.; Rizzardo, E.; Thang, S. H. *ACS Symposium Series* **2009**, *1024*, 3–18.
98. Klumperman, B.; McLeary, J. B.; van den Dungen, E. T. A.; Pound, G. *Macromol. Symp.* **2007**, *248*, 141–149.
99. Brar, A. S.; Saini, T. *J. Polymer Sci., Part A: Polym. Chem.* **2006**, *44*, 2955–2971.
100. Puskas, J. E.; Seo, K. S.; Sen, M. Y. *Eur. Polym. J.* **2011**, *47*, 524–534.
101. Padovani, M.; Hilker, I.; Duxbury, C. J.; Heise, A. *Macromolecules* **2008**, *41*, 2439–2444.
102. Mita, N.; Rawaki, S.; Uyama, H.; Kobayashi, S. *Bull. Chem. Soc. Jpn.* **2004**, *77*, 1523–1527.
103. Alam, T. M.; Jenkins, J. E.; Seitz, M. E.; Buitrago, C. F.; Winey, K. I.; Opper, K.; Baughman, T. W.; Wagner, K. B. ACS Symposium Series 1077; American Chemical Society: Washington, DC, 2011; Chapter 7.
104. Geppi, M; Borsacchi, S; Mollica, G; Veracini, C. A. *Appl. Spectrosc. Rev.* **2009**, *44* (1), 1–89.
105. Olejniczak, S; Kazmierski, S; Pallathadka, PK; Potrzebowski, M. *Polimery* **2007**, *52*, 713–721.
106. Brown, S. P. *Macromol. Rapid Comm.* **2009**, *30* (9-10), 688–716.
107. White, J. L.; Wachowicz, M. *Ann. Rep. NMR Spectrosc.* **2008**, *64*, 189–209.
108. Asano, A. ACS Symposium Series 1077; American Chemical Society: Washington, DC, 2011; Chapter 5.
109. Ediger, M.; Zhao, J. *ACS Polym. Prepr.* **2008**, *49* (1), 706.
110. White, J.; Wachowicz, M.; Gill, L. *ACS Polym. Prepr.* **2008**, *49* (1), 711.

Downloaded by 89.163.35.42 on June 19, 2012 | http://pubs.acs.org
Publication Date (Web): October 14, 2011 | doi: 10.1021/bk-2011-1077.ch001

111. Foston, M.; Leisen, J.; Beckham, H. *ACS Polym. Prepr.* **2008**, *49* (1), 665–666.

112. Papon, A.; Saalwachter, K.; Schaler, K.; Guy, L.; Lequeux, F.; Montes, H. *Macromolecules* **2011**, *44* (4), 913–922.

113. Liu, H. H.; Chaudhary, D.; Yusa, S.; Tade, M. O. *Carbohydrate Polym.* **2011**, *83* (4), 1591–1597.

114. Powers, D. S.; Vaia, R. A.; Koerner, H.; Serres, J.; Mirau, P. A. *Macromolecules* **2008**, *41*, 4290–4295.

115. Causemann, S.; Schonhoff, M.; Eckert, H. *Phys. Chem. Chem. Phys.* **2011**, *13* (19), 8967–8976.

116. Fortier-McGill, B.; Reven, L. *Macromolecules* **2009**, *42*, 247–254.

117. Walderhaug, H.; Soderman, O. *Curr. Opin. Colloid Interface Sci.* **2009**, *14* (3), 171–177.

118. Mirau, P.; Lyons, M.; Powers, D.; Koerner, H.; Vaia, R. *ACS Polym. Prepr.* **2008**, *49* (1), 704–705.

119. Jeschke, G. *ACS Polym. Prepr.* **2008**, *49* (1), 737–738.

120. Metin, B.; Blum, F. D. *J. Chem. Phys.* **2006**, *125*, 054707–9.

121. Okuom, M. O.; Metin, B.; Blum, F. D. *Langmuir* **2008**, *24*, 2539–2544.

122. Stapf, S.; Ayalur-Karunakaran, S.; Blumich, B. *ACS Polym. Prepr.* **2008**, *49* (1), 661–662.

123. VanderHart, D.; Prabhu, V.; Lavery, K.; Lin, E.; Dennis, C. *ACS Polym. Prepr.* **2008**, *49* (1), 739–740.

124. Nakazawa, Y.; Suzuki, Y.; Saito, H.; Asakura, T. ACS Symposium Series 1077; American Chemical Society: Washington, DC, 2011; Chapter 18.

125. Laschewsky, A.; Marsat, J.-N.; Skrabania, S.; von Berlepsch, H.; Bottcher, C. *Macromol. Chem. Phys.* **2010**, *211*, 215–221.

126. Guan, Z. *Polym. Int.l* **2007**, *56*, 467–473.

127. Kentgens, A. P. M.; van Eck, E.; Gowda, C.; Nolte, R.; Cornelissen, J.; Rowan, A. E. *ACS Polym. Prepr.* **2008**, *49* (1), 693–694.

128. Flynn, P. F.; Simorellis, A. K.; Van Horn, W. D. *Ann. Rep. NMR Spectrosc.* **2007**, *62*, 179–219.

129. Nucci, N. V.; Marques, B. S.; Bedard, S.; Dogan, J.; Gledhill, J. M.; Moorman, V. R.; Peterson, R. W.; Valentine, K. G.; Wang, A. L.; Wand, A. J. *J. Biomol. NMR* 2011, online, PMID: 21748265.

130. Peterson, R. W.; Pometun, M. S.; Shi, Z.; Wand, A. J. *Protein Sci.* **2005**, *14*, 2919–2921.

131. Tanaka, S.; Kawata, Y.; Otting, G.; Dixon, N. E.; Matsuzaki, K.; Hoshino, M. *Biochim. Biophys. Acta* **2010**, *1804*, 866–871.

132. Huckerby, T.; Lauder, R. *ACS Polym. Prepr.* **2008**, *49* (1), 702–703.

133. Bernin, D.; Goudappel, G. J.; van Ruijven, M.; Altskar, A.; Strom, A.; Rudemo, M.; Hermansson, A. M.; Nyden, M. *Soft Matter* **2011**, *7* (12), 5711–5716.

134. Kasaai, M. R. *Carbohydrate Polym.* **2010**, *79*, 801–810.

135. Uccello-Barretta, G.; Nazzi, S.; Balzano, F.; Sanso, M. *Int. J. Pharm.* **2011**, *406* (1-2), 78–83.

136. Suarez, S; Greenbaum, S. *Chem. Rec.* **2010**, *10* (6), 377–393.

137. Ye, G.; Goward, G. *ACS Polym. Prepr.* **2008**, *49* (1), 714–715.

Downloaded by 89.163.35.42 on June 19, 2012 | http://pubs.acs.org
Publication Date (Web): October 14, 2011 | doi: 10.1021/bk-2011-1077.ch001

138. Bai, Z.; Shumaker, J. A.; Houtz, M. D.; Mirau, P. A.; Dang, T. D. *Polymer* **2009**, *50*, 1463–1469.
139. Ekanayake, P; Dissanayake, M. A. K. L. *J. Solid State Electrochem.* **2009**, *13* (12), 1825–1829.
140. Rahman, M. H.; Chen, H. L.; Chen, S. A.; Chu, P. P. J. *J. Chin. Chem. Soc.* **2010**, *57* (3) Special Issue, 490-495.
141. Kaji, H. *ACS Polym. Prepr.* **2008**, *49* (1), 736.
142. Yamada, K. ACS Symposium Series 1077; American Chemical Society: Washington, DC, 2011; Chapter 8.
143. Spevacek, J. *Curr. Opin. Colloid Interface Sci.* **2009**, *14* (3), 184–191.
144. Hubbard, H.; Ward, I. *ACS Polym. Prepr.* **2008**, *49* (1), 709–710.
145. Saalwachter, K.; Gottlieb, M.; Liu, R. G.; Oppermann, W. *Macromolecules* **2007**, *40* (5), 1555–1561.

Downloaded by 89.163.35.42 on June 19, 2012 | http://pubs.acs.org
Publication Date (Web): October 14, 2011 | doi: 10.1021/bk-2011-1077.ch001

Downloaded by STANFORD UNIV GREEN LIBR on June 19, 2012 | http://pubs.acs.org
Publication Date (Web): October 14, 2011 | doi: 10.1021/bk-2011-1077.ch002

Chapter 2

Overview of NMR of Bulk Polymers

Hans Wolfgang Spiess*

**Max-Planck-Institute for Polymer Research, P. O. Box 3148,
D-55021 Mainz, Germany
*E-mail: spiess@mpip-mainz.mpg.de**

The favorable properties of bulk polymers are primarily due to their molecular structure but also heavily depend on their organization in bulk and their molecular dynamics. Solid state NMR techniques provide unique information on the local conformation of macromolecules as well as time scale and amplitude of rotational motions in bulk. Moreover, translational motions of the chains on mesoscopic length scales can be elucidated by advanced NMR techniques. In order to obtain this information, homo- and heteronuclear dipole-dipole couplings, involving ^{1}H and heteronuclei such as ^{13}C and ^{15}N, isotropic as well as anisotropic chemical shifts, in particular of ^{13}C, and quadrupole coupling of ^{2}H are employed. Experiments can be performed on static samples and under magic angle spinning (MAS). Double quantum and multidimensional NMR techniques are especially informative. The methods will be briefly introduced and illustrated by recent experimental examples from different fields of polymer science, such as chain microstructure, defects and dynamics, chain packing in polymers for plastic electronics, proton motion in proton conductors and packing of macrocycles in nanotubes.

Introduction

Precise knowledge of structure and dynamics of macromolecules of well-defined architectures is key when tailoring them for specific functions. For instance, such diverse technological challenges as efficient fuel cells, photonic sensors and devices or gene delivery systems all require transport of electrones, holes, protons or other ions. Likewise, the properties of conventional polymers

In NMR Spectroscopy of Polymers: Innovative Strategies for Complex Macromolecules; Cheng, H., et al.;
ACS Symposium Series; American Chemical Society: Washington, DC, 2011.

can be substantially improved by controlling, e.g., their microstructure and the processing conditions. Properties of macromolecular systems critically depend on the arrangement of the building blocks relative to each other and their mobility on different length- and time scales. Therefore, success in polymer science requires development of characterization techniques that are able to provide information on these aspects. Scattering of light, X-rays and neutrons, the various forms of microscopy as well as mechanical and dielectric relaxation are well-established in polymer science (*1*).

NMR spectroscopy, on the other hand, is often considered just as an analytical tool, monitoring the various synthetic steps, which eventually lead to the new polymers or supramolecular systems. High-resolution NMR in one- and two dimensions (*2*) provides a number of important parameters, which are specific to macromolecules. Examples include stereochemical configuration, geometrical isomerism, and regioregularity.

More recently, the rapid development of solid state NMR has substantially broadened the application of NMR to polymers (*3*). In particular, molecular and collective motions can be characterized in unprecedented detail. The new NMR methods use concepts well established in X-ray and neutron scattering, yet on much longer timescales. These techniques provide structural information with atomic resolution even for systems that lack crystalline order in the traditional sense (*4*). Moreover, solid state NMR concepts can also be applied to partially mobile systems such as liquid crystals. Further examples are highly viscous materials such as polymer melts in the vicinity of the glass transition or elastomers.

This chapter is intended as an overview rather than a detailed description of the different possibilities NMR provides. It is based on previous reviews of the author (*1*, *4*); for further details we refer to recent reviews of the subject (*5*–*7*).

NMR Background

NMR spectroscopy is remarkably versatile and, therefore, is widely applied in many fields of science, in particular physics, chemistry, biology, materials science, and in medicine. This form of spectroscopy combines a number of features that makes it an almost ideal tool: NMR is non-destructive, sample preparation is easy, the possibility to observe different nuclei and isotopes provides extreme structural selectivity. Moreover, dynamic features can be studied over many decades of characteristic times, from picoseconds to minutes, and length scales from interatomic distances in the 100 pm range up to a meter or so in NMR imaging.

The wealth of information accessible by NMR spectroscopy results from the fact that a variety of interactions of the nuclear spins with their surroundings can be exploited. The structure of polymers and other supramolecular systems can be elucidated along several routes. The chemical shift provides the basis of site selectivity. Geometric parameters such as internuclear distances as well as dihedral angles are encoded in the dipole-dipole and the J-coupling. Of the great variety of molecular motions possible in polymers, rotations have the most pronounced effects on NMR spectra and relaxation parameters, because the spin interactions

Downloaded by STANFORD UNIV GREEN LIBR on June 19, 2012 | http://pubs.acs.org
Publication Date (Web): October 14, 2011 | doi: 10.1021/bk-2011-1077.ch002

In NMR Spectroscopy of Polymers: Innovative Strategies for Complex Macromolecules; Cheng, H., et al.;
ACS Symposium Series; American Chemical Society: Washington, DC, 2011.

are angular-dependent. But conformational dynamics and translational motions can be tackled as well. The anisotropic nuclear spin interactions also offer a means to probe the alignment of residues in partially ordered systems such as drawn fibers or oriented liquid crystals. Therefore, a brief outline of these anisotropic spin interactions is given here.

Anisotropic Spin Interactions

As noted above, the information that can be extracted from solid state NMR spectra is encoded via spin interactions such as the chemical shift, the quadrupolar interaction, homo- and heteronuclear dipolar interactions, as well as J-couplings. For convenience, these couplings and the information that is accessible through them are listed in Table 1.

A common characteristic of the relevant spin interactions is that they are anisotropic and can be described by second-rank tensors. The resulting orientation-dependent NMR frequency for each of the interactions is alike and of the following form:

$$\omega(\alpha,\beta) - \omega_L = \omega_{iso} + \frac{\delta}{2}(3\cos^2\beta - 1 - \eta\sin^2\beta\cos 2\alpha)\,. \qquad (1)$$

Here ω_L is the Larmor frequency, ω_{iso} is the isotropic chemical shift and the other terms reflect the deviations due to angular-dependent contributions. The strength of the anisotropic interaction is specified by δ, and η ($0 \leq \eta \leq 1$) is the asymmetry parameter which describes the deviation from axial symmetry. The polar angles α, β, relate the orientation of the principal axes system of the interaction tensor with the external magnetic field.

The most important interaction with respect to chemical information is the *chemical shift*. It results from the shielding of the magnetic field at the position of the nucleus by the electrons. Major advances have been achieved recently in quantum chemical calculations of this parameter in bulk at different levels of precision and calculational cost (*8*). The NMR frequency is thus shifted by an isotropic contribution ω_{iso} and by angular dependent terms. Assuming an equal probability for all directions the powder average can be calculated and a broad powder spectrum is obtained, which reflects the chemical-shift anisotropy. For the case of an axially symmetric chemical-shift tensor, η is zero and the angular-dependent term simplifies to $\delta\,(3\cos^2\beta - 1)/2$. Usually the chemical shift in polymers spans about 10 ppm for ^{1}H, 200 ppm for ^{13}C, and 400 ppm for ^{15}N nuclei, see Fig. 1.

Downloaded by STANFORD UNIV GREEN LIBR on June 19, 2012 | http://pubs.acs.org
Publication Date (Web): October 14, 2011 | doi: 10.1021/bk-2011-1077.ch002

Downloaded by STANFORD UNIV GREEN LIBR on June 19, 2012 | http://pubs.acs.org
Publication Date (Web): October 14, 2011 | doi: 10.1021/bk-2011-1077.ch002

Table 1. Interactions of nuclei in NMR providing access to structure and dynamics of polymers.

Interaction	*Electronic Structure*	*Geometry*	*Nuclei*	*Structure*	*Dynamics*
Chemical shift	Yes	Intrinsic and orientation	^{1}H, ^{13}C, ^{15}N, ^{19}F, ^{29}Si, ^{31}P	Conformation, through-space proximities	Conformational transitions, rotational motions
Dipole-dipole coupling	No	Internuclear distance and orientation	^{1}H, ^{13}C, ^{15}N, ^{19}F, ^{29}Si, ^{31}P	Through-space distances	Translational and rotational motions
J-Coupling	Yes	Intrinsic, internuclear distance and orientation	^{1}H, ^{13}C, ^{15}N, ^{19}F, ^{29}Si, ^{31}P	Conformation and intergroup binding	Conformational transitions, rotational motions
Quadrupole Coupling	Yes	Intrinsic and orientation	^{2}H, ^{14}N, ^{17}O, ^{23}Na, ^{27}Al	Electronic environment, chemical bonding	Rotational motions

For abundant nuclei with spin ½, the spectrum is often dominated by heteronuclear or homonuclear *dipole-dipole interactions*, i.e. the interactions between the magnetic moments of two neighboring spins. In this case there is no isotropic contribution and the interaction is axially symmetric, η=0, so that Eq. (1) simplifies correspondingly. For a two-spin system the interaction Hamiltonian, which defines the frequencies, reads

$$H_D = \left(\frac{\mu_0}{4\pi}\right)\frac{\gamma_1\gamma_2\hbar}{r_{12}^3}\left(\frac{3\cos^2\theta - 1}{2}\right)(3I_{1z}I_{2z} - \vec{I}_1\vec{I}_2) \qquad (2)$$

where r_{12} is the magnitude of the vector connecting the two spins, θ is the angle of this vector to the magnetic field. The I_i are spin operators and the γ_i (i=1,2) are the magnetogyric ratios of the spins. That is, the strength of the resulting line splitting depends strongly on the distance between the two spins, so that distance information can be extracted from such spectra. Homonuclear interaction (equivalent spins with $\gamma_1 = \gamma_2 = \gamma$ and heteronuclear interaction (non-equivalent spins with $\gamma_1 \neq \gamma_2$) have to be distinguished. In the latter case, the flip-flop term which is part of the product $\boldsymbol{I_1}\ \boldsymbol{I_2}$ in Eq. (2) can be neglected. For a powder sample one has again to take into account all angles β and thus obtains the so-called Pake spectrum with a considerable anisotropic line-broadening of up to 50 kHz for homonuclear ^{1}H-^{1}H and up to 25 kHz for heteronuclear ^{13}C-^{1}H or ^{15}N-^{1}H dipolar interaction. Since the dipole-dipole coupling is a through-space interaction, however, we have in principle to evaluate the sum over all possible

Downloaded by STANFORD UNIV GREEN LIBR on June 19, 2012 | http://pubs.acs.org
Publication Date (Web): October 14, 2011 | doi: 10.1021/bk-2011-1077.ch002

pair interactions. This and the presence of molecular motions lead to considerable complications. Therefore, in practice a relatively structureless line-shape rather than a Pake spectrum but is observed.

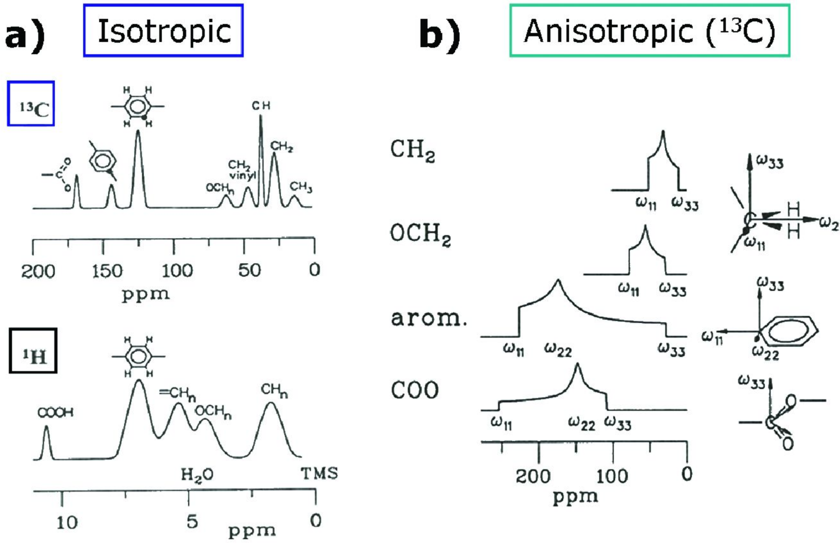

Figure 1. Chemical shift ranges of organic compounds. (3)

In the case of a deuterated sample (^{2}H, spin I=1), the spectra are usually dominated by the *quadrupole interaction*, that is, the coupling of the nuclear quadrupole moment with the electric field gradient of the C-^{2}H bond. For deuterons in C-^{2}H bonds this can lead to a splitting of about 250 kHz. As in the case of the dipole-dipole interaction, a Pake spectrum is obtained for a powder sample. The z-principal axis of the quadrupolar interaction is oriented along the bond axis. This makes deuteron NMR particularly useful for studies of segmental orientations and molecular dynamics (reorientation), where the line shapes strongly depend on the orientation of an oriented sample such as a polymer fiber, or on the geometry of rotational motions generating averaged spectra, Fig. 2a. It is important to note that in the fast limit where the averaging is complete, the anisotropic interaction can still be described by an expression as Eq. (1) with averaged coupling parameters and angles. Even if an interaction is axially symmetric in the static case, it can become asymmetric upon motional averaging (*3*) and Fig. 2a.

In sufficiently mobile (i.e. liquid-like) systems where the residues undergo rapid *isotropic* thermal motions, the anisotropy is typically averaged out completely, leaving only the isotropic contributions.

Downloaded by STANFORD UNIV GREEN LIBR on June 19, 2012 | http://pubs.acs.org
Publication Date (Web): October 14, 2011 | doi: 10.1021/bk-2011-1077.ch002

Manipulation of Spin Interactions

The rich information content of solid state spectra makes them difficult to handle, in particular if more than one of the interactions introduced above has to be taken into account. NMR methodology, however, provides the possibility to decouple and recouple spin interactions nearly as desired (see (*9*) for a comprehensive introduction). Moreover, the different sources of information can be separated and correlated using the two-dimensional techniques discussed below.

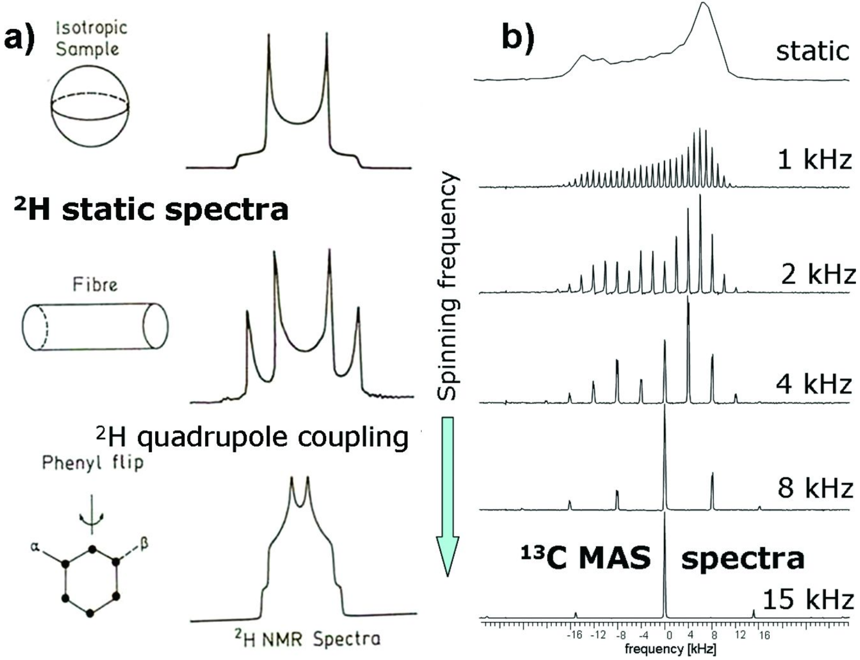

Figure 2. Solid state NMR spectra; a) static, b) under MAS.

The most prominent example of a technique for decoupling or line-narrowing is magic-angle spinning (MAS). Here, the angular dependent part of the interactions is modulated by rapidly spinning the sample around an axis inclined at an angle Θ to the magnetic field. If the spinning axis is chosen along the so-called magic-angle Θm=54.7°, the relevant scaling factor $(3\cos^2\Theta-1)/2$ becomes zero and the anisotropic part of the interaction vanishes, see Fig. 1. Today, fast MAS with rotation frequencies reaching 70 kHz is possible. This paves the way for easy access to high spectral resolution in solid state ^{1}H-NMR and, more important, largely simplifies the dipolar coupled network that prevents the dipole-dipole coupling between ^{1}H from being used for specific structural investigations in non-spinning samples.

In addition, it is possible to manipulate the spin interactions by pulse techniques (*5–9*) These act on the spin operators in the corresponding Hamiltonians rather than on the geometric part. Depending on the applied pulse sequence, a given spin interaction can be switched on and off in order to discriminate the different contributions to the desired information. For instance, heteronuclear dipole-dipole couplings are averaged out by MAS, yet a simple train of 180^0 pulses properly synchronized with the rotor phase reintroduces the coupling for a well-defined period of time. This so-called Rotational-Echo Double-Resonance (REDOR) technique can be seen as the basis of many more sophisticated ways of reintroducing homo- and heteronuclear dipole-dipole as well as anisotropic chemical shift interactions under MAS. Pictorially speaking the mechanical rotation by MAS in real space is partially offset by counter rotations in spin space.

Magic angle spinning modulates the spin interactions periodically. This means it generates rotational echoes and data acquisition can be performed in two ways: First, if only the echo-height is monitored (rotor synchronized acquisition) a single line results in the spectrum for each resolved site and information about the anisotropic coupling is lost. Secondly, if the whole echo-train is monitored, a side band pattern results, which retains information about the anisotropic coupling, yet with spectral resolution of the different sites. This is important for precise structural elucidation, based on the dipole-dipole coupling as well as using this interaction to study molecular dynamics resulting in reduction of the coupling, Fig. 2b.

Downloaded by STANFORD UNIV GREEN LIBR on June 19, 2012 | http://pubs.acs.org
Publication Date (Web): October 14, 2011 | doi: 10.1021/bk-2011-1077.ch002

Double Quantum NMR

The basic concept for using the distance- and angular dependent dipole-dipole coupling for structural studies is described in extended reviews (*5*, *7*). In a two-dimensional experiment, double quantum coherence (DQ) is created, e.g. between two ^{1}H with like or different chemical shifts Fig. 3a. During excitation of the DQ coherence, the dipole-dipole coupling between the two spins, which is largely reduced by MAS, is recoupled by a suitable pulse sequence. In the evolution time of DQ coherence recoupling is turned off, such that the different residues can be distinguished by their different chemical shifts. In the subsequent reconversion to single quantum coherence needed for signal detection, recoupling is again applied. Thus, a 2D spectrum, as shown in Fig. 3b is recorded, in which information about internuclear distances is, first of all, encoded in the strength of the DQ peaks.

It should be appreciated that the technique is based on analyzing signals resulting from a *coherence* originating from two spatially separated nuclei. Thus the basic physics is *analogous* to coherent X-ray or neutron *scattering*, where the coherent superposition of scattered waves is exploited to deduce the distance between the scattering centers. In NMR, however, no translational symmetry is necessary to determine distances in the range of 0.5 nm. In fact, proximities of ^{1}H in the same or different moieties can be probed by DQ NMR by analyzing the intensities of a so-called rotor-synchronized spectrum, which can typically be recorded in about 10 min for 10 mg as-synthesized samples, without the need of isotopic labeling. If the dipole-dipole coupling needs to be determined more accurately, for more precise determination of internuclear distances or molecular dynamics, *see above*, DQ sideband spectra, as displayed in Fig. 3c are recorded. The measurement time is then considerably longer, typically overnight.

Downloaded by STANFORD UNIV GREEN LIBR on June 19, 2012 | http://pubs.acs.org
Publication Date (Web): October 14, 2011 | doi: 10.1021/bk-2011-1077.ch002

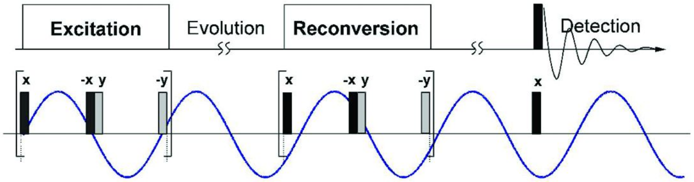

a) Pulse Sequence for Double Quantum NMR

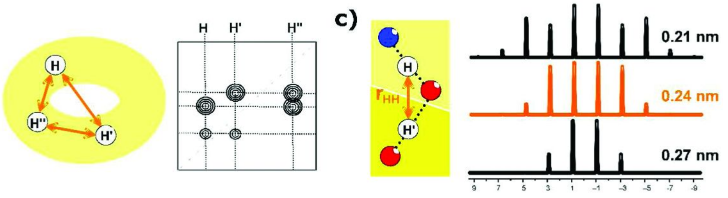

b) Double Quantum Spectra c) Sideband Patterns

Figure 3. Principle of double quantum NMR. a) pulse sequence; b) double quantum NMR spectra; c) sideband patterns.

Such DQ spectra can be recorded for both homonuclear ^{1}H-^{1}H, or heteronuclear ^{1}H-^{13}C, ^{1}H-^{15}N coherences, exploiting the much higher site selectivity of ^{13}C and ^{15}N chemical shifts. In the heteronuclear case polarization transfer and recoupling take advantage of the popular REDOR technique introduced above usually applied to isotopically labeled samples.

Two-Dimensional NMR Spectroscopy

Most of the advanced NMR techniques make use of two-dimensional (2D) spectroscopy, because of the superb increase of resolution and ease of information encoding. There is not enough space to explain these techniques in detail here, but comprehensive books are available (*3*, *10*) and only the basics are described here. In general, a 2D NMR experiment is divided in several time periods that follow each other. In order to record a 2D NMR spectrum, a two-dimensional data set is acquired as a function of two time variables t_1 and t_2 as shown schematically in Fig. 3a for the specific case of double quantum NMR. This is preceded by the so-called preparation period in which coherences are excited by a suitable pulse sequence, which in the simplest case is only one radio-frequency pulse. Unlike conventional (1D) NMR spectroscopy, the excited signal is not directly acquired, but is allowed to evolve in the so-called evolution period under influence of the relevant spin interactions. The evolution time t_1 is incremented in subsequent experiments and provides the first time dimension of the experiment. After the evolution period (and an optional mixing time), the remaining signal is directly detected in the detection period for each time increment thus generating a 2D data set. Two-dimensional Fourier transformation then gives the 2D spectrum. Optionally, a so-called mixing period of length t_m can be inserted between the evolution and detection periods. During t_m changes in the system can occur, for instance, by molecular motions, spin interactions, relaxation or by spin manipulation (for instance recoupling).

The different aspects of 2D NMR spectroscopy are reflected in the different variants that can be distinguished. One variant, *separation* spectroscopy, is used to separate different interactions by taking advantage of the spin manipulation techniques For instance, during the evolution period the spin manipulation can be made such that only the isotropic chemical shift is acquired while in the detection period the full spectrum is acquired. This leaves the anisotropy to be studied site-selectively.

Other 2D NMR techniques, so-called *correlation* techniques, aim at obtaining new information by correlating different interactions. For instance, the ^{13}C chemical shift anisotropy can be correlated with the heteronuclear dipolar powder pattern in order to obtain information on the relative orientation of the two tensors. Moreover, since no signal is detected during the evolution time, it can conveniently be used to provide the basis for recording a double quantum spectrum which correlates single and double quantum coherences. Considering the manifold of spin manipulation techniques there is a wealth of such 2D NMR techniques that can be derived for different purposes.

Finally, introducing a mixing time t_m, 2D *exchange* spectroscopy can be performed, Fig. 4. The most important application of such exchange techniques, with respect to polymer investigations, is the study of slow molecular dynamics. In these experiments, reorientations due to molecular dynamics are allowed to take place during the mixing time t_m and lead to characteristic off-diagonal patterns in the resulting 2D spectra. If the mixing time is increased in a series of 2D experiments, slow dynamics in the range of milliseconds to seconds can be investigated in detail. For instance, rotation of molecules by a well-defined angle leads to an elliptical exchange ridge for a powder. This can be viewed as a Lissajous-figure, from which the angle, by which the molecules have rotated, can directly be read off by a ruler. Measuring time can be dramatically reduced in a 1D variant under MAS. Likewise, exchange of magnetization can also occur by cross relaxation or mutual spin-flips, the latter being designated as *spin-diffusion*. It can be described by a diffusion equation and provides access to domain dimensions in phase separated systems.

Applications

The chapters in this book describe NMR studies of polymers or supramolecular structures in the solid-, the liquid crystalline-, or the liquid state. Often one or the other aspect of the techniques introduced above is used. Therefore, in this overview I have refrained from trying to describe a comprehensive set of NMR applications in polymer science. Instead, I have just included a few recent examples of our own work.

Downloaded by STANFORD UNIV GREEN LIBR on June 19, 2012 | http://pubs.acs.org
Publication Date (Web): October 14, 2011 | doi: 10.1021/bk-2011-1077.ch002

Downloaded by STANFORD UNIV GREEN LIBR on June 19, 2012 | http://pubs.acs.org
Publication Date (Web): October 14, 2011 | doi: 10.1021/bk-2011-1077.ch002

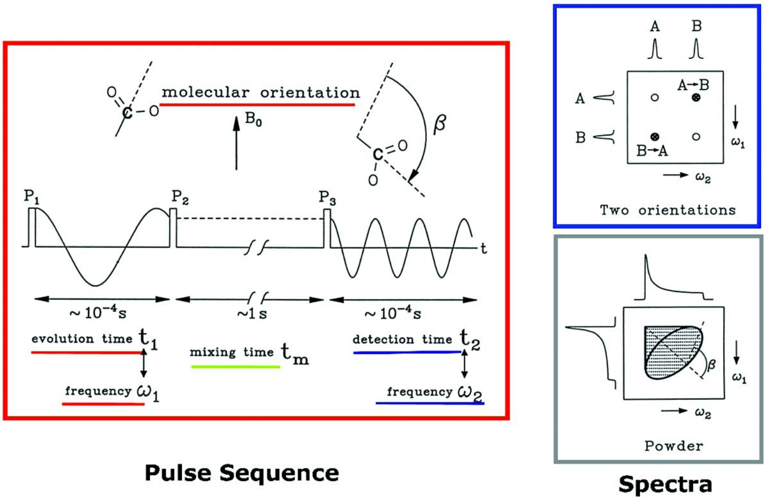

Figure 4. Principles of 2D exchange NMR for studying molecular motions.

Chain Microstructure, Defects, and Dynamics

The macroscopic properties of polyolefins strongly depend on the chain microstructure. In recent years, new single site catalysts have enabled much greater synthetic control over the polydispersity, type of branch, and branch content. In polyethylene, the physical properties of both the solid and the melt can be tuned by the presence of branches of various lengths in the polymer backbone. Short-chain branches (SCB) can be introduced by copolymerization of ethylene with short alkenes, or by isomerisation reactions during ethylene homopolymerization Such branches form structural defects during crystallization and thus strongly affect crystallization rates, ultimate crystallinity, and other bulk mechanical properties. Similarly, long-chain branches (LCB) are formed by macromonomer incorporation during polymerization. With these branches typically being longer than the entanglement molecular weight their presence strongly affects the processability of the bulk polymer. Long-chain branching is known to influence the zero-shear viscosity even at concentrations of 2 LCB per 100 000 CH_2 groups. Thus, it is very important to quantify the degree of chain branching and $_{13}$C NMR in solution seems to be the method of choice as the chemical shifts of branch points as well as adjacent carbon positions can be distinguished from the backbone resonances (*2*).

However, when applied to polyethylene a number of problems arise. The most important being the low solubility of polyethylene, even at high temperatures. The low concentration of ^{13}C nuclei results in low NMR signals requiring extended measurement times, especially for the quantification of very low levels of branching. In specific cases up to two million transients had to be acquired at high field in order to determine branch contents of 3–8 branches per 100 000 CH_2. Another inherent limitation of solution-state NMR is the lack of access to crosslinked and other non-soluble fractions of polyethylene. Solid state type NMR, under magic-angle spinning (MAS), on the other hand, can be used to overcome these limitations, despite the substantial loss of spectral resolution as compared to solution NMR. Under optimal conditions time savings of about two orders of magnitude are achieved, allowing quantification of 7-9 branches in 100 000 CH_2 groups within 13 h (*11*), see Fig. 5a.

In commercial polymer samples the irregular distribution of the branching sites along the main chain results in uncertainty of the branching influence on morphology, chain dynamics, and other physical properties. Here polyethylene samples with regularly spaced methyl branches obtained by Acyclic Diene METathesis (ADMET) polycondensation (*12*) provide much more specific information. By deuteration of the methyl branches, the molecular dynamics of the defect site can be studied selectively via ^2H NMR, whereas molecular reorientations of the polymer chain between the branching sites can be monitored separately via ^{13}C chemical shift anisotropy. Combining these results with studies of local conformations, a twist motion was identified, which is centered at the branching sites for a spacing of more than twenty CH_2 units between subsequent branching points. In methyl branched PE samples with shorter spacing, e.g. 14 CH_2 units between subsequent methyl branches, a collective dynamic process emerges from this twist motion, which ultimately leads to the formation of a rotator phase as indicated in Fig. 5b. Thus, localized and collective mobility induced by the defects can clearly be distinguished. The superb spectral resolution of a 850 MHz solid state NMR spectrometer was essential for obtaining these results.

Dynamics in Polymeric Proton Conductors

The growing necessity for clean energy sources to substitute fossil energy has created high demands for batteries and fuel cells. Therefore, various approaches have been proposed aiming at developing new classes of proton conducting membranes for high temperature applications (*13*). One promising approach to the development of such a material is to combine the functions of the protogenic group and the proton solvent in a single molecule. Such molecules must be amphoteric in the sense that they behave as both a proton donor (acid) and proton acceptor (base), and they must form dynamical hydrogen bond networks. The first leads to the formation of a high concentration of intrinsic protonic defects as a result of self-dissociation, and the latter may promote a high mobility of these protonic charge carriers (excess and deficient protons). The mobility of intrinsic defects is generally higher than that of extrinsic defects, which may be introduced by acid or basic doping disturbing the local symmetry of the hydrogen bond network.

Typical amphoteric liquids include phosphonic acid and diverse heterocycles such as imidazole, pyrazole, benzimidazole and triazole. In the liquid state, they all show relatively high proton conductivities with significant contributions from structure diffusion, i.e. the motion of protonic defects (excess or deficient protons) via intermolecular proton transfer, coupled to hydrogen bond breaking and forming processes. A promising approach to eliminate the liquid electrolyte is to attach the protic groups of the liquid electrolyte to the backbone of the polymer,

Downloaded by STANFORD UNIV GREEN LIBR on June 19, 2012 | http://pubs.acs.org
Publication Date (Web): October 14, 2011 | doi: 10.1021/bk-2011-1077.ch002

such that only chemical decomposition would result in a loss of ion carriers, a prominent example being poly (vinyl phosphonic acid). From ^{1}H, ^{2}H, ^{13}C, and ^{31}P NMR combined with computer simulation, detailed information on the proton mobility, water content, and the unwanted condensation of the phosphonic acid groups can be obtained. The protons are highly mobile, but on the same time scale no mobility associated with reorientation of the phosphonic acid groups or the polymer backbone is observed. The ^{1}H chemical shifts of P-OH protons provide evidence for the presence of a complex hydrogen bond network, see Fig. 6, which allows for proton transport via a Grotthus-type mechanism along a given chain as well as between adjacent chains. The MD simulations further show that proton vacancies can be trapped in the anhydride defect produced by the condensation. More important, as shown in Fig. 6, the highest intrinsic proton mobility with essentially isotropic geometry arises in systems like poly(vinyl phosphonic acids), where the hydrogen bonded network is highly *disordered*, characteristic of a hopping mechanism for proton conductivity (*14*).

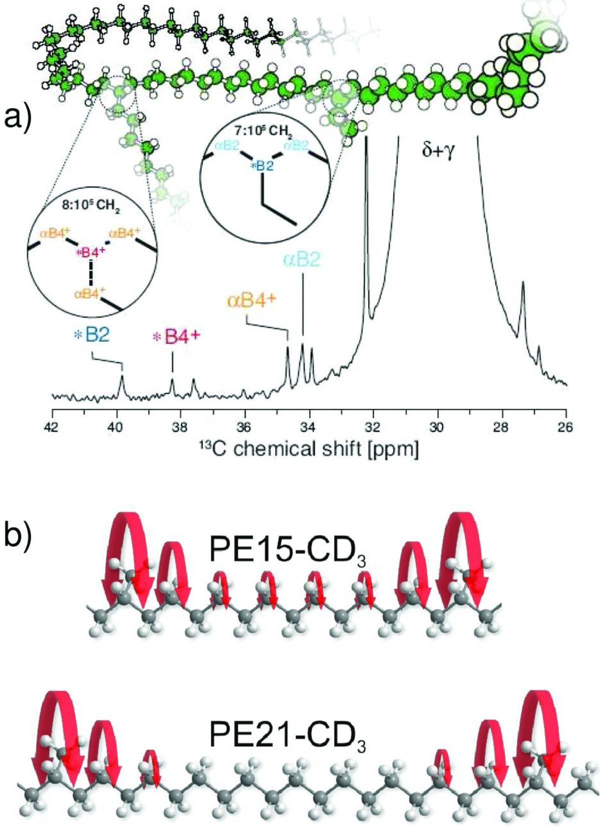

Figure 5. a) Quantification of low branch content in optimized melt state ^{13}C-NMR under MA. b) Local and Collective Motions in precise polyethylene with CD_3 Branches spaced every 15th and every 21st CH2 group.

Downloaded by STANFORD UNIV GREEN LIBR on June 19, 2012 | http://pubs.acs.org
Publication Date (Web): October 14, 2011 | doi: 10.1021/bk-2011-1077.ch002

Downloaded by STANFORD UNIV GREEN LIBR on June 19, 2012 | http://pubs.acs.org
Publication Date (Web): October 14, 2011 | doi: 10.1021/bk-2011-1077.ch002

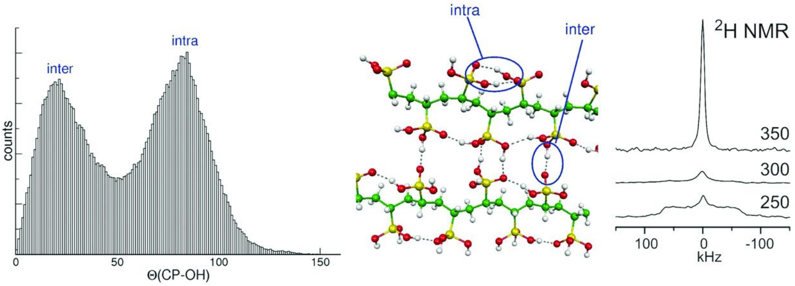

Figure 6. Left: Distribution of the CP-OH angle within a given phosphonic acid group of poly(vinyl phosphonic acid) PVPA, predicted from first-principles molecular dynamics simulations. Right: Experimental ^{2}H NMR lineshapes as a function of temperature, illustrating motional narrowing due to the hydrogen bond dynamics, exhibiting an effectively isotropic motion.

Hydrogen Bonding and Side Chain Conformation in Rigid-Rod Copolymers

In recent years the interest in polymer science has shifted considerably to include liquid crystals (*15*) and supramolecular structures (*16*). As a recent example, let us consider rod-coil copolymers such as oligo(p-benzamide)-poly(ethylene glycol) (OPBA-PEG) copolymers with an oligomeric rod and flexible PEG chains. They aggregate on a nanometer length scale, which is important for many applications such as organic photovoltaics. However, this aggregation behavior and the driving forces such as hydrogen bonding and π-π interactions, as well as the role of the side groups, are not yet fully understood. These non-covalent interactions can be studied by advanced solid state NMR, combined with X-ray diffraction (XRD), differential scanning calorimetry (DSC), and polarization optical microscopy (POM) (*17*). As shown in Fig. 7, longer OPBAs form layered ß-sheet like aggregates stabilized by amide hydrogen bonds, similar to polyamides with flexible side groups attached to the repeat units rather than the end groups (*18*). These aggregates are remarkably stable and apparently represent an equilibrium structure in both unsubstituted OPBAs and OPBA-PEG rod coil copolymers. The binding of the PEG also introduces a liquid-crystalline phase and the local structural order is improved in the copolymer, if the sample is preorganized in that phase. Thus, by combining different methods of structural investigation a model of local aggregation and packing in both the liquid-crystalline and the solid state could be developed.

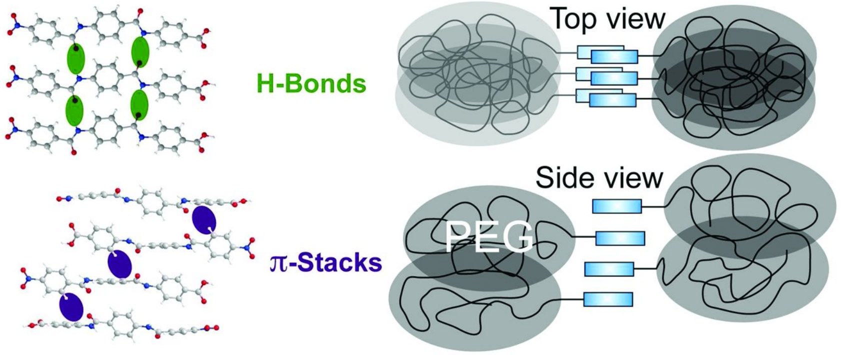

Figure 7. Scheme packing of rod-coil copolymers. The rigid rods are held together by intermolecular hydrogen bonds and the space between the stacks is filled by the PEG side chains adopting a Gaussian coil-like conformation.

Packing in Polymers with Ultrahigh Charge Carrier Mobility for Field-Effect Transistors

Applications in plastic electronics like flexible displays or smart tags call for organic semiconductors that can be easily processed into thin films and show field-effect transistor (FET) charge carrier mobilities exceeding 0.1 cm^2/Vs. To this end a copolymer consisting of an alternating arrangement of cyclopentadithiophene (CDT) as a donor and benzothiadiazole (BTZ) as an acceptor unit has recently been examined (*19*), Fig. 8. The planar arrangement of the conjugated backbone ensures a close π-stacking which is required for efficient inter-molecular charge carrier transport. Moreover, it was assumed that the close packing of the polymer chains might originate from assisting donor-acceptor interactions. Indeed, for the optimum molar mass, charge carrier motilities up to 3.3 cm^2/Vs were achieved.

For the first time such a macromolecular system was recently examined by solid state nuclear magnetic resonance (NMR) to provide a molecular scale picture of the packing, Fig. 8. The ^1H 2D DQ NMR spectra clearly reveal the relevant packing contacts, confirming the expected π-π stacking for the polymer backbone. The packing of the donor and the acceptor groups, however, was found to be more delicate. Donor-acceptor groups are π-π stacked in a lamellar fashion and these groups are ordered in an alternating way as shown in Figure 8d. Thereby, the acceptor groups in one layer are located on top of the acceptor groups in adjacent layers, however, not always in the exact same position, leading to a heterogeneous packing. This model derived from NMR is consistent with the findings of X-ray scattering. It also allows for optimal packing of the side chains that in the case of long and bulky alkyl chains (C_{16}) should be advantageous in order to avoid steric clash. Conclusively, solid state NMR does not reveal a donor-acceptor overlap within 0.4 nm. Thus, donor-acceptor interaction between the neighboring CDT and BTZ groups located a adjacent chains apparently contributes little, if any to the observed improvement in charge carrier mobility. NMR rather shows the complexity of this remarkable CDT-BTZ copolymer system. This implies that the enhanced packing order resulting in improved thin film crystallinity with

Downloaded by STANFORD UNIV GREEN LIBR on June 19, 2012 | http://pubs.acs.org
Publication Date (Web): October 14, 2011 | doi: 10.1021/bk-2011-1077.ch002

increasing M_n results primarily from π-stacking interactions of the planar extended conjugated backbones. (*19*).

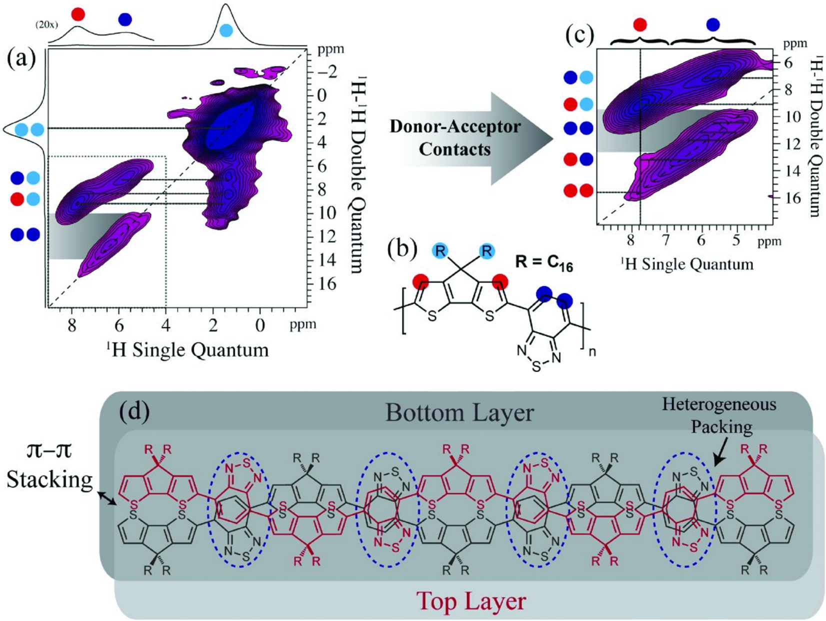

Figure 8. Local packing and organization of the donor-acceptor groups in a CDT-PTZ copolymer. (a) 2D contour plot of the ^1H-^1H DQ NMR spectrum. (b) Color scheme used for assignments. (c) Expansion of the backbone region showing the contacts between donor and acceptor groups. (d) Schematic drawing illustrating the local packing of donor-acceptor groups in two neighboring CDT-BTZ copolymer chain.

Downloaded by STANFORD UNIV GREEN LIBR on June 19, 2012 | http://pubs.acs.org
Publication Date (Web): October 14, 2011 | doi: 10.1021/bk-2011-1077.ch002

Empty Helical Nano-Channels from Low-Symmetry Macrocycles

Natural channel-forming structures are mandatory for connecting different compartments within a living organism. For instance, trans-membrane proteins function as ion-channels, transporters, or antibiotics. Recently, synthetic nanochannels as large as 1.3 nm in diameter in a tight tubular supramolecular superstructure have been generated from shape-persistent macrocycles. Solid state NMR combined with computer simulation was able to provide the details of the packing. The interplay of charge-transfer type interactions and steric effects due to the side chains were unraveled (*20*). Moreover, it was shown that the channels are empty and do not host solvent molecules or back-folded alkyl chains.

Fig. 9b displays the 2D NMR $^{13}C\{^1H\}$ hetero-nuclear correlation (HETCOR) spectrum for the macrocycle in the LC phase. In this spectrum a remarkable spectral resolution is observed, with ^{13}C line widths in the order of ~100 Hz for the core of the macrocycle, implying a very high degree of local order. From the 2D NMR spectrum in Fig. 9b the complete assignment given in Fig. 9a is obtained. It includes only one fourth of the total number of ^{13}C signals possible for the macrocycle indicating that the macrocycles are located in highly symmetric environments, which can be envisaged in a helical arrangement of the macrocycles in a column.

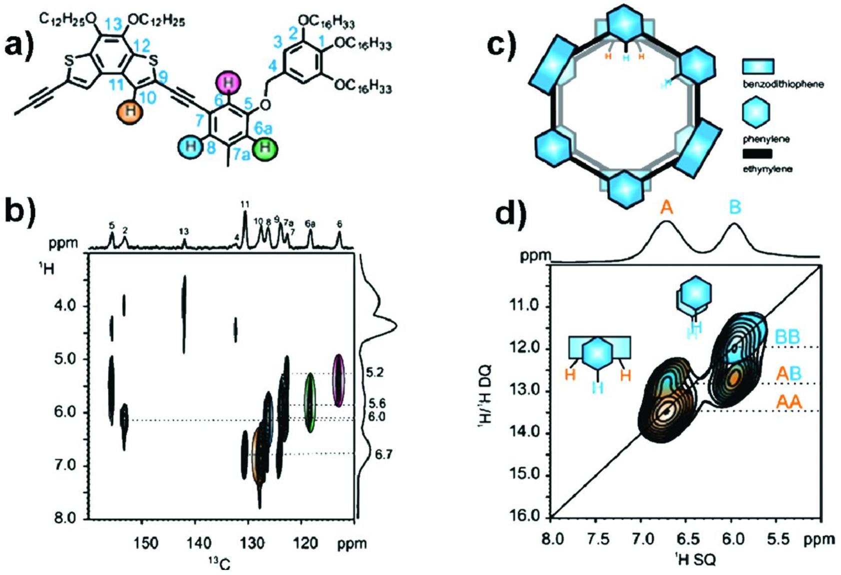

Figure 9. Spectroscopic fingerprints of the helical assembly in an empty nanochannel from solid state NMR. a) Assignment of the aromatic carbon and proton resonances. b) 2D $^{13}C\{^1H\}$ HETCOR NMR spectrum in the liquid crystalline phase. c)The helical packing with a pitch of 60° leads to intermolecular correlation peaks AB and BB observed in the ^1H-^1H DQ- NMR spectrum d).

The packing environment is also reflected in the ^1H chemical shifts for the core protons of the macrocycle. These differ substantially from each other (Fig. 9b), and also from the values found in solution, which is a clear indication of π-π stacking. The specific pitch angle can be determined by combining 2D NMR ^1H-^1H DQ-SQ (Double-Quantum Single-Quantum) correlation spectroscopy with *ab initio* calculations. This fixes the pitch angle between adjacent macrocycles to ~60° as illustrated by Fig. 9c and the inset of Fig. 9d. Within the stack every fourth molecule is eclipsed, i.e. related by translation, resulting in a helical arrangement (Fig. 10), as also observed in other self-assembled organic compounds. The pitch angle of 60° is supported by additional NMR experiments and *ab initio* calculations investigating the packing of pairs of macrocycles considering their energetics and the ^1H chemical shifts of neighboring macrocycles. These show excellent agreement between experimental and calculated values. Thus, the internal order of the channels can be molecularly controlled and adjusted for future applications in recognition, stabilization, or organization of nanoparticles.

Downloaded by STANFORD UNIV GREEN LIBR on June 19, 2012 | http://pubs.acs.org
Publication Date (Web): October 14, 2011 | doi: 10.1021/bk-2011-1077.ch002

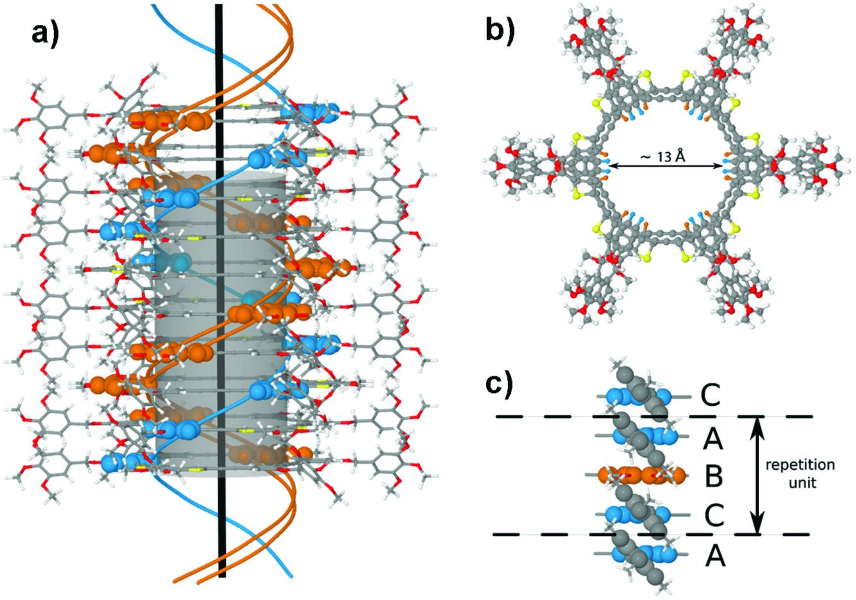

Figure 10. a) Overall view of the helical packing arrangement of the macrocyclic channel with a pitch angle of 60°. b) Top view of the macrocycle. c) Packing arrangement for the side chains illustrating the stabilizing effect of the outer phenylene groups.

Conclusions and Outlook

Advances in synthesizing, characterizing, as well as understanding macromolecular and supramolecular systems lead to an enormous variety and complexity in the field of polymer science (*21*). The traditional separation in terms of structure vs. dynamics, crystalline vs. amorphous, or experiment vs. theory is increasingly overcome (*1*). As far as characterization of such materials is concerned, no experimental or theoretical/simulation approach alone can provide full information. Instead, a combination of techniques is called for and conclusions should be backed by results provided by as many complementary methods as possible, see Table 2, where NMR and scattering are compared. Combining scattering or NMR spectroscopy with computer simulation is well established today in the study of structure and dynamics of biomacromolecules. The examples described here show the power of such an approach in the supramolecular field involving the combination of spectroscopy, scattering and computer simulation. Last, but not least, the development of NMR spectroscopy is far from complete. In particular, in order to meet the ever-increasing demands of miniaturization, the sensitivity of NMR spectroscopy has to be increased substantially and several approaches in response to that challenge are underway (*22*).

Downloaded by STANFORD UNIV GREEN LIBR on June 19, 2012 | http://pubs.acs.org
Publication Date (Web): October 14, 2011 | doi: 10.1021/bk-2011-1077.ch002

Downloaded by STANFORD UNIV GREEN LIBR on June 19, 2012 | http://pubs.acs.org
Publication Date (Web): October 14, 2011 | doi: 10.1021/bk-2011-1077.ch002

Table 2. Comparison of scattering and NMR techniques as well as the information provided about structure and dynamics of materials. WAXS: Wide Angle X-ray scattering; SAXS: Small Angle X-ray Scattering; SANS: Small Angle Neutron Scattering.

		SCATTERING		**NMR**	
		inco-herent	**coherent**	**single quantum**	**double quantum**
DYNAMICS					
	Molecular	n-quasi-elastic	n-quasi-elastic	2D-, 3D-, 4D-exchange, pulsed field gradient	MAS sidebands
	Collective		n-spin-echo	2D-exchange	decay of DQC
STRUCTURE					
	Molecular		WAXS, WANS	chemical shift, MAS-sidebands	2D pattern, MAS-sidebands
	Collective (packing)		X-ray pole figures, SAXS, SANS	DECODER chemical shift	2D signal pattern

Acknowledgments

This paper is based on and concludes my work at the Max Planck Institute for Polymer Research for more than 25 years. It has provided me with a unique scientific environment, in which new ideas and approaches prospered. It gives me great pleasure to thank my colleagues and co-workers for all their contributions.

References

1. Spiess, H. W. *Macromolecules* **2010**, *43*, 5479–5491.
2. Al Amri, A.; Sahoo, S. K.; Monwar, M.; McCord, E. F.; Rinaldi, P. L. *Macromolecules* **2006**, *39*, 5768–5776.
3. Schmidt-Rohr, K.; Spiess, H. W. *Multidimensional Solid-State NMR and Polymers*; Academic Press: New York, 1994.
4. Spiess, H. W. In *Macromolecular Engineering: Precise Synthesis, Materials Properties, Applications*; Matyjaszewski, K., Gnanou, Y., Leibler, L., Eds.; Wiley-VCH: Weinheim, 2007; pp 1937−1965

5. Brown, S. P. *Macromol. Rapid Comm.* **2009**, *30*, 688–716.
6. Saalwaechter, K. *Prog. Nucl. Magn. Reson. Spectrosc.* **2007**, *51*, 1–35.
7. Schnell, I.; Spiess, H. W. *J. Magn. Reson.* **2001**, *151*, 153–227.
8. Sebastiani, D. *ChemPhysChem* **2006**, *33*, 164–175.
9. Hafner, S.; Spiess, H. W. *Concepts Magn. Reson.* **1998**, *10*, 99–128.
10. Ernst, R. R.; Bodenhausen, G.; Wokaun, A. *Principles of Nuclear Magnetic Resonance in One and Two Dimensions*; Clarendon Press: Oxford, 1987.
11. Klimke, K.; Parkinson, M.; Piel, C.; Kaminsky, W.; Spiess, H. W.; Wilhelm, M. *Macromol. Chem. Phys.* **2006**, *207*, 382–395.
12. Wei, Y.; Graf, R.; Sworen, J. C.; Cheng, C. Y.; Bowers, C. R.; Wagener, K. B.; Spiess, H. W. *Angew. Chem. Int. Ed.* **2009**, *48*, 4617–4620.
13. Steininger, H.; Schuster, M.; Kreuer, K. D.; Kaltbeitzel, A.; Bingöl, B.; Meyer, W. H.; Schauff, S.; Brunklaus, G.; Maier, J.; Spiess, H. W. *Phys. Chem. Chem. Phys.* **2007**, *9*, 1764–1773.
14. Lee, Y. J.; Murakhtina, T.; Sebastiani, D.; Spiess, H. W. *J. Am. Chem. Soc.* **2007**, *129*, 12406–12407.
15. *Handbook of Liquid Crystals*; Demus, D., Goodby, J., Gray, G. W., Spiess, H. W., Vill, V., Eds.; Wiley-VCH: Weinheim, 1998.
16. Lehn, J. M. *Science* **2002**, *295*, 2400–2403.
17. Bohle, A.; Brunklaus, G.; Hansen, M. R.; Schleuss, T. W.; Kilbinger, A. F. M.; Seltmann, J.; Spiess, H. W. *Macromolecules* **2010**, *43*, 4978–4985.
18. Clauss, J.; Schmidt-Rohr, K.; Adam, A.; Boeffel, C.; Spiess, H. W. *Macromolecules* **1992**, *25*, 5208–5214.
19. Tsao, H. N.; Cho, D. M.; Park, I.; Hansen, M. R.; Mavrinskiy, A.; Yoon, D. Y.; Graf, R.; Pisula, W.; Spiess, H. W.; Muellen, K. *J. Am. Chem, Soc.* **2011**, *133*, 2605–2612.
20. Fritzsche, M.; Bohle, A.; Dudenko, D.; Baumeister, U.; Sebastiani, D.; Richardt, G.; Spiess, H. W.; Hansen, M. R.; Höger, S. *Angew. Chem. Int. Ed.* **2011**, *50*, 3030–3033.
21. Ober, C. K.; Cheng, S. Z. D.; Hammond, P. T.; Muthukumar, M.; Reichmanis, E.; Woolex, K. L.; Lodge, T. P. *Macromolecules* **2009**, *42*, 465–471.
22. Spiess, H. W. *Angew. Chem. Int. Ed.* **2008**, *47*, 639–642.

Downloaded by STANFORD UNIV GREEN LIBR on June 19, 2012 | http://pubs.acs.org
Publication Date (Web): October 14, 2011 | doi: 10.1021/bk-2011-1077.ch002

Downloaded by DUKE UNIV on June 20, 2012 | http://pubs.acs.org
Publication Date (Web): October 14, 2011 | doi: 10.1021/bk-2011-1077.ch003

Chapter 3

Tutorial on Solution NMR of Polymers

Peter L. Rinaldi*

Department of Chemistry, The University of Akron, Akron, Ohio 44325-3601
***E-mail: peterrinaldi@uakron.edu**

This paper is derived from a tutorial on the use of solution NMR methods to characterize polymers. The presentation has a dual purpose: 1) to orient new scientists who are just starting to use NMR methods in polymer science; and 2) to introduce new developments in NMR to experienced practitioners of solution NMR of polymers. After a brief introduction to using one-dimensional (1D-) NMR for quantitative analysis of polymers, the presentation covers recent developments in pulse sequences/software, hardware developments and methodology that combines the two. For the benefit of novice NMR users, an introduction to some basic NMR methodology is incorporated into these discussions. The work cited includes NMR papers on polymers as well as recent work on small-molecule NMR that has potential for helping with polymer analysis.

Introduction

The most important aspect of polymer synthesis is to identify the structures of the newly synthesized materials. Once a material with desirable properties is prepared, it is important to know the structures present and their quantities, so that the synthesis of the desired material can be reproduced. If properties of synthesized materials are not reproducible, the polymer chemist must determine whether the structure and composition of the material has changed to cause the change in properties. Furthermore, systematic changes in polymer structure can often be correlated with changes in mechanical and physical properties. This in turn can lead to educated choices in designing the structures of new polymers with desired properties. Finally, it is desirable to identify the nature and quantity of adulterants which undesirably alter the properties of materials.

In NMR Spectroscopy of Polymers: Innovative Strategies for Complex Macromolecules; Cheng, H., et al.;
ACS Symposium Series; American Chemical Society: Washington, DC, 2011.

Solution state NMR is ideally suited for determining the structures and compositions of organic materials. There are a wealth of pulsed 1D- and 2D-NMR techniques for resolving the resonances of many unique atoms (especially hydrogen and carbon) present in the mixtures of organic structure components that make up a polymer. These methods can be used for determining how these atomic components are linked to form molecules. In most cases, the structures of unknown compounds can be determined by straightforward examination and interpretation of NMR spectra.

Once the structures have been identified and NMR resonances have been attributed to the structures present, NMR spectra can be used to quantitatively determine the compositions of these structures in the polymer. In fact, NMR is unique among spectroscopic methods in that a correctly acquired and processed NMR spectrum has a simple one-to-one relationship between the strengths of signals and the number of atoms producing those signals. Other spectroscopic methods require calibration procedures to determine extinction coefficients for different functional groups before they can be used for quantitative analysis.

For the benefit of novice NMR users, this work contains a brief introduction to polymer structure and some general comments on collection of quantitative 1D-NMR spectra. It is followed by a description of some recently available (last 5 years) NMR methods which will have an impact on the field of solution NMR of polymers. For more comprehensive descriptions of polymer NMR, the reader is refered to some recent works (*1*, *2*). For an excellent introduction to the use of 1D- and 2D-NMR for characterization of organic structures, the reader is referred to an excellent textbook on the subject (*3*).

Polymer Structure

It is desirable to identify a number of structure elements in polymers. These include: chain-ends, monomer composition, monomer sequence, sequences from inverse monomer addition, stereosequence effects, branches and cross-link points and polymer block junctions. It is also desirable to identify structure defects that might be caused from side reactions during the polymerization, and to determine the presence and amount of adulterants such as low molecular weight impurities like solvents and unreacted monomer.

Chain-Ends

Equations (1)–(6) outline the general mechanism for polymerization including initiation, propagation and termination steps.

Initiation:

$$In \rightarrow In^{*} \xrightarrow{M} In - M^{*} \qquad (1)$$

Propagation:

$$In - M^{*} \xrightarrow{nM} In - M - (M)_{n-1} - M^{*} \qquad (2)$$

In NMR Spectroscopy of Polymers: Innovative Strategies for Complex Macromolecules; Cheng, H., et al.;
ACS Symposium Series; American Chemical Society: Washington, DC, 2011.

Downloaded by DUKE UNIV on June 20, 2012 | http://pubs.acs.org
Publication Date (Web): October 14, 2011 | doi: 10.1021/bk-2011-1077.ch003

Downloaded by DUKE UNIV on June 20, 2012 | http://pubs.acs.org
Publication Date (Web): October 14, 2011 | doi: 10.1021/bk-2011-1077.ch003

Termination:

Coupling $$In - (M)_n - M^{\bullet} + In - (M)_m - M^{\bullet} \rightarrow In - (M) \quad (3)$$

Disproportionation $$In - (M)_n - CH_2^{\bullet} + In - (M)_m - CH_2^{\bullet} \rightarrow M - (M)_m = CH_2 \quad (4)$$

Chain transfer:

Chain transfer to monomer $$In - (M)_n - M^{\bullet} \xrightarrow{M} In - (M)_n - M + M^{\bullet} \quad (5)$$

Chain transfer to solvent $$In - (M)_n - M^{\bullet} \xrightarrow{HS} In - (M)_n - MH + S^{\bullet} \quad (6)$$

The relative rates of propagation and termination pathways determine the molecular weights of the polymers produced. From a knowledge of the various termination processes, the chemist can alter the reaction conditions to control the polymer's molecular weight. Additionally, many polymer degradation processes start by reactions at the chain terminus. If the structures of the predominant chain-ends are known, the reaction chemistry can be altered, or chain-end capping reactions can be performed, to reduce the number of reactive chain-ends, leading to a stable polymer.

Monomer Sequence

When a polymer is synthesized from two monomers, A and B, the monomers can add in an alternating fashion (**1**), in a statistical manner (**2**), in a manner to form blocks of A and blocks of B (**3**), or such that sequences of B can be grafted to a chain of A sequences (**4**).

Alternating	-ABABABABABABABABAB-	**1**
Random	-ABABBBABBAABBAABAA-	**2**
Block	-AAAAAAAAABBBBBBBBB-	**3**
Graft	-AAAAAAAAAAAAAAAAA- | BBBBBBBBB-	**4**

The prevalence of these various structures is dependent upon the relative reactivities of A and B monomer with themselves or with each other, and on the

Downloaded by DUKE UNIV on June 20, 2012 | http://pubs.acs.org
Publication Date (Web): October 14, 2011 | doi: 10.1021/bk-2011-1077.ch003

reaction conditions. The prevalence of these various structures has a dramatic influence on polymer properties and is of intense interest to polymer chemists.

The relative reactivities of A/B monomers with themselves and with each other can be derived from the analysis of n-ad sequences. Often, the resonances of triads (AAA, AAB/BAA, BAB, ABA, ABB/BBA, BBB) can easily be resolved, even at relatively low field. From an analysis of the relative compositions of these triads, the predisposition of a particular copolymer to form alternating, random or block structures can be quantitatively described (*4*). With the routine availability of instruments with ^{1}H resonance frequencies as high as 700 to 800 MHz, it is sometimes possible to resolve resonances from heptads or even nonads. When it is possible to resolve and measure the intensities of signals from different n-ads, accurate information about relative reactivities is obtainable.

Stereosequence

When certain monomers such as 1-substituted ethylenes (e.g. styrene) polymerize, they create stereogenic centers on alternating carbons along the polymer backbone. In most cases the absolute stereochemistry is not important, as a racemic mixture of polymer chains is created. However, the relative stereochemistry of adjoining stereogenic centers is important, and has a dramatic effect on polymer properties.

If the backbone of a vinyl polymer is drawn in a planar zig-zag orientation as in structures **5**–**7**, two relative orientations are seen: the *meso* (*m*) structure has two adjoining R substituents on the same face of the polymer as in the two dyads in **5**; and the *racemic* (*r*) structure has two adjoining R substituents on opposite faces of the polymer as in the two dyads in **6**. If triads are considered, isotactic polymers have the same orientations of all R substituents to produce polymers with all *m* dyad placements. Syndiotactic polymers have alternating orientations of R substituents to produce polymers with all *r* dyad placements. Atactic polymers have random orientations of R substituents to produce polymers with equal numbers of randomly placed *m* and *r* dyads.

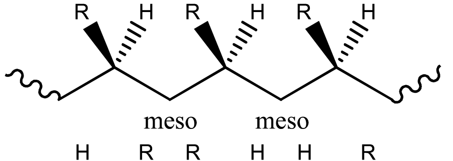

Isotactic **5**

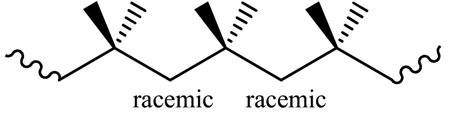

Syndiotactic **6**

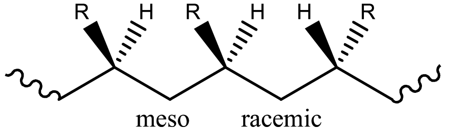

Atactic **7**

Since the properties of polymers are related in part to their tacticity, measurement of *m* and *r* dyad composition is crucial. NMR is ideally suited to this measurement, as the NMR resonance positions are influenced by relative stereochemistry (*5*).

Other Defects

NMR is ideally suited for determining the structures and quantities of polymer defects, whether they are incorporated intentionally or accidentally. These include branch points, junctions between two polymer blocks, cross-link junctions and other defects. Finally, adulterants such as residual solvents or monomer, and additives such as antioxidants can usually be detected and identified.

Structure proofs can usually be accomplished by comparison of resonance positions with those in the spectra of authentic material. When authentic materials are difficult to obtain or are not available, combinations of 2D-NMR methods can be used to determine atomic attachments, prove structure elements and simultaneously assign resonances.

Downloaded by DUKE UNIV on June 20, 2012 | http://pubs.acs.org
Publication Date (Web): October 14, 2011 | doi: 10.1021/bk-2011-1077.ch003

Quantitative One-Dimensional NMR

Once the presence of the above structure elements is determined and their resonances identified, it is desirable to quantitatively evaluate the amounts of these structures present in the polymer. This is usually accomplished with 1D-NMR experiments. While NMR is unique among spectroscopic methods in that peak areas can be directly related to the number of atoms of each type, it is important to properly obtain NMR spectra in order to get reliable and accurate analysis of composition and purity. Accurate quantitative analysis of polymers requires attention to the details at the data acquisition stage as well as the data processing stage.

Data Acquisition

The most important factor in generating good quality 1D-NMR spectra for quantitative analysis it to measure the T_1 relaxtion times for the nuclei whose signals are to be measured. This is accomplished using an inversion recovery experiment (relaxation delay-180^o-τ-90^o-acquire, where τ is a variable relaxation delay) experiment. By fitting the exponentially decaying peak intensity variation vs. τ from a series of spectra obtained with varying τ delays, the exponential recovery time constant T_1 for each peak in the spectrum is determined (*1*). In setting up a quantitative 1D-NMR experiment, the relaxation delay should be 5-10 times the longest T_1 among the signals of interest.

If decoupling is performed (as is the case when ^{13}C NMR is used) then in most cases, the nuclear Overhauser effect (NOE) resulting from saturation of the decoupled nuclei must be suppressed, since signals of different ^{13}C atoms are differentially enhanced depending upon the unique relaxation characteristics of each nucleus. To accomplish NOE suppression, a gated decoupling experiment must be used, where the ^{1}H decoupler is turned off except during the acquisition time, and a 90° excitation pulse is used. Under these circumstances complete suppression of the NOE requires a relaxation delay (during which the ^{1}H decoupler is turned off) of at least $10xT_1$. In rare instances, when signals of very similar atoms are compared, spectra with NOE enhancement can be used if the enhancement is the same for all signals to be compared.

Data accumulation should be performed with an acquisition time such that the NMR signal decays (at least $3xT_2$*, the apparent transverse relaxation of the NMR signal). In selecting the spectral window, the effective excitation window of the pulse should be considered. A square pulse produces an excitation window in which peak height vs. offset from the transmitter (center of the spectral window) is defined by a sin(x)/x function. A good rule of thumb is that for a 5μs pulse only the middle 50 kHz of the spectral window experiences uniform excitation. Outside of this window, the peak heights will be attenuated by incomplete flipping of the spins. If the pulse width is doubled (10 μs) then the useable spectral window will be halved (25 kHz).

A second factor to consider when setting the spectral window is hardware filtering of the audio signal. Older NMR instruments mix the rf signal down to the audio frequency range where it can be digitized by older analog-to-digital converters (ADC's). To prevent aliasing of high frequency signal components from outside of the spectral window (thus maintaining good signal-to-noise) audio filters are used. These hardware filters have non-ideal response and can attenuate signals outside of the middle half of the spectral window; attenuation of signals near the edges of the spectral window is often 50% or more, depending on the age of the instrument. Thus, only the middle half of the spectral window is useable for quantitative analysis.

Instruments manufactured in the past five years use digital manipulation over a much larger portion of the signal receiver path. In these newer instruments, the NMR signal is digitized in the rf range, and mathematical filtering is used to prevent aliasing of signals from outside of the desired spectral window. Mathematical filters have more desirable "brick wall" behavior; completely attenuating signals from outside of the spectral window, while leaving signals within the spectral window unperturbed. In these newer digital instruments, signals in the middle 90% or more of the spectral window can be used for quantitative analysis.

Once the spectral window is determined, the delay between the end of the pulse and start of data acquisition should be adjusted such that in the final spectrum all peaks can be phased correctly with adjustment of only the zero order phase correction. The spectrum should be properly phased without the use of first order phase correction. The optimum preacquisition delay is spectral window dependent, so that once analysis parameters are determined, it is unnecessary to make further adjustments and the parameters can be used for subsequent analyses. If the spectrum is collected with an incorrect preacquistion delay, then a sinusoidal roll will be introduced into the baseline. The intensity and number of cycles will be dependent on the extent of the misset, and the spectral window. The problems introduced will be more severe for data collected with larger spectral windows.

Downloaded by DUKE UNIV on June 20, 2012 | http://pubs.acs.org
Publication Date (Web): October 14, 2011 | doi: 10.1021/bk-2011-1077.ch003

Finally, for good quantitative analysis, spectra with good signal-to-noise (S:N) are required. Analytical criteria specify that a minimum S:N of 10:1 is required before quantitative measurements can be performed. However, for accurate analyses, S:N levels an order of magnitude or greater should be used.

Data Processing

In order to accurately measure a peak integral, the peak must be accurately represented in the digital domain. Typically, it is desirable to have approximately 10 points to define the top half of the peak shape. A good rule of thumb is to zero fill a properly collected time domain signal (free induction decay, FID) to 2 or 4 times the original dataset size. To improve S:N and to further contribute to sufficient digital resolution of the peaks, it is also useful to apply an exponentially decaying function to the decaying FID. Optimum S:N is achieved when the decay of weighting function matches the decay of the FID. Often, in real spectra there will be a mixture of broad and sharp peaks from polymer backbone and side-chain resonances, respectively. Therefore, it is usually desirable to examine the spectral with different weighting functions.

A properly phased spectrum is essential for good quantitative analysis. As mentioned above, if the data are properly collected, it should be possible to phase the spectrum solely by adjustment of the zero order phase parameter. Often the operator will phase spectra by zooming in on the peak and attempting to make the peak symmetrical. If the peak is inherently asymmetric due to a signal component producing a shoulder on the main peak, or due to an asymmetric shape from incorrect shimming, then integration error will result. There are many published protocols for phasing. Some of these involve phase adjustments to produce a maximum peak integral and numerically monitoring the baseline on either side of the peak. When phasing, it is useful to examine the true baseline regions on either side of the peak and to adjust the phase so the extensions of these baseline components to the peak center, intersect at the same vertical point.

Distortions in the baseline should be removed with the operator's favorite baseline correction algorithm. For properly collected data, the distortions should not be too severe and a spline fit is effective. Other more involved procedures involve fitting the baseline to an nth order polynomial, or to a sum of sinusoidal functions. In all cases the baseline (peak-free regions of the spectrum) needs to be identified. This is often accomplished by dividing the integral regions of the spectrum (e.g. such that odd regions are peak-free). When defining the baseline regions it is important to consider the fact that Lorenzian peaks typically found in NMR spectra extend for quite a distance from the frequency of the peak maximum. Approximately 99% of the peak area is found over a region 20 times the peak width at half height ($\Delta\upsilon_{1/2}$); 98% of the peak area is found within a region with 10 times $\Delta\upsilon_{1/2}$; and only 95% of the peak area is found within a region with 5 times $\Delta\upsilon_{1/2}$. While it might be desirable to integrate the spectra with narrower integral regions surrounding the peak maxima, it is necessary to select baseline regions of the spectrum that do not fall within 10-20 peak widths of the intense signals in the spectrum. If this is not done, baseline correction will shift the baseline offsets due to the presence of real signals, and lead to inaccurate peak integrals.

Downloaded by DUKE UNIV on June 20, 2012 | http://pubs.acs.org
Publication Date (Web): October 14, 2011 | doi: 10.1021/bk-2011-1077.ch003

Downloaded by DUKE UNIV on June 20, 2012 | http://pubs.acs.org
Publication Date (Web): October 14, 2011 | doi: 10.1021/bk-2011-1077.ch003

Accurate quantitative analysis requires that all of the resonance assignments be known and properly counted. Some particular problems include contributions from ^{13}C satellites and the outer wings of AB patterns in ^{1}H and ^{19}F NMR spectra. Failure to count these signals properly can cause errors in quantitative analysis, especially if the intensities of weak and strong signals are being compared.

Figure 1 shows an excellent example of how both of these factors can cause complications in quantitative analysis. This region of the ^{19}F spectrum of poly(hexafluoropropylene oxide) (pHFPO) contains two AB patterns, labeled a_2 and a'_2 from the two diastereotopic CF_2 fluorines shown on the two structures at the bottom of the figure. The structures differ by inversion of the central $–CF(CF_3)CF_2$ monomer unit. The central parts of these AB pattern are off scale. They are components of the AB patterns from the chain-ends groups of pHFPO containing CF_2 signals from normal (a_2) and inverse addition (a_2') of the second monomer unit in the chain. The two weak signals at the outer edges of this spectral region are the outer satellites of the AB pattern from the a_2 fluorines. The measured couplings in this AB pattern are $^{2}J_{FF}$ = 285 Hz, which is typical of a two-bond ^{19}F-^{19}F homonuclear coupling. The corresponding outer parts of the AB pattern from the a'_2 fluorines are too weak to detect; they are ca. 10 fold weaker due to the lower concentration of structures from monomer inversion.

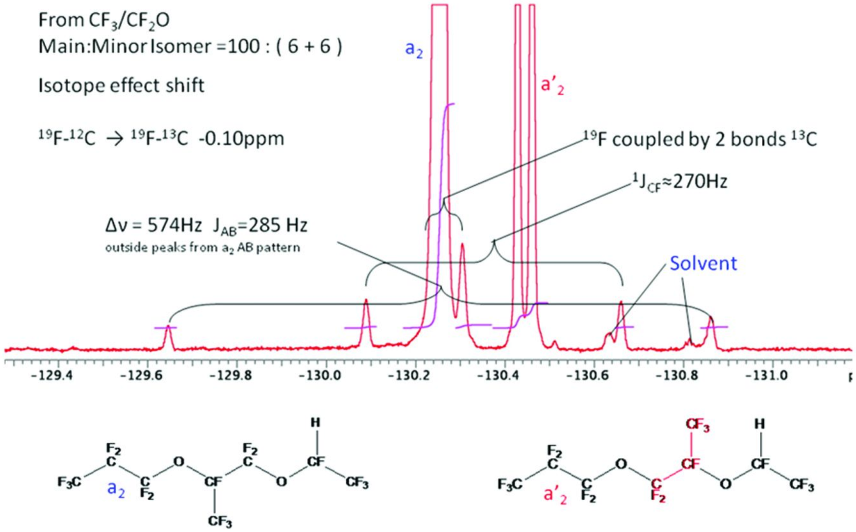

Figure 1. Section of the 470 MHz ^{19}F 1D -NMR spectrum from pHFPO showing the region containing the a_2 and a'_2 CF_2 resonances as labeled on the structures at the bottom of the figure. The ratio of the two structures is ca. 100:12.

Satellites of the a_2 resonance from 1.1% ^{19}F-^{13}C and 2.2% ^{19}F-C-^{13}C are seen with couplings of $^{1}J_{CF}$ = 270 and $^{2}J_{CF}$ = 40 Hz, respectively. The center of the doublet from $^{1}J_{CF}$ is shifted upfield by ca. 0.1 ppm by a ^{13}C istotope shift. The center of the doublet from $^{2}J_{CF}$ is shifted upfield by ca. 0.01 ppm by a ^{13}C istotope shift. Additionally, the latter doublet (from $^2J_{CF}$) is twice as large as the former doublet (from $^1J_{CF}$) because the probability of coupling to ^{13}C is twice as large (^{13}C's can be present at two sites, CF_2 and CF_3, which are two bonds away from the a_2 fluorines). These signals from coupling to ^{13}C could easily be misinterpreted as weak resonances from other minor chain-end structures, especially because they are asymmetrically spaced around the central ^{19}F resonance. Corresponding ^{13}C satellite signals from the weaker a'_2 resonances are not seen in the spectrum because these structures are present in ca. 10-fold lower concentration.

Also, if these satellites had fallen beneath weaks signals of minor structure components, they could easily lead to enormous errors in compositional calculations.

If very accurate compositional calculations are needed, one should compare integrals which are a similar multiple of the peak width. Usually, 10 peak widths is acceptable. However, one must also consider overlap of neighboring resonances and the effect of J-couplings on the width of multiplets in deciding integral reset positions. When doing compositional calculation with a high degree of accuracy, one must also decide whether to incorporate ^{13}C satellites, and to be consistent in their inclusion or omission.

Once the peak areas are determined, there are several strategies for calculating compositions of various monomer- or stereo-sequences. The traditional strategy involves determining the relationship between peak areas and various n-ad structure elements (monomer sequences or stereosequences). A set of linear equations is obtained which can be solved for n-ad compositions. In many cases some of the resonances are associated with odd-numbered n-ads such as triads, and other resonances are associated with even number m-ads such as dyads and tetrads. These can be related to each other through necessary relationships, which also provide additional linear relationships (*2*).

On occasion problems with incorrectly counting structure units occur when more than one n-ad is considered in the compositional analysis. Researchers from Dow proposed an alternative method for extracting polymer compositions from NMR data (*6*). Their method involves examining resonances and attributing them to the central monomer of odd-numbered n-ads, thus counting atoms only once. From these assignments, a set of linear equations can be obtained that relate peak integrals to a set of structures. The compositions can be solved by numerically fitting calculated peak areas to those experimentally determined. Recently, Momose et al. (*7*) described the use of multivariate analysis as a method for studying the compositions of copolymers and homopolymer blends.

New Experiments and Pulse Sequences

Over the past decade, 2D-NMR methods have become routine for studying the structures of complex polymers and producing the unequivocal resonance assignments that are needed for quantitative analyses. Complete spectral analysis usually involves collection of two or more 2D-NMR spectra and using complementary information from the spectra to construct an entire structure.

Downloaded by DUKE UNIV on June 20, 2012 | http://pubs.acs.org
Publication Date (Web): October 14, 2011 | doi: 10.1021/bk-2011-1077.ch003

2D-NMR Methodologies for Determining Polymer Structure

Various methodologies have been developed for determining polymer structure. Reference (*3*) serves as an excellent initial source for learning how to determine organic structure and resonance assignments from NMR data. Two commom methodologies for extracting structures from multidimensional NMR spectra involve the use homonuclear or heteronuclear 2D-NMR methods.

Homonuclear 2D-NMR

In the case where sample quantity and/or sensitivity is an issue, methodologies involving ^{1}H - ^{1}H (or ^{19}F - ^{19}F) correlation 2D-NMR experiments are useful. Such situations include cases where sub-milligram quantites of material are available, or where very weak signals from structures such as chain ends are to be studied. In these homonuclear experiments the natural abundance of both nuclei is 100%, and high sensitivity detection of nuclei with large magnetic moments (^{1}H or ^{19}F) is performed.

Downloaded by DUKE UNIV on June 20, 2012 | http://pubs.acs.org
Publication Date (Web): October 14, 2011 | doi: 10.1021/bk-2011-1077.ch003

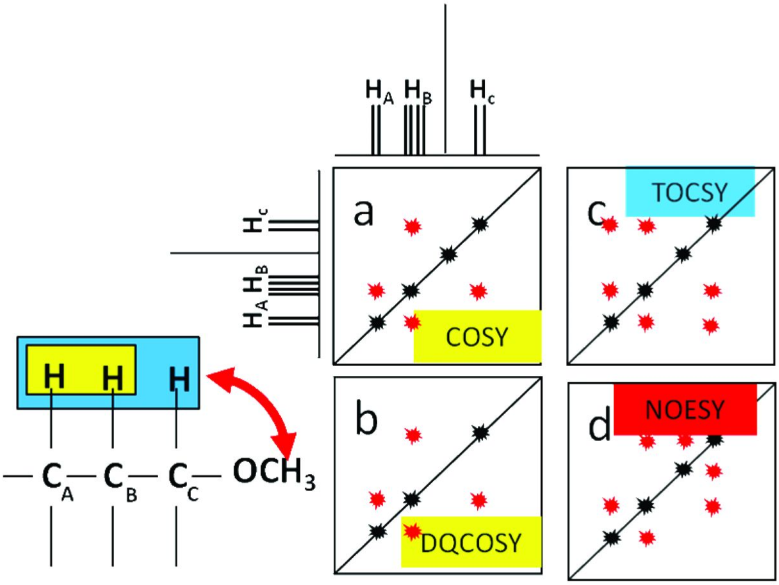

Figure 2. Schematic representation of homonuclear 2D-NMR experiments and the structure information available from them: a) COSY, b) DQCOSY, c) TOCSY, and d) NOESY. Reprinted with permission from reference (1).

The structure information available from homonuclear 2D-NMR experiments is illustrated schematically in Figure 2. The atomic connectivities in the structure in Figure 2 are highlighted by colored boxes that match the color codes of the experiment names which provide that structure connectivity information.

The COSY (correlation spectroscopy, highlighted in yellow) 2D-NMR experiment produces a spectrum schematically illustrated by Figure 2a with the identical homonuclear chemicals shifts plotted along the two axes. Peaks are found along a diagonal at the shifts of the resonances in the spectrum. If there is germinal or vicinal coupling between protons, cross-peaks appear off the diagonal at the intersection of the two shifts indicating atomic connectivity highlighted in the yellow box (i.e. the vicinal relationship between H_A and H_B) on the chemical structure in the figure. Similar information from the COSY spectrum identifies the vicinal relationship between H_B and H_C (not shown on the figure).

The DQCOSY (double quantum filtered COSY, also highlighted in yellow) NMR experiment produces a 2D spectrum (Figure 2b) similar to that in COSY, but with signals from singlets (resonance not coupled) filtered from the spectrum. These signals do not produce useful information in COSY spectra and only serve to hide cross-peaks that fall near the diagonal, so their absence from the 2D spectrum is an advantage.

TOCSY (total correlation spectroscopy, highlighted in blue) 2D-NMR spectra (Figure 2c) have an appearance similar to COSY spectra, but with correlations among resonances of all protons that are part of the same spin system as illustrated by the structure elements highlight in blue on the structure in the figure. Note crosspeaks between H_A and H_C in this spectrum, even though they are not coupled to each other. These TOCSY crosspeaks are produced because they are part of the same spin system, where H_A is coupled to H_B and H_B in turn is coupled to H_C.

NOESY (NOE spectroscopy) 2D-NMR experiments produce spectra (Figure 2d) with cross-peak patterns similar to those found in COSY spectra, but with cross-peaks appearing at the intersection of the chemical shifts of protons that are close (usually within 0.5 nm) in space. They provide structure information about the spacial proximity of groups (regardless of coupling) like those shown by the red arrow on the structure in the figure.

From a set of homonuclear experiments, it is usually possible to determine chemical structures. However, these experiments suffer from the limited chemical shift dispersion of ^1H (10 ppm). If many structures are present with slight environmental differences, such as those found from stereosequence effects, it can be difficult to resolve all of the cross-peaks needed to determine structure.

Furthermore, the distinction/resolution between cross-peaks is complicated by the fact that the cross-peak pattern are a cluster of (n x m) peaks where n and m are the multiplicities of the coupled peaks in the 1D-NMR spectrum. For example, the cross-peaks between H_A and H_B resonances in Figure 2a are a 2x4 set of peaks. The projection of these cross-peaks produce a 2-line pattern at the chemical shift of the H_A resonance, which is a doublet; and a 4-line pattern at the chemical shift of H_B, which is a doublet of doublets. If two sets of cross-peaks occur at similar shifts, it is often difficult to distinguish between them.

Finally, the individual peaks within a cross-peak pattern are a series of positive and negative contours, determined by the relative signs of the J-couplings. In low resolution 2D-NMR spectra, overlap between adjoining anti-phase peaks can lead to signal cancellation, especially if the J-couplings are small compared to the digital resolution and/or the peak width. In these circumstances it is easy to miss cross-peaks, leading to misassignments and incorrect interpretation of the spectra. This is especially true with spectra of polymers, which contain broader lines than those found in the spectra of small molecules.

Downloaded by DUKE UNIV on June 20, 2012 | http://pubs.acs.org
Publication Date (Web): October 14, 2011 | doi: 10.1021/bk-2011-1077.ch003

For these reasons, when adequate signal is present, it is often preferable to study structures using a methodology involving two or more heteronuclear 2D-NMR experiments.

Heteronuclear 2D-NMR

Downloaded by DUKE UNIV on June 20, 2012 | http://pubs.acs.org
Publication Date (Web): October 14, 2011 | doi: 10.1021/bk-2011-1077.ch003

In the case where ample quantities of material are available (1-100 mg depending upon the abundance of the structure to be detected and the field strength of the instrument used) heteronuclear 2D-NMR experiments can be performed. These experiments most commonly involve sensitive detection of a nucleus such as ^1H or ^{19}F, which has a large magnetic moment and is also present in high natural abundance. However, the shifts of these nuclei are correlated with a low abundance nucleus such as ^{13}C (1.1% abundance), so that NMR signal is detected from one molecule in 100. These experiments have the advantage that the chemical shift dispersion in the indirectly detected dimension is determined by the shift range of the heteronucleus (200 ppm in the case of ^{13}C). Also, the correlation is a (1 x n) pattern as there is usually no coupling in the ^{13}C dimension (unless there is a third NMR-active nucleus in the structure). Thus, it is possible to resolve many resonances from chemically similar structure fragements.

Figure 3 schematically illustrates the most useful heteronuclear 2D-NMR spectra. As in the previous section, the connectivities on the structure in the figure are highlighted with colored boxes to match the colors of the boxes around the experiment names from which the atomic connectivities are derived. The HSQC (heteronuclear single quantum coherence, colored in yellow) and HMQC (heteronuclear multiple quantum coherence) experiments use one-bond C-H couplings to produce spectra (Figure 3a) with cross-peaks indentifying direct C-H attactment, as illustrated by the fragments highlighted by the yellow boxes on the structure in the figure. The HMQC experiment was originally used for this purpose, but has been replaced by the HSQC experiment which produces more intense signals and less complicated cross-peak patterns. Variations of the HSQC experiment that use adiabatic 180^o pulses usually give better signal to noise levels than spectra from HSQC experiments using simple 180^o pulses (*8*).

The HSQC experiment is usually used in combination with data from the HMBC (heteronuclear multiple bond correlation, highlighted by the blue boxes) experiment which produces spectra similar to that illustrated by Figure 3b. The HMBC spectrum shows correlations between ^{13}C and ^1H atoms coupled through 2- and 3-bonds. Structure fragments highlighted in blue on the structure in the figure are identified. Complications arise in distinguishing between 2- and 3-bond C-H correlations. One method to enhance one or the other set of cross-peaks is to perform the experiment twice with different delays optimized for 2- and 3-bond couplings (80 and 50 ms usually work for the former and the latter). Some judgement of relative cross-peak intensity in the two spectra is necessary, and the results are often ambiguous.

Downloaded by DUKE UNIV on June 20, 2012 | http://pubs.acs.org
Publication Date (Web): October 14, 2011 | doi: 10.1021/bk-2011-1077.ch003

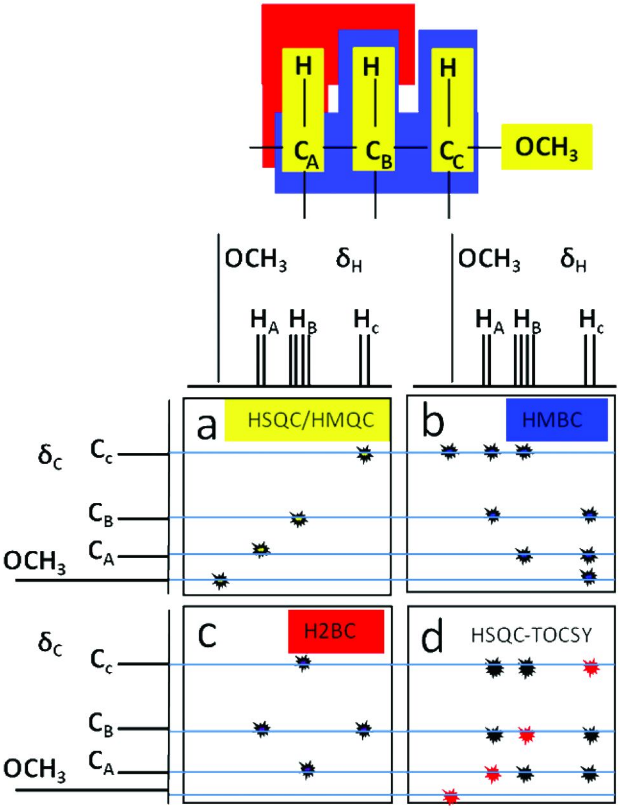

Figure 3. Schematic illustration of heteronuclear correlated 2D-NMR spectra from the hypothetical structure fragment shown at the top of the figure: a) HSQC or HMQC, b) HMBC, c) H2BC, d) HSQC-TOCSY. Reproduced with permission from reference (1).

The advantage of this experiment is that correlations across heteratoms and quaternary carbons can be detected (e.g. in this case a correlations can be seen between the resonances of the methoxyl protons and C_C). Distinction between 2- and 3-bond correlations in the HMBC spectra is usually the "Achilles heel" of this heteronuclear 2D-NMR methodology. Many variations of the HMBC experiment have been devised to help differentiate between between 2-bond and 3-bond correlations. Most of these work nicely for small molecules, but because polymers give spectra with broader lines from shorter relaxation times, these experiments rarely work well for polymers. The exception is the H2BC (heteronuclear two-bond correlation) experiment which produces spectra illustrated by Figure 3c (*9*). This experiment uses a combination $^1J_{CH}$ and $^3J_{HH}$ to produce correlations among the atoms in the structure fragment highlighted by the red box on the structure in the figure. In this example a 2-bond correlation is seen between C_A and H_B. The H2BC cross-peak patterns are considerably simpler that those in the HMBC spectra because ^{13}C decoupling can be used during the acquisition time in the former experiment. Furthermore, the cross-peaks are independent of $^2J_{CH}$;

Downloaded by DUKE UNIV on June 20, 2012 | http://pubs.acs.org
Publication Date (Web): October 14, 2011 | doi: 10.1021/bk-2011-1077.ch003

two bond C-H couplings are often small leading to inefficient coherence transfer between nuclei in the HMBC experiment. When polymers are studied, for the same experiment time, signals in H2BC spectra are considerably more intense than signals in HMBC spectra. The drawback of H2BC is that correlations to quaternary carbons are not detected.

In the HSQC-TOCSY spectrum (Figure 3d), at the shift of each proton bearing ^{13}C, a C-H correlation is detected at the intersection of the chemical shifts of directly bound carbon and hydrogen (e.g. between C_A and H_A). In addition, at this ^{13}C shift, additional TOCSY correlations are observed to the shifts of all the other protons (H_B and H_C in this case) that are part of the consecutively coupled proton spin system. The experiment is usually run to produce positive contours (red spots) to indicate correlations between the resonances of directly bound carbons and hydrogens, and negative contours (blue spots) to indicate correlations between the resonances of the initial C-H carbon and protons not directly bound to that carbon but part of the same coupled proton spin system.

Figure 4 shows selected regions from the heteronuclear 2D-NMR spectra of poly(lactate-co-glycolate)-b-poly(ethylene glycol) capped with folate end groups on the polyester chain-end (PLGA-PEG-FOL). These data show the regions which support the assignments of resonances from the lactate portion of polymer, as shown on the structure in the figure. Figure 4a contains the HSQC data showing a one-bond correlation for the methyl group. Figure 4c shows the portion of the HMBC spectrum containing correlations from lactate methyl protons to the lactate methine and ester carbonyl carbons (correlations A1 and A2, respectively), two- and three-bonds away, respectively. On its own, this spectrum does not permit distinction between the two- and three-bond correlations. Figure 4b shows the relevant region from the H2BC spectrum; it identifies the A1 cross-peak as the one associated with the two-bond HMBC correlation.

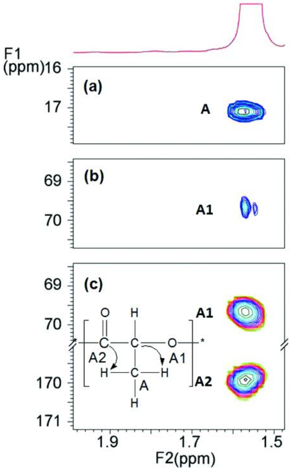

Figure 4. Polylactic acid regions from the 2D-NMR spectra of PLGA-PEG-Folate: a) HSQC, b) H2BC, and c) HMBC of PLGA-PEG-folate.

Quantitative NMR

The spectral dispersion provided by 2D-NMR methods is enormously powerful for resolving and assigning resonances in complicated polymer structures. However, once resonance assignments are made, it is desirable and often necessary to use this information to perform quantitative analysis of polymer composition. This can be a problem if resonances are not resolved in standard 1D-NMR spectra. There are alternatives for getting resolved peaks for quantitative analysis.

2D-NMR

Downloaded by DUKE UNIV on June 20, 2012 | http://pubs.acs.org
Publication Date (Web): October 14, 2011 | doi: 10.1021/bk-2011-1077.ch003

The utilization of 2D-NMR peak integrals for quantitative analysis is complicated by several factors that produce non-linear instrument response which hampers quantification. These include: 1) resonance offset effects on both transmitter and decoupler channels; 2) inconsistent polarization transfer efficiency due to ranges of J-couplings; 3) variations in ^{1}H T_1 causing inconsistent return of the magnetization to its equilibrium state during the relaxation delays; 4) differential polarization transfer due to variations in T_2's; 5) effects from inadequate digital resolution; and 6) multiplicity effects (CH, CH_2 and CH_3 signals do not provide identical responses).

Lemaster et al. (*10*) first used quantitative 2D-NMR analysis for the study polymers by examining the spectra of polyester urethanes from 1,4-butanediol/ 4,4'-diphenylmethane diisocyanate and adipic acid. They used 2D-HSQC and 3D-TOCSY-HSQC spectra to obtain resonance assignments. They then used HSQC spectra under conditions so that the resonance offset effects were insignificant. They determined relative ^{1}H T_1's and corrected for shorter T_1's of the backbone protons relative to the chain-end groups. They compared the 2D-NMR integrals of CH_2 groups which were expected to have similar $^1J_{CH}$ couplings. They determined that inconsistent T_2's did not contribute to the integration errors. Digital resolution problems were eliminated by collecting higher resolution 2D-NMR data, and by using signal processing methods to extend the acquired signal (especially in the evolution time dimension). Only signals of CH_2 groups were compared. After accounting for these issues, they obtained excellent results when they were able to determine the monomer distribution ratio and the ratio of backbone to chain-end units.

Most often, inadequate resolution in 1D-NMR spectra occurs when comparing resonances of similar structures, as these are the resonances most likely to overlap. This was the case in research reported by Qiu et al. where they were concerned with the composition of poly(ethylene-co-octene) (*6*). 1D- and 2D-NMR data from the αα-CH_2 region of one of their samples of poly(ethylene-co-1-octene)s (polyEO) containing 64 mole% 1-octene are shown in Figure 5.

The quantitative ^{13}C 1D-NMR spectrum is shown across the top of the corresponding region from the HSQC spectrum collected under conditions where the 2D-peak volumes are expected to be quantitative. Since the αα-CH_2 resonances are being compared, identical J_{CH} couplings are expected, identical relaxation is expected, effects of resonance offset are identical in both the ^{1}H and ^{13}C dimensions, and multiplicity effects are identical. ^{1}H T_1 could not be measured directly because the αα-protons are not resolved; however, T_1's for these protons (0.2s) could be measured indirectly through detection of the resolved αα- ^{13}C resonances. The bar graph at the bottom compares the 1D-(blue) and 2D-(purple) peak integrals for the three resolved resonances. Excellent comparisons are seen, indicating the utility of 2D-NMR spectra for quantitative analysis.

Diffusion

NMR diffusion measurements have played an increasingly important role in characterizing components in polymer systems. Although the first NMR diffusion measurement using pulsed magnetic field gradients was described by Stejskal and Tanner (*11*), the development of a 2D-pulsed field gradient NMR method, DOSY (diffusion ordered spectroscopy), really sparked applications of diffusion measurements (*12*). A good summary of applications and methodology can be found in reference (*13*).

New Hardware

Over the past decade, hardware improvements have been made in several areas. Modern instruments provide precise and accurate control of the rf amplitude, phase and frequency. After decades of incremental improvements in instrument sensitivity, new detection circuitry has provided a quantum jump in signal-to-noise level. Incorporation of multiple receivers permits simultaneous detection of two or more spectra.

Control of Rf

Modern instruments provide unimaginable control of the rf signals to permit flexible and arbitrary schemes for manipulating the states of nuclear spins. Many of these schemes reduce the demands of collecting high resolution 2D-NMR data by accomplishing selective excitation of the information containing regions of the spectrum, while ignoring other uninteresting regions of the spectrum. There are a number of options for accomplishing this; only a few of these will be discussed here.

Selective Excitation

The COSY pulse sequence is the most basic 2D-NMR experiment, consisting of only two rf pulses separated by an evolution period. It is simple to perform, tolerant of miscalibrations, has good sensitivity, and requires very little expertise to perform. When dealing with hydrocarbon-based structures, it is the first 2D-NMR experiment performed and it generally provides useful structure information.

Downloaded by DUKE UNIV on June 20, 2012 | http://pubs.acs.org
Publication Date (Web): October 14, 2011 | doi: 10.1021/bk-2011-1077.ch003

Downloaded by DUKE UNIV on June 20, 2012 | http://pubs.acs.org
Publication Date (Web): October 14, 2011 | doi: 10.1021/bk-2011-1077.ch003

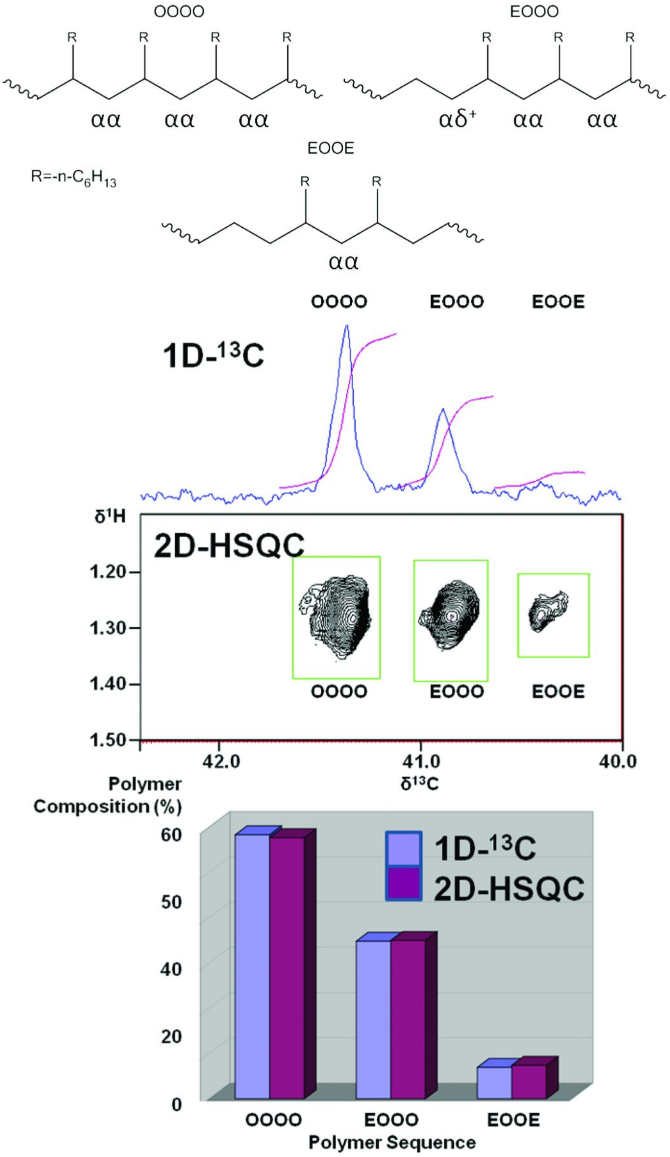

Figure 5. Backbone αα-CH_2 region from the quantitative 1D-^{13}C and 2D-HSQC NMR spectra poly(ethylene-co-octene) containing predominantly racemic relative orientations (top of figure). A bar graph is shown comparing compositions of monomer sequences OOOO, EOOO and EOOE determined from 1D- (blue) and 2D- (purple) integrals (bottom part of figure). Reproduced with permission from reference (6).

When working with fluoropolymers, the huge ^{19}F spectral window (200 ppm compared with 10 ppm for ^{1}H) is an advantage in that the resonance positions are well dispersed and sensitive to the chemical environment of the fluorine atoms.

Downloaded by DUKE UNIV on June 20, 2012 | http://pubs.acs.org
Publication Date (Web): October 14, 2011 | doi: 10.1021/bk-2011-1077.ch003

When COSY experiments are perfomed with ^{19}F, many FID's with different values of the t_1 evolution period must be collected to digitize the indirectly detected dimension of the 2D-NMR spectrum.

Figure 6a shows a small fraction of the entire ^{19}F-^{19}F COSY spectrum (ca. 1% of the total spectrum area) from tetrameric(hexafluoropropylene oxide) T(HFPO), which is a model compound for Krytox® fluoropolymer, a poly(hexafluoropropylene oxide) P(HFPO). To obtain this data, a spectrum with several thousand t_1 increments was collected over the course of a weekend. The experiment was long because many FID's were needed, not because signal averaging was required to obtain good signal-to-noise. Only the region shown was needed to obtain the desired correlation information between the CF_2-O-CF structure fragments illustrated by the red arrows on the structure in the figure. Despite the long experiment, spectral detail in the multiplets is not resolved.

Figure 6b shows the entire 2D-NMR spectrum from a selective COSY (*14*) experiment in which shaped pulses were used to produce a spectrum containing only CF resonances in the f_1 dimension and CF_2 resonances in the f_2 dimension, corresponding to the same spectral window shown in Figure 6a. The experiment required less than 30 minutes of instrument time in which several hundred FID's were collected (*15*, *16*). The experiment required hardware to produce arbitrary rf pulse shapes with arbitrary frequency offsets, not just the simple square pulses centered at the frequency in the center of the spectral window as are commonly used in NMR. Note that the selective COSY spectrum contains far more detail than is seen in the corresponding region from the standard COSY spectrum.

Figure 6c contains a spectrum obtained from a selective COSY spectrum collected with inversion pulses centered in the middle of the evolution period, in order to remove homonuclear couplings. The flexible hardware permits resolution of unprecedented spectral detail. The cross-peaks all appear as singlets in the f_1 dimension; multiplet pattern containing coupling information are retained in the f_2 dimension where collection of high resolution data has little impact on the total experiment time. Two sets of four cross-peak patterns are observed; one set showing the B_2-C_1 correlation between fluorine resonances from the central CF_2OCF groups, and a second set showing A_2-B_1 correlations between the fluorine resonances of the CF_2OCF fragment on the left part of the structure at the top of the figure. Four cross-peak patterns are observed for each C-F group because the three stereogenic centers in the structure produce four diastereomers and their mirror images.

Homonuclear Decoupling

Once multidimensional NMR experiments provide resolution and resonance assignments, the next immediate need is to measure how much of each structure component is present using peak area integration. ^{13}C 1D-NMR experiments are ideally suited for this purpose since all of the protons can be decoupled with broadband irradiation, to produce a spectrum with a single line for each unique carbon atom. Since the natural abundance of ^{13}C is only 1.1 %, homonuclear coupling between ^{13}C atoms does not complicate the spectrum because coupled ^{13}C-^{13}C spin pairs occur in only $1/10^4$ molecules.

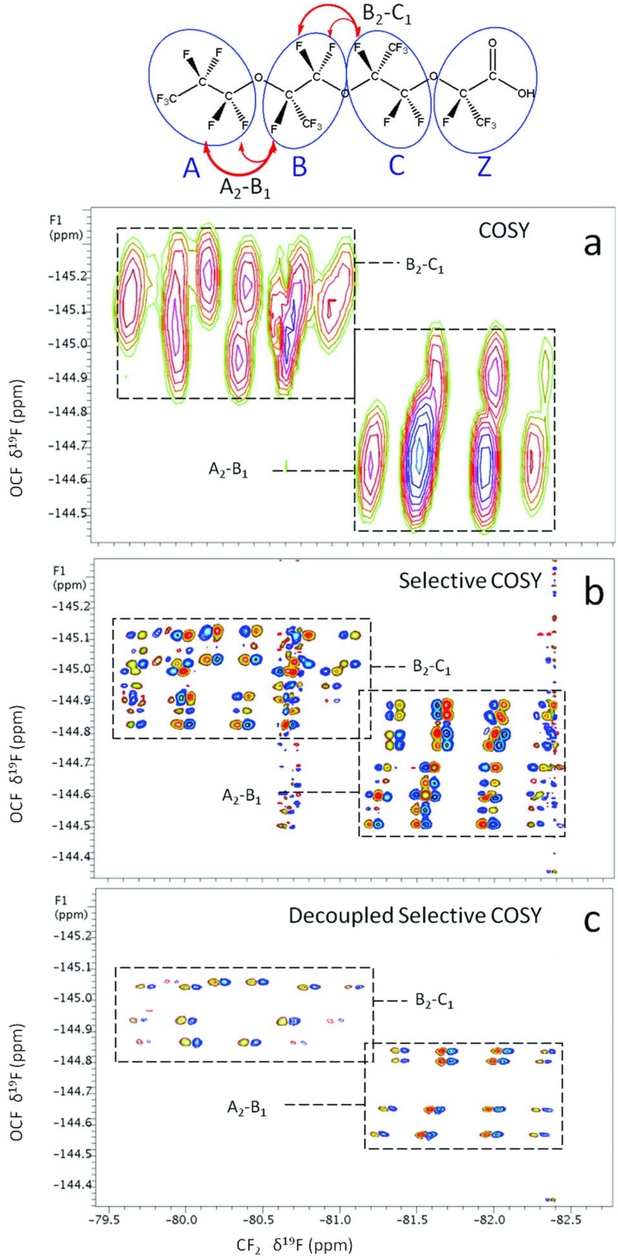

Figure 6. 2D-COSY spectra of hexafluoropropylene oxide tetramer: a) segment from a standard COSY spectrum; b) full spectrum from a selective COSY experiment; and c) full spectrum from a selective COSY experiment with homonuclear decoupling in the f_1 dimension.

Downloaded by DUKE UNIV on June 20, 2012 | http://pubs.acs.org
Publication Date (Web): October 14, 2011 | doi: 10.1021/bk-2011-1077.ch003

When doing NMR of abundant spins such as ^{1}H or ^{19}F, homonuclear coupling produces spectra with complex multiplets. In complex molecules, these multiplets result in overlapping patterns which can't be resolved from one another, and can't be easily integrated. Although many attempts have been made, until now it has not been generally possible to accomplish broadband decoupling of homonuclear spins to produce 1D-NMR spectra with integrable singlets. Until recently, it has only been possible to obtain spectra with single frequency irradiation of the resonance of a single atom, or at best to perform homonuclear decoupling of a narrow multiplet.

Recently, Espindola et al. (*17*) described the use of state-of-the-art rf hardware to produce shaped inversion pulses. These capabilities were used to decouple an arbitrary combination of nuclei with resonances in various spectral windows, and produce a spectrum of singlets with broadband decoupling of the rest of the nuclei in the spectrum.

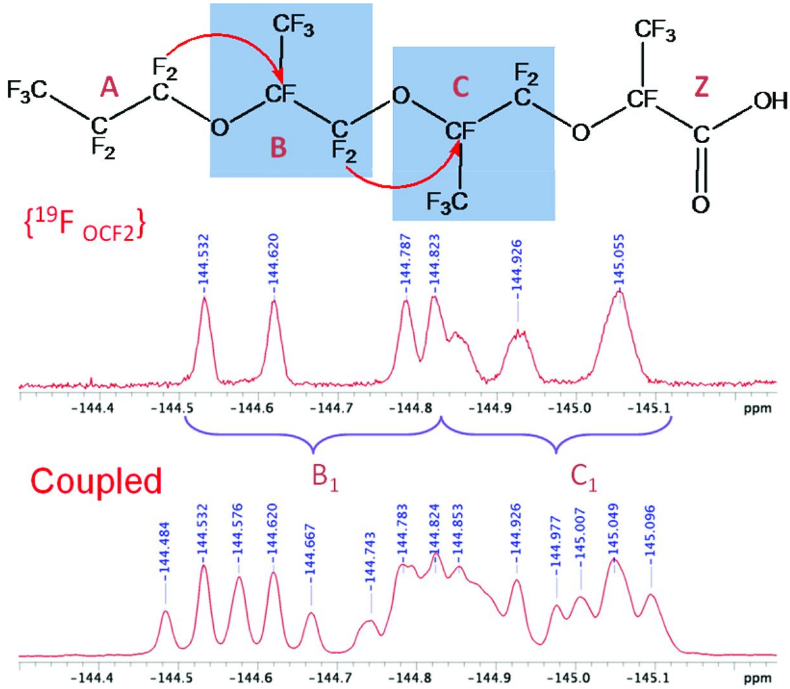

Figure 7. Selected (CF containing) regions from the 470 MHz ^{19}F 1D-NMR spectra of hexafluoropropylene oxide tetramer: (bottom) standard spectrum; (top) spectrum with broadband decoupling of CF_2 resonances.

This is illustrated with the spectra of T(HFPO) shown in Figure 7, where the C-F containing regions of the 470 MHz ^{19}F spectra are shown. In the bottom spectrum, coupled C-F multiplets from the middle (B and C) monomer units shown in the structure at the top of the figure (B_n and C_n designate the fluorines of CF_n groups in monomer units B and C in the structure). These resonances were resolved and assigned with the aid of the selective COSY spectra shown above. It is impossible to resolve and integrate the 8 separate sets of resonances due

Downloaded by DUKE UNIV on June 20, 2012 | http://pubs.acs.org
Publication Date (Web): October 14, 2011 | doi: 10.1021/bk-2011-1077.ch003

Downloaded by DUKE UNIV on June 20, 2012 | http://pubs.acs.org
Publication Date (Web): October 14, 2011 | doi: 10.1021/bk-2011-1077.ch003

to large couplings with the CF_2 groups. In structure such as this, the four-bond couplings are usually large (20-40 Hz), compared with the three-bond couplings to the CF_3 groups.

The top spectrum was collected with shaped inversion pulses between data point samplings in the FID, such that the CF_2 atoms (resonances between -75 and -90 ppm) are inverted. As a consequence, homonuclear couplings that evolve during the first half of the dwell time (period between sampling of two data points in the FID) are refocused during the second half of each dwell time. From the homonuclear decoupled spectrum, shown in the top of the figure, it is possible to separately integrate most of the resonances. At worst, it is possible to perform peak deconvolution on some of the overlapping resonances to obtain quantitative information.

Sensitive Detection

As with most spectroscopic techniques, in NMR there has been a constant struggle to improve the receptivity of instruments so that spectra can be obtained with smaller quantities of material. Over the past 60 years, this improvement has been incremental, and resulted from improvements in instrument stability, magnet homogeneity, magnetic field strength, rf electronics, solid state circuitry and probe design. The exception has been the introduction of Fourier transform techniques in the late 1960's and early 1970's, which lead to a quantum leap in receptivity. The cumulative effect of these many incremental improvements has been a 10^5-10^6 fold gain in receptivity such that with the most sensitivie NMR instruments it is now possible to get ^1H NMR spectra from 10-100 ng of material compared with 100mg of material required to obtain spectra from instruments available in the early 1960's.

After many years of instrument improvements, the major sources of noise in the NMR experiment are now the detection coil and the sample itself. In the past decade, probes with the detection coil cooled to cryogenic temperatures have become commercially available. In these probes the detection coil is typically cooled to 20^0K, while the sample located a few mm away, remains at ambient temperature. Such probes provide a factor of 4-5 gain in receptivity compared to older style probes in which the coil remains at ambient temperature. Most of these commercial probes are designed to operate with the sample near ambient temperature, using 5mm sample tubes for sensitive detection of ^1H, while decoupling ^{13}C and ^{15}N. These probes are primarily designed and used for biological applications. For polymer applications we are not usually sample limited, so that it is desirable to study larger samples. Also, often polymers require high temperature to dissolve or swell the material for high resolution solution NMR studies.

Zhou et al. (*18*) describe a new commercial "cryoprobe" designed for ^{13}C detection using 10 mm sample tubes, heated at temperatures up to 420^oK, while the coil temperature remains at 20^oK. Under these conditions, they observed almost 6-fold increase in receptivity compared to a standard 10 mm probe designed for

^{13}C detection. This new cryoprobe permitted them to study the minor structure components in poly(propylene-co-1-octene) using ^{13}C NMR.

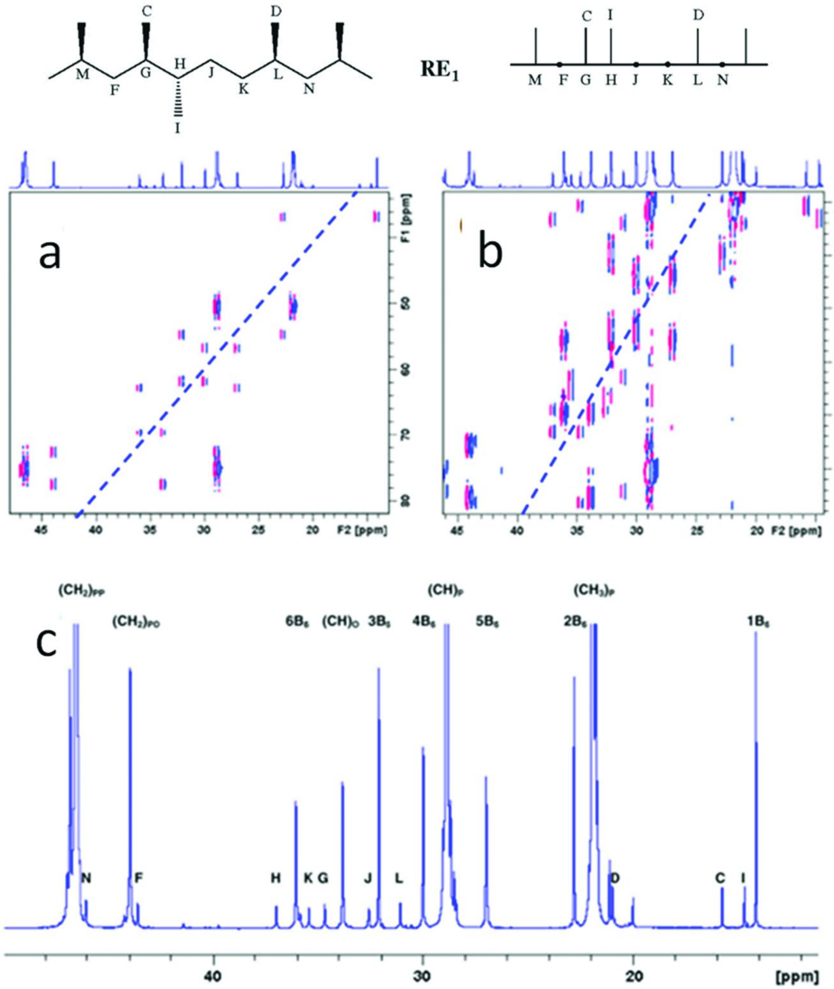

Figure 8. 100 MHz ^{13}C NMR spectra of poly(propylene-co-1-octene): a) INADEQUATE spectrum showing correlations of the major structure components; b) vertical amplification of the spectrum in (a) revealing additional correlations from minor structure components; and c) 1D-NMR spectrum. Reproduced with permission from reference (18).

In this copolymer, the major structure component is polypropylene; the next major component is derived from insertions of 1-octene units within the polypropylene backbone; and finally the smallest component is derived from inverse addition of propylene units. The study of this polymer's structure

Downloaded by DUKE UNIV on June 20, 2012 | http://pubs.acs.org
Publication Date (Web): October 14, 2011 | doi: 10.1021/bk-2011-1077.ch003

requires sensitive detection of the weakest signal components. The 100 MHz ^{13}C 1D-NMR spectrum is shown in Figure 8c; the three signals that are off scale (labeled $(CH_2)_{PP}$, $(CH_2)_{PO}$, $(CH)_P$ and $(CH_3)_P$) are derived from CH, CH_2 and CH_3 carbons of "normal" polypropylene segments; the set of signals that fall near half scale (labeled $1B_6$ – $6B_6$ and $(CH)_O$) are from 1-octene units incorporated into the polymer; and the weak signals that are labeled with capital letters (C, D and F-N) are derived from inverse addition of propylene units. The latter labels indicate resonance assignments corresponding to the labels on the structure at the top of Figure 8.

The 2D-INADEQUATE experiment provides correlations among the resonances of carbons related by ^{13}C-^{13}C attachments in a structure. Because these spins occur together in only $1/10^4$ molecules, obtaining an INADEQUATE spectrum is 100 times more difficult than performing a simple ^{13}C 1D-NMR experiment. Their plot of an INADEQUATE spectrum in Figure 8a, showing correlations identifying the major structure fragments in the polymer, represents the capabilities of most state-of-the-art NMR spectrometers. The vertical amplification of this spectrum, shown in Figure 8b, reveals additional correlations identifying low concentration structures from inverse propylene addition. These structures are present in 3-5 times lower concentration.

Their 2D-INADEQUATE spectrum took 2.6 days to collect using a "cryoprobe" with a 10 mm coil. They estimated that it would take 2.6 months to collect a similar spectrum on a 400 MHz spectrometer using a standard probe with a detection coil at ambient sample temperature. If quantitative ^{13}C 1D-NMR experiments are to be performed with senstitive detection of weak signals, cryoprobes like the one described here could boost an instrument's productivity by 30-fold when long-term signal averaging is necessary. Alternatively, it might be possible to detect weak signals in a weekend using this cryoprobe, when another lab with a standard probe would never be able to dedicate 3 months to collection of a single spectrum.

Multiple Receiver Systems

Multiple receiver systems have been used to speed up collection of image data in magnetic resonance imaging (MRI) applications. These multiple receiver systems are beginning to appear in labs doing high resolution NMR in chemistry related applications.

In one paper, representative of one application area, Kupce et al. (*19*) were able to nest $^{1}H\{^{13}C\}$-HSQC and $^{19}F\{^{13}C\}$-HSQC 2D-NMR experiments and to use an instrument with two receiver channels to simultaneously detect the ^{1}H and ^{19}F signals (Figure 9). Such work had not been reported with a polymer sample so the illustration here is with data from a small molecule. Two separate experiments were performed simultaneously to double the productivity of the instrument. The reader is encouraged to look at the cited literature in this paper to learn of other possible variations. These experiments can increase the productivity of instruments that are dedicated to routine screening of samples.

Downloaded by DUKE UNIV on June 20, 2012 | http://pubs.acs.org
Publication Date (Web): October 14, 2011 | doi: 10.1021/bk-2011-1077.ch003

Downloaded by DUKE UNIV on June 20, 2012 | http://pubs.acs.org
Publication Date (Web): October 14, 2011 | doi: 10.1021/bk-2011-1077.ch003

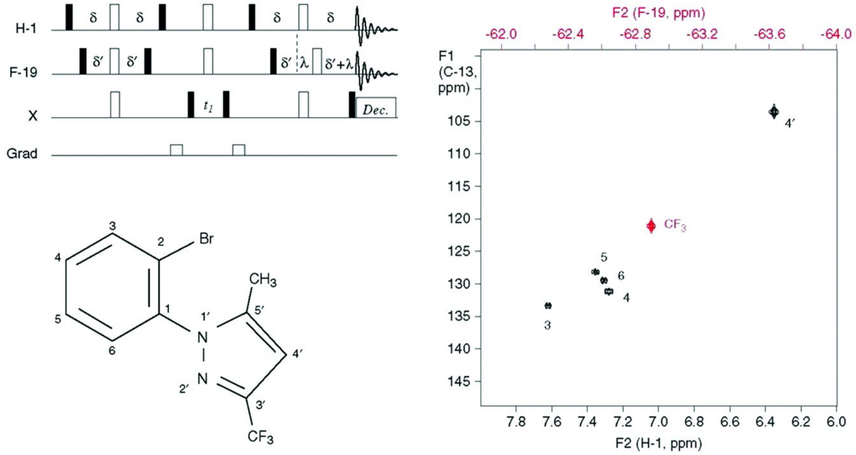

Figure 9. Nested HSQC pulse sequences (left) to produce ^1H (black) and ^{19}F detected HSQC spectra (right). Reproduced with permission from reference (19).

Alternative Lock Channel

Another valuable use of instruments with a second receiver systems is as an alternative to the field-frequency locking system. In order for the NMR signal to add coherently, the peak frequencies must remain fixed from one transient (and one spectrum) to the next. To compensate for magnetic field drift, instruments have a third complete rf channel to monitor the frequency of a third nucleus and to adjust B_o to maintain a constant resonance frequency. In almost all cases, this third nucleus is ^2H from a deuterated solvent. Deuteration of the solvent also has the fringe benefit of reducing the solvent signal strength, especially in ^1H NMR.

In solution NMR studies of polymers, it is often necessary to use exotic solvents to dissolve the material, or to heat and swell the polymer. For example, chlorinated solvents such as tetrachloroethylene or dichlorobenzenes are often used to study polyolefins, because they permit heating the sample to 120-140°C. At these temperatures, the polymers swell and produce high resolution spectra. Often deuterated forms of these solvents are expensive or unavailable and alternatives are needed to provide the needed lock signal. These range from incorporating a small amount of a deuterated cosolvent, to addition of a capillary containing a high boiling deuterated solvent to the center of the NMR tube.

Kupce and Freeman (*20*) used their second receiver system to monitor the frequency of an independent NMR signal and to calculate a correction factor to be applied to the spectrum during the data processing stage. Their results are shown in Figure 10. In Figure 10a and b, the results from plotting a ^{13}C NMR signal from a 0.1 M solution of sucrose are shown without and with compensation for field drift, respectively. Figure 10c and d show the effects of field drift on the HMBC spectrum without and with compensation, respectively.

Downloaded by DUKE UNIV on June 20, 2012 | http://pubs.acs.org
Publication Date (Web): October 14, 2011 | doi: 10.1021/bk-2011-1077.ch003

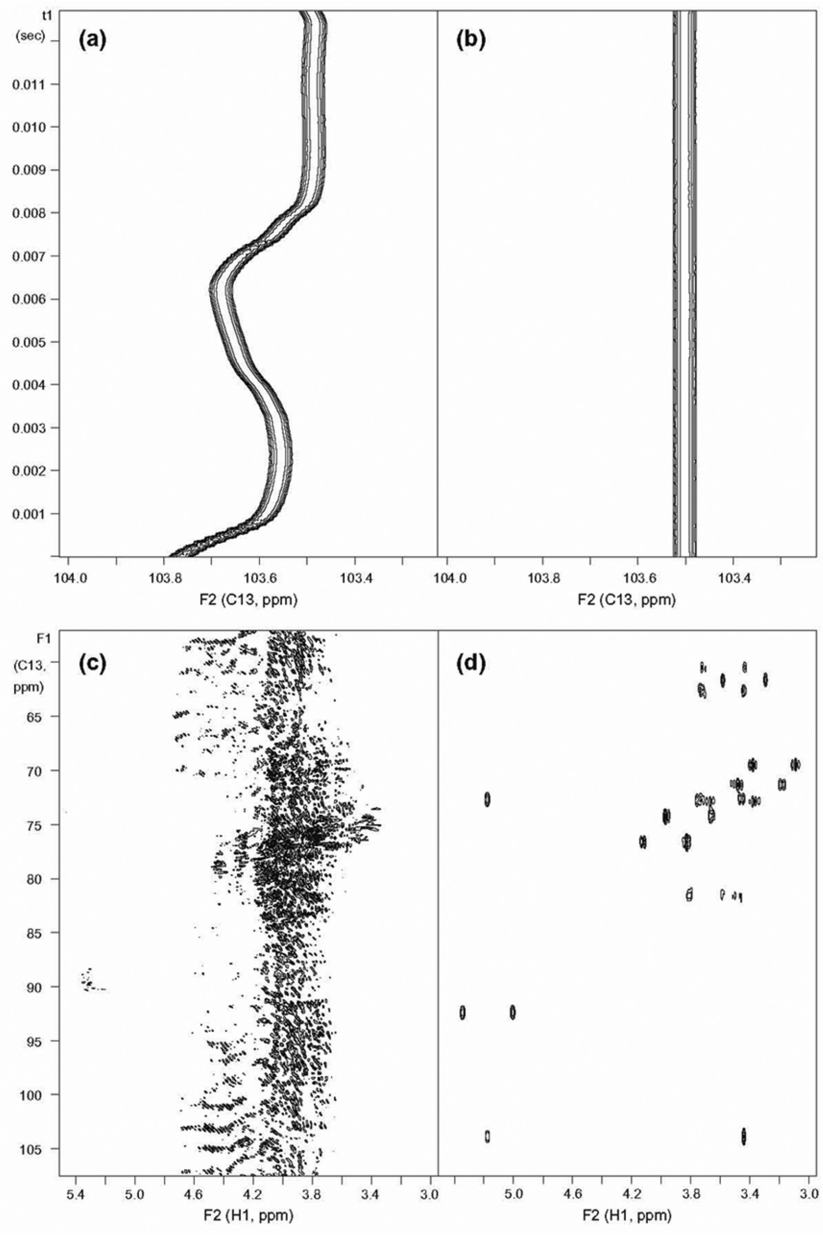

Figure 10. Results from using a second receiver as an alternate lock channel while collecting HMBC spectra of 0.1 M sucrose in D_2O: a) ^{13}C signal monitored without lock and b) the same signal as in (a), but with digital compensation for field drift; c) HMBC spectrum without lock and d) same spectrum as in (c), but with compensation for field drift. Reproduced with permission from reference (20).

Summary

This paper presents a small sampling of the new NMR capabilities that can potentially impact polymer NMR spectroscopy. There are many advances in NMR hardware, software and methodology that could not be mentioned here. Space limitations require that the list stop at some point. If anything, the NMR field seems to be advancing at a more rapid pace than ever before. Advancements continue to contribute to improving the sensitivity of the NMR experiment so that it is possible to work with smaller samples (or detect lower occurrence structure components). New NMR methodologies help to provide information about new structure components so that detailed structure information can be resolved. New computers and software automate experiment setup so that once methodology is developed, it can be applied by users who are not expert in NMR. Development of powerful computers and software will make it easier to extract information from complicated spectra or groups of spectra. For new workers in this field, the times are as exciting as ever.

Acknowledgments

The author wishes to thank the National Science Foundation (DMR-0905120) for financial support during the preparation of this work. The author also wishes to thank current and former research group members, University of Akron NMR Center staff members (past and present) and collaborators who are too numerous to mention here. They have contributed in countless ways to exciting research and learning experiences over the past few decades.

References

1. Rinaldi, P. L.; Li, L.; Li, X.; Paudel, L.; Twum, E. B. Solution NMR of Polymers. In *Comprehensive Encyclopedia of Polymer*; Spiess, H., Ed.; Elsevier: New York, 2011; Chapter 2.06 (in press).
2. Mirau, P. A. *A Practical Guide to Understanding the NMR of Polymers*; Wiley-Interscience: New York, 2004.
3. Silverstein, R. M.; Webster, F. X.; Kiemle, D. J. *Spectrometric Identification of Organic Compounds*, 7th ed.; John Wiley & Sons: Hoboken, NJ, 2005.
4. Cheng, H. N.; Bennett, M. A. *Anal. Chem.* **1984**, *56*, 2320–2327.
5. Miri, M. J.; Pritchard, B. P.; Cheng, H. N. *J. Mol. Model.* 2010, DOI 10.1007/s00894-010-0880-8.
6. Qui, X.; Redwine, D.; Gobbi, G.; Nuamthanom, A.; Rinaldi, P. L. *Macromolecules* **2007**, *40*, 6879–6884.
7. Momose, H.; Hattori, K.; Hirano, T.; Ute, K. *Polymer* **2009**, *50*, 3819–3821.
8. Hu, J.; Krishnamurthy, K. *Magn. Reson. Chem.* **2008**, *46*, 683.
9. Nyber, N. T.; Duus, J. O.; Sorensen, O. W. *J. Am. Chem. Soc.* **2005**, *127*, 6154.
10. LeMaster, D. M.; Hernandez, G. *Macromolecules* **2000**, *33*, 3569–3576.
11. Stejskal, E. O.; Tanner, J. E. *J. Chem. Phys.* **1968**, *49*, 1768–1777.
12. Morris, K. F.; Johnson, C. S., Jr. *J. Am. Chem. Soc.* **1992**, *114*, 3139–3141.

Downloaded by DUKE UNIV on June 20, 2012 | http://pubs.acs.org
Publication Date (Web): October 14, 2011 | doi: 10.1021/bk-2011-1077.ch003

13. Antalek, B. *Concepts Magn. Reson.* **2002**, *14*, 225–258.
14. Huth, J.; Kurur, N.; Bodenhausen, G. *J. Magn. Reson., Ser. A* **1996**, *118*, 286–290.
15. Li, X.; McCord, E. F.; Baiagern, S.; Fox, P.; Howel, J. L.; Sahoo, S. K.; Rinaldi, P. L. *Magn. Reson. Chem.* In press, DOI 10.1002/mrc.2763.
16. Rinaldi, P. L.; Baiagern, S.; Fox, P.; Howel, J. L.; Li, L.; Li, X.; Lyons, D.; McCord, E. F.; Sahoo, S. K.; Twum, E. B.; Wyzgoski, F. J. *Advanced Solution 2D-NMR of Fluoropolymers*; Cheng, H. N., Asakura, T., English, A., Eds.; ACS Symposium Series 1077; American Chemical Society: Washington, DC, 2011; Chapter 21.
17. Espindola, A. P. D. M.; Crouch, R.; De Bergh, J. R.; Ready, J. M.; MacMillan, J. B. *J. Am. Chem. Soc.* **2009**, *131*, 15994–15995.
18. Zhou, Z.; Kummerle, R.; Stevens, J. C.; Redwine, D.; He, Y.; Qiu, X.; Cong, R.; Klosin, J.; Monanez, N.; Roof, G. *J. Magn. Reson.* **2009**, *200*, 328–333.
19. Kupce, E.; Cheatham, S.; Freeman, R. *Magn. Reson. Chem.* **2007**, *45*, 378–380.
20. Kupce, E.; Freeman, R. *J. Magn. Reson.* **2010**, *206*, 147–153.

Downloaded by DUKE UNIV on June 20, 2012 | http://pubs.acs.org
Publication Date (Web): October 14, 2011 | doi: 10.1021/bk-2011-1077.ch003

Chapter 4

New Insights into Amorphous Macromolecules and Their Mixtures from Advanced Magnetic Resonance Experiments

Jeffery L. White,*,[1] Marcin Wachowicz,[1] Lance Gill,[1] Joshua Damron,[1] and Justyna Wolak-Dinsmore[2]

[1]Department of Chemistry, Oklahoma State University, Stillwater, OK 74078
[2]Department of Chemistry, North Carolina State University, Raleigh, NC 27695-8204
(Current address: Liposciences, Inc., Raleigh, NC)
***E-mail: jeff.white@okstate.edu**

Amorphous blends of high molecular weight macromolecules present some uniquely challenging problems in structure-function investigations, and pose some interesting fundamental questions regarding dynamics and thermodynamics. In the absence of ordered morphologies or extensive isotopic labeling, traditional diffraction and spectroscopic techniques may not provide component-specific information. In this contribution, we review experimental methods which have been developed to specifically probe the dynamics and thermodynamics of mixing in amorphous blends. Our approach is based on advanced NMR techniques that provide chain-specific data over a wide temperature range without introduction of any isotopic labeling or probe molecules.

Introduction

The science related to polymer blends has historically enjoyed a productive marriage between intellectual pursuit and economic utility, as recently discussed in a national workshop hosted by the National Science Foundation (*1*). The notion that the polymer blend area is a mature science can be challenged by simply assessing the lack of understanding surrounding mixtures of amorphous

In NMR Spectroscopy of Polymers: Innovative Strategies for Complex Macromolecules; Cheng, H., et al.;
ACS Symposium Series; American Chemical Society: Washington, DC, 2011.

macromolecules of even the most simple chemical structure. As the polymer science community, both from an intellectual and engineering motivation, pursues increasingly complex systems, tailored composites, hybrid and hierarchical structures, self-assembly, and biologically inspired materials as outlined in a recent *Macromolecules* "Perspectives" article (*2*), we find that the same key questions that characterize problems in mixtures of amorphous polymers continue to arise in these emerging interdisciplinary areas. For example, simply measuring with confidence the length scales within which two polymers are mixed in a binary mixture of two non-crystalline macromolecules can be very challenging, even for very simple polymer chain architectures. Also, what causes amorphous mixtures to have a homogeneous, intimately mixed arrangement of its constituent chains versus a heterogeneous, phase separated morphology? If intimate mixing of the two polymer species occurs, does this mean that the chains assume new "identities" relative to their pure component characteristics, and if so, in what ways? Can we synthetically manipulate the macroscopic properties of the end-result blend by systematic variation of chemical structure? Amorphous polymer blends, which for the purposes of this contribution mean mixtures of high polymers with no crystalline regions in the final blend, represent the first step in generating complex polymer systems. As such, fundamental understanding of how they behave, and connections between microscopic structure versus end-use properties is paramount to continued progress in key areas of macromolecular science, ranging from synthetic to engineered to biological materials. In addition, the science of "soft matter" is growing as an interdisciplinary focal point for researchers from physical, biological, and materials science areas (*3*), revealing an increasingly apparent need for rigorous experimental techniques capable of providing component-specific information in heterogeneous amorphous systems. We note in passing that much of the same language that has pervaded the polymer science community is now beginning to emerge in protein and enzyme science (*4*).

In this review, we will discuss experimental strategies developed to address key questions originally motivated by our interest in understanding miscibility in technologically important polyolefin blends, which are composed of completely saturated (i.e., only sp^3 carbons and hydrogens) high-molecular weight macromolecules. Since polyolefin blends have no chemical heterogeneity, they are very difficult to study with chain-level specificity in the absence of extensive isotopic labeling. In addition, they often are composed of chains with similar dipole moments, or no permanent dipole at all, and as amorphous mixtures, exhibit broad and diffuse glass transitions. Therefore, traditional methods like dielectric spectroscopy and differential scanning calorimetry are not generally applicable to amorphous polyolefin mixtures. As various polymer combinations were examined, we found that the selectivity inherent to our experimental approach based on variable-temperature CODEX[5] solid-state NMR experiments addressed many general questions in the current polymer blend literature related to thermodynamics of mixing, differential chain dynamics, time-temperature superposition, dynamic heterogeneity, and glass transition time-scales. Guiding principles for the strategies discussed here include: [1] Non-invasive access to quantitative chain-specific information before and after formation of mixtures;

[2] Data outputs in a format accessible to the general polymer science (i.e., non-NMR) community; [3] Experimental measures of average/mean chain behavior as well as heterogeneity/distributions in chain behavior; [4] Quantitative conclusions related to the thermodynamics of macromolecular mixing; [5] General applicability to amorphous materials. These will be discussed in the ensuing sections.

Experimental Section

Complete details for the synthesis, acquisition, and characterization of the polymers have been described (*6–9*). In general, all polymers used in our studies have molecular weights in the range 30,000 – 1,000,000, i.e., synthetic high polymers well above the entanglement molecular weight. The individual systems will be described in the text when appropriate, but include polymers and various binary blends composed of atactic polypropylene (aPP), head-to-head polypropylene (hhPP: made via anionic polymerization of dienes and hydrogenation), polyethylene-co-butene (PEB: monodisperse copolymer made via anionic polymerization and hydrogenation), polyisobutylene (PIB-a commercial material), polyvinylethylene (PVE: 88% 1,2-polybutadiene enchainment), and polyisoprene (PI: 97% cis-1,4 enchainment). Representative structures for the repeat units are shown in Scheme 1.

All systems were studied in bulk, i.e., without any solvents. Miscible blends (either equimolar or 50/50 wt%) were made by casting from solutions in a good solvent, and were exposed to vacuum pumping for several days prior to use. Characterization by TGA and ^{1}H NMR revealed that no residual solvent existed in any blend.

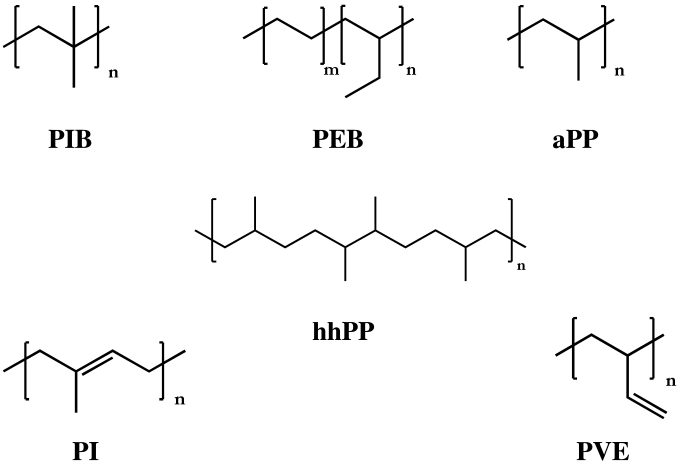

Scheme 1

In this review, we will primarily focus on an experimental strategy based on variable-temperature CODEX (Centerband-Only Detection of EXchange) experiments. However, several other experiments (including spin-diffusion measurements to verify miscibility, GPC, and DSC) were completed prior to CODEX analysis, as previously described (*7–9*). The CODEX experiment, first described by Schmidt-Rohr and coworkers in 1999 (*5*), is ideally suited for studying slow motions in macromolecules. Stated simply, it is a one-dimensional chemical exchange experiment that relies on incomplete refocusing of a chemical shift anisotropy (CSA) echo based on molecular reorientation during a mixing time. Complete details have been explained previously (*10*, *11*), but the process is schematically represented by the pulse sequence shown in Figure 1 below which is applied under magic-angle spinning (MAS) conditions.

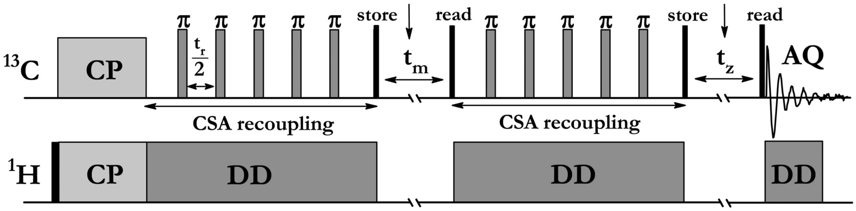

Figure 1. CODEX experiment pulse sequence applied under conditions of MAS. The value of the exchange mixing time $\boldsymbol{t_m}$ *ranges from 0.05 to 0.20 seconds for all data reported here. The total CSA evolution time corresponding to the sum of the first and second recoupling periods was* $2Nt_r = (2)(4)(0.22\ ms) = 1.76\ ms$*. The* t_z *period, to ensure a constant time experiment, was 1 millisecond.*

It is important to note that the any dynamics which occur during the mixing time are events which are detected in real time, albeit indirectly based on their attenuation of the chemical shift echo. Although we have typically used mixing times t_m values ranging from 0.050 – 0.20 seconds, in theory this value could range widely, with an upper limit defined by spin-lattice relaxation. All ^{13}C and ^{1}H measurements were collected on a Bruker DSX-300 with field strength = 7.05T. The probe temperature was calibrated using $PbNO_3$ to within ±1 K. All CODEX exchange data was acquired with an actively-controlled MAS speed (typically 4-5 kHz), a 1-ms cross-polarization contact time, rotor synchronization, and as a precaution, CODEX measurements were altered between the CODEX and reference signal every 256 scans to eliminate spectrometer drift. In practice, one acquires a reference spectrum by interchanging the constant 1-ms t_z time with the mixing time. Since this time value is too short relative to slow chain dynamics, no motion can occur during such a short mixing period. This reference experiment yields a signal of maximum amplitude (S_o), which is then compared to the experiment where the much longer mixing time t_m is used (S). The normalized difference of the two experiments is referred to as the exchange intensity **E** = $(S_o - S)/S_o$, or $\Delta S/S_o$, which quantitatively reflects slow segmental dynamics. The exchange intensity **E** is a direct function of the length of the mixing time t_m, the characteric correlation time constant for whatever type of motion occurs (τ_c), and the temperature T. The complete equations describing the quantitative relationship between **E** and these variables have been described in detail in previous publications (*7–11*). In all cases, ^{13}C spectra were analyzed.

We are cognizant of concerns arising from possible inhomogeneous polymer chain sampling based on experiments that begin with a cross-polarization step. While our primary interests revolve around very slow backbone chain dynamics at temperatures slightly below, near, and above the glass transition temperature (but much lower than terminal dynamics region), we do not wish to preferentially select chain segments that are much more rigid than the bulk. Rather, homogeneous sampling of all polymer chains in mixtures is desired. To address this concern in the context of amorphous polymer blends, we devised a modified version of the experiment employing only direct carbon polarization as the initial step in the experiment. Based on quantitative comparisons of the modified direct polarization versus CP-based CODEX results over a wide temperature range (including T_g) for atactic polypropylene (aPP), we demonstrated that results representative of all polymer chains in the sample are obtained in both experimental approaches (*12*). Therefore, we have confidence that CP-based CODEX-based exchange methods provide chain-level information representative of the bulk mixing and miscibility in amorphous macromolecules.

Results and Discussion

Using the experimental approach described above, one can extract exchange intensities E(T) versus temperature for chain specific locations, i.e., backbone CH_2 versus side-group CH_3. Whenever possible, signals from carbons in the backbone are used as reporters for slow segmental dynamics. In other cases, a methyl side group might be advantageous in that the signal is well-resolved from other signals once mixtures are formed. We will discuss examples from each approach in the following sections.

Figure 2 shows systematic comparisons of CODEX exchange intensities measured from backbone CH_2 versus side-group CH_3 in the two pure polymers (PEB and aPP) over the entire temperature range for which a measurable exchange signal is detected. This is an important control experiment, since it eliminates any uncertainty associated with additional side group dynamics that might influence the interpretation of the CODEX results in the blend, and their relevance to slow segmental dynamics. The onset of detectable exchange intensity for either functional group, as well as the temperature of the maximum E(T) value, is identical within each polymer. The absolute value of the maximum E(T) is markedly different for the backbone CH_2 vs. side-chain CH_3 signals in the PEB-66 polymer, indicative of additional ethyl branch motions which further reduce the magnitude of the chemical shift anisotropy for that pendant methyl group relative to backbone moeties, thereby decreasing E(T) values compared to the backbone CH_2. The exchange intensity for this CH_3 group in PEB-66 did increase, as expected, in experiments with longer recoupling times (not shown here). Since only a single carbon-carbon bond separates the CH_3 group from the main-chain in aPP, this dramatic difference in exchange intensity relative to the backbone is not observed. Two important points from this control experiment are:

In NMR Spectroscopy of Polymers: Innovative Strategies for Complex Macromolecules; Cheng, H., et al.;
ACS Symposium Series; American Chemical Society: Washington, DC, 2011.

(1) the temperature of the maximum E(T) value is independent of which group is measured, which means that the CH_3 signals can accurately report conformational exchange in the blend, an advantage given that they are better resolved than their respective CH or CH_2 backbone counterparts and can be deconvoluted accurately; (2) the onset of detectable E(T) signal in the CODEX experiment agrees with DSC data, in that the first one or two data points on the low temperature side of each curve coincide with the DSC T_g (PEB66 = 219 K and aPP = 262 K). Finally, in all cases a decrease in E(T) amplitude occurs when temperatures are high enough that thermally activated conformational rearrangements occur with a frequency larger than the magnitude of the CSA; this eliminates the possibility of detecting any signal differences between the exchange and reference spectrum since there is no longer orientation-dependent shielding information preserved in the system due to motional averaging.

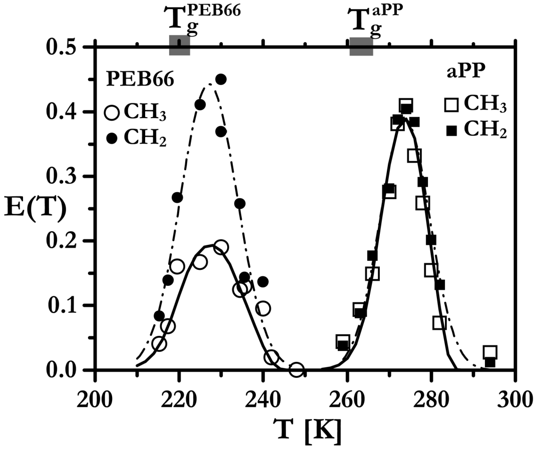

Figure 2. Normalized exchange intensities E(T) for methyl and methylene signals of pure PEB66 (a copolymer of ethylene and 66 wt% 1-butene) and pure aPP. The solid lines are Arrhenius model fits (see below) to the data, whereas the dash-dot lines are drawn through the methylene experimental points only to guide the eye. For reference, the Tg ranges via DSC are shown at the top of the figure. (Reproduced from reference (8))

From these example results, we observe that the CODEX experiment under MAS conditions provides dynamic information for slow chain reorientation/segmental motions on timescales similar to that probed by DSC methods, the latter being most familiar to practicing polymer scientists. However, as we will demonstrate in subsequent sections, and as has been described in detail in references 7-9, the overall information content and the chain specificity in mixed systems are much higher with the CODEX approach.

Figure 3 shows temperature dependent exhange intensities **E** for the same polymers described in Figure 2, and their miscible blend. We will use this miscible aPP/PEB-66 blend to illustrate the wide range of information (both model-independent and model-dependent) accessible using the variable-temperature CODEX approach, and then conclude with brief representative results from other amorphous polymer blends. The data in Figure 3 represent the outcome of three independent temperature dependent experiments; one each for the two pure polymers and a single experiment for the blend from which polymer specific exchange intensities were extracted at each temperature. This latter point is important. In contrast to other experimental approaches, a single experiment on a mixed polymer system can provide data for all components in the mixture, which eliminates sample preparation uncertainties/reproducibility that often plague sequential methods where only one component may be analyzed in any one experiment (e.g., selective deuteration, dielectric spectroscopy, etc.)

Prior to any consideration of a quantitative model to fit the results, several key points may be discerned via simple inspection of the raw data in Figure 3, comparing the response of the ^{13}C signals in the CODEX experiment for each pure polymer to the response of that same polymer in the blend. First, the PEB66 exchange intensity curve shifts to higher temperature in the blend relative to pure chains (PEB66 is the lower T_g component). Similarly, the exchange intensity curve shifts to lower temperature for the aPP in the blend compared to its pure response. For the PEB66, the E(T) maximum shifts from 227 K to 247 K upon blend formation, while the aPP E(T) maximum changes from the pure value of 273 K to 253 K in the blend. Although each curve exhibits an identical 20 K change, they do not converge to an identical common value (5-7 K difference in E(T) maxima) even though the chains are intimately mixed. While omitted from the figure in order to maintain clarity, the E(T) versus T curve for the backbone CH_2 peak of aPP *in the blend* has a maximum at the same 252-253 K position as the CH_3 peak shown in Figure 3. Secondly, the breadth of each E(T) curve increases for either component in the blend relative to the pure polymer, especially for aPP. Finally, the absolute value of E(T) at each temperature across the detectable range decreases in the blend relative to the unmixed result for both polymer components. Although each temperature dependent exchange intensity curve decreases in intensity and increases in breadth for the polymers in the blend compared to the pure polymers, the overall integrated area under the curve fits (vide infra) remains constant for each polymer, within the error of the data analysis. While the intermediate temperature values for the E(T) curves are reminiscent of DSC results on blends, the ability to extract these specific details for each polymer in an amorphous mixture by simultaneous detection of the two unique E(T) curves is difficult using traditional thermal analysis methods. Typically, DSC traces on multicomponent miscible blends are broad and featureless, and one cannot discern individual behaviors for the polymer components. We conclude from these points that the overall dynamic heterogeneity for both polymer chains increases in the blend, and in addition, it is also known that the CODEX exchange intensity decreases with increasing number of sites involved in the exchange process for a fixed recoupling and mixing time (*11*). The details specifying exactly how the dynamic heterogeneity increases for both chains will be discussed in the following sections, and the reader can consult references 7-9 (and references therein) for additional details.

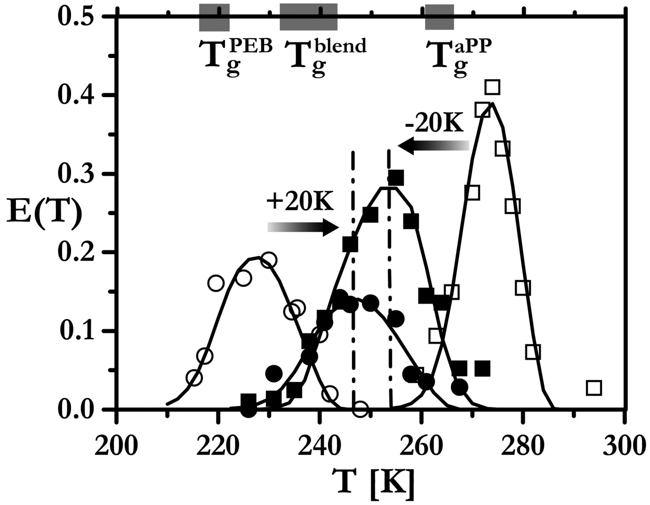

*Figure 3. Normalized exchange intensities **E(T)** for pure PEB66 (O), PEB66 in the blend (•), pure aPP (□), and aPP in the blend (■). The smooth lines are fits to the data using an Arrhenius model as described in the text. Note shifts of equal but opposite magnitude for each component upon blend formation, but a lack of complete convergence to a common temperature for the exchange intensity maximum of each polymer in the blend. The 5K/min scan DSC T_g range for each polymer and the blend is plotted for reference on the top of the figure, with the box length representing the beginning and end of the endotherm. (Reproduced from reference (8))*

Historically, the polymer science community espouses a miscible blend is characterized by identical Tg's for each polymer component in the miscible blend. While this can be true, it should not be taken as a criterion for miscibility, since Figure 3 above and Figure 8 (see below for further discussion of the PI/PVE miscible blend) clearly demonstrate that unique glass transitions (or "effective Tg's") can occur for constituent polymers in a miscible blend. Our results are in agreement with recent publications by Lodge discussing inequivalent Tg's for the polymers in miscible blends (*13*, *14*).

The fits to the experimental data shown in Figures 2 and 3 were obtained by combining isotropic rotational diffusion with a temperature-dependent discrete log Gaussian correlation time distribution/Arrhenius model (*15–19*). The absolute value of the exchange intensity E(T) at each temperature, for a fixed recoupling and mixing time, depends on the correlation time constant characteristic of the motion modulating the chemical shift anisotropy as well as the distribution of correlation time constants for all of the segments in the amorphous polymer or polymer mixture. We use a linear model that relates the width of the correlation time distribution to increasing temperature (*20*). Key results that can be obtained from the analyses include central correlation time constants for slow backbone reorientations in the pure and mixed systems (beginning from slightly below the glass transition to higher temperatures, but still in segmental dynamics regime), the width of the correlation time constant distribution in both pure and mixed systems, and activation energies for segmental dynamics in the neat and blended polymers.

We recognize that other temperature dependent models may be more familiar to the polymer scientist. Figure 4 shows a comparison of the correlation time distribution/log Gaussian/Arrhenius model discussed above with a KWW/WLF analysis for the exchange intensity data from pure aPP and aPP in the blend; this is the same aPP raw data shown in Figure 3. The KWW/WLF fitting parameters are reported in the captions to Figures 4 and 5; we observe excellent agreement between the two models in terms of correlation time values over the temperature range of our data. Such low β values upon blend formation are consistent with increased dynamic heterogeneity in aPP,[11] as is apparent from direct inspection of the E(T) exchange curve intensities in Figure 3 and 4. Detailed comparisons of KWW β values to corresponding values of the correlation time distribution widths **g(τ)** are provided in the Supporting Information to Reference (*8*). That equivalent correlation times for the center of the distribution (τ_c) are obtained using either model is more clearly evident by the representation of their temperature dependence for both polymer components in Figure 5. One observes that the temperature dependence of the slow chain dynamics for PEB66 and aPP are very different. Figure 5 also shows that while the magnitude of the change in τ_c values upon blend formation differs between the two polymers significantly at any temperature (ca. 5 decade decrease in aPP versus ca. 2.5-3 decade increase in PEB66), the two polymer components *in the blend* have identical values of τ_c near 250 K.

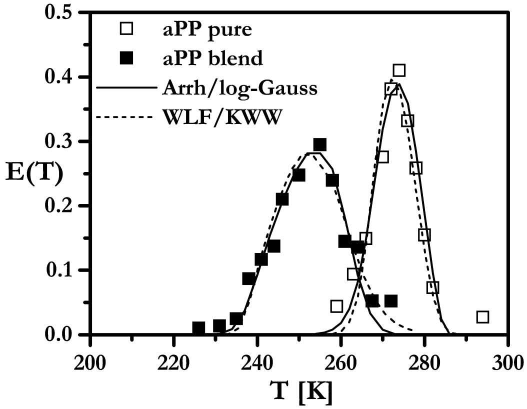

Figure 4. Comparison of fits to the aPP exchange data obtained using two different models: (1) Arrhenius temperature dependence of correlation times with variable-width log-Gaussian distribution, and (2) WLF temperature dependence combined with KWW distribution. The WLF/KWW parameters for pure aPP were $C_1 = 15.5$, $C_2 = 41$ K, $\tau(T_g) = 100$ s, $T_g = 259$ K, $\beta = 0.8$, whereas for aPP in blend $T_g = 237$ K and $\beta = 0.2$ was used. (Reproduced from reference (8))

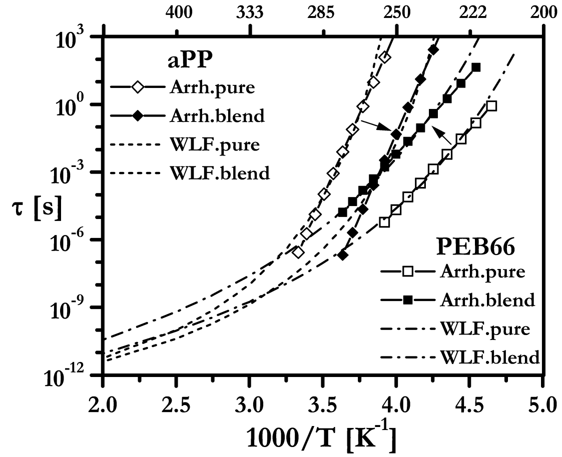

Figure 5. Temperature dependence of correlation times obtained using Arrhenius and WLF models for the aPP/PEB66 miscible blend. The WLF parameters for pure aPP were: $C_1 = 15.5$, $C_2 = 41$ K, $\tau(T_g) = 100$ s, $T_g = 259$ K, whereas for aPP in blend $T_g = 237$ K was used. For pure PEB66 we used $C_1 = 15.5$, $C_2 = 55$ K, $\tau(T_g) = 100$ s, $T_g = 210$ K, and the best fit for PEB66 in blend was obtained with $C_2 = 68$ K and $T_g = 224$ K. An Arrhenius model can be treated as linear approximation to the WLF curve, since both Arrhenius and WLF models give similar results over the temperature range for slow motions near Tg. (Reproduced from reference (8))

Figure 5 also clearly demonstrates that quantitative T_g timescales are revealed by these experiments, both for the pure polymers and the polymers in the blends. The correlation time constants for T_g in pure PEB and pure aPP both appear to be between 10 and 100 seconds (PEB near 10 and aPP nearer 100), but most importantly the data indicates that the change in T_g timescales, as well as their absolute values, for either component once the miscible blend is formed are quite different outside of a very narrow temperature range (250-260K).

Figure 6 shows calculated correlation time distributions from the fits to data in Figures 2 and 3 for the aPP component, demonstrating how the correlation time distribution function **g(τ)** can influence **E(T)** (*21*). We note how much broader the correlation time distributions become upon formation of the blend, and also, the increased distribution width near the T_g value (low T) for a pure polymer. By comparing Figures 5 and 6, we immediately observe that while central correlation time constants converge for each component in the miscible blend, albeit changing by largely different values, that the correlation time distributions actually diverge. Figure 6 shows that aPP, i.e. the high Tg component, becomes much more dynamically heterogeneous relative to its pure state, which is a common result for binary blends we have examined to date. Indeed, the total dynamic heterogeneity in the blend is much larger than the sum of the two unmixed polymer components, an important concept as one considers the thermodynamics of mixing in amorphous macromolecules (*vide*

In NMR Spectroscopy of Polymers: Innovative Strategies for Complex Macromolecules; Cheng, H., et al.;
ACS Symposium Series; American Chemical Society: Washington, DC, 2011.

infra). The reader may consult references 7-9 to see more detailed representations of correlation time distributions, and different schematics depicting their width as a function of temperature for pure and mixed states.

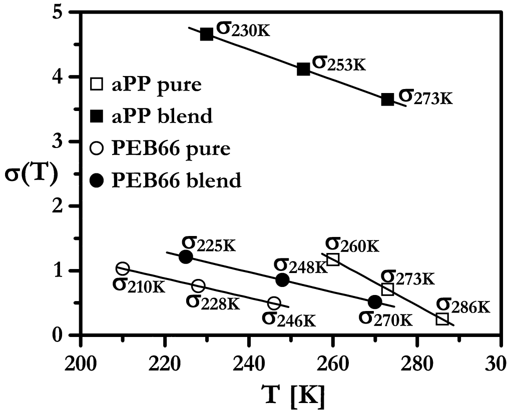

Figure 6. Temperature dependence of correlation time distribution widths σ for pure versus blended aPP and PEB66. (Reproduced from reference (8))

For brevity, only the variable temperature CODEX exchange curves are shown for two additional blend systems in Figures 7 (PIB/hhPP) and 8 (PI/PVE), along with fits to the raw data using the techniques described above. PIB/hhPP is unique among miscible blends we have studied to date in that the CODEX exchange curves do converge to the same value (as defined by onset of detectable exchange intensity, or more definitively by the maximum in the curve). If one determines the central correlation time constant for the temperature corresponding to the maximum in the E(T) curve, an identical value is observed for each polymer component in the blend. However, the change in segmental correlation time constants upon formation of the miscible blend is again much larger (by several orders of magnitude) for the high-Tg component hhPP than the low-Tg PIB component. Interestingly, the temperature where maximum exchange intensity occurs, as indicated by the vertical arrows in Figure 7, is 5-7 degrees lower than predicted by Gordon-Taylor/Fox equation mixing rules. In other words, it does not agree with composition-weighted average values, and qualitatively suggests an entropically driven mixing. Quantitative calculations based on central correlation time constants determined experimentally for the pure and mixed polymers, using the approach described here, confirm that positive configurational entropies of mixing exist for this blend, as well as other miscible polyolefin blends we have examined to date.

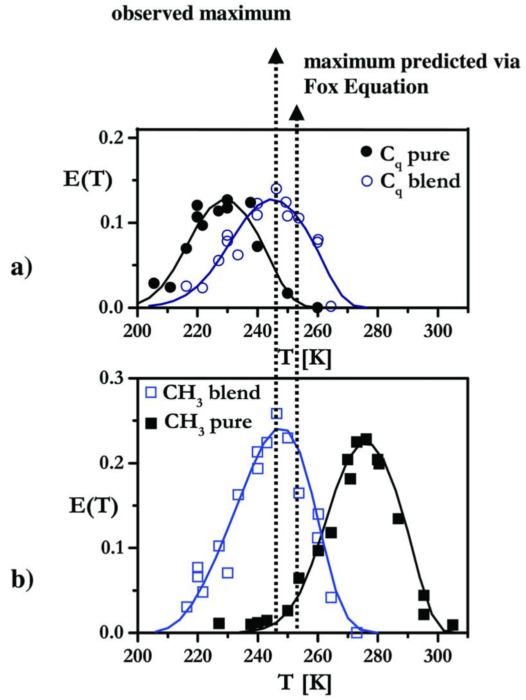

Figure 7. Normalized exchange intensities ***E(t_m)*** *for* ***a)*** *pure PIB measured at the quaternary backbone carbon (•) and PIB in the blend (o), and* ***b)*** *pure hhPP (■) and hhPP in the blend (□). Note the common exchange maximum temperature T=246 K for each polymer in the blend (left arrow) and the Fox equation prediction (right arrow). The smooth lines are fits to the data as described in the text. (Reproduced from reference (7))*

Figure 8 shows exchange curves for the PI/PVE miscible blend system. Note the apparent similarities between the general shape/location of the four curves and those in Figure 3, in that the curves for the polymers in the miscible blend do not converge to the same values (unlike the PIB/hhPP system in Figure 7). In total, these three results suggest that one cannot assume how slow segmental chain dynamics, which are the macromolecular dynamics most important for mechanical properties, change when a miscible blend is formed. Stated differently, one cannot assume that (a) a common glass transition will occur for the polymers in a miscible blend, and (b) composition-weighted averaged chain behavior takes place.

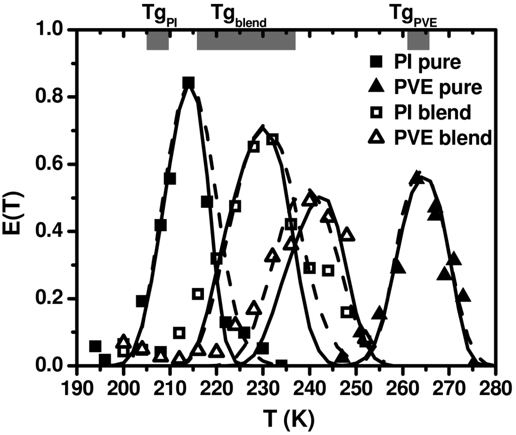

Figure 8. Normalized 200-ms exchange intensity ***E(T)*** *curves for pure PI and PVE and the same components measured independently in the blend. All data shown here reflect only backbone aliphatic carbons, not side chains or olefinic groups. The solid lines are fits to the data using an Arrhenius model with a variable-width log-Gaussian correlation time distribution. The dashed lines are fits to the data using the WLF/KWW model. The thick gray lines at the top of the figure indicate the 10 K/min DSC T_g range for the two pure polymers and the miscible blend. (Reproduced from reference (9))*

Complete quantitative analysis, using both Arrhenius and WLF/KWW models, of the data in Figures 7 and 8, including effective T_g's, central correlation time constants, correlation time distributions, and activation energies are reported in references (*7*) and (*9*). It is worth mentioning here that the PI/PVE system was an important control case as this blend has been studied by multiple investigators using a wide variety of techniques (*22–27*). However, as ours was the first method to get chain-selective information non-invasively from a single set of experiments on a single blend sample, we were pleased to find good agreement between quantitative data from our approach and selective deuteration techniques involving multiple blend preparations, as previously described (*26*, *27*). In addition to central correlation time constants, correlation time distributions, and activation energies, segmental friction coefficients were determined for each component in the PI/PVE system using a KWW/WLF treatment of the central correlation time data, where the characteristic segment length was taken as equal to the Kuhn length, or 1.1 nm.

During this review, we have deliberately pointed out model-independent and model-dependent conclusions accessible via the variable-temperature CODEX approach. Given that many of the key quantitative results come from fitting the raw E(T) data, it is appropriate to consider a mechanism by which the central correlation time constants τ_c can be evaluated independently.

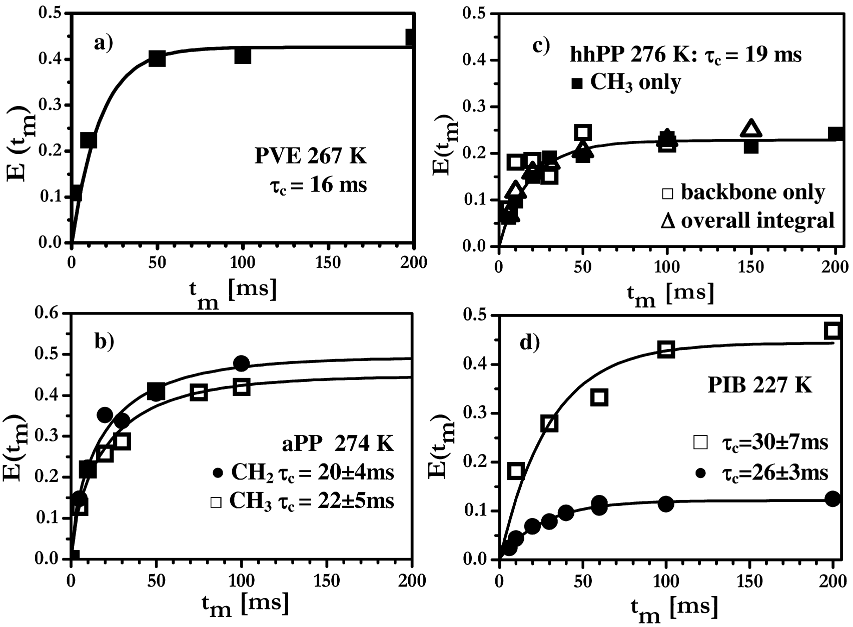

Figure 9. Exchange time constants extracted from an exponential fit to the rising exchange intensity curves are indicated on each of the Figures 9a-d for PVE, atactic PP (PP), head-to-head PP (hhPP), and polyisobutylene (PIB), respectively. For each of these same four polymers, at the same temperature as indicated on each plot, the respective central correlation time constants obtained from full analysis of the variable temperature exchange intensity curves of the type represented by the data in Figures 3, 4, 7, and 8, are: (a) τ_c = 14 ms (b) τ_c = 24 ms (c) τ_c = 20 ms (d) τ_c = 25 ms. The temperatures indicated in a-d are equal or very nearly equal to the exchange intensity maximum temperature for each polymer, resulting in similar values of τ_c. (Reproduced from reference (9)).

In Figure 9, we show results from such an independent evaluation, in which τ_c's were determined at temperatures near the maxima in the E(T) curves, using variable mixing time experiments for four different pure polymers including PVE, atactic polypropylene (PP), head-to-head polypropylene (hhPP), and polyisobutylene (PIB) at the indicated temperatures. The correlation time constants, extracted from an exponential fit to the rising intensity curve, are indicated on each of the Figures 9a-d, while values extracted from fitting the

CODEX data are listed in the Figure 9 caption. (In figures where there are multiple data points, either multiple carbon positions in the polymer chain were probed, or as in Figure 9d, two different recoupling times in the CODEX experiment were compared.) The results in Figure 9 indicate that the correlation time constants obtained by full analysis of the raw data of the type shown in Figures 3, 4, 7, and 8 are accurate, with the largest difference for the polymers shown equal to 12% for PVE, and significantly less in the other three cases. While the time required to generate the experimental data in Figure 3, 7, or 8 is not trivial, such an approach is significantly shorter (by a factor of 5 to 10) than the time required to obtain full variable mixing time exchange curves, like those shown in Figure 9, over wide temperature ranges. This control experiment, as well as comparisons of PI and PVE data to previously reported correlation time values (*9*), indicate the quantitative robustness of our approach for macromolecular mixtures.

Given that we can calculate central correlation time constants characteristic of slow segmental reorientation for pure and mixed polymers over a wide temperature range, we can use the Adams-Gibbs formalism to quantitatively assess entropy changes that occur upon formation of a miscible blend (*28*). The relationship between configurational entropy $\mathbf{S_c}$ and $\boldsymbol{\tau_c}$ is:

$$\tau_c = \tau_o \exp(c/TS_c),$$

where we equate τ_c the value of the correlation time at the center of the distribution for either a pure polymer or the same polymer in a blend. Using data of the type shown in Figure 5, and assuming τ_o ranging from 10^{-12} s to 10^{-15} seconds and c as constant for each polymer in pure versus mixed state at a fixed temperature (usually taken as the temperature corresponding to maximum exchange intensity), we have determined that the total change in configurational entropy for PIB/hhPP and aPP/PEB-66 blends ranges from +10 to +20% upon formation of the miscible blend (and relative to the unmixed components). Therefore, one must conclude that an increase in the number of surface contacts either between dissimilar polymer chains or within chains themselves (an enthalpic model) in miscible polyolefin blends simply does not exist relative to the unmixed pure polymers. We view this as a conservative limit, since it does not quantitatively capture the large increases in the distribution of correlation times, or dynamic heterogeneity, associated with forming the miscible blend. The PI/PVE system is somewhat different in that it possesses sp^2 functional groups, and therefore free electron density which increases polarizability and induced association. Even so, Figure 10 clearly demonstrates that there is a slight positive entropy of mixing associated with forming the miscible blend, relative to the sum of the configurational entropy for the two unmixed components. The ability to non-invasively, selectively, and quantitatively determine this kind of data for amorphous polymers in a miscible mixture is a key advantage of this experimental approach.

In NMR Spectroscopy of Polymers: Innovative Strategies for Complex Macromolecules; Cheng, H., et al.;
ACS Symposium Series; American Chemical Society: Washington, DC, 2011.

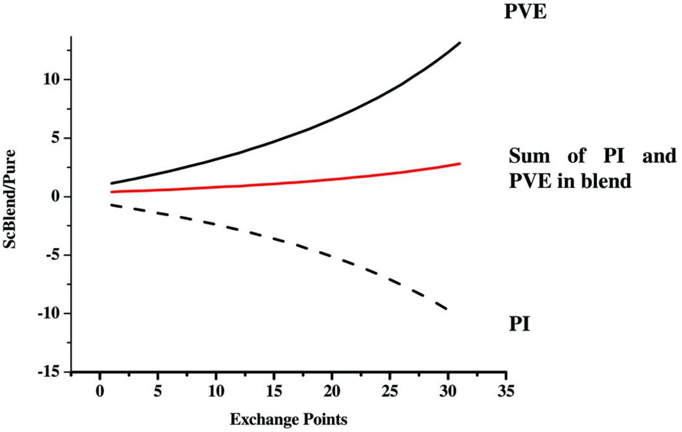

*Figure 10. Calculated values of the ratio of the total configurational entropy in the miscible blend to the sum of the pure component entropies (**S_c** Blend / **S_c** Pure), expressed in percent, versus the position on the exchange intensity curves shown in Figure 8 moving from low to high temperature. Each trace represents a calculation across the entire temperature range of the curve.*

Conclusions

A chain-specific experimental approach based on variable-temperature solid-state CODEX NMR experiments reveals that the effective glass transitions for each chain type in miscible blends may be inequivalent, and slow segmental dynamics for each polymer in the blend are characterized by unique central correlation times and unique correlation time distributions. Quantitative analyses of the raw data indicate that good agreement exists between effective Tg's, central correlation time constants, correlation time distributions, and friction coefficients extracted from this approach versus those obtained by other well-documented methods. Results from an isotropic rotation diffusion model with Arrhenius/log-Gaussian or WLF/KWW treatments of temperature dependence show clear sensitivity to changes that occur upon blend formation relative to the unmixed components. Positive configurational entropies of mixing are detected experimentally. That such quantitative information may be obtained for either polymer component in an amorphous mixture, without isotopic labeling, electric dipole moment constraints, or introduction of probe molecules, is a unique advantage of this experimental strategy and illustrates applicability to a wide range of multicomponent macromolecular systems beyond miscible blends, including polymer nanocomposites, organic/inorganic hybrids, biological macromolecules, and block copolymers.

In NMR Spectroscopy of Polymers: Innovative Strategies for Complex Macromolecules; Cheng, H., et al.;
ACS Symposium Series; American Chemical Society: Washington, DC, 2011.

Acknowledgments

The principal investigator gratefully acknowledges support from the National Science Foundation Division of Materials Research through grant DMR-0756291 and DMR-0611474.

References

1. National Science Foundation Report. *Interdisciplinary Globally-Leading Polymer Science and Engineering*, 2007, available via the Web at http://www.nsf.gov/mps/dmr/reports.jsp.
2. Ober, C. K.; Cheng, S. D.; Hammond, P. T.; Muthukumar, M.; Reichmanis, E.; Wooley, K. L.; Lodge, T. P. *Macromolecules* **2009**, *42*, 465.
3. Donald, A. M. *MRS Bulletin* **2010**, *35*, 702.
4. Frauenfelder, H.; Chen, G.; Berendzen, J.; Fenimore, P. W.; Jansson, H.; McMahon, B. H.; Stroe, I. R.; Swenson, J.; Young, R. D. *Proc. Nat. Acad. Sci. U.S.A.* **2009**, *106*, 5129.
5. deAzevedo, E.; Hu, W. G.; Bonagamba, T. J; Schmidt-Rohr, K. *J. Am. Chem. Soc.* **1999**, *121*, 8411–8412.
6. Wolak, J. E.; Jia, X.; White, J. L. *J. Am. Chem. Soc.* **2003**, *125*, 13660.
7. Wachowicz, M.; White, J. L. *Macromolecules* **2007**, *40*, 5433.
8. Wachowicz, M.; Wolak, J. E.; Gill, L.; White, J. L. *Macromolecules* **2008**, *41*, 2832.
9. Wachowicz, M.; Gill, L.; Damron, J.; White, J. L. *Macromolecules* **2010**, *43*, 3903.
10. deAzevedo, E.; Hu, W. G.; Bonagamba, T. J; Schmidt-Rohr, K. *J. Chem. Phys.* **2000**, *112*, 8988–9001.
11. deAzevedo, E. R.; Tozoni, J. R.; Schmidt-Rohr, K.; Bonagamba, T. J. *J. Chem. Phys.* **2005**, *122*, 154506.
12. Wachowicz, M.; Gill, L.; White, J. L. *Macromolecules* **2009**, *42*, 553.
13. Lodge, T. P.; McLeish, T. C. B. *Macromolecules* **2000**, *33*, 5278.
14. Haley, J. C.; Lodge, T. P. *J. Rheology* **2005**, *49*, 1277.
15. Wefing, S.; Kaufmann, S.; Spiess, H. W. *J. Chem. Phys.* **1988**, *89*, 1234.
16. Wind, M.; Brombacher, L.; Heuer, A.; Graf, R.; Spiess, H. W. *Solid State Nucl Magn. Reson.* **2005**, *27*, 132.
17. Kaufmann, S.; Wefing, S.; Schaefer, D.; Spiess, H. W. *J. Chem. Phys.* **1990**, *93*, 197.
18. Saalwachter, K.; Fischbach, I. *J. Magn. Reson.* **2002**, *157*, 17.
19. O'Connor, R. D.; Ginsburg, E. J.; Blum, F. D. *J. Chem. Phys.* **2000**, *112*, 7247.
20. deAzevedo, E. R.; Reichert, D.; Vidoto, E. L. G.; Dahmouche, K.; Judeinstein, P.; Bonagamba, T. J. *Chem Mater* **2003**, *15*, 2070.
21. See references 7−9 for discrete versus continuous plots illustrating this relationship.
22. Hefner, S.; Mirau, P. A. *Macromolecules* **1994**, *27*, 7283.
23. Roovers, J.; Toporowski, P. M. *Macromolecules* **1992**, *25*, 1096.
24. Roovers, J.; Toporowski, P. M. *Macromolecules* **1992**, *25*, 3454.

25. Alegria, A.; Colmonero, J.; Ngai, K. L.; Roland, C. M. *Macromolecules* **1994**, *27*, 4486.
26. Chung, G. C.; Kornfield, J. A.; Smith, S. D. *Macromolecules* **1994**, *27*, 964.
27. Chung, G. C.; Kornfield, J. A.; Smith, S. D. *Macromolecules* **1994**, *27*, 5729.
28. Adam, G.; Gibbs, J. H. *J. Chem. Phys.* **1965**, *43*, 139.

Downloaded by CORNELL UNIV on June 20, 2012 | http://pubs.acs.org
Publication Date (Web): October 14, 2011 | doi: 10.1021/bk-2011-1077.ch005

Chapter 5

Solid-State NMR Investigations of Semi-Crystalline PVIBE/ε-PL and PK/PA Blends: Crystallite Size, Type, and Morphology Related to Physical Properties

Atsushi Asano*

Department of Applied Chemistry, National Defense Academy,
1-10-20 Hashirimizu, Yokosuka, 239-8686 Japan
***E-mail: asanoa@nda.ac.jp**

Crystallinity and the size of crystalline phase of poly(ε-L-lysine) (ε-PL) were determined by solid-state ^{13}C NMR . The decrease in the melting temperature with increasing ε-PL content ascribed to the crystalline phase of ε-PL in poly(vinyl isobutyl ether) (PVIBE)/ε-PL blends was interpreted by the decrease in total lamellar thickness in the crystalline phase of ε-PL. Furthermore, the independence of the melting temperature with ε-PL content for PVIBE/ε-PL/saponite-clay nanocomposites was also explained in a similar way. For polyketone/nylon 6 (PK/PA) blends, the high impact resistance under the wet condition was explained by the characteristic morphology of PK crystalline phase, the increased elasticity due to water absorption in the amorphous phase of PA, and conversion of γ crystallite to the α crystallite morphology of PA (as shown by solid-state ^{15}N NMR).

Introduction

Polymer blends and nanocomposites have been widely used for engineering purposes. Their favorable mechanical and physical properties are closely related to their morphology (especially in semi-crystalline polymers), the domain size of the crystalline phase, and the crystalline type. Hence, the morphology of crystalline phase and the degree of crystallinity are among the important information

In NMR Spectroscopy of Polymers: Innovative Strategies for Complex Macromolecules; Cheng, H., et al.;
ACS Symposium Series; American Chemical Society: Washington, DC, 2011.

that we have to know to understand the physical and chemical properties of semi-crystalline polymers, their polymer blends, and their nanocomposites. To obtain the degree of crystallinity, we can choose any appropriate method, such as differential scanning calorimetry (DSC), X-ray diffraction, Raman and infrared (IR) spectroscopies, and nuclear magnetic resonance (NMR) (*1*, *2*). Among these methods, NMR can detect the crystalline phase of a component polymer even in a blend or a nanocomposite distinguishably and also estimate correctly the amount of microcrystalline phase (*3*–*5*). It is valuable to analyze the domain size, type, and morphology of crystalline and non-crystalline phases (including inter-phase and amorphous phase) separately to reveal the relationship between morphological information and physical properties, such as melting temperature, impact strength, modulus, and elasticity.

In this review, I shall first discuss the determination of crystallinity via NMR parameters, especially for poly(ε-L-lysine) (ε-PL). There are several ways in NMR to study the crystalline phase, such as ^{13}C spin-lattice relaxation time ($T_1{}^{C}$), ^{1}H spin-spin relaxation time ($T_2{}^{H}$), and ^{13}C NMR spectral editing. We shall compare these parameters with the results from X-ray diffraction (XRD) (*3*). Secondly, I shall discuss the effects of inorganic clay fillers on crystallinity and melting temperatures of ε-PL and poly(vinyl isobutyl ether) (PVIBE) blends, and their nanocomposites with saponite clay (*6*, *7*). The melting temperature of ε-PL measured from differential scanning calorimetry (DSC) showed a dependence on composition in the PVIBE/ε-PL blends, but compositional independence in the PVIBE/ε-PL/saponite nanocomposites. These interesting phenomena were explained by the domain size of the crystalline phase in ε-PL, i.e., the Gibbs-Thomson effect (*1*). Finally, I shall discuss the analysis of the morphology of polyketone/polyamide (PK/PA) blends. The high impact property of the PK/PA blend with water absorption is due to the effects of change of PA crystalline phase type and the increase of elasticity of PA amorphous phase under wet conditions. Furthermore, transmission electron microscopy (TEM) shows a characteristic crystalline lamella-like picture of PK. The ^{1}H spin-diffusion study via well-resolved ^{13}C NMR signals indicates that both the domain sizes of PK and PA are not affected by the moisture absorption (*8*–*10*).

Downloaded by CORNELL UNIV on June 20, 2012 | http://pubs.acs.org
Publication Date (Web): October 14, 2011 | doi: 10.1021/bk-2011-1077.ch005

Experimental Section

Materials

Poly(ε-L-lysine) (ε-PL: repeat unit $-NH(CH_2)_4CH(NH_2)CO-$) was provided by Chisso Corporation as a solid powder, with an average degree of polymerization approximately 30. ε-PL is known as a biodegradable hydrophilic semi-crystalline polymer and nontoxic toward humans and environment (*11*). Semi-crystalline poly(vinyl isobutyl ether) (PVIBE: repeat unit $-CH_2CH(OCH_2CH(CH_3)_2-)$ was obtained from Scientific Polymer Products, Inc, and its M_w is 600,000. Polyketone (PK, an ethylene/propylene/CO copolymer $-(CH_2CH_2CO)_m-(CH_2CH(CH_3)CO)_n-)$ is a commercial material (Carilon D26HM100), provided by Shell Co. Polyamide-6 (PA; repeating unit $-NH(CH_2)_6CO-$) is a commercial material (Amilan CM1017), provided by Toray Ind. Both PK and PA are semi-crystalline

Downloaded by CORNELL UNIV on June 20, 2012 | http://pubs.acs.org
Publication Date (Web): October 14, 2011 | doi: 10.1021/bk-2011-1077.ch005

polymers. Saponite clay, which is synthetic and a smectite clay, was obtained from Kunimine Industries Co., Ltd. It has a relatively small aspect ratio when compared to montmorillonite and has no paramagnetic center such as Fe^{3+}.

The PVIBE/ε-PL blend and PVIBE/ε-PL/saponite nanocomposite films were prepared by casting 90:10 (v/v) chloroform/methanol mixed solutions that contained those polymers at a concentration of 15 (w/v) % on a Teflon plate at 313K, which were further dried under vacuum at 313K for 1 or 2 days. The film thus obtained was opaque and elastic. In order to exfoliate the saponite clay layers, the saponite clay was dissolved in ε-PL/water solution at 3 wt% concentration prior to mixing with PVIBE (ε-PL/saponite-clay=1/0.03). The ε-PL/saponite-clay mixed powder was obtained by drying the ε-PL water solution.

The PK/PA blends were obtained by mechanical mixing. We used a simple terminology for the PK/PA blend: PK60PA40 means a blend of 60 weight % PK (volume fraction 0.578) and 40 weight % of PA (volume fraction 0.422). The PK/PA blends were moisture-conditioned by holding them at 50% or 95% relative humidity (RH) and a temperature of 296 K for three weeks or longer. Dry test specimens were prepared by drying them in vacuum at 373K for 72 h. The moisture absorption rate was measured by the Karl Fisher method.

Measurements and Instruments

Nuclear Magnetic Resonance (NMR)

High-resolution solid-state ^{13}C NMR spectra were obtained using a Varian 400WB NMR spectrometer or a Bruker DMX500 spectrometer. The ramped-amplitude cross-polarization (CP) (*12*, *13*) and magic-angle spinning (MAS) with ^{1}H high-power dipolar decoupling technique was used, employing a rotor with 4.0 mm diameter for both NMR systems. The radio-frequency field strength for ^{1}H decoupling was 120 kHz for the Varian and 56 kHz for the Bruker instrument, and the two-pulse-phase-modulation (TPPM) method (*14*) was used. The MAS frequencies used were 10 to 16 kHz. ^{13}C chemical shifts were measured relative to tetramethylsilane (TMS) using the benzene carbon signal at 132.07 ppm for solid hexamethylbenzene or 29.47 ppm for solid adamantane as an external reference. High-resolution solid-state ^{15}N NMR spectra were measured using the Varian NMR 400WB spectrometer at a MAS rate of 5 kHz and a ^{1}H decoupling frequency of 65 kHz with a 7.5 mm diameter rotor. ^{15}N chemical shifts were measured relative to the glycine signal as an external reference at 0 ppm.

The ^{1}H spin-lattice relaxation times in the laboratory frame (T_1^{H}) were indirectly measured from well-resolved ^{13}C signals enhanced by 500 μs to 2 ms CP contact times. These parameters were chosen to obtain the maximum enhanced signal, applied after the inversion-recovery pulse sequence for the ^{1}H nucleus. T_1^{C} decay was indirectly measured from protons through the CP enhancement as proposed by Torchia (*15*).

In NMR Spectroscopy of Polymers: Innovative Strategies for Complex Macromolecules; Cheng, H., et al.;
ACS Symposium Series; American Chemical Society: Washington, DC, 2011.

Downloaded by CORNELL UNIV on June 20, 2012 | http://pubs.acs.org
Publication Date (Web): October 14, 2011 | doi: 10.1021/bk-2011-1077.ch005

Differential Scannning Calorimetry (DSC)

DSC curves were observed using a Perkin-Elmer 7 instrument with the temperature increasing at a rate of 2 K·min^{-1} from 233 K to 473 K.

Transmission Electron Microscopy (TEM)

TEM images were collected using a Hitachi H-800 instrument with an accelerating voltage of 200 kV. Electron staining was done with phosphotungstic acid. Three-dimensional TEM images were examined using a FEI Tecnai G2 F20 TEM with a tilting angle that ranged from -70 to +70° for every 2° step.

X-ray Diffraction (XRD)

XRD patterns were collected using MAC Science M21X diffractometer with Cu Kα radiation of λ= 0.154 nm at 293 K. For the XRD experiments, we prepared a sample of ε-PL which was mostly non-crystalline. A ε-PL sample sealed in a glass tube with nitrogen atmosphere was heat treated at 458 K for 20 min: the crystalline phase was completely melted. After the heat treatment, the glass tube was immediately immersed in liquid nitrogen to quench the amorphous phase.

Results and Discussion

Crystallinity and Crystal Size (Gibbs-Thomson Relationship)

Figure 1 shows the observed ^{13}C CPMAS NMR spectra of (a) PVIBE, (b) PVIBE/ε-PL=10/3, (c) PVIBE/ε-PL/saponite=10/3/0.09, (d) ε-PL, and (e) ε-PL/saponite-clay=1/0.03. The expanded spectra for the CH-O-CH$_2$ region of PVIBE and C$_\alpha$H region of ε-PL are also shown in (b) and (c). Furthermore, the spectra for the carbonyl carbon region of ε-PL are depicted in the left-hand side of (b) to (e) and the peak assignments are also shown in the figure. Although the peak intensities are enhanced individually by CP, we determined the real composition of PVIBE/ε-PL blends and nanocomposites via ^{1}H dipolar-decoupling (DD)-MAS spectra. The spectrum of the ε-PL/saponite-clay=1/0.03 (e) shows that the relative ratio of broad lines is much more than that of ε-PL (d). For example, the CH$_2$ peaks at 20 to 40 ppm region, which consists of apparently four narrow peaks plus broad lines, show much broader features. This suggests that the degree of crystallinity is decreased by adding saponite clay. Similarly, the spectrum of PVIBE/ε-PL/saponite=10/3/0.09 nanocomposite (c) shows more broadening as compared to that of PVIBE/ε-PL=10/3 (b). The broadening can be particularly seen at the C$_\alpha$H peak of ε-PL from 50 to 65 ppm. This is ascribed to the effect of adding clay, too. For the carbonyl (C=O) peak at ca. 178 ppm, the tendency is clearly observed; a sharp doublet peak of the crystalline (CR) phase (d), which is observed on top of the broad peak attributed to the non-crystalline (NC) phase, becomes small by adding saponite clay (e). Interestingly such a significant broadening does not appear in the PVIBE/ε-PL=10/3 blend (b); however, the sharp doublet peak was obscured after blending with both PVIBE and saponite clay (c). However, the CH-O-CH_2 region of PVIBE from 65 to 85 ppm does not show such a broadening by adding saponite clay, as shown in (b) and (c).

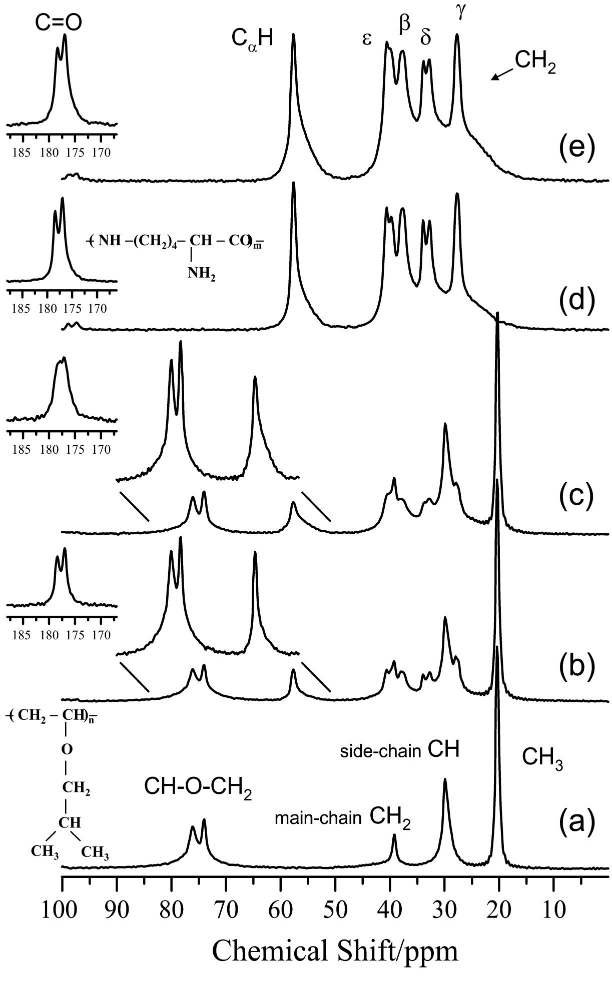

Figure 1. Observed ^{13}C CPMAS NMR spectra of (a) PVIBE, (b) PVIBE/ε-PL=10/3 blend, (c) PVIBE/ε-PL/saponite=10/3/0.09 nanocomposite, (d) ε-PL, and (e) ε-PL/saponite-clay=1/0.03 powder, respectively.

To investigate the degree of crystallinity, we examined the ^{13}C CPMAS NMR spectra separated into contributions from the CR and NC phases on the basis of the differences in the intrinsic ^{1}H spin-lattice relaxation time in the rotating frame that characterize CR and NC phases (*4*, *16*). This method provides the same quality for the degree of crystallinity as well as XRD measurement for each component even in polymer blends. Furthermore, it can be examined at room temperature basically and usually. For the T_1^C measurement, it is not easy to select appropriate

Downloaded by CORNELL UNIV on June 20, 2012 | http://pubs.acs.org
Publication Date (Web): October 14, 2011 | doi: 10.1021/bk-2011-1077.ch005

temperature for both component polymers. The differences among NMR, XRD, and $T_1{}^C$ measurements for detection of the crystallinity are briefly discussed later. Figure 2(A) shows an example of the spectral separation to the CR (dotted line, sharp component) and the NC (broken line, broad component) signals for the $C_\alpha H$ peak of pure ε-PL (*3*) as shown in Figure 1(d). The dotted and broken lines are the results of linear combinations of the spectra obtained from the different spin-locking times of 1 µs and 5 ms prior to the CP contact time of 800 µs, respectively. In order to obtain each line, we have attempted to null the NC and CR signal contributions, respectively (*4*, *16*). The solid line spectrum is obtained by the sum of the spectra of the CR and the NC signals.

It is noteworthy that both CR and NC spectra depend on the difference in chain order only and not on molecular motion. Since the peak intensities decrease during CP irradiation depending on the contact time, it is necessary to obtain the efficiency factors of CP enhancement to estimate the correct crystallinity using both CR and NC integrals. We examined the CP dependency with various CP contact times from 25 µs to 7 ms to obtain the relative CP efficiencies for both CR and NC phases at a CP contact time of 800 µs.

The estimated degree of the crystallinity for pure PVIBE was ca. 20 % and for pure ε-PL ca. 54 %. These values have an experimental uncertainty of 5 %. The obtained crystallinity for PVIBE in the PVIBE/ε-PL blends was approximately a half of that of the pure one (around 10%). However, the values in the PVIBE/ε-PL/saponite nanocomposites were not affected and remained unchanged at ca. 20 %. This is also confirmed by comparing the expanded spectra of $CH\text{-}O\text{-}CH_2$ region between Figures 1(b) and 1(c). The degree of crystallinity of ε-PL in the blends remained unchanged at 54 ± 5% except for PVIBE/ε-PL=10/1 blend where the value was ca. 30% (*6*, *7*). In the case of nanocomposites, the crystallinity of ε-PL was changed to be around 45%, except for PVIBE/ε-PL/saponite=10/1/0.03 where the value was 36% (*7*).

Here, we discuss briefly the difference in sensitivity to both CR and NC phases towards spectral separation, $T_1{}^C$ curve, and XRD (*3*). Figure 2(B) shows the $T_1{}^C$ curves of the $C_\alpha H$ peak of pure ε-PL. The insert is the decay curve obtained from the whole integral. The solid circles are obtained from the integrals of the CR phase and the open circles from those of the NC phase. The data were obtained from the integrals of the peaks depicted by the dotted line (CR) and by the broken line (NC), respectively, in Figure 2(A). The sum of both decays is equal to the curve of the insert. The $T_1{}^C$ decay in the insert shows double exponentials and the fraction of the long component was obtained to be 62 ± 11% by the least square fit with a conventional double-exponential function. The $T_1{}^C$ decay curve of the CR phase shows single exponential (●) and that of the NC phase non-single exponential (○). For the CR decay, we obtained the $T_1{}^C$ value of 25 ± 2 s by a least-square fit with a conventional single-exponential curve. This value is comparable to the value of the long $T_1{}^C$ component obtained from the decay of the insert (22 ± 3 s) but not completely the same: the value obtained from the CR phase is longer than that of the whole integral. This indicates that the molecular motion of the intrinsic CR phase is much slower than that estimated from the long $T_1{}^C$ component, and the long $T_1{}^C$ component includes the inter-phase, where the molecular motion is comparable to that of the CR phase. Thus, the value obtained becomes slightly

Downloaded by CORNELL UNIV on June 20, 2012 | http://pubs.acs.org
Publication Date (Web): October 14, 2011 | doi: 10.1021/bk-2011-1077.ch005

shorter than that obtained from the CR phase. Actually, the T_1^{C} curve of the NC phase shows a non-single exponential decay. The dashed and dotted lines in Figure 2(B) represent the decays of short and long components in the insert, respectively. The combination of both lines reproduces the T_1^{C} curve of the NC phase (○) well, suggesting that the broad NC component includes both inter-phase and amorphous regions. It is also important to discuss herewith the accuracy of crystallinity determined from NMR. The XRD experiment can estimate the crystallinity reflecting the chain order but not mobility. Figure 2(C) shows the XRD patterns of whole ε-PL (regular solid line), mostly CR phase (bold solid line), and almost all NC phase (dotted line). The XRD pattern of the mostly CR phase was obtained from the linear combination of both XRD patterns of whole ε-PL and almost all NC phase. The estimated value from XRD is ca. 58 % with an uncertainly of 5-10% (*3*). This value is in excellent agreement with that estimated from spectral separation, 54%, within experimental error. These observations indicate that spectral separation spectral separation provides the same quality and accuracy for the crystallinity as well as XRD observation. Of course, it is also true that T_1^{C} provides accurate crystallinity if the appropriate temperature is chosen because mobility is largely affected by temperature chosen. Furthermore, it has a potential to provide morphological information ascribed to mobility difference. Actually, the combination study of the spectral separation and T_1^{C} experiments gives us information on the fraction of inter-phase in the material (*3*).

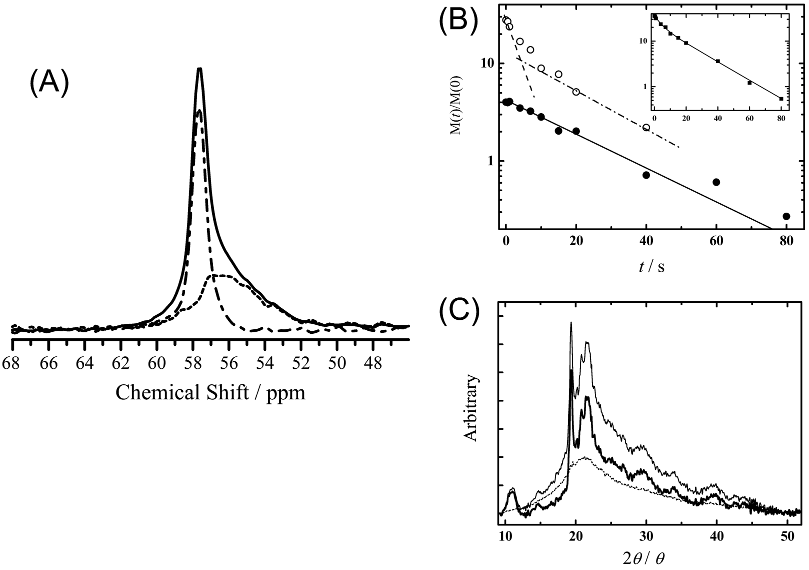

Figure 2. (A) Observed and expanded ^{13}C CPMAS NMR spectra of $C_{\alpha}H$ carbon of ε-PL: dotted line and broken lines represent the CR and the NC phases, respectively. (B) The observed ^{13}C spin-lattice relaxation curve obtained from the CR phase (●) and the NC phase (○). The insert is obtained from the entire integral. (C) Observed XRD patterns of ε-PL (regular solid line),ε-PL mainly consisted of NC phase (dotted line), and the CR phase (bold solid line).

Downloaded by CORNELL UNIV on June 20, 2012 | http://pubs.acs.org
Publication Date (Web): October 14, 2011 | doi: 10.1021/bk-2011-1077.ch005

Downloaded by CORNELL UNIV on June 20, 2012 | http://pubs.acs.org
Publication Date (Web): October 14, 2011 | doi: 10.1021/bk-2011-1077.ch005

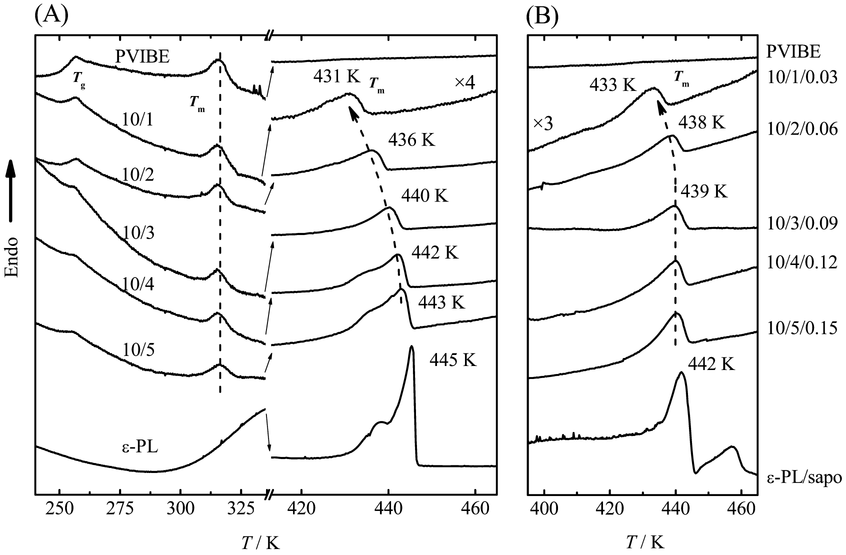

Figure 3. DSC curves of PVIBE/ε-PL blends (A) and PVIBE/ε-PL/saponite-clay nanocomposites (B).

A discussion is needed of the relationship between melting temperature and the domain size of crystalline phase. For PVIBE/ε-PL blends and PVIBE/ε-PL/saponite nanocomposites, we found an interesting DSC phenomenon shown in Figure 3. Figure 3(A) shows DSC curves of pure PVIBE, PVIBE/ε-PL blends, and pure ε-PL. Similarly, Figure 3(B) depicts DSC curves of the melting temperature, T_m, region of ε-PL for the PVIBE/ε-PL/saponite nanocomposites. From Figure 3(A), we recognize that the T_m transition of ε-PL shifts towards lower temperatures with increasing PVIBE composition although T_m for PVIBE remains unchanged with ε-PL addition. On the other hand, the T_m transition of ε-PL in the PVIBE/ε-PL/saponite nanocomposites do not show such a composition dependence as shown in Figure 3(B). For the PVIBE/ε-PL/saponite=10/3/0.09 to 10/5/0.15 regions, the T_m transition does not change with composition and shows a constant value of 439 K. This value is comparable to that of PVIBE/ε-PL=10/3 blend. With increasing ε-PL composition, this value decreases to 433 K at PVIBE/ε-PL/saponite=10/1/0.03. This value is somewhat higher than that of PVIBE/ε-PL=10/1 blend. Here, if the diluent effect is predominant, the shift tendency of T_m towards lower temperature with composition is reasonable for the change of PVIBE/ε-PL/saponite-clay=10/2/0.06 to 10/1/0.03. However, the constancy of T_m values for PVIBE/ε-PL/saponite-clay=10/3/0.09 to 10/5/0.15 cannot be interpreted as well. On the basis of the Gibbs-Thomson effect (*1*), the same lamellar thickness exhibits the same T_m value. The DSC results shown in Figure 3 imply that the change of T_m is attributable to the lamellar thickness in the crystalline domain of ε-PL but not to the diluent effect by adding PVIBE.

To investigate the domain size of crystalline phase, we employed the ^{1}H spin-lattice relaxation decay analysis. The crystalline domain size can be inferred from

Downloaded by CORNELL UNIV on June 20, 2012 | http://pubs.acs.org
Publication Date (Web): October 14, 2011 | doi: 10.1021/bk-2011-1077.ch005

the ^{1}H spin-diffusion rate between PVIBE and ε-PL. Figure 4 shows the T_1^H curves observed from PVIBE (CR: ●, NC: ○) and ε-PL (CR: ▲, NC: △) in PVIBE/ε-PL=10/1 blend. For pure PVIBE and pure ε-PL, the observed T_1^H curve of the CR phase agrees with that of the NC phase due to the fast ^{1}H spin diffusion between the CR and NC domains; the dotted straight lines represent the respective relaxation curves of pure PVIBE (0.8 s) and pure ε-PL (2.8 s), respectively. This figure indicates that PVIBE and ε-PL are heterogeneous on a scale of 20-100 nm, because both T_1^H curves are not consistent with each other. Furthermore, the T_1^H curve of the CR (▲) for ε-PL is different from that of the NC (△), while that of CR for PVIBE (●) is the same as that of NC (○). This observation indicates that insufficient ^{1}H spin diffusion occurs between PVIBE and ε-PL during the T_1^H measuring period, and similarly even between the CR and NC phases of ε-PL for the PVIBE/ε-PL=10/1 blend. This is because the molecular motion of NC chains of ε-PL becomes much faster after blending with a large amount of mobile PVIBE enough to hinder the ^{1}H spin diffusion between NC and CR domains even in the same ε-PL. This indicates that NC chains of PVIBE coexist with and penetrate into the NC domain of ε-PL intimately much more than the other blends, and then PVIBE chains are close proximity of the CR chains of ε-PL. Thus, the ^{1}H spins of PVIBE exchange smoothly with ^{1}H spins in the CR domain of ε-PL as well as in the NC domain of ε-PL. This results in the three-spin system. Actually, the observed T_1^H curves show the typical curvature in the case of insufficient ^{1}H spin-diffusion rate for a three-spin system (*17*): T_1^H curves are one concave (PVIBE) and two convex (ε-PL). For the other compositions, the T_1^H curves show the typical two-spin system decay: the CR curve is in good agreement with the NC curve for each polymer (*6*, *7*).

The proton magnetizations $M_i(t)$ of i spin for two- and three-spin systems are expressed by equations (1) and (2), respectively as follows:

$$\frac{d}{dt}\begin{pmatrix} M_A(t) \\ M_B(t) \end{pmatrix} = \begin{pmatrix} -\xi_A & f_A k \\ f_B k & -\xi_B \end{pmatrix}\begin{pmatrix} M_A(t) \\ M_B(t) \end{pmatrix} \tag{1}$$

where $\xi_A = K_A + f_B k$ and $\xi_B = K_B + f_A k$. Symbols A and B denote ^{1}H spins of PVIBE and ε-PL, respectively. The sum of f_A and f_B equals to 1.

$$\frac{d}{dt}\begin{pmatrix} M_1(t) \\ M_2(t) \\ M_3(t) \end{pmatrix} = \begin{pmatrix} -\xi_1 & f_1 k_{12} & f_1 k_{13} \\ f_2 k_{12} & -\xi_2 & f_2 k_{23} \\ f_3 k_{13} & f_3 k_{23} & -\xi_3 \end{pmatrix}\begin{pmatrix} M_1(t) \\ M_2(t) \\ M_3(t) \end{pmatrix} \tag{2}$$

where $\xi_1 = K_1 + f_2 k_{12} + f_3 k_{13}$, $\xi_2 = K_2 + f_1 k_{12} + f_3 k_{23}$, and $\xi_3 = K_3 + f_1 k_{13} + f_2 k_{23}$. Parameters *f*, *K*, and *k* represent ^{1}H molar fraction, intrinsic ^{1}H relaxation rate, and ^{1}H spin-diffusion rate, respectively. Numbers 1, 2, and 3 express ^{1}H spins of PVIBE, NC of ε-PL, and CR of ε-PL, respectively. The sum of f_1, f_2 and f_3 equals to 1.

The simulated 'best-fit' curves are depicted as solid, dashed, and dotted lines in Figure 4. The simulated lines are in good agreement with the observed data points. The obtained values are $K_1 = 1.12$ s^{-1}, $K_2 = 0.39$ s^{-1}, $K_3 = 0.25$ s^{-1}, $k_{12} = 0.57$

In NMR Spectroscopy of Polymers: Innovative Strategies for Complex Macromolecules; Cheng, H., et al.;
ACS Symposium Series; American Chemical Society: Washington, DC, 2011.

s^{-1}, $k_{23} = 2.0\ s^{-1}$, and $k_{13} = 0.33\ s^{-1}$. The uncertainty is approximately 10 %. The repeating unit length, L, can be estimated from the relation of $L = 2\sqrt{D/\pi k}\,/(f_{\mathrm{PVIBE}}\,f_{\varepsilon\text{-PL}})$: D is the ^{1}H spin-diffusion coefficient for PVIBE/ε-PL system (380 nm^2s^{-1}) and obtained from the ^{1}H spin-spin relaxation time (*18–20*).

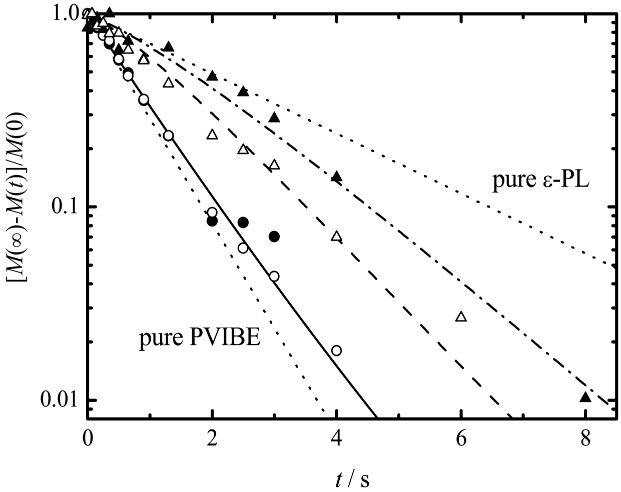

Figure 4. Observed T_1^H relaxation curves of PVIBE (CR: ●, NC: ○) and ε-PL (CR: ▲, NC: △) for the PVIBE/ε-PL=10/1 blend. Each solid line represents the calculated curve from equation (2). The T_1^H relaxation curves for pure PVIBE and ε-PL are represented by the dotted lines.

The obtained k, the estimated L, the degree of crystallinity, x_C, of ε-PL, and the domain size which is related to the total lamellar thickness, L_C, of the crystalline phase of ε-PL are listed in Table 1. There exists a good relationship between the decrease of L_C values and the depression of the melting point with decreasing ε-PL for blends. On the other hand, the L_C values for PVIBE/ε-PL/saponite=10/3/0.09 to 10/5/0.15 exhibit the same value of 30-33 nm within an error of 10%. For further PVIBE-rich compositions, L_C values decreases with PVIBE as well as those of blends. The L_C values for PVIBE/ε-PL/saponite =10/3/0.09 to 10/5/0.15 are comparable to that for the PVIBE/ε-PL=10/3 blend (35 nm). It is also interesting and surprising that the T_m values of the PVIBE/ε-PL/saponite=10/3/0.09 to 10/5/0.15 nanocomposites show the same value of 439 K with each other. Furthermore, this value is in excellent agreement with that of the PVIBE/ε-PL=10/3 blend at 440K. For PVIBE/ε-PL=10/2 or 10/1 compositions, similar relationship also remains; i.e., T_m value depends on the L_C value. These results clearly prove that the T_m value is governed by the lamellar thickness in crystalline domain and not by the diluent effect in PVIBE/ε-PL.

Downloaded by CORNELL UNIV on June 20, 2012 | http://pubs.acs.org
Publication Date (Web): October 14, 2011 | doi: 10.1021/bk-2011-1077.ch005

Table 1. ^{1}H spin-diffusion rates, *k*, the estimated repeat lengths, *L*, of both PVIBE and ε-PL domains, and the degree of crystallinity, x_C, of ε-PL

composition	k / s^{-1}	L / nm	$L \times f_{\varepsilon\text{-}PL}$ / nm	x_C / %	L_C / nm
10/1	0.33	569	41	30	12
10/2	0.37	309	42	58	24
10/3	0.20	320	61	57	35
10/4	0.12	350	83	55	46
10/5	0.10	345	97	59	57
10/1/0.03	0.25	654	47	36	17
10/2/0.06	0.38	305	41	46	19
10/3/0.09	0.15	369	70	47	33
10/4/0.12	0.18	286	68	44	30
10/5/0.15	0.21	238	67	49	33

L is estimated from k and the formula of $L = 2\sqrt{D/\pi k}\,/(f_{\text{PVIBE}}\,f_{\varepsilon\text{-PL}})$. L_C is caluculated from $L \times f_{\varepsilon\text{-PL}} \times x_C/100$.

Downloaded by CORNELL UNIV on June 20, 2012 | http://pubs.acs.org
Publication Date (Web): October 14, 2011 | doi: 10.1021/bk-2011-1077.ch005

The crystallinity of ε-PL in the PVIBE/ε-PL/saponite=10/5/0.15-10/2/0.06 nanocomposites (around 45%) is lower than that of PVIBE/ε-PL blends (around 55 %). In order to clarify the effect of adding clay on crystallite growth, I employed the Gibbs-Thomson relation between the lamellar thickness and T_m. According to the Gibbs-Thomson relation (*1*), the depression of T_m is inversely proportional to the CR thickness. The estimated total lamellar thickness, *d*, is not suitable for applying the relation directly because we never know the intrinsic and single lamellar thickness by this NMR simple estimation. However, if the intrinsic lamellar thickness does not change but the amount of lamellar decreases with decreasing of the domain size to keep the constancy of crystallinity from 10/5 to 10/2 compositions, the T_m values do not change. Thus, the change of T_m should be explained by a diluent effect of adding PVIBE. However, the constancy of T_m for PVIBE/ε-PL/saponite=10/5/0.15 to 10/3/0.09 cannot be interpreted by the diluent effect. It is reasonable to consider, instead, that the thickness of the single lamellar layer decreases with decreasing of the crystalline domain size of ε-PL but the amount increases in the crystalline phase to keep the constant crystallinity: namely, the estimated value *d* will correspond to an integral multiple of the intrinsic and single lamellar thickness, *x*. Here, I adapt the value, *d*, to the Gibbs-Thomson relation instead of the intrinsic and single lamellar thickness of *x* to elucidate the effect of adding saponite clay on the crystalline growth of ε-PL.

Downloaded by CORNELL UNIV on June 20, 2012 | http://pubs.acs.org
Publication Date (Web): October 14, 2011 | doi: 10.1021/bk-2011-1077.ch005

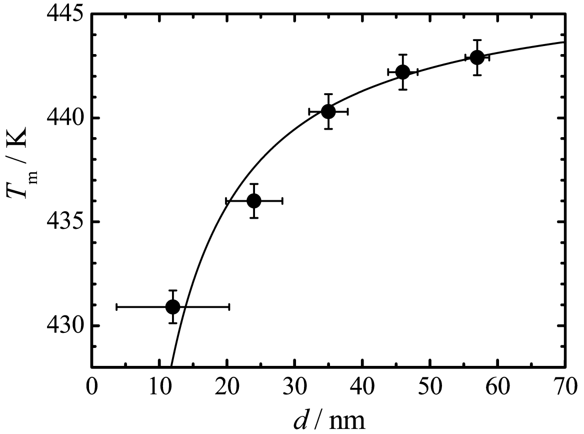

Figure 5. Plot of T_m and the total lamellar thickness of ε-PL, d, for the PVIBE/ε-PL blends. The solid curve is obtained from equation (3).

Figure 5 shows the plot of T_m against the total thickness of the CR phase of ε-PL, d, in the PVIBE/ε-PL blends. The Gibbs-Thomson effect is given as following equation.

$$T_m(x) = T_m^{\ 0} - \frac{\theta}{x}, \quad \theta = 2\sigma \cdot T_m^{\ 0} / \Delta H_m^{\ 0} \qquad (3)$$

Here, T_m^0, σ, ΔH_m^0, and x are, respectively, the melting temperature of a complete crystal of ε-PL, surface energy at the lamella interface, equilibrium enthalpy per a unit cell, and the thickness of CR. The solid line is the least-square fitted curve to the data points by substituting x to d. The fitted curve is in excellent agreement with the observed data points. The estimated T_m^0 and θ are 446.8 ± 0.2 K and 220 ± 10 K·nm, respectively. By using these parameters, the thickness of CR for pure ε-PL can be estimated to be ca. 120 nm and that of ε-PL/saponite to be ca. 46 nm. This suggests that adding clay has a large ability of depression of crystalline size for ε-PL. The degree of crystallinity of pure ε-PL is approximately 54 % but that of ε-PL/saponite is 42 %. The decrease ratio of crystalline size (1.0 – 46/120 = 0.62) is much larger than the depression ratio of crystallinity (1.0 – 42/54 = 0.22). This indicates that the crystalline phase of the ε-PL/saponite probably consists mainly of microcrystallites.

Morphology and Impact Resistence

The impact resistence of PK/PA blends becomes much better in the wet condition, particularly for the range of PK/PA=10/90 to 70/30 (*8–10*). Surprisingly, the impact energy under dry condition is around 25 kJ m^{-2}, but at > 1.5% humidity the value exceeds 160 kJ m^{-2}. This large increase of impact energy occurs for the PK/PA blends with a PA content of over 30 weight % only, and it is interesting that the wet pure PA sample does not show such an improvement, though it is seen even for the PK10PA90 blend. The improvement of impact resistence under the wet condition is limited to the compositions of 80/20 and 90/10. Furthermore, no improvement is seen for either pure PA or pure PK. Therefore, the pronounced improvement in impact resistance should be related to both morphology and humidity.

Figure 6 shows sliced sections of three-dimensional (3D) TEM images of PK10PA90, PK60PA40, PK80PA20, and PK90PA10 blends. The white color represents mainly the amorphous region and the black color the crystalline region. It is clear in the image of PK60PA40 that there is a lamellar-like structure shown in black ascribed to the crystalline region. Furthermore, there are many co-continuous spherical amorphous regions. For both pure PK and pure PA, the lamellar-like structure is not clearly observed in the TEM image. However, the lamellar-like structure is detected even in the PK90PA10 blend in the 3D-TEM image, albeit not clearly. It is confirmed from electron energy loss spectroscopy (EELS) image (*9*, *10*) that this region mainly comes from PK; hence the lamellar-like structure is assigned to the crystalline lamellar of PK. For PK80PA20 and PK90PA10 blends, both 3D-TEM images show a characteristic spherical amorphous domain filled with lamellar structure. For PK10PA90 blend, the 3D-TEM image shows poor contrast but there is a lamellar network in the deep white region (perhaps amorphous). Considering the PK loading, it is inconceivable that the entire lamellar network is attributed to the PK chains. From small angle X-ray scattering (SAXS) study (*9*, *10*), the long period of lamellae for PK-rich blends is estimated to be ca. 14 nm but that for PA-rich blends decreases from 14 to 9 nm gradually (*21*). The long periods of both pure PK and pure PA are ca. 14 nm and ca. 8 nm, respectively. Therefore, the lamellar network for the PA-rich blends consists of a mixture network of both PK and PA. Furthermore, the impact strength of both PK80PA20 and PK90PA10 does not show the pronounced improvement under the wet condition. This suggests that the existences of PK lamellae and the co-continuous spherical amorphous region are strongly related to the improvement in impact resistance.

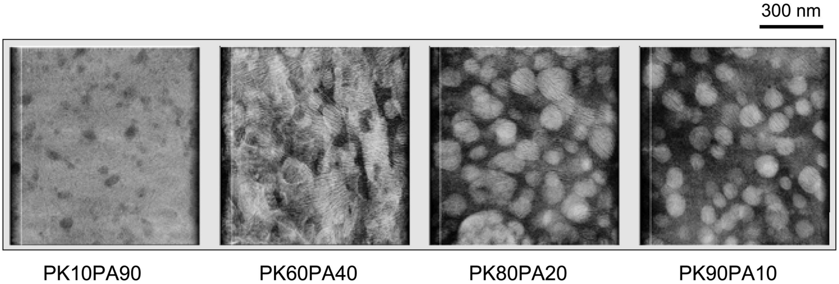

Figure 6. The 3D-TEM images in are views selected at arbitrary angles for PK10PA90, PK60PA40, PK80PA20, and PK90PA10 blends.

In order to investigate the structure of the crystalline phase, domain size, and the effect of humidity on polymer chain, ^{13}C CPMAS NMR spectra were obtained for both dry and wet conditions. Figure 7 shows the observed and enlarged solid-state ^{13}C CPMAS NMR spectra of the PK60PA40 blend in the aliphatic (a) and carbonyl (b) carbon regions. The solid and broken lines represent the ^{13}C CPMAS

In NMR Spectroscopy of Polymers: Innovative Strategies for Complex Macromolecules; Cheng, H., et al.;
ACS Symposium Series; American Chemical Society: Washington, DC, 2011.

Downloaded by CORNELL UNIV on June 20, 2012 | http://pubs.acs.org
Publication Date (Web): October 14, 2011 | doi: 10.1021/bk-2011-1077.ch005

Downloaded by CORNELL UNIV on June 20, 2012 | http://pubs.acs.org
Publication Date (Web): October 14, 2011 | doi: 10.1021/bk-2011-1077.ch005

NMR spectra for dry and wet conditions, respectively. By comparing both dry and wet spectra, it is clear that the signal intensity under the wet condition is lower than that under the dry condition. The relative intensity of the amorphous peak of PA decreases more markedly in the presence of moisture, while those of PK remains unchanged. This indicates that the CP efficiency of the amorphous phase of PA declines selectively. When water absorption occurs predominantly in the amorphous phase, the polymer chains display higher mobility than in the crystalline phase. Since CP works effectively between the ^{13}C and ^{1}H spin pairs at a lower level of mobility, the CP efficiency in the mobile spins becomes worse. Similarly, the carbonyl (C=O) peak of PK does not change after water absorption, while the C=O signal of PA decreases. This observation suggests that water is absorbed predominantly in the amorphous phase of PA but not in the crystalline phase of PA and PK and the amorphous phase of PK.

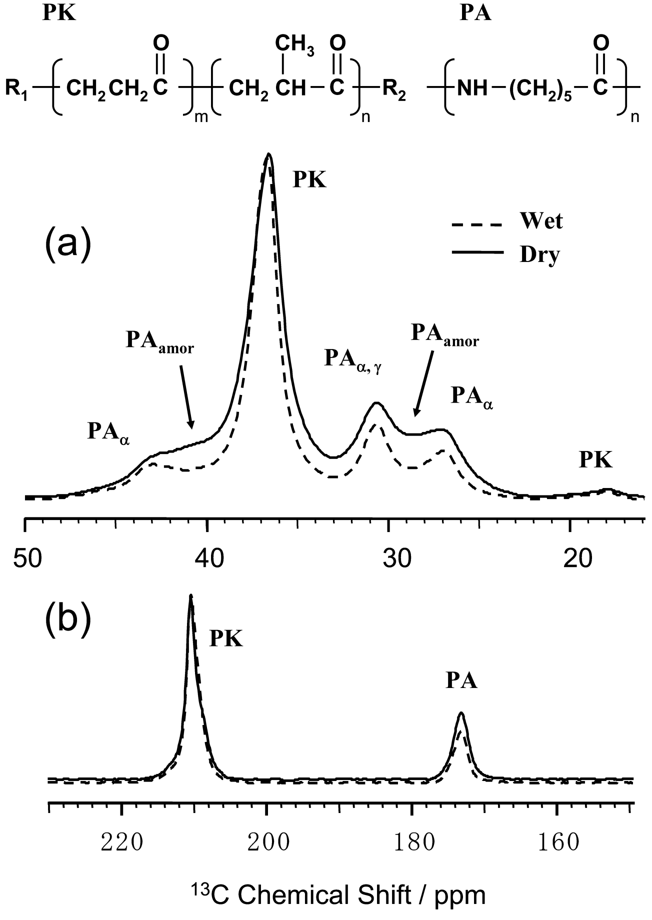

Figure 7. Observed and enlarged ^{13}C CPMAS SSNMR spectra for (a) the aliphatic and (b) the carbonyl carbon regions of PK60PA40 blend under dry and wet (broken line) conditions.

PA is known to have the two crystalline phases, α and γ crystallites (*22–26*). In order to clarify the change in the crystalline phase of PA after blending with PK, we examined the ^{15}N CPMAS NMR spectra of PK60PA40 blend and pure PA. Figure 8 shows the ^{15}N CPMAS NMR spectra of (a) the PK60PA40 blend and (b) pure PA under the wet condition.

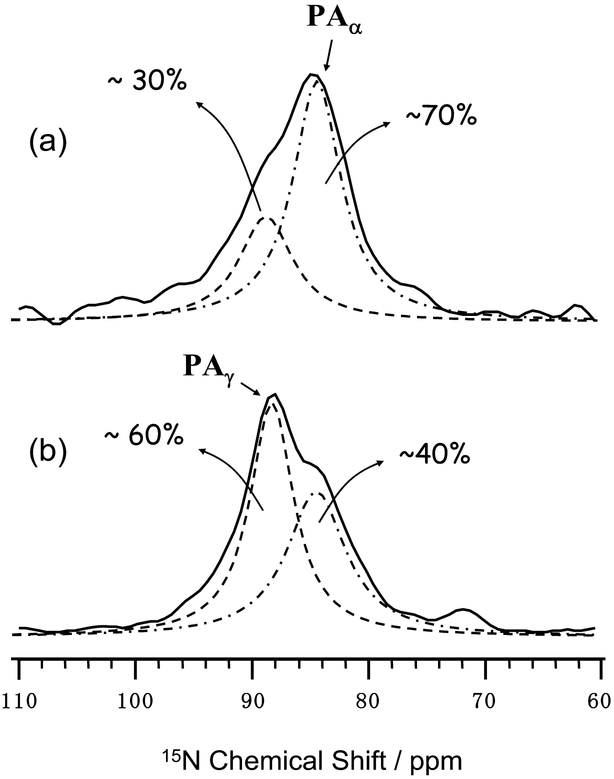

Figure 8. Observed ^{15}N CPMAS NMR spectra of (a) PK60PA40 blend and (b) pure PA.

For the wet condition, the amorphous phase of PA is water-absorbed, so that the CP efficiency of the amorphous phase is depressed. Thus the amorphous peak is obscured in Figure 8. It is well known that the ^{15}N NMR signal is sensitive to the difference in the polymer chain direction between the α and γ crystalline phases of PA and shows a different chemical shift, which is due to the difference in the circumstances of hydrogen bonding (*24–26*). The signal ascribed to the α crystalline phase of PA resonates at 84 ppm and that to the γ crystalline phase at 89 ppm (*25*). Obviously, the α crystalline phase of PA in the PK60PA40 blend is dominant compared with that of pure PA: rapid cooling of PA induced the growth of the γ crystalline phase in pure PA, although the α crystalline phase is thermally stable usually. This indicates that PK induces the growth of the α crystalline phase of PA in the blend rather than α crystallites. The relative fraction of the α crystalline phase of PA changes from 40% to 70% after blending with

Downloaded by CORNELL UNIV on June 20, 2012 | http://pubs.acs.org
Publication Date (Web): October 14, 2011 | doi: 10.1021/bk-2011-1077.ch005

PK. This observation suggests that PK induces the thermally stable α crystalline phase of PA in the blend. Presumably, the lamellar-like structure of PK will be stabilized by the alternation of the crystalline phase of PA between parallel (γ) and anti-parallel (α) chain directions. It is also revealed that PK causes the crystallization temperature of PA to decrease; a higher crystallization temperature induces γ crystallites (*9*). The change in the crystalline form of PA is related to the complicated morphology detected in the TEM image and to the high impact properties under the wet condition.

Figure 9 shows the observed T_1^H curves of both PK and PA in the PK60PA40 blend for both dry and wet conditions. These T_1^H curves were obtained from the C=O carbon peaks of PK and PA, respectively. Because both C=O carbons are close to the protons of the main chain aliphatic carbons or NH, ^{1}H spin diffusion occurs efficiently even though protons are not bonded directly to carbon within the CP contact time of 2 ms. The T_1^H curves of both pure PK and pure PA (dashed lines) show single exponential decay, resulting in semi-log plots in a straight line. The T_1^H values for pure PK and pure PA under the dry condition are 2.06 ± 0.03 s ($1/T_1^H = K = 0.485$ s^{-1}) and 1.06 ± 0.01 s ($K = 0.943$ s^{-1}), respectively. The values under the wet condition are 1.50 ± 0.01 s ($K = 0.667$ s^{-1}) for PK and 0.86 ± 0.01 s ($K = 1.163$ s^{-1}) for PA. The T_1^H rates, K, under the wet condition are faster than those under the dry condition. This indicates that the molecular motion of both polymers is affected and is increased by water absorption. For PA, water is absorbed predominantly in the amorphous phase and the humidity is 1.9%; for the PA-rich alloys, the humidity is 1.7%. On the other hand, PK absorbs water without selectivity, and the amount of absorbed water is only 0.6%. This difference in water absorption shows that the ^{13}C CPMAS NMR spectrum of PK remains unchanged under the wet condition, but that there is sufficient water absorption to change the molecular motion and to affect the T_1^H of PK.

To obtain the information on domain size, the observed data points are fitted by equation (1) with f_{PA} of 0.548. The solid lines, which are obtained by the least-square fit to the data, are in excellent agreement with the observed T_1^H decay curves (● and ○) in the PK60PA40 blend. The K values obtained for the dry condition are 0.53 ± 0.02 s^{-1} (1.90 s) for PK and 0.81 ± 0.02 s^{-1} (1.21 s) for PA, respectively: the values in parenthesis are $1/K$. The ^{1}H spin-diffusion rate, k, was 0.8 ± 0.3 s^{-1}. The values obtained for the wet condition are $K_{PK} = 0.66 \pm 0.04$ s^{-1} (1.51 s), $K_{PA} = 0.95 \pm 0.04$ s^{-1} (1.05 s), and $k = 0.7 \pm 0.5$ s^{-1}, respectively. The initial relaxation rate of PA, K_{PA}, in the blend is more affected by blending with PK than that of PK. The K_{PA} value is slower than that of pure PA by ca. 0.2 s^{-1}, whereas that of PK in the blend is comparable to that of pure PK. This observation suggests that PA is dispersed and located in the PK matrix. It also indicates that the molecular motion of PA is greatly affected after blending with PK. Since the molecular motion of the rigid PK lamellar structure is not influenced by PA, the initial relaxation rate does not change after blending, whereas that of PA is altered. On the other hand, the ^{1}H spin-diffusion rate, k, is comparable to the initial relaxation rate of both polymers and intermediate between K_{PK} and K_{PA}. This value indicates that ^{1}H spin diffusion is slow, but that the two polymers are not completely phase-separated on a scale of several tens to several hundreds of nm. The maximum diffusive path

Downloaded by CORNELL UNIV on June 20, 2012 | http://pubs.acs.org
Publication Date (Web): October 14, 2011 | doi: 10.1021/bk-2011-1077.ch005

length, $\sqrt{<r^2>}$ (*i.e.*, average value of *r*), for the three-dimensional diffusion model is estimated by $\sqrt{6D/k}$; *D* is the diffusion coefficient for proton spin energy. From the TEM images that show that the direction of the lamellae is not uniform, and we employed the $\sqrt{<r^2>}$ to estimate the domain size. The effective *D* value (*27*, *28*) has been estimated to be ca. 700 nm^{2}s^{-1} from both diffusion coefficients D_{PK} = 840 nm^{2}s^{-1} and D_{PA} = 600 nm^{2}s^{-1}, which are obtained from the ^{1}H spin-spin relaxation rate (*20*). The estimated path length, *r*, is about 77 nm. Thus, the average domain size is approximately 150 nm which is twice as large as *r*. This value is consistent with the averaged overall size of the elliptical (or spherical or cylindrical) domains measured from the 3D TEM.

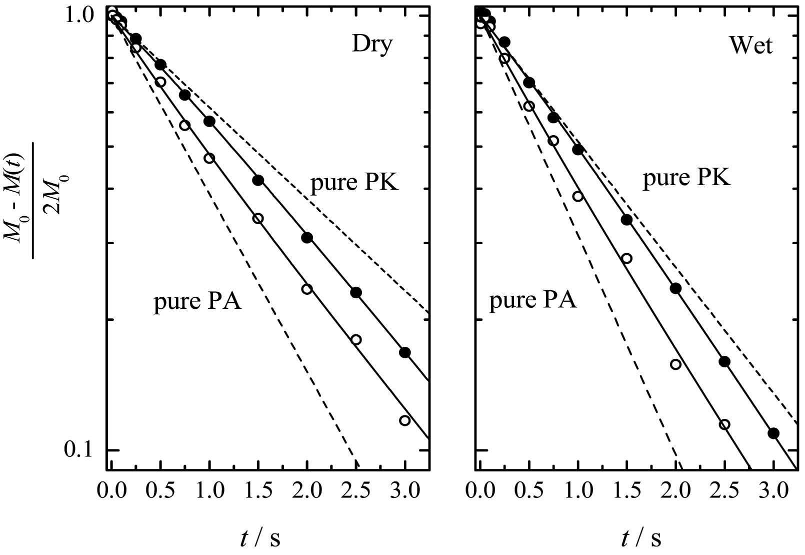

Figure 9. Semi-logarithmic plots of normalized T_1^H decay curves for PK (●) and PA (○) in the PK60PA40 blend under the dry and wet conditions. Dashed lines represent T_1^H decay curves for pure PA and pure PK. The solid lines were obtained with equation 1.

Thus, the domain size under the wet condition did not change as compared to that under the dry condition. From 3D TEM image, however, it was suggested that the creation of the co-continuous spherical amorphous region contributes the high impact resistance, and PK crystalline lamellae are evidently formed only by blending with PA. From the NMR study, it was futher revealed that the γ crystalline phase is converted to the α crystalline phase for PA by blending with PK, and water absorption occurs selectively in the amorphous region of PA. These observations indicate that the water-absorbing amorphous phase of PA plays an important role in enabling PK/PA blends to exhibit high impact resistance and toughness. Actually, from SAXS the long period of PK lamellae becomes wider by approximately 1 nm under the wet condition through the swelling of PA amorphous phase (*9*, *21*). Hence, the combination of both rigidity of PK lamellae and elasticity of water-

Downloaded by CORNELL UNIV on June 20, 2012 | http://pubs.acs.org
Publication Date (Web): October 14, 2011 | doi: 10.1021/bk-2011-1077.ch005

absorbing amorphous phase of PA is needed to obtain high impact properties, modulus, and toughness.

Conclusion

In this article, I first showed the relationship between the domain size of crystalline phase and T_m of ε-PL for both PVIBE/ε-PL blends and PVIBE/ε-PL/saponite nanocomposites. The T_m values are associated with the total lamellar thickness estimated from an analysis of the effect of ^{1}H spin diffusion on T_1^H. Even so, it is disputable whether the calculated value is really related to the single lamellar thickness. As I mentioned above, there are two possibilities for the lamellar thickness in the case of similar crystallinity. One is that the lamellar thickness does not change but the amount of lamellar decreases with decreasing domain size. Another one is that the thickness of the single lamellar layer decreases with decreasing crystalline domain size of ε-PL but the amount increases in the crystalline phase to keep the crystallinity constant. The mostly constant crystallinity has been estimated, as listed in Table 1 for 10/2 to 10/5 compositions. In the latter case, T_m changes as expected with the estimated L_C value and obeys the Gibbs-Thomson relation. If the actual morphology is similar to the former condition, the decreasing T_m can be explained by the diluent effect of adding PVIBE. In actual fact, we cannot distinguish between the diluent effect and the Gibbs-Thomson effect from the L_C estimation for the blends only. However, it is also true that the diluent effect cannot explain the constancy of T_m observed for the nanocomposites. The decrease of the lamellar thickness gives unambiguous solution of the shift and the constancy of T_m values observed for both blends and nanocomposites, if the estimated L_C value is comparable to the summation of a single lamellar layer thickness.

Furthermore, the relationship between the crystalline structure and impact property for the PK/PA blends is elucidated. The high impact resistance and toughness of PK/PA blends are the result of the interactions among the water-absorbing amorphous phase of PA, the existence of lamellar-like structure of PK, and the conversion of PA crystallite types.

Downloaded by CORNELL UNIV on June 20, 2012 | http://pubs.acs.org
Publication Date (Web): October 14, 2011 | doi: 10.1021/bk-2011-1077.ch005

Acknowledgments

I am very grateful to collaborators at National Defense Academy, NISSAN ARC LTD., and Industrial Technology Center of Okayama Prefecture for their helpful and valuable cooperation with this study.

References

1. Strobl, G. R. *The physics of polymers*; Springer-Verlag: Berlin, 1996; Chapter 4.
2. Kitamaru, R.; Kaji, K. Kobunshi Jikken-gaku. In *Kobunshi no Kotai Kouzou II (Solid structure of polymer II)*; Kyoritsu Shuppan Co., Ltd.: Tokyo, 1984; Vol. 17, Chapter 6 (in Japanese).

3. Asano, A.; Tanaka, C.; Murata, Y. *Polymer* **2007**, *48*, 3809–3816.
4. VanderHart, D. L.; Asano, A.; Gilman, J. W. *Chem. Mater.* **2001**, *13*, 3781–3795.
5. VanderHart, D. L.; Asano, A.; Gilman, J. W. *Chem. Mater.* **2001**, *13*, 3796–3809.
6. Asano, A.; Murata, Y.; Kurotsu, T. *e-J. Soft Mater.* **2007**, *3*, 1–8.
7. Asano, A.; Tanak, C.; Kurotsu, T. *Macromolecules* **2008**, *41*, 9469–9473.
8. Asano, A.; Nishioka, M.; Kato, A.; Takahashi, Y.; Sawabe, H.; Arao, M.; Sato, S.; Sato, H.; Izumi, T.; Drozdova, O.; Ishikawa, D.; Hasegawa, T.; Okamura, T.; Nagata, K.; Hikasa, S.; Iwabuki, H. *Polym. Prep.* **2008**, *49*, 682–683.
9. Asano, A.; Nishioka, M.; Takahashi, Y.; Kato, A.; Hikasa, S.; Iwabuki, H.; Nagata, K.; Sato, H.; Hasegawa, T.; Sawabe, H.; Arao, M.; Suda, T.; Isoda, A.; Mukai, M.; Ishikawa, D.; Izumi, T. *Macromolecules* **2009**, *42*, 9506–9514.
10. Kato, A.; Nishioka, M.; Tkahashi, Y.; Suda, T.; Sawabe, H.; Isoda, A.; Drozdova, O.; Hasegawa, T.; Izumi, T.; Nagata, K.; Hikasa, S.; Iwabuki, H.; Asano, A. *J. Appl. Polym. Sci.* **2010**, *116*, 3056–3069.
11. Shih, I. L.; Shen, M. H.; Van, Y. T. *Bioresource Tech.* **2006**, *97*, 1148–1159.
12. Bennet, A. E.; Rienstra, C. M.; Auger, M.; Lakshmi, K. V.; Griffin, R. G. *J. Chem. Phys.* **1996**, *103*, 6951–6958.
13. Peersen, O. B.; Wu, X.; Kustanovich, I.; Smith, S. O. *J. Magn. Reson.* **1993**, *A104*, 334–339.
14. Metz, G.; Wu, X.; Smith, S. O. *J. Magn. Reson.* **1994**, *A110*, 219–227.
15. Torchia, D. A. *J. Magn. Reson.* **1978**, *30*, 613–616.
16. VanderHart, D. L.; Pérez, E. *Macromolecules* **1986**, *19*, 1902–1909.
17. Asano, A.; Takegoshi, K.; Hikichi, K. *Polymer* **1994**, *35*, 5630–5636.
18. VanderHart, D. L.; McFadden , G. B. *Solid State Nucl. Magn. Reson.* **1996**, *7*, 45–66.
19. Demco, D. E.; Johansson, A.; Tegenfeldt, J. *Solid State Nucl. Magn. Reson.* **1995**, *4*, 13–38.
20. Assink, R. A. *Macromolecules* **1978**, *11*, 1233–1237.
21. Takahasi, Y.; Nishioka, M.; Kato, A.; Hikasa, S.; Iwabuki, H.; Nagata, K.; Asano, A. *Kobunshi Ronbunshu* **2009**, *66*, 577–584.
22. Weeding, T. L.; Veeman, W. S.; Gaur, H. A.; Huysmans, G. B. *Macromolecules* **1988**, *21*, 2028–2032.
23. Okada, A.; Kawasumi, M.; Tajima, I.; Kurauchi, T.; Kamigaito, O. *J. Appl. Polym. Sci.* **1989**, *37*, 1363–1371.
24. Hatfield, G. R.; Glans, J. H.; Hammond, W. B. *Macromolecules* **1990**, *23*, 1654–1658.
25. Mathias, L. J.; Davis, R. D.; Jarrett, W. L. *Macromolecules* **1999**, *32*, 7958–7960.
26. Andreis, M.; Koenig, J. L. *Adv. Polym. Sci.* **1995**, *124*, 191–237.
27. Clauss, J.; Schmidt-Rohr, K.; Spiess, H. W. *Acta Polym.* **1993**, *44*, 1–17.
28. Mellinger, F.; Wilhelm, M.; Spiess, H. W. *Macromolecules* **1999**, *32*, 4686–4691.

Downloaded by CORNELL UNIV on June 20, 2012 | http://pubs.acs.org
Publication Date (Web): October 14, 2011 | doi: 10.1021/bk-2011-1077.ch005

Downloaded by UNIV OF DELAWARE MORRIS LIB on June 19, 2012 | http://pubs.acs.org
Publication Date (Web): October 14, 2011 | doi: 10.1021/bk-2011-1077.ch006

Chapter 6

Investigation of Filler-Matrix Interactions and Confinement Effect in Polymer Nanocomposites

K. P. Pramoda,*,[1] K. Y. Mya,[1] T. T. Lin,[1] J. Wang,[1] and C. B. He[1,2]

**[1]Institute of Materials Research and Engineering (IMRE),
(A*STAR) Agency for Science, Technology and Research,
3 Research Link, Singapore 117602
[2]Department of Materials Science and Engineering, National University of
Singapore, 7 Engineering Drive 1, Singapore 117574
*E-mail: pramoda-kp@imre.a-star.edu.sg**

Although nanocomposites are known for decades, the molecular interactions under the confined environments of such composites are not well understood. In this article we report the influence of two types of fillers, viz., graphite (G) and graphene oxide (GO) nanosheets, on polyimide (PI) matrix with varying filler content. Solid state NMR and thermo-mechanical analysis were deployed to characterize the morphology of hybrid materials and the interactions between the polymer and the filler. CP-MAS and relaxation experiments were performed to probe the interaction between inorganic and organic phases on a molecular level and to elucidate polymer dynamics. NMR relaxation measurements further helped in elucidating the polymer dynamics and were supplemented by thermo-mechanical relaxation. From the relaxation data it is clear that GO interacts better than G with the polyimide matrix. This is further confirmed by the higher modulus observed for PI-GO nanocomposites than for PI-G.

Introduction

Nanocomposites are a newly emerged class of composite materials that incorporate relatively small percentages of nanometer-sized filler particles. Nanocomposites with carbon as filler materials exhibit improved electrical,

In NMR Spectroscopy of Polymers: Innovative Strategies for Complex Macromolecules; Cheng, H., et al.;
ACS Symposium Series; American Chemical Society: Washington, DC, 2011.

thermal and mechanical properties (*1*, *2*). Among the various other carbon additives, graphite is much more attractive to researchers as it is comparable to carbon nanotube (CNT) in properties. Moreover, it has a layered structure (similar to clay) constituted by a large number of graphene sheets held by van der Waals forces (*3*, *4*). Therefore, pretreatment and modification of graphite is necessary to achieve the nanosheet distribution of graphene. Surface treatment of graphene makes it more compatible to polymer matrix which helps good dispersion in a polymer matrix, resulting in nanocomposites with excellent mechanical and electrical properties. Polymer nanocomposites find applications in automobile, food packaging and biomedical industries due to improvements in thermal, physical and gas permeability properties of the polymers attributed to the nanoscale filler materials. For silicates, these enhancements are achieved with less than 10% wt addition of the exfoliated nanoscale dispersion of 1 nm thick layers, with diameters between 20 and 500 nm. This is in stark contrast to conventional polymer fillers, such as talc, mica, silica, and carbon black, which require high concentrations (>30 wt %) and may cause deterioration of fracture toughness and in processibility.

Daniel et al (*5*) reported a 15% improvement in elastic modulus of 1 wt % expanded graphite (EG)-epoxy nanocomposite over pure epoxy and attributed it to the in-situ formation of graphite nanosheets as well as to their uniform dispersion and exfoliation in the epoxy matrix. High density polyethylene reinforced with EG and untreated graphite by a melt compounding process also shows an improvement in the electrical and mechanical properties of nanocomposite (*6*). Poly(methyl methacrylate)-EG composites prepared by in-situ polymerization exhibits better mechanical and electrical properties than those prepared using solution blending methods (*7*). Although epoxy and thermoplastic nanocomposites with graphite/graphene oxide nanosheet fillers have been studied, to our knowledge, there have been no reports available on polyimide (PI)-based graphite nanocomposites.

Polyimides (PIs) are widely used in defense and aerospace applications as well as in the electronics industry for a variety of applications because of their high temperature resistance, low dielectric constant, inertness to solvent, and long-term stability (*8*). Polyimide nanocomposites with various fillers such as CNT, clay, and POSS (Poly Oligomer SilSesquioxane) have been studied (*9–12*). In this article we report on the influence of two types of fillers, namely, graphite (G) and graphene oxide (GO) nanosheets, on polyimide matrix with varying filler content. Solid state nuclear magnetic resonance (SSNMR) spectroscopy and thermo-mechanical analysis were deployed to characterize the morphology of hybrid materials and the interaction between the polymer and the filler. The chemical oxidations of graphite to graphite oxide are confirmed by XRD. The interaction between filler and the polymer matrix is further studied by XPS analysis. In addition, dynamic mechanical thermal analysis (DMTA), and thermomechanical analysis (TMA) are applied to characterize the glass transition temperature (T_g), storage modulus (E′), and coefficient of thermal expansion (CTE).

Downloaded by UNIV OF DELAWARE MORRIS LIB on June 19, 2012 | http://pubs.acs.org
Publication Date (Web): October 14, 2011 | doi: 10.1021/bk-2011-1077.ch006

Downloaded by UNIV OF DELAWARE MORRIS LIB on June 19, 2012 | http://pubs.acs.org
Publication Date (Web): October 14, 2011 | doi: 10.1021/bk-2011-1077.ch006

Experimental Section

Materials and Synthesis of Polyimide Composites

Biphenyltetracarboxylic dianhydride, phenylene diamine, and N-methyl-2-pyrrolidinone (NMP) were purchased from Sigma-Aldrich. All the monomers were purified before use. Graphite, donated generously by Asbury Carbons (Asbury, NJ, 3775 grade) was used as received and also oxidized by a modified Hummer's method (*13*). The poly(amic acid) (PAA) precursor solution was prepared through polycondensation reaction between dianhydride and diamine in NMP. The resulting PAA solutions were controlled to have solid contents of 10-15wt%. In a separate flask, the filler (G/GO) was first uniformly dispersed in NMP using an ultrasonic bath to obtain their respective nanosheet. After that, the required amount of G-NMP/GO-NMP was added to the PAA solution and stirred continuously. The solution was then cast on a glass plate using automatic film applicator and thermally treated at 100°C for 1 h, 200°C for 1 h, and 300°C for 4 h, respectively. The films were then removed from the glass substrate with the aid of warm water and dried at 50°C in a vacuum oven for 2 days. The thickness of the films was ~100 μm. Hereafter, the PI composite film with G filler was denoted as "PI-G" and the film with GO filler "PI-GO."

Characterization

X-ray diffraction (XRD) patterns of the samples were recorded by using a Bruker GADDS diffractometer, with an area detector operating under 40 kV and 40mA, using CuK$_\alpha$ radiation ($\lambda = 0.154\ 18$ nm). X-ray photoelectron spectroscopy (XPS) data were recorded using a VG Scientific EscaLab 220 IXL spectrometer with an Al K$_\alpha$ X-ray source (hν = 1 486.6 eV). The spectra were corrected for carbon shift binding energy, Cs = 284.5 eV in order to determine the accurate binding energies. SSNMR measurements were carried out with Varian 400 MHz (9.4 T) wide bore spectrometer and the samples were spun at the magic angle at the rate of 15 kHz using a 4 mm double resonance probe. The spectrometer was operated at resonance frequencies of 100 and 400 MHz to obtain ^{13}C and ^{1}H spectra, respectively. The spectra were referenced using tetramethylsilane (TMS). Thermomechanical behavior of the composites was analyzed with the help of dynamic mechanical thermal analyzer (DMTA) and thermo mechanical analyzer (TMA) from TA Instruments. The modeling and simulation on these complexes were done using Materials Studio software and DMol^3 (*14*). The binding energy was calculated using the density functional theory (DFT) calculation with the following equation:

Binding energy (kcal/mol) = total energy of the model (complex) - total energy of the model (G/GO) - total energy of the model (PI).

Downloaded by UNIV OF DELAWARE MORRIS LIB on June 19, 2012 | http://pubs.acs.org
Publication Date (Web): October 14, 2011 | doi: 10.1021/bk-2011-1077.ch006

Results and Discussion

Chemically oxidized graphite (G) is known as graphene oxide (GO) which forms a stable dispersion in water or other organic solvents leading to GO nanosheets. The extent of oxidation and the surface structure of GO are the key parameters to improve their compatibility with the polymer. The oxidation of graphite may affect its chemical structure and was confirmed by XRD and FTIR (*15*). Figure 1 represents the XRD pattern of G and GO together with its polymer composites. A strong peak is observed at 2θ = 26.6° for G and a scattering signal at 2θ = 9° for GO. The peak at 26.6° represents the intact crystal lattice in G and the peak at 9° for GO corresponds to a layer spacing of 10 Å (*16*). The absence of the peak at 26.6° (2θ) in GO implies that the crystal lattice structure of G has been disrupted. On the other hand, a small peak that appears at 26.6° (2θ) in the PI-G composites shows the intercalation of graphite in the PI matrix. However, the absence of the peak at 9° (2θ) that is the characteristic of GO in the PI-GO composites indicates that the packing of the GO has been entirely disrupted by PI-chains.

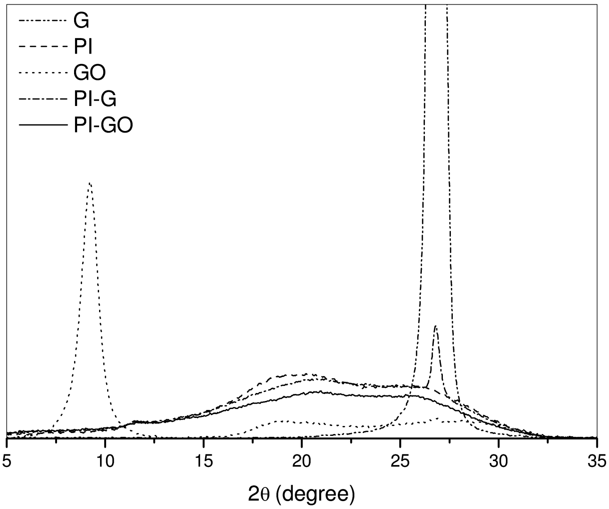

Figure 1. XRD spectra for G and GO along with the neat PI, PI-G and PI-GO systems, respectively.

The interaction between filler and the PI matrix plays a critical role in the property enhancement in the nanocomposites and therefore it is studied by XPS and SSNMR analyses. XPS provides information on the specific interaction in polymer nanocomposites as the binding energy (BE) of a core-level electron depends on its chemical environment (*17*). SSNMR reveals the structure, conformation and dynamics of polymer chains in the composites, and thereby the interactions between the polymer and the filler. However, there have been only a few papers on the application of SSNMR to the structure and dynamics of organic-inorganic hybrid nanomaterials. VanderHart's research group at

NIST has studied Nylon-6/clay nanocomposites, including clay dispersion, crystal stratification, and stability of organic modifiers, using ^{1}H T$_1$ relaxation times. Nanodispersion in polystyrene-montmorillonite nanocomposites was also investigated by Gilman and coworkers (*18–20*).

Figure 2 shows the ^{1}H NMR spectra of the PI nanocomposites. It is observed that the peak shifts upfield from 7.73 ppm in neat PI to 7.16 ppm along with the presence of shoulder peaks (3.01 and 0.84 ppm) in PI-GO system. It is clearly indicated that the interaction between filler and the matrix depends on the structure and relaxation of polymer chains. In addition, the incorporation of GO shows a better intensified peak compared to G, indicating better compatibility between the filler and the matrix in PI-GO system.

Downloaded by UNIV OF DELAWARE MORRIS LIB on June 19, 2012 | http://pubs.acs.org
Publication Date (Web): October 14, 2011 | doi: 10.1021/bk-2011-1077.ch006

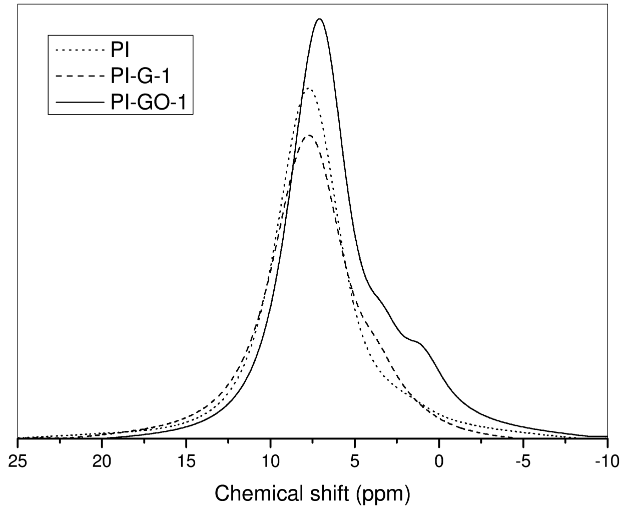

Figure 2. ^{1}H SS NMR spectra for neat PI, and 1 wt% of PI-G, PI-GO.

Relaxation measurements on these samples can be informative as well. The T$_1$ relaxation times for ^{1}H and ^{13}C are tabulated in Table 1. The T$_1$ values for the composites are reduced compared to neat PI. The T$_1$ values for both ^{1}H and ^{13}C are reduced in the following order PI > PI-G > PI-GO. This trend suggests strong filler-matrix interaction between PI chains and GO nanosheets compared to PI-G. This was further verified by thermomechanical properties such as modulus and CTE enhancement (discussed later) in PI-GO composites as compared to PI-G.

The N 1s binding energies (BEs) for PI composites are displayed in the Table 1. As seen in the Table, the peak at 400.8 eV in neat PI is shifted by 0.8 eV for 1 wt% GO (400 eV) and the shift is only 0.4 eV in the case of 1 wt% G (400.4 eV). The magnitude of the changes in BEs of N 1s correlates well to the strength of interaction, indicating that the interaction between PI and GO is stronger than that in PI-G composite. The observed strong interaction in PI-GO system is possibly due to the presence of functional groups such as OH, COOH, and epoxy, which becomes the preferable site for the interaction with the linear chain packing of PIs.

However, the observed decrease in the BE values are not prominent, mainly due to the lower sensitivity of N1s in the XPS measurement.

Table 1. N1s XPS and ^{1}H SS NMR fit data along with their relaxation time

	BE N1s XPS (eV)	*T_1 (s)*	
		^{13}C	*^{1}H*
PI	400.8	38	1.5
PI-G-1%	400.4	32	1.0
PI-GO-1%	400.0	22	0.3

Thermomechanical properties of PI composites were determined by DMTA and TMA analyses. Figure 3 shows the DMTA curves for PI-G and PI-GO composites with 1 wt% of G and GO, respectively. The storage modulus (E′) increased with increasing filler (G/GO) content as seen in Figure 3. Table 2 summarizes the storage modulus (E′) at 100°C along with α and β transition temperature (T_α and T_β). T_α or T_g ~ 340°C; the presence of filler did not affect much the T_g of the PI matrix. The observed modulus enhancement was greater with GO addition as compared to PI-G system. A ca. 38% improvement in E′ for 1 wt% of G loading was observed versus an increase of ca. 106% with GO loading for PI-GO composites. The extent of increase in E′ was greater in the PI-GO system, which is possibly due to the better interaction between the GO and the PI, leading to both physical and chemical cross-linking between filler and the PI matrix, as evidenced by the ^{1}H-NMR spectra. In comparison to our system, PI-clay composites (*10*) showed a modulus increase of ~42% with 2 wt% clay loading relative to that of neat PI. Similarly, Zhu et al (*11*) also reported that the modulus of the PI-multi-walled carbon nanotube (MWCNT) composites exhibited 40% increase with 5 wt% of MWCNTs content.

Table 2. Storage modulus, (E′@100°C), T_β, $T_\alpha(T_g)$, and CTE values

	T_β (°C)	*$T_\alpha(T_g)$ (°C)*	*E′ (GPa) @ 100°C*	*CTE (100-250°C) ppm/°C*
PI	191	341	8.41	15.70
PI-G-1%	187	340	11.6	3.98
PI-GO-1%	186	344	17.3	1.67

Downloaded by UNIV OF DELAWARE MORRIS LIB on June 19, 2012 | http://pubs.acs.org
Publication Date (Web): October 14, 2011 | doi: 10.1021/bk-2011-1077.ch006

Downloaded by UNIV OF DELAWARE MORRIS LIB on June 19, 2012 | http://pubs.acs.org
Publication Date (Web): October 14, 2011 | doi: 10.1021/bk-2011-1077.ch006

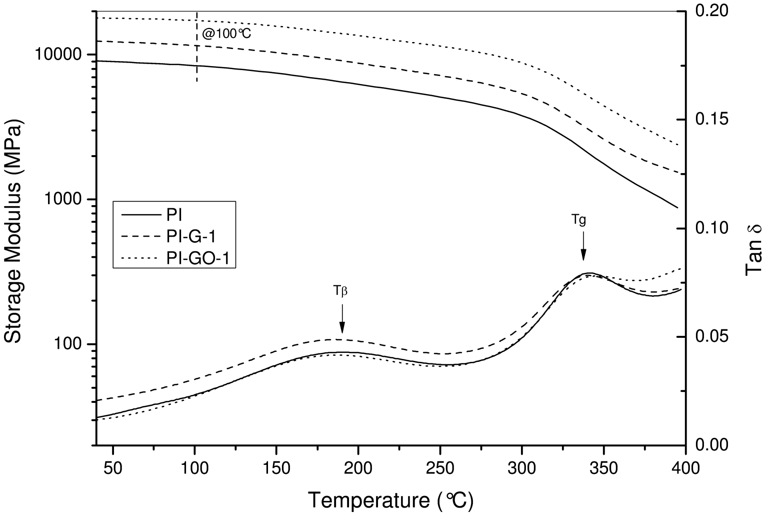

Figure 3. Temperature dependant storage moduli and tangent delta for the neat PI and its composites.

The influences of G/GO on the CTE of the PI composites were also investigated, and the results are shown in Table 2. It was found that the CTE decreased when G and GO were incorporated into the PI matrix. The CTE of the PI composite films is significantly reduced by about 75% and 90%, for 1% loading of G and GO, respectively. Since CTE depends on the rigidity of PI-chain and the interaction between PI and the fillers, the observed decreases in the CTE for PI-G and PI-GO composite systems suggested that the interaction between PI-chain and the G/GO nanosheet were strong which hindered the motion of the PI-chain. On the other hand, the relatively lower CTE observed in PI-GO when compared with PI-G could be attributed to the strong interaction between the GO with PI-chain, which has been confirmed by XPS and NMR studies. Furthermore, our DFT calculation also suggests that the binding energy for the composite PI-GO was found to be 10.7 kcal/mol with an orbital cutoff 3.7 Å while it was only 3.7 kcal/mol for PI-G with same value of cutoff (i.e. 3.7 Å). The theoretical calculations also supported our experimental findings; i.e., the interactions between the PI-chains and the GO nanosheets are much stronger than that in the PI-G.

Downloaded by UNIV OF DELAWARE MORRIS LIB on June 19, 2012 | http://pubs.acs.org
Publication Date (Web): October 14, 2011 | doi: 10.1021/bk-2011-1077.ch006

Conclusions

Spectroscopic investigation was carried out to determine the relaxation behavior of PI composites. The relaxation times obtained from NMR analysis indicate that the interaction between PI chain and GO nanosheet is stronger than that in PI-G composites. In agreement, the DFT calculations revealed that the chemical compatibility achieved between PI and filler were mainly with GO rather than G. Dynamic mechanical thermal analysis shows that the incorporation of GO nanosheets significantly enhance the storage moduli of PI nanocomposites compared to that of G nanosheets. The moduli improved ~106% with only 1 wt% GO nanosheets while it is only ~38% with G nanosheets. The extent of thermal expansion coefficient drop in the case of GO incorporation is greater than that of G.

Acknowledgments

The authors thank IMRE and Agency for Science, Technology, and Research (A*STAR), Singapore for financial support.

References

1. *Polymer Nanocomposites: Synthesis, Characterization and Modeling*; Krishnamoorti, R., Vaia, R. A., Eds.; ACS Symposium Series 804; American Chemical Society: Washington, DC, 2002.
2. Pinnavaia, T. J.; Beall, B. W. *Polymer-Clay Nanocomposites*; Wiley: New York, 2001.
3. Chung, D. D. L. *J. Mater. Sci.* **2004**, *39*, 2645–2661.
4. Jang, B. Z.; Zhamu, A. *J. Mater. Sci.* **2008**, *43*, 5092–5101.
5. Yashmin, A.; Luo, J. J.; Daniel, I. M. *Compos. Sci. Technol.* **2006**, *66*, 1182–1189.
6. Zheng, W.; Lu, X.; Wong, S. C. *J. Appl. Polym. Sci.* **2004**, *91*, 2781–2788.
7. Ramanathan, T.; Abdala, A. A.; Stankovich, S.; Dikin, D. A.; Herrera-Alonso, M.; Piner, R. D.; Adamson, D. H.; Schniepp, H. C.; Chen, X.; Ruoff, R. S.; Nguyen, S. T.; Aksay, I. A.; Prud'homme, R. K.; Brinson, L. C. *Nat. Nanotechnol.* **2008**, *3*, 327–331.
8. Ghosh, K. L.; Mittal, K. L. *Polyimides: Fundamentals and Applications*; Marcel Dekker: New York, 1996.
9. Wahab, M. A.; Khine, M. Y.; He, C. B. *J. Polym. Sci., Part A: Polym. Chem.* **2008**, *46*, 5887–5896.
10. Agag, T.; Koga, T.; Takeichi, T. *Polymer* **2001**, *42*, 3399–3408.
11. Zhu, B.-K.; Xie, S.-H.; Xu, Z.-K.; Xu, Y.-Y. *Compos. Sci. Technol.* **2006**, *66*, 548–554.
12. Mya, K. Y.; Wang, K.; Chen, L.; Lin, T. T.; Pallathadka, P. K.; Pan, J.; He, C. B. *Macromol. Chem. Phys.* **2008**, *209*, 643–650.
13. Hummers, W. S.; Offeman, R. E. *J. Am. Chem. Soc.* **1958**, *80*, 1339.
14. Delley, B. *J. Chem. Phys.* **1990**, *92*, 508–517.

15. Pramoda, K. P.; Hussain, H.; Koh, H. M.; Tan, H. R.; He, C. B. *J. Polym. Sci., Part A: Polym. Chem.* **2010**, *48*, 4262–4267.
16. Jeong, H. K.; Lee, Y. P.; Lahaye, R. J. W. E.; Park, M. H.; An, K. H.; Kim, I. J.; Yang, C. W.; Park, C. Y.; Ruoff, R. S.; Lee, Y. H. *J. Am. Chem. Soc.* **2008**, *130*, 1362–1366.
17. Beamson ,G.; Briggs, D. *High Resolution XPS of Organic Polymers*; John Wiley and Sons: Chichester 1992.
18. Bourbigot, S.; VanderHart, D. L.; Gilman, J. W.; Awad, W. H.; et al. *J. Polym. Sci., Part B: Polym. Phys.* **2003**, *41*, 3188–3213.
19. VanderHart, D. L.; Asano, A.; Gilman, J. W. *Chem. Mater.* **2001**, *13*, 3781–3795.
20. VanderHart, D. L.; Asano, A.; Gilman, J. W. *Macromolecules* **2001**, *34*, 3819–3822.

Downloaded by UNIV OF DELAWARE MORRIS LIB on June 19, 2012 | http://pubs.acs.org
Publication Date (Web): October 14, 2011 | doi: 10.1021/bk-2011-1077.ch006

Chapter 7

^{1}H MAS NMR Spectroscopy of Polyethylene Acrylic Acid Copolymers and Ionomers

Todd M. Alam,*,[1] Janelle E. Jenkins,[1] Michelle E. Seitz,[2] C. Francisco Buitrago,[3] Karen I. Winey,[2] Kathleen L. Opper,[4] Travis W. Baughman,[4] and Kenneth B. Wagener[4]

[1]Electronic and Nanostructured Materials, Sandia National Laboratories, Albuquerque, NM 87185
[2]Department of Materials Science and Department of Chemical and Biomolecular Engineering, University of Pennsylvania, Philadelphia, PA 19104
[3]Department of Chemical and Biomolecular Engineering, University of Pennsylvania, Philadelphia, PA 19104
[4]Department of Chemistry, University of Florida, Gainesville, FL 32611
***E-mail: tmalam@sandia.gov**

High speed solid-state ^{1}H MAS NMR spectroscopy has been used to characterize a series of poly(ethylene-*co*-acrylic acid) P(E-AA) materials where the distributions of the pendant carboxylic acid group along the polymer backbone are precisely controlled. Ionomers obtained from partial neutralization of the carboxylic acid within these P(E-AA) materials with Zn^{2+} or Li^{+} were also investigated. Using a combination of 1D ^{1}H MAS NMR and 2D ^{1}H MAS NMR double quantum (DQ) and NOESY correlation experiments, details about the local P(E-AA) structure were obtained. The influence of precise versus random spacing of the carboxylic acid and the impact of Li- and Zn-neutralization on the polymer structure is discussed.

Introduction

The control and tailoring of polymer microstructure to suit the final application of the material remains an important objective. In addition, the ability to precisely locate ions within the polymer structure and morphology is predicted to provide

In NMR Spectroscopy of Polymers: Innovative Strategies for Complex Macromolecules; Cheng, H., et al.; ACS Symposium Series; American Chemical Society: Washington, DC, 2011.

control over the performance of ionomer membranes. Advances in the acyclic diene metathesis (ADMET) and ring-opening metathesis polymerization (ROMP) chemistry have now allowed production of polymers where the functional groups are precisely and pseudo-randomly placed along the polyethylene chain. Recent examples include the introduction of alkyl chains, halogens, phosphonic acids, and carboxylic acid groups with very controlled chain spacing (*1–4*). Understanding the local structure and morphology variations that occur with the inclusion of these functional groups is an area of active research. Characterization of these precise polymer materials has included the use of solid-state NMR spectroscopy; with ^{13}C, ^{19}F and ^{31}P magic angle spinning (MAS) NMR (*2*, *3*, *5*), and static ^{2}H NMR (*4*) investigations exploring the impact of random versus precise functional group incorporation on polymer crystallization.

In this chapter, we present then high speed ^{1}H MAS NMR characterization of a series of poly(ethylene-*co*-acrylic acid) copolymers, P(E-AA), and both Zn- and Li-neutralized P(E-AA) ionomers. The term ionomer has found use in literature to describe polymers that have ionic functional groups in humidified environments. For example, Nafion in considered an ionomer in both the acidic and neutralized salt form, because the sulfonic acid readily ionizes with water. In the present discussion we will refer to the non-neutralized P(E-AA) materials as acid copolymers, and the Li- or Zn-neutralized P(E-AA) systems as ionomers. This distinction arises because the P(E-AA) copolymer acts as a weak acid, with the carboxylic acids not being extensively ionized in a humid environment.

The ^{1}H MAS NMR spectra of polymers below T_g are commonly broad unresolved lines due to the presence of strong ^{1}H-^{1}H dipolar coupling (*6*, *7*). Utilizing high speed (> 30 kHz) MAS spinning, this dipolar coupling is significantly reduced producing spectra with increased spectral resolution (*8*). Even though the ^{1}H MAS NMR spectra for the P(E-AA) materials detailed here are relatively simple, details about the local hydrogen bonding environment and spatial connectivity between different functional groups can readily be obtained using variable temperature (VT) and multi-dimensional NMR spectroscopy correlation experiments as described below.

Experimental Section

Material Preparation

The synthesis and characterization of the linear poly(ethylene-*co*-acrylic acid), P(E-AA), materials have been previously described (*1*). Polymers with precisely spaced carboxylic acid groups were prepared using the ADMET chemistry. These polymer samples are designated as p9AA, p15AA and p21AA, and reflect samples where the carboxylic acid groups are precisely (p) located every 9th, 15th and 21st carbon along the backbone, respectively. The relative acid concentrations are 22, 13.3, and 9.5 mol%, respectively. A ROMP synthesis method was used to produce materials of equivalent acid concentrations, but with the carboxylic acid groups pseudo-randomly distributed along the polymer backbone. The designation r15AA, r21AA and r44AA reflect the random (r) nature and the average number of carbons between acid groups. The structures of these random and precise materials are shown in Scheme 1.

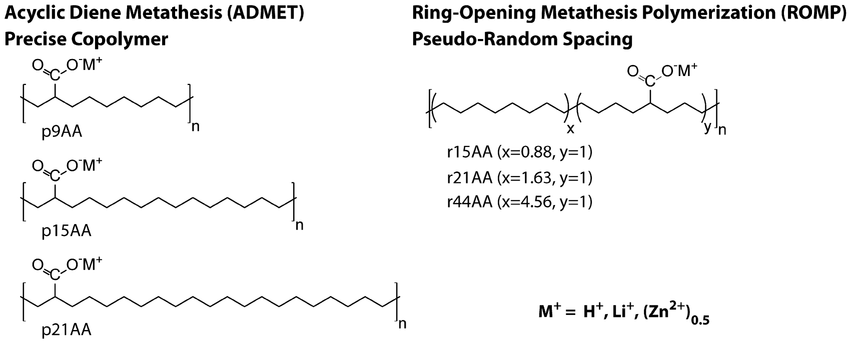

Scheme 1. Structures of poly(ethylene-co-acrylic) acid copolymers and the corresponding Li- and Zn-neutralized ionomers.

The Zn^{2+} neutralization of the P(E-AA) copolymers has been previously described (*9*). These polymer samples are designated as p21AA-56%Zn, p21AA-116%Zn, p15AA-82%Zn and p9AA-66%Zn to reflect the initial precise copolymer and the extent of neutralization. The Li^{+} neutralized material was prepared by dissolving the acid copolymer in a 1:4 mixture of 1,4-dioxane and 1-butanol at 90 °C, adding the appropriate amount of lithium acetate salt, followed by filtration of the resultant precipitant. These Li-neutralized materials are designated as p22AA-43%Li, p15AA-45%Li and r15AA-31%Li. The extent of Zn^{2+} or Li^{+} neutralization achieved was determined using inductively coupled plasma elemental analysis performed by Galbraith Laboratories (Knoxville, TN). The generalized structure for the exchanged P(E-AA) copolymers is shown in Scheme 1. The materials utilized for the NMR studies had previously been hot pressed at 150 °C (~ 0.4 mm film thickness) for X-ray scattering analysis. These polymer films were used as received unless otherwise noted.

Solid-State ^{1}H NMR Spectroscopy

The solid-state 1D ^{1}H magic angle spinning (MAS) NMR spectra were obtained on a Bruker AVANCE-III spectrometer operating at 600.13 MHz using a 2.5 mm broadband MAS probe, using N_2 for spinning. A rotor-synchronized Hahn spin echo pulse sequence was employed (Figure 1a), with 2.5 μs $\pi/2$ pulse, 16 scan averages, and a 5 s recycle delay. The rotor spinning speed for analysis was 30 kHz, unless specifically noted. Spin regulation was maintained at ± 1Hz through the experiments. It is known that significant frictional heating occurs at high MAS speeds. The actual sample temperature was calibrated using the ^{207}Pb chemical shift change of a secondary $Pb(NO_3)_2$ sample (*10*, *11*), with all temperatures reported in this chapter reflecting this correction. The ^{1}H MAS NMR chemical shifts were referenced to the secondary external standard adamantane, $\delta = +1.63$ ppm with respect to TMS $\delta = 0.0$ ppm.

The 2D ^{1}H MAS NMR double quantum (DQ) to single quantum (SQ) correlation experiments utilized the chemical shift anisotropy (CSA) and off-set compensated Back-to-Back (BaBa) multiple pulse sequence for the excitation and reconversion of the multiple quantum coherences as shown in Figure 1b (*8*). The $0 \rightarrow \pm 2 \rightarrow 0 \rightarrow 1$ coherence pathway was selected using a 64 step phase cycle, 128-256 non-rotor synchronized t_1 increments, a 2.5 μs π/2 pulse length, 8-64 scan averages, and an excitation/reconversion length τ_{exc} of 66.66 μs, and a dephasing delay of τ_0 = 10 μs. Phase sensitive detection in the F_1 dimension was obtained using the States-TPPI method (*12*). For this excitation time the observation of signal in the DQ NMR spectra reveals the existence of dipolar coupling between a pair of nuclei with ^{1}H-^{1}H distances < 5 Å. The solid-state 2D ^{1}H NOESY MAS NMR correlation experiments utilized a standard non-rotor-synchronized sequence (Figure 1c) with mixing times τ_{mix} ranging to 1 ms. Typically 8 to 16 scan averages were employed with 512 to 1024 t_1 increments. Spectral deconvolutions were performed using the DMFIT software package (*13*). The average ^{1}H-^{1}H dipolar coupling constants were obtained from simulation of the ^{1}H MAS NMR spectra using in house software written in MATLAB 2010a (The Mathworks, Inc.).

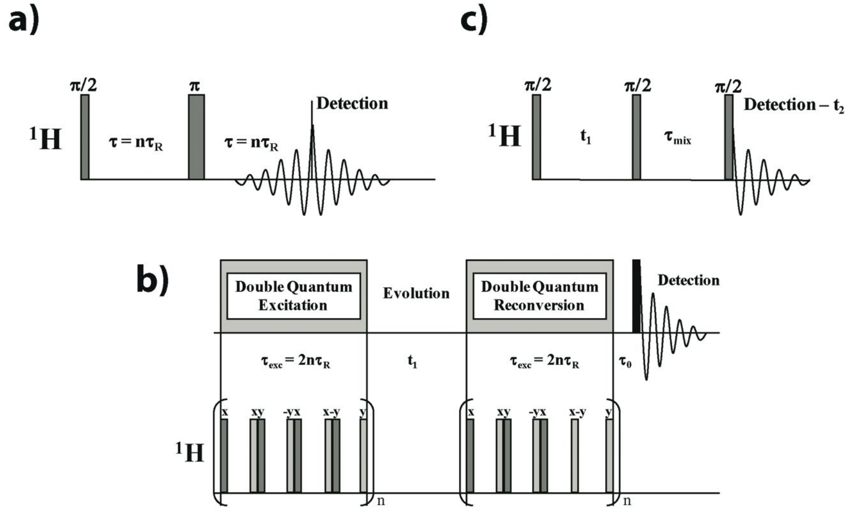

Figure 1. Solid-state ^{1}H MAS NMR pulse sequences utilized: a) 1D rotor-synchronized Hahn spin echo, b) 2D DQ-SQ MAS NMR correlation experiment using the DQ BaBa excitation/reconversion sequence, and c) 2D ^{1}H MAS NMR NOESY. In these sequences the rotor period is defined as τ_R.

Ab Initio Calculations

The small acid-, ester- and Li-containing clusters were optimized in the Gaussian 09 software (*14*) (Gaussian Inc., Wallingford CT) using the 6-311++G(2d,2p) basis set (*15*, *16*), and density functional theory (DFT) utilizing

Becke's three parameter exchange functional (*17*), and the LYP correlation function (B3LYP). The optimizations utilized a surrounding PCM solvent with a dielectric of $\varepsilon = 2.3$ to represent the surrounding continuum of a PE polymer. The integral equation formalism (IEF-PCM) model was implemented for these calculations (*18*). The chemical shielding tensors, σ, were calculated using the Gaussian 09 program utilizing the gauge-including atomic orbital (GIAO) method at the DFT level (*19*). All NMR shielding calculations for the small acid clusters used the same exchange and correlation functionals and basis sets as for the structure optimization. The NMR chemical shift is defined with respect to the chemical shielding of the TMS reference species by

$$\delta(\text{ppm}) = \sigma_{iso}^{\text{TMS}} - \sigma_{iso} \qquad (1)$$

where positive δ values represent environments that are deshielded and resonate at a higher frequency.

Results and Discussion

^{1}H MAS NMR

The solid state ^{1}H MAS NMR spectra for the different random and precise P(E-AA) materials are shown in Figure 2. As predicted for such a simple copolymer, two major resonances were observed corresponding to protons in a methylene (CH_2) environment ($\delta \sim +1.5$ ppm) and to protons in carboxylic acid (COOH) environment ($\delta \sim +12$ ppm). The high chemical shifts suggest that the carboxylic acids are strongly hydrogen bonded and were assigned to acid-acid dimers as shown in Scheme 2. The relative intensity of the COOH resonance scales correctly with the overall acrylic acid mol % (see Figure 2). For example, the p9AA (22 mol %) copolymer has the largest relative COOH intensity. The methine CH resonance ($\delta \sim +2.2$ ppm), and the CH_2 groups α to the COOH functionality ($\delta \sim 1.5$ to 1.7 ppm) were not resolved below T_g under the current MAS conditions. At very high temperatures in the melt (> T_g or T_m) the methine resonance was observable in the 1D ^{1}H MAS NMR spectra. The ^{1}H NMR chemical shifts and full width at half maximum (FWHM) line widths for the observed resonances are given in Table 1.

Minor proton environments were also observed in several of these P(E-AA) materials, and include small amounts of adsorbed water ($\delta \sim +4.8$ ppm), and a carboxylic ester resonance at $\delta \sim +3.4$ ppm (see r15AA in Figure 2). The assignment of this ester resonances is based on the presence of additional minor OCH_3 carbon species, $\delta(^{13}C) \sim +51$ ppm, and an additional minor C=O species, $\delta = +174$ ppm, observed in both the solution and the solid state ^{13}C NMR. It should be noted that this lot of the r15AA polymer had some residual adsorbed methanol remaining from polymer precipitation and processing, which was finally removed after extensive vacuum pumping at 80 °C (see upper spectral inset, Figure 2). For the final (vacuum dried) r15AA sample, the carboxylic ester resonance represents a minor proton species and corresponds to ~1 to 3% (assuming a CH_3 integration) of the entire ^{1}H concentration. For samples containing observable carboxylic ester, a second carboxylic acid resonance ($COOH_b$) was also observed at $\delta \sim +7$ ppm. The smaller ^1H chemical shift of this acid species reflects a reduction in the hydrogen bond strength, and is assigned to carboxylic acids that are free or complexed to the carboxylic acid ester, instead of the strong hydrogen bonded acid-acid dimer structure. Additional discussion concerning the local $COOH_b$ proton environment is provided in the section on 2D correlation experiments below. The relative integration of the $COOH_a$ and $COOH_b$ carboxylic acid resonances are given by the a/b ratio in Table 1, and range between 10 and 3 for the r15AA and r21AA samples, respectively.

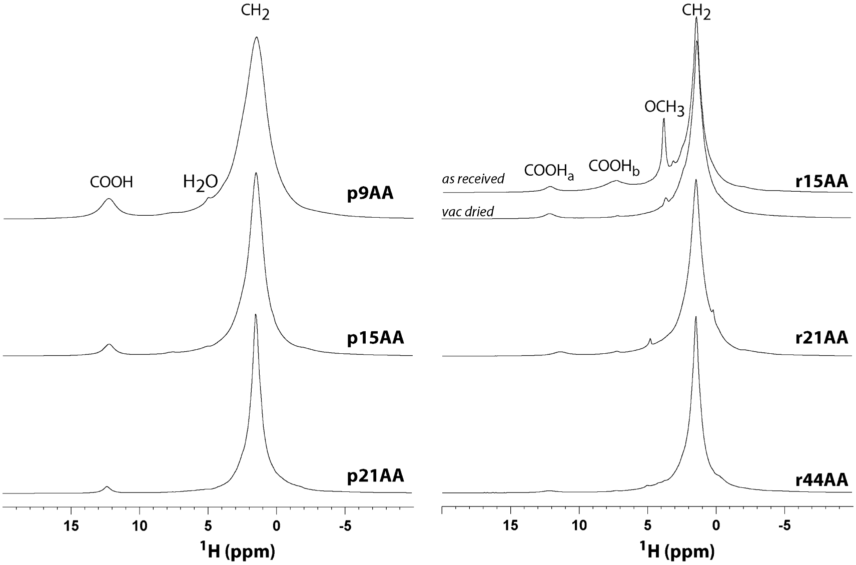

Figure 2. The solid-state ^1H MAS NMR spectra (ν_r = 30 kHz, 332 K) for the precise and pseudo-random P(E-AA) copolymers. The NMR spectra are dominated by protons in the methylene and carboxylic acid environments.

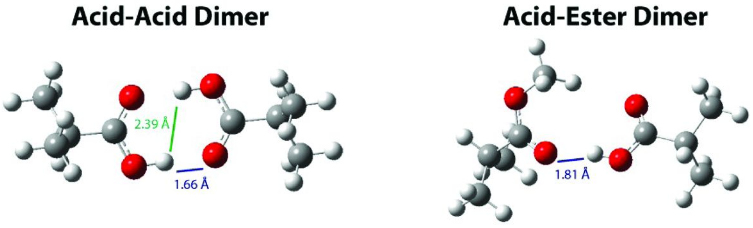

Scheme 2. Proposed carboxylic acid dimer structure and carboxylic acid – carboxylic acid ester structure based on small cluster optimizations using ab initio DFT B3LYP/6-311++(2d,2p) methods. Simulation details are given in the experimental section.

While the methylene can be deconvoluted into a broad and narrow component resonance under high speed (30 kHz) MAS, there are no clear ^1H NMR spectral signatures that allow quantification of the amorphous and crystalline morphologies known to be present within these pseudo-random and precise P(E-AA) acidic copolymers. The different contribution to the methylene line width are better resolved by analysis of static ^{1}H spectral line shapes and DQ buildups, but are not discussed here. The crystalline and amorphous morphologies are clearly identifiable in the solid-state ^{13}C MAS NMR spectra, vary with the degree of neutralization and preparation method, but will be presented and discussed in a subsequent publication (Jenkins and Alam, unpublished results). The changes in the crystallinity does not appear to significantly impact the observed ^{1}H NMR chemical shifts. There are some generalized observations concerning the methylene line width that can be made. For the precise copolymer (Figure 2, left side) there is an increase in the CH_2 line width as the spacing between carboxylic acids decreases. This inhomogeneous line width most likely reflects differences in the relative concentrations of the crystalline and amorphous component, along with the increased disorder in the CH_2 environment for the copolymers with higher acid concentrations. This variation in the methylene line width was not as pronounced in the random copolymers (Figure 2, right side), where the relative contributions to narrow and broad line width components do not change significantly with increased spacing between acid groups. This is also consistent with the invariance in the amorphous/crystalline morphology ratio observed for these random materials using ^{13}C MAS NMR (Jenkins and Alam, unpublished results).

It has been shown that ^{1}H MAS NMR can provide a wealth of information concerning hydrogen bonding (*20*), and in general, the chemical shift of the OH species gets larger with increasing hydrogen bond strength (*21*). The variation of the ^{1}H NMR chemical shifts for the COOH environment with temperature in the P(E-AA) acidic copolymers is shown in Figure 3a. The $\delta > +12$ ppm resonances have been assigned to acid protons in a strong hydrogen bonding environment such as that present in the acid-acid dimer structure (Scheme 2). For the random materials (r15AA and r21AA), the observation of distinct $COOH_a$ and $COOH_b$ resonances over the temperature range investigated (270 to 340 K) demonstrates that the proton exchange rate between these two different carboxylic acid hydrogen environments is significantly slower than the NMR time scale of the chemical shift difference ($1/\tau_{exchange} < 3500$ Hz).

For the precise and random P(E-AA) acidic copolymers studied, the high frequency $COOH_a$ resonance shows the largest temperature variation (Figure 3a) ranging from $\delta = +13.3$ ppm to +12.2 ppm ($\Delta\delta = 1.1$ ppm), and is very similar for all materials. The exception to this trend is the p15AA acidic copolymer which has a shifted chemical shift variation ranging from $\delta = +12.9$ to $\delta = +11.9$ ppm. The low frequency (weakly hydrogen bonded) $COOH_b$ environment also exhibits temperature variation (data not shown), but with a greatly reduced variation ($\Delta\delta = 0.3$ ppm). Several of these acidic copolymers have transitions (T_g and T_m) in the temperature range studied by this NMR study (i.e. p9AA, p21AA and r15AA); which do not appear to have an impact of magnitude of the COOH temperature variation. The presence of semi-crystalline components appears to have little impact on the hydrogen bond strength. The consistent ^{1}H NMR chemical shift temperature behavior between these different acidic copolymers demonstrates that the local COOH environments are not significantly changed by the spacing between AA groups, or by the random or precise arrangement of these carboxylic acid functional groups. The lower ^{1}H NMR chemical shift of the p15AA acidic copolymer argues that for this material the hydrogen bonding is weaker, again consistent with the lowest T_g observed (see Table 1). This reduced hydrogen bond strength most likely results from the energetic competition between acid dimer formation and the chain packing in the amorphous phase produced for this acid group spacing.

Table 1. The ^{1}H MAS NMR (332 K) chemical shifts and line widths for the random and precise PE-AA copolymers, and the Zn^{2+} and Li^+ ionomers

	Mol% AA	*T_g(K) [T_m]*	*δ (ppm) [FWHM][a]*		
			$COOH_a$	*$COOH_b$*	*CH_2*
Precise					
p9AA	22	295[c]	12.3 [778]	--	2.5 [1403, 23.2%][b] 1.5 [1070,76.8%] [b]
p15AA	13.3	269[c]	12.3 [577]	--	1.9 [1660, 36.6%] [b] 1.1 [670,63.4%] [b]
p21AA	9.5	318[c,d]	12.4 [650]	--	1.7 [1564, 56.5%] [b] 1.6 [333, 44.5%] [b]
Random					
r15AA(dried)	13.3	347 [c,d]	12.3 [455]	7.3 [365] [a/b ~ 10][e]	1.65 [1940, 55.3%] [b] 1.54 [410, 44/7%] [b]
r21AA	9.5	358 [c,d]	12.5 [750]	7.23 [360] [a/b ~ 3.2][e]	1.51 [1790, 43.9%] [b] 1.48 [460, 56.1%] [b]
r44AA	4.5	371 [c,d]	12.2 [925]	--	1.7 [2130, 45%] [b] 1.5 [385, 55%]
Zn-Neutralized					
p9AA-66%Zn	22	--[i]	12.2 [1260]		1.53 [1110]
p15AA-82%Zn	13.3	-- [i]	12.8 [970]		1.62 [975]
p21AA-56%Zn	9.5	326[f]	12.4 [1275]		1.7 [3560, 11.5%] 1.6 [705, 88.5%]
p21AA-116%Zn	9.5	327[g]	--		1.55 [2365, 40%] 1.55 [745, 60%]
Li- Neutralized					

Continued on next page.

Table 1. (Continued). The ^{1}H MAS NMR (332 K) chemical shifts and line widths for the random and precise PE-AA copolymers, and the Zn^{2+} and Li^+ ionomers

	Mol% AA	*T_g(K) [T_m]*	*δ (ppm) [FWHM]*[a]		
			$COOH_a$	*$COOH_b$*	*CH_2*
p9AA-43%Li	22	-- [i]	14.5 [1700] 13.2 [1710]	--	1.59 [1415]
p15AA-45%Li	13.3	-- [i]	14.5 [1700]	--	1.61 [995]
r15AA-31%Li	13.3	-- [i]	14.5 [1725]	--	1.53 [775]

[a] δ = chemical shift (± 0.05 ppm), FWHM = full width at half maximum (±5 Hz). [b] The relative % contributions of the different line width components. [c] Reference (*1*). [d] T_m, since this copolymer contained significant crystalline component. [e] a/b = ratio of integrals between the $COOH_a$ and $COOH_b$ species. [f] Reference (*9*). [g] Obtained from static ^{1}H NMR line width analysis. [i] Not measured.

A linear correlation between the solid-state ^{1}H NMR chemical shift and the H···O hydrogen bond length has been described for inorganic crystals (*22*)

$$\delta^{^{1}\mathrm{H}}(\mathrm{ppm}) = 44.68 - 19.3\mathrm{d}_{\mathrm{OH\cdots O}}(\text{Å}) \qquad (2)$$

While this relationship was developed for crystalline materials, it can still provide some quantitative information about the hydrogen bonding in these P(E-AA) copolymers and ionomers. For the acidic copolymer, the observed ^{1}H NMR chemical shifts of the COOH environment vary between δ = +13.3 and +12.2 ppm (Figure 3a), with Equation (2) predicting a hydrogen bond length between 1.63 to 1.68 Å. The lengthening of the hydrogen bond at higher temperatures (approaching or above T_g) is consistent with increased local motions of the polymer chains that disrupt hydrogen bonding. Interestingly, these ^{1}H NMR chemical shift-predicted bond lengths are very close to the 1.66 Å predicted from *ab initio* modeling of small carboxylic acid dimer (Scheme 2). Direct Gaussian GIAO modeling of the acidic dimmers predicts a δ ~ +13.7 ppm. Details for these simulations are provided in the experimental section. These NMR results demonstrate that the majority of the carboxylic acid protons in the P(E-AA) acidic copolymers reside in strongly hydrogen bonded-type dimer complexes. Only in the acidic copolymers, where an observable concentration of carboxylic acid ester was observed (see discussion above), are free or weakly complexed carboxylic acids resonances present. The *ab initio* predicted structure of the acid-ester dimer complex (Scheme 2) predicts an increase in the hydrogen bond length to 1.81 Å, corresponding to a predicted δ = 9.75 ppm (Gaussian GIAO δ = 10.6 ppm). While this decrease in the ^{1}H NMR chemical shift is in the correct direction, it is not as large as that observed experimentally (δ ~ +7.3 ppm), arguing that the hydrogen bonding in the $COOH_b$ species is disrupted to a larger extent than predicted using this simple model. The predicted ^1H NMR chemical shift for a free, uncomplexed COOH species is $\delta = +6.6$ ppm in a continuum dielectric of $\varepsilon = 2.3$ (polyethylene) using Gaussian GIAO methods.

This lack of free acid groups in the P(E-AA) copolymers and Zn- and Li-neutralized ionomers (see those results below) is consistent with previous FTIR studies on poly(ethylene-*ran*-methacrylic acid) ionomers (*23*). It should also be noted that at a sample temperature of 270K (the lower limit of our fast MAS VT capabilities) the temperature changes in the chemical shift had not yet reached a plateau, suggesting that the dynamics of these carboxylic acid protons that influence the chemical shift are still dominant at this temperature.

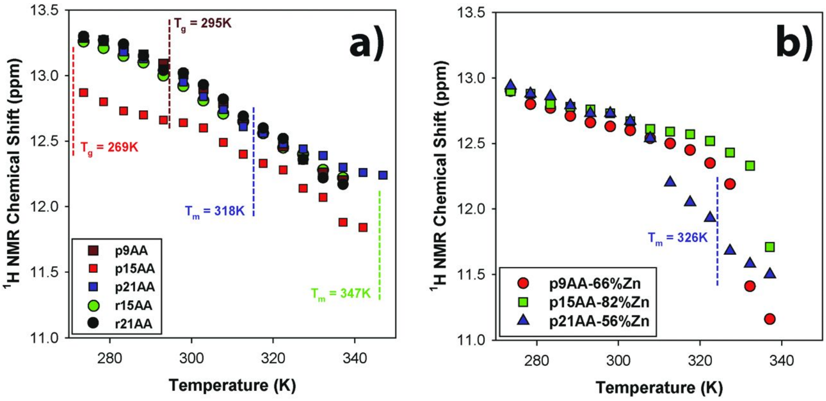

Figure 3. The temperature variation of the COOH proton chemical shift for a) P(E-AA) acidic copolymers and b) Zn-neutralized P(E-AA) ionomers. The T_g and T_m values (Table 1) for different P(E-AA) materials in this temperature range are shown for comparison.

The solid-state ^1H MAS NMR spectra for the partially Zn- and Li-neutralized P(E-AA) copolymers are shown in Figure 4. The chemical shift and FWHM line width for the different exchanged materials are presented in Table 1. Similar to the acidic copolymers, the CH_2 protons give rise to the dominant resonance, with the COOH resonance being reduced in intensity with increasing neutralization. For example, the inset (Figure 4) shows an expansion of the COOH resonance for the p21AA copolymer with different levels of Zn^{2+} neutralization, clearly revealing the loss of the COOH proton with Zn^{2+} incorporation into the material. For the p21AA-116%Zn material there is no visible COOH ^1H NMR signal remaining showing complete removal of the carboxylic acid proton. For the Zn-neutralized materials the COOH chemical shifts are unchanged with respect to the un-neutralized materials, suggesting that the COOH groups retain strong dimer-type hydrogen bonding and that the neutralization with Zn^{2+} does not drastically impact the COOH environments. In contrast, the ^1H NMR chemical shift of the COOH protons in the Li-neutralized ionomers are larger (higher frequency) arguing an *increase* in the hydrogen bond strength following partial Li-neutralization. Using Equation (1), the observed $\delta = +14.5$ and $+13.2$ ppm predicts a *shortened* hydrogen bond distance between 1.56 and 1.63 Å.

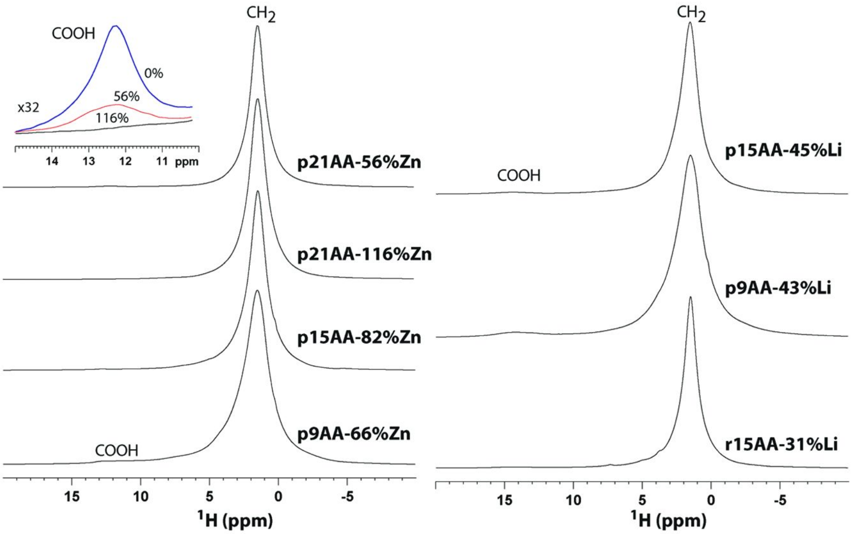

Figure 4. The ^1H MAS NMR spectra ($\nu_r = 30$ kHz) for the Zn- and Li-neutralized precise and pseudo-random P(E-AA) copolymers at 332K. The inset shows an expansion of the COOH proton region for the p21AA Zn neutralized materials: 0% (blue), 56% (red) and 116% (black) demonstrates the loss of this proton with increasing exchange.

This is quantitatively captured in the *ab initio* cluster calculations for the Li-containing dimer and tetramer clusters shown in Scheme 3. For the partially neutralized Li-acid dimer the predicted hydrogen bond length was 1.60 Å (predicted $\delta = +13.8$ ppm). The preferred oxygen coordination of Li^+ is 4, such that the tetramer cluster containing the partially Li+ neutralized carboxylic acid groups is perhaps a better description of the Li-acid clusters being formed. This tetramer cluster has a range of hydrogen bond lengths (1.71, 1.62 and 1.51 Å), with the average 1.61 Å hydrogen bond distance predicting a $\delta = +13.6$ ppm. It should be noted that these *ab initio* clusters are representative of the type of changes that are occurring in these ionomers, and are probably simplistic in the description of the overall structure. For example, in the Zn-neutralized ionomers, large ionic aggregates containing numerous Zn-acid environments have been proposed to described the overall polymer structure, (*9*) and that the NMR spectra would be an average over these different configurations. Clearly the ^1H MAS NMR chemical shift remains a sensitive probe to changes in the hydrogen bond strength in these P(E-AA) ionomers during neutralization.

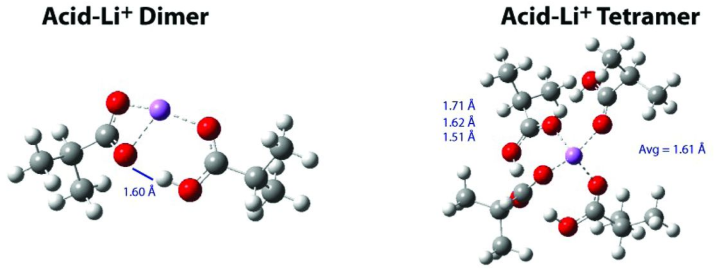

Scheme 3. Proposed carboxylic acid – Li^+ neutralized dimer structure and the carboxylic acid – Li^+ neutralized tetramer structure based on small optimized cluster models obtained using ab initio DFT B3LYP/6-311++(2d,2p) methods.

The temperature variation of the ^{1}H NMR chemical shifts for the $COOH_a$ resonance in the Zn-neutralized P(E-AA) ionomers is shown in Figure 3b. The p21AA-116%Zn ionomer has no observable COOH resonance, and is therefore these values are not included. At low temperatures the chemical shifts are similar to those observed in the acidic copolymers, but show a marked deviation at higher temperatures. This may reflect changes that are occurring during the melting transition, which is in contrast to the temperature invariance of the acidic copolymers during transition. This would suggest differences in the polymer structure between the Zn-neutralized ionomers and the original acidic copolymers. The temperature variation of COOH environment in the Li P(E-AA) ionomers was very complex and revealed multiple COOH domains with differing concentration of coordinated Li^+. This differential segregation was explored using ^{1}H-^{7}Li REDOR MAS NMR spectroscopy and will be presented elsewhere (Alam, unpublished results).

2D MAS NMR Correlation Experiments

Additional details about the local structural environment are obtained using 2D NMR correlation experiments. Figure 5a shows the 2D ^{1}H MAS NMR DQ-SQ correlation spectrum for the p9AA acid copolymer. Similar results were observed for the p21AA copolymer. These 2D DQ experiments provide a sensitive tool to measure spatial proximity of protons within these materials, with the intensity of the DQ peaks being a function of the distance between interacting spins ($\sim 1/r^6$). The 2D DQ-SQ NMR experiments reveal the expected interactions for the proposed structures in these P(E-AA) copolymers. There is a strong autocorrelation peak on the diagonal (dashed line) for the CH_2 proton environments, consistent with strong dipolar couplings (close spatial interactions) within the polymer backbone. In these experiments, a lack of an autocorrelation resonance would show that protons of the same chemical shift (i.e. the same environment) are not dipolar coupled to each other, or that local dynamics are large enough to average the ^{1}H-^{1}H dipolar coupling. For the p9AA copolymer, the observation of a COOH autocorrelation resonance proves close proton-proton distances between acid groups, and supports the argument for an acid dimer structure in these materials (*ab initio* predicted ^1H-^1H distance 2.4 Å). Due to exchange effects for the acid proton, (see previous temperature variation of chemical shift discussion) we are unable to directly measure the ^1H-^1H distance using the DQ NMR experiments. A water autocorrelation resonance was also observed, and is consistent with either water-water clustering in the material, or strongly absorbed water molecules with very limited mobility (*24*). The off diagonal resonances in the 2D NMR DQ-SQ correlation experiments reveal spatial contact between different types of protons, including the predicted COOH-CH_2 cross peak. By increasing the sample temperature to 332 K (above T_g) the COOH-COOH cross peak completely disappears in the 2D NMR DQ-SQ spectrum, consistent with the motional averaging of the ^1H-^1H dipolar coupling due to increased polymer backbone dynamics. Figure 5b shows the 2D ^1H MAS NMR NOESY correlation experiment, which reveals similar spatial interaction for the off-diagonal resonances. No information about the spatial interaction between similar proton environments (autocorrelation type resonances) can be extracted from these NOESY experiments as the diagonal resonances in these 2D experiments represent magnetization that has not exchanged.

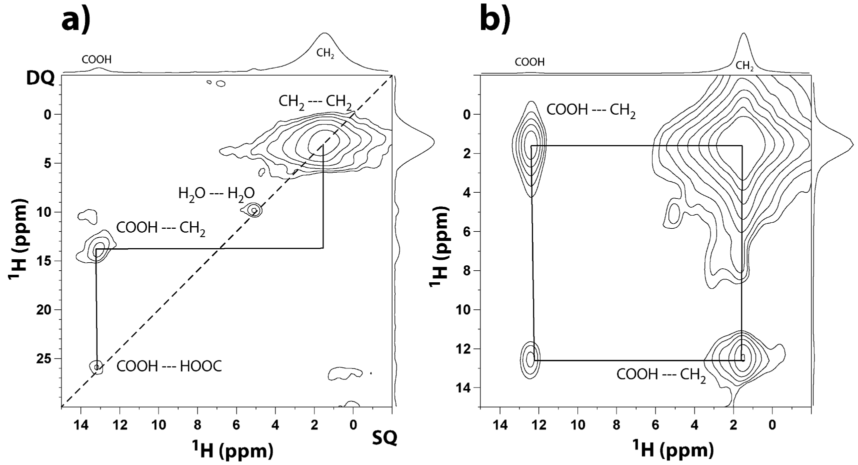

Figure 5. The a) 2D ^1H MAS NMR DQ-SQ correlation spectra obtained at 273K (ν_r = 30 kHz) and the b) 2D ^1H MAS NOESY (τ_{mix} = 10 ms) at 332K (ν_r = 30 kHz) for the precise p9AA copolymer. Several different cross peaks resulting from through space conductivities were observed, including the carboxylic acid auto-correlation resonance in the 2D DQ spectra. Additional discussion provided in the text.

The 2D ^1H MAS NMR DQ-SQ correlation experiments (data not shown) for the pseudo-random P(E-AA) acid copolymers are very similar, with the exception of those containing significant concentrations of the carboxylic ester proton species. Additional information concerning the local structure in these ester-containing materials can be realized by inspection of the 2D ^1H MAS NMR NOESY spectra shown in Figure 6. The protons in the carboxylic ester environments (δ ~ 3.8 ppm) are more mobile (have a longer T_2), such that the 2D NMR NOESY spectrum tends to emphasizes these spectral features at τ_{mix} =

10ms, allowing strong correlations to be observed even for these minor species. Interestingly, Figure 6 shows that the strongly bonded carboxylic acid protons ($COOH_a$) only have spatial contacts to the CH_2 protons (similar to that in Figure 5b), and does not appear to be spatially located near either the weakly hydrogen bonded carboxylic acid ($COOH_b$) or the carboxylic ester. Similarly, the protons in the $COOH_b$ species only show through space contact with the ester protons, consistent with the previous assignment of a weakly bonded interaction. These results suggest that these different types of carboxylic acids are not within the same cluster.

Dynamic Heterogeneity

The ^1H MAS NMR spectra reveal that strong ^1H-^1H dipolar interaction are present within both the P(E-AA) copolymers and ionomers. Below T_g, relatively broad CH_2 resonances with spinning sidebands (SSB) were observed due to strong ^1H-^1H dipolar couplings not completely removed by fast MAS spinning (30 kHz) or local chain dynamics. These SSB occur at integer values of the spinning speed around the dominant CH_2 resonance, as shown in Figure 7a. The previous sections have concentrated on analysis of the isotropic resonance region to extract chemical shift information, and have ignored the SSB patterns present within the NMR spectra. Simulations of the SSB patterns in the ^1H MAS NMR spectra can provide an *effective* or average dipolar coupling values (D_{eff}).

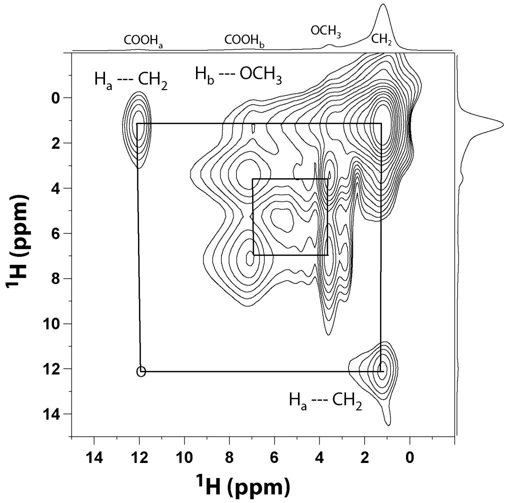

Figure 6. The 2D ^1H MAS NOESY (τ_{mix} = 10 ms) at 332K (ν_r = 30 kHz) for the r15AA acid copolymer. The strongly hydrogen bonded carboxylic acid ($COOH_a$) environment reveals only through space proton-proton contacts with the backbone CH_2 protons, while the more weakly hydrogen bonded carboxylic acid ($COOH_b$) has dominant through space interactions with the methyl ester protons (OCH_3). No contact between the $COOH_a$ and $COOH_b$ protons is observed. Additional discussion provided in the text.

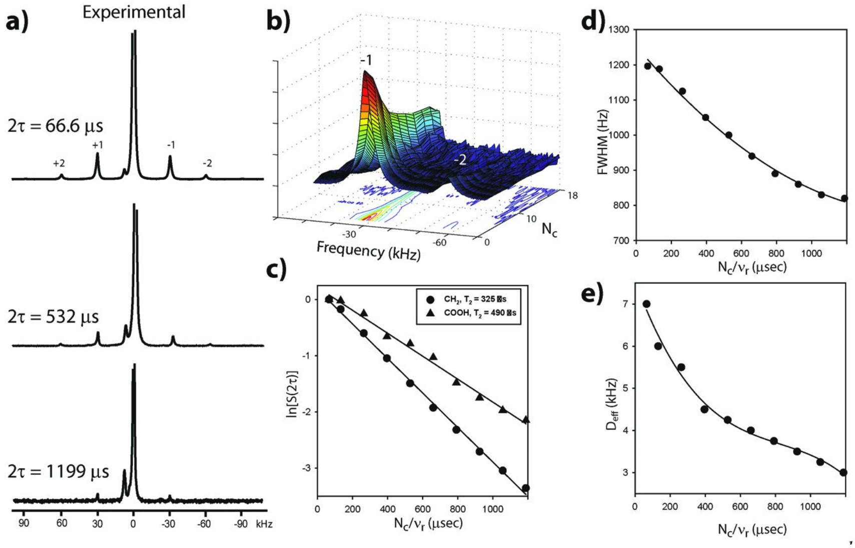

Figure 7. The influence of inhomogeneous T_2 relaxation on: a) The observed 1D ^1H MAS NMR line shape for the p15AA-45%Li ionomer as a function of the echo time. b) Expansion of the -1 and -2 SSB spectral region showing this heterogeneous loss, c) Change in overall signal intensity for the COOH and CH^2 resonances, d) Variation of the FWHM for the isotropic resonance and e) Change in the effective dipolar coupling constant extracted from simulation of the 1D ^1H MAS NMR spectra in (a).

The polymer dynamics on the other hand produce averaging of the dipolar coupling, which is readily reflected in changes to the SSB patterns in the MAS NMR spectra. While it is tempting to discuss the local structure and environment of these P(E-AA) copolymers as being uniform, it is important to remember that these co-polymers are heterogeneous in both their structure and dynamics. For example, heterogeneous dynamics were readily observed during ^1H MAS NMR echo spin-spin T_2 relaxation experiments, where changes in the MAS NMR spectra result with increasing echo times. For example, Figure 7a shows the T_2-Hahn echo spectra for the pAA15-45%Li ionomer sample as a function of rotor-synchronized echo delays (N_c = number of rotor cycles, ν_r = spinning speed). Even though the overall signal intensity for the CH_2 and COOH resonances reveals a single exponential decay (Figure 7c), close inspection of the ^1H MAS NMR spectra (Figure 7a) reveal heterogeneous changes in the spectra. Most importantly are the change in relative intensity of the ±1 and ±2 spinning sideband (SSB) shown in Figure 7b, where the spectra have been normalized to the isotropic peak intensity. The SSB intensities decrease with increasing echo time as a result of differential T_2 relaxation. Simulations of these SSB changes correspond to a decrease in the effective dipolar coupling D_{eff} (Figure 7d). These spectral changes occur because the polymer fractions with smaller D_{eff} (fewer SSB) have longer T_2 relaxation times, with this signal from these fractions being preferentially retained at longer echo periods. A reduction in the line width of the isotropic resonance as a function of echo time (Figure 7e) was also observed. The MAS line width of the isotropic resonance is known to be impacted by dipolar coupling involving higher order spin correlation, which are diminished (narrower line widths) for those polymer environment that are more dynamic, and have a longer T_2 relaxation. These heterogeneous dynamics and the averaging inherent in NMR measurements should always be considered when comparing information obtained using other structural refinement methods (dielectric, neutron scattering, etc.), or to structural details extracted from other NMR experiments employing multiple pulse sequences where heterogeneous relaxation may be involved.

Conclusions

High speed solid-state ^{1}H MAS NMR has been presented for a series of precise and pseudo-random P(E-AA) acidic copolymers and the related Li- and Zn-neutralized ionomers. Even though the ^{1}H NMR spectra were relatively simple, a wealth of information concerning the local carboxylic acid hydrogen bonding environment in these materials was obtained. These NMR results demonstrate the formation of strong acid-acid dimers, with very little free acid present within the P(E-AA) materials. While the Zn-neutralization does not produce a large change in the acid-acid hydrogen bonding environment, the introduction of Li^+ into the P(E-AA) ionomers actually increases the strength of the acid hydrogen bonding.

Acknowledgments

Sandia National Laboratories is a multi-program laboratory operated by Sandia Corporation, a wholly owned subsidiary of Lockheed Martin Company, for the U.S. Department of Energy's National Nuclear Security Administration under contract DE-AC04-94AL85000.

The NMR portion of this research was funded entirely through Sandia's LDRD program. KIW acknowledges funding from the National Science Foundation Polymers Program, Grant DMR 0549116.

References

1. Baughman, T. W.; Chan, C. D.; Winey, K. I.; Wagener, K. B. *Macromolecules* **2007**, *40*, 6564–6571.
2. Alamo, R. G.; Jeon, K.; Smith, R. L.; Boz, E.; Wagener, K. B.; Bockstaller, M. R. *Macromolecules* **2008**, *41*, 7141–7151.
3. Opper, K. L.; Fassbender, B.; Brunklaus, G.; Spiess, H. W.; Wagener, K. B. *Macromolecules* **2009**, *42*, 4407–4409.
4. Wei, Y.; Graf, R.; Sworen, J. C.; Cheng, C.-Y.; Bowers, C. R.; Wagener, K. B.; Spiess, H. W. *Angew. Chem. Int. Ed.* **2009**, *48*, 4617–4620.
5. Boz, E.; Wagener, K. B.; Ghosal, A.; Fu, R.; Alamo, R. G. *Macromolecules* **2006**, *39*, 4437–4447.

6. Mirau, P. A. *A Practical Guide to Understanding the NMR of Polymers*; John Wiley & Sons, Inc.: Hoboken, 2005; p 418.
7. Schmidt-Rohr, K.; Spiess, H. W. *Multidimensional Solid-State NMR and Polymers*; Academic Press Inc.: San Diego, 1994.
8. Schnell, I.; Spiess, H. W. *J. Magn. Reson.* **2001**, *151*, 153–227.
9. Seitz, M. E.; Chan, C. D.; Opper, K. L.; Baughman, T. W.; Wagener, K. B.; Winey, K. I. *J. Am. Chem. Soc.* **2010**, *132*, 8165–8174.
10. Bielecki, A.; Burum, D. P. *J. Magn. Reson, Ser. A* **1995**, *116* (2), 215–20.
11. Takahashi, T.; Kawashima, H.; Sugisawa, H.; Baba, T. *Solid State Nucl. Magn. Reson.* **1999**, *15* (2), 119–23.
12. Marion, D.; Ikura, M.; Tschudin, R.; Bax, A. *J. Magn. Reson.* **1989**, *85* (2), 393–9.
13. Massiot, D.; Fayon, F.; Capron, M.; King, I.; Le Calvé, S.; Alonso, B.; Durand, J. O.; Bujoli, B.; Gan, Z.; Hoatson, G. *Magn. Reson. Chem.* **2002**, *40*, 70–76.
14. M. J. Frisch, G. W. Trucks, H. B. Schlegel, G. E. Scuseria, M. A. Robb, J. R. Cheeseman, G. Scalmani, V. Barone, B. Mennucci, G. A. Petersson, H. Nakatsuji, M. Caricato, X. Li, H. P. Hratchian, A. F. Izmaylov, J. Bloino, G. Zheng, J. L. Sonnenberg, M. Hada, M. Ehara, K. Toyota, R. Fukuda, J. Hasegawa, M. Ishida, T. Nakajima, Y. Honda, O. Kitao, H. Nakai, T. Vreven, J. A. Montgomery, Jr., J. E. Peralta, F. Ogliaro, M. Bearpark, J. J. Heyd, E. Brothers, K. N. Kudin, V. N. Staroverov, R. Kobayashi, J. Normand, K. Raghavachari, A.Rendell, J. C. Burant, S. S. Iyengar, J. Tomasi, M. Cossi, N. Rega, J. M. Millam, M. Klene, J. E. Knox, J. B. Cross, V. Bakken, C. Adamo, J. Jaramillo, R. Gomperts, R. E. Stratmann, O. Yazyev, A. J. Austin, R. Cammi, C. Pomelli, J. W. Ochterski, R. L. Martin, K. Morokuma, V. G. Zakrzewski, G. A. Voth, P. Salvador, J. J. Dannenburg, S. Dapprich, A. D. Daniels, O. Farkas, J. B. Foresman, J. V. Ortiz, J. Cioslowski, D. J. Fox, *Gaussian 09*, Revision A.02.; Gaussian, Inc.: Wallingford, CT, 2009.
15. McLean, A. D.; Chandler, G. S. *J. Chem. Phys.* **1980**, *72* (10), 5639–5648.
16. Krishnan, R.; Binkley, J. S.; Pople, J. A. *J. Chem. Phys.* **1980**, *72* (1), 650–654.
17. Becke, A. D. *J. Chem. Phys.* **1992**, *98* (7), 5648–5652.
18. Scalmani, G.; Frisch, M. J. *J. Chem. Phys.* **2010**, *132* (1-15), 114110.
19. Cheeseman, J. R.; Trucks, G. W.; Keith, T. A.; Frisch, M. J. *J. Chem. Phys.* **1996**, *104* (14), 5497–5509.
20. Brown, S. P. *Macromol. Rapid Commun.* **2009**, *30*, 688–716.
21. Lutz, H. D. *J. Mol. Sci.* **2003**, *646*, 227–236.
22. Jeffrey, G. A.; Yeon, Y. *Acta Cryst.* **1986**, *B42*, 410–413.
23. Walters, R. M.; Sohn, K. E.; Winey, K. I.; Composto, R. J. *J. Polym. Sci., Part B: Polym. Phys.* **2002**, *41*, 2833–2841.
24. Alam, T. M.; Nyman, M.; McIntyre, S. K. *J. Phys. Chem. A* **2007**, *111*, 1792–1799.

Chapter 8

A Solid-State NMR Study of Boric Acid Doped in Poly(vinyl alcohol)

Kazuhiko Yamada[*]

Department of Chemistry and Materials Science, Graduate School of Science and Engineering, Tokyo Institute of Technology, 2-12-1-E4-5 Ookayama Meguro-ku, Tokyo, Japan
[*]E-mail: kyamada@polymer.titech.ac.jp

A multinuclear solid-state NMR study of boric acid doped in poly(vinyl alcohol) (PVA) is presented. The experiments used for PVA films include ^1H windowed Phase-Modulated Lee-Goldburg (wPMLG), and ^{11}B Magic-Angle Spinning (MAS), ^{11}B stationary NMR, ^{11}B Multiple-Quantum MAS, and ^1H-^{11}B CP and HETCOR at 14.1 and/or 21.6 T. The present analysis strongly suggests the possibility that the boric acid serves as a crosslinker with a coordination number other than four.

Introduction

Polyvinyl alcohol (PVA) is industrially important and is used in a variety of materials including vinylon fiber, textile sizing agent, adhesive agents, and paper coatings (*1–3*). The versatility of PVA is due to its water solubility, and its emulsifying, film forming, and adhesive properties. Usually a small amount of a boric acid is added to modify the physical properties of PVA, such as mechanical strength and water resistance. It is believed that the doped boric acid plays an important role in crosslinking. Thus far, several schematic representations for the crosslinked structures have been proposed, most of which are known as the di-diol model (*4*, *5*). In this model, a boron site involved in the formation of crosslinks has a coordination number of four.

Nevertheless, the detailed structure for the boric acid crosslink is not understood completely probably because it is difficult to obtain the molecular structure of a crosslinker in a polymer that contains both crystalline and

In NMR Spectroscopy of Polymers: Innovative Strategies for Complex Macromolecules; Cheng, H., et al.; ACS Symposium Series; American Chemical Society: Washington, DC, 2011.

non-crystalline regions. For example, X-ray diffraction patterns reflect the crystalline parts only. Solid-state NMR is known as one of the most powerful techniques to study non-crystalline samples (*6–8*). Moreover, it has a clear advantage of nuclear selectivity, which means that it is possible to obtain detailed information on the structural and electronic properties of the nucleus of interest. In the present case, boron, the key atom for crosslinking, contains two NMR-active nuclei: ^{10}B (γ = 2.8746 × 10^7 rad/T s, I = 3, natural abundance = 19.6 %) and ^{11}B (γ = 8.5843 × 10^7 rad/T s I = 3/2, natural abundance = 80.4 %), and PVA contains ^1H and ^{13}C. Thus, through ^1H, ^{11}B, or ^{13}C NMR, the interactions between boric acid and PVA can be investigated at the molecular level. In this paper, a study has been made of the molecular properties of boric acid doped in a PVA film obtained by ^1H and ^{11}B solid-state NMR, and a possible conformation of the boron crosslinker is proposed.

Experimental Section

All polyvinyl alcohol (PVA) films used in the present work were kindly provided by KURARAY Co., Ltd. (Tokyo, Japan). For the preparation of PVA film containing boric acid, PVA was dissolved in aqueous solutions of boric acid, which was dried and heat-treated at 200ºC to produce the polymer film. The final content of the boric acid in the PVA film was found to be less than 1.0 wt%. For reference, a PVA film without boric acid was also prepared with the same procedure without boric acid. Prior to NMR measurements, all PVA films were dried at approximately 90ºC under reduced pressures for several hours in order to remove residual water. Borax and boric acid, which were used as reference compounds, were purchased from Wako Pure Chemical Industries, Ltd. (Tokyo, Japan) and were employed without further purification.

All NMR experiments were performed on JEOL ECA 500 and 930 spectrometers (*9*), operating at frequencies of 160.5 and 298.1 MHz, respectively. PVA films or polycrystalline borax and boric acid were packed into 4-mm rotors of zirconium oxide. An external sample of aqueous solutions of a boric acid was used for chemical shift referencing and pulse-length determination. The recycle delay was typically 10 – 180 s. The ^1H decoupling power was around 80 – 100 kHz. Magic angle spinning (MAS) frequencies were set to be 10.00 kHz. ^1H and ^{11}B T_1 relaxation times were measured by using the saturation recovery method. ^{11}B 3QMQMAS experiments were carried out on the JEOL ECA 500 spectrometer. The z-filter pulse sequence proposed by Amoureux *et al.* (*10*) was employed. For ^1H-^{11}B CP experiments, pre-saturation pulses were added to avoid unwanted signals from the direct polarizations. The contact time was set to be 2 ms. For ^1H windowed Phase-Modulated Lee-Goldburg (wPMLG) experiments (*11*), the optimized pulse length was found to be 2.9 μs and the ^1H offset position was -3ppm. For ^1H-^{11}B dipolar HETCOR experiments (*12*), the CP condition was adjusted for the boron site with a coordination number of three, which will be discussed in the text. All the NMR spectra were processed by Delta (JEOL USA, Inc.) software. Spectral simulations were performed on a personal computer using the program written by the author on MATLAB (The Math Works, Inc.).

Results and Discussion

For convenience, the results will be presented in four sections: (1) peak assignments in ^{11}B MAS spectra of PVA film and extraction of ^{11}B NMR parameters, (2) quantitative analysis of boron sites as a crosslinker, (3) investigation of the relationship between boric acids and polymer chains at the molecular level, and (4) a proposal for the possible conformation of boric acid doped in a PVA film.

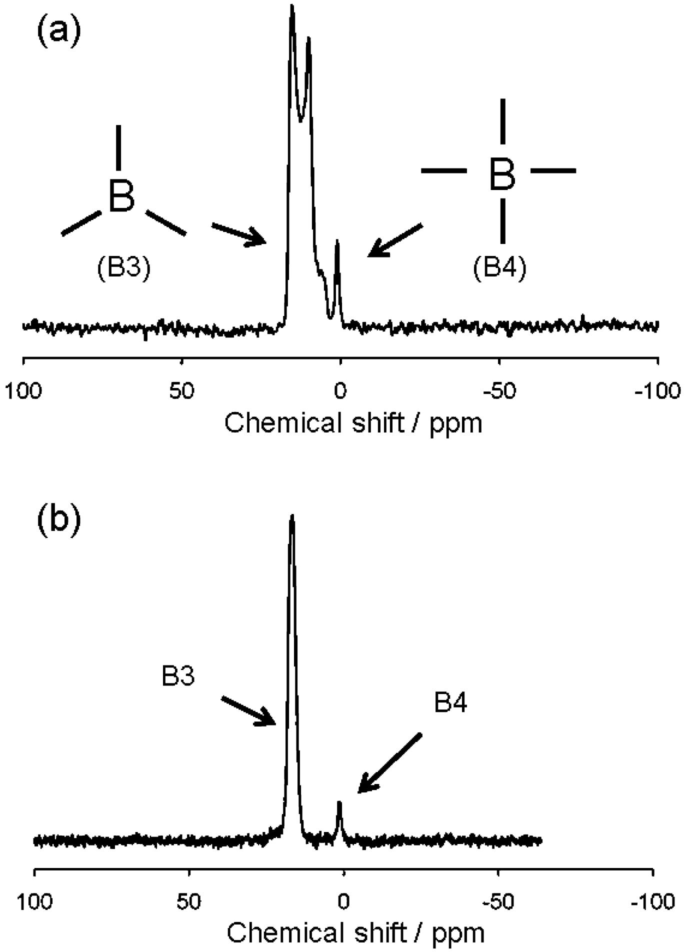

Figure 1. Experimental ^{11}B MAS spectra of the boric acid/PVA film, measured at (a) 11.7 and (b) 21.6 T.

^{11}B MAS NMR of Boric Acid in PVA Films

Figure 1 shows the experimental ^{11}B MAS NMR spectra of boric acid/PVA films observed at (a) 11.7 and (b) 21.6 T with sample spinning frequencies of 10.00

kHz. At 11.7 T, the low-field peak exhibits the typical lineshape arising from second-order quadrupolar interactions, and the high-field peak appears as a singlet. At 21.6 T, the two ^{11}B sites can be clearly separated because in quadrupole nuclei the line width is inversely proportional to the strength of the applied magnetic field (*13*). Unfortunately, the spectrum measured at 21.6 T exhibits shapeless peaks so that it is difficult to analyze it. Although the spectral width is large, the spectrum obtained at 11.7 T is used for analysis. For the assignments of the two peaks and extraction of the ^{11}B NMR parameters, we first study borax as a reference compound.

The experimental ^{11}B MAS NMR spectrum of borax observed at 11.7 T is shown in Figure 2. As in boric acid/PVA film, there are two boron sites in the spectrum; a broad line shape at the low-field and a sharp one at the high-field.

From the result of X-ray diffraction (*14*), this compound contains two chemically different boron; one associated with a coordination number of three and the other with four. In the rest of this paper, these boron sites are called B3 and B4, respectively. It was reported from the pioneer work of single-crystal ^{11}B NMR experiments (*15*) that the broad (low-field) and sharp (high-field) peaks were assigned to be B3 and B4, respectively. This assignment is quite reasonable in that the line width depends on the magnitudes of quadrupolar interactions, reflecting the local electric-field-gradient around the boron nucleus. For example, the electric-field-gradient of B4 is small due to the tetrahedral structure so that it exhibits a small magnitude of the quadrupolar interactions, thereby a narrow line shape.

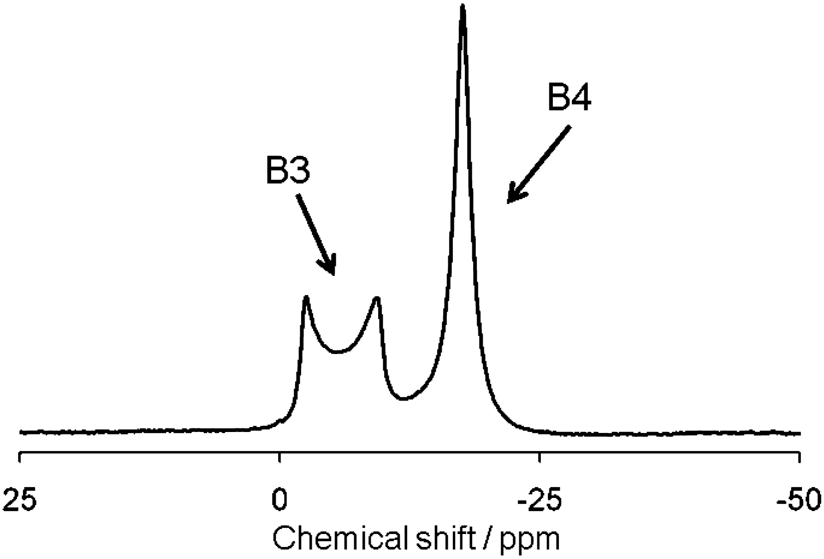

Figure 2. Experimental ^{11}B MAS spectrum of borax, measured at 11.7 T.

The analysis of the 1D MAS spectrum of borax yielded the following parameters for B3: $\delta_{iso} = 19 \pm 2$ ppm, $C_Q = 2.5 \pm 0.1$ MHz, $\eta_Q = 0.09 \pm 0.06$. The results are reasonably consistent with those reported for B3 of borax (*15*). Unfortunately, the spectral analysis of B4 provides no information on quadrupole

NMR parameters due to the shapeless peak. At this point, it is difficult to judge whether B4 contains non-quadrupolar interaction, or just a small one. Yet, it was found that the π/2 pulse width for B4 of the PVA film was different from that determined in boric acid solution, which implies that B4 contains some quadrupolar interactions. Note that, in the literature, a single-crystal of borax was used so that the ^{11}B NMR parameters could be accurately determined.

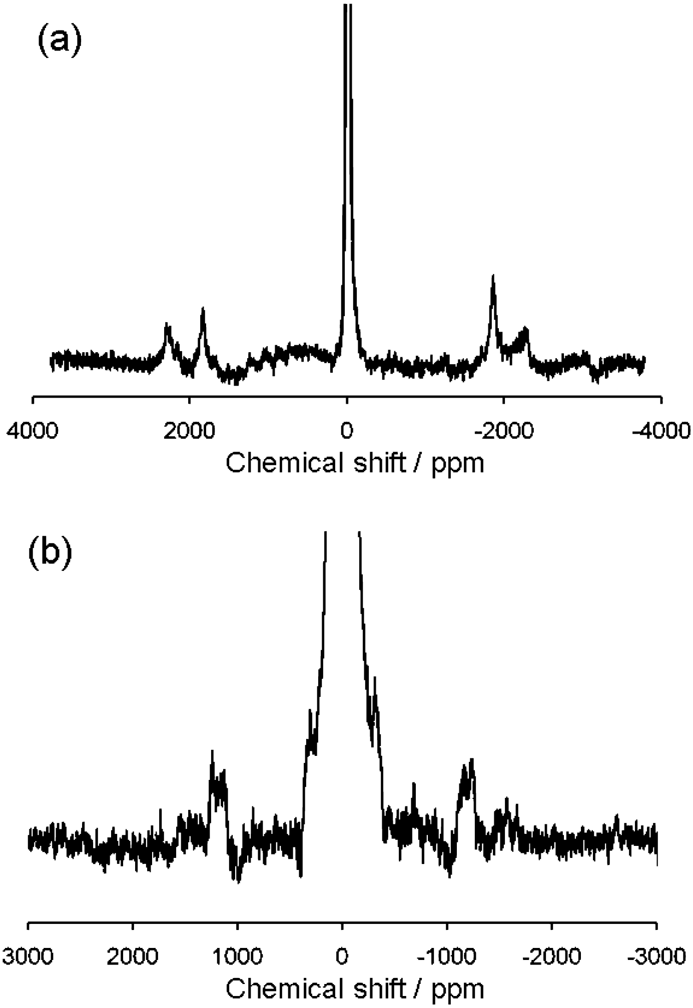

Figure 3. Stationary NMR spectra of (a) sodium nitride (^{23}Na) and (b) borax (^{11}B).

To obtain ^{11}B quadrupole NMR parameters for B4 of borax, the first order effect of the quadrupolar interactions was used instead of the second order. This method was reported by Mao et al (*16*). The procedure is based on the detection of satellite transition by FTNMR, which is useful for analyzing such a shapeless peak. As a test case, the stationary ^{23}Na NMR spectrum of sodium nitride is shown in Figure 3(a). The spectral width was set to be 8000 ppm. When quadrupolar interactions exist, the satellite transitions may be observed. Because of the wide spectral width, all NMR transitions cannot be excited. As a result, only line singularities such as peaks and shoulders remain in the spectrum and broad parts of the line shapes are lost. By measuring the frequency between the remaining peaks or shoulders, the NMR parameters can be successfully determined. Such analyses of the 1D stationary NMR spectra of sodium nitride yielded the following ^{23}Na NMR parameters: C_Q = 1.095 ± 0.005 MHz, η_Q = 0.106 ± 0.005, which are in good agreement with literature values (*17*). The same spectral analysis is applied for B4 of borax, which is shown in Figure 3(b), and the following ^{11}B NMR parameters were obtained: C_Q = 0.5412 ± 0.0008 MHz, η_Q = 0.637 ± 0.008. The isotropic chemical shift, δ_{iso}, was determined to be 2 ± 1ppm from Figure 2. In the ^{11}B NMR spectrum of Figure 3(b), the spectral width was set to be 6000 ppm, and the large broad peaks observed in the middle were associated with B3.

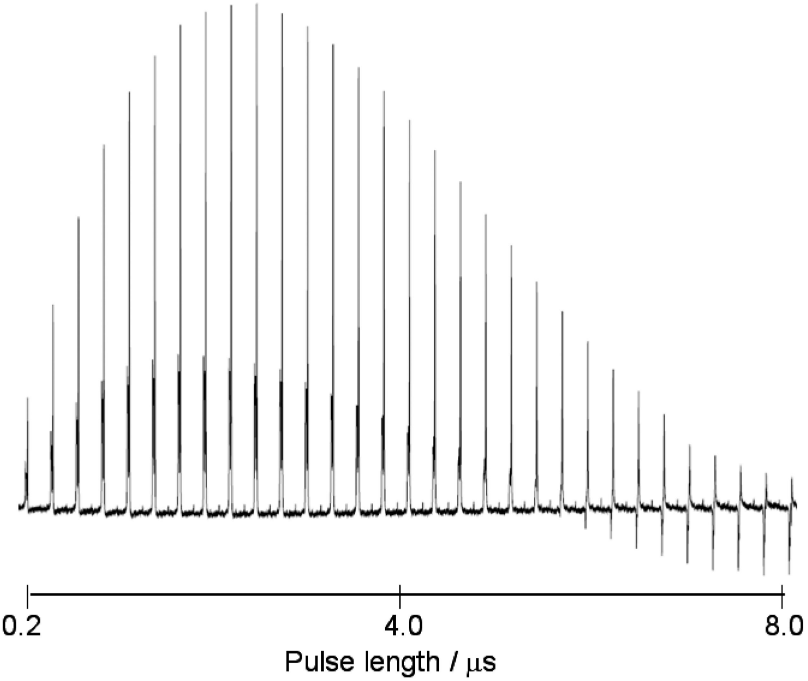

Figure 4. Dependence of signal intensities on the pulse length for borax, measured at 11.7 T.

The above procedure has been applied to obtain ^{11}B NMR parameters for B3 and B4 of the boric acid/PVA film. The ^{11}B NMR parameters for B3 are: δ_{iso} = 19±2 ppm, C_Q = 2.4 ± 0.1 MHz, η_Q = 0.09 ± 0.08, which are similar to borax. Unfortunately, the NMR signals of the satellites were too small to be observed for B4. Therefore, it was assumed that the ^{11}B NMR parameters are the same as those for B4 of borax.

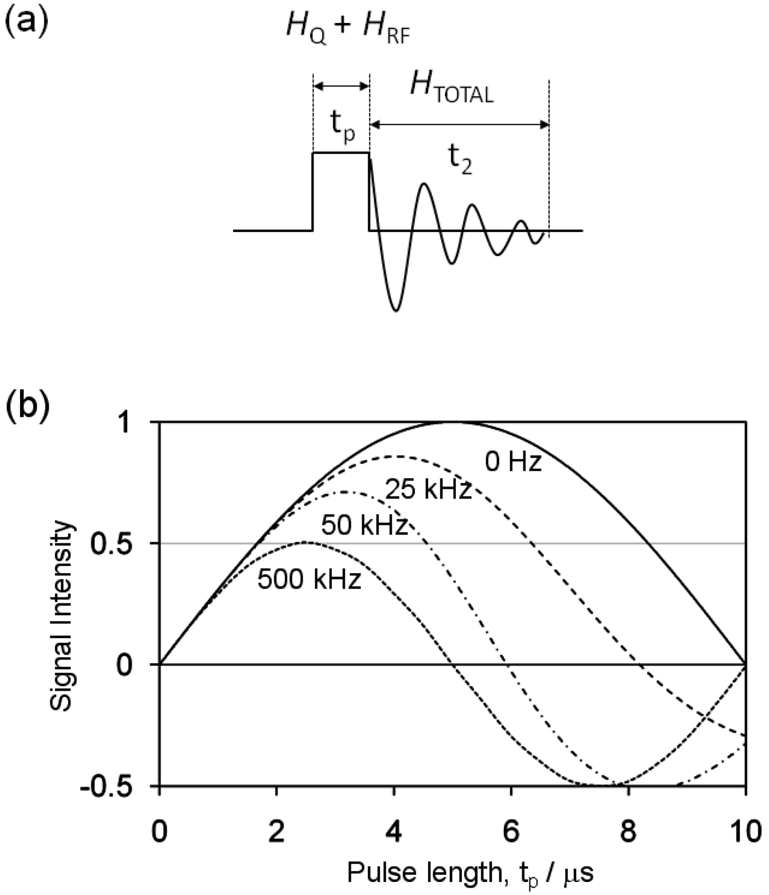

Figure 5. (a) A pulse sequence for direct polarization (b) Plot of signal intensity against the pulse length.

Quantitative Analysis of Boric Acid Doped in PVA Films

For quadrupole nuclei, the strength of the RF field and its pulse length affect the line shapes as well as relative intensities (*18*). Therefore, information on relative populations is sometimes difficult to obtain. Figure 4 shows the relationship between signal intensities of B3 and B4 in borax, and the corresponding pulse lengths. The pulse lengths were varied from 0.5 to 10.0 μs with 0.1μs steps. The π/2 pulses for B3 and B4 were 1.7 and 2.7 μs, respectively. The magnetization of the ^{11}B nuclei of B3 seems to process faster than that of B4. In order to obtain accurate quantitative information, such effect must be considered in the spectral simulation. Let us consider the direct polarization sequence given in Figure 5(a). The initial value of the FID is equal to the area of the NMR peak. This initial point can be calculated by using the density matrix at the end of the pulse width, t_p. If there is quadrupolar interaction, the total Hamiltonian during t_p must be the sum of Hamiltonians of the effect of RF field,

H_{RF}, and the quadrupolar interaction, H_Q. To calculate the expected value, we need to carry out diagonalization. The details are well explained in the literature by Man (*19*). Figure 5(b) shows the calculated signal intensity of a central transition line for $I = 3/2$ system against the pulse length for several different magnitudes of quadrupolar interactions. In the calculations, the pulse power was fixed to be 50 kHz, and the magnitudes of quadrupolar interactions were varied from 0 to 500 kHz, as described in the figure. When there was no quadrupolar interaction, the $\pi/2$ pulse length became 5μs, which corresponds to the situation of $I = 1/2$ in the solution state. As the quadrupole interactions became larger, the $\pi/2$ pulse lengths tended to be shorter with lower intensities. When the magnitude of the quadrupolar interaction was much larger than that of the pulse power, the $\pi/2$ pulse length became one-half of that for non-quadrupole interaction, which is 2.5 μs, with the reduced intensities of 2/5. These observations are in good agreement with the experimental results. Similar calculation has been done for the relative populations of the boric acid/PVA film.

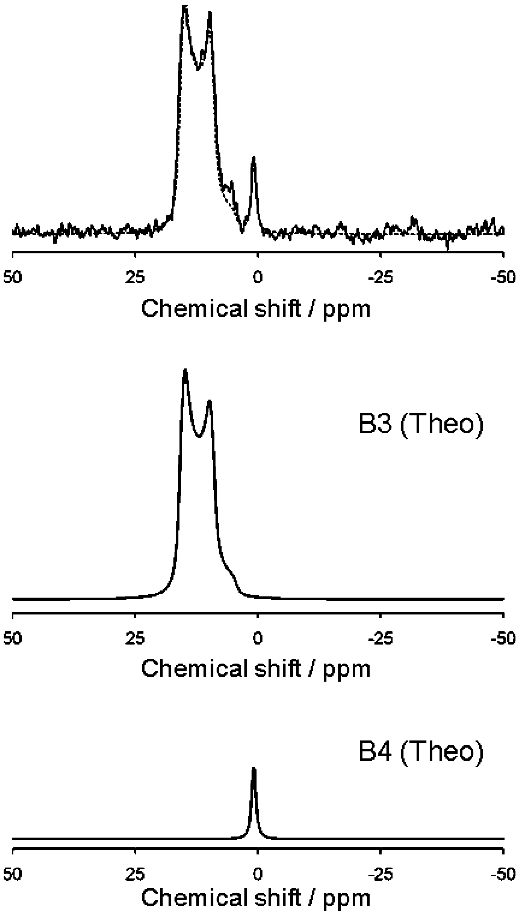

Figure 6. Experimental and calculated ^{11}B MAS spectra of the PVA film.

Figure 6 shows experimental and calculated 1D ^{11}B NMR spectra of the boric acid/PVA film measured at 11.7 T. The calculated spectrum was the sum of those of B3 and B4. In the spectral simulation, the ^{11}B NMR parameters obtained in the above were fixed and the intensity of each sub-spectrum was varied until the total theoretical spectrum fitted to the experimental one. From the present analysis, the ratio of B3 to B4 was found to be around 14. Contrary to the di-diol model in which the coordination number of boron crosslinks is four, the population of B4 was found to be minor. The crystal structure of a boric acid (*20*) shows that the boron site has the B3 structure. Thus, it may be expected that crystalline boric acid (with B3 structure) is present in the PVA polymer. There is also the possibility that B3 plays an important role in crosslinking because of its high abundance.

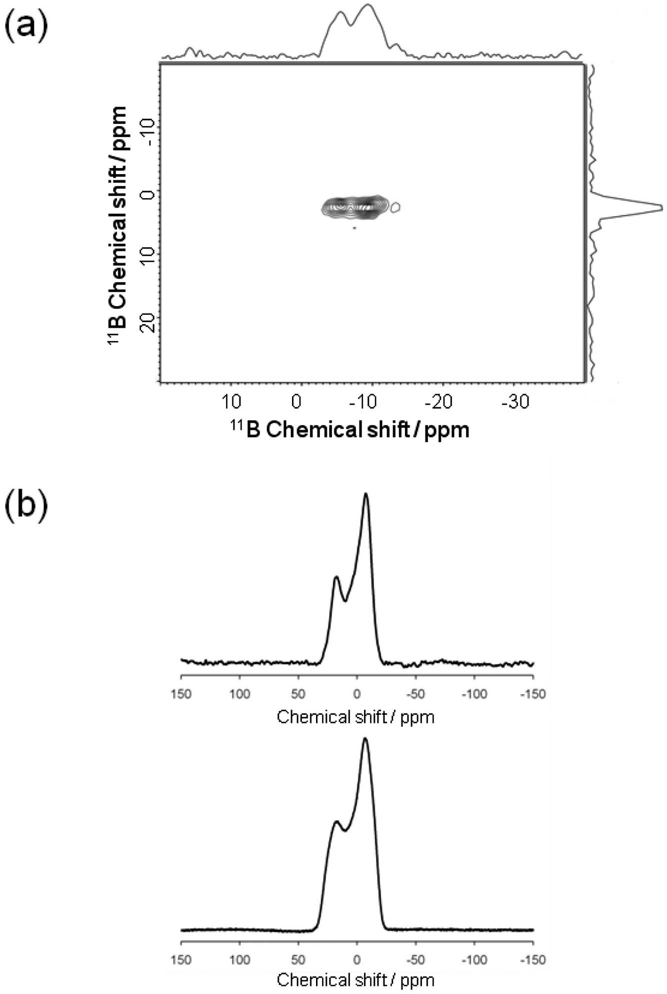

Figure 7. (a) 2D experimental ^{11}B 3QMQMAS spectrum of the boric acid/PVA film. (b) ^{11}B stationary NMR spectra of (upper) the boric acid/PVA film and (lower) the crystalline boric acid.

Interactions between Boric Acid and Polymer Chains

Next we explore the relationship between doped boric acid and the polymer chains at the molecular levels, focusing in particular on the majority component, B3. Figure 7(a) shows a contour plot of the ^{11}B z-filter 3QMQMAS spectrum of the PVA film measured at 11.7 T. Both the F1 and F2 projections of the 2D MQMAS spectra are given on the side and at the top, respectively. Obviously, one major peak can be observed, suggesting that B3 is a single component. Figure 7(b) shows experimental ^{11}B stationary spectra of the boric acid/PVA film (upper) and crystalline boric acid (lower), obtained at 11.7 T. Relatively similar line shapes are obtained for both NMR spectra. Apparently, B4 is too small to be detected. From Figure 7, it is expected that the boric acid/PVA film contains a single boron site, B3, in which the chemical environment may be close to that of the polycrystalline boric acid. However, it was also found that T_1 relaxation time for the boric acid/PVA film, which was determined to be less than 2 s, was much shorter than that for the polycrystalline boric acid (36 s). This is probably because, in polymers, there are additional relaxation mechanisms, or the electronic properties around the boron nuclei may be different.

Horii and co-workers previously reported the ^{1}H chemical shifts of PVA by analyzing high-resolution ^{1}H NMR spectra in details (*21*). According to their results, there are three kinds of hydroxyl groups involved in intramolecular and intermolecular hydrogen and non-hydrogen bonding. The chemical shifts of these protons are reported to be in the range of 2.85-5.80 ppm. The chemical shifts of CH_2 and CH groups are found at 1.40-1.60 and 4.20 ppm, respectively. Figure 8 shows ^{1}H windowed Phase-Modulated Lee-Goldburg (wPMLG) spectra of PVA films with (a) and without (b) boric acids. The present ^{1}H NMR spectrum of the PVA film could be assigned on the basis of the results reported by Horii and co-workers (*16*). It is important to point out that there is no signal corresponding to polycrystalline boric acid, whose chemical shift was 5.5-7.0 ppm, observed under the same experimental conditions of ^{1}H wPMLG experiments (data not shown). As shown in Figure 8, there is no difference in lineshapes between the two NMR spectra, indicating that the chemical shift of B3 may be overlapped on the major peaks of the CH and CH_2 groups, or that the PVA polymer does not contain polycrystalline boric acid.

The adequate ^{1}H-^{11}B CP conditions were evaluated in order to investigate the chemical environment around B3 in the PVA film. Figure 9 shows experimental ^{1}H-^{11}B CP MAS spectra of boric acid/PVA films in which the ^{11}B CP power was varied from 45 to 90% at 5% step while the ^{1}H CP power was fixed. The adequate CP conditions were found to be quite different between B3 and B4 due to the fact that they depend on the magnitude of quadrupolar interactions. The maximal peaks for B3 and B4 were at 60 and 90%, respectively. For reference, the adequate CP condition for the polycrystalline boric acid was found to be at 40%, suggesting that the proton environment around B3 is different from that of the crystalline counterpart.

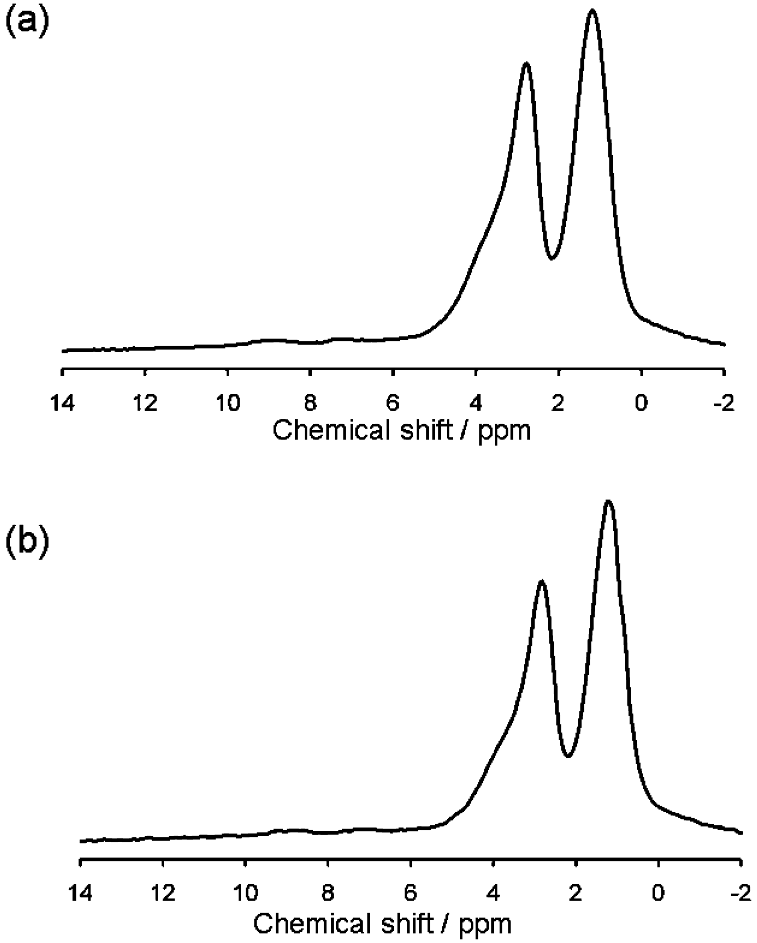

Figure 8. ^{1}H wPMLG NMR spectra of PVA films (a) with and (b) without boric acids.

It is useful to carry out heteronuclear correlation experiments in order to understand the relationship between the doped boric acid and the polymer chains. Figure 10 shows a contour plot of the ^{1}H-^{11}B HETCOR spectrum of the PVA film observed at 11.7 T. Both the F1 (^{1}H) and F2 (^{11}B) projections of the 2D spectra are also given on the side and at the top, respectively. In the experiment, the ^{11}B CP power was set to be 60%, which is the appropriate CP condition for B3. In this setting, little cross peak could be observed for B4. It can be seen that there are strong cross peaks between B3 and the CH and CH_2 groups. From a careful analysis of the F1 projection, i.e., the high-resolution ^{1}H NMR spectrum in which there is a small shoulder at the peak arising from the CH group, it is deduced that there are small cross peaks between B3 and the OH groups. Importantly, no cross peak between B3 and the polycrystalline boric acid is confirmed. In summary, B3 is not attributed to the polycrystalline boric acid itself, but it is surrounded by the PVA main and side chains. It should be noted that a cross peak appears via dipole-dipole interactions, which implies that the two atoms may not be connected by chemical bonds, but are spatially close to each other.

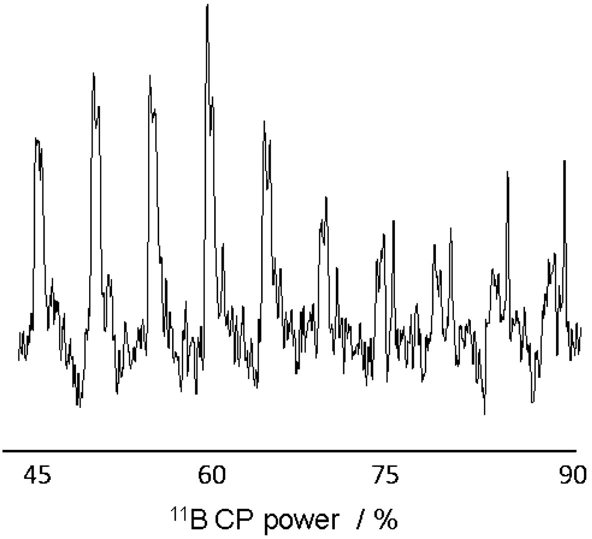

Figure 9. ^{1}H-^{11}B CP profiles of boric acid/PVA films in which the ^{11}B CP power was varied from 45 to 90 % with 5% step while the ^{1}H CP power was fixed.

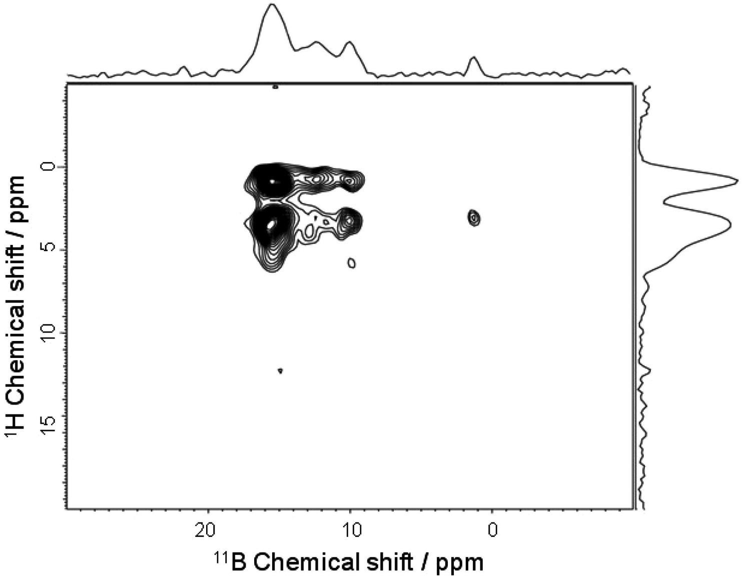

Figure 10. 2D experimental ^{1}H-^{11}B HETCOR spectrum of boric acid doped in PVA.

Possible Conformation of Boric Acid Doped in PVA Films

From the author's previous work and experience, the mechanical strength of a PVA film is known to depend critically on the amount of boric acid. The higher the concentration of the doped boric acid, the greater is the mechanical strength of the PVA film. Therefore, it is deduced that a doped boric acid somehow forms a chemical bond between the polymer and the boric acid. Assuming that boric acid and PVA are linked by hydrogen bonds, the present results indicate that the boric acid crosslinker has a coordination number of three instead of four.

Conclusion

This work aims to investigate the molecular properties of boric acid doped in PVA film via multinuclear solid-state NMR. Contrary to expectations from the previously proposed the di-diol model, the major boron site was found to have a coordination number of three. The chemical environment of the boron site is quite different from that of the polycrystalline boric acid. The boron is surrounded by polymer main chain and side chains. Because the amount of doped boric acid is related to the polymer properties such as mechanical strengths and water-resistance, it can be assumed that the doped boric acid are linked to the polymer, e.g., through hydrogen bonds. To the best of the author's knowledge, this is the first report of boron/PVA crosslinker with a coordination number of three. Finally, it has been demonstrated that solid-state NMR is useful for studying the molecular properties of crosslinkers in crystalline and non-crystalline polymers, and it will be applied in this laboratory to a variety of crosslinkers in rubbers and gels in the near future.

Acknowledgments

Polyvinyl alcohol was kindly supplied by KURARAY Co., Ltd. (Okayama, Japan). This work was supported by the Ministry of Education, Culture, Sports, Science and Technology (MEXT) Grant-in-Aid for Young Scientists (B) (22750009). I thank Dr. Tadashi Shimizu and Kenzo Deguchi for their technical assistance with the solid-state NMR experiments at National Institute for Materials Science. Finally I wish to thank Takahiro Ishii, Hideki Kamada, Hiroshi Kawai, and Toshiaki Kobayashi for helpful comments on the fabrication and properties of PVA films.

References

1. Sakurada, I. *International Fiber Science and Technology Series 6, Polyvinyl Alcohol Fibers*; Marcel Dekker Inc.: New York, 1985.
2. Finch, C. A. *Polyvinyl Alcohol—Developments*; John Wiley & Sons Ltd.: Oxford, England, 1992.
3. Goodship, V.; Jacobs, D. *Polyvinyl Alcohol: Materials, Processing and Applications*; Smithers Rapra Technology, 2009.

4. Kurokawa, H.; Shibayama, M.; Ishimaru, T.; Nomura, S. *Polymer* **1992**, *33*, 2182.
5. Deuel, H.; Neukom, A. *Makromol. Chem.* **1949**, *3*, 113.
6. Schmidr-Rohr, K.; Spiess, H. W. *Multidimensional Solid-state NMR and Polymers*; Academic Press Limited, New York, 1994.
7. Saito, H.; Ando, I.; Naito, A. *Solid-state NMR Spectroscopy for Biopolymers: Principles and Applications*; Springer: Amsterdam, Netherlands, 2006.
8. Ando, I., Asakura, T., Eds.; *Studies in physical and theoretical chemistry 84, Solid State NMR of Polymers*; Elsevier Science: Amsterdam, 1998.
9. Tsukuba Magnet Laboratory, National Institute for Materials Science, Tsukuba city, Japan. http://www.nims.go.jp/TML/.
10. Amoureux, J. P.; Fernandez, C.; Steuernagel, S. *J. Magn. Reson.* **1996**, *123*, 116.
11. Vinogradov, E; Madhu, P. K.; Vega, S. *Chem. Phys. Lett.* **2002**, *354*, 193.
12. Caravatti, P; Braunschweiler, L; Ernst, R. R. *Chem. Phys. Lett.* **1983**, *100*, 305.
13. Slichter, C. P. *Principles of Magnetic Resonance, Springer Series in Solid-state Sciences*; Springer: Berlin, 1996.
14. Gainsford, G. J.; Kemmitt, T.; Higham, C. *Acta Cryst.* **2008**, *E64*, i24.
15. J. D. Cuthbert, J. D.; Petch, H. E. *J. Chem. Phys.* **1963**, *38*, 1912.
16. Mao, D; Bray, P. J. *Solid State Nucl. Magn. Reson.* **1992**, *1*, 255.
17. Weiss, A. *Z. Naturforsch.* **1960**, *15a*, 536.
18. Man, P. P. *J. Magn. Reson.* **1988**, *77*, 148.
19. Man, P. P. *Molec. Phys.* **1993**, *78*, 307.
20. Zachariasen, W. H. *Z. Kristallogr.* **1934**, *88*, 150.
21. Masuda, K; Kaji, H; Horii, F. *Polym. J.* **2001**, *33*, 190.

Chapter 9

NMR Characterization of Canopy Dynamics in Nanoscale Ionic Materials

Michael L. Jespersen,[1,2] Peter A. Mirau,[*,1] Ernst von Meerwall,[3]
Richard A. Vaia,[1] Robert Rodriguez,[4,5] Nikhil J. Fernandes,[4]
and Emmanuel P. Giannelis[4]

[1]Materials and Manufacturing Directorate, Air Force Research Laboratory,
Wright-Patterson AFB, OH 45433
[2]UES, Inc., Dayton, OH 45432
[3]Department of Physics, University of Akron, Akron, OH 44325
[4]Department of Materials Science and Engineering and School of Applied
and Engineering Physics, Cornell University, Ithaca, NY 14853
[5]Current address: Intel Corp., 2501 NW 229th Ave., Hillsoboro, OR 97124
[*]E-mail: peter.mirau@wpafb.af.mil

Downloaded by DUKE UNIV on June 21, 2012 | http://pubs.acs.org
Publication Date (Web): October 14, 2011 | doi: 10.1021/bk-2011-1077.ch009

Nanoscale ionic materials (NIMs) are organic-inorganic hybrids in which a core nanoparticle is functionalized with a covalently attached corona and an ionically tethered polymer canopy. NIMs exhibit liquid-like character under ambient conditions in the absence of solvent and are of interest for a variety of applications. We have used nuclear magnetic resonance (NMR) relaxation and pulsed-field gradient (PFG) diffusion experiments to measure the canopy dynamics of NIMs prepared from 18-nm silica nanoparticles. NMR studies show that the fast (ns) local dynamics of the canopy are insensitive to the presence of the silica nanoparticles. Canopy diffusion in the NIMs is slowed relative to the neat copolymer, but not all canopy molecules are slowed equally due to crowding at the nanoparticle surface, resulting in a strongly bound fraction at the surface and a weakly bound outer sphere. Electrostatic interactions with other ionic (Na^+) species alter the dynamics by screening interactions with the nanoparticle.

In NMR Spectroscopy of Polymers: Innovative Strategies for Complex Macromolecules; Cheng, H., et al.;
ACS Symposium Series; American Chemical Society: Washington, DC, 2011.

Downloaded by DUKE UNIV on June 21, 2012 | http://pubs.acs.org
Publication Date (Web): October 14, 2011 | doi: 10.1021/bk-2011-1077.ch009

Introduction

Nanoscale ionic materials (NIMs) are an emerging class of functionalized nanoparticles that have recently generated a great deal of interest due to their unique characteristics (*1–3*). NIMs are organic-inorganic hybrids consisting of a core nanoparticle functionalized with a covalently bound ionic corona and a bulky counter-ion as the canopy (Figure 1). NIMs are nanoparticles stabilized by an organic ionic liquid coating and either behave as liquids at room temperature or undergo reversible, macroscopic solid-to-liquid transitions near room temperature in the absence of solvent. The library of NIMs reported to date has grown to include NIMs based on metal oxides (SiO_2 (*1*, *4*, *5*), Fe_2O_3 (*5*), TiO_2 (*2*), and ZnO (*6*)), metals (Au (*7–9*), Pt (*7*, *9*), Pd (*7*), and Rh (*7*)), quantum dots (*10*), carbon nanotubes (*11*, *12*), nanorods (*13*) and fullerols (*14*).

The room temperature liquid character of NIMs allows for the design of liquids that retain the unique size-dependent properties of the core nanoparticles (*e.g.*, magnetic fluids with high viscosity, etc.). Exploiting the versatility of the NIMs platform in widespread applications (*9*, *15*, *16*) will depend on the degree to which NIMs properties can be tuned by modifying their structure and composition (core shape and size, canopy composition and structure, and ionic content). Flexibility in NIMs design also presents an opportunity to investigate the influence of structure and composition on the dynamics of the canopy, which will likely have a strong impact on the macroscopic properties of NIMs.

In this study we report the NMR relaxation and diffusion studies of silica-based NIMs with a polymer canopy in order to determine the relationship between chemical structure and dynamics. The results show how the properties of the canopy relate to the macroscopic properties.

Experimental Section

Materials

Silica nanoparticles (LUDOX® HS-30 colloidal silica, 30 wt. % suspension in H_2O, 18-nm diameter, Aldrich Chemical Co.), 3-(Trihydroxysilyl)-1-propanesulfonic acid (30-35 wt. % solution in H_2O, Gelest, Inc.), and Jeffamine® M-2070 Polyetheramine (M_n=2263, M_w=2334, PDI=1.03, Huntsman Corporation) were used as received. Deionized water (18.2 MΩ-cm) was purified using a Barnstead Nanopure system.

NIMs Preparation

Silica nanoparticles were functionalized according to a previously reported procedure using (trihydroxysilyl)-1-propanesulfonic acid (SIT, 30-35 wt. % in deionized water) (*1*). The functionalized nanoparticles were purified by dialysis to remove excess SIT and then stirred in the presence of an ion exchange resin (HCR-W2) for at least 48 hours in order to exchange sodium atoms for protons. NIMs were prepared by titration of the bound sulfonic acid groups with M-2070 in deionized water. The equivalence point of the titration represents a 1:1 ratio of canopy to bound corona. The canopy:corona ratio can be tuned by adding the appropriate amount of M-2070 relative to that required to reach stoichiometric equivalence. Samples were prepared at 100% (NIMs100) and 60% (NIMs60) neutralization of the anionic surface of the silica nanoparticles. Once the appropriate amount of M-2070 had been added to generate the targeted corona:canopy ratio, solvent was removed under vacuum at 35-45 °C for several days, resulting in a pale yellow product that flows as a viscous liquid at room temperature.

NMR Characterization

^{13}C relaxation experiments were conducted using a Tecmag Apollo 500 MHz NMR spectrometer equipped with a DOTY Scientific magic-angle spinning probe. Diffusion coefficients were measured at 50.5 °C using proton pulsed-gradient spin-echo NMR as previously described (*17*) using the stimulated echo sequence with pulsed magnetic field gradients of magnitude G = 652 Gauss/cm.

The magnetization decay as a function of gradient field strength was used to determine the diffusion coefficient. In the case of a single diffusing species, the signal decay is given by (*18*, *19*)

$$M(G) = M_0 e^{-\gamma^2 G^2 \delta^2 D(\Delta - \delta/3)}$$

where γ is the gyromagnetic ratio of the nucleus of interest, δ is the time of the gradient pulse, Δ is the diffusion delay time in the pulse sequence, G is the gradient strength, and the diffusion coefficient D is related to the hydrodynamic radius r_H by the Stoke-Einstein equation (*19*, *20*).

$$D = \frac{k_B T}{6\pi\eta r_H}$$

In those cases where single-exponential decay is not observed (*vide infra*), we have chosen to fit the data to a stretched exponential function, given by

$$M(G) = M_0 e^{-\left[\gamma^2 G^2 \delta^2 D(\Delta - \delta/3)\right]^{\beta}}$$

where β is a fitting parameter relating to the deviation from single-exponential behavior. In cases where the stretched exponential did not give a good fit, the data was fit to a double exponential function, given by

$$M(G) = M_f e^{-\gamma^2 G^2 \delta^2 D_f(\Delta - \delta/3)} + M_s e^{-\gamma^2 G^2 \delta^2 D_s(\Delta - \delta/3)}$$

where the subscripts *f* and *s* refer to fast and slow diffusion processes.

Results and Discussion

The dynamics of the NIMs corona-canopy interface were evaluated from the ^{13}C spin-lattice relaxation times and the proton diffusion coefficients measured

Downloaded by DUKE UNIV on June 21, 2012 | http://pubs.acs.org
Publication Date (Web): October 14, 2011 | doi: 10.1021/bk-2011-1077.ch009

Downloaded by DUKE UNIV on June 21, 2012 | http://pubs.acs.org
Publication Date (Web): October 14, 2011 | doi: 10.1021/bk-2011-1077.ch009

by pulsed-field gradient (PFG) NMR. The NIMs of interest consist of an 18-nm silica nanoparticle core functionalized with a monolayer of trihydroxysilylpropyl sulfonic acid (SIT). The anionic SIT corona is paired with an amine-terminated (cationic) ethylene oxide/propylene oxide diblock copolymer canopy (Figure 1). NIMs have been described as monolithic hybrid materials with liquid properties, where each nanostructure "carries" its share of the solvent (*1*, *21*). For this reason, a canopy: corona ratio of 1:1 was chosen as the most reasonable starting point for examining the molecular-level dynamics of NIMs using NMR.

The first step in characterizing the dynamics by NMR relaxation is measurement of the T_1 relaxation across a range of temperatures and identification of the ^{13}C T_1 minimum. The T_1 minimum occurs when the molecular motions are near the spectrometer frequency (125 MHz) (*22*). The dynamics of the free canopy (M-2070) and the NIMs canopy in neat, dry samples were measured from the carbon T_1 of the methylene carbon peak at 74 ppm, which is attributed primarily to the ethylene oxide segments. Figure 2 compares the temperature dependence of the carbon T1's for the bulk M-2070 and NIMs samples prepared with 100% and 60% neutralization of the sulfonic acid groups. The most remarkable feature of this plot is that the relaxation times versus temperature are identical and that the T_1 minimum occurs at the same temperature for the NIMs100 and NIMs60 samples as for the bulk M-2070.

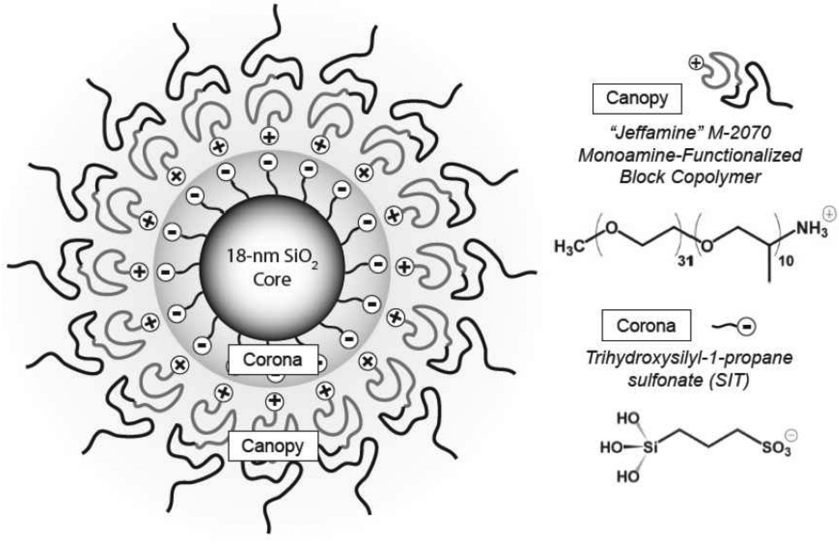

Figure 1. NIMs diagram showing the core, corona and canopy.

A more quantitative understanding of canopy dynamics in NIMs can be obtained by fitting the temperature dependence of the relaxation to a specific model. A number of models for the C-H autocorrelation function were explored to determine the rotational correlation times from the T_1 relaxation data. We observed that the T_1 minimum (0.1 s) calculated from the isotropic reorientation model for the C-H autocorrelation function did not adequately predict the

Downloaded by DUKE UNIV on June 21, 2012 | http://pubs.acs.org
Publication Date (Web): October 14, 2011 | doi: 10.1021/bk-2011-1077.ch009

experimentally observed T_1 minimum (0.26 s) for either the neat canopy or the NIMs. Given that the canopy molecules are smaller than an entangled polymer in the melt, we have chosen to use the Lipari-Szabo (LS) model (*23*, *24*) for the autocorrelation function rather than a more sophisticated model like the modified KWW model (*25*) commonly used for high molecular weight polymers. The key assumption of the LS model is that the overall molecular reorientation is decoupled from faster internal motions, and the autocorrelation function $C(t)$ is given by the product of the correlation functions for overall reorientation $C_0(t)$ and the internal motion $C_i(t)$ as

$$C(t) = C_0(t)C_i(t)$$

The spectral densities in the LS model are given by

$$J(\omega_i) = \frac{S^2\tau_r}{\left(1+\omega_i^2\tau_r^2\right)} + \frac{\left(1-S^2\right)\tau_i}{\left(1+\omega_i^2\tau_i^2\right)}$$

where S^2 is the generalized order parameter and $\tau = \tau_r\tau_i/\left(\tau_r+\tau_i\right)$ where τ_i is the correlation time for rapid librational motions and τ_r is the rotational correlation time.

The LS model with a generalized order parameter of 0.4 gave a good fit to the T_1 minimum (268 K) and was used to calculate correlation times as a function of temperature. The key conclusions from the T_1 fits are that the carbon relaxation is due to a combination of rapid (10 ps) librational motions and slower (0.1-2 ns) reorientation. The local dynamics do not appear to depend on the presence of the 18-nm silica nanoparticle for NIMs100 and NIMs60.

The silica nanoparticles in the NIMs are functionalized at nearly every surface hydroxyl group on the silica nanoparticle, resulting in an estimated corona density of 4.5/nm^2. At this density, the average distance between between acid groups is less than the radius of gyration of the canopy (1.25 nm) calculated for a freely jointed chain (*26*). The resultant crowding could result in stretched chain configurations extending away from the surface, analogous to a brush. At lower canopy densities than those studied here, configurations where the chain folds back onto the nanoparticle surface, allowing interactions between the oxygen atoms in the ethylene oxide/propylene oxide monomers and the sulfonic acid groups or water molecules strongly bound to the sulfonic acids, are more likely. We are currently investigating systems with the possibility for these interactions, which we would expect to result in slower local dynamics.

One of the key assumptions in NIMs design is that each functionalized nanoparticle carries its share of the solvent (*i.e.*, the canopy) because the charge on the ionic terminal functionality of the corona is balanced by a strongly associated, oppositely-charged canopy molecule (*1*, *21*). In the case of strong association of the canopy with the nanoparticle surface, significant differences between the diffusion coefficients measured for the bulk M-2070 and NIMs canopy would be expected. To evaluate this hypothesis, we have measured the canopy diffusion coefficients using the stimulated-echo PFG pulse sequence with corrections for gradient artifacts (*27*).

The first measure of the interaction between the anionic terminal functionality on the nanoparticle and the cationic corona is to compare the diffusion coefficients in solutions of the canopy and the NIMs. Figure 3 compares the diffusion curves for 8% (w/w) solutions of the canopy and the NIMs in D_2O at 50°C. The most notable feature is that the diffusion coefficients are very similar for the two samples. In both cases, the data was fit to a stretched exponential function and the results are listed in Table I (*28*).

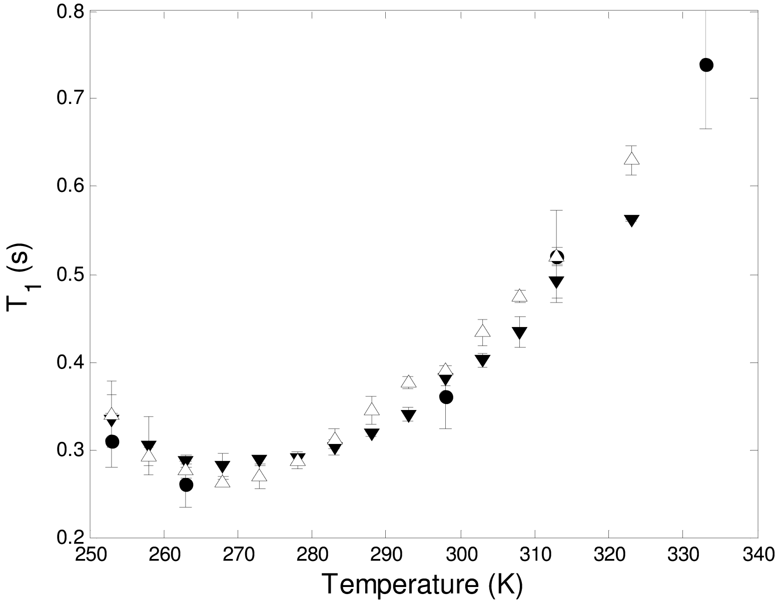

Figure 2. The carbon T_1 vs. temperature for M-2070 (●), NIMs100 (▵), and NIMs60 (▾).

The magnetization decay for M-2070 in D_2O appears as a single exponential (β=0.98) within experimental error, as expected for a nearly monodisperse polymer (PDI=1.03) (*29*). The measured diffusion coefficient for M-2070 closely agrees with the value of 2.1 x 10^{-6} cm^2/s calculated from the Stokes-Einstein relation using the viscosity of D^2O at 50 °C and a hydrodynamic radius of 1.25 nm, calculated assuming a freely jointed chain (*26*). We note that r_H =1.25 nm compares favorably to the value determined from dynamic light scattering experiments (1.15 nm). By comparison, the decay curve for the NIMs100 canopy shows only a 15% decrease in the diffusion coefficient compared to dissolved M-2070. We can estimate the diffusion coefficient expected if the canopy molecules were bound to the nanoparticles by calculating the hydrodynamic radius for the silica nanoparticle (9 nm), the corona (0.5 nm) and the canopy (2 x 1.25 nm). This gives a hard-sphere radius of 12 nm, from which we would expect the

In NMR Spectroscopy of Polymers: Innovative Strategies for Complex Macromolecules; Cheng, H., et al.;
ACS Symposium Series; American Chemical Society: Washington, DC, 2011.

Downloaded by DUKE UNIV on June 21, 2012 | http://pubs.acs.org
Publication Date (Web): October 14, 2011 | doi: 10.1021/bk-2011-1077.ch009

diffusion coefficient to decrease by a factor of 9.6 relative to a dissolved canopy molecule in D_2O. The fact that we observe only a 15% decrease in the diffusion coefficient shows that the NIMs canopy does not undergo hard-sphere diffusion in solution. Rather, the canopy is exchanging between free molecules and other nanoparticles in D_2O on the time scale (ms) of the diffusion measurements.

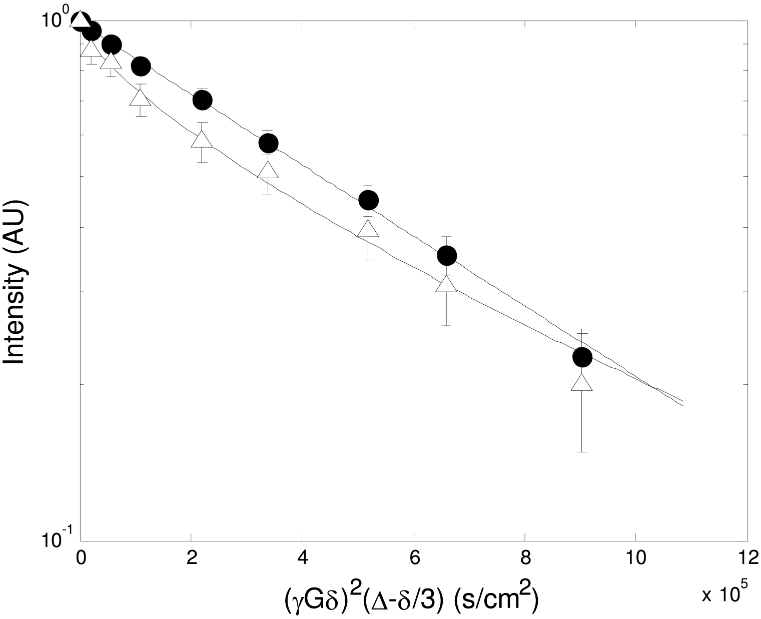

Figure 3. PFG NMR diffusion for M-2070 (●) and NIMs100 (▵) in D_2O. (Reproduced with permission from reference (28). Copyright 2010 American Chemical Society.)

Table I. Self-diffusion coefficients and fitting parameters for the canopy and NIMs in D_2O at 50°C

Sample	*D (cm²/s)*	*β*
M-2070	1.84×10^{-6}	0.98
NIMs100	1.56×10^{-6}	0.73

Figure 4 compares the self-diffusion decay curves for neat, dry samples of the free canopy, NIMs100, and NIMs100 spiked with NaCl (SIT:Na=1:1). We observe curvature on the semilog plots and good fits to the stretched exponential function for free canopy and Na^+-spiked NIMs100. The data for NIMs 100 is fit by a double exponential function, and the diffusion coefficients and fit parameters are listed in Table II.

Downloaded by DUKE UNIV on June 21, 2012 | http://pubs.acs.org
Publication Date (Web): October 14, 2011 | doi: 10.1021/bk-2011-1077.ch009

Downloaded by DUKE UNIV on June 21, 2012 | http://pubs.acs.org
Publication Date (Web): October 14, 2011 | doi: 10.1021/bk-2011-1077.ch009

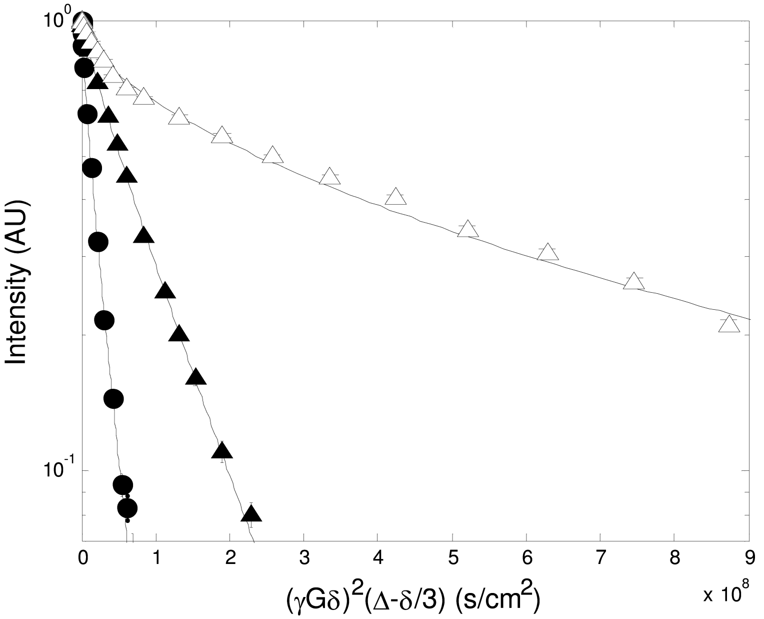

Figure 4. PFG diffusion for bulk M-2070 (●), NIMs100 (△) and NIMs100 spiked with NaCl (▲).

Table II. Self-diffusion coefficients for neat M-2070, NIMs100 and NIMs100 spiked with NaCl

Sample	***D (cm²/s)***	***β***
Bulk M-2070	5.3×10^{-8}	0.83
NIMs100	3.2×10^{-8} (fast) 1.4×10^{-9} (slow)	--
NIMs100/NaCl	1.3×10^{-8}	0.90

Even though we observed single exponential decay for M-2070 in D_2O solution, Figure 4 and Table II show that a stretched exponential function (β=0.83) is required to fit the data for the neat canopy. Since the solution experiments eliminate polydispersity as an explanation for curvature in the signal decay, we believe the curvature results from self-association of M-2070 in the neat state, which does not occur when the molecule is dissolved in D_2O at 50 °C (Figure 3). We note that M-2070 is similar in structure to Pluronic block copolymers, which are known to self-associate in solution, giving rise to distributions in diffusion coefficients (*30*). We have also observed self-association of M-2070 in dilute solutions of by GPC and in both dilute solutions of M-2070 and neat M-2070 by small angle x-ray scattering (not shown).

Downloaded by DUKE UNIV on June 21, 2012 | http://pubs.acs.org
Publication Date (Web): October 14, 2011 | doi: 10.1021/bk-2011-1077.ch009

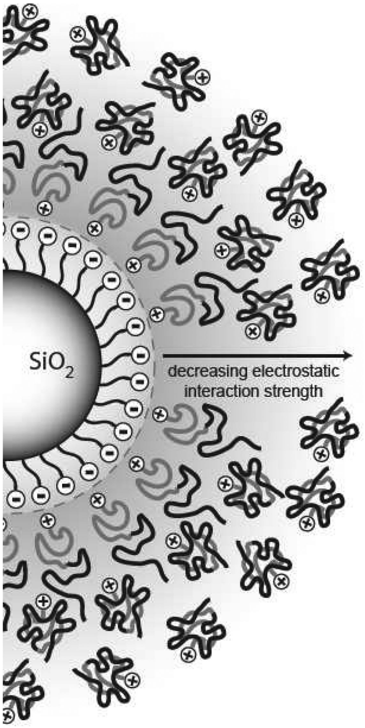

Figure 5. Diagram showing the crowding of polymer chains at the surface of the nanoparticle.

Canopy diffusion in NIMs100 is significantly slower than in bulk M-2070 and is best fit with a double exponential function. The double-exponential nature of the curve demonstrates that there are two populations of canopy polymers, one of which is not exchanging on the time scale (ms) of the diffusion experiment. We believe this can be explained by polymer crowding at the particle surface because the radius of gyration of the M-2070 is larger than the spacing between anionic groups on the nanoparticle surface, as shown schematically in Figure 5. A balance of electrostatic attractions between sulfonic acid and amine groups and entropic repulsion arising from stretched chain conformations would result in a diffuse electrostatic coupling zone extending away from the anionic corona. This hypothesis is further supported by the observation that the slow diffusion coefficient (1.4 x 10^{-9} cm^2/s) gives a hard-sphere radius of 14 nm, which closely agrees with the estimated hard-sphere radius (12 nm), defined by the silica nanoparticle diameter plus the SIT layer and two times the hydrodynamic radius of the canopy. The outer sphere canopy molecules are attracted to the surface by Coulombic interactions, but they are unable to reach the surface due to the molecular crowding. We note that the fast diffusion in the NIMs100 sample is similar to that of bulk M-2070. We previously reported that the diffusion

Downloaded by DUKE UNIV on June 21, 2012 | http://pubs.acs.org
Publication Date (Web): October 14, 2011 | doi: 10.1021/bk-2011-1077.ch009

coefficients are not sensitive to the diffusion delay time, which demonstrates the diffusion is not restricted to the surface of the nanoparticle (*28*).

Canopy exchange is slowed in neat NIMs100, but it is greatly increased in the presence of NaCl. This is illustrated in Figure 4 (▲) for the sample spiked with NaCl at a level of one sodium atom per acid group. Under these conditions, the diffusion coefficient is an average of that observed for hard-sphere diffusion and for the bulk canopy. The diffusion coefficient measured for the NaCl-spiked sample is similar to that reported for another NIMs sample which we have subsequently determined also contained approximately one sodium ion per acid group (*28*). This behavior suggests that the presence of small amounts of contaminant ions can have a dramatic effect on the canopy dynamics in NIMs and that the diffusion properties can potentially be tuned by controlling the concentration and valence of additional ions in the NIMs.

Conclusion

In summary, we have studied the dynamics and diffusion of the organic canopy in SiO_2 NIMs using a combination of NMR relaxation and pulsed-field gradient diffusion. The local molecular relaxation times are similar for the bulk canopy and the completely neutralized NIMs, suggesting that the dynamics are liquid-like at the surface of the nanoparticle. The diffusion experiments reveal two different populations of canopy polymers with different translational diffusion characteristics. The canopy polymers strongly tethered to the surface exhibit hard-sphere-like diffusion, whereas the outer sphere layer of the canopy exhibits bulk-like M-2070 diffusion. These data are explained with a model in which canopy crowding at the nanoparticle surface prevents all of the amine-terminated canopy from interacting directly with the acid groups on the surface. We are currently investigating the effects of canopy molecular weight, canopy:corona ratios, nanoparticle size, and contaminant ion concentrations on the dynamics and rheology of NIMs.

Acknowledgments

Funding provided by the Air Force Office of Scientific Research is gratefully acknowledged. The diffusion portion of this work was supported by the National Science Foundation under Grant No. DMR 04 55117. This publication is based on work supported by Award No. KUS-C1-018-02, made by King Abdullah University of Science and Technology (KAUST). A portion of this research was carried out while M. Jespersen was a National Research Council Associate at the Air Force Research Laboratory. Jeffamine M-2070 was generously donated by Huntsman Corporation (Houston, TX). The authors would like to thank George Fultz and Timothy Reid (University of Dayton Research Institute) for viscosity and ICP-MS data supporting this research. M. Tchoul and H. Koerner (AFRL/RX) contributed GPC and SAXS data, respectively, in support of this study. The authors also thankfully acknowledge Dr. Rajiv Berry and Phuong Ngo (AFRL/RX) for helpful discussions regarding this work.

References

1. Rodriguez, R.; Herrera, R.; Archer, L. A.; Giannelis, E. P. *Adv. Mater.* **2008**, *20*, 4353–4358.
2. Bourlinos, A. B.; Chowdhury, S. R.; Herrera, R.; Jiang, D. D.; Zhang, Q.; Archer, L. A.; Giannelis, E. P. *Adv. Funct. Mater.* **2005**, *15*, 1285–1290.
3. Rodriguez, R.; Herrera, R.; Bourlinos, A. B.; Li, R.; Amassian, A.; Archer, L. A.; Giannelis, E. P. *Appl. Organomet. Chem.* **2010**, *24*, 581–589.
4. Bourlinos, A. B.; Chowdhury, S. R.; Jiang, D. D.; An, Y.-U.; Zhang, Q.; Archer, L. A.; Giannelis, E. P. *Small* **2005**, *1*, 80–82.
5. Bourlinos, A. B.; Herrera, R.; Chalkias, N.; Jiang, D. D.; Zhang, Q.; Archer, L. A.; Giannelis, E. P. *Adv. Mater.* **2005**, *17*, 234–237.
6. Bourlinos, A. B.; Stassinopoulos, A.; Anglos, D.; Herrera, R.; Anastasiadis, S. H.; Petridis, D.; Giannelis, E. P. *Small* **2006**, *2*, 513–516.
7. Warren, S. C.; Banholzer, M. J.; Slaughter, L. S.; Giannelis, E. P.; DiSalvo, F. J.; Wiesner, U. B. *J. Am. Chem. Soc.* **2006**, *128*, 12074–12075.
8. Zheng, Y.; Zhang, J.; Lan, L.; Yu, P.; Rodriguez, R.; Herrera, R.; Wang, D.; Giannelis, E. P. *ChemPhysChem* **2010**, *11*, 61–64.
9. Voevodin, A. A.; Vaia, R. A.; Patton, S. T.; Diamanti, S.; Pender, M.; Yoonessi, M.; Brubaker, J.; Hu, J.-J.; Sanders, J. H.; Phillips, B. S.; MacCuspie, R. I. *Small* **2007**, *3*, 1957–1963.
10. Sun, L.; Fang, J.; Reed, J. C.; Estevez, L.; Bartnik, A. C.; Hyun, B.-R.; Wise, F. W.; Malliaras, G. G.; Giannelis, E. P. *Small* **2010**, *6*, 638–641.
11. Bourlinos, A. B.; Georgakilas, V.; Boukos, N.; Dallas, P.; Trapalis, C.; Giannelis, E. P. *Carbon* **2007**, *45*, 1583–1595.
12. Bourlinos, A. B.; Georgakilas, V.; Tzitzios, V.; Boukos, N.; Herrera, R.; Giannelis, E. P. *Small* **2006**, *2*, 1118–1191.
13. Bhattacharjee, R. R.; Li, R.; Estevez, L.; Smilgies, D.-M.; Amassian, A.; Giannelis, E. P. *J. Mater. Chem.* **2009**, *19*, 8728–8731.
14. Fernandes, N.; Dallas, P.; Rodriguez, R.; Bourlinos, A. B.; Georgakilas, V.; Eiannelis, E. P. *Nanoscale* **2010**, *2*, 1653–1656.
15. Eastman, J. A.; Choi, S. U. S.; Li, S.; Yu, W.; Thompson, L. J. *Appl. Phys. Lett.* **2001**, *78*, 718–720.
16. Park, S. I.; Lim, J. H.; Kim, J. H.; Yun, H. I.; Roh, J. S.; Kim, C. G.; Kim, C. O. *Phys. Status Solidi B* **2004**, *241*, 1662–1664.
17. Iannacchione, G.; Von Meerwall, E. *J. Polym. Sci., Part B: Polym. Phys.* **1991**, *29*, 659–668.
18. Price, W. S. *Concepts Magn. Reson.* **1998**, *104*, 299–336.
19. Johnson, C. S. *Prog. Nucl. Magn. Reson. Spectrosc.* **1999**, *34*, 203–256.
20. Price, W. S. *Concepts Magn. Reson.* **1998**, *104*, 197–237.
21. Agarwal, P.; Qi, H.; Archer, L. A. *Nano Lett.* **2010**, *10*, 111–115.
22. Mirau, P. *A Practical Guide to the NMR of Polymers*; John Wiley & Sons: Hoboken, 2004; p 418.
23. Lipari, G.; Szabo, A. *J. Am. Chem. Soc.* **1982**, *104*, 4546–4559.
24. Lipari, G.; Szabo, A. *J. Am. Chem. Soc.* **1982**, *104*, 4559–4570.
25. Qiu, X.; Moe, N. E.; Ediger, M. D.; Fetters, L. J. *J. Chem. Phys.* **2000**, *113*, 2918–2926.

Downloaded by DUKE UNIV on June 21, 2012 | http://pubs.acs.org
Publication Date (Web): October 14, 2011 | doi: 10.1021/bk-2011-1077.ch009

26. Hiemenz, P. C. *Polymer Chemistry, The Basic Concepts*; Marcel Dekker, Inc.: New York, 1984.
27. Von Meerwall, E.; Kmat, M. *J. Magn. Reson.* **1989**, *83*, 309–323.
28. Jespersen, M. L.; Mirau, P. A.; von Meerwall, E.; Vaia, R. A.; Rodriguez, R.; Giannelis, E. P. *ACS Nano* **2010**, *4*, 3735–3742.
29. Hakansson, B.; Nyden, M.; Soderman, O. *Colloid Polym. Sci.* **2000**, *278*, 399–405.
30. Nilsson, M.; Hakansson, B.; Soderman, O.; Topgaard, D. *Macromolecules* **2007**, *40*, 8250–8258.

Downloaded by DUKE UNIV on June 21, 2012 | http://pubs.acs.org
Publication Date (Web): October 14, 2011 | doi: 10.1021/bk-2011-1077.ch009

In NMR Spectroscopy of Polymers: Innovative Strategies for Complex Macromolecules; Cheng, H., et al.;
ACS Symposium Series; American Chemical Society: Washington, DC, 2011.

Chapter 10

Dynamics of Disordered Structure of π-Conjugated Polymers Investigated by Solid-State NMR

N. Asakawa,*,[1] Y. Inoue,[2] T. Yamamoto,[3] R. Shimizu,[4] M. Tansho,[4] and K. Yazawa[2]

[1]Department of Chemistry and Chemical Biology, Graduate School of Engineering, Gunma University, 1-5-1 Tenjincho, Kiryu, Gunma 376-8515, Japan
[2]Department of Biomolecular Engineering, Graduate School of Bioscience and Biotechnology, Tokyo Institute of Technology, 4259 Nagatsuta-cho, Midori-ku, Yokohama, Kanagawa 226-8501, Japan
[3]Chemical Resources Laboratory, Tokyo Insitute of Technology, 4259 Nagatsuta-cho, Midori-ku, Yokohama, Kangawa 226-8503, Japan
[4]National Institute for Materials Science, 3-13 Sakura, Tsukuba, Ibaraki 305-0003, Japan
***E-mail: asakawa@chem-bio.gunma-u.ac.jp**

Stochastically excitable threshold units using functional materials will potentially be among the key devices for the production of noise-driven bio-inspired sensors and information processors with ultra-low energy consumption. In particular, a noise generator and threshold unit will be able to be fabricated utilizing the fluctuations found in materials that include structural, electric dipole, magnetic, and spin. This article deals with studies of polymer dynamics mainly by ^{13}C solid-state NMR and structural fluctuations due to twist dynamics of π-conjugated polymers near the order-disorder phase transition or twist glass transition. The twist dynamics of π-conjugated polymers will be important in the design and production of future electronic devices such as bio-inspired stochastic information processors.

In NMR Spectroscopy of Polymers: Innovative Strategies for Complex Macromolecules; Cheng, H., et al.;
ACS Symposium Series; American Chemical Society: Washington, DC, 2011.

Introduction

Biological systems employ a mechanism of sensoring and information transmission/processing with ultra low energy consumption, which are found in their sensory (*1–3*) and central (*4–6*) nervous systems. This situation contrasts sharply with conventional digital computers, where energy consumption is quite high. The low energy consumption of biological information processing is due to its mechanism of environmental noise utilization.

Conventional digital technology has been developed based on "noise suppression." Because of this design, the system consumes high energy, say 3 or 5 volts and 10-100 watts per CPU in order to ensure error-less, deterministic operation with Boolean logic. On the other hand, it is known that, for instance, a human brain consumes at most 10 W (*7*) for information processing although the number of elements (neurons) are at least hundreds of times larger than a typical central processing unit (CPU). This is due to noise tolerant mechanism of information transmission and processing.

Sensory nerves of several biological systems including crickets (*1*), crayfish (*2*), and paddlefish (*3*) exploit the phenomenon of *stochastic resonance* (SR) for weak signal detection within a noisy environment (*4*). Counterintuitively, the signal/noise ratio (SNR) of weak sensory signal is enhanced by internal and/or external noise to these systems. Thus. biological systems enhance their performance with progressive utilization of noise. Similar phenomena can be found in several layers of biological hierarchy, including membrane proteins (*8*), cells (*9*), nervous tissues (*10*), brains (*11*), and individuals (*12*). Recently, the concept of neuronal computations with stochastic network in the brain has also been accepted (*13*). If one seeks to bio-mimick artificial agents with high adaptability to unpredictable, abrupt environmental change, it would be difficult to do with conventional digital technology, where operations based on "If…Then…Else" are prerequisite. In such a case, one needs to establish novel information sensors and processors with ultra-low energy consumption that employs biological mechanisms of progressive utilization of noise.

Recently, Asakawa et al. (*14*) demonstrated that a delayed feedback network of stochastic threshold units have the ability of noise-driven autonomous switching depending on a sensory signal. Below we listed the four important characteristics that can be realized with such a device element.

i) nonlinear response to external field,
ii) noise generation,
iii) one-directional signal transmission, and
iv) dynamic modulation of inter-elemental connectivity.

Historically, polymeric materials had not been used for active electronic device materials mainly because many polymers show unstable electric properties due to poor heat resistance or heat deflection, large structural fluctuation, or chemical instability. Of course, recent developments in organic light emitting diodes(OLED) (*15*), organic field effect transistors(OFET) (*16*), and organic photovoltaic cells(OPV) (*17*) have been remarkable, and these applications related to polymers will form a mainstream of polymer electronics. Even so, unstable properties, or (more correctly) large time and/or spatial fluctuations of physical properties, e.g., carrier mobility and electric conductivity, can be an important determinant in producing noise-driven bio-inspired devices that we are interested in.

Poly(alkylthiophene)s [P3ATs] are a class of π-conjugated polymers soluble in ordinary organic solvents. Previous x-ray diffraction (*18*) and differential scanning calorimetry (DSC) measurements (*19*, *20*) indicate that P3ATs show an order-disorder phase transition. By tuning the length of alkyl side-group, one can observe a transition temperature near room temperature. It is also well known that P3ATs without doping show nonlinear electrical conductivity. Since it is theoretically predicted that static (*21*) and dynamic (*22*) disorder affect the carrier mobility of π-conjugated polymers, the dynamics associated with the transition could be the origin of random electric properties and would have the potential to be utilized for a stochastic threshold unit or a molecular noise generator. An interacting ensemble of such stochastic threshold units can be thought of as a complex system that generates such emergent properties as "synchronization" (*23*, *24*) and "chaotic state" (*25*) (Fig.1). We believe that such cooperative dynamics produced by an ensemble of stochastic elements will be able to be used for noise-driven information sensoring and processing in the future.

In this article, we shall show our recent works (*26–28*) concerning dynamics of P3ATs investigated by DSC, Fourier transform infrared (FTIR), and ^{13}C solid-state nuclear magnetic resonance (NMR) spectroscopies. The knowledge obtained here will be useful for material selection/screening in the fabrication of stochastic threshold units using π-conjugated polymers.

Results and Discussions

Molecular Dynamics of Regioregulated P3AT

We have recently investigated the phase diagram for P3ATs (*26–28*). There are various thermodynamic and non-equilibrium states including crystalline (C), glassy crystalline (GC), plastic crystalline (PC), liquid glass (G), and isotropic lipuid (I). The complex diagram can be understood using the concept of *frustration against crystallization* (*29*). In this article, we focus on the structure and dynamics of poly(3-butylthiophene) [P3BT] and poly(3-hexylthiophene) [P3HT]. P3BT shows the richest phase diagram among P3AT, and P3HT is the most widely used polymer in P3ATs mainly because it shows the largest carrier mobility among P3ATs (*30*).

DSC of Regioregulated P3BT and P3HT

Figure 2A shows the DSC chart of P3BT. We found an endothermal peak at 333 K as well as a melting peak (520 K). The peak at 333 K is probably different from the heat capacity jump at 303K for the glass transition of the quenched sample by liquid nitrogen (Figure 2B). (Here, *glass transition* means conventional liquid-glass transition.) Thus, the peak at 333 K is attributable to some sort of solid-solid transition. The endothermal peak at 333 K could not be observed in the second DSC heating scan after cooling at a rate of 50 K/min., inferring that the kinetics of the transition is quite slow. An x-ray diffraction study of P3BT is available (*31*), where the authors concluded that there is a side-group transition from a mixture of end-to-end (phase I) and interdigitation (phase II) packings to the pure phase I state. Nevertheless, on the DSC of P3HT, we could not detect anything other than the melting peak around 500 K (Figure 2C).

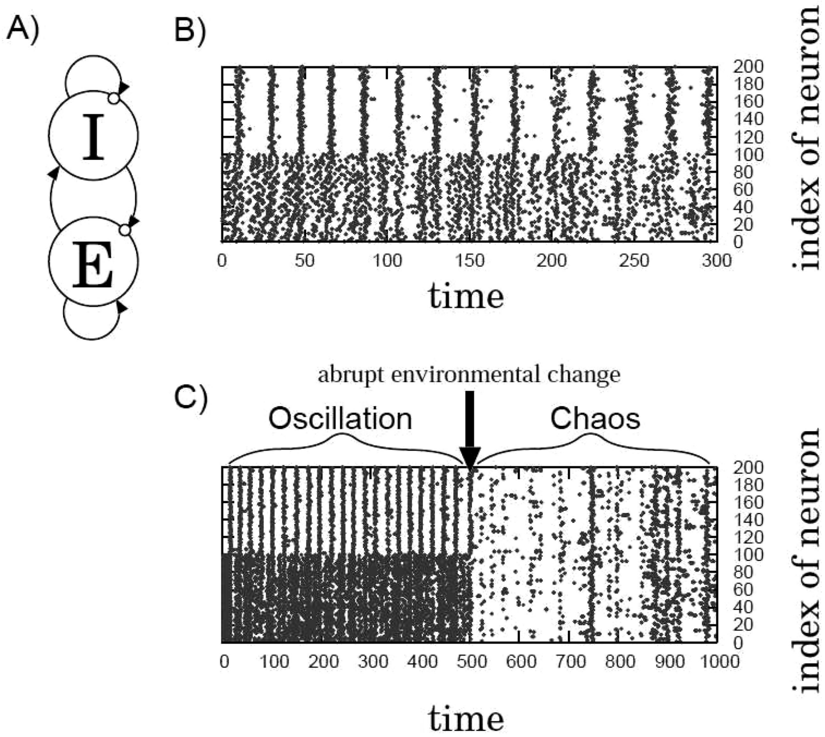

Figure 1. An example of Langevin dynamics simulation for an ensemble of stochastic threshold units. Gray dots stands for the timing when the unit outputs a firing pulse. A) Schematic drawing of a neural network consisting of 100 excitatory units (shown as "E") and 100 inhibitory neurons ("I"). All the excitatory units are connected to one another and the same is true for the inhibitory units. B) "oscillation" emergent from an ensemble of units. External noise input or internal noise is required for the network to emerge from the cooperative dynamics. C) Typical bifurcation phenomenon from oscillation ("limit cycle") to chaos when inter-unit interaction is modified through sensory input by abrupt environmental change.

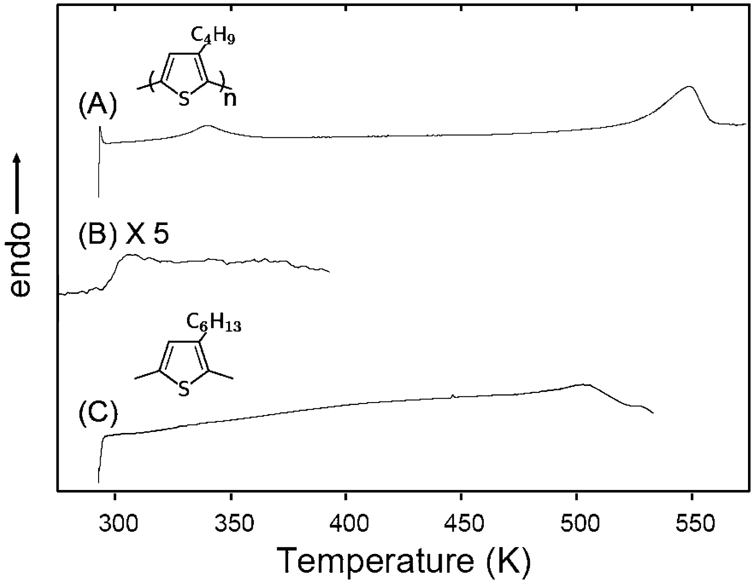

Figure 2. Differential scanning calorimetry (DSC) charts for powdered samples for regioregulated P3ATs. (A) the first heating scan for pristine P3BT, (B) the second heating scan for a quenched sample by liquid nitrogen after the first heating scan in DSC measurements, and (C) the first heating scan for P3HT.

Here, three questions remain. First, why did the π-π stacking peak in the x-ray powder pattern smear out below 323 K, while the same peak was visible above 323 K? Secondly, what is the driving force of transition? Thirdly, why is the difference between P3BT and P3HT? We performed FTIR and solid-state NMR measurements in order to address these problems.

FTIR Measurements for Regioregulated P3BT and P3HT

Figure 3 shows variable temperature FTIR measurements for P3BT and P3HT. The spectra are for the out-of-plane deformation mode for the C_4-H bond in the main chain. For P3BT, there are two peaks, one at 825 cm^{-1} and the other at 810 cm^{-1}. With increasing temperature, these signals are merged to the 820 cm^{-1} band (Fig.3A, right). At higher temperatures, the absorption of the 820 cm^{-1} band is reduced and that of the 837 cm^{-1} band for melting is increased. In total, we observed four peaks. At lower temperatures, the 825 cm^{-1} band is constant down to 173 K, and the 820 cm^{-1} band is gradually shifted to 810 cm^{-1}. From these experiments, we assigned the four peaks as follows: 837 cm^{-1} (liquid), 825 cm^{-1}(unknown from IR measurements), 820 cm^{-1} (metastable crystalline state), and 810 cm^{-1} (crystalline state, energetically stabler than that of 820 cm^{-1}).

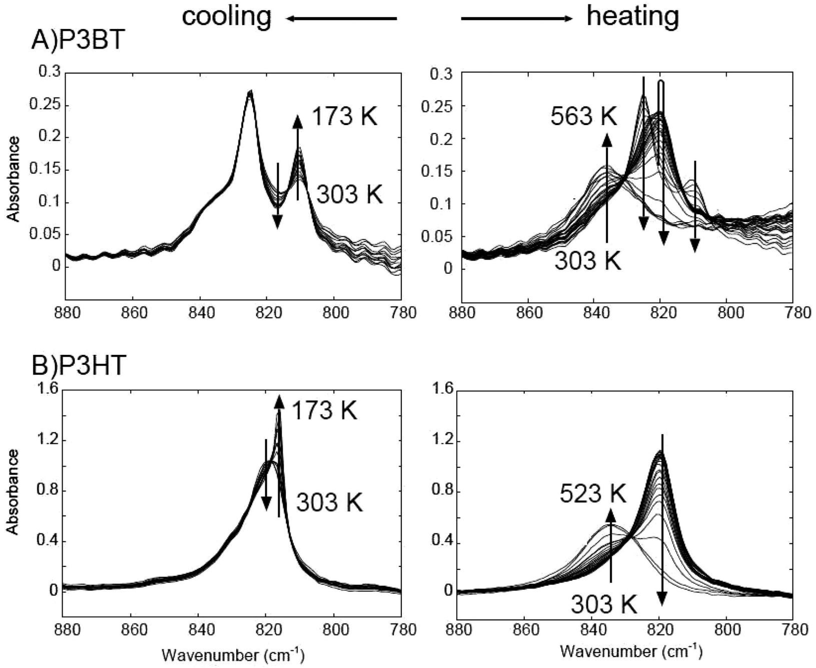

Figure 3. Variable temperature FTIR spectra for thin films of regioregulated P3ATs, P3BT (A) and P3HT (B).

For P3HT, the IR spectrum was similar to but simpler than that for P3BT. Below 300 K (=T_{cp}, the transition temperature between the crystalline and plastic crystalline states; *vide infra* for the detailed definition), two main peaks were observed at 816 and 820 cm^{-1}. From curve fitting, a small signal at 826 cm^{-1} was also detected as a minor component. Above 300K, the 820 cm^{-1} peak is dominant up to the melting temperature (500 K).

^{13}C CPMAS NMR Measurements of Regioregulated P3BT

In order to investigate the transition around 333 K, we performed ^{13}C cross-polarization magic-angle sample spinning (CPMAS) experiments for powdered samples of P3BT and P3HT.

The chemical structure of 3-butylthiophene unit and ^{13}C CPMAS spectra of P3BT are shown in Figure 4A and B, respectively. The clear shoulder signal of the C4 methyl carbon of P3BT can be seen around 16.0 ppm below 333 K, whereas the spectra at the higher temperatures show a unique component (14.6 ppm), meaning that at least two chemically inequivalent methyl carbons in P3BT exist below 333 K (Fig.4C). Because the methylene carbons show no peak splitting, only the end of the butyl chain shows two or more distinct states.

In Figure 4D, the signals of the thiophene ring for P3BT appear at 120–145 ppm as noted in previous studies of oligothiophene (*32*) and regiorandom poly(3-

octylthiophene) (*33*). Broadening and shift of C2 and C5 peaks with heating were also observed. We shall discuss the broadening and shift later in conjunction with spin-lattice relaxation times. Results of FTIR and CPMAS NMR show that the structural change of P3BT occurs markedly around 333 K. At temperatures greater than 333 K, the state of the main chain is attributed almost uniquely to 820 cm^{-1} in FTIR. The side chain is also at a unique state, as shown by the results of CPMAS NMR. Below 333 K, the main chain consists of mainly two states: the main component attributed to 825 cm^{-1} and the other to 810 cm^{-1}. From these, the fact that the methyl moiety of the side chain also shows at least two components is probably related to the main-chain states.

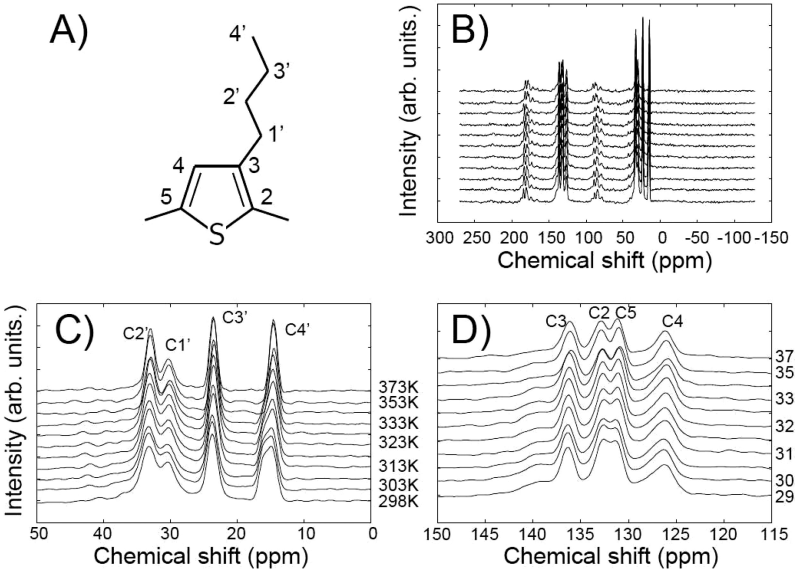

Figure 4. Variable temperature 67.8MHz ^{13}C CPMAS NMR spectra for a powdered sample of P3BT. A) chemical structure of 3-butylthiophene unit, B) full range spectra, C) expanded spectra for alkyl carbon, and D) expanded spectra for thiophene ring carbons.

Let us recall the three aforementioned questions. What explains the absence of the (010) peak (π-π stacking) and the weakness of (100) peaks (inter-chain packing parallel to the planar π-conjugation) below 323 K in the WAXD measurement (*31*)? Even if both phases (phase I and phase II) coexist, the respective scattering peaks of x-ray diffraction should be observed. Furthermore, the peak shifts in the IR spectrum from 825 and 810 cm^{-1} to 820 cm^{-1} with heating do not agree with the argument by Causin *et al.* (*31*), i.e., the transition from phase I and phase II to phase I, because no common IR absorption peak attributable to phase I is visible below and above the transition temperature. Furthermore, what is the driving force of the transition? What is the difference between P3BT and P3HT? Clarifying these issues would be the key to rationalizing the data obtained from DSC, FTIR, CPMAS NMR, and WAXD. Here, we specifically examine the dynamics of the twisting motion of the main chain in the crystalline state.

^{13}C Spin-Lattice Relaxation Time Measurements for Regioregulated P3BT

We performed ^{13}C spin-lattice relaxation time measurements for P3BT using the Torchia method (*34*) at various temperatures to investigate the molecular dynamics. An Arrhenius plot of the spin-lattice relaxation rate (R_1=T_1^{-1}) for each carbon is shown in Figure 5.

For the side group (Figure 5A), each R_1 value was obtained using a simple exponential fitting curve. The figure shows the subtle change of slopes around 333 K, but the decrease of R_1 was observed throughout the measured temperature range with heating (from 303 to 373 K). This tendency is visible in the extremely narrowed regime according to the classical Bloembergen-Pound-Purcell (BPP) theory (*35*), indicating that the side chains behave similarly to liquid. The subtle change of slopes was inferred to result from the conformational change of the main chain because it would be difficult to believe that further changes in average conformation should occur in the side group in the liquid state.

On the other hand, the relaxation of main-chain carbons showed no single exponential decay in the measured temperature range. For that reason, we tried to fit the decay curves using a Kohlrausch-Williams-Watts (KWW) function (*36*). In general, the KWW function is used to express magnetization near and below the glass-transition temperature (T_g) because the distribution of the relaxation rate gave rise to nonexponential recoveries (*37*).The temperature dependences of R_1 for each aromatic carbon are shown in Figure 5B. This figure shows that the main chain must be in the slow motion regime because of the increase of R_1 with heating. More noteworthy is the fact that discontinuous slope changes are apparent around 333 K. In many cases, similar tendency is apparent in ^{2}H NMR measurements, at the glass transition for many glass formers (*38–40*). In the case of NMR spin-lattice relaxation measurements, we can distinguish three temperature regions for the arguments of glass transition. (i) $T<T_g$: the R_1 of glass formers is dominated by the slow β process (Johari-Goldstein process (*41*)), which follows the Arrhenius-type thermal activation process. (ii) $T_g<T<1.2T_g$: Both the α process and the Johari-Goldstein process affect R_1, where the α process is described as stretched exponential (KWW) functions. (iii) $T>1.2T_g$: R_1 is dominated only by the α process. Below 333 K, we observed the Arrhenius-type thermally activated process for all carbons. That tendency is similar to the Johari-Goldstein process. Above 333 K, although the measured temperature range is insufficient to consider the condition of (ii) or (iii) because of the limitation of the available temperature range of our instrument, discontinuous slope changes can be a fingerprint for the effect of α process.

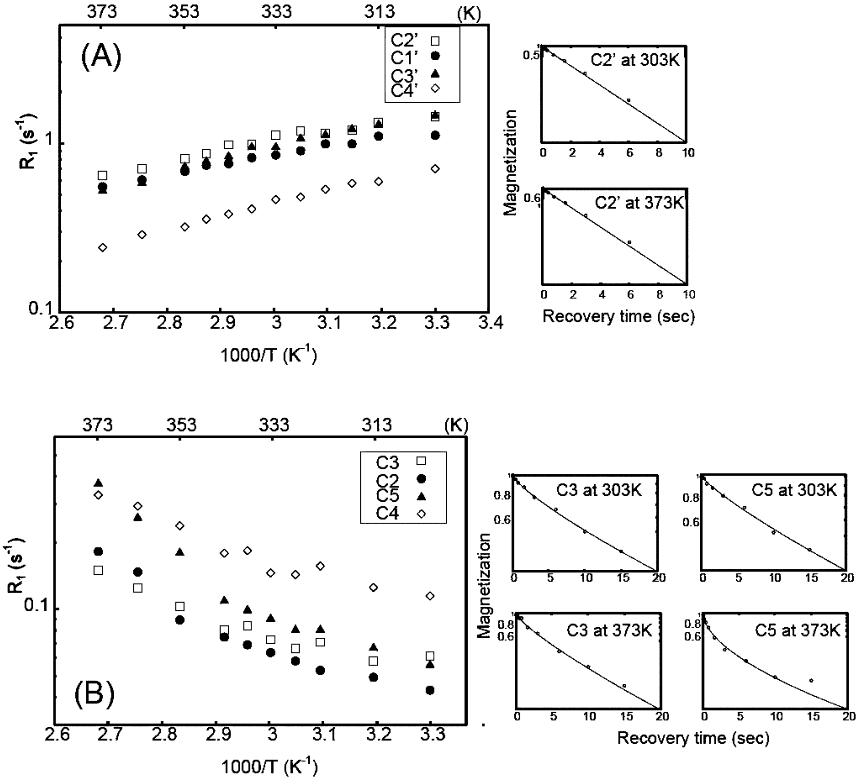

Figure 5. Temperature dependence of ^{13}C spin-lattice relaxation time at 67.8 MHz for alkyl side group carbons (A) and for thiophene ring carbons (B). Insets are typical decay curves measured using Torchia's method.

Figure 5B illustrates another point. For the CPMAS ^{13}C measurements, relaxation occurs through two paths: one is due to the local field fluctuation by ^{13}C-^{1}H magnetic dipolar coupling and the other is due to fluctuation of ^{13}C chemical-shift anisotropy (CSA). C4 carbon that is directly connected to a proton has larger dipolar coupling effect than those of unconnected carbons. Below 333 K, only the C4 carbon shows larger R_1 than other carbons, indicating that the relaxation is caused mainly by ^{13}C-^{1}H magnetic dipolar coupling. That is, the thiophene ring does not undergo reorientations sufficient to fluctuate the chemical-shift anisotropy. Above 333 K, the other carbons (C2,C3,C5) showed individually specific slopes, indicating that the reorientation of the thiophene ring brings about fluctuations in CSA as well. In view of both IR and NMR detectability, the most plausible reorientation is *twist motion*. Similar low-energy excitations of twist motion were observed in structural phase transitions in oligophenylenes using Raman (*42*) and NMR (*43*, *44*).

The above arguments indicate that the glass transition with respect to the thiophene twisting in the crystalline state occurs around 333 K. We define the transition as a *twist glass transition*. Around the twist glass transition, it is thought that the translational symmetry with respect to the molecular axis remains almost unchanged. Although the side group is in the liquid state, there exist residual thiophene π-stacking and then P3BT assumes a kind of crystalline state. But since the π-stacking would not be strong, the planarity of π-conjugation would be far from the perfect. If we think of the thiophene twisting as rotational degree of freedom, the crystalline phase with thiophene twisting is *twist plastic crystalline phase* (PC), and the corresponding non-equilbrium state with frozen twist below the transition temperature is *twist glassy crystalline* (GC). Therefore, twist glass transition is called PC-GC transition and the transition temperature is expressed as T_{gp}. Accordingly, the four peaks observed in FTIR are assigned a follows; 825 cm^{-1} (GC), 820 cm^{-1} (PC), 837 cm^{-1} (I), and 810 cm^{-1} (C), respectively.

Back to the ^{13}C spin-lattice relaxation of P3BT, the temperature dependence of the stretching parameter β does not accord with the results of other glass formers. In general, for $T>T_g$, β is nearly unity because the motional correlation time is much shorter than the spin-lattice relaxation time, which means that ergodicity is achieved. Around T_g, the value of β begins to decrease with decreasing temperature because of the T_1 distribution caused by the slowing of the α process. Then, the value of β increases again slightly with further cooling (*40*, *45*, *46*). In these cases, the single form of the spectral density function $J(\omega)$ is used to determine T_1 because it allows the specific examination of intramolecular motions if we ignore intermolecular interactions. In our case, because of the crystalline state of strong packing, we cannot ignore the fluctuation of intermolecular interaction, especially above the transition temperature where twist motion exists. For that reason, two kinds of spectral-density functions are needed $J_{intra}(\omega)$ and $J_{inter}(\omega)$. Because two interactions, magnetic dipolar coupling and chemical shift anisotropy, should affect each $J(\omega)$ in a specific ratio depending on the second moment of interactions, the decay curve cannot be expressed by a single stretched-exponential function, indicating that β cannot express the T_1 distribution directly at higher temperatures. At $T < 333$ K, where a twist motion is absent, the magnetization curve can be expressed using a single stretched exponential function. As mentioned above, however, at least two states exist, which are attributed to 825 and 810 cm^{-1} in the FTIR spectrum in the temperature region. Therefore, the value of β does lose the conventional meaning of the distribution parameter in the case of P3BT.

^{13}C CPMAS NMR of Regioregulated P3HT

Combining the results of FTIR for P3BT and P3HT and solid-state NMR of P3BT, we assigned the absorption bands in FTIR spectra for P3HT thus: 816 cm^{-1} (C), 820 cm^{-1} (PC), 826 cm^{-1} (GC), and 832 cm^{-1} (I), respectively. The gradual transition was observed in FTIR (Fig.3B, left) and C and GC phases disappears around 300K, which is expressed as T_{cp}, the C-PC transition temperature. Since the fraction of GC phase is quite low, it would be appropriate to express the C-PC transition rather than GC-PC transition. In this section, in order to investigate the structure and molecular dynamics of P3HT around T_{cp} observed in the FTIR study (*27*), we first performed ^{13}C CPMAS measurements for P3HT at various temperatures. The chemical structure of the 3-hexylthiophene unit and the spectra are shown in Figure 6A and 6B, respectively. The peaks higher than 40 ppm correspond to the aliphatic carbon atoms of the side group (Figure 6C) and four aromatic peaks at 120-140 ppm correspond to the four carbons of the thiophene unit(Figure 6D). The assignments of each carbon were made by comparing with the solution NMR of P3HT (*47*). Notably the signals narrow with increasing temperature for both the main chain and the side group. The narrowing probably indicates the onset or acceleration of molecular motion of the P3HT main chain and side group. Figure 6E and 6F show the change in the full width at half-maximum (FWHM) of each peak for the side group and the main chain, respectively.

For the side group, the FWHM decreased gradually with heating, and the slope turned particularly steeper between 200 and 250 K. After that, they showed a weak temperature dependence (note the plateau) between 270 and 300 K, and finally decreased again above 300 K. Interestingly, this transition temperature region for the steeper slope between 200 and 250 K corresponds to that of the FTIR study (*27*), where the C_4-H out-of-plane vibration band gradually shifted with heating from two peaks, 826 and 816 cm^{-1}, to a single peak, 820 cm^{-1}, which corresponds to GC-PC (although the fraction is quite small) and C-PC transition, respectively. In the FTIR study, we focused only on the behavior of the thiophene ring moiety, that is, the change in absorption of the C_4-H out-of-plane region around the transition temperature (*27*). The CPMAS spectra, however, imply that the conformation or the dynamics of the side group changes around the transition temperature. There was no noticeable peak shift in the IR spectra from trans to gauche in the CH_2 asymmetric band in the measured temperature range (*28*). Thus, the FTIR data shows that the alkyl side group keeps the gauche conformation even below T_{cp}, although the line width of the CPMAS spectra changed in this temperature region. The ^{13}C chemical shift of CPMAS spectra for the alkyl group is consistent with the IR results. The methylene peaks (C1′-3′) at 30.5 ppm maintain its height even below T_{cp}. From the chemical shift of the methylene peak, the side group mainly takes on the gauche conformation even below T_{cp}. In fact, CPMAS spectra below T_{cp} showed small shoulders around 25 and 34 ppm in the C5′ and C1′-3′ signals, respectively, indicating at least two or more chemically inequivalent methylene carbons in the side group below T_{cp}. Our FTIR study showed that several phases, PC, GC, C, and amorphous, coexist in this temperature region. These various phases may affect the chemical shift of the side group. Therefore, CPMAS spectra below T_{cp} should have a complicated shape. Unfortunately, the signal of C4′ carbon which appears around 33 ppm overlaps with the all-trans signal of other methylene carbons. This makes it difficult to assign the conformation at the lower temperature accurately. However, the fact that the signal at 30 ppm is clearly apparent and still being a main component even down to 173 K means that at least a certain amount of the gauche conformation exists below T_{cp}. It has often been claimed that the side groups of P3ATs take a perfect all trans conformation at lower temperatures. However, it is not true in the case of P3HT.

Consequently, one can say that the increase of FWHM below T_{cp} originates from the slowing of the side group dynamics. At the transition temperature, the side group froze without a conformational change similar to a glass transition. As mentioned above, P3ATs with longer alkyl side group, such as poly(3-dodecylthiophene) [P3DDT], show a melting behavior of the side group, and it leads to polymorphism (*48*, *49*).

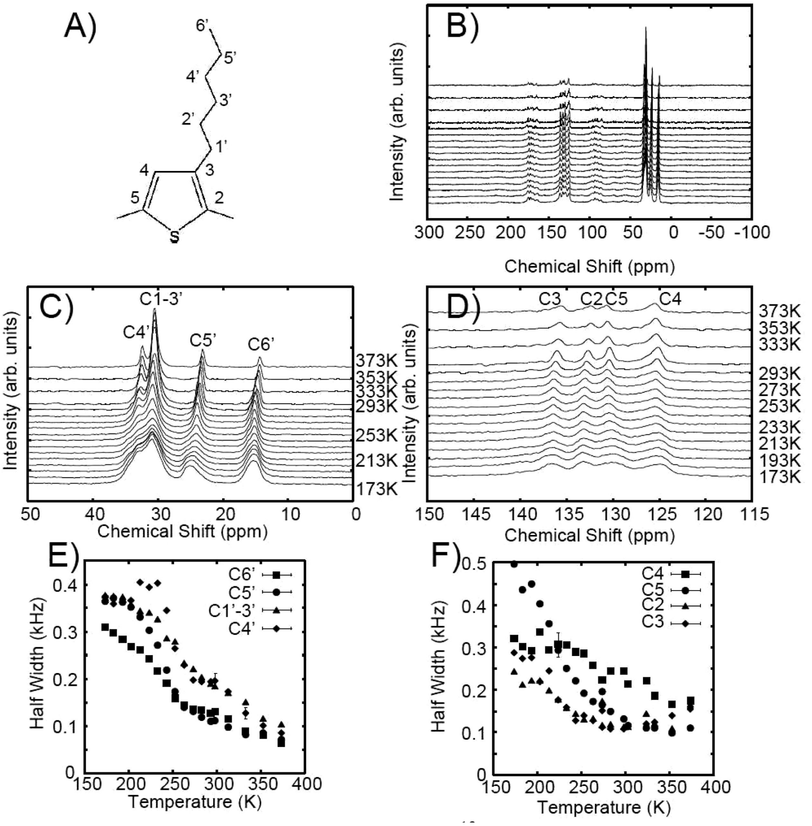

Figure 6. Variable temperature 125.8 MHz ^{13}C CPMAS NMR spectra for a powdered sample of P3HT. A) chemical structure of 3-hexylthiophene unit, B) full range spectra, C) expanded spectra for alkyl carbon, D) expanded spectra for thiophene ring carbons, E) full width at half maximum (FWHM) for alkyl carbons, and F) FWHM for thiophene carbons.

Nonetheless, the side group transition in P3HT is not an order-disorder transition but a glass transition because of its short side group. Pankaj et al. (*50*) investigated side chain dynamics in a series of regiorandom P3ATs by dynamic mechanical analysis, and a process of the alkyl side group for P3HT was observed at 186 K. The fact that the temperature at which the narrowing of the CPMAS spectrum started is almost consistent with their results confirms the glass transition of the alkyl side group in the crystalline state. Similar to the behavior of the side group, the line width for the main chain also narrowed with heating (see Figure 6D and 6F). Below 300 K, similar temperature dependence of FWHM to the side group was observed, although slope changes around 190-210 K are not so clear as observed in the side group. The narrowing with heating below 300K should be attributed to an inhomogeneity-homogeneity change in the conformation or to acceleration of the thiophene ring twisting motion. Indeed, the IR band of the C4-H out-of-plane vibration below 300 K (=T_{cp}) was able to be decomposed to four components, PC, C, GC, and amorphous, while it could be decomposed to two states, PC and amorphous, above T_{cp} (*27*). Therefore, both the decrease of conformational distribution and the increase of molecular dynamics must have contributed to the narrowing of CPMAS signals.

^{13}C Spin-Lattice Relaxation Time Measurements of Regioregulated P3HT

Next, we performed ^{13}C spin-lattice relaxation-time measurements for P3HT (*28*). The relaxation rates (R_1) for each carbon at various temperatures are plotted in Figure 7. For the side groups (Figure 7A), each R_1 value was obtained using a KWW function. Whereas below 230 K the relaxation rates were distributed, the value of β showed nearly unity above 250 K (see the relaxation curves in the inset of Figure 7A); i.e., the obtained fitting curve was a simple exponential. It suggests that an inhomogeneity-homogeneity transition was occurred with heating. The temperature range where the β value is turned into unity corresponds to the peak narrowing of the CPMAS spectrum, suggesting side group transition. However, a clear transition of R_1 was not observed probably due to the noise in R_1 measurement, which is very susceptible to plots with low amplitude in the relaxation curve. With further heating, R_1 reached the maximum value around 270-300 K, except for the methyl carbon of the side group, which monotonously decreased with heating, meaning that the correlation time, τ_c, for the inner side group reached the inverse of Larmor frequency, 125 MHz. At a temperature greater than 300 K, the molecular motion of these carbons entered the extremely narrowing regime (*35*), and eventually the value of R_1 decreased with heating. Interestingly, the onset temperature of extremely narrowing regime is consistent with T_{cp}, indicating that rapid alkyl group motion occurs in the PC state. As mentioned above, the decay of magnetization of the side group carbon obeyed Debye type relaxation in this temperature range. In this case, we were able to determine the activation energy, E_a, of 8.2-15.0 kJ/mol. This is consistent with the recent result of quasi-elastic neutron scattering by Obrzut et al. (*51*).

For the main chain carbons, the decay of magnetization obeyed the stretched exponential fitting curve in all measured temperature ranges as shown by the representative curves in the inset of Figure 7B. This distribution of R_1 is reasonable for the similar reasons as P3BT. Obtained value of R_1 are shown in Figure 7B. Two step jumps with heating are visible around 240 and 310 K. The abrupt slope change in the lower temperature region seems to coincide with the FWHM change observed in the alkyl side group. We can describe a plausible scenario of the transition; the alkyl chain begins to undergo molecular motion around 200 K, which is the onset of slope change in the FWHM upon heating, and then the thiophene begins to twist around 240 K in response to the side group motion accelerated enough to stimulate the main chain motion. Around 270-310 K, R_1 show almost constant values. This plateau of R_1 is probably related to the critical behavior of C-PC transition. At a temperature greater than 310 K, R_1 increases again with heating. The steep rise of R_1 was observed in the case of the twist glass transition for P3BT as well (*26*). We believe that all thiophene rings undergo twisting, which means that they are in the PC state. However, various factors derived from the same reasons as P3BT prevent an estimation of exact activation energy for the thiophene twist. As mentioned above, R_1 remains almost constant around 270-310 K. Similar phenomenon has been reported for the phase transition of the second kind between a high-temperature normal phase and an incommensurately modulated phase, T_i, particularly named "partial slow motion limit" in some insulating crystals (*52*). Just above the critical temperature, R_1 is temperature independent due to the critical slowing down of order parameter dynamics (*52*). The fact that the temperature independent region is observed just above T_{cp} for P3HT might indicate that the transition might be a second-order phase transition as well. The absence of remarkable latent heat in DSC (*26*) also supports the second-order phase transition. However, the phenomenon that violates the general property of second-order transition has also been observed; i.e., PC can exist even below Tgp (=T_{cp}) as the supercooling liquid (*27*). Further investigations such as the frequency dependence of T_1 NMR measurements are necessary to determine the classification of the phase transition occurring in P3HT.

Comparison between P3BT and P3HT

This section is devoted to the aforementioned third question. The temperature dependent R_1 also provides information about the difference of dominant structures between P3BT and P3HT around T_{gp} or T_{cp}. For P3BT, only the C4 carbon, which is directly connected to a proton, showed larger R_1 than other carbons below the twist glass transition temperature (T < T_{gp}=340K) (*26*), indicating that the relaxation was mainly due to fluctuation of ^{13}C-^{1}H magnetic dipolar coupling. The thiophene ring would not undergo reorientations sufficient to fluctuate the chemical shift anisotropy (CSA). Above the T_{gp}, on the other hand, the other carbons (C2, C3, C5) showed specific slopes individually, where reorientation of the thiophene ring, i.e., twisting, brought about fluctuations in CSA as well. For P3HT, however, all carbons showed similar R_1 in the measured temperature range, suggesting that the relaxation occurred not only by the fluctuation of magnetic dipolar coupling but also by that of chemical shift anisotropy even below T_{cp}. This difference between P3BT and P3HT seems to be consistent with our argument based on the IR results; GC and C, in which thiophene does not undergo twisting motion, are dominant in P3BT, whereas PC is dominant in P3HT below T_{gp} or T_{cp}. This tendency can be explained by the degree of frustration against crystallization due to interchain interaction (*27*). In the case of P3BT, locally favored structures ("cooperative rearrangement region"-like structure) exist with strong frustration. Consequently, GC and C are preferentially realized with respect to a decrease of temperature. For P3HT, in contrast, PC is the dominant structure instead of GC or C because of its weak frustration. The relationship between the molecular mobilities of the side group and main chain supports this hypothesis. The C-PC transition occurred in P3HT when the hexyl group entered the extreme narrowing regime, which is confirmed by a negative slope of R_1 vs T^{-1}. In other words, π-π stacking is easily weakened by the rapid side group's motion. On the other hand, P3BT kept GC and C states even though the butyl group was in the extremely narrowing regime.

In NMR Spectroscopy of Polymers: Innovative Strategies for Complex Macromolecules; Cheng, H., et al.;
ACS Symposium Series; American Chemical Society: Washington, DC, 2011.

The stronger intermolecular interaction in P3BT yields a more rigid crystal as well as a large amount of GC. The temperature dependence of optical absorption measurements for P3HT support these argument (*28*).

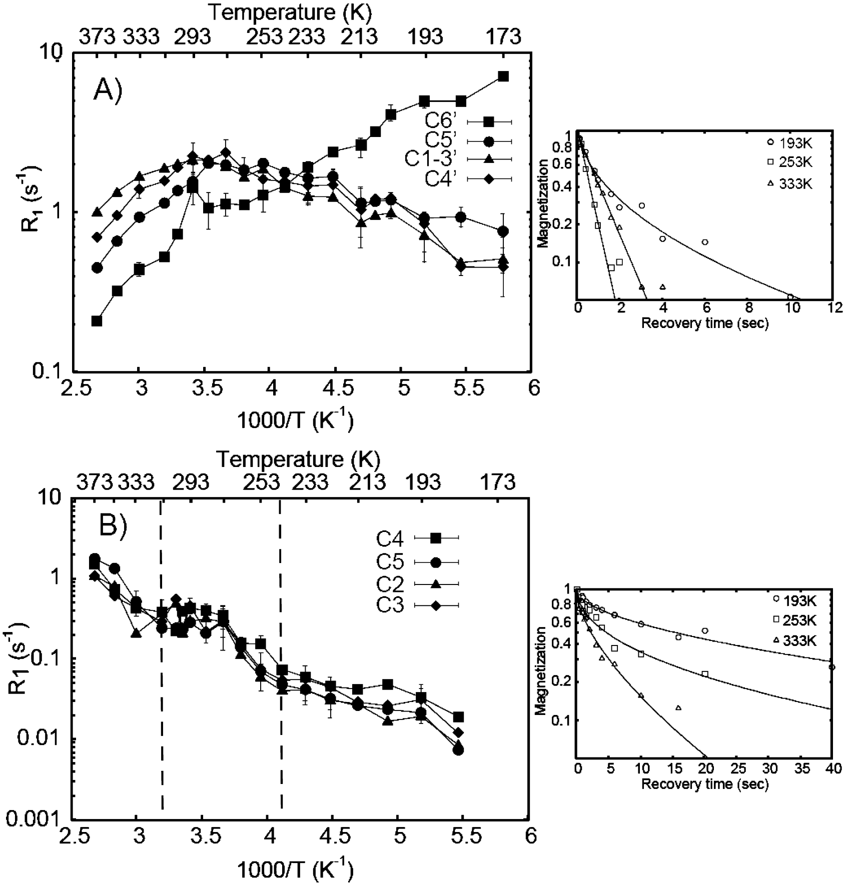

Figure 7. Temperature dependence of ^{13}C spin-lattice relaxation time at 125.8 MHz for alkyl side group carbons (A) and for thiophene ring carbons (B). Insets are typical decay curves measured using Torchia's method.

Conclusion

In this article, we summarized our recent results concerning the phase diagram for P3ATs. There are various thermodynamic and non-equilibrium states including crystalline, glassy crystalline, plastic crystalline, liquid glass, and isotropic liquid. Figure 8 illustrates the phase diagrams for P3BT and P3HT including the thermodynamical phases and non-equilibrium states. This complex situation is due to frustration against crystallization in P3ATs. The strength of the frustration depends on the length of alkyl side-groups. For example, RR-P3BT is GC rich, while RR-P3HT is PC rich for a wide temperature range.

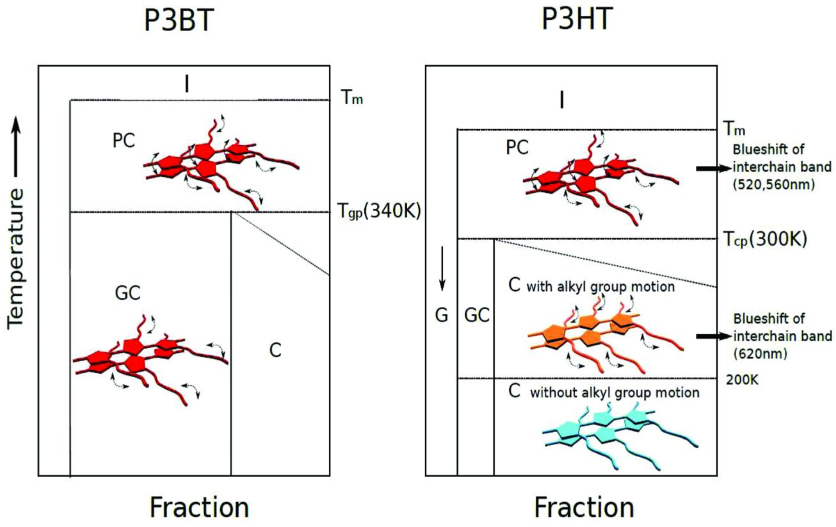
P3BT
P3HT
Temperature
I
Tm
PC
Tgp(340K)
GC
C
Fraction
I
Tm
PC
Blueshift of interchain band (520,560nm)
Tcp(300K)
G
GC
C with alkyl group motion
Blueshift of interchain band (620nm)
200K
C without alkyl group motion
Fraction

Figure 8. Proposed phase diagram for P3BT and P3HT. The horizontal axis stands for the fraction of thermodynamical phasesand non-equilibrium states estimated by the FTIR measurements and the fractions are presumably connected to the degree of frustration against crystallization of P3AT.

Acknowledgments

One of the authors (N.A.) is supported by the Ministry of Education, Culture, Sports, Science and Technology (Japan) through a Grant-in-Aid for science research (21350125).

References

1. Levin, J. E.; Miller, J. P. *Nature (London)* **1996**, *380*, 165–168.
2. Douglas, J. K.; Wilkens, L.; Pantazelou, E.; Moss, F. *Nature (London)* **1993**, *365*, 337–340.
3. Russell, D. F.; Wilkens, L. A.; Moss, F. *Nature (London)* **1999**, *402*, 291–294.
4. Gluckman, B. J.; Netoff, T. I.; Neel, E. J.; Ditto, W. L.; Spano, M. L.; Schiff, S. J. *Phys. Rev. Lett.* **1996**, *77*, 4098–4101.
5. T. Mori, T.; S. Kai, S. *Phys. Rev. Lett.* **2002**, *88*, 218101-1–218101-4.
6. K. Kitajo, K.; Nozaki, D.; Ward, L. M.; Yamamoto, Y. *Phys. Rev. Lett.* **2003**, *90*, 218103-1–218103-4.
7. Merkle, R. C. *Foresight Update* 1989, August, 6.
8. Berzukov, S. M.; Vodyanoy, I. *Nature* **1995**, *378*, 362–364.
9. Ueda, M.; Ueda, M.; Takagi, H.; Sato, M. J.; Yanagida, T.; Yamashita, I.; Setsune, K. *Physica A* **2008**, *387*, 4475–4481.
10. Gluckman, B. J.; Netoff, T. I.; Neel, E. J.; Ditto, W. L.; Spano, M. L.; Schiff, S. J. *Phys. Rev. Lett.* **1996**, *77*, 4098–4101.
11. Hidaka, I.; Nozaki, D.; Yamamoto, Y. *Phys. Rev. Lett.* **2000**, *85*, 3740–3743.

12. Priplata, A.; Niemi, J.; Salen, M.; Harry, J.; Lipsitz, L. A.; Collins, J. J. *Phys. Rev. Lett.* **2002**, *89*, 238101-1–238101-4.
13. Destexhe, A.; Contreras, D. *Science* **2006**, *314*, 85–90.
14. Asakawa, N; Hotta, Y.; Kanki, T.; Kawai, T.; Tabata, H. *Phys. Rev. E* **2009**, *79*, 021902-1–021902-8.
15. Wessling, B. In *Handbook of Conducting Polymers, 3rd ed.: Processing and Applications*; Skotheim, T. A.,Reynolds, J. R., Eds.; CRC Press: Boca Raton, FL, 2007; pp 1-3 - 1-75.
16. Tessler, N.; Veres, J.; Globerman, O.; Rappport, N.; Preezant, Y.; Roichman, Y.; Solomesch, O.; Tal, S.; Gershman, E.; Adler, M.; Zolotarev, V.; Gorelik, V.; Eichen, Y. In *Handbook of Conducting Polymers, 3rd ed.: Processing and Applications*; Skotheim, T. A., Reynolds, J. R., Eds.; CRC Press: Boca Raton, FL, 2007; pp 7-1 – 7-42.
17. Mozer, A. J.; Sariciftci, N. S. In *Handbook of Conducting Polymers, 3rd ed.: Processing and Applications*; Skotheim, T. A., Reynolds, J. R., Eds.; CRC Press: Boca Raton, FL, 2007; pp 10-1 – 10-37.
18. Łużny, W.; Proń, A. *Synth. Metals* **1996**, *79*, 37–41.
19. Bolognesi, A.; Porzio, W.; Provasoli, F. *Makromol. Chem.* **1993**, *194*, 817–827.
20. Bolognesi, A.; Botta, C.; Mercogliano, C.; Marinelli, M.; Porzio, W.; Angiolini, L.; Salatelli, E. *Polym. Adv. Tech.* **2003**, *14*, 537–543.
21. Yu, Z. G.; Smith, D. L.; Saxena, A.; Martin, R. L.; Bishop, A. R. *Phys. Rev. Lett.* **2000**, *84*, 721–724.
22. Troisi, A.; Orlandi, G. *Phys. Rev. Lett.* **2006**, *96*, 086601-1–086601-4.
23. Gerstner, W.; van Hemmen, J. L. *Phys. Rev. Lett.* **1993**, *71*, 312–315.
24. Hotta, Y.; Kanki, T.; Asakawa, N.; Tabata, H.; Kawai, T. *Appl. Phys. Exp.* **2008**, *1*, 088002-1–088002-3.
25. Kanamaru, T.; Sekine, M. *Phys. Rev. E* **2003**, *67*, 031916-1–031916-8.
26. Yazawa, K.; Inoue, Y.; Yamamoto, T.; Asakawa, N. *Phys. Rev. B* **2006**, *74*, 094204-0–094204-12.
27. Yazawa, K.; Inoue, Y.; Yamamoto, T.; Asakawa, N. *J. Phys. Chem. B* **2008**, *112*, 11580–11585.
28. Yazawa, K.; Inoue, Y.; Shimizu, T.; Tansho, M.; Asakawa, N. *J. Phys. Chem. B* **2010**, *114*, 1241–1248.
29. Shintani, H.; Tanaka, H. *Nat. Phys.* **2006**, *2*, 200–206.
30. Babel, A.; Jenekhe, S. A. *Synth. Metals* **2005**, *148*, 169–173.
31. Causin, V.; Marega, C.; Marigo, A.; Valentini, L.; Kenny, J. M. *Macromolecules* **2005**, *38*, 409–415.
32. Barbarella, G; Casarini, D.; Zambianchi, M.; Favaretto, L.; Rossini, S. *Adv. Mater.* **1996**, *8*, 69–73.
33. Bolognesi, A.; Porzio, W.; Provasoli, A.; Botta, C.; Comotti, A.; Sozzani, P.; Simonutti, R. *Macromol. Chem. Phys.* **2001**, *202*, 2586–2591.
34. Torchia, D. A. *J. Magn. Reson.* **1978**, *30*, 613–616.
35. Bloembergen, N.; Purcell, E. M.; Pound, R. V. *Phys. Rev.* **1948**, *73*, 679–712.
36. Ngai, K. L. *Solid State Ionics* **1981**, *5*, 27–33.
37. Schnauss, W.; Fujara, F.; Hartmann, K.; Sillescu, H. *Chem. Phys. Lett.* **1990**, *166*, 381–384.

38. Böhmer, R.; Diezemann, G.; Hinze, G.; Rössler, E. *Prog. Nucl. Magn. Reson. Spectrosc.* **2001**, *39*, 191–267.
39. Rössler, E.; Warschewske, U.; Eiermann, P.; Sokolov, A. P.; Quitmann, D. *J. Non-Cryst. Solids* **1994**, *172-174*, 113–125.
40. Döß, A.; Hinze, G.; Diezemann, G.; Böhmer, R. *Acta Polym.* **1998**, *49*, 56–58.
41. Johari, G. P.; Goldstein, M. *J. Chem. Phys.* **1970**, *53*, 2372–2388.
42. Guha, S.; Graupner, W.; Resel, R.; Chandrasekhar, M.; Chandrasekhar, H. R.; Glaser, R.; Leising, G. *Phys. Rev. Lett.* **1999**, *82*, 3625–3628.
43. Kohda, K.; Nakamura, N.; Chihira, H. *J. Phys. Soc. Jpn.* **1982**, *51*, 3936–3941.
44. Liu, S.-B.; Conradi, M. S. *Phys. Rev. Lett.* **1985**, *54*, 1287–1290.
45. Hinze, G.; Sillescu, H. *J. Chem. Phys.* **1996**, *104*, 314–319.
46. Böhmer, R.; Hinze, G.; Jörg, T.; Qi, F.; Sillescu, H. *J. Phys.: Condens. Matter* **2000**, *12*, A383–A390.
47. Ferrari, M.; Mucci, A.; Schenetti, L.; Malmusi, L. *Magn. Reson. Chem.* **1995**, *33*, 657–663.
48. Prosa, T. J.; Winokur, M. J.; McCullough, R. D. *Macromolecules* **1996**, *29*, 3654–3657.
49. Meille, S. V.; Winokur, M. J.; McCullough, R. D. *Macromolecules* **1997**, *30*, 7898–7905.
50. Pankaj, S.; Hempel, M.; Beiner, M. *Macromolecules* **2009**, *42*, 716–724.
51. Obzrut, J.; Page, K. A. *Phys. Rev. B* **2009**, *80*, 195211-1–195211-7.
52. Decker, F.; Petersson, J.; Irsch, M.; Michel, D. *Phys. Rev. B* **2001**, *65*, 014110-1–014110-11.

Downloaded by UNIV OF GUELPH LIBRARY on June 21, 2012 | http://pubs.acs.org
Publication Date (Web): October 14, 2011 | doi: 10.1021/bk-2011-1077.ch011

Chapter 11

Molecular Mobility and Phase Composition in Polyolefins: From Fundamental to Applied Research

V. M. Litvinov[*]

DSM Resolve, P.O. Box 18, 6160 MD Geleen, The Netherlands
[*]E-mail: Victor.Litvinov@DSM.com

Molecular mobility, phase composition and morphology of polyethylenes (PE), polypropylenes (PP) and random poly(ethylene-co-propylene) (PPR) were studied by solid-state low-field ^{1}H NMR, X-ray, DSC and microscopy methods. Influence of the following factors on the phase composition and molecular mobility is discussed: (1) the effect of the amount and the type of comonomers in PE and PP chains, (2) thermal aging, and (3) deformation. Small changes in the chemical composition, thermal history and mechanical load can significantly influence molecular mobility in the amorphous phase. A series of studies by the author shows that solid-state NMR provides a unique and complementary tool to traditional methods in obtaining information about physical structures and local dynamics in polyolefins. This information is useful to achieve a better understanding of deformation behavior of this class of polymers.

Introduction

The physical and mechanical properties of semi-crystalline polymers are significantly influenced by morphology, phase composition and molecular mobility in different phases. Therefore, a quantitative characterization of these meso-/nano-scopic characteristics of semi-crystalline polymers is of great importance to advance our understanding of their properties. In this respect, the phase composition is probably one of the most important morphological parameters, mainly because the amorphous and crystalline phases exhibit vastly

In NMR Spectroscopy of Polymers: Innovative Strategies for Complex Macromolecules; Cheng, H., et al.;
ACS Symposium Series; American Chemical Society: Washington, DC, 2011.

different behavior and their relative contributions to the material properties should be accurately known. Numerous ^{1}H, ^{2}H and ^{13}C solid-state NMR studies of polyolefins have provided detailed information on phase structure and morphology, especially with respect to crystalline polymorphs, phase composition, chain conformation, and molecular motions. In this paper, a series of studies of polyolefins using low-field ^{1}H NMR is reviewed. Several examples of methods and applications are provided, which help improve our understanding of the physical structures of polyolefins and the role of the physical structures in the different applications.

Downloaded by UNIV OF GUELPH LIBRARY on June 21, 2012 | http://pubs.acs.org
Publication Date (Web): October 14, 2011 | doi: 10.1021/bk-2011-1077.ch011

Results and Discussion

Methods for Crystallinity Determination

The most common methods for crystallinity determination are X-ray diffraction, density measurement, and differential scanning calorimetry. Each of these methods is based on a different physical property and gives rise to a different definition of the crystalline phase. In general, crystallinity determination using different methods does not always yield the same result on even the same sample (*1*) because of the following reasons: (i) The complex morphology of semi-crystalline polymers requires different sets of assumptions for the analysis of the data recorded by different techniques. (ii) The discrimination of the crystalline and amorphous phases is made on the basis of different characteristics, such as the enthalpy of melting (DSC), long range periodicity (WAXD), and the specific volume (density analysis). (iii) The two-phase model, which is traditionally used for determining crystallinity, is rather simplified for the description of semi-crystalline polymers due to the presence of a crystal-amorphous interface or rigid amorphous fraction, which can be detected either as crystalline or amorphous fraction depending on the method used. In other words, the borderline is difficult to draw between crystalline and amorphous phases for different methods.

Several experimental methods, such as neutron scattering, dielectric relaxation, calorimetry, and solid-state NMR, have shown that an intermediate layer separates crystalline and amorphous phases, and the properties of this layer, i.e., crystal-amorphous interface (*1*, *4*, *5*) or rigid amorphous fraction (*6*, *7*), are intermediate between those for crystalline and amorphous phases. A *three-phase model,* in which the interface is taken into account, could provide better description of the experimental data. Therefore, the term “phase composition” is perhaps more appropriate than simply “crystallinity” to emphasize the multi-phase nature of semi-crystalline polymers. The interfacial layer is usually thought to be a transitional region located in between the crystals and the mobile amorphous regions. The interface has distinct chain dynamic and is characterized by a degree of order perpendicular to the lamellae surface but disorder in the lateral direction (*8*).

Solid-state NMR is one of the most informative techniques for the characterization of molecular mobility and molecular scale heterogeneity in materials. Over the years, different solid-state NMR methods with relatively basic or sophisticated features were used for the investigation of morphology and molecular mobility in polyolefins. ^{13}C NMR spectroscopic methods provide detailed information about molecular mobility in the different phases of PE because of high phase selectivity, which exploits differences in chemical shifts for crystalline and amorphous phases (*9–12*). However, quantitative studies of phase composition, domain sizes, and molecular mobility in PE by ^{13}C NMR could suffer from a lack of accuracy due to very long ^{13}C T_1 value for PE crystals. For the characterization of a large series of samples, one should choose the most robust, convenient and accurate NMR method. ^{1}H NMR T_2 relaxometry was widely used for this purpose. The high sensitivity of ^{1}H NMR makes this method very attractive for the characterization of crystallization kinetics (*13*), premelting behavior (*14*), and quality control (*15*). Wide-line ^{1}H NMR and relaxation experiments were frequently applied to study the effect of the chemical structure, molar mass and temperature on the phase composition and molecular mobility (*16–20*).

Downloaded by UNIV OF GUELPH LIBRARY on June 21, 2012 | http://pubs.acs.org
Publication Date (Web): October 14, 2011 | doi: 10.1021/bk-2011-1077.ch011

Phase Composition Analysis by NMR T_2 Relaxometry

When the term crystallinity is used in connection with low-resolution NMR technique, this refers to the rigid fraction at temperatures well above T_g, i.e., the fraction of material possessing the lowest molecular mobility; this term is also distinguished from semi-rigid (interfacial) and soft non-crystalline phases (either oriented or non oriented) in a material. Characterization of the three-phase structure is important from a theoretical viewpoint, and it is a key factor in determining the overall crystalline structure, the morphology and (thus) the mechanical properties.

Optimum Analysis Temperature for Phase Composition by NMR T_2 Relaxometry

At room temperature, a significant fraction of the amorphous phase in *i*-PP and HDPE is rigid. With increasing temperature, molecular mobility begins to increase in the inner/softer part of the amorphous phase towards the lamellae surface resulting in decrease in the amount of the rigid fraction, which is composed of the crystalline phase and the rigid fraction of the amorphous phase (Figure 1). To observe distinct differences in molecular mobility of the crystalline and amorphous phases, and consequently in the T_2 relaxation, the temperature of the sample should substantially exceed the dynamic glass transition temperature (T_g^d) at the time scale of the NMR experiment, i.e., in the range of 10^{-4} - 10^{-5} sec. Since the T_2 relaxation experiments should be performed at temperatures well above T_g, the sample exposure to elevated temperatures can cause irreversible changes in the phase composition and in molecular mobility. Therefore, the temperature for the experiments should not be too high to prevent annealing of the sample during the NMR experiment.

The amount of the rigid fraction in HDPE (*21*) and *i*-PP (*22*) is almost constant in the temperature range from ~70°C to 100 °C, and its value is close to the crystallinity measured by DSC and X-ray. In this temperature range, the difference in molecular mobility in rigid, semi-rigid and soft fractions is high enough for (i) accurate deconvolution of the decay of the transverse magnetization relaxation (T_2 decay) into the relaxation components originating from different phases, and (ii) annealing can be avoided during NMR experiments at these temperatures. Therefore, this temperature range is optimal for phase composition analysis in HDPE and *i*-PP.

Analysis of the Decay of the Transverse Magnetization Relaxation

Precautions should be taken for accurate measurements of the T_2 relaxation function of materials which are composed of rigid and soft phases, like semi-crystalline polymers above T_g of the amorphous phase (*23–26*). The T_2 decay – the time dependence of the M_{xy} component of the macroscopic magnetization vector - is a weighted sum of T_2 decays from phases with distinct difference in molecular mobility. The relative fraction of the T_2 relaxation components is proportional to the content of hydrogen in these phases. The T_2 relaxation time of these relaxation components allows the determination of relative difference in molecular mobility in different phases and in a series of samples of the same chemical origin. The longer the T_2 relaxation time, the larger the frequency (and/or the amplitude) of molecular motions is.

Downloaded by UNIV OF GUELPH LIBRARY on June 21, 2012 | http://pubs.acs.org
Publication Date (Web): October 14, 2011 | doi: 10.1021/bk-2011-1077.ch011

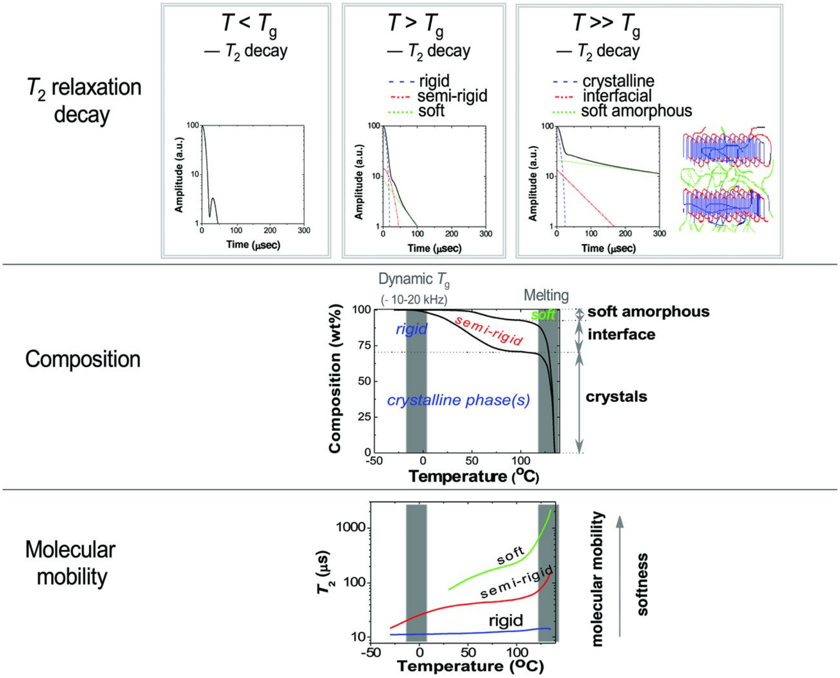

Figure 1. Schematic drawing of the effect of temperature on the amount of rigid, semi-rigid ands soft fractions of melt-crystallized PE, and molecular mobility in these fractions as determined by the analysis of T_2 decay.

Downloaded by UNIV OF GUELPH LIBRARY on June 21, 2012 | http://pubs.acs.org
Publication Date (Web): October 14, 2011 | doi: 10.1021/bk-2011-1077.ch011

Analysis of the phase composition in complex polymeric materials using T_2 relaxation data is usually complicated due to several reasons: (a) *multiphase/component composition*; (b) *morphological heterogeneities* of materials, such as distribution of domain sizes resulting in a distribution of frequency of molecular motions; (c) *spatial heterogeneity of materials on the micrometer scale*, which is formed during processing, i.e., heterogeneous distribution of components, differences in morphology through the sample volume because of variation in temperature gradient and flow induced orientation in different parts of a sample, for example in skin layer versus core part; (d) *molecular-scale and morphological heterogeneity,* which is caused by the chemical heterogeneity, such as molar mass distribution and a variation in the chain composition, chain sequences and tacticity along a single chain; (e) *complexity of molecular motions* causing a complex shape of the decay of the transverse magnetization relaxation. Because of these reasons, a thorough study of the T_2 relaxation as a function of temperature both for a polymeric material and for the separate components that were used for its preparation, is desired for reliable data analysis.

The theoretical description of the T_2 decay shape for semicrystalline polymers above the T_g^d is still under debate and a purely phenomenological analysis of the decay shape with two- or more components is commonly used. Different functions were used for describing the T_2 decay for semicrystalline polyolefins (*20*, *26–31*). The shape of the relaxation component for the crystalline phase was described either by an Abragamian or a Gaussian function. A Gaussian, Weibull or an exponential function was used to describe the T_2 relaxation of the crystal-amorphous interface. The relaxation of the soft amorphous fraction was described either with a single exponential or a sum of two exponential functions. It should be noted that the phase composition, as characterized by the NMR method, is affected to some extent by the temperature of the experiment (*25*), and by a fitting function used for the deconvolution of the T_2 decay into the separate components (*13*, *20*, *30*, *32*). Nevertheless, the amount of rigid phase, which is determined from the T_2 relaxation analysis, corresponds rather well with crystallinity values obtained by other methods.

Temperature Dependence of Phase Composition and Molecular Mobility in Polyolefins

1. HDPE, Ethylene-Octene Copolymer (m-PE) and i-PP

The three-phase model provides the most appropriate description of the phase composition in HDPE (*21*) and *i*-PP (*22*) at temperatures of ~70 - 100 °C. Above these temperatures, the phase composition is affected by annealing and partial melting. Crystallinity values, as determined by the NMR method, are in good agreement with those determined for the same samples using SAXS. Crystallinity of *m*-PE is significantly lower than that of HDPE (*33*). Above room temperature, crystallinity of *m*-PE with 30 wt% octane chain units gradually decreases with increasing temperature and approaches zero at 70°C.

2. Random Poly(Ethylene-co- propylene) (PPR)

The phase structure of PPR is more complex than that of *i*-PP due to the presence of small amount of ethylene chain units in the main chain, as well as atactic propylene chain units. Four different phases/fractions with different molecular mobility are determined at 110°C by the T_2 relaxation method (*26*): (i) crystalline phase, (ii) semi-rigid crystal-amorphous interface, (iii) soft fraction of the amorphous phase, and (iv) small amount of the amorphous fraction, which has molecular mobility similar to that of rubbers.

Downloaded by UNIV OF GUELPH LIBRARY on June 21, 2012 | http://pubs.acs.org
Publication Date (Web): October 14, 2011 | doi: 10.1021/bk-2011-1077.ch011

3. Thermoplastic Vulcanizates (TPV) Composed of i-PP, EPDM, and Paraffinic Oil

TPV's are rubbery materials, which are processable as thermoplastics but exhibits properties similar to those of vulcanized rubbers at usage temperatures. TPV's are produced by dynamic vulcanization of blends containing a thermoplast and an elastomer. At 110 °C, the NMR relaxation method allows us to perform a rather accurate determination of the amount of different phases/components of TPV – namely, crystalline and amorphous phases of PP, EPDM and paraffinic oil – and molecular mobility in these phases (*34*). Crystallinity of PP is hardly affected by the TPV's composition and is close to 70 wt %. A small fraction of oil molecules plasticizes the amorphous phase of PP and the plasticization effect is proportional to oil : PP mass ratio in the TPV composition. Results suggest that a thin interfacial layer is formed by propylene-rich chain fragments of EPDM of EPDM/oil rubbery phase and by PP chains of the PP phase. The interface is the source of physical junctions, which are formed at the shell of EPDM rubber particles and at the surface of PP particles occluded in the EPDM phase.

NMR allows quantitative determination of the network density in the rubbery phase of the TPV's (*34*). The network structure is formed by chemical crosslinks, physical junctions at the EPDM/PP interface, temporary and trapped chain entanglements. The total network density in EPDM rubbery phase is affected by the following changes in the TPV composition: (i) the network density increases with increasing amount of the crosslinker per weight unit of EPDM; (ii) decreases with increasing oil content because of chain disentanglements; and (iii) increases with increasing PP/EPDM weight ratio due to an increase in the density of physical junctions at the EPDM/PP interface. The EPDM network density largely influences the translational and rotational mobility of oil molecules; i.e. the higher the crosslink density, the more the mobility of oil molecules is hindered. Some relationships between the TPV composition, network density and mechanical properties are established (*34*).

Domain Size Determination by NMR Spin-Diffusion Experiments

Traditionally, transmission electron micrograph (TEM) and small-angle X-ray scattering (SAXS) are two major techniques used to determine the lamellar thickness. The former offers the advantage of direct access to the morphology. SAXS is a well-developed method to quantitatively determine the thicknesses of alternating layers of the crystalline and amorphous regions of the lamellae morphology. The NMR experiments permit unambiguous identification of the three-phase morphology due to a large difference in the relaxation behavior of the chain units in mobile amorphous fraction, semi-rigid crystal-amorphous interface and crystalline phase (*21*, *22*). The domain thickness in HDPE and *i*-PP, which is determined by NMR in the temperature range from ~70 to 100°C, is in good agreement to those measured by SAXS and TEM on the same sample. The thickness of the interface is nearly constant in the studied temperature range and equals 1.1 – 1.3 nm. This value is in the same range as previously estimated for PE value by Monte Carlo simulations (*35*). It should be noted that the interface thickness is close to the length of the statistical segment of PE and *i*-PP chains, which consists of 6 – 7 carbon–carbon bonds and equals to ~0.8 nm for fully extended polyolefinic chain. Therefore, distinct differences in molecular mobility in different fractions of HDPE are apparently caused by short-range correlations of chain motion due to the short length of the statistical segment.

The Effect of Annealing on Phase Composition, Molecular Mobility, and Domain Sizes

Annealing at Temperatures Close to Melting Temperature Range

Chain rearrangements upon prolonged annealing of HDPE and *i*-PP at elevated temperatures result in an increase in the lamellar thickness at the expense of the interfacial layer and the soft amorphous phase (*21*, *22*). Annealing also causes a decrease in molecular mobility in the crystalline phase due to perfecting of the crystalline order. Lamellae thickening and a slight increase in the crystallinity would cause additional slippage of chain entanglements towards the inner part of inter-lamellar amorphous regions causing additional immobilization of the soft fraction of the amorphous phase. The following mechanism of morphological changes during annealing at elevated temperatures is suggested. Upon approaching the melting temperature, molecular mobility increases both in the amorphous phase, the crystal-amorphous interface, and in the crystalline phase. An increase in molecular mobility is accompanied by partial melting of small crystals and less ordered fragments of lamellae. An increased mobility in the amorphous phase and chain diffusion in and out of the crystals (α_c-relaxation) facilitates structural reorganizations, which occur in the amorphous layer adjacent to the lamella surface, causing a continuous shift of the interface towards the inner part of the amorphous regions and thus reducing the thickness of the amorphous layer and increasing the lamellae thickness. The thickness of rigid (crystalline) domains increases linearly as a function of the logarithm of the annealing time,

Downloaded by UNIV OF GUELPH LIBRARY on June 21, 2012 | http://pubs.acs.org
Publication Date (Web): October 14, 2011 | doi: 10.1021/bk-2011-1077.ch011

which is in good agreement with theoretical predictions and experimental results for other polymers (*36*, *37*).

Aging of i-PP at Temperatures Slightly Exceeding T_g

A significant change in impact strength, flexural modulus and dimensions of injection molded part, which are made from *i*-PP, occurs upon prolonged aging at ambient temperature (*38*). The exact origin of these changes is not well understood. NMR T_2 relaxation experiments has helped in understanding this phenomenon (*38*). Molecular mobility of the rigid fractions, which at 28°C is composed of crystalline phase and rigid amorphous fraction, is hardly affected by aging for 1000 hours. The amount of the rigid fraction increases by ~1–2 wt%. Aging causes a significant decrease in molecular mobility in the soft amorphous fraction. This decrease can be caused by two different phenomena: (i) the formation of small crystals in inter-spherolitic amorphous domains during the secondary crystallization, and (ii) an increase in the density of the amorphous phase due to relaxation of residual stresses. The results obtained suggest that aging-induced changes in the macroscopic properties of injection molded articles largely originate from a decrease in molecular mobility in the amorphous phase.

Long Term Aging at Elevated Temperatures and Hydrostatic Pressure

One of the important applications of random propylene copolymers (PPR) is the production of hot water pipes. The pipes can be used under hydrostatic pressure and at elevated temperatures up to 70°C continuously for 50 years and for a short time at 80°C. Breakage of pipes can occur if aging time at a certain temperature exceeds that of the specification. It has been shown that ^{1}H NMR T_2 relaxation analysis is the most sensitive tool for determining changes in PPR samples that are caused by storage of PPR pipes at these conditions (*26*). The long term aging causes the following changes in the phase composition and molecular mobility. The crystallinity increases by ≤5% with increasing storage temperature. The amount of semi-rigid and soft amorphous fractions slightly decreases upon storage at the expense of the highly mobile chain fragments in the amorphous phase, which have a higher concentration of ethylene comonomer units than chain fragments in the soft amorphous fraction.

The following processes, which occur in PPR due to exposure to hydrostatic pressure at elevated temperatures, are suggested (*26*). (i) Creep upon hydrostatic pressure causing chain elongation in the amorphous phase. (ii) The increase in crystallinity, which can occur due to the attachment of chain fragments in the amorphous phase to existing crystals and/or due to the formation of new crystals. In both cases, mobility in the amorphous phase decreases due to a decrease in the chain length between adjacent crystals, i.e., the length of tie molecules. (iii) A better phase separation of ethylene-rich chain fragments from the PP matrix. The better phase separation results in an additional decrease in molecular mobility in the PPR matrix, since more mobile chain fragments with ethylene chain units,

Downloaded by UNIV OF GUELPH LIBRARY on June 21, 2012 | http://pubs.acs.org
Publication Date (Web): October 14, 2011 | doi: 10.1021/bk-2011-1077.ch011

if they are mixed on the molecular scale with PP chain fragments, cause some increase in molecular mobility of the PP matrix due to intermolecular coupling of chain motions. All these changes cause embrittlement of pipes followed by their breakage. It was shown that the combination of DSC and NMR relaxometry is a powerful tool for the investigation of the molecular origin of damages in broken PPR pipes and fittings, and for estimating their usage temperature and time.

The Effect of Deformation on Phase Composition, Molecular Mobility, and Domain Sizes

Ethylene Copolymers

Downloaded by UNIV OF GUELPH LIBRARY on June 21, 2012 | http://pubs.acs.org
Publication Date (Web): October 14, 2011 | doi: 10.1021/bk-2011-1077.ch011

Changes in phase composition and molecular mobility were studied for vulcanized semi-crystalline ethylene-octene copolymer (*m*-PE) and amorphous EPDM rubber using a specially designed device, which made it possible to perform NMR experiments under fixed uniaxial compression and to record applied force (*33*). These two samples differ as regards network structure, i.e., EPDM has a larger density of chemical crosslinks, whereas the total network density in *m*-PE is significantly larger because small crystallites act as physical network junctions. These differences in the network structure largely influence the elastic properties. Despite the larger total network density in *m*-PE, strain-induced orientation of EPDM chains in compressed sample is significantly greater, suggesting that the density of chemical crosslinks largely determines the elastic behavior. Crystallinity of *m*-PE does not increase upon compression. It appears that compression causes rearrangements of crystallites due to chain detachment from the crystal surface and its attachment to neighboring crystals. It can be concluded that physical network junctions, which originate from chains anchoring to crystallites, would not be efficient in bearing the force, and the applied force is mainly carried by chemical crosslinks and trapped chain entanglements. Thus, an increase in the density of chemical crosslinks is required for improvement the elastic recovery (the compression set) of *m*-PE. It has been demonstrated that ^{1}H NMR T^2 relaxation experiments under uniaxial compression can provide useful information to help in a better understanding the viscoelastic behavior of heterogeneous elastomeric materials, such as semi-crystalline polymers, filled elastomers, thermoplastic elastomers and thermoplastic vulcanizates.

Isotactic Polypropylene

Changes in phase composition, molecular mobility and domain thickness in uniaxially stretched *i*-PP have been investigated as a function of temperature, draw ratio (λ), drawing temperature and drawing rate (*39*). The NMR experiments have been performed on samples after strain recovery. For the drawing temperature range between 25 and 110°C, typical ductile deformation behavior with a yield point, neck formation and propagation, and strain hardening have been found.

Downloaded by UNIV OF GUELPH LIBRARY on June 21, 2012 | http://pubs.acs.org
Publication Date (Web): October 14, 2011 | doi: 10.1021/bk-2011-1077.ch011

The Effect of Drawing Rate

Deformation-induced changes in the phase composition and molecular mobility are hardly affected by changes in drawing speed which is varied from 1 to 100 mm/min. This suggests that chain rearrangements, which lead to changes in morphology and physical structures upon drawing, are fast as compared to the total time scale of deformation used, or the effect of drawing speed diminishes during strain recovery.

The Effect of Drawing Ratio

Drawing to $\lambda = 7$, which corresponds to beginning of the strain hardening, causes a small increase in the amount of the rigid fraction, which indicates the presence of highly strained tie molecules in the amorphous phase. Upon increase in λ from 10 to 16, a further increase in the amount of the rigid fraction is observed. This increase can be attributed to strain-induced crystallization and/or large immobilization of chains in the amorphous phase. At $\lambda = 7$, molecular mobility in the semi-rigid and soft fractions is already largely decreased, and it continues to decrease up to the highest draw ratio.

The Effect of Drawing Temperature

Drawing temperature has a large effect on the strain-induced transformation of the spherulitic morphology of *i*-PP to fibrillar morphology. The amount of the rigid fraction increases with increasing drawing temperature for all draw ratios. Molecular mobility in crystalline and amorphous phases is lower at higher deformation temperatures. Relative differences in imperfections in the crystalline structure can be identified by comparing T_2 relaxation time for the rigid fraction - T_2^r. At the same λ, T_2^r is longer at lower deformation temperatures. This indicates larger imperfections in the crystalline phase of *i*-PP, which is stretched at 25°C, as compared to the undeformed sample. At drawing temperature of 25°C, the long period and the thickness of the rigid domains slightly decrease at the expense of the thickness of the semi-rigid and soft domains, which suggests defragmentation and disordering of crystals. At higher drawing temperatures, an increase in the long period and lamellae thickness is observed upon increasing the draw ratio and drawing temperature, whereas the thickness of amorphous layer, which separate adjacent crystals, slightly decreases. As far as molecular mobility is concerned, it decreases with increasing draw ratio both in the rigid and soft phases. The decrease is more pronounced at higher deformation temperatures, which points out a more perfect structure organization due to partial melting followed by recrystallization at higher deformation temperatures. The observed changes in the phase composition and molecular mobility suggest that faster rate of chain motions in the crystalline phase (α_c-relaxation) facilitates transformation of the spherulitic morphology to a fibrillar one. Moreover, partial melting followed by strain-induced crystallization can possibly occur at higher temperatures.

Downloaded by UNIV OF GUELPH LIBRARY on June 21, 2012 | http://pubs.acs.org
Publication Date (Web): October 14, 2011 | doi: 10.1021/bk-2011-1077.ch011

Conclusions

A series of studies of polyolefins shows that solid-state low-field ^{1}H NMR provides a powerful and complementary tool to traditional methods to obtain information about physical structures, the phase composition, molecular mobility in different phases. Even small changes in the chemical composition, thermal history and a mechanical load can significantly influence molecular mobility in the amorphous phase. This information is useful to achieve a better understanding of yield and deformation behavior of polyolefins. If more detailed information about physical phases and their chemical origin is required, high-field ^{13}C NMR spectroscopy should be used .

Acknowledgments

The studies of the author were sponsored by DSM and SABIC-Europe. The author thanks D. Demco, C. Hedesiu, K. Remerie, M. Soliman, G. Vanden Poel, R. Kleppinger, R. Deblieck, W. Gijsbers, B. Blümich and V. Mathot for collaboration on topics presented in this paper.

References

1. Isasi, J. R.; Mandelkern, L.; Galante, M. J.; Alamo, R. G. *J. Polym. Sci., Polym. Phys.* **1999**, *37*, 323.
2. Baker, A. M. E.; Windle, A. H. *Polymer* **2001**, *42*, 667.
3. Hiss, R.; Hobeika, S.; Lynn, C.; Strobl, G. *Macromolecules* **1999**, *32*, 4390.
4. Iwata, K. *Polymer* **2002**, *43*, 6609.
5. Sajkiewicz, P.; Hashimoto, T.; Saijo, K.; Gradys, A. *Polymer* **2005**, *46*, 513.
6. Schick, C.; Wurm, A.; Mohammed, A. *Thermochim. Acta* **2003**, *396*, 119.
7. Androsch, R.; Wunderlich, B. *Polymer* **2005**, *46*, 12556.
8. Gautman, S.; Balijepalli, S.; Rutledge, G. C. *Macromolecules* **2000**, *33*, 9136.
9. Schmidt-Rohr, K.; Spiess, H. W. *Macromolecules* **1991**, *24*, 5288.
10. Hillebrand, L.; Schmidt, A.; Bolz, A.; Hess, M.; Veeman, W.; Meier, R. J.; Van der Velden, G. *Macromolecules* **1998**, *31*, 5010.
11. Kuwabara, K.; Kaji, H.; Tsuji, M.; Horii, F. *Macromolecules* **2000**, *33*, 7093.
12. Litvinov, V. M.; Mathot, V. B. F. *Solid State Nucl. Magn. Reson.* **2002**, *22*, 218.
13. Kristiansen, P. E.; Hansen, E. W.; Pedersen, B. *J. Phys. Chem. B* **1999**, *103*, 3552.
14. Kristiansen, P. E.; Hansen, E. W.; Pedersen, B. *Polymer* **2000**, *41*, 311.
15. Tanzer, C. I.; Roy, A. K. *Proc. SPE ANTEC '95: Boston, MA, USA* **1995**, *2*, 2700.
16. Bergmann, K. *J. Polym. Sci., Polym. Phys.* **1978**, *16*, 1611.
17. Fedotov, V. D.; Abdrashitiva, N. A. *Polym. Sci. USSR* **1985**, *27*, 287.
18. Kakudate, T.; Kakizaki, M.; Hideshima, T. *J. Polym. Sci.: Polym. Phys.* **1985**, *23*, 787.
19. Eckman, R. R.; Henrichs, P. M.; Peacock, A. J. *Macromolecules* **1997**, *30*, 2474.

20. Hansen, E. W.; Kristiansen, P. E.; Pedersen, B. *J. Phys. Chem. B* **1998**, *102*, 5444.
21. Hedesiu, C.; Kleppinger, R.; Demco, D. E.; Buda, A.; Blümich, B.; Remerie, K.; Litvinov, V. M. *Polymer* **2007**, *48*, 763.
22. Hedesiu, C.; Demco, D. E.; Kleppinger, R.; Vanden Poel, G.; Gijsbers, W.; Blümich, B.; Remerie, K.; Litvinov, V. M. *Macromolecules* **2007**, *40*, 3977.
23. Zhang, L.; Hansen, E. W.; Helland, I.; Hinrichsen, E.; Larsen, A.; Roots, J. *Macromolecules* **2009**, *42*, 5189.
24. Mauri, M.; Thomann, Y.; Schneider, H.; Saalwächter, K. *Solid State Nucl. Magn. Reson.* **2008**, *34*, 125.
25. Litvinov, V. M.; Penning, J. P. *Macromol. Chem. Phys.* **2004**, *205*, 1721.
26. Litvinov, V. M.; Soliman, M. *Polymer* **2005**, *46*, 3077.
27. Tanaka, H.; Inoue, Y. *Polym. International.* **1993**, *31*, 9.
28. Dadauli, D.; Harris, R. K.; Kenwright, A. M.; Say, B. J.; Sünnetçioĝlu, M. M. *Polymer* **1994**, *35*, 4083.
29. Dujourdy, L.; Bazile, J. P.; Cohen-Addad, J. P. *Polym. Int.* **1999**, *48*, 558.
30. Schreurs, S.; François, J. P.; Adriaensens, P.; Gelan, J. *J. Phys. Chem. B* **1999**, *103*, 1393.
31. Weglarz, W. P.; Peemoeller, H.; Rudin, A. *J. Polym. Sci., Part B: Polym. Phys.* **2000**, *38*, 2487.
32. Kenwright, A. M.; Say, B. J. In *NMR Spectroscopy of Polymers*; Ibbett, R. N., Ed.; Blackie Academic & Professional: London, 1993; p. 231.
33. Litvinov, V. M. *Macromolecules* **2001**, *34*, 8468.
34. Litvinov, V. M. *Macromolecules* **2006**, *39*, 8727.
35. In't Veld, P. J.; Hütter, M.; Rutledge, G. C. *Macromolecules* **2006**, *39*, 439.
36. Peterlin, A. *Polymer* **1967**, *6*, 25.
37. Sanchez, I. C.; Peterlin, A.; Egy, R. K.; McCrackin, F. L. *J. Appl. Phys.* **1974**, *45*, 4216.
38. Hedesiu, C.; Demco, D. E.; Kleppinger, R.; Vanden Poel, G.; Remerie, K.; Litvinov, V. M.; Blümich, B.; Steenbakkers, R. *Macromol. Mater. Eng.* **2008**, *293*, 847.
39. Hedesiu, C.; Demco, D. E.; Remerie, K.; Blümich, B.; Litvinov, V. M. *Macromol. Chem. Phys.* **2008**, *2009*, 734.

Downloaded by UNIV OF GUELPH LIBRARY on June 21, 2012 | http://pubs.acs.org
Publication Date (Web): October 14, 2011 | doi: 10.1021/bk-2011-1077.ch011

Downloaded by UNIV OF DELAWARE MORRIS LIB on June 20, 2012 | http://pubs.acs.org
Publication Date (Web): October 14, 2011 | doi: 10.1021/bk-2011-1077.ch012

Chapter 12

Molecular Dynamics and Structure of the Crystalline Region of Isotactic-Polyolefins Characterized by Solid-State NMR

Toshikazu Miyoshi*

Department of Polymer Science, The University of Akron,
Akron, OH 44325, U.S.A.
***E-mail: miyoshi@uakron.edu**

A review is given of recent solid–state NMR work on structure and molecular dynamics of polyolefins such as isotactic poly(1–butene) (iPB1) and isotactic polypropylene (iPP). In iPB1, melt–crystallization leads to metastable form II, and subsequent solid–solid transition results in stable form I. ^1H–^{13}C wide line separation (WISE) and center bands only detection of exchange (CODEX) NMR techniques provided geometric and time–kinetic parameters of molecular dynamics for overall and side chains in both forms at natural abundance. The ^1H line–shape analysis using a two–spin approximation and ^{13}C T_1 results indicate that form II chains perform uniaxially rotational diffusions accompanying side–chain conformational transitions in the fast motional limit (correlation time < 10^{-7} s). After irreversible solid transition, ^{13}C CODEX results indicate that crystalline stems and side–chain conformations are completely fixed, up to the melting points (correlation time > 10 s). The effects of the unusual molecular dynamics on the mechanical properties are discussed. The second part of this article deals with a re–investigation (by high resolution ^{13}C NMR) of packing structures of the α form of iPP. Two–Pulse Phase–Modulation decoupling during a rather long acquisition time results in significantly narrowed signals corresponding to ordered packing. The enhanced spectral resolution allows us to properly evaluate order–disorder phenomenon in polymer crystals. From CODEX experiments, lamellar thickness and packing order apparently suppress helical jumps in the crystalline regions. These experiments provide valuable information on chain–level structures and dynamics, particularly on the variations in lamellae thickness as a function of supercooling.

Downloaded by UNIV OF DELAWARE MORRIS LIB on June 20, 2012 | http://pubs.acs.org
Publication Date (Web): October 14, 2011 | doi: 10.1021/bk-2011-1077.ch012

Introduction

Understanding relationship between structure and molecular dynamics is one of the particularly important subjects in polymer science. There are continuous interests to understand molecular dynamics in the crystalline (*1*), amorphous (*2*), and interfacial regions as well as in the limited dimensions such as thin films (*3*) and nanopores (*4*). Molecular dynamics in several crystalline polymers has been well characterized by solid–state NMR (*1*). Dynamic geometry and time kinetics of molecular dynamics in the crystalline regions are significantly affected by conformation, packing, and, inter–stem interaction. Schmidt–Rohr and Hu categorized polymer crystals as either mobile or fixed crystals (*1*). The flexible polymer chains such as polyethylene (PE) (*5*), isotactic–poly(propylene) (iPP) (*6*), poly(oxy methylene) (*7*), and poly(ethylene oxide) (*8*), *etc*. are categorized in mobile, which commonly shows helical jump motions that combine the dynamics of well defined discrete jump motions and translations along chain axis. On the other hand, Nylon and poly(ethylene terephtalate) (PET), *etc*. are examples of fixed crystals. English et al (*9*) demonstrated using ^{2}H line shape that Nylon essentially does not perform overall molecular motions in the crystalline region up to melting temperature (T_m).

Polyolefins consists of hydrocarbons and do not have specific functional groups. They are ideal semi–crystalline polymers to further investigate i) the relationship between structure and molecular dynamics, and ii) the roles of molecular dynamics for bulk property and structural organization of polymer crystals.

In this work, a review is conducted of our recent works on detailed dynamic analysis of iPB1 (*10*, *11*) and iPP (*12*) by using center bands only detection of exchange (CODEX) (*13*) and wide line separation (WISE) NMR (*14–16*). On the basis of the experimental data, useful information has been obtained on molecular dynamics, structure, and bulk material properties.

Experimental Section

Samples

iPB1 with an average molecular weight of M_w = 186,000 and a polydispersity of M_w/M_n = 3.3 and isotacticity, (*mmmm*) = 92 % was purchased from Polysciences, Inc. iPP with M_w of 360,000 and M_w/M_n of 3.3 and isotacticity, (*mmmm*) of 97 % was purchased from Polysciences, Inc. The sample was melted and crystallized at a required crystallization temperature, T_c under nitrogen atmosphere. Equilibrium melting temperature, T_m^0, of iPB and iPP were 135 ± 2 and 184 ± 4 °C, respectively.

Measurements

NMR

The solid–state ^{13}C NMR experiments were carried out on a BRUKER AVANCE 300 spectrometer, equipped with 4 and 7 mm VT CPMAS NMR probe. The ^{1}H and ^{13}C carrier frequencies are 300.1 and 75.6 MHz, respectively. The MAS frequency was set to 4000 and 6800 ± 3 Hz. The 90° pulses for ^{1}H and ^{13}C were 4.5−5.0 μs. The recycle delay and cross–polarization (CP) time were 2 s and 1 ms, respectively. High power ^{1}H Two–Pulse Phase–Modulation (TPPM) decoupling with a field strength of 65 kHz was used during acquisition time of 80 ms. For iPP, severe decoupling conditions with a field strength of 110 kHz and acquisition time of 160 ms were used. Phase sensitive ^{1}H–^{13}C 2D WISE NMR spectrum was obtained in TPPI mode. The data matrix had 512 points along the t_2 dimension and 128 points along the t_1 dimension with a dwell time of 2 and 7 μs. A short CP of 50 μs was utilized. Continuous wave (CW) decoupling with a field strength of 55 kHz was applied in t_1 dimension to suppress ^{1}H–^{13}C hetero–nuclear interaction (*15*, *16*). The CODEX experiments utilize the recoupling of chemical shift anisotropy (CSA) interaction by 180° pulses trains in the two evolution periods sandwiching a mixing period, t_{mix} (*13*). The MAS frequency was 4000 ± 3 Hz. The ^{1}H rf field strength for CW decoupling during ^{13}C 180° pulse with pulse length of 15 μs was set to 100 kHz. All other rf parameters were the same as for the CPMAS experiments. The reference and exchange experiments were obtained alternatively by every 128 transients, to suppress drift of the NMR spectrometer. The $T_{1\rho\mathrm{H}}$ filter was incorporated into CODEX pulse program, for suppression of the amorphous signal contribution to CODEX results at ambient temperature and –10 °C. Totally, each spectrum was obtained by accumulating 1024 transients. The total experimental time for mixing–time dependence up to 4 s was approximately 24 hs. The total experimental time of a typical Nt_{r} experiment was about 12 hs.

SAXS

SAXS studies were carried out using a CuKα radiation generated by a Rigaku Ultrax 4153A 172B X–ray diffractometer, and a point–focusing SAXS camera. The camera length used was 740 mm and the images were recorded using an image plate (IP) with an exposure time of 2.5 h. Digitized data were then read from the IP using the image plate reader. Using IP, very small change in SAXS patterns could be obtained with a very short exposure time. The corrected pattern of an empty sample holder was subtracted from each pattern. To calculate he long period and lamellar thickness, a correlation-function method by Rigaku R–axis software was used.

Downloaded by UNIV OF DELAWARE MORRIS LIB on June 20, 2012 | http://pubs.acs.org
Publication Date (Web): October 14, 2011 | doi: 10.1021/bk-2011-1077.ch012

Downloaded by UNIV OF DELAWARE MORRIS LIB on June 20, 2012 | http://pubs.acs.org
Publication Date (Web): October 14, 2011 | doi: 10.1021/bk-2011-1077.ch012

DSC

All the samples were measured with an updated computer interfaced Perkin–Elmer DSC–7. Both temperature and heat–flow levels were corrected by standard materials. Measurements of the melting points were performed at a heating rate of 10 °C /min. To prevent thermal degradation, nitrogen gas was circulated around the sample pan.

Results and Discussion

iPB1

iPB1 is an important industrial material due to outstanding mechanical strengths relative to chemically similar polyolfins such as PE, iPP, and *isotactic*–poly(4–methyl–1–pentene) (iP4M1P) (*17*). iPB1 crystallizes from melt under stationary conditions, kinetically favoring the metastable tetragonal crystal with 11_3 helices (form II) (*18*, *19*). This form II spontaneously transforms into the stable trigonal crystal of 3_1 helices (form I) (*20*) at ambient temperature via solid–solid transition (*21*). This solid transition leads to superior mechanical property without changing lamellae thickness and crystallinity (*17*, *22*). However, origin of the mechanical property is not fully understood.

Figures 1(a) and (b) show the ^{1}H MAS spectra of a form II–rich sample at 100 °C at a MAS frequency of 4 kHz. The spectrum is dominated by the isotropic component with intense SSB patterns. The isotropic signal corresponds to the amorphous component and SSB envelop originates from form II. Very intense SSB patterns reflect fast and anisotropic complex dynamics in polymer backbones (*23*), conformational transitions in the ethyl group (*24*), and methyl rotations (*25*). The ^{13}C relaxation time, T_1 is sensitive to high frequency motions with a minimum value of ~ 0.1 s when τ_c of molecular dynamics approaches to an inverse of ~ 75 MHz. In fact, the main–chain (m–) CH_2, side chain (s–) CH_2, and CH have T_1 values of 0.25, 0.32, and 0.38 s, respectively, at 100 °C. This simple T_1 result suggests the dynamic frequency for the coupled side group and backbone motions is in the order of ~ 10 MHz or higher. Such high frequency dynamics are rare in the solid state and are rather close to the frequency range in the melted state.

^{1}H–^{13}C WISE NMR spectrum was obtained to further investigate functional mobility at a MAS frequency of 6.8 kHz at 100 °C. Figure 1(c) and (d) shows ^{1}H slice data of m–CH_2 and s–CH_2 protons obtained through highly resolved ^{13}C signals. A short CP (CP time = 50 μs) and ^{13}C CW decoupling in t_1 dimension were applied to selectively observe the crystalline signals and to quench spin diffusions between the different functional groups in the crystalline region and suppress heteronuclear dipolar interactions, respectively. The slice data clearly indicate that isotropic components corresponding to the amorphous ones are not polarized to ^{13}C signals.

Downloaded by UNIV OF DELAWARE MORRIS LIB on June 20, 2012 | http://pubs.acs.org
Publication Date (Web): October 14, 2011 | doi: 10.1021/bk-2011-1077.ch012

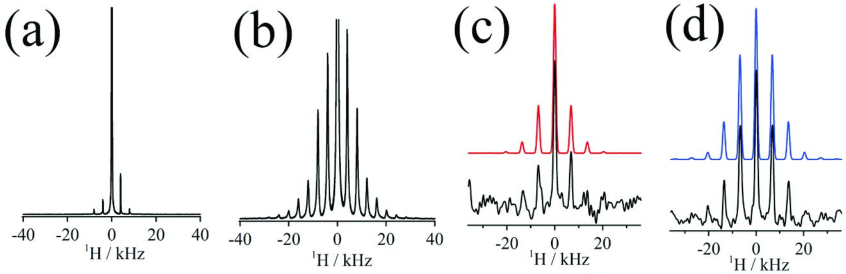

Figure 1. (a) ^{1}H MAS NMR spectrum, (b) amplified vertically by 20 times at a MAS frequency of 4 kHz at 100 °C; and c) ^{1}H slice date of ^{1}H–^{13}C WISE NMR spectra of (c) the main chain (m–CH_2) and (d) side chains CH_2 (s–CH_2) protons through high resolved corresponding ^{13}C signals at a MAS frequency of 6.8 kHz at 100 °C. The (c) red and (d) blue spectra showing best fitted curves to the experimental data with best–fit parameters of (c) $\bar{\delta} / \delta = 0.44 \pm 0.02$ and $\bar{\eta} = 0$ ($D_{II}/2\pi = 9.0 \pm 0.5$ kHz) and (d) $\bar{\delta} / \delta = 0.61 \pm 0.02$ and $\bar{\eta} = 0$ ($D_{II}/2\pi = 12.5 \pm 0.5$ kHz), respectively. (see color insert)

Schnell et al (*26*) simulated third spin effects on the ^{1}H SSB signals at *n* order depending on geometry and distances. They realized that if a third spin significantly interacts with the isolated spin pairs, asymmetric line shapes shall appear, depending on the relative geometry, the mutual distances of three spins, and the MAS frequency. Our experimental data indicate that all SSB signals at *n* order are symmetric and have similar line widths as the center band. Thus, it can be safely assumed that the two spin approximation holds for CH_2 geminal protons. Under two spin approximation, the dipolar patterns were calculated under an assumption of averaged asymmetry parameter, $\bar{\eta} = 0$. The calculated line shapes are well consistent with the experimental data.

Surprisingly, the s–CH_2 geminal protons show much larger dipolar coupling constant, $D_{\text{II}} / 2\pi = 12.5 \pm 0.5$ kHz than 9.0 ± 0.5 kHz for m–CH_2. These results were unexpected for the dynamics of the polymer with a side chain, since side–chain protons are influenced by the complex dynamics of both the main and side chains. Generally, two independent dynamic processes with different dynamic axes result in a smaller dipolar coupling constant in the side group than that in the main chain. In fact, Mirau et al (*16*) detected smaller linewidths for the side group than that in main chain of poly(ethyl methacrylate) (PEMA) at a temperature above T_g. Our experimental results in form II are opposite to those expected in the side–chain polymers in glassy polymers but shall be explained by the assumption of an anisotropic dynamical process.

In the crystalline region, parallel packing of the stems restricts the overall dynamics to uniaxial motions around the stem axes. For several conformational disordered (CONDIS) crystals such as PE in the hexagonal phase (*27*), 1,4–*trans*–polybutadiene in the high temperature phase (*28*), and poly(diethyl siloxane) (PDES) (*29*), it has been reported by SS–NMR that stems commonly show uniaxial diffusions around the stem axes. Under such conditions, $\bar{\eta}$ is 0 and absolute averaged anisotropy parameter, $|\bar{\delta}|$ is described in terms of a following equation:

$$|\bar{\delta}| = \frac{1}{2}\,\delta\,|3\cos^2\phi - 1| \tag{1}$$

where δ is the anisotropy parameter of CH_2 geminal protons under no motion (20.6 kHz), φ is an angle between dipolar vector of the germinal protons and dynamic axis (*24*).

Figure 2 illustrates a part of 11_3 helix of form II and possible dynamic models. The m–CH_2 protons were colored by red. The dipolar vector of germinal protons of m–CH_2 in 11_3 helix is inclined by an angle of 82° with respect to the stem axis. Under uniaxial diffusion in a fast limit, the $|\bar{\delta}|/\delta$ value for m–CH_2 geminal protons is calculated to be 0.47. This value is consistent with the experimentally obtained value of 0.44 ± 0.02. The small reduction in the observed value may be due to small librations around the C–C bonds of main chains and/or slight conformational deviations from an ideal 11_3 helix.

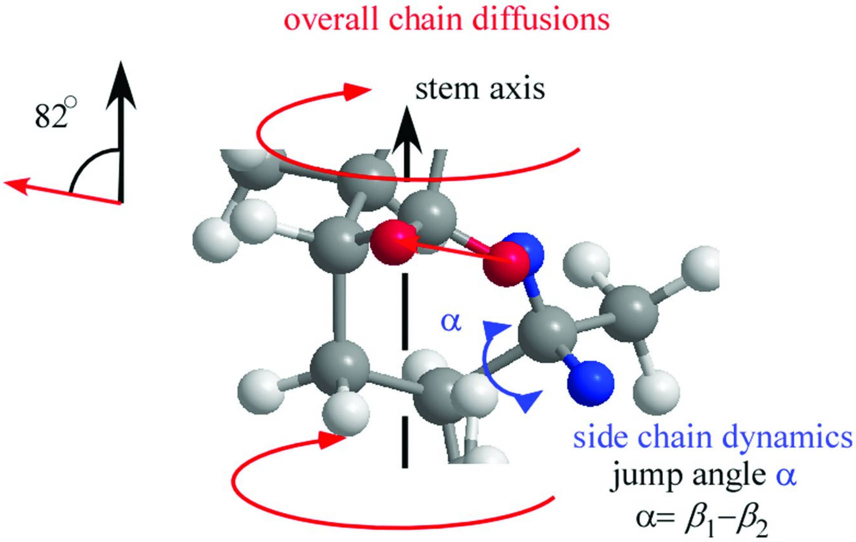

Figure 2. Schematic illustration of dynamic effects of overall chain diffusions and conformational transitions on m– and s–CH_2 dipolar vectors which being colored by red and blue, respectively, of form II of iPB1. The side–chain dynamics being defined by a jump angle α, where α being a difference angle between two interchanging conformations defined by dihedral angles, β_1 and β_2. (see color insert)

Former high resolution ^{13}C NMR (*24*) indicated that ethyl groups in form II adopt two conformations and perform conformational transitions at temperatures above –110 °C. The complex dynamics of side–chain and overall dynamics would contribute to the $|\bar{\delta}|/\delta$ value for the s–CH_2 geminal protons (0.61 ± 0.02) (Figure

Downloaded by UNIV OF DELAWARE MORRIS LIB on June 20, 2012 | http://pubs.acs.org
Publication Date (Web): October 14, 2011 | doi: 10.1021/bk-2011-1077.ch012

Downloaded by UNIV OF DELAWARE MORRIS LIB on June 20, 2012 | http://pubs.acs.org
Publication Date (Web): October 14, 2011 | doi: 10.1021/bk-2011-1077.ch012

2). Two independent dynamic effects on dipolar patterns were numerically calculated as functions of dihedral angle, β and conformational transition angle, α, where α corresponds to a difference between dihedral angles in two interchanging conformations, $|\beta_1 - \beta_2|$, where lower numbers 1 and 2 denote two different conformations. Here, the population ratios of two conformations obtained in former high resolution NMR at –110 °C were used (*24*). The calculated result on $|\bar{\delta}|/\delta$ value is illustrated in Figure 3. The overall dynamic effect of s–CH$_2$ protons in different conformations with a dihedral angle, β, on $|\bar{\delta}|/\delta$ is shown along a horizontal axis. The conformational transition effect with a jump angle, α, on $|\bar{\delta}|/\delta$ is shown as vertical axis, The calculated vales of $|\bar{\delta}|/\delta$ = 0.4, 0.5, and 0.6 are shown as dotted solid black, and red curves, respectively, in Figure 3. It is clearly seen that only β = 88 and 268 ± 10° and their transitions with α = 180 ± 20° or no dynamics (0 ± 20°) satisfy the experimental value. Other conformations and jump angles show much smaller values than the experimental result ($|\bar{\delta}|/\delta$ = 0.61). The obtained structures and dynamics (β = 88 and 268 ± 10°, and α = 0 and 180 ± 20°) also satisfy $\bar{\eta}$ = 0. However, the lack of lateral dynamics does not average out higher spin interactions within the stem. In view of multi–spin interactions, it is concluded that chains in form II of *i*PB1 performs uniaxial diffusions accompanying the conformational transition (α = 180 ± 20°) of the side chain between two conformations at β = 88 and 268 ± 10° in the fast motional limit (*10*). The obtained molecular dynamics clearly indicate that form II is a CONDIS crystal.

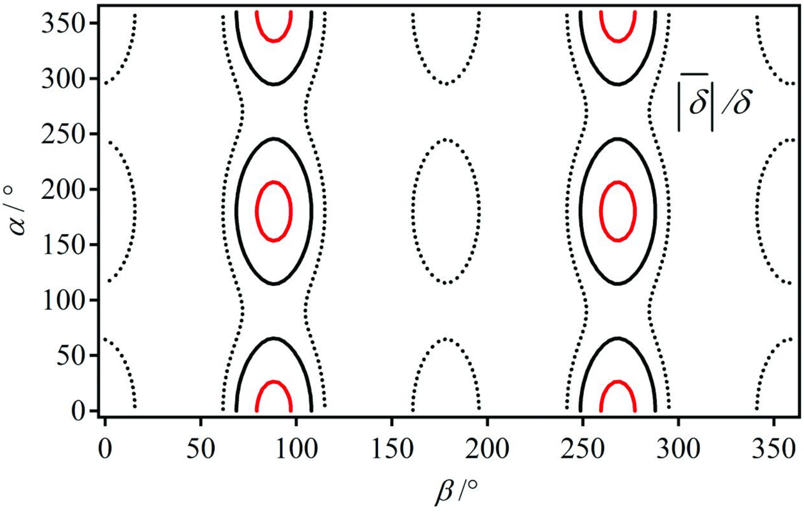

Figure 3. Effects of overall motions and side-chain conformational transition with a jump angle, α on $\bar{\delta}/\delta$ value of s–CH$_2$ geminal protons at a dihedral angle of β under two spin approximation. α corresponding to a difference angle between dihedral angle in two interchanging conformations. The dotted and solid black and red curves corresponding to $\bar{\delta}/\delta$ = 0.4, 0.5, and 0.6,

respectively. Reproduced with permission from ref (10). Copyright 2010 ACS. (see color insert)

Figure 4(a) shows ^{1}H MAS NMR spectrum for form I–rich sample of iPB1 enlarged vertically by 20 times at 118 °C. The spectrum consists of two components of the broad crystalline and narrow amorphous signals. The observed ^{1}H line shape in crystalline regions show a typical rigid spectral pattern which is largely different from those of form II. Figure 4(b) and (c) shows ^{1}H slice data of ^{1}H–^{13}C WISE spectra in the main and side chains, respectively. The obtained line shapes were fitted by Gaussian functions. The best fitted results indicate that ^{1}H full line width at half height (flwhh) is 57, 57, 54, and 37 kHz, for m–CH_2, CH, and s–CH_2, and CH_3 protons, respectively. This result indicates that overall and side–chain conformation in form I do not perform large amplitude motions at frequency over ~ mid 10 kHz even at high temperature of 118 °C close to equilibrium melting temperature (T_m^0 = 135 °C).

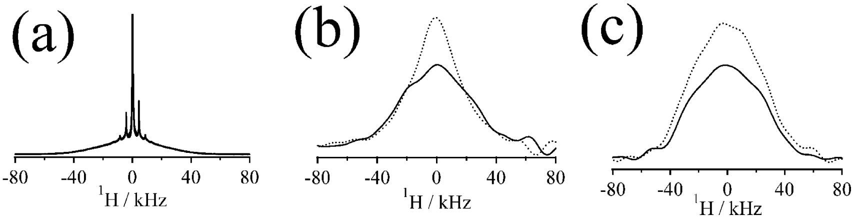

Figure 4. (a) ^{1}H MAS NMR spectrum amplified vertically by 20 times and ^{1}H slice date of ^{1}H–^{13}C MAS WISE NMR spectra of (b) the side chains and (c) main chains of the form I rich–sample at 118 °C. The dotted lines showing ^{1}H slice date through ^{13}C CH and CH_3 signals, and solid lines showing ^{1}H ones through ^{13}C s–CH_2 and m–CH_2 signals.

The CODEX experiments were carried out to investigate molecular dynamics of from I in slow dynamic range. If there is molecular motion during t_{mix}, the orientation–dependent frequency before and after t_{mix} will be different, and the magnetization will not completely be refocused. The resulting dephasing leads to a decay of the signal–intensity in the exchange spectrum (S). If there is no molecular motion during t_{mix}, the evolutions in the two evolution periods will cancel each other, and there will be no decay of the signal intensity. To remove relaxation effects during t_{mix} and Nt_r, a reference spectrum is acquired. The signal intensity in the reference spectrum (S_0) is not sensitive to exchange process but is only dominated by T_1, T_2, and pulse length errors. The motional correlation time and information about the motional geometry can be obtained by plotting the ratio (S/S_0) versus t_{mix} and (S/S_0) versus Nt_r, respectively.

Figure 5(a) shows CODEX reference, exchange, and different spectra of iPB1 form I with a t_{mix} = 200 ms and Nt_r = 2 ms at ambient temperature. S - S_0 is nearly zero in all the functional signals. This means that there is no slow molecular dynamics which reorients CSA interactions in all functional carbons during t_{mix} at Nt_r= 2 ms.

Downloaded by UNIV OF DELAWARE MORRIS LIB on June 20, 2012 | http://pubs.acs.org
Publication Date (Web): October 14, 2011 | doi: 10.1021/bk-2011-1077.ch012

Figure 5(b) and (c) shows t_{mix} dependence of $(S/S_0)^*$ intensity ratios of m–CH_2, CH, CH_3 at ambient temperature and 118 °C, respectively, where * means pure CODEX (S/S_0) decay after spin–diffusion corrections. The $(S/S_0)^*$ intensity ratios of m–CH_2 and CH carbons do not show essential decay up to t_{mix} = 4 s with a fixed Nt_{r} = 2 ms at ambient temperature and 118 °C. Here, it is noted that 118°C is a few degree lower than onset of melting. The $(S/S_0)^*$ ratios of CH_3 signal at $t_{\mathrm{mix}} \geq 2$ s are fluctuated and shows large experimental errors. This is caused not by molecular dynamics but by short ^{13}C T_1 value. The solid curve to the experimental data of CH signal shows $<\tau_c> = 860 \pm 5000$ s at 118 °C. This long value is out of dynamic window in our experiments (≤ 10 s). Thus obtained $<\tau_c>$ is not reliable.

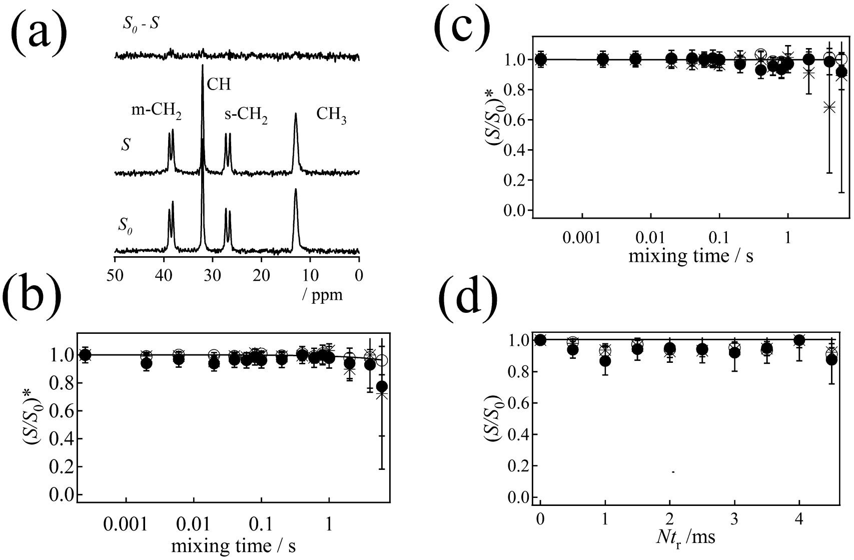

Figure 5. (a) ^{13}C CODEX reference, exchange, and difference spectra of iPB1 form I at a mixing time of 200 ms and Nt_r =2.0 ms at ambient temperature. (b) and (c) CODEX t_{mix} dependence of $(S/S_0)^*$ and (d) Nt_r dependence of (S/S_0) intensity ratios of m–CH_2 (●), CH (○), and CH_3 (*) with Nt_r = 2 ms at (b) ambient temperature, and (c) and (d) 118°C. Reproduced from ref (11).

Figure 5(d) shows Nt_{r} dependence of (S/S_0) intensity rations of m–CH_2, CH, and CH_3 ^{13}C signals with a t_{mix} = 200 ms at 118 °C. The (S/S_0) intensity ratios of all the signals do not decay with increasing Nt_{r} up to 4.5 ms even at high temperature of 118 °C. The solid line with a jump angle of 0° is well consistent with the experimental data within the experimental errors. Therefore, both t_{mix} and Nt_{r} dependences of CODEX results indicate that there is no evidence supporting overall and side–chain motions which induce re–orientations of CSA principle axes of all the functional signals of iPB1 crystal in slow dynamic range even at very high temperatures close to melting point. Thus, polymer chains in forms I and II show markedly different mobility. According to crystallographic data (*14*), solid–solid transition leads to 15 % contraction in *ab* plane and 12 %

Downloaded by UNIV OF DELAWARE MORRIS LIB on June 20, 2012 | http://pubs.acs.org
Publication Date (Web): October 14, 2011 | doi: 10.1021/bk-2011-1077.ch012

extension along *c* axis (chain axis). Such densifications lead to huge dynamic differences in geometry and time kinetic parameters in different polymorphs of the same polymer.

Here, we consider how molecular dynamics in forms I and II contribute to structural organization and superior mechanical property even at very high temperatures of iPB1. Extremely high mobility in form II is highly related to crystallization process. For example, crystallization of form II of iPB1 completes within 3 days at 110 °C (ΔT = 25°C)) The crystallized sample shows lamellae thickness, <*l*>, of ~ 28 nm at ΔT = 25°C (*11*). For comparison, iPP which is an example of mobile crystals shows <*l*> of ~ 23 nm at similar supercooling (ΔT = 23°C) (*12*). This crystallization takes about 12 days. Namely, extremely fast dynamics in form II shows much faster crystallization and makes much thicker lamellae than mobility in a typical mobile crystal.

Irreversible solid–solid transitions not only lead to drastic changes of stem mobility from extremely fast to slow–limit dynamics. Slow–limit dynamics of chains in form I is largely different from mobility of similar polyolefins such as PE (*5*), iPP (*6*), and iP4M1P (*30*). In these polymers, it is suggested that dissipation of mechanical property is related to chain dynamics in the crystalline regions (*5*). Thus, it is indicated that immobility of chains in form I crystal plays a critical role for superior mechanical property. Additionally, solid–solid transition process preserves very thick lamellae and high crystallinity which extremely fast chain dynamics in form II makes (*22*). One step crystallization into fixed crystal leads to thin lamellae with a low crystallinity (*11*). Therefore, it is reasonably concluded that molecular dynamics in two step processes of i) crystallization into form II (extremely mobile crystal) and ii) subsequently irreversible solid–solid transitions into form I (fixed crystal) play critical roles for superior mechanical strength of iPB1 even at very high temperatures.

iPP

We have shown that extremely high mobility in form II of iPB1 results in significant thickness at very high temperatures. This result simply suggests that crystalline mobility plays a critical role in lamellar thickness. Hereinafter, we investigate contributions of other structural factors to lamellar thickness.

Stereoregular polymers adopt one of four types of helical structure consisting of two independently structural factors of handness (right (*R*) or left (*L*)) and orientation (upward ($_u$) or downward ($_d$)) in the crystalline region (*31*), namely, R_u, R_d, L_d, and L_u, each of which shows an identical rotational energy in isolated states. The chain conformation and packing in α form of iPP have been well characterized by XRD. α form shows two limit packing structures as shown in Figure 6 (a) and (b) (*32*). The chains in two limiting structures adopt 3_1 helices but different orientations along *c* axis. There is no upward and downward disorder of stem orientations in full limit order. On the other hand, the disorder statistically occurs at each site in full limit disorder. Full limit disorder appears at a low T_c. The ordered packing fraction increases with increasing crystallization temperatures T_c, and reaches to 90–100 % at T_c = 150 °C (*33–35*). Previous high resolution ^{13}C NMR also supported these XRD results (*36–38*). However, spectral resolutions in

Downloaded by UNIV OF DELAWARE MORRIS LIB on June 20, 2012 | http://pubs.acs.org
Publication Date (Web): October 14, 2011 | doi: 10.1021/bk-2011-1077.ch012

previous NMR was insufficient to properly evaluate order–disorder phenomenon due to strong ^1H–^{13}C dipolar interactions.

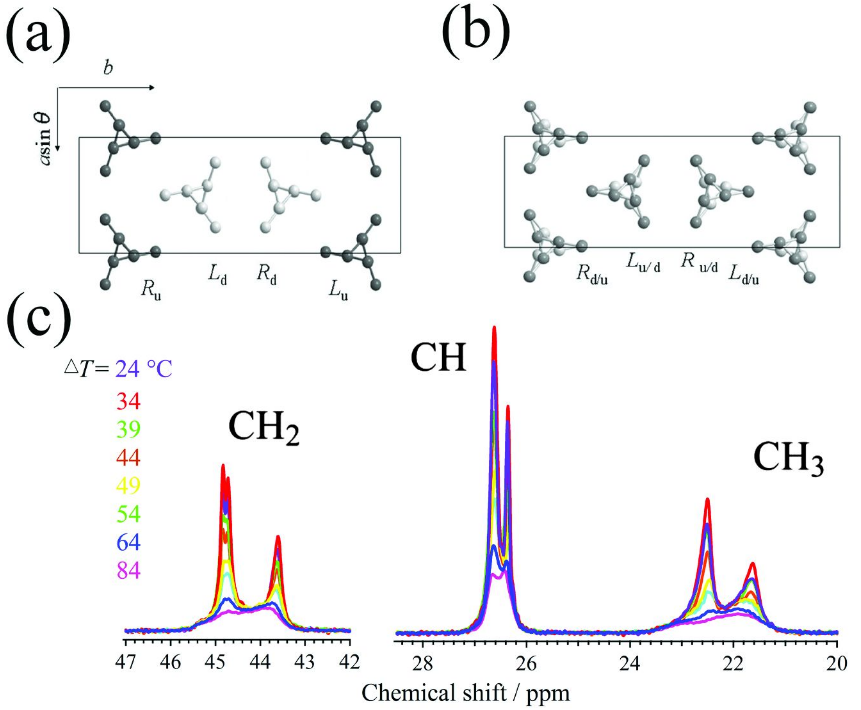

Figure 6. Unit-cell structures in (a) full limit order and (b) full limit disorder for α form of iPP. (c) The ^{13}C $T_{1\rho H}$ filter CPMAS NMR spectra for α form of iPP depending on supercooling at ambient temperature and signal assignments. Reproduced with permission from ref (12). Copyright 2010 ACS. (see color insert)

Figure 6(c) shows ^{13}C $T_{1\rho H}$ filtered CPMAS NMR spectra for pure *α* form crystallized at various Δ*T*. TPPM decoupling with a filed strength of 110 kHz during a long acquisition time of 160 ms were applied to fully detect free induction decays of the crystal signals. The structure less and inhomogeneously broadened ^{13}C signals were observed at Δ*T* = 84 °C. These line shapes correspond to packing structures in full limit disorder. With decreasing Δ*T*, newly narrowed doublet signals corresponding to those in full limit order appear and grow on the disordered line shapes. The observed spectral changing features are similar to the formers. However, current result shows much higher spectral resolution, and clearly indicates that the doublet signals reach to maximum intensities at Δ*T* = 34 °C and disordered and ordered structures co–exist even at very high temperatures less than Δ*T* = 34 °C. Considering CP and relaxation effects, improved ^{13}C signals determine the maximum ordered packing fraction, f_{order} = 62 % at Δ*T* = 34 °C (*12*). This result is mostly different from former XRD (*33–35*) and NMR results (f_{order} = 90 – 100 %) (*38*). The obtained discrepancy is attributed to characterization tools. XRD analysis uses very minor differences in diffraction as an evidence

Downloaded by UNIV OF DELAWARE MORRIS LIB on June 20, 2012 | http://pubs.acs.org
Publication Date (Web): October 14, 2011 | doi: 10.1021/bk-2011-1077.ch012

of order–disorder phenomenon. This minor difference is affected by amorphous halo, background, and neighboring peaks. Additionally, three–dimensional periodicity and sizes also influence the results. For these reasons XRD might overestimate f_{order}.

Current NMR results clearly indicate that polymer crystals include a large amount of structural disorders even at a very low supercooling. This result suggests that a host of factors (viz., packing energy, kinetics, chemical and physical features, such as molecular weights, stereo–regularity, regio–defects, entanglements, and chain folding) influence the packing structures of α form of iPP under bulk crystallization (*12*).

The relationship between molecular dynamics and structures were further investigated. As reported before (*6*), iPP shows helical jump motions in the crystalline regions. Figure 7 shows the temperature dependence of $<\tau_c>$ of helical jumps of *α* form of iPP obtained by CODEX, crystallized at ΔT = 34 ($<l>$ = 10 nm) and 84 °C ($<l>$ = 23 nm). The $<\tau_c>$ of helical jumps in the ordered packing of *i*PP_Δ*T*34 is 1270 ± 20 ms at 95 °C and is 37–fold longer than that in the disordered packing of *i*PP_Δ*T*84 ($<\tau_c>$ = 34 ± 1 ms) at the same temperature. The $<\tau_c>$ vs. $1/T$ plot exhibits Arrhenius behavior with activation energies of E_a = 102 ± 5 and 72 ± 4 kJ/mol for the ordered packing form of *i*PP_Δ*T*34 (This sample crystallize at ΔT= 34 °C) and for the disordered packing of *i*PP_Δ*T*84, respectively (*12*). These experimental results clearly indicate that both $<\tau_c>$ and E_a highly depend on packing order and lamellae thickness. If chain mobility alone plays a critical role in increasing lamellae thickness, annealing would lead to very thick lamellae without structural change. Thus, we investigate the relationship between $<l>$ and f_{order} of iPP samples annealed at various temperatures.

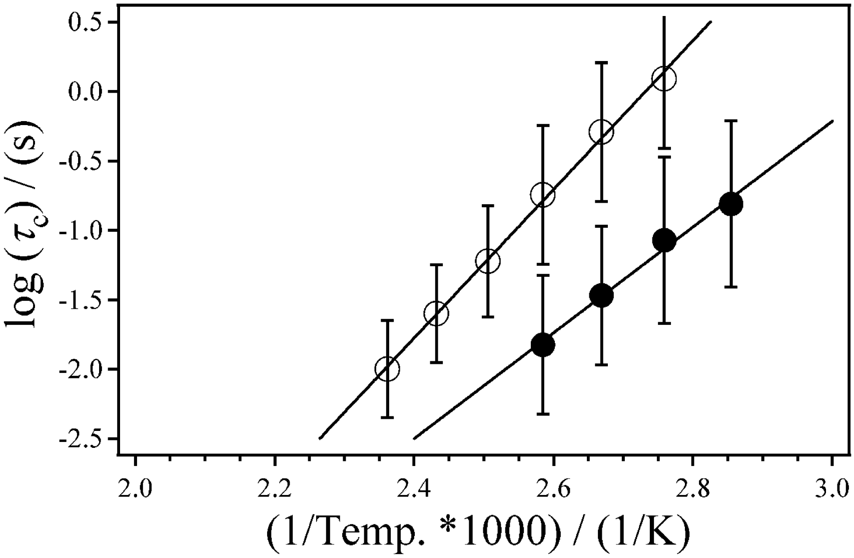

Figure 7. Arrhenius plot of $<\tau_c>$ for helical jump motions of stems in ordered packing of iPP_ΔT 34 (○) and in disordered packing of iPP_ΔT 84 (●) with best

Downloaded by UNIV OF DELAWARE MORRIS LIB on June 20, 2012 | http://pubs.acs.org
Publication Date (Web): October 14, 2011 | doi: 10.1021/bk-2011-1077.ch012

fitted values of E_a = 102 ± 5 and 72 ± 4 kJ/ mol, respectively. Reproduced with permission from ref (12). Copyright 2010 ACS.

Figure 8 shows the <l> vs. f_{order} curve during annealing at various temperatures (T_a). The starting conditions of <l> and f_{order} are 9 nm and 0 %, respectively. With increasing T_a, the lamellar thickness increases by only 3 nm without changing f_{order} up to 140 °C. At T_a = 150 °C, f_{order} suddenly increases to 25 %, and <l> also increases. Further increase of T_a induces further increases in f_{order}, accompanying large <l> enhancement. Figure 8 clearly indicates that <l> significantly increases in the f_{order} region of > 50 %. Actually, replacement of upward and downward orientations (stem orientations) is impossible in the limited spaces of solid crystals. This structural change requires partial melt and re–crystallization. Therefore, it is reasonable to consider thin lamellae that partially melt, and after re–crystallization which accompanies rearrangement of polymer chains packing ordering, <l> significantly increases.

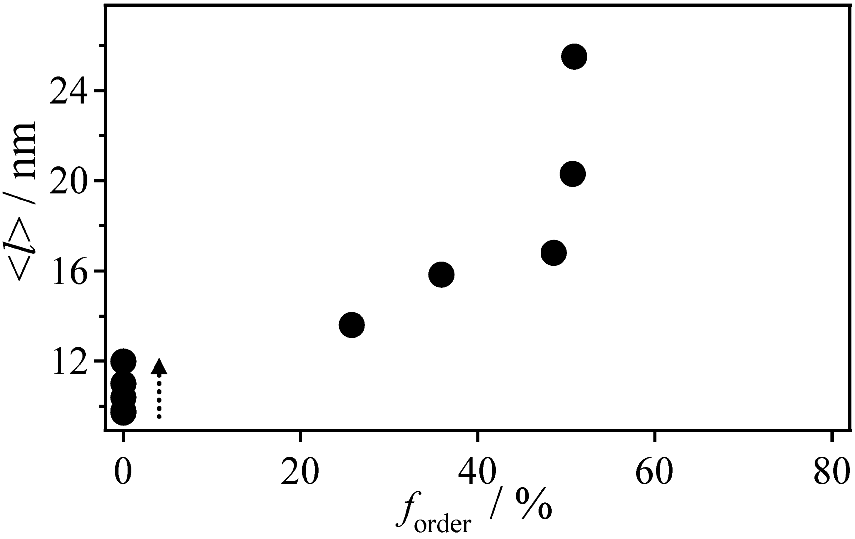

Figure 8. <l> versus f_{order} of α form of iPP under (b) annealing at 110 – 170 °C. Reproduced with permission from ref (12). Copyright 2010 ACS.

Here, we extract chain–level information from the packing structures under the hypothesis of adjacent reentry structure. In the case of stereoregular polymers, chain folding is allowed between antichiral isomorphous or isochiral antimorphous chains. This selection rule leads to a strong relationship between packing structures and chain–folding directions. In the case of full limit order, chain folding is possible only between alternating *R* and *L* stems along *a**axis (Figure, 9 (a)). On the other hand, there is no restriction on chain–folding directions in full limit disorder (Figure 9(b)). Therefore, two limiting structures on packing levels mean markedly different trajectories on chain levels. Thus, T_a dependence of f_{order} represents a degree of ordering of chain–level structures under hypothesis of adjacent re–entry structures. Actual lamellae thickening

In NMR Spectroscopy of Polymers: Innovative Strategies for Complex Macromolecules; Cheng, H., et al.;
ACS Symposium Series; American Chemical Society: Washington, DC, 2011.

Downloaded by UNIV OF DELAWARE MORRIS LIB on June 20, 2012 | http://pubs.acs.org
Publication Date (Web): October 14, 2011 | doi: 10.1021/bk-2011-1077.ch012

process at different T_a accompanies changes of chain–folding directions inside of crystals. This fact indicates that not only molecular dynamics but also chain–level structures contribute to T_a dependence of lamellar thickness in the polymer crystals. The same discussion would hold for isothermal crystallization ($1/\Delta T$ dependence of $<l>$).

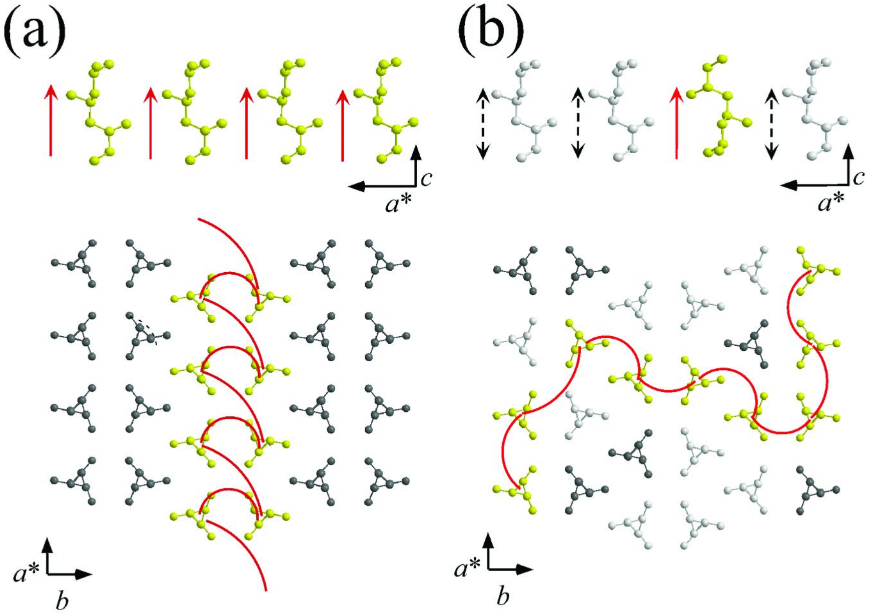

Figure 9. Possible models for of polymer chain trajectory of iPP in the crystalline region in (a) full limit order and (b) full limit disorder. Reproduced with permission from ref (12). Copyright 2010 ACS.

Conclusion

In the first part, extremely fast and slow–limit dynamics of polymer backbone are shown to be sources for unusual mechanical property of iPB1. This experiment clearly indicates that available dynamic spaces induce different dynamic geometry and time kinetics in different polymorphs of the same polymer. Extremely fast dynamics result in very thick lamellae within a relatively short crystallization time at high T_c. After irreversible solid–solid transition, crystalline stems in form I do not perform any overall and side–chain dynamics up to melting points in slow motional limit ($<\tau_c> > 10$ s). The huge contrasts in these dynamics play a critical role in the structural organization and the resulting material property of iPB1.

In the second part, we revisited packing order of α form of iPP by high resolution ^{13}C NMR. Strong dipolar decoupling significantly sharpens ^{13}C signals of the ordered packing structures. Improved resolution of ^{13}C crystalline signals properly accesses order–disorder phenomenon of the packing structures depending on T_c and T_a. The experiments provide not only molecular dynamics

Downloaded by UNIV OF DELAWARE MORRIS LIB on June 20, 2012 | http://pubs.acs.org
Publication Date (Web): October 14, 2011 | doi: 10.1021/bk-2011-1077.ch012

but also structural ordering information at molecular levels and the effects on the lamellae thickening process.

Acknowledgments

We really appreciate Dr. H. N. Cheng for carefully checking our manuscript.

References

1. Hu, W−G.; Shimidt−Rohr, K. *Acta Polym.* **1999**, *50*, 271–285.
2. Ediger, M. D. Spatially Heterogeneous Dynamics in Supercooled Liquid. *Ann. Rev. Phys. Chem.* **2000**, *51*, 99–128.
3. Serghei, A.; Kremer, F. *Phys. Rev. Lett.* **2003**, *91*, 16702, 1–4.
4. Uemura, T.; Horike, S.; Kitagawa, K.; Mizuno, M; Endo, K.; Bracco, K.; Comotti, A.; Sozzani, P.; Nagaoka, M.; Kitagawa, S. *J. Am. Chem. Soc.* **2008**, *138*, 6781–6788.
5. Hu, W. G.; Boeffel, C.; Schmidt−Rohr, K. *Macromolecules* **1999**, *32*, 1611–1619.
6. Schaefer, D.; Spiess, H. W.; Suter, U. W.; Fleming, W. W. *Macromolecules* **1990**, *23*, 3431–3439.
7. Kentgens, A. P. M.; de Boer, E.; Veeman, W. S. *J. Chem. Phys.* **1987**, *87*, 6859–6865.
8. Schmidt−Rohr, K.; Spiess, H. W. *Multidimensional Solid–state NMR and Polymers*, 1994 Academic Press.
9. Hirschinger, J.; Miura, H.; Gardner, K. H.; English, A. D. *Macromolecules* **1990**, *23*, 2153–2169.
10. Miyoshi, T.; Mamun, A.; Reichert, D. *Macomoelcules* **2010**, *43*, 3986–3989.
11. Miyoshi, T.; Mamun, A. *Polym. J., in press*.
12. Miyoshi, T.; Mamun, A.; Hu, W. *J. Phys. Chem. B.* **2010**, *114*, 92–100.
13. deAzevedo, E. R.; Hu, W. G.; Bonagamba, T. J.; Schmidt−Rohr, K. *J. Am. Chem. Soc.* **1999**, *121*, 8411–8412.
14. Schmidt−Rohr, K.; Clauss, J.; Spiess, H. W. *Macromolecules* **1992**, *25*, 3273–3277.
15. Tekely, P.; Palmas, P.; Mutzenhardt, P. *Macromolecules* **1992**, *26*, 7363–7365.
16. Qiu, X.; Mirau, A. P. *J. Magn. Reson.* **2000**, *142*, 183–189.
17. Lugiani, L.; Seppälä, J.; Löfgren, B. *Prog. Polym. Sci.* **1988**, *13*, 37–62.
18. Turner−Jones, A. *J. Polym. Sci. Part B.* **1963**, *1*, 455–456.
19. Petraccone, V.; Pirozzi, B.; Frasci, A.; Corradini, P. *Eur. Polym. J.* **1976**, *12*, 323–327.
20. Natta, G.; Corradini, P.; Bassi, I. W. *Nuov. Chim. Suppl.* **1960**, *15*, 52–67.
21. Maruyama, M.; Sakamoto, Y.; Nozaki, K.; Yamamoto, T.; Kajioka, H.; Toda, A.; Yamada, K. *Polymer* **2010**, *51*, 5532–5538.
22. Azzuri, F.; Flores, A.; Alfonso, G. C.; Sics, I.; Hsiao, B. S.; Balta; Calleja, F. J. *Polymer* **2003**, *44*, 1641–1645.

Downloaded by UNIV OF DELAWARE MORRIS LIB on June 20, 2012 | http://pubs.acs.org
Publication Date (Web): October 14, 2011 | doi: 10.1021/bk-2011-1077.ch012

23. Beckham, H. W.; Schmidt−Rohr, K.; Spiess, H. W. *ACS Symp. Ser.* **1995**, *598*, 243–253.
24. Miyoshi, T.; Hayashi, S.; Imashiro, F.; Kaito, A. *Macromolecules* **2002**, *35*, 6060–6063.
25. Maring, D.; Meurer, B.; Weill, G. *J. Polym. Sci., Part B: Polym. Phys.* **1995**, *33*, 1235–1247.
26. Schnell, I.; Spiess, H. W. *J. Magn. Reson.* **2001**, *151*, 153–227.
27. de Langen, M.; Prins, K. O. *Chem. Phys. Lett.* **1999**, *299*, 195–200.
28. Möller, M. *Makromol. Chem. Rapid Commun.* **1988**, *9*, 107–114.
29. Litvinov, V. M.; Macho, V.; Spiess, H. W. *Acta Polym.* **1997**, *48*, 471–477.
30. Miyoshi, T.; Pascui, O.; Reichert, D. *Macromolcules* **2004**, *37*, 6460–6471.
31. Petraccone, V.; Pirozzi, B.; Meille, S. V. *Polymer* **1986**, *27*, 1665–1668.
32. Hikosaka, M.; Seto, T. *Polym. J.* **1973**, *5*, 111–127.
33. Radhakrishnan, J.; Ichikawa, K.; Yamada, K.; Toda, A.; Hikosaka, M. *Polymer* **1998**, *39*, 2995–2997.
34. Auriemma, F.; de Ballesteros, O. R.; De Rosa, C.; Corradini, P. *Macromolecules* **2000**, *33*, 8764–8774.
35. Nakamura, K.; Shimizu, S.; Umemoto, S.; Thierry, A.; Lotz, B.; Okui, N. *Polym. J.* **2008**, *40*, 915–922.
36. Bunn, A.; Cudby, M. E. A.; Harris, R. K.; Packer, K. J.; Say, B. J. *Polymer* **1982**, *23*, 694–698.
37. Saito, S.; Moteki, Y.; Nakagawa, M.; Horii, F.; Kitamaru, R. *Macomolecules* **1990**, *23*, 3256–3260.
38. Caldas, V.; Brown, G. R.; Nohr, R. S.; Macdonald, J. G. *J. Polym. Sci., Part B: Polym. Phys.* **1996**, *34*, 2085–2098.

Downloaded by UNIV OF DELAWARE MORRIS LIB on June 20, 2012 | http://pubs.acs.org
Publication Date (Web): October 14, 2011 | doi: 10.1021/bk-2011-1077.ch012

Downloaded by OHIO STATE UNIV LIBRARIES on June 21, 2012 | http://pubs.acs.org
Publication Date (Web): October 14, 2011 | doi: 10.1021/bk-2011-1077.ch013

Chapter 13

Chain Mobility in Crosslinked EPDM Rubbers. Comparison of ^{1}H NMR T_2 Relaxometry and Double-Quantum ^{1}H NMR

Pieter C. M. M. Magusin,[*,1] **Ramona A. Orza,**[1,2] **Victor M. Litvinov,**[2,3]
Martin van Duin,[4] **and Kay Saalwächter**[5]

[1]Eindhoven Univ. of Technology, P.O. Box 513, 5600 MB Eindhoven, The Netherlands
[2]Dutch Polymer Institute, P.O. Box 902, 5600 AX Eindhoven, The Netherlands
[3]DSM Resolve, P.O. Box 18, 6160 MD Geleen, The Netherlands
[4]Lanxess Elastomers Global R&D, P.O. Box 1130, 6160 BC Geleen, The Netherlands
[5]Martin-Luther-Universität Halle-Wittenberg, Institut für Physik, Friedemann-Bach-Platz 6, D-06108 Halle, Germany
[*]E-mail: p.c.m.m.magusin@tue.nl

^{1}H NMR transverse relaxation and double-quantum (DQ) build up have been compared for a series of EPDM grades crosslinked with different amounts of sulfur or peroxide. The modulus at 100% elongation of the same EPDM samples correlates linearly to the effective transverse-relaxation and DQ build-up rate, suggesting that both rates are proportional to the total network density caused by chain entanglements and crosslinks. For none of the rates, however, the linear trends of sulfur- and peroxide-crosslinked EPDM coincide. This suggests that sulfur- and peroxide-crosslinked EPDM networks are qualitatively different, which is confirmed by different distributions of residual dipolar coupling constants.

Introduction

Elastomers, like ethylene-propylene copolymers (EPM) or ethylene-propylene-diene terpolymers (EPDM), are crosslinked to improve their

In NMR Spectroscopy of Polymers: Innovative Strategies for Complex Macromolecules; Cheng, H., et al.;
ACS Symposium Series; American Chemical Society: Washington, DC, 2011.

Downloaded by OHIO STATE UNIV LIBRARIES on June 21, 2012 | http://pubs.acs.org
Publication Date (Web): October 14, 2011 | doi: 10.1021/bk-2011-1077.ch013

performance, such as elasticity, tensile strength and resistance to solvents. Traditionally, sulfur vulcanization is applied, which, however, suffers from S-S bond cleavage at elevated temperatures. Peroxide cure results in more thermally stable networks (*1*). The mechanical properties of the rubber networks are not only determined by the chemical crosslinks but also by the physical entanglements between the polymer chains. Macroscopic characterization techniques, like mechanical measurements, yield overall information of the crosslink density. Solid-state ^{1}H NMR gives a more detailed picture of the network density and the heterogeneity thereof in different parts of the rubber network. The higher the density of crosslinks and entanglements, the more restricted the polymer-chain mobility and thus the higher the residual proton dipole coupling, as reflected in the ^{1}H NMR lineshape, transverse (T_2) relaxation (*2*, *3*) and the build up of double-quantum coherenc (*4*, *5*) For rigid non-oriented polymers the orientation dependence of the dipolar ^{1}H-^{1}H coupling leads to broad ^{1}H NMR lineshapes. In mobile polymers the dipole coupling is partly averaged by chain motions, which are fast compared to the static dipole coupling constant D_0 (~10^4 Hz),. Since in a real mobile polymer the cumulative rotational effect of chain motions is not isotropic, a residual dipole coupling (RDC) with reduced coupling constant D remains. This is reflected in the NMR spectrum by a narrower lineshape. The less restricted the chain motion, the narrower the lineshape.

Although, in principle, the linewidth in a ^{1}H NMR spectrum can be used as a source of information about chain mobility, it tends to be polluted by other linebroadening mechanisms, like chemical-shift heterogeneity and magnetic susceptibility. For mobile polymers with narrow ^{1}H NMR lines, such as weakly crosslinked elastomers above T_g, this inhomogeneous broadening can significantly spoil the interpretation. Therefore as an improved approach, ^{1}H NMR transverse relaxation, reflected in Hahn-echo decays, is often investigated for characterization of chain mobility in polymer networks (*2*, *6–8*). By reflecting the overall anisotropy of sub-millisecond polymer motions, the T_2 relaxation time for elastomer networks is sensitive to the conformational mean position of the network chains, which is affected by the presence of chemical and physical network junctions. Long network chains undergo less restricted motions, resulting in strongly averaged dipole couplings and thus long T_2 values. Short network chains have short T_2 relaxation times.

For ideal polymer networks, a direct relation exists between the crosslink density and proton transvere relaxation far above the glass transition T_g, where chain mobility is fast and only restricted by the network junctions (*6*, *7*, *9*, *10*). In practice, however, one has to deal with network defects, such as dangling chain-ends, chain loops and sol. Careful analysis of the T_2 decay curves often allows separating the relaxation behavior of the network defects from that of network chains. The theory of the transverse relaxation in crosslinked rubbers is based on the submolecule concept of network chains with both ends fixed in a laboratory system of coordinates regardless of the origin of the junctions. By assumption, the network chain consists of a number of statistical segments between the network junctions. The Kuhn and Grün model of freely jointed chains is used to calculate the conformational mean of the chain function in elastomers with low crosslink density (network chains obeying the Gaussian chain statistics). The weight average molar mass of polymer chains between neighboring network junctions in crosslinked elastomers can be calculated from the transverse relaxation rate at the high temperature plateau.

^{1}H NMR T_2 relaxation of a polymer reflects the overall anisotropy of chain motions that are fast on the sub-millisecond timescale. It is also particularly sensitive to intermediate motions at the millisecond timescale. If intermediate motions are significantly present in the broad range of timescales governing polymer dynamics, the validity of standard theories relating network density via the anisotropy of sub-millisecond motions to T_2 relaxation can be questioned (*11*). As further improvement, Double-Quantum (DQ) NMR has therefore been advocated (*5*). The same residual dipolar coupling that underlie T_2 relaxation can also be used to generate double-quantum coherences in hydrogen spin pairs. By a strategic combination of NMR signals, the DQ NMR technique is able to distinguish between a coherent build-up of double-quantum coherence, and incoherent loss of transverse magnetization. The DQ build-up rate measured in this way only reflects the residual dipole coupling averaged by the fast chain motions. The effect of intermediate motions ends up in the incoherent part and is not included in analysis in terms of network density. The advantage is that the technique zooms in on the anisotropy of fast motions, which is more correctly analyzed by use of the submolecule theories for rubber networks. In the previous investigation (*12–14*) of chemical structures and density of crosslinks in peroxide-cured EPDM the main focus was on MAS ^{1}H and ^{13}C NMR spectroscopy and static ^{1}H NMR T_2 relaxometry. In the present paper we want to compare the outcome of T_2 relaxometry and DQ build-up measurements for a series of sulfur- and peroxide-crosslinked EPDM grades, and get a more detailed picture of different network distributions caused by the different crosslinking method.

Downloaded by OHIO STATE UNIV LIBRARIES on June 21, 2012 | http://pubs.acs.org
Publication Date (Web): October 14, 2011 | doi: 10.1021/bk-2011-1077.ch013

Experimental Section

Materials

Amorphous EPM and EPDM co- and terpolymers with 0, 2, 4.5 and 9 wt.% ethylidene norbonene (ENB) and respective ethylene content of 49, 54, 52, 48 wt.% were obtained from DSM Elastomers (K3200, V2727, K4802 and K4703). For the systematic T_2 relaxometry study of peroxide crosslinking illustrated in Fig. 1, the EP(D)M grades were cured with 1.25, 2.5, and 5 parts per hundred rubber parts (phr) of bis (t-butylperoxy-i-propyl)benzene), commercially available as Perkadox Px-14-40 (AKZO). The *combined* T_2 relaxometry and double-quantum build-up study described in this chapter was applied to five sulfur-vulcanized EPDM systems with 9 wt.% ENB and varied sulfur levels of 0.7, 0.8, 1.2, 5 and 4.5 phr (as well as accelerating additives), and three peroxide-cured EPDM systems with peroxide levels of 1.25, 2.5 and 5 phr and co-varying ENB content of 0, 2 and 9 wt.% ENB, respectively. Further sample-preparation details can be found elsewhere (*2*, *13*).

Downloaded by OHIO STATE UNIV LIBRARIES on June 21, 2012 | http://pubs.acs.org
Publication Date (Web): October 14, 2011 | doi: 10.1021/bk-2011-1077.ch013

^{1}H NMR

^{1}H NMR Transverse Relaxometry

^{1}H NNMR transverse relaxation was measured by use of the Hahn-echo pulse sequence on a Bruker Minispec MQ spectrometer at a proton frequency of 20 MHz. All decays of the transverse magnetization were obtained and analyzed as described previously (*6*, *7*). Briefly, the Hahn-echo decays were decomposed into three relaxation components with in total 6 fit parameters. To avoid overfitting artefacts only the weight-average relaxation rate $R_2 = 1/T_2$ of the three components was used for the analysis. According to submolecule model of crosslinked rubbers, the effective relaxation rate R_2 in a polymer network is proportional to the average density of network junctions resulting from quasi-permanent chain entanglements and chemical crosslinks. For EPDM the proportionality constant, which depends on the molecular structure and the flexibility of the polymer chains, equals 0.285 mmol s kg^{-1}.

Multiple-Quantum ^{1}H NMR

^{1}H multiple-quantum NMR measurements were performed on a Bruker Minispec mp20 at 90 °C. The adjustment procedures and pulse sequences applied are specified in references (*5*) and (*15*).

Results and Discussion

^{1}H NMR Transverse Relaxometry

Fig. 1a shows the effective transverse relaxation rate $R_2 = 1/T_2$ of ethylene-propylene copolymer (EPM) and three ethylene-propylene-diene terpolymer (EPDM) grades, respectively, containing 2, 4.5 and 9 wt% of 5-ethylidene-2-norbonene (ENB) as the third monomer, crosslinked with a varied amount of peroxide. The transverse relaxation rate is proportional to the underlying total rubber network density, i.e. the sum of physical entanglements and chemical crosslinks. Thus, for the given proportionality constant determined by the molecular structure and flexibility of the polymer chains, the relaxation rates can be directly translated into network densities (Fig. 1a, vertical axis righthand side). Up to 5 phr peroxide the network density of the crosslinked EP(D)M grades depend linearly on the peroxide level. Extrapolation to zero peroxide yields similar chain entanglement densities in the range 0.20 - 0.24 mol/kg, This is consistent with the outcome of previous NMR and other studies (*2*, *16*). The higher network density after peroxide crosslinking is caused by the formation of chemical crosslinks. The presence of ENB monomers in the EPDM chain leads to enhanced crosslink formation. These ENB monomers are involved in crosslinking reactions via addition of macro-radicals to the pendent ENB unsaturation and via combination of ENB-derived allyl radicals (*14*).

In NMR Spectroscopy of Polymers: Innovative Strategies for Complex Macromolecules; Cheng, H., et al.;
ACS Symposium Series; American Chemical Society: Washington, DC, 2011.

Downloaded by OHIO STATE UNIV LIBRARIES on June 21, 2012 | http://pubs.acs.org
Publication Date (Web): October 14, 2011 | doi: 10.1021/bk-2011-1077.ch013

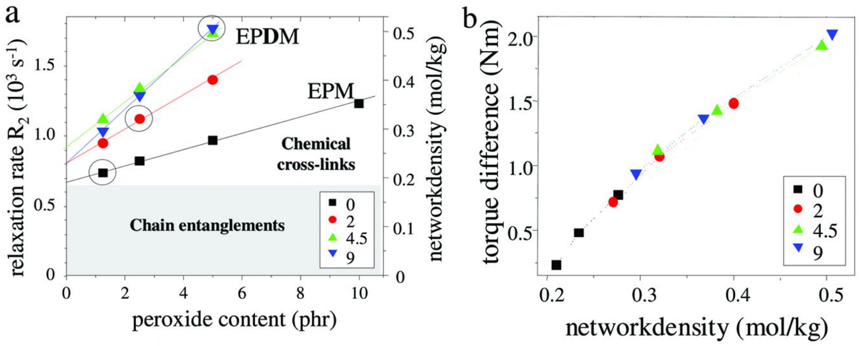

Figure 1. (a) ^{1}H NMR transverse relaxation rates $R_2 = 1/T_2$ and network density of EP(D)M grades with 0, 2, 4.5 and 9 wt.% ENB crosslinked with varied initial peroxide content. The three peroxide-cured EP(D)M systems that have also been studied with DQ NMR are encircled. (b) Correlation of rheometer torque difference of the EPM and EPDM grades with total network crosslink density derived from ^{1}H NMR relaxometry.

Figure 1b shows the excellent correlation between separately measured rheometer torque difference for the complete set of peroxide-cured EPM and EPDM grades and the total network density determined from NMR. Apparently, the network density calculated from T_2 relaxometry has a real physical meaning and is relevant for the macroscopic properties of the crosslinked EPDM rubbers.

Multiple-Quantum ^{1}H NMR

The left side of Fig. 2 shows DQ build-up curves of EPDM with 9 wt.% ENB and crosslinked with sulfur amounts of 0.7, 1.5 and 4.5 phr. The results are compared with the DQ build-up curves of three peroxide-cured EP(D)M systems with 0, 2 and 9 wt.% ENB and respective peroxide levels of 1.25, 2.5 and 5 phr (Fig. 2, right). The three peroxide-cured systems represent a typical selection across the set of EP(D)Ms already characterized with T_2 relaxometry (encircled points in Fig. 1a). Both the DQ build up S_{DQ} and the reference decay S_{ref} were recorded. Fig. 2 shows the S_{DQ}, S_{ref} and the sum $S_{\Sigma} = S_{DQ}+S_{ref}$ as a function of evolution time τ_{DQ} (sum of excitation and reconversion time). For comparison the curve fits to the Hahn-echo decays of the same samples are also shown. S_{ref} and S_{DQ} show the typical decay - and build-up behavior, respectively. For an isotropic ensemble of isolated spin pairs without relaxation and spin diffusion, S_{ref} and S_{DQ} should approach each other at sufficient long evolution time. This is indeed observed for the sulfur-vulcanized systems, but not for peroxide-cured EPDM, where S_{ref} is always bigger than S_{DQ}. Apparently the latter contains a comparably large fraction (~10 % monomer units, *vide infra*) of mobile chain fragments, such as long network chains or "dangling ends". The DQ build-up rate of these fragments is low compared to the overall loss of coherence due to T_2 relaxation. As a result, these mobile chain fragments will only contribute to S_{ref} and hardly to S_{DQ}, which causes S_{ref} to be systematically larger than S_{DQ} even at long DQ evolution time. The loss of overall coherence is reflected by the decay of S_Σ. The observed sum-intensity decays (~5 ms) are always slower than the corresponding Hahn-echo decays (~1 ms).

The difference between S_{ref} and S_{DQ} at long time is a signature of "incoherent" components, of which the loss of overall coherence is faster than the build-up of DQ coherence. To remove these components from the NMR data we have therefore fitted a bi-exponential model to the difference intensity $S_{ref} - S_{DQ}$ over the range 5 – 18 ms, and used this to normalize the DQ build up according to:

$$S_{DQ}^{N}(\tau_{ex}) \equiv \frac{S_{DQ}(\tau_{ex})}{S_{ref}(\tau_{ex}) + S_{DQ}(\tau_{ex}) - a\exp(-\tau_{ex}/T_{2a}) + b\exp(-\tau_{ex}/T_{2b})} \quad [1]$$

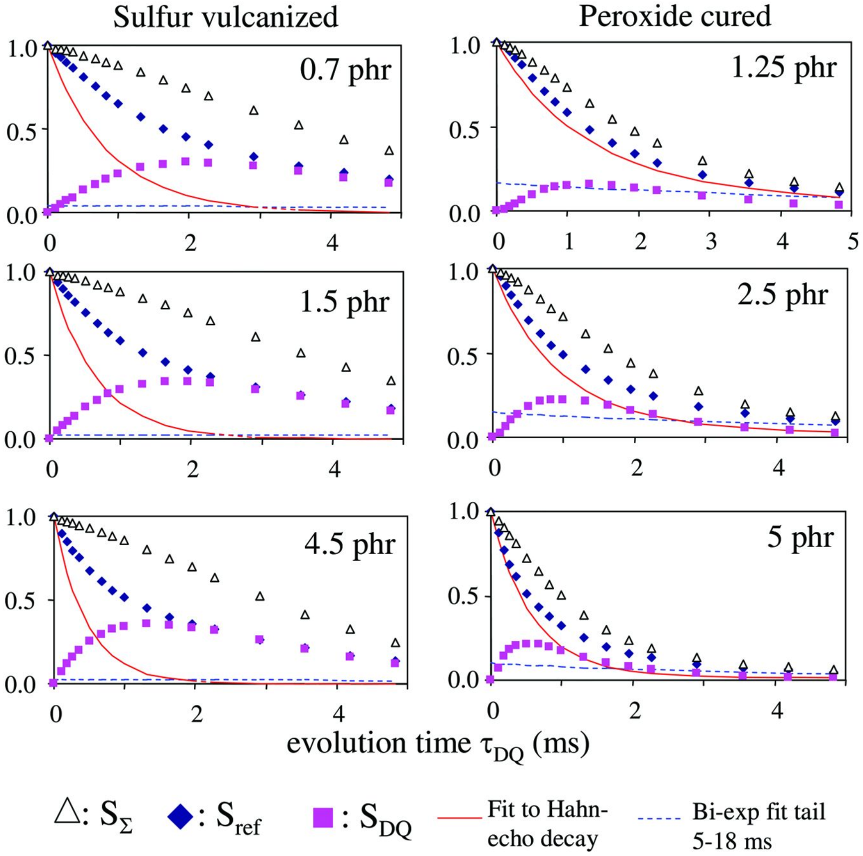

Figure 2. DQ build-up intensity S_{DQ}, reference intensity S_{ref} (magnetization not converted into DQ coherence) and their sum S_Σ versus the evolution time τ_{DQ}, as compared to Hahn-echo decay curves, and bi-exponential curves fitted to the tail of S_{ref} between 5 and 18 ms.The results shown here are (left) for EPDM with 9 wt.% ENB vulcanized with 0.7, 1.5 and 4.5 phr sulfur and (right) for EP(D)M with 0, 2 and 9 wt.% ENB cured with 1.25, 2.5 and 5 phr peroxide, respectively.

Downloaded by OHIO STATE UNIV LIBRARIES on June 21, 2012 | http://pubs.acs.org
Publication Date (Web): October 14, 2011 | doi: 10.1021/bk-2011-1077.ch013

Downloaded by OHIO STATE UNIV LIBRARIES on June 21, 2012 | http://pubs.acs.org
Publication Date (Web): October 14, 2011 | doi: 10.1021/bk-2011-1077.ch013

The bi-exponential correction is negligible for the sulfur-vulcanized EPDM (Fig. 2, left), and corresponds to the removal of ~10 % of the initial intensity for the peroxide-cured EPDM, with a tendency to decrease at increasing peroxide-level (Fig. 2, right).

The normalized DQ build-up curves for the same sulfur- and peroxide-crosslinked EPDM rubbers are depicted up to 5 ms in Fig. 3. As expected, the DQ build-up becomes faster at higher sulfur and peroxide/ENB levels. The respective shapes reflect the underlying distribution of residual dipole coupling constants. Before giving a detailed analysis in terms of specific distribution models, we note an interesting shape similarity among the build-up curves of the sulfur-vulcanized EPDM systems when plotted along a logarithmic time axis (Fig. 4a). Up to 1.5-phr sulfur the curves coincide upon scaling the evolution time (Fig. 4c). The same is true for peroxide-cured EPDM up to peroxide levels of 2.5 phr (Fig. 4b and 4d).

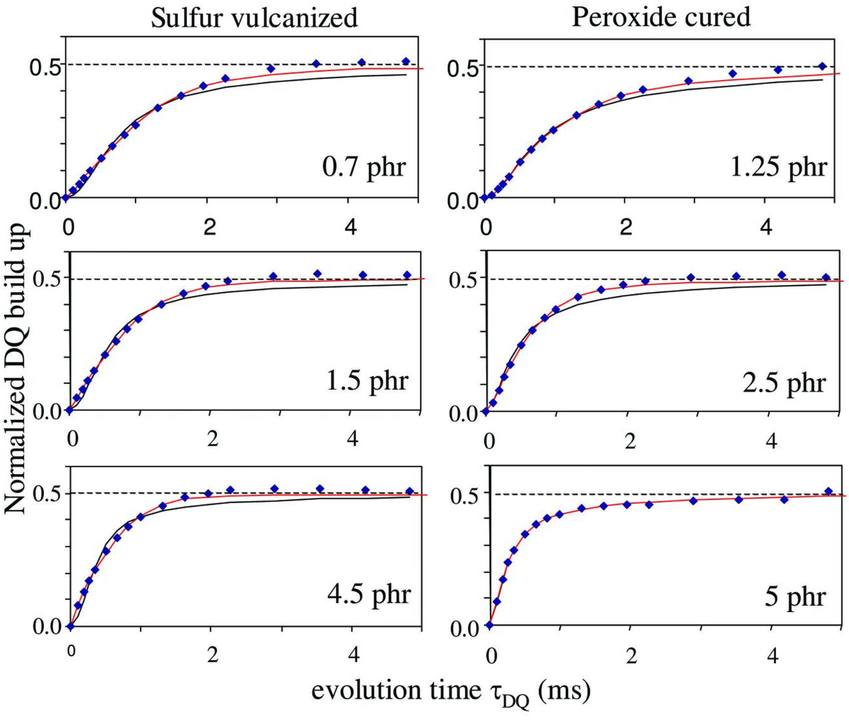

Figure 3. Normalized DQ build-up curves with curve fits based on a Gaussian and bi-Gaussian distribution of residual dipole coupling (RDC) constants for the same sulfur- and peroxide-crosslinked EP(D)M systems as in Fig. 2. Simulated curves for a bi-Gaussian distribution of RDC constants fit better to the observed DQ build ups than those for a Gaussian RDC distribution.

The faster the DQ build-up, the bigger the required scaling factor, which thus represents a *model-free* “relative build-up rate” R_{DQ}. Arbitrarily taking the curve of 1.25-phr peroxide-cured EPM as the reference, we have determined the time-scaling factors of the other curves with respect to this curve. There is a systematic shape difference between sulfur- and peroxide-cured EP(D)M, which cannot be removed by time scaling (Fig. 5). This makes comparison of the relative build-up rates between sulfur- and peroxide-cured EPDM slightly ambiguous, but a rough comparison is still possible.

R_{DQ} depends similarly on the sulfur and peroxide levels as the (weighted-average) Hahn-echo decay rate $R_2 = 1/T_2$ (Fig. 6a and 6b). As shown in Fig. 1a, the effective relaxation rate R_2 of peroxide-cured EP(D)M varies linearly with the peroxide level below 5 phr. In contrast, for sulfur-cured EPDM R_2 and R_{DQ} follow a kind of saturation curve. This indicates that at sulfur levels > 4 phr the content of third monomers becomes limiting for the crosslink density, which agrees with earlier observations (*2*).

Since R_2 and R_{DQ} appear to follow different slopes for sulfur- and peroxide-cured EPDM, one could wonder which of the two, R_2 or R_{DQ}, correlates best with the macroscopic mechanical properties. The ideal behavior would be an NMR parameter predicting, e.g., the modulus, independent of the applied curing method. Fig. 6c and 6d shows plots of the modulus at 100 % elongation (M_{100}) versus either R_2 or R_{DQ}. For each of the two crosslinking types there is a linear correlation between the modulus and R_2 and R_{DQ}, respectively. However, for neither R_2 nor R_{DQ} the crosslinking-type dependence disappears. This confirms that the R_2 and R_{DQ} difference between sulfur- and peroxide-crosslinked networks is not so much caused by NMR artifacts related to the selected NMR parameter, but may actually be related to the even qualitatively different types of networks formed.

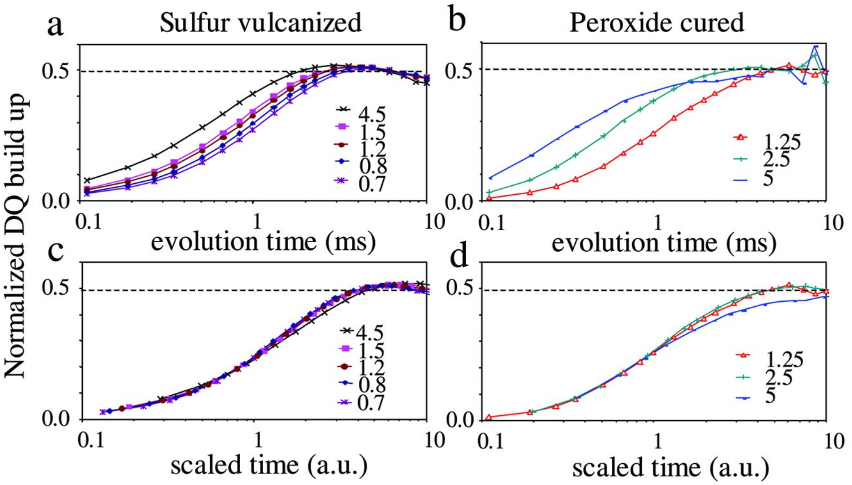

Figure 4. Normalized quantum build-up curves of (a,c) sulfur-vulcanized and (b,d) peroxide-cured EPDM crosslinked at varied levels of sulfur and peroxide, respectively, versus (a,b) evolution time and (c,d) scaled evolution time. The five sulfur-vulcanized EPDM rubbers all contained 9 wt.% ENB. The three peroxide-cured EPDM systems are the same as in Fig. 2.

In NMR Spectroscopy of Polymers: Innovative Strategies for Complex Macromolecules; Cheng, H., et al.; ACS Symposium Series; American Chemical Society: Washington, DC, 2011.

Downloaded by OHIO STATE UNIV LIBRARIES on June 21, 2012 | http://pubs.acs.org
Publication Date (Web): October 14, 2011 | doi: 10.1021/bk-2011-1077.ch013

Downloaded by OHIO STATE UNIV LIBRARIES on June 21, 2012 | http://pubs.acs.org
Publication Date (Web): October 14, 2011 | doi: 10.1021/bk-2011-1077.ch013

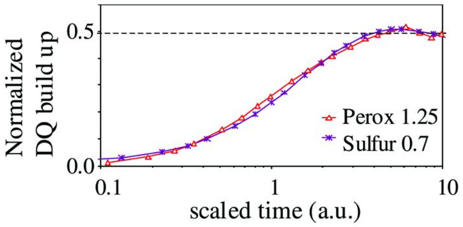

Figure 5. Normalized quantum build-up curves of EPDM vulcanized with 0.7 phr sulfur and EPM cured with 1.25 phr peroxide versus the scaled DQ evolution time.

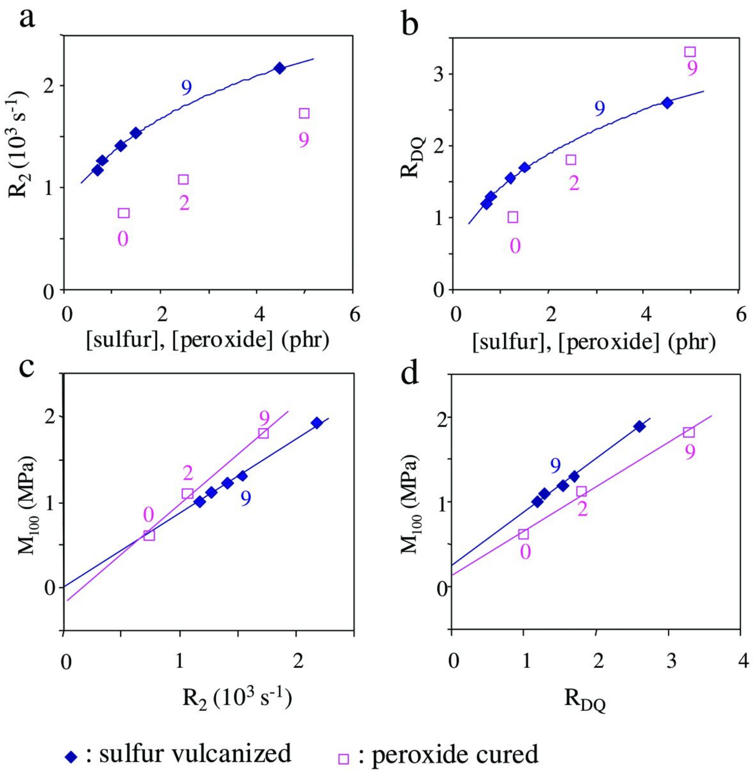

Figure 6. (a) Effective relaxation rates R_2 and (b) relative DQ build-up rates R_{DQ} for the same sulfur- and peroxide-crosslinked EP(D)M rubbers as in Fig. 4. (c,d) correlation between the modulus at 100% elongation M_{100} and (c) R_2 and (d) R_{DQ}. For clarity the data are labeled with the ENB content of the specific EP(D)M grade, i.e. 9 wt.% for the five sulfur-vulcanized systems, and 0, 2 and 9 wt.% for the three peroxide-cured systems. The curved lines connecting the data for the sulfur-vulcanized systems in (a) and (b) are guides for the eye only.

The similar dependence of R_2 and R_{DQ} on the sulfur- or peroxide levels is also clear from the linear correlations between the two (Fig. 7). Sulfur- and peroxide-crosslinked EPDM samples show different slopes, which may

Downloaded by OHIO STATE UNIV LIBRARIES on June 21, 2012 | http://pubs.acs.org
Publication Date (Web): October 14, 2011 | doi: 10.1021/bk-2011-1077.ch013

reflect the difference in the underlying network topology. Peroxide can generate radicals anywhere along the EPDM chains, whereas sulfur requires the residual unsaturation of the third monomer to generate crosslinks. Interestingly, the linear correlations between R_2 and R_{DQ} for sulfur-vulcanized and peroxide-cured EPDM cross each other at $R_{DQ} = 0$ and a positive value $R_2^* \sim 300\ \mathrm{s}^{-1}$. This may indicate that the entanglements, which determine R_2 and R_{DQ} in the absence of chemical crosslinks, may be different. Alternatively, $R_2^* = 1/T_2^{BWR}$ may represent Bloch-Wangsness-Redfield type of relaxation contributions (*17*, *18*) associated with *incoherent* loss of transverse magnzetization:

$$\frac{1}{T_2^{eff}} = \frac{1}{T_2^{BWR}} + \frac{1}{T_2^{coh}} \qquad [2]$$

where $1/T_2^{coh}$ denotes the decay rate of the Hahn echo under the influence of the coherent dipolar dephasing.

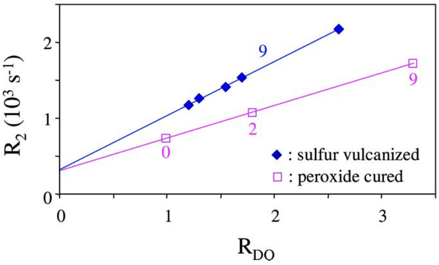

Figure 7. Correlation between effective relaxation rate R_2 and R_{DQ} for the same sulfur- and peroxide-cured EP(D)M samples as in Fig. 4.

After this essentially model-free analysis we have also analyzed the DQ build-up curves in terms of mono- and bi-modal Gaussian distributions:

$$g^{(n)}(D) = \sum_{k=1}^{n} \frac{f_k}{\sigma_k \sqrt{\pi}} \exp\left(-\frac{(D - D_c^{(k)})^2}{\sigma_k^2} \right) \qquad [3]$$

with $n = 1$ or 2 , respectively, and in the latter case $f_1 + f_2 = 1$, $D_c^{(1)}$, $D_c^{(2)}$, σ_1 and σ_2 the center values and widths of the two Gaussian components describing the distribution of residual dipolar coupling (RDC) constants. This distribution can be convoluted with the Gaussian initial behavior of the DQ build-up curves for an isotropic ensemble of isolated spin pairs with *identical* residual couplings D:

$$S_{DQ}^{N}(D\, \tau_{DQ}) \approx 0.5 \left\{ 1 - \exp\left(-0.4 D^2 \tau_{DQ}^2 \right) \right\} \qquad [4]$$

The resulting analytical expression for the DQ build-up curve is (*15*):

$$S_{DQ}^{N}(D_{av}, \sigma, \tau_{DQ}) = \tag{5}$$

$$= 0.5 \sum_{k=1}^{n} f_k \left\{ 1 - \frac{\exp\left(- \dfrac{0.4\left(D_{av}^{(k)}\right)^2 \tau_{DQ}^2}{1 + 0.8\,\sigma_k^2 \tau_{DQ}^2} \right)}{\sqrt{1 + 0.8\,\sigma_k^2 \tau_{DQ}^2}} \right\}$$

Curves based on a single Gaussian distribution of RDC constants with the maximum at 0 fit well to the initial part of the DQ build-up curves of the *peroxide*-cured EPDM (Fig. 3, right hand side). At increasing peroxide content the width of the half-Gaussian RDC distribution increases (Fig. 8b), but the maximum stays at 0. This indicates that the chains between the network junctions become shorter at increasing peroxide content, but there is always a significant fraction with long chain segments (D_{res}=0) even at high peroxide content. Such network structure could indicate a tendency of peroxide to form heterogeneous networks with parts of the EPDM chains non-crosslinked. One of the chemical pathways in the peroxide crosslinking of EPDM is the addition of EPDM macro-radicals to the residual unsaturation of ENB monomers in the polymer chain. This is followed by a hydrogen transfer, generating a new EPDM macro-radical which can add to the unsaturation of another ENB monomer, or combine with another EPDM macro-radical (*13*). The net result is a cluster of two or four crosslinks. In addition, a side reaction of peroxide curing is main chain degradation yielding a rubber network with dangling ends. Other types of chain reactions, such as formation of multifunctional crosslinks by double-bond polymerization, may also play a role during peroxide curing. These various reactions lead to a broad distribution of chain mobility, and thus to a broad RDC distribution. Similar observations were in fact previously reported for peroxide cross-linked natural and butadiene rubbers (*19*).

In contrast to the *peroxide*-cured samples, mono-modal curves based on Eq. 5 do not fit well to the DQ build-up curves of *sulfur*-crosslinked EPDM (Fig. 3, left). Bi-modal distributions consisting of a broad Gaussian centered at 0 and a narrow Gaussian with variable center and width fit better. In this case both the center and the width of the dominant narrow Gaussian component increases at increasing sulfur content (Fig. 8c). The good fit with the bimodal model should not be interpreted as indication of pronounced inhomogeneity, as the RDC distribution is in fact dominated by the narrower component. (Note the logarithmic scale in Fig. 8.) As support for this argument, sulfur vulcanization of natural rubber, i.e., poly(isoprene), also yields homogeneous networks (*19*). Sulfur vulcanization requires the residual unsaturation of the ENB monomer which is known to be

Downloaded by OHIO STATE UNIV LIBRARIES on June 21, 2012 | http://pubs.acs.org
Publication Date (Web): October 14, 2011 | doi: 10.1021/bk-2011-1077.ch013

incorporated randomly into the EPDM chains. Sulfur vulcanization thus produces crosslinks more homogeneously distributed along the chain.

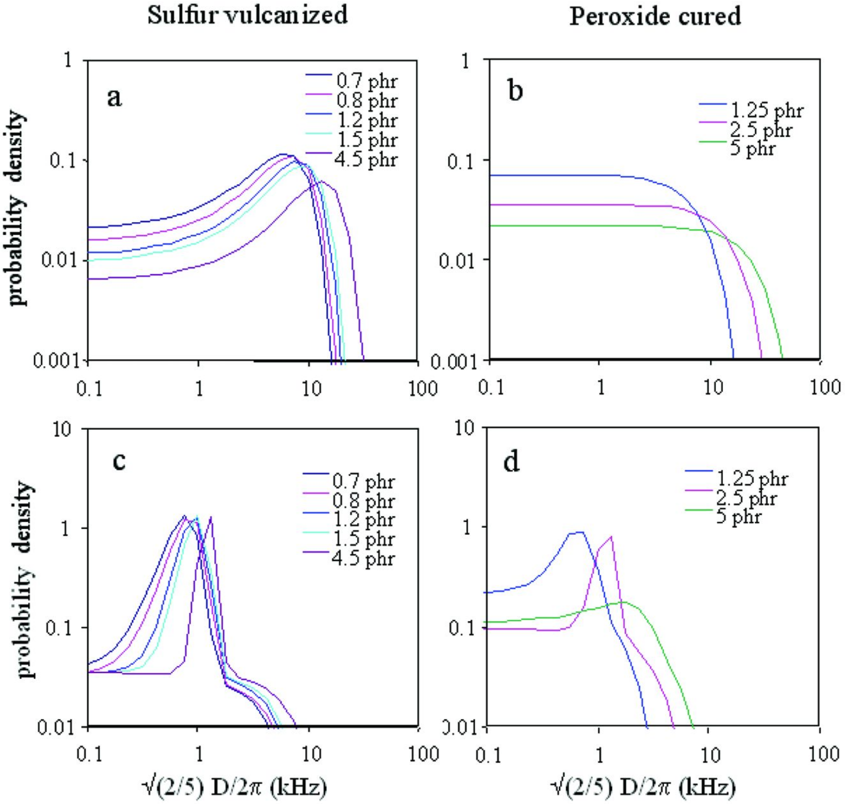

Figure 8. (a,b) (single-)Gaussian and (c,d) bi-Gaussian RDC distributions yielding DQ build-up curves which fit best to the experimentaldata of the (a,c) sulfur- and (b,d) peroxide-crosslinked EPDM grades.

Conclusion

We have compared ^{1}H NMR transverse relaxation and double-quantum (DQ) build up for sulfur- and peroxide-crosslinked EPDM grades with varied sulfur- and peroxide content. The network density derived from transverse relaxation correlates well with macroscopic properties such as the rheometer torque difference and the modulus at 100% elongation. For peroxide-cured EPDM DQ NMR indicates a heterogeneous network with a significant amount of dangling ends, whereas sulfur-vulcanized EPDM shows the features of a more homogeneous polymer network. For both types of crosslinking, the DQ build up is faster at increasing curative content, which is consistent with an increased immobilization of the polmer chains. The DQ build-up curves of the sulfur-crosslinked EPDM samples have similar shapes, and can be made to coincide by time scaling. The DQ build-up curves of the peroxide-cured EPDM

Downloaded by OHIO STATE UNIV LIBRARIES on June 21, 2012 | http://pubs.acs.org
Publication Date (Web): October 14, 2011 | doi: 10.1021/bk-2011-1077.ch013

grades have a different shape. Whereas the peroxide-crosslinked EPDM grades show a *linear* increase of the effective relaxation rates R_2 and relative DQ build-up rates up to 4.5 phr peroxide, the corresponding rates for sulfur-vulcanized EPDM grades level off already at initial sulfur content > 1.5 phr. Mechanical properties, like the modulus at 100% elongation, correlate linearly with both the effective relaxation rate R_2 and the relative DQ build up rate R_{DQ}, but for neither of the two rates the linear trends for sulfur- and peroxide EPDM grades coincide. This is probably a consequence of the underlying different types of rubber networks. A difference between sulfur- and peroxide-crosslinking is that the first requires the unsaturation of the ENB monomers which are randomly distributed along the EPDM chain, whereas peroxide radicals create combination crosslinks anywhere along the chain, as well as addition crosslinks and other possible chain reactions.

Downloaded by OHIO STATE UNIV LIBRARIES on June 21, 2012 | http://pubs.acs.org
Publication Date (Web): October 14, 2011 | doi: 10.1021/bk-2011-1077.ch013

Acknowledgments

This work was part of the research program of the Dutch Polymer Institute (DPI Project No. 511).

References

1. van Duin, M.; Dikland, H. G. *Rubber Chem. Technol.* **2003**, *7*, 132–144.
2. Litvinov, V. M.; Barendswaard, W.; van Duin, M. *Rubber Chem. Technol.* **1998**, *71*, 105–118.
3. Fulber, C.; Demco, D. E.; Weintraub, O.; Blümich, B. *Macromol. Chem. Phys.* **1996**, *197*, 581.
4. Schneider, M.; Gasper, L.; Demco, D. E.; Blümich, B. *J. Chem. Phys.* **1999**, *111*, 402–415.
5. Saalwächter, K.; Ziegler, P.; Spyckerelle, O.; Haidar, B.; Vidal, A.; Sommer, J.-U. *J. Chem. Phys.* **2003**, *119*, 3468–3482.
6. Litvinov, V. M.; Dias, A. A. *Macromolecules* **2001**, *34*, 4051–4060.
7. Litvinov, V. M. *Spectroscopy of Rubbers and Rubbery Materials*; RAPRA: Shawbury, U.K., 2002; p 353.
8. Rastogi, S.; Lippits, D. R.; Peters, G. W. M.; Graf, R.; Yao, Y.; Spiess, H. W. *Nat. Mater.* **2005**, *4*, 635–641.
9. Cohen-Addad, J. P. *Prog. Nucl. Magn. Reson. Spectrosc.* **1993**, *25*, 1–316.
10. Brereton, M. G. *Macromolecules* **1991**, *24*, 2068–2074.
11. Saalwächter, K. *Macromolecules* **2005**, *38*, 1508–1512.
12. Orza, R. A.; Magusin, P. C. M. M.; Litvinov, V. M.; van Duin, M.; Michels, M. A. J. *Macromol. Symp.* **2005**, *230*, 144–148.
13. Orza, R. A.; Magusin, P. C. M. M.; Litvinov, V. M.; van Duin, M.; Michels, M. A. J. *Macromolecules* **2007**, *40*, 8999–9008.
14. Orza, R. A.; Magusin, P. C. M. M.; Litvinov, V. M.; van Duin, M.; Michels, M. A. J. *Macromolecules* **2009**, *42*, 8914–8924.
15. Saalwächter, K. *Prog. Nucl. Magn. Reson. Spectrosc.* **2007**, *51*, 1–35.
16. Richter, D.; Farago, B.; Butera, R.; Fetters, L. J.; Huang, J. S.; Ewen, B. *Macromolecules* **1993**, *26*, 795–804.

17. Wangsness, R. K.; Bloch, F. *Phys. Rev.* **1953**, *89*, 728–739.
18. Redfield, A. G. *IBM J. Res. Dev.* **1957**, *1*, 19–31.
19. Valentín, J. L.; Posadas, P.; Fernández-Torres, A.; Malmierca, M. A.; González, L.; Chassé, W.; Saalwächter, K. *Macromolecules* **2010**, *43*, 4210–4222.

Downloaded by OHIO STATE UNIV LIBRARIES on June 21, 2012 | http://pubs.acs.org
Publication Date (Web): October 14, 2011 | doi: 10.1021/bk-2011-1077.ch013

Chapter 14

Diffusion NMR of Polymers in Bicelles

Peter M. Macdonald[*]

Department of Chemical and Physical Sciences,
University of Toronto Mississauga,
Mississauga, Ontario, Canada L5L 1C6
[*]E-mail: pm.macdonald@utoronto.ca

This mini-review describes diffusion NMR studies of polymers in bicelles using the pulsed field gradient (PFG) NMR technique. Bicelles are first introduced and their morphology and applications as membrane mimetics and confinement media are briefly covered. The PFG NMR diffusion method is then introduced, emphasizing its specific advantages and limitations when applied to diffusion measurements in macroscopically-oriented lamellar systems such as magnetically-aligned bicelles. The utility of PFG NMR diffusion measurements in bicellar model membrane systems for examining lateral diffusion of membrane-bound, surface-grafted poly(ethylene glycol) (PEG) molecular species is demonstrated, focusing on those features of lateral diffusion and / or bicelle morphology that such studies illuminate. Further, PFG NMR diffusion studies of various molecular weight soluble PEG species confined within the parallel-plate geometry of magnetically aligned bicelles are reviewed, again focusing on revelations concerning bicelle morphology. The discussion concludes with an outline of future prospects for diffusion NMR studies in bicelles.

Introduction

The sensitivity of the NMR experiment to diffusion was recognized virtually from the inception of NMR spectroscopy (*1*). In the succeeding decades, diffusion NMR, i.e., the use of NMR spectroscopy to detect and characterize diffusion, has matured into a sophisticated suite of techniques and been applied widely in a host

In NMR Spectroscopy of Polymers: Innovative Strategies for Complex Macromolecules; Cheng, H., et al.;
ACS Symposium Series; American Chemical Society: Washington, DC, 2011.

of physical, chemical, biological and medical investigations. Much of the impetus for these developments stems from the recognition that knowledge of diffusion properties often can offer key insights into the structural features of complex, or otherwise intractable, systems.

In this mini-review the focus is diffusion NMR applications in bicelles; a novel biomembrane mimetic system increasingly employed in NMR studies of membrane-associating molecules (*2–7*) and as an orienting medium for NMR structural studies of soluble proteins and nucleic acids (*8–11*). Like any good membrane mimetic, bicelles provide an environment mirroring the lipid bilayer structural foundation of biological membranes and thus encourage the adoption by membrane-bound species of their proper functional form. However, it is the propensity of bicelles to align in a magnetic field, and the enhanced NMR spectral resolution that this engenders, that is the ultimate source of their ever increasing popularity; a popularity evident from the ongoing effusion of reviews of bicelle properties and applications (*12–23*). Notwithstanding their popularity, certain key questions regarding fundamental bicelle properties remain unresolved. And because of their broad utility, new bicelle compositions continue to be introduced (*24*), while novel bicelle properties continue to emerge (*25–27*).

Here, after reviewing some fundamental properties of bicelles, an overview of the diffusion NMR experiment is provided, followed by an examination of its particulars as applied to magnetically-aligned bicelle systems in our laboratory. Of special interest will be the insights gleaned from diffusion NMR of polymers incorporated into bicelles: insights regarding bicelle morphology, the resolution of controversies thus provided and the description of new properties. Of course, diffusion NMR is but one technique and the contributions of the multitude of other techniques that have informed the present understanding of bicellar systems will be acknowledged as they come to bear on the subject at hand.

Bicelle Fundamentals

Bicelles are self-assembled mixtures of short-chain and long-chain amphiphiles (*28*, *29*), typified by the canonical combination of dihexanoylphosphatidylcholine (DHPC) and dimyristoylphosphatidylcholine (DMPC) first reported by Sanders and Schwonek (*30*). As shown in Figure 1, DMPC, being roughly cylindrical in shape, on its own in water assembles into a bilayer structure such that its hydrophobic tetradecyl chains are sequestered away from water in the bilayer interior, while its polar phosphocholine headgroup occupies the interface between the hydrophobic interior and the aqueous bathing medium. To eliminate the exposure of hydrophobic acyl chains at the edge of the bilayer to water, the DMPC bilayer assembly vesiculates into a macroscopically spherical morphology. DHPC, in contrast, being roughly conical in shape due to its shorter acyl chains, prefers a highly curved, micellar assembly. Mixtures of DMPC and DHPC, however, assemble into single bilayer-thickness DMPC-rich lamellar sheets stabilized by a DHPC-rich coating along the edge regions. Since the DMPC tetradecyl acyl chains at the edge regions are masked from water by the coating of DHPC, there is no drive to vesiculate, and the resulting morphology is macroscopically planar. Because bicelles are self-assembled structures, their morphology is subject to both compositional and environmental influences, and exhibits a plasticity that is at once both beguiling and bedeviling.

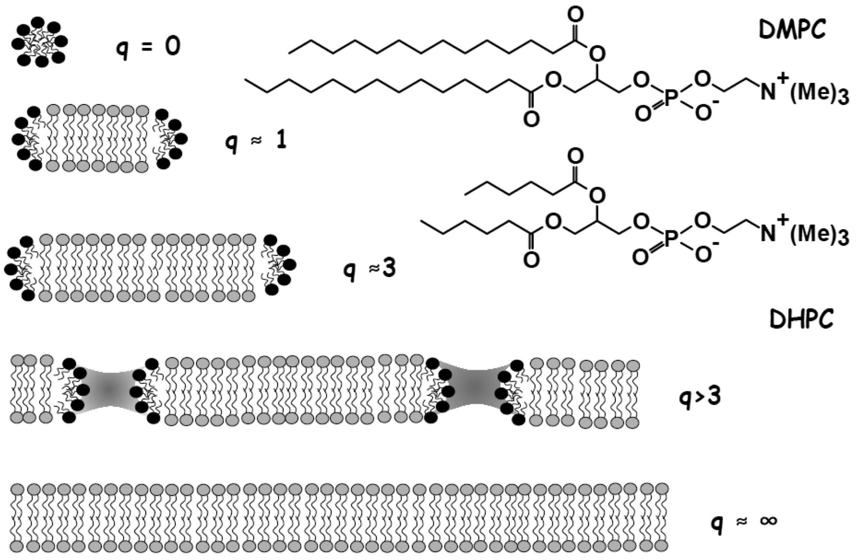

Figure 1. Schematic of the morphological evolution of bicellar self-assemblies as a function of the molar ratio q = DMPC/DHPC. Pure DHPC (black) forms micelles, while pure DMPC (gray) forms lamellae. Mixtures of the two form disks at low q, or perforated lamellae at higher q, with DHPC occupying curved edge regions while DMPC forms a planar bilayer.

The current consensus understanding of bicelle morphology is the result of studies using a host of physical techniques including electron microscopy (EM) (*31–33*), fluorescence spectroscopy (*34*), NMR (*35–38*), small angle X-ray scattering (SAXS) (*39*) and small angle neutron scattering (SANS) (*19*, *25*, *26*, *39–42*). A major influence on this morphology is the molar ratio of long-chain to short-chain amphiphiles, i.e., DMPC / DHPC, typically given the designation “q”. As illustrated in Figure 1, at low q bicelles adopt a discoidal morphology with DHPC populating the highly curved outer edge regions encircling a DMPC-rich planar bilayer disc, as per the “ideal” bicelle model (*43*), and in close analogy to the discoidal amphiphilic self-assemblies described and characterized by Reeves and co-workers in the 1970’s (see (*44*) for a review of this early work). With increasing q, the morphology evolves towards a perforated lamellar structure having dimensions far larger than envisaged by the ideal bicelle model and wherein DHPC populates the highly curved inner edges of toroidal perforations decorating the DMPC-rich bilayer lamella.

From an NMR perspective, bicelles should be regarded as “soft” materials, self-assembled as the result of an accumulation of otherwise weak interactions, and retaining, therefore, considerable freedom of molecular vibrational, rotational and translational motion. Because of the constraints imposed by the planar bilayer structure, the motional averaging is anisotropic, so that an NMR spectrum obtained from bicelles will be influenced by residual anisotropic, i.e., orientation-dependent, interactions such as those arising from chemical shift, or dipolar or quadrupolar interactions. Both the size of any such residual orientation-dependent interactions and the distribution of orientations across the sample will influence the NMR spectrum. When there is a random distribution of bicelle orientations across the sample a so-called powder spectrum results, as shown in Figure 2A for the case of the ^{31}P NMR spectrum of DMPC / DHPC bicelles at a temperature below the DMPC gel-to-liquid-crystalline phase transition temperature ($T_m \sim 25^0$C) where bicelles cannot magnetically align. The width of the powder spectrum $\Delta\sigma = \sigma_{\|} - \sigma_{\perp}$ reflects the residual ^{31}P chemical shift anisotropy difference between the extrema of the parallel, $\sigma_{\|}$, and perpendicular, $\sigma_{\perp}$, orientations of the phospholipid long axis (and bilayer normal) relative to the direction of the magnetic field. The line shape observed reflects the powder distribution of bicelle orientations between those extrema. Because DHPC resides in highly curved edge regions, it experiences effectively isotropic motional averaging and hence exhibits an isotropically narrow ^{31}P NMR resonance.

Magnetic alignment of bicelles becomes possible once the temperature is raised above the T_m of DMPC so that the self assembly becomes flexible and able to reorganize. Such spontaneous magnetic alignment of amphiphilic self-assembled bilayers was first reported by Lawson and Flautt in 1967 (*45*). It is the interaction between the magnetic field and the magnetic susceptibility anisotropy of the self-assembly that drives the magnetic alignment (*46*). Individual amphiphiles generally possess only a small negative magnetic susceptibility anisotropy, but when assembled into a bilayer, and aided by cooperative interactions between neighbouring assemblies, the volume magnetic susceptibility anisotropy is sufficient to overcome thermal fluctuations.

For DMPC / DHPC bicelles the spontaneous, so-called negative, alignment is such that the normal to the bilayer plane lies perpendicular to the magnetic field direction. As shown in Figure 2B, the resulting ^{31}P NMR resonance now consists of a narrow resonance having a frequency corresponding to $\sigma_{\perp}$, reflecting the narrow distribution of alignments about the direction perpendicular to the magnetic field.

In the presence of certain membrane-associating species having intrinsic positive magnetic susceptibility anisotropy the direction of bicelle alignment is such that the bilayer normal lies parallel to the magnetic field – the so-called positive alignment. The pioneering work of Reeves and co-workers demonstrated that simple variations in the counterion composition of the electric double layer could induce a “flip” from the negative to the positive alignment (*44*). For bicelles, such a “flip” to the positive alignment was first reported by Prosser and co-workers (*47–50*) who added lanthanides which bind to the bicelle surface. Subsequently, the same positive alignment was shown to occur upon incorporating phosphatidylcholines containing biphenyl groups (*51–53*), or peptides having phenyl ring side chains (*54*), or lipophilic aromatic compounds (*55*). As illustrated in Figure 2C, the resulting ^{31}P NMR resonance now consists of a narrowed resonance having a frequency corresponding to σ‖, reflecting the narrow distribution of alignments about the direction parallel to the magnetic field.

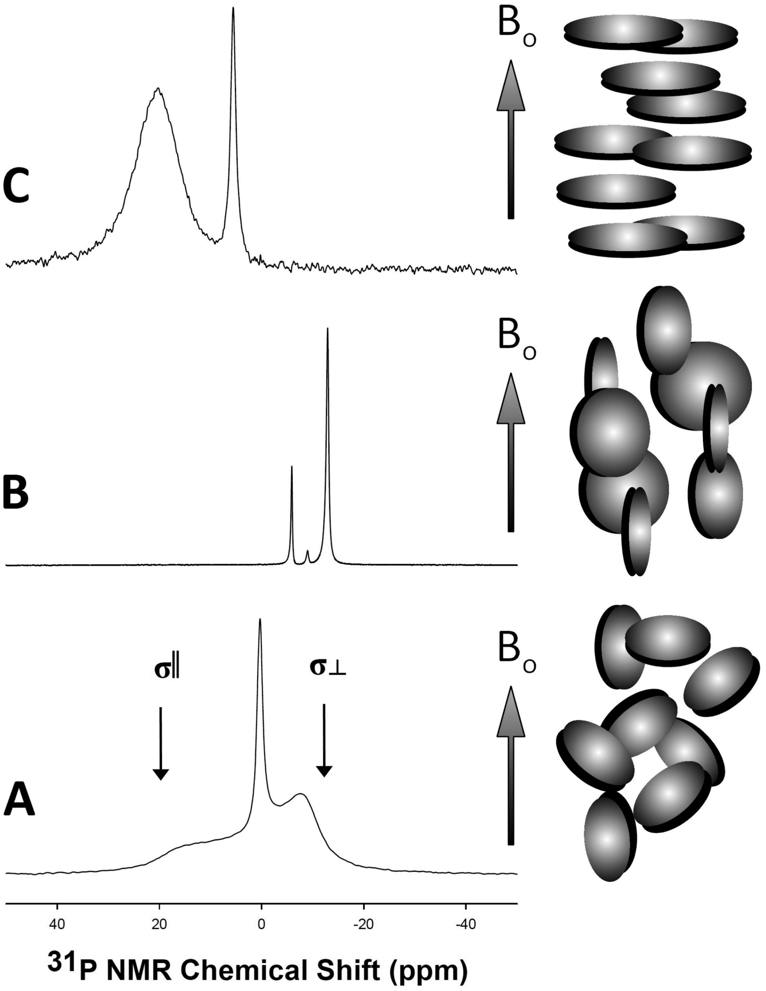

Figure 2. Magnetic alignment of bicelles and corresponding ^{31}P NMR spectra. (A) At temperatures below the Tm of DMPC the bicelles are randomly aligned. (B) At T > Tm, spontaneous negative magnetic alignment can occur. (C) At T > Tm upon addition of lanthanides, like Yb^{3+}, positive magnetic alignment results. The paramagnetic Yb^{3+} ions also cause NMR line broadening. Spectrum (B) was adapted from Soong and Macdonald (159). Spectra (A) and (C) were provided courtesy of Hannah Morales (personal communication).

It is this ability to align in a magnetic field, and the consequently enhanced resolution relative to powder-type NMR spectra, while still manifesting orientation-dependent interactions, that have made bicelles so popular as biomembrane mimetics for solid state (*56–76*) and solution state (*77–82*) NMR structural studies of membrane proteins and membrane associating molecules (*83–95*), and as an orienting medium for solution state NMR structural studies of soluble proteins and nucleic acids (*96–108*).

This very popularity has engendered continuing re-examinations of bicelle morphology, new aspects of which continue to emerge, along with reports of novel bicelle compositions with enhanced properties. For example, both SANS (*25*, *26*) and cryo-TEM (*32*) methods indicate that the morphology of neutral DMPC / DHPC bicelles is actually a ribbon-like aggregate which converts to a smectic phase upon addition of a negatively-charged amphiphile like phosphatidyglycerol. A further example concerns the location of DHPC, originally believed to be confined to highly-curved edge regions, but now recognized to be miscible with DMPC and to reside partly within the planar bilayer region (*109*). Most recently, bicelles having DHPC replaced with the detergent Triton X100 (*24*) have been reported to yield assemblies with enhanced structural features.

The remainder of this mini-review will highlight the contributions of diffusion NMR studies from our laboratory to the description of bicelle structure, to the resolution of certain controversies regarding their morphology, and our use of bicelles as a platform for diffusion NMR studies of lateral diffusion within and between lipid bilayers. It will commence with a review of diffusion NMR fundamentals, as follows.

Diffusion NMR Fundamentals

Self-diffusion is the thermally-generated centre-of-mass translational motion occurring in the absence of a concentration gradient. For isotropic diffusion of a spherical object of hydrodynamic radius R_H in an isotropic medium of viscosity η, the diffusion coefficient is given by the Stokes-Einstein equation,

$$D = \frac{k_B T}{6\pi\eta R_H}$$

where k_B is the Boltzmann constant and T is the absolute temperature.

Most generally, however, diffusion will be anisotropic so that the diffusion coefficient is properly described in terms of a second-rank symmetric tensor,

$$D = \begin{vmatrix} D_{xx} & D_{yx} & D_{zx} \\ D_{xy} & D_{yy} & D_{zy} \\ D_{xz} & D_{yz} & D_{zz} \end{vmatrix}$$

requiring the determination of six independent tensor components D_{ij} to completely specify the diffusion coefficient (*110*).

For the special case of lateral diffusion within a planar bilayer membrane, or diffusion confined between two parallel plates, only two independent diffusion tensor components need be considered: $D_{\|}$ and $D_{\perp}$ corresponding to diffusion parallel and perpendicular, respectively, to the direction of the bilayer normal (*111*, *112*), as shown schematically in Figure 3. Consequently, the diffusion tensor is given by,

$$D = \begin{vmatrix} D_{\perp} & 0 & 0 \\ 0 & D_{\perp} & 0 \\ 0 & 0 & D_{//} \end{vmatrix}$$

where $D_{\perp}$ is the diffusion coefficient within, or along the direction of, the plane of the lipid bilayer membrane.

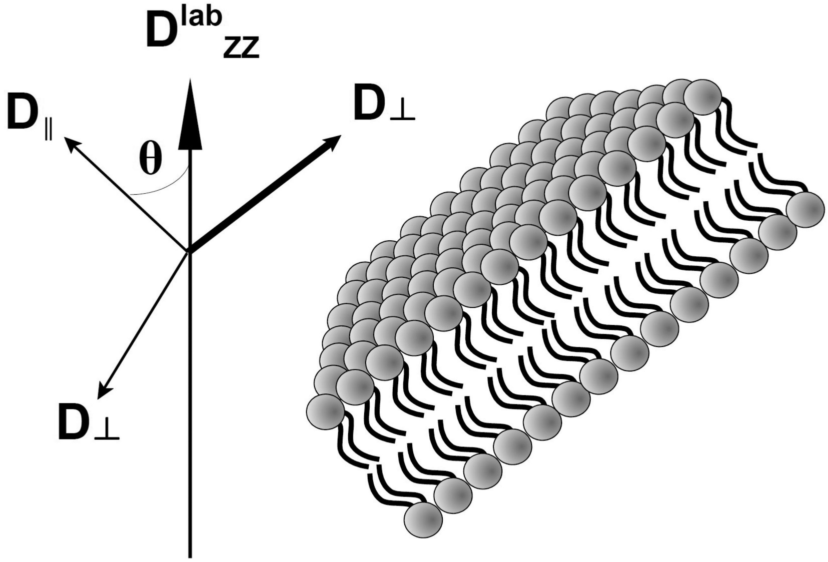

Figure 3. The diffusion tensor in the membrane frame of reference, relative to the laboratory frame of reference as defined by the magnetic field gradient direction, here assumed to lie parallel to the static magnetic field.

Techniques for measuring membrane diffusion abound, with fluorescence-based methods such as fluorescence recovery after photobleaching (FRAP), fluorescence correlation spectroscopy (FCS) and single particle tracking (SPT) being the most sensitive and widely employed. Obviously, fluorescence techniques require the presence of an observable fluorophore attached to the species of interest. NMR methods for measuring membrane diffusion do not necessarily require specific isotropic enrichment with an NMR sensitive nucleus. They may be divided broadly into those based on exchange in the presence of orientation-dependent interactions and those based on the application of field gradients to confer spatial sensitivity. The latter will be the specific focus of the following discussion.

Pulsed field gradient (PFG) diffusion NMR was introduced more than four decades ago by Stejskal and Tanner in their now classic article (*110*). Their original spin echo PFG NMR experiment is often replaced by the stimulated echo

(STE) PFG NMR sequence (*113*) shown schematically in Figure 4, where the diffusion time, Δ, is limited only by the longitudinal relaxation time, T_1, rather than the transverse relaxation time, T_2, which limits the diffusion time in the spin echo case: an advantage when, as is often the case, $T_1 > T_2$. During the evolution period between the first and the second 90^0 radio frequency (rf) pulse the nuclear spins precess in the transverse plane, acquiring a phase angle proportional to their relevant interaction Hamiltonian, i.e., chemical shift, scalar coupling, dipolar coupling, or quadrupolar coupling. The second 90^0 rf pulse places the spin magnetization along the z-axis where it may be stored for a duration $\tau_1 < T_1$. The third 90^0 rf pulse returns the spin magnetization to the transverse plane where a stimulated echo forms after a time τ_2. The experiment is rendered sensitive to diffusion by applying gradient pulses of amplitude g (T m^{-1}) and duration δ (s) during the evolution periods following the first and third rf pulse. The gradient pulse induces an additional phase shift of angle $\varphi_i = \gamma g \delta z_i$, where γ (rad T^{-1} s^{-1}) is the magnetogyric ratio and z_i is the position of an individual nuclear spin along the direction of the applied field gradient, assumed to lie parallel to the static magnetic field. Thus, the first gradient pulse encodes the nuclear spins according to their position. If no diffusion occurs during the diffusion time Δ, then the second gradient pulse exactly decodes, i.e., reverses, the position-dependent phase shift due to the first gradient pulse and the stimulated echo forms with its amplitude unchanged. If diffusion occurs then the stimulated echo amplitude is reduced as per,

$$I = I_o \exp\left(\frac{-2\tau_2}{T_2}\right) \exp\left(\frac{-\tau_1}{T_1}\right) \exp\left[-D(\gamma g \delta)^2 (\Delta - \delta/3)\right]$$

where D is the diffusion coefficient along the direction of the applied field gradient. Experimentally, either the gradient pulse duration δ, or its amplitude g, or the diffusion time Δ, is varied progressively. For the case of simple Gaussian diffusion, a semi-log plot of I/I_o versus $k=(\gamma g\delta)^2(\Delta-\delta/3)$ produces a linear decay, assuming constant τ_1 and τ_2, with a slope proportional to the diffusion coefficient.

An in-depth analysis of the theory underlying the PFG NMR experiment is beyond the scope of this mini-review, but the reader interested in greater detail may refer to several authoritative reviews (*114–117*). Since its introduction, the basic PFG NMR experiment has been greatly refined as techniques have been introduced to surmount problems such as the presence of background gradients (*118*), or convection (*119*), or the need for solvent suppression (*120*). In our laboratory, for example, we find it particularly useful to employ a slice-selection strategy (*121–123*) to avoid the effects of non-linear field gradients.

For simple Gaussian diffusion the observed diffusive decay described above is linear with *k* while the observed diffusion coefficient is independent of the diffusion time Δ. There exist many situations, however, in which the diffusive decay is non-linear while the measured diffusion coefficient depends on the diffusion time. Such non-Gaussian diffusion behavior typically involves complex heterogeneous systems wherein centre-of-mass diffusion is confined due to morphological constraints (*124–126*). Indeed, it is in exactly such situations that the PFG NMR diffusion experiment can prove advantageous in extracting morphological details.

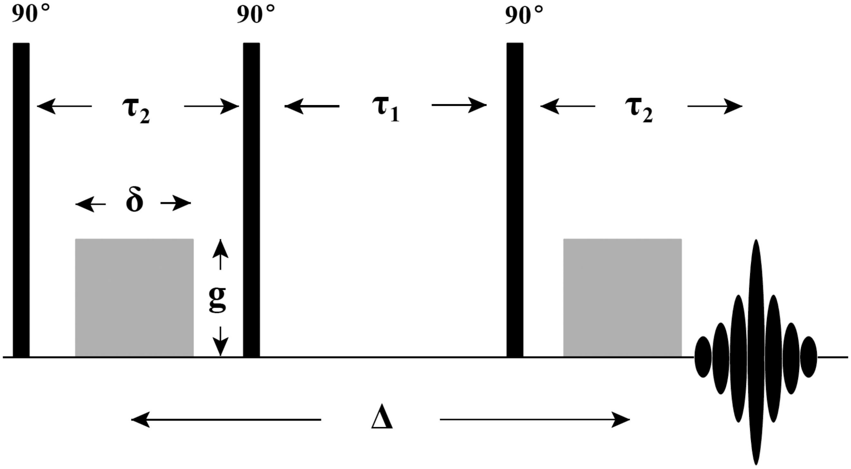

Figure 4. The stimulated echo pulsed field gradient NMR pulse sequence introduced by Tanner (113) for measurement of molecular diffusion. Black bars represent radio-frequency pulses, while grey rectangles represent field gradient pulses. See the text for further details.

Diffusion NMR in Lipid Bilayer Membranes

When applied to lipid bilayer membranes the PFG NMR experiment encounters two fundamental difficulties. First, due to residual anisotropic interactions, and dipolar interactions especially, the NMR resonances in lipid bilayers are typically broad, which produces rapid loss of coherence during the evolution times in a PFG NMR sequence and consequent loss of signal. Second, in a normal spherical lipid bilayer vesicle there is a powder distribution of local bilayer normal orientations and this complicates considerably the extraction of a diffusion coefficient from any observed intensity decay.

One means to overcome the broad resonance problem is to combine magic angle spinning (MAS) with field gradients applied co-directional with the spinning axis (*127*). MAS produces line narrowing while the gradient configuration ensures that all nuclear spins experience an identical gradients strength throughout a rotor cycle. Gawrisch and co-workers have employed this approach to considerable effect in their studies of the lateral diffusion of various membrane-associating compounds (*128–134*). In such measurements cognizance must be taken of the need to correct the diffusive decay for the powder distribution of bilayer orientations within the sample, and a further correction made for the radius of curvature of the bilayers as it affects the apparent diffusion coefficient (*128*).

One means to overcome the distribution of bilayer orientations problem is to macroscopically align lipid bilayers between planar solid supports. Lindblom and Wennerström (*135*) first used this strategy in lateral diffusion measurements, while Lindblom and Öradd have been its principal proponents ever since, reporting, for example, the characterization of domain composition and properties in various binary and ternary lipid mixtures (*112*, *136–140*). For such planar supported lipid bilayers there is a single bilayer orientation across the entire sample. The diffusion coefficient extracted from a plot of Ln I/Io versus k depends, however, on the angle θ defining the orientation of the bilayer normal relative to the direction of the applied field gradient as per (*111*, *112*)

$$D_{zz}^{lab} = D_{\perp}\sin^2\theta + D_{\parallel}\cos^2\theta$$

where the geometry is shown in Figure 3. In order to minimize the line broadening problem, the planar aligned lipid bilayer is placed such that the bilayer normal is at an orientation of 54.74^0 relative to the direction of the static magnetic field (assumed to be co-linear with the field gradient direction). At the so-called magic angle $\theta=54.74^0$ residual line broadening effects, including in particular for ^{1}H NMR measurements dipolar broadening, disappear. Since for molecular species confined within a planar lipid bilayer milieu $D_{\perp} >> D_{\parallel}$, the cosine term in the above equation can be ignored and the experiment measures a scaled lateral diffusion coefficient $D_{zz}^{lab} = 0.667\ D_{\perp}$.

Another solution to the distribution of bilayer orientations problem involves the use of magnetically-aligned bicelles. As may be ascertained from inspection of Figure 2, for negatively magnetically-aligned bicelles, where $\theta=90^0$, it follows that $D_{zz}^{lab} = 0.667\ D_{\perp}$, so the experiment measures directly the lateral diffusion coefficient of any NMR-observable membrane-associated species. On the other hand, for positively magnetically-aligned bicelles, where $\theta=0^0$, it follows that $D_{zz}^{lab} = D_{\parallel}$, so the experiment measures only transbilayer diffusion, i.e., of soluble species. The latter is a function, principally, of the number and size of any DHPC-rich perforations in the bicellar lamellae, as will be discussed in a subsequent section.

Neither orientation, however, eliminates the line width problem. In fact, for the STE PFG ^{1}H NMR sequence, the residual dipolar broadening in magnetically-aligned bicelles is sufficient to render most lipid resonances undetectable due to loss of coherence during the evolution periods. Nevertheless, instances abound in which, due to inherently near-isotropic motional averaging, the resulting narrow resonances can be used for lateral diffusion measurements.

The first demonstration of this possibility involved a PEGylated lipid incorporated into negatively magnetically-aligned bicelles (*141*). PEGylated lipids consist of a water-soluble poly(ethylene glycol), i.e., PEG, group covalently attached to the polar head group of a lipid moiety such as dimyristoylphosphatidylethanolamine (DMPE). The DMPE intercalates into a lipid bilayer, leaving the PEG group displayed at the aqueous interface, thereby effectively grafting the polymer to the lipid bilayer surface. PEGylated lipids are used in the fabrication of "stealth" liposomes for drug delivery applications (*142*), where the steric barrier created by the PEG coating at the liposomal surface delays liposome clearance by the reticulo-endothelial system. In bicelles, PEGylated lipids enhance bicelle stability, again by virtue of steric stabilization

(*143*). Marsh et al (*144*) have recently reviewed the voluminous research into the physicochemical properties of these enormously useful bio-compatibilizing agents. Of particular virtue for the purposes of diffusion NMR measurements is the fact that essentially all of the protons of the ethylene oxide (EO) units of which PEG is composed are equivalent, while the EO units undergo rapid and facile rotational isomerizations such that, overall, even rather large PEG species, even when attached at a surface, exhibit a single, nearly isotropically narrow ^{1}H NMR resonance.

A typical series of STE PFG ^{1}H NMR spectra as a function of *k* for DMPC / DHPC negatively magnetically aligned bicelles containing DMPE-PEG 2000 is shown in Figure 5. Proton resonances from the DMPC and DHPC are more-or-less absent due to their short transverse relaxation time relative to the transverse evolution times. The remaining significant proton resonances are those from water and the EO protons of the PEGylated lipid. The water resonance decays rapidly with increasing *k* as expected for the rapid diffusion of such a small molecule. The EO proton resonance decays far more slowly as expected for a larger lipid molecule associated with the lipid bilayer.

The diffusion coefficients are extracted from the slope in plots of $Ln\ I/I_o$ versus $k=(\gamma g\delta)^2(\Delta-\delta/3)$ of the type shown in Figure 6. The water diffusion coefficient for the case shown in Figure 5 is 1.6 x 10^{-9} m^2s^{-1} indicating significantly (30%) slower diffusion than that of bulk water at the same temperature (*145*) the difference being attributable to the population of lipid bilayer surface-bound water in fast exchange with bulk water. Note that the water diffusion being measured here is along the direction of the two-dimensional channels lying between the "parallel plates" formed by the negatively magnetically aligned bicelles.

Figure 6 compares specifically the diffusive decays for DMPE-PEG 2000 and free, i.e., non-hydrophobically modified, PEG 2000, both incorporated into DMPC / DHPC bicelles which have been negatively magnetically aligned.

DMPE-PEG 2000 becomes intercalated into the lipid bilayers while free PEG 2000 resides within the aqueous interstices separating the bicelles. For DMPE-PEG 2000, the intensity decay over most of the range of *k* values is linear, i.e., monoexponential, indicating normal Guassian diffusion. (There is a small contribution at lower k values from an overlapping proton resonance that decays rapidly and is assigned to the choline methyl resonance of DHPC.) The lateral diffusion coefficient for 1 mole% (relative to DMPC) DMPE-PEG 2000 was 1.35 x 10^{-11} m^2s^{-1}. Increasing the DMPE-PEG 2000 content to 2 mole% reduced its lateral diffusion coefficient to 1.15 x 10^{-11} m^2s^{-1}. By comparison, the diffusion of free PEG 2000 present in the aqueous interstices between these bicelles, although hindered relative to PEG 2000 in bulk solution, was a factor of 30 times faster than that of DMPE-PEG 2000 and was essentially concentration independent.

Diffusion NMR and Bicelle Morphology

Given the basic themes described above, that diffusion NMR in magnetically aligned bicelle systems provides useful and facile membrane lateral diffusion measurements, the focus of the remainder of this article will concern the insights provided by such techniques regarding lateral diffusion of PEGylated lipids and bicelle morphology.

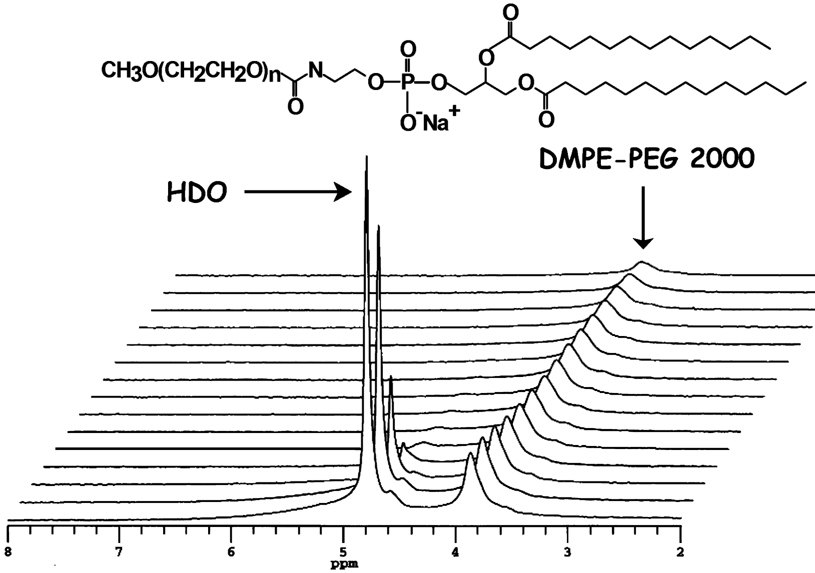

Figure 5. STE PFG ^{1}H NMR spectral series obtained at 35 ^{0}C with q = 4.5 DMPC/DHPC negatively magnetically aligned bicelles containing 1 mol% DMPE-PEG 2000 as a function of increasing gradient pulse duration in the STE PFG NMR pulse sequence. The HDO resonance decays rapidly as expected given the fast diffusion of water. The ethylene oxide (EO) resonance of DMPE-PEG 2000 decays much more slowly as expected for a large molecule bound to the lipid bilayer regions of the bicelle. Other resonances are largely absent due to their fast transverse relaxation. Adapted from Soong and Macdonald (141).

PEGylated Lipid Diffusion Obeys the Free Area Model

The free area model of lateral diffusion in membranes posits that, when the diffusing species is of a size comparable to that of the "solvent", in this case the solvent being the lipids of which the lipid bilayer is composed, lateral diffusion is dictated by the availability of "free area" within the lipid bilayer relative to the cross-sectional area occupied by the diffusant within the lipid bilayer (*146–148*). The fact that the lateral diffusion coefficient of DMPE-PEG 2000 at 1 mole% ($D = 1.35 \times 10^{-11}$ m^2s^{-1}) is virtually identical to values reported for DMPC at similar temperatures using FRAP (*149*) demonstrates the validity of this notion, since DMPE-PEG 2000 and DMPC will occupy virtually identical cross-sectional areas. The size of the extra-membranous PEG moiety is entirely secondary because it experiences only the aqueous bathing medium where the viscosity is a fraction of that of the lipid bilayer proper. Non-hydrophobically anchored PEG 2000 diffusing between bicelles diffuses at least an order of magnitude faster.

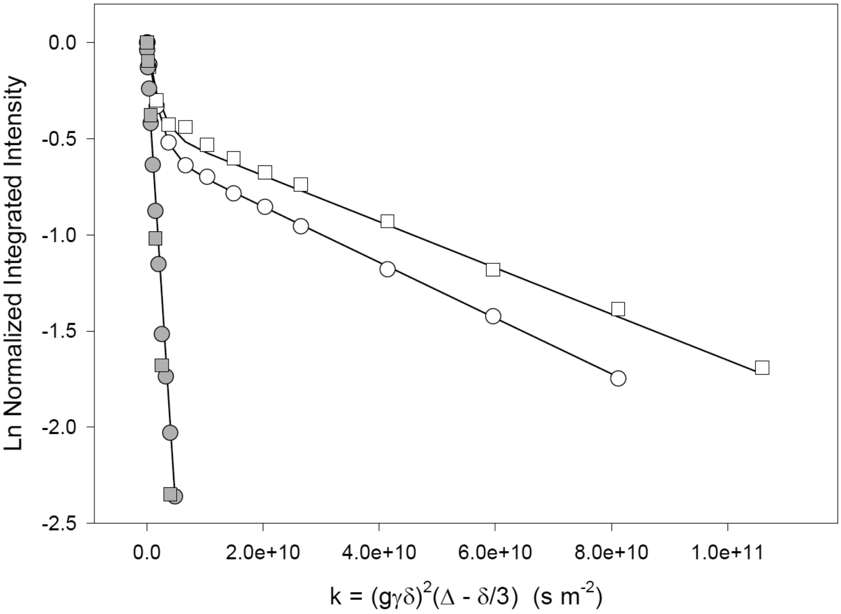

Figure 6. STE intensity decays as a function of DMPE-PEG 2000 concentration in STE PFG ^{1}H NMR spectra (35 ^{0}C) of magnetically aligned DMPC / DHPC (q = 4.5) bicelles plus various levels of either DMPE-PEG 2000 or free (i.e. non-hydrophobically-modified) PEG 2000. Open circles: 1 mole% DMPE-PEG 2000, $D_{PEG} = 1.35 \times 10^{-11}$ m^{2}s^{-1}. Open squares: 2 mole% DMPE-PEG 2000, $D_{PEG} = 1.15 \times 10^{-11}$ m^{2}s^{-1}. Closed circles: 1 mole% free PEG 2000, $D_{PEG} = 5.00 \times 10^{-10}$ m^{2}s^{-1}. Closed squares: 2 mole% free PEG 2000, $D_{PEG} = 5.23 \times 10^{-10}$ m^{2}s^{-1}. Adapted from Soong and Macdonald (141).

Membrane Crowding Slows Lateral Diffusion

The slower lateral diffusion measured for 2 mole% relative to 1 mole% DMPE-PEG 2000 can be attributed directly to the onset of surface crowding of the PEG groups. Polymer theory indicates that for unperturbed surface grafted polymers, a situation pertinent to the PEG group of DMPE-PEG 2000 incorporated into bicelles at the 1 mole% level, the shape of the polymer may be modeled as a half-sphere or "mushroom" extending out from the surface a distance equivalent to the Flory radius, R_F, and covering an area $A=\pi R_F^2$ (*150*). The Flory radius is calculated using the Flory equation, $R_F=N^{3/5}a$ where N is the number of monomer units and a is the length of one such monomer (*151*). For DMPE-PEG 2000, where $N=45$ and $a=3.5$ Å (*152*), $R_F=35$ Å and $A=3850$ Å^2. Hence, assuming DMPC occupies 60 Å^2, complete surface coverage with PEG is achieved at 1.6 mole% DMPE-PEG 2000. Thus, at 2 mole% DMPE-PEG 2000 overlap and entanglement of PEG groups has commenced, leading to crowding and slower lateral diffusion. The effect is exacerbated by further increasing the

DMPE-PEG 2000 concentration or by increasing the size of the PEG group of DMPE-PEG (*153*) Surface crowding is one reason postulated to explain the observation that lateral diffusion is generally slower in real biological membranes relative to model lipid bilayer membranes (*154–158*).

The Bicelle Disk versus Perforated Lamellae Question

For some time controversy percolated regarding whether bicelles should be regarded as disks encircled by a "bikini" of DHPC, or as lamellae perforated by toroidal holes lined with DHPC. The PFG NMR lateral diffusion measurements on DMPE-PEG 2000 demonstrate unequivocally that, at least under the particular conditions of q = DMPC / DHPC = 4.5 and T = 35 ^{0}C, bicelle morphology is that of a perforated lamella. Specifically, the fact that the semi-log diffusive intensity decays for the PEGylated lipid as shown in Figure 5 are linear with k and are diffusion time-independent is indicative of normal Gaussian diffusion, as opposed to, for example, restricted diffusion. This permits a straightforward calculation of the root-mean-square (rms) displacement undergone by the PEGylated lipid during the experimental diffusion time via the Einstein equation, $<z^2>^{1/2}=\sqrt{4D\Delta}$ yielding rms displacements on the order of 6 μm for the case D = 1.35 x 10^{-10} m^{2}s^{-1} and $\Delta = 600$ ms. This distance far exceeds the radial dimensions of 300 Å predicted for "ideal" diskoidal bicelles (*43*). Further, if truly diskoidal, given the operative diffusion coefficient and diffusion time, such bicelles should have lead to restricted diffusion behaviour in the PFG NMR diffusion experiment characterized by a slope of zero at large *k* values in plots such as those in Figure 5. One must conclude that the perforated lamellae model pertains.

DHPC Is Not Strictly Segregated to Regions of High Curvature

As originally conceived, in DMPC / DHPC bicelles DHPC was regarded as remaining completely segregated into regions of high curvature due to its immiscibility with DMPC. Recent ^{31}P NMR results have called this view into question, providing evidence that in fact DHPC does migrate from highly-curved regions into DMPC-rich planar regions at elevated temperatures (*109*). Corroborative evidence for the "mixed bicelle" model proposed by these researchers is provided by diffusion NMR experiments.

Examples of the type of ^{31}P NMR spectra obtained in our laboratory, which conform with those reported by Triba et al (*109*) and prompted their mixed bicelle model proposal, are shown in Figure 7 for the case of positively magnetically aligned bicelles as a function of q (at constant temperature 35 ^{0}C) and of temperature (at constant q = 4.5) (*159*). An essential observation is that the narrow resonance assigned to DHPC migrates towards the broader resonance assigned to DMPC as either temperature or q increases. The interpretation is that DHPC is in fast exchange between highly-curved regions (isotropic chemical shift) and planar regions (anisotropic chemical shift), so that the chemical shift observed for DHPC reflects its equilibrium distribution between the two environments. Given certain conservative assumptions (*109*, *159*), the ^{31}P NMR data may be used to calculate an effective ratio of planar-to-edge phospholipid populations, $q^*=(q+\omega^*)/(1-\omega^*)$, where q = DMPC/DHPC and $\omega^* = \omega_{DHPC} / \omega_{DMPC}$, with ω_{DHPC} and ω_{DMPC} being the observed chemical shifts for DHPC and DMPC, respectively.

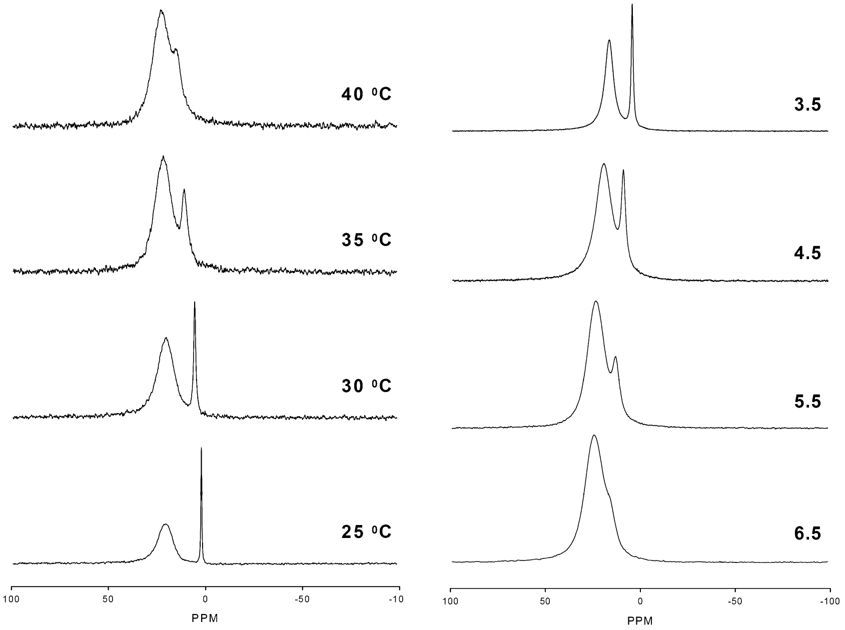

Figure 7. ^{31}P NMR spectra of (left) positively magnetically aligned bicelles composed of 100 / 5 / 1 (mol/mol/mol) DMPC / DMPG / DMPE-PEG2000 + DHPC in the ratio q = (DMPC+DMPG+DMPE-PEG2000) / DHPC = 4.5 as a function of temperature, and (right) at 35 °C as a function of q as indicated. All samples contained 25% w/w lipid/water and included ytterbium in the ratio Yb^{3+} / P = 1 / 75 to achieve positive magnetic alignment. Adapted from Soong and Macdonald (159).

If the mixed bicelle model is correct, then the number and/or size of DHPC-dependent perforations in the lamellae must decrease as the equilibrium distribution of DHPC shifts away from the edge, and towards the planar, environment. One means to test this prediction is to conduct diffusion NMR measurements of transbilayer diffusion in the same positively magnetically aligned bicelles. Transbilayer diffusion of a small molecule such as water will depend principally on the total surface area of perforations in the lamellar sheets which otherwise act as barriers to diffusion. This suggests a simple relationship between the reduced transbilayer water diffusion coefficient $D_{\|}/D_o$, (D_o being the bulk water diffusion coefficient at the corresponding temperature), and q*,

$$D_{\|}/D_o = f_{pore} = (1+A_{lam}/A_{perf})^{-1} = (1+Bq^*)^{-1}$$

where f_{pore} is the surface fraction of pores, A_{lam} and A_{perf} are the respective areas of lamellar and perforation regions, while B is a model dependent scaling factor relating the number of DHPC occupying perforations to the fractional area of perforations.

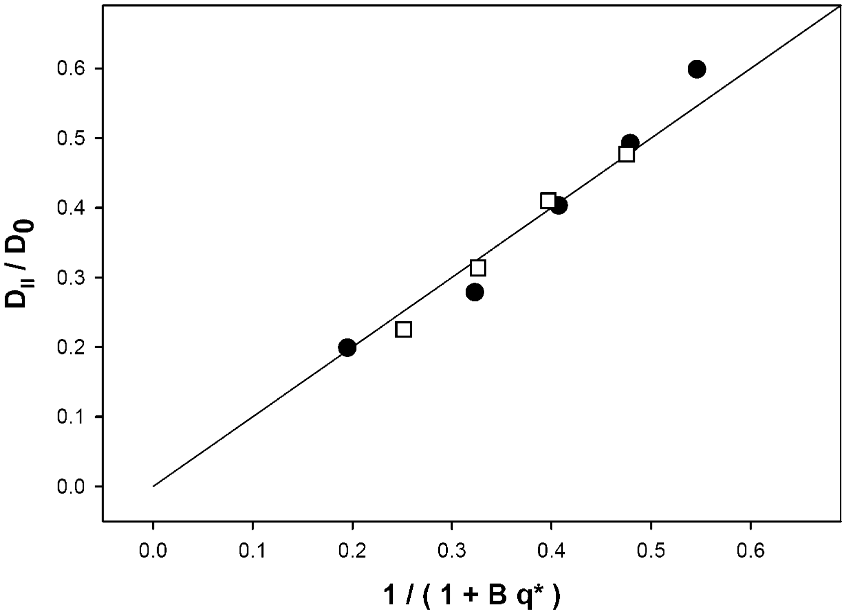

Figure 8. Reduced transbilayer water diffusion coefficient $D_{\|}/D_0$ as a function of the proportion of phospholipids q resident in planar versus edge regions of the bicelles. $D_{\|}/D_0$ was measured in positively magnetically aligned bicelles as a function of temperature at constant q = 4.5 (closed circles), and as a function of q at a constant temperature of 35 ^0C (open squares). q* was calculated from ^{31}P NMR spectra as described in the text and is assumed to be inversely proportional to the fractional surface area of bicellar perforations. For the line of best 1:1 fit shown in the figure, B=0.16. Adapted from Soong and Macdonald (159).*

As shown in Figure 8, there is excellent correspondence between the decrease in transbilayer water diffusion observed via diffusion NMR and the shift of the DHPC population away from curved regions and into planar regions as quantified via ^{31}P NMR. Note that transbilayer water diffusion actually decreases with increasing temperature, an effect that is counter-intuitive, but readily explicable in terms of the corresponding decrease in the total area of transbilayer perforations if the mixed bicelle model interpretation of the ^{31}P NMR observations is correct. The fact that both the temperature dependence and, separately, the q dependence of $D_{\|}/D_o$ obey the same q* dependence strongly suggests that the common element is indeed the fraction of DHPC available to form perforations, and strongly supports the mixed bicelle model of Triba et al (*109*).

An interesting aspect of the interdependence of q* and $D_{\|}/D_o$ concerns the fate of the water displaced as the DHPC-rich perforations decrease in size and/or number with increasing temperature (*160*). Specifically, one may interpret the reduced transbilayer water diffusion coefficient as directly reflecting the fractional surface area of lamellar perforation or pores, f_{pores}. Thus, Figure 8 indicates that the fractional surface area of pores decreases from roughly 60% at a temperature near the T_m of DMPC to as small as 20% at 40 ^{0}C. The volume of water thus displaced may be estimated using

$$\Delta V_{bilayer} \,/\, unit\ area = (d_B f_{pore})_{final} - (d_B f_{pore})_{initial}$$

where d_B is the bilayer thickness at a given temperature as determined from SANS (*160*).

The same SANS measurements (*160*) show that in such bicelles, as in lipid bilayers in general, d_B decreases with increasing temperature due to the corresponding increase in the probability of *trans-gauche* isomerizations along the hydrocarbon chains of the phospholipids. However, SANS measurements also demonstrate that, unlike lipid bilayers in general, for bicelles the interlamellar spacing, *d*, increases with increasing temperature. It follows that the interstitial volume between adjacent bicelles must be increasing with increasing temperature. The change in interstitial volume may be estimated via:

$$\Delta V_{intersticial} \,/\, unit\ area = (d - d_B)_{final} - (d - d_B)_{initial}$$

The obvious question becomes whether the increase in interstitial volume matches the volume of water displaced by annealing of lamellar perforations with increasing temperature. In fact, we found that $\Delta V_{\mathrm{bilayer}} / \Delta V_{\mathrm{intersticial}} = 0.93$ using values of f_{pore} derived from diffusion NMR and values of *d* and d_B obtained from SANS (*160*).

A schematic summarizing the temperature dependence of bicelle morphology, as derived from the combination of SANS, ^{31}P NMR and diffusion NMR results, is provided in Figure 9. At a lower temperature, i.e., near the T_m of DMPC, DHPC resides almost exclusively within, and lines the inner highly-curved edges of, toroidal perforations decorating the DMPC-rich lamellar bicelles. With increasing temperature DHPC becomes more readily miscible with DMPC, and is able to migrate into the DMPC-rich lamellar regions. Consequently, the number and/or size of the toroidal perforations decrease, so that transbilayer water diffusion decreases correspondingly. Further, the water displaced by this temperature-dependent annealing of the perforations migrates into the interstitial spaces, thereby increasing the interlamellar spacing.

Water being a small molecule, its transbilayer diffusion depends principally on the fractional area of lamellar perforations. Hence, such measurements say little regarding the specific pore size or shape, assuming the pores are large relative to water. One possible means to investigate pore size would be to examine transbilayer diffusion of various size probe molecules in positively magnetically aligned bicelles. A good candidate for such probes would be PEG.

PEG Diffusion Confined Between Bicellar Parallel Plates

As a prelude to probing pore sizes in bicelles via measurements of transbilayer PEG diffusion, we first inspected PEG diffusion in negatively aligned bicelles (*161*). In this situation the adjacent bicellar lamellae will form a set of confining two-dimensional parallel-plate channels along which PEG may diffuse. Figure 10 A shows the PEG diffusion coefficients obtained via diffusion NMR for a series of

11 different molecular weight PEG varying from 200 to 20,000 Daltons, comparing results for PEG free in solution and confined between bicellar lamellae. For the case of a flexible random coil polymer free in solution in a good solvent, such as the case of PEG in water, *D* is expected to vary as $1/\sqrt{M_w}$. Thus, in a plot of *Log D* versus *Log N*, where *N* is the degree of polymerization, i.e., the number of EO units, the slope should be close to -0.5. As shown by the solid line, where the slope = -0.473, this expectation is fulfilled for free PEG. From such diffusion coefficients one calculates the hydrodynamic radius R_H via the Stokes-Einstein equation and, subsequently, the critical overlap concentration for a given polymer molecular weight (*162*). The PEG concentration used here (3.33 mg /ml) was well below the overlap concentration in all cases, so issues of polymer entanglement will not complicate the interpretation of the diffusion data.

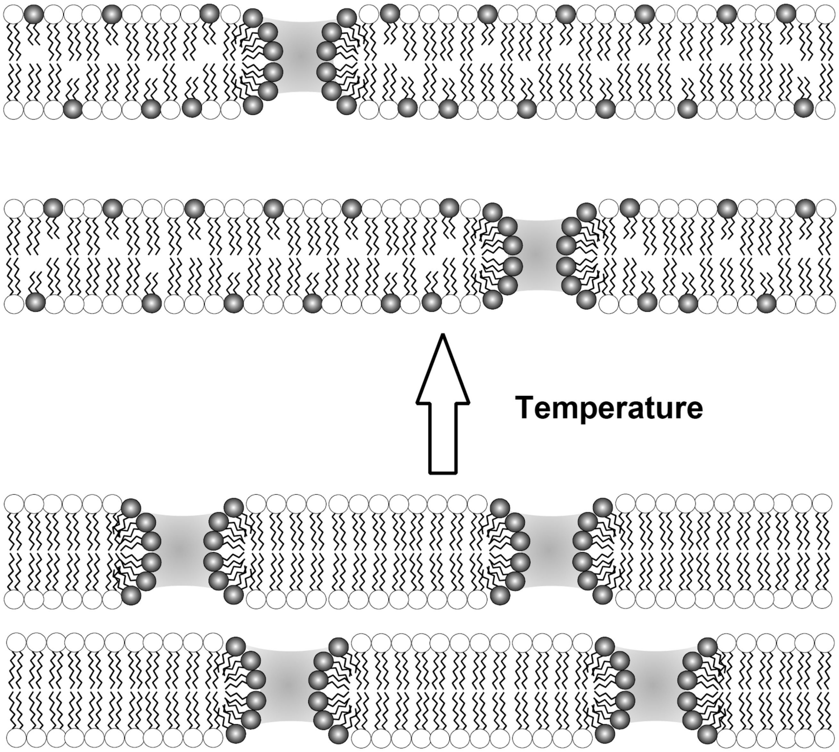

Figure 9. Schematic cross-section through a set of stacked perforated lamellae of DMPC (white) /DHPC (grey) bicellar mixtures, illustrating temperature effects on morphology. Adapted from Nieh et al (160).

As show in Figure 10 A, at the low end of the molecular weight range, bicellar-confined PEG diffusion parallels the size effects seen for free PEG, but is reduced by roughly 30% relative to free PEG; an effect that can be attributed to the approximately 30% viscosity increase in the interlamellar space. With increasing PEG size, there is a progressively greater hindrance of PEG diffusion in the confined relative to the free situation. This additional slowing of diffusion with larger PEG must be attributed to hindrance due to confinement effects.

For diffusion confined to a two-dimensional parallel-plate geometry, the important scalar is the ratio R_H/H, where H is the separation between the confining plates. For bicelles, H is the interlamellar spacing, i.e., the width of the aqueous interstices between adjacent bicellar lamellae. This may be determined via SANS and has been reported to equal 60 Å for bicelles of composition virtually identical to those investigated here (*41*, *163*). The free PEG diffusion data mentioned above serve to demonstrate that the ratio R_H/H will always be less than unity for the range of PEG sizes investigated here. De Gennes' scaling arguments (*164–166*) predict $D/D_o \sim (R_H/H)^{-2/3}$ for strong confinement regimes, defined by De Gennes as $R_H/H > 1$. In Figure 10 B, the normalized diffusion coefficient, D/D_o, where D_o is the diffusion coefficient of free PEG in aqueous solution, is plotted as a function of R_H/H in a log-log format. It is evident that strong confinement effects commence once $RH/H > 0.4$, i.e., far sooner than predicted by scaling theory, although the -2/3 exponent is born out. This reflects one of the challenges of scaling arguments; that of defining the cross-over point between bulk and confined behavior. Describing confinement effects on polymer diffusion in terms of the expected behavior of an equivalently-sized hard sphere, as modeled by Pawar and Anderson (*167*) and shown as the dashed line in Figure 10 B, fails utterly to capture the quantitative details of the diffusion of the flexible PEG in the two-dimensional confinement imposed by the bicellar lamellae. Newer simulations using a "Brownian dynamics combined with hydrodynamic interactions" approach (*168*) predict that strong confinement commences when $R_H/H > 0.5$ and that in this regime $D/D_o \sim (R_H/H)^{-2/3}$. This agrees well with the diffusion behavior observed in our laboratory for PEG confined between bicelles (*161*), as well as that of double-stranded DNA confined between parallel plates as reported by others (*169*).

Probing Bicellar Pore Size via Transbilayer PEG Diffusion NMR

The basic notion here is that smaller PEG will succeed in entering the lamellar perforations in bicelles and thus be able to diffuse in the transbilayer direction, while larger PEG will not. Consequently, the relationship between the PEG molecular weight and its transbilayer diffusion coefficient should reflect the size of the pores through which it must diffuse.

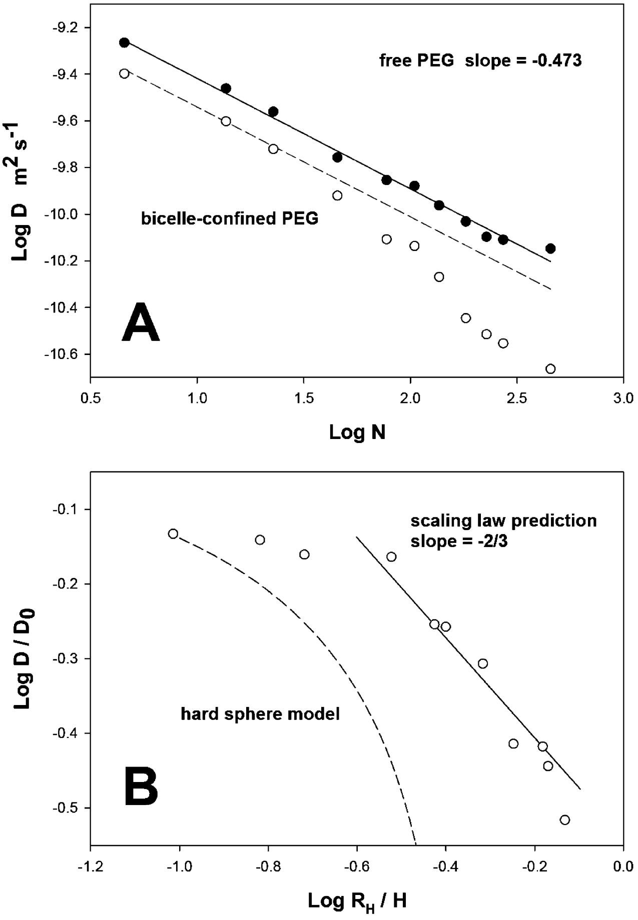

Figure 10. (A) Log - log plot of the PEG diffusion coefficient versus the degree of polymerization N. Closed circles: free PEG in aqueous solution (3.33 mg/ml, 35 ^{0}C). Open circles: PEG confined between the lamellae of negatively magnetically aligned q = (DMPC+DMPG) / DHPC = 4.5 bicelles containing 5 mol % DMPG (25 wt% lipid, 35 ^{0}C) in the presence of 3.33 mg ml^{-1} PEG . The solid line is from a regression analysis of the free PEG data and has a slope equal to -0.473. The dashed line has the same slope as the solid line but was scaled lower by 30% to account for the increased aqueous viscosity within the bicelle interlamellar aqueous space. (B) Log - log plot of the reduced diffusivity D/D_o, where D is the diffusion coefficient of the bicelle-confined PEG and D_o is that of the same molecular weight PEG free in aqueous solution, versus the ratio of the hydration radius to the confinement dimension R_H/H. R_H was calculated from the diffusion coefficient of PEG free in solution as per the Stokes-Einstein equation. H was take to be 60 Å (41, 163). The dashed line shows the results for the Pawar-Anderson equation (167) simulating a hard sphere confined between two walls. The solid line shows the de Gennes scaling prediction (166) wherein $D/D_o \sim (R_H/H)^{-2/3}$. Adapted from Soong and Macdonald (161).

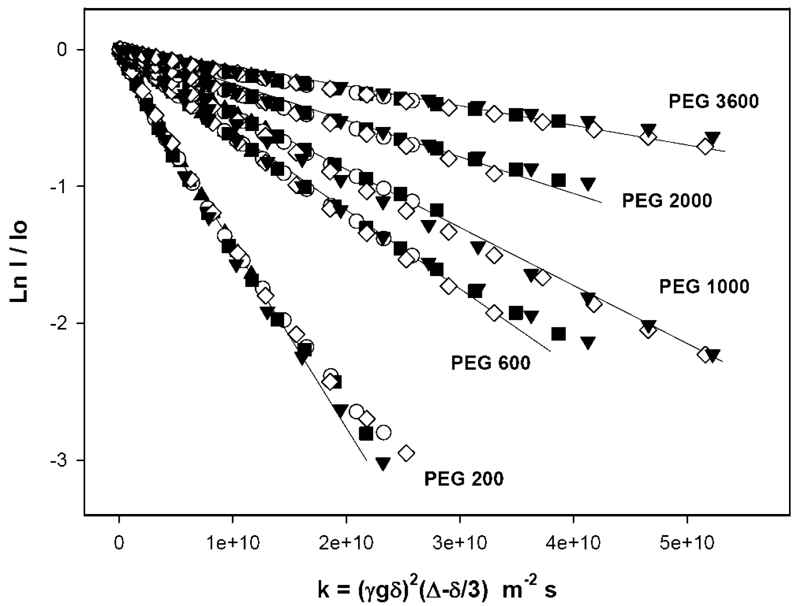

Figure 11. Normalized diffusive intensity decays from STE PFG ^{1}H NMR spectra (35 ^{0}C) of various molecular weight PEG (as indicated) confined within positively magnetically aligned bicelles. Symbols represent different diffusion times: 210 ms (closed triangles), 410 ms (open circles), 610 ms (closed squares), 810 ms (open diamonds), 1010 ms (closed inverted triangles). The solid lines are the fits used to obtain the diffusion coefficient. Adapted from Soong et al (170).

Figure 11 shows the diffusive decays obtained via STE PFG ^{1}H NMR of various size PEG in positively magnetically aligned bicelles (*170*). The bicelles act as a series of stacked, equally-spaced semi-permeable barriers to diffusion so that, in general, the apparent diffusion coefficient should be diffusion-time dependent, i.e., different diffusion coefficients would be measured for different experimental diffusion times. Only in Tanner's asymptotic limit that the rms displacement exceeds many multiples of the barrier spacing (roughly 100 Å in this case (*41*)) does the apparent diffusion coefficient become diffusion-time independent (*171*). As shown in Figure 11 this is indeed the case, in that for each size PEG the decays overlap for all different experimental diffusion times. Hence, the diffusion coefficient is obtained by simply fitting the slope in the usual fashion. The rms displacement calculated for PEG 4600, where $D \leq 1x10^{-11}$ m^{2}s^{-1}, is several microns, equivalent to several hundred barrier spacings, confirming that Tanner's asymptotic limit indeed should apply.

The profound decrease in the transbilayer diffusion coefficient with increasing PEG size is illustrated in Figure 12, where the reduced transbilayer diffusion coefficient, $D_{\|}/D_o$, is plotted as a function of the corresponding hydrodynamic radius R_H. D_o is the diffusion coefficient of the particular PEG free in solution (see Figure 10 A) from which RH is derived via the Stokes-Einstein equation.

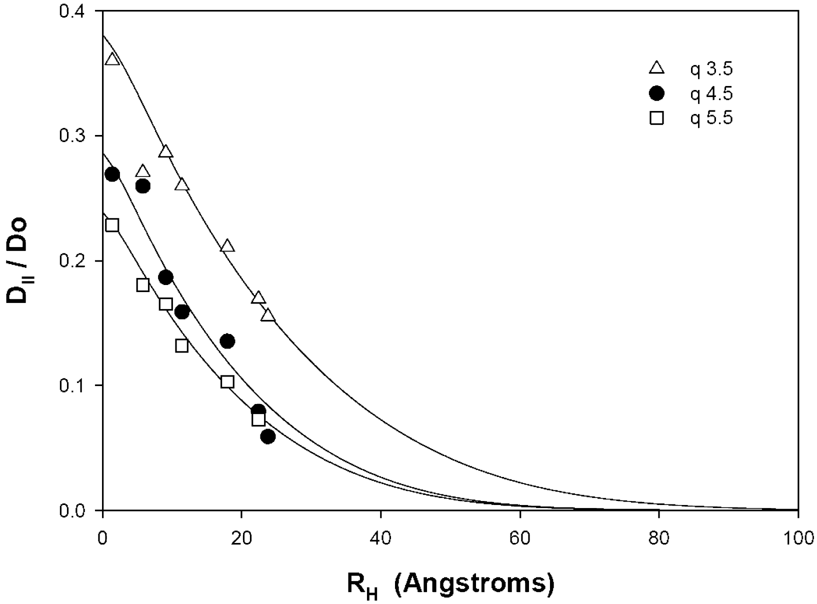

Figure 12. Reduced transbilayer diffusion coefficients $D_{\|}/D_o$ for various molecular weight PEG as a function of the corresponding Stokes-Einstein radius R_H. Data are shown for three q values: 3.5 (triangles), 4.5 (circles) and 5.5 (squares). Solid curves show the best-fit Davidson and Deen model (172, 173) predictions for the mean pore radii <Rp> as described in the text. Adapted from Soong et al (170).

To obtain pore size information from data such as those in Figure 12 requires an appropriate model for diffusion of flexible polymers through pores. In this regard, the Davidson and Deen hydrodynamic model is particularly useful (*172–174*), in that both steric exclusion from the pore and increased hydrodynamic drag within the pore are taken into consideration,

$$D_{\|}/D_o = f_{pore}\varphi K^{-1}$$

where φ is the partition coefficient accounting for the energy cost of inserting a polymer into a pore, K^{-1} quantifies the increased hydrodynamic drag experienced by the polymer inside the pore, and f_{pore} is the surface area fraction of pores as derived from transbilayer water diffusion measurements such as shown in Figure 8. Details regarding the derivation of the expressions for φ and K^{-1} are provided in the original references by Davidson and Deen (*172*, *173*) and the comprehensive review by Deen (*174*). The key point is their dependence on the ratio R_H/R_p, i.e., the size of the polymer to the pore radius.

Fitting the Davidson – Deen model to the transbilayer diffusion of PEG in positively aligned bicelles, as shown in Figure 12, yields values for the average pore radius for three different values of the ratio q = DMPC/DHPC. For the case q = 3.5, the best fit value of R_p is 165 Å, while for both q = 4.5 and 5.5, the best fit value yielded R_p equal to 125 Å. These experimentally-derived values for R_p

are consistently larger than those derived from static models, whether a diskoidal or lamellar morphology is assumed (*109*, *159*) and the trend with changing q is diametrically opposite. One possible factor contributing to this discrepancy is that real bicelles undergo fluctuations, both in-plane and out-of-plane, and such fluctuations can contribute to transbilayer diffusion (*175*). Static geometric models do not capture the effects of such fluctuations.

Conclusions and Future Propsects

Bicelles are a model system for membrane diffusion studies, while simultaneously providing a insights into bicelle morphology. Diffusion measurements have resolved certain controversies, but new aspects of bicelle morphological plasticity continue to emerge, more complex lipid compositions than the canonical DMPC/DHPC mixtures continue to be a focus of interest, and always one wishes to incorporate and investigate proteins. Thus, it seems likely that diffusion NMR in bicelles will continue to yield results of significance.

Attaching a PEG moiety to the diffusant of interest is one means by which to obtain a readily visible NMR resonance, which is a prerequisite for straightforward bicelle diffusion measurements via PFG NMR diffusion. PEGylation of virtually any chemical species of interest is now possible. The high internal mobility of the PEG group, even when effectively grafted to the membrane surface, is the property which renders PEG so useful for such measurements. But many membrane associating species, proteins in particular, exhibit regions of high internal mobility and thus may prove amenable to diffusion measurements even without PEGylation.

Bicelle morphology is still far from fully understood, as witness the nematic ribbon structure observed via SANS and PFG NMR for neutral, i.e., uncharged, bicelles, where diffusion is confined to an apparently one-dimensional path (*176*). The physical origin of this morphology is still obscure.

New bicelle compositions with improved alignment properties have been reported recently (*24*) but morpholigcal details are so far lacking. One composition of interest that has not yet been described in bicelles is that containing raft-forming lipids, which form domains and are of intense interest biologically. Indeed, domain formation in bicelles, other than segregation of DMPC and DHPC, has yet to be demonstrated convincingly. No doubt this has to do with the technical challenge of mixing together lipids which, by definition, prefer to demix from the common membranous milieu.

As for membrane-associating proteins, it seems likely that diffusion NMR in bicelles should be able readily to differentiate oligomerization states of membrane surface-associating peptides, where surface association may catalyze aggregation. As for the state of oligomerization of transmembrane helical proteins, however important biologically, diffusion NMR seems unlikely to provide useful measurements given the expected weak dependence of the lateral diffusion coefficient on the membrane cross-sectional area in the hydrodynamic size regime relevant to membrane proteins.

Finally, PFG NMR diffusion techniques may prove useful for the study of ligand-membrane protein association studies. Membrane proteins, such as G protein coupled receptors, are common drug targets. Thus, on might imagine that magnetically aligned bicelles containing reconstituted membrane proteins could serve as a platform for diffusion NMR studies of drug-membrane protein interactions.

Acknowledgments

The research described here was supported by grants from the Natural Sciences and Engineering Research Council (NSERC) of Canada. The author wishes to thank Hannah Morales for providing certain NMR spectra presented here.

References

1. Hahn, E. L. *Phys. Rev.* **1950**, *80*, 580–594.
2. Sanders, C. R., II; Landis, G. C. *J. Am. Chem. Soc.* **1994**, *116*, 6470–6471.
3. Sanders, C. R., II; Landis, G. C. *Biochemistry* **1995**, *34*, 4030–4040.
4. Struppe, J.; Komives, E. A.; Taylor, S. S.; Vold, R. R. *Biochemistry* **1998**, *37*, 15523–15527.
5. Whiles, J. A.; Brasseur, R.; Glover, K. J.; Melacini, G.; Komives, E. A.; Vold, R. R. *Biophys. J.* **2001**, *80*, 280–293.
6. Glover, K. J.; Whiles, J. A.; Wood, M. J.; Melacini, G.; Komives, E. A.; Vold, R. R. *Biochemistry* **2001**, *40*, 13137–13142.
7. Marcotte, I.; Dufourc, E. J.; Ouellet, M.; Auger, M. *Biophys. J.* **2003**, *85*, 328–339.
8. Tjandra, N; Bax, A. *Science* **1997**, *278*, 1111–114.
9. Vold, R. R.; Deese, A. J.; Prosser, R. S. *J. Biomol. NMR* **1997**, *9*, 329–335.
10. Boyd, J.; Redfield, C. *J. Am. Chem. Soc.* **1999**, *121*, 7441–7442.
11. Cavagnero, S.; Dyson, H. J.; Wright, P. E. *J. Biomol. NMR* **1999**, *13*, 387–391.
12. Sanders, C. R.; Hare, B. J.; Howard, K. P.; Prestegard, J. H. *Progr. Nucl. Magn. Reson. Spectrosc.* **1994**, *26*, 421–444.
13. Sanders, C. R.; Oxenoid, K. *Biochim. Biophys. Acta* **2000**, *1508*, 129–145.
14. Whiles, J. A.; Deems, R.; Vold, R. R.; Dennis, E. A. *Bioorg. Chem.* **2002**, *30*, 431–442.
15. Nevzorov, A. A.; Mesleh, M. F.; Opella, S. J. *Magn. Reson. Chem.* **2004**, *42*, 162–171.
16. Sanders, C. R.; Hoffmann, A. K.; Gray, D. N.; Keyes, M. H.; Ellis, C. D. *ChemBioChem* **2004**, *5*, 423–426.
17. De Angelis, A. A.; Jones, D. H.; Grant, C. V.; Park, S. H.; Mesleh, M. F.; Opella, S. J. *Methods Enzymol.* **2005**, *394*, 350–382.
18. Marcotte, I.; Auger, M. *Concepts Magn. Reson., Part A* **2005**, *24A*, 17–37.
19. Katsaras, J.; Harroun, T. A.; Pencer, J.; Nieh, M. P. *Naturwissenschaften* **2005**, *92*, 355–366.

20. Sanders, C. R.; Sönnichsen, F. *Magn. Reson. Chem.* **2006**, *44*, S24–S40.
21. Prosser, R. S.; Evanics, F.; Kitevski, J. L.; Al-Abdul-Wahid, M. S. *Biochemistry* **2006**, *45*, 8453–8465.
22. Poget, S. F.; Girvin, M. E. *Biochim. Biophys. Acta* **2007**, *1768*, 3098–3106.
23. Kim, H. J.; Howell, S. C.; Van Horn, W. D.; Jeon, Y. H.; Sanders, C. R. *Progr. Nucl. Magn. Reson. Spectrosc.* **2009**, *55*, 335–360.
24. Park, S. H.; Opella, S. J. *J. Am. Chem. Soc.* **2010**, *132*, 12552–12553.
25. Nieh, M. P.; Raghunathan, V. A.; Glinka, C. J.; Harroun, T. A.; Pabst, G.; Katsaras, J. *Langmuir* **2004**, *20*, 7893–7897.
26. Nieh, M.-P.; Raghunathan, V. A.; Glinka, C. J.; Harroun, T. A.; Katsaras, J. *Macromol. Symp.* **2005**, *219*, 135–145.
27. Nieh, M. P.; Raghunathan, V. A.; Pabst, G.; Harroun, T.; Nagashima, K.; Morales, H.; Katsaras, J.; Macdonald, P. M. *Langmuir* **2011**, *27*, 4838–4847.
28. Ram, P.; Prestegard, J. H. *Biochim. Biophys. Acta* **1988**, *940*, 289–294.
29. Sanders, C. R.; Prestegard, J. H. *Biophys. J.* **1990**, *58*, 447–460.
30. Sanders, C. R.; Schwonek, J. P. *Biochemistry* **1992**, *31*, 8898–8905.
31. Arnold, A.; Labrot, T.; Oda, R.; Dufourc, E. J. *Biophys. J.* **2002**, *83*, 2667–2680.
32. Van Dam, L.; Karlsson, G.; Edwards, K. *Biochim. Biophys. Acta* **2004**, *1664*, 241–256.
33. Van Dam, L.; Karlsson, G.; Edwards, K. *Langmuir* **2006**, *22*, 3280–3285.
34. Rowe, B. A.; Neal, S. L. *Langmuir* **2003**, *19*, 2039–2048.
35. Ottinger, M.; Bax, A. *J. Biomol. NMR* **1998**, *12*, 361–372.
36. Raffard, G.; Steinbruckner, S.; Arnold, A.; Davis, J. H.; Dufourc, E. J. *Langmuir* **2000**, *16*, 7655–7662.
37. Sternin, E.; Nizza, D.; Gawrisch, K. *Langmuir* **2001**, *17*, 2610–2616.
38. Boltze, J.; Fujisawa, T.; Nagao, T.; Norisada, K.; Saito, H.; Naito, A. *Chem. Phys. Lett.* **2000**, *329*, 215–220.
39. Luchette, P. A.; Vetman, T. N.; Prosser, R. S.; Hancock, R. E.; Nieh, M. P.; Glinka, C. J.; Krueger, S.; Katsaras, J. *Biochim. Biophys. Acta* **2001**, *1513*, 83–94.
40. Nieh, M. P.; Ginka, C. J.; Krueger, S.; Prosser, R. S.; Katsaras, J. *Langmuir* **2001**, *17*, 2629–2638.
41. Nieh, M. P.; Ginka, C. J.; Krueger, S.; Prosser, R. S.; Katsaras, J. *Biophys. J.* **2002**, *82*, 2487–2498.
42. Harroun, T. A.; Koslowsky, M.; Nieh, M.-P.; de Lannoy, C. F.; Raghunathan, V. A.; Katsaras, J. *Langmuir* **2005**, *21*, 5356–5361.
43. Vold, R. R.; Prosser, R. S. *J. Magn. Reson., Ser. B* **1996**, *113*, 267–271.
44. Forrest, B. J.; Reeves, L. W. *Chem. Rev.* **1981**, *81*, 1–14.
45. Lawson, K. D.; Flautt, T. J. *J. Am. Chem. Soc.* **1967**, *89*, 5489–5491.
46. Boroske, E.; Helfrich, W. *Biophys. J.* **1978**, *24*, 863–868.
47. Prosser, R. S.; Hunt, S. A.; DiNatale, J. A.; Vold, R. R. *J. Am. Chem. Soc.* **1996**, *118*, 269–270.
48. Prosser, R. S.; Hwang, J. S.; Vold, R. R. *Biophys. J.* **1998**, *74*, 2405–2418.
49. Prosser, R. S.; Bryant, H; Bryant, R. G.; Vold, R. R. *J. Magn. Reson.* **1999**, *141*, 256–260.
50. Prosser, R. S.; Shiyanovskaya, I. V. *Concepts Magn. Reson.* **2001**, *13*, 19–31.

51. Cho, G.; Fung, B. M.; Reddy, V. B. *J. Am. Chem. Soc.* **2001**, *123*, 1537–1538.

52. Tan, C.; Fung, B. M.; Cho, G. *J. Am. Chem. Soc.* **2002**, *124*, 11827–11832.

53. Loudet, C.; Manet, S.; Gineste, S.; Oda, R.; Achard, M.-F.; Dufourc, E. J. *Biophys. J.* **2007**, *92*, 3949–3959.

54. Picard, F.; Paquet, M. J.; Levesque, J.; Bélanger, A.; Auger, M. *Biophys. J.* **1999**, *77*, 888–902.

55. Sanders, C. R.; Schaff, J. E.; Prestegard, J. H. *Biophys. J.* **1993**, *64*, 1069–1080.

56. Sanders, C. R.; Landis, G. C. *Biochemistry* **1995**, *34*, 4030–4040.

57. Drechsler, A.; Separovic, F. *IUBMB Life* **2003**, *55*, 515–523.

58. Williamson, P. T. F.; Zandomeneghi, G.; Barrantes, F. J.; Watts, A.; Meier, B. H. *Mol. Membr. Biol.* **2005**, *22*, 485–496.

59. Triba, M. N.; Zoonens, M.; Popot, J. L.; Devaux, P. F.; Warschawski, D. E. *Eur. Biophys. J.* **2006**, *35*, 268–275.

60. De Angelis, A. A.; Howell, S. C.; Nevzorov, A. A.; Opella, S. J. *J. Am. Chem. Soc.* **2006**, *128*, 12256–12267.

61. Park, S. H.; De Angelis, A. A.; Nevzorov, A. A.; Wu, C. H.; Opella, S. J. *Biophys. J.* **2006**, *91*, 3032–3042.

62. De Angelis, A. A.; Opella, S. J. *Nat. Protoc.* **2007**, *2*, 2332–2338.

63. Nevzorov, A. A.; Park, S. H.; Opella, S. J. *J. Biomol. NMR* **2007**, *37*, 113–116.

64. Durr, U. H. N.; Yamamoto, K.; Im, S. C.; Waskell, L.; Ramamoorthy, A. *J. Am. Chem. Soc.* **2007**, *129*, 6670–6671.

65. Park, S. H.; Opella, S. J. *Protein Sci.* **2007**, *16*, 2205–2215.

66. Muller, S. D.; De Angelis, A. A.; Walther, T. H.; Grage, S. L.; Lange, C.; Opella, S. J.; Ulrich, A. S. *Biochim. Biophys. Acta* **2007**, *1768*, 3071–3079.

67. Mahalakshmi, R.; Franzin, C. M.; Choi, J.; Marassi, F. M. *Biochim. Biophys. Acta* **2007**, *1768*, 3216–3224.

68. Durr, U. H. N.; Waskell, L.; Ramamoorthy, A. *Biochim. Biophys. Acta* **2007**, *1768*, 3235–3259.

69. McKibbin, C.; Farmer, N. A.; Jeans, C.; Reeves, P. J.; Khorana, H. G.; Wallace, B. A.; Edwards, P. C.; Villa, C.; Booth, P. J. *J. Mol. Biol.* **2007**, *374*, 1319–1332.

70. Mahalakshmi, R.; Marassi, F. M. *Biochemistry* **2008**, *47*, 6531–6538.

71. Park, S. H.; Loudet, C.; Marassi, F. M.; Dufourc, E. J.; Opella, S. J. *J. Magn. Reson.* **2008**, *193*, 133–138.

72. Xu, C. Q.; Gagnon, E.; Call, M. E.; Schnell, J. R.; Schwieters, C. D.; Carman, C. V.; Chou, J. J.; Wucherpfennig, K. W. *Cell* **2008**, *135*, 702–713.

73. Daily, A. E.; Greathouse, D. V.; van der Wel, P. C. A.; Koeppe, R. E. *Biophys. J.* **2008**, *94*, 480–491.

74. Diller, A.; Loudet, C.; Aussenac, F.; Raffard, G.; Fournier, S.; Laguerre, M.; Grelard, A.; Opella, S. J.; Marassi, F. M.; Dufourc, E. J. *Biochimie* **2009**, *91*, 744–751.

75. Naito, A. *Solid State NMR* **2009**, *36*, 67–76.

76. Cui, T. X.; Canlas, C. G.; Xu, Y.; Tang, P. *Biochim. Biophys. Acta* **2010**, *1798*, 161–166.

77. Bocharov, E. V.; Pustovalova, Y. E.; Pavlov, K. V.; Volynsky, P. E.; Goncharuk, M. V.; Ermolyuk, Y. S.; Karpunin, D. V.; SchulgaA.A.; Kirpichnikov, M. P.; Efremov, R. G.; Maslennikov, I. V.; Arseniev, A. S. *J. Biol. Chem.* **2007**, *282*, 16256–16266.
78. Poget, S. F.; Girvin, M. E. *Biochim. Biophys. Acta* **2007**, *1768*, 3098–3106.
79. Wang, G. S. *Curr. Protein Pept. Sci.* **2008**, *9*, 50–69.
80. Lee, D.; Walter, K. F. A.; Bruckner, A. K.; Hilty, C.; Becker, S.; Griesinger, C. *J. Am. Chem. Soc.* **2008**, *130*, 13822–13823.
81. Hiller, S.; Wagner, G. *Curr. Opin. Struct. Biol.* **2009**, *19*, 396–401.
82. Kim, H. J.; Howell, S. C.; Van Horn, W. D.; Jeon, Y. H.; Sanders, C. R. *Prog. Nucl. Magn. Reson. Spectrosc.* **2009**, *55*, 335–360.
83. Sanders, C. R.; Landis, G. C. *J. Am. Chem. Soc.* **1994**, *116*, 6470–6471.
84. Struppe, J.; Komives, E. A.; Taylor, S. S.; Vold, R. R. *Biochemistry* **1998**, *37*, 15523–15527.
85. Losonczi, J. A.; Tian, F.; Prestegard, J. H. *Biochemistry* **2000**, *39*, 3804–3816.
86. Yu, K.; Kang, S.; Kim, S. D.; Ryu, P. D.; Kim, Y. *J. Biomol. Struct.* **2001**, *18*, 595–606.
87. Whiles, J. A.; Brasseur, R.; Glover, K. J.; Melacini, G.; Komives, E. A.; Vold, R. R. *Biophys. J.* **2001**, *80*, 280–293.
88. Glover, K. J.; Whiles, J. A.; Wood, M. J.; Melacini, G.; Komives, E. A.; Vold, R. R. *Biochemistry* **2001**, *40*, 13137–13142.
89. Marcotte, I.; Dufourc, E. J.; Ouellet, M.; Auger, M. *Biophys. J.* **2003**, *85*, 328–339.
90. Lindberg, M.; Biverstahl, H.; Graslund, A.; Maler, L. *Eur. J. Biochem.* **2003**, *270*, 3055–3063.
91. Biverstahl, H.; Andersson, A.; Graslund, A; Maler, L. *Biochemistry* **2004**, *43*, 14940–14947.
92. Ellena, J. F.; Moulthrop, J.; Wu, J.; Rauch, M.; Jaysinghne, S.; Castle, J. D.; Cafiso, D. S. *Biophys. J.* **2004**, *87*, 3221–3233.
93. Anderluh, G.; Razpotnik, A.; Podlesek, Z.; Macek, P.; Separovic, F.; Norton, R. S. *J. Mol. Biol.* **2005**, *347*, 27–39.
94. Dvinskikh, S. V.; Durr, U. H. N.; Yamamoto, K.; Ramamoorthy, A. *J. Am. Chem. Soc.* **2007**, *129*, 794–802.
95. Al-Abdul-Wahid, M. S.; Neale, C.; Pomes, R.; Prosser, R. S. *J. Am. Chem. Soc.* **2009**, *131*, 6452–6459.
96. Tjandra, N; Bax, A. *Science* **1997**, *278*, 1111–1114.
97. Vold, R. R.; Deese, A. J.; Prosser, R. S. *J. Biomol. NMR* **1997**, *9*, 329–335.
98. Bax, A.; Tjandra, N. *J. Biomol. NMR* **1997**, *10*, 289–292.
99. Clore, G. M.; Gronenborn, A. M.; Bax, A. *J. Magn. Reson.* **1998**, *133*, 216–221.
100. Ottiger, M.; Bax, A. *J. Biomol. NMR* **1999**, *13*, 187–191.
101. Fischer, M. W. F.; Losonczi, J. A.; Weaver, J. L.; Prestegard, J. H. *Biochemistry* **1999**, *38*, 9013–9022.
102. Markus, M. A.; Gerstner, R. B.; Draper, D. E.; Torchia, D. A. *J. Mol. Biol.* **1999**, *292*, 375–387.
103. Boyd, J.; Redfield, C. *J. Am. Chem. Soc.* **1999**, *121*, 7441–7442.

104. Cavagnero, S.; Dyson, H. J.; Wright, P. E. *J. Biomol. NMR* **1999**, *13*, 387–391.
105. Cornilescu, G.; Bax, A. *J. Am. Chem. Soc.* **2000**, *122*, 10143–10154.
106. Schwalbe, H.; Grimshaw, S. B.; Spencer, A.; Buck, M.; Boyd, J.; Dobson, C. M.; Redfield, C.; Smith, L. J. *Protein Sci.* **2001**, *10*, 677–688.
107. Ohnishi, S.; Shortle, D. *Proteins: Struct., Funct., Genet.* **2003**, *50*, 546–551.
108. Luhrs, T. T.; Zahn, R.; Wuthrich, K. *J. Mol. Biol.* **2006**, *357*, 833–841.
109. Triba, M. N.; Warschawski, D. E.; Devaux, P. F. *Biophys. J.* **2005**, *88*, 1887–1901.
110. Stejskal, E. O.; Tanner, J. E. *J. Chem. Phys.* **1965**, *42*, 288–295.
111. Callaghan, P. T.; Söderman, O. *J. Phys. Chem.* **1983**, *87*, 1737–1744.
112. Lindblom, G.; Orädd, G. *Prog. Nucl. Magn. Reson. Spectrosc.* **1994**, *26*, 483–515.
113. Tanner, J. E. *J. Chem. Phys.* **1970**, *52*, 2523–2526.
114. Stilbs, P. *Prog. Nucl. Magn. Reson. Spectrosc.* **1987**, *19*, 1–45.
115. Kärger, J.; Pfeifer, H.; Heink, W. *Adv. Magn. Opt. Reson.* **1988**, *12*, 1–89.
116. Price, W. S. *Concepts Magn. Reson.* **1997**, *9*, 299–336.
117. Price, W. S. *Concepts Magn. Reson.* **1998**, *10*, 197–237.
118. Cotts, R. M.; Hoch, M. J. R.; Sun, T.; Marker, J. T. *J. Magn. Reson.* **1989**, *83*, 252–266.
119. Momot, K. I.; Kuchel, P. W. *J. Magn. Reson.* **2005**, *174*, 229–236.
120. Price, W. S.; Elwinger, F.; Vigouroux, C.; Stilbs, P. *Magn. Reson. Chem.* **2002**, *40*, 391–395.
121. Antalek, B. *Concepts Magn. Reson.* **2002**, *14*, 225–258.
122. Antalek, B.; Hewitt, J. M.; Windig, W.; Yacobucci, P. D.; Mourey, T.; Le, K. *Magn. Reson. Chem.* **2002**, *40*, S60–S71.
123. Park, K. D.; Lee, Y. J. *Magn. Reson. Chem.* **2006**, *44*, 887–891.
124. Kärger, J. *Diffus. Fundam.* **2005**, *2*, 78–1.
125. Mitra, P. P.; Sen, P. B.; Schwatrz, L. M. *Phys. Rev. B* **1993**, *47*, 8565–8574.
126. Mitra, P. P.; Sen, P. B. *Phys. Rev. B* **1992**, *45*, 143–156.
127. Maas, W. E.; Laukien, F. H.; Cory, D. G. *J. Am. Chem. Soc.* **1996**, *118*, 13085–13086.
128. Gaede, H. C.; Gawrisch, K. *Biophys J.* **2003**, *85*, 1734–1740.
129. Scheidt, H. A.; Pampel, A.; Nissler, L.; Gebhardt, R.; Huster, D. *Biochim. Biophys. Acta* **2004**, *1663*, 97–107.
130. Kimura, T.; Cheng, K.; Rice, K. C.; Gawrisch, K. *Biophys. J.* **2009**, *96*, 4916–4924.
131. Gaede, H. C.; Yau, W.-Y.; Gawrisch, K. *J. Phys. Chem. B* **2005**, *109*, 13014–13023.
132. Scheidt, H. A.; Huster, D.; Gawrisch, K. *Biophys. J.* **2005**, *89*, 2504–2512.
133. Polozov, I. V.; Gawrisch, K. *Biophys. J.* **2004**, *87*, 1741–1751.
134. Polozov, I. V.; Bezrukov, L.; Gawrisch, K.; Zimmerberg, J. *Nat. Chem. Biol.* **2008**, *4*, 248–255.
135. Lindblom, G.; Wennerström, H. *Biophys. Chem.* **1977**, *6*, 167–171.
136. Orädd, G.; Lindblom, G. *Magn. Reson. Chem.* **2004**, *42*, 123–131.
137. Orädd, G.; Lindblom, G. *Spectroscopy* **2005**, *19*, 191–198.

138. Lindblom, G.; Gröbner, G. *Curr. Opin. Colloid Interface Sci.* **2006**, *11*, 24–29.

139. Lindblom, G.; Orädd, G. *J. Dispersion Sci. Technol.* **2007**, *28*, 55–61.

140. Lindblom, G.; Orädd, G. *Biochim. Biophys. Acta* **2009**, *1788*, 234–244.

141. Soong, R.; Macdonald, P. M. *Biophys. J.* **2005**, *88*, 255–268.

142. Lasic, D. D.; Needham, D. *Chem. Rev.* **1995**, *95*, 2601–2628.

143. King, V.; Parker, M.; Howard, K. P. *J. Magn. Reson.* **2000**, *142*, 177–182.

144. Marsh, D.; Bartucci, R.; Sportelli, L. *Biochim. Biophys. Acta* **2003**, *1615*, 33–59.

145. Mills, R. *J. Phys. Chem.* **1973**, *77*, 685–688.

146. Vaz, W. L. C.; Clegg, R. M.; Hallmann, D. *Biochemistry* **1985**, *24*, 781–768.

147. Almeida, P. F. F.; Vaz, W. L. C.; Thompson, T. E. *Biochemistry* **1992**, *31*, 6739–6747.

148. Almeida, P. F. F.; Vaz, W. L. C.; Thompson, T. E. *Biochemistry* **1992**, *31*, 7198–7210.

149. Tocanne, J.-F.; Dupou-Cézanne, L.; Lopez, A. *Progr. Lipid Res.* **1994**, *33*, 203–237.

150. de Gennes, P. G. *Macromolecules* **1980**, *13*, 1069–1075.

151. Flory, P. *Principles of Polymer Chemistry*; Cornell University Press: Ithica, NY, 1971.

152. Hristova, K.; Needham, D. *Macromolecules* **1995**, *28*, 991–1002.

153. Soong, R.; Macdonald, P. M. *Biochim. Biophys. Acta* **2007**, *1768*, 1805–1814.

154. Jovin, T. M.; Vaz, W. L. C. *Methods Enzymol.* **1989**, *172*, 471–513.

155. Tocanne, J.-F.; Dupou-Cézanne, L.; Lopez, A. *Progr. Lipid Res.* **1994**, *33*, 203–237.

156. Haustein, E.; Schwille, P. *Annu. Rev. Biophys. Biomolec. Struct.* **2007**, *36*, 151–169.

157. Saxton, M. J.; Jacobson, K. *Annu. Rev. Biophys. Biomol. Struct.* **1997**, *26*, 373–399.

158. Kusumi, A.; Nakada, C.; Richie, K.; Murase, K.; Suzuki, K.; Murakoshi, H.; Kasai, R.; Kondo, J.; Fujiwara, T. *Annu. Rev. Biophys. Biomol. Struct.* **2005**, *34*, 351–378.

159. Soong, R.; Macdonald, P. M. *Langmuir* **2009**, *25*, 380–390.

160. Nieh, M. P.; Raghunathan, V. A.; Pabst, G.; Harroun, T.; Nagashima, K.; Morales, H.; Katsaras, J.; Macdonald, P. *Langmuir* **2011**, *27*, 4638–4647.

161. Soong, R.; Macdonald, P. M. *Langmuir* **2008**, *24*, 518–527.

162. Doi, M.; Edwards, S. F. In *The Theory of Polymer Dynamics*; Oxford University Press: New York, 1986; p 141.

163. Nieh, M.-P.; Ginka, C. J.; Krueger, S; Prosser, R. S.; Katsaras, J. *Biophys. J.* **2002**, *82*, 2487–2498.

164. Brochard, F.; de Gennes, P. G. *J. Chem. Phys.* **1977**, *67*, 52–56.

165. Daoud, M.; de Gennes, P. G. *J. Phys. (Paris)* **1977**, *38*, 85–93.

166. de Gennes, P.-G. In *Scaling Concepts in Polymer Physics*; Cornell University Press: Ithica, NY, 1979.

167. Pawar, Y.; Anderson, J. L. *Ind. Eng. Chem. Res.* **1993**, *32*, 743–746.

168. Jendrejack, R. M.; Schwartz, D. C.; Graham, M. D.; de Pablo, J. J. *J. Chem. Phys.* **2003**, *119*, 1165–1173.
169. Chen, Y.-L.; Graham, M. D.; de Pablo, J. J.; Randall, G. C.; Gupta, M.; Doyle, P. S. *Phys. Rev. E* **2004**, *70*, 0609011–0609014.
170. Soong, R.; Majonis, D.; Macdonald, P. M. *Biophys. J.* **2009**, *97*, 796–805.
171. Tanner, J. E. *J. Chem. Phys.* **1978**, *69*, 1748–1754.
172. Davidson, M. G.; Suter, U.; Deen, W. M. *Macromolecules* **1987**, *20*, 1141–1146.
173. Davidson, M. G.; Deen, W. M. *Macromolecules* **1988**, *21*, 3474–3481.
174. Deen, W. M. *AIChE J.* **1987**, *33*, 1409–1425.
175. Lutti, A.; Callaghan, P. T. *Appl. Magn. Reson.* **2008**, *33*, 293–310.
176. Soong, R.; Nieh, M.-P.; Nicholson, E.; Katsaras, J.; Macdonald, P. M. *Langmuir* **2010**, *26*, 2630–2638.

Downloaded by STANFORD UNIV GREEN LIBR on June 21, 2012 | http://pubs.acs.org
Publication Date (Web): October 14, 2011 | doi: 10.1021/bk-2011-1077.ch015

Chapter 15

Understanding Anisotropy, Transport, and Ion Associations Inside Ionic Polymers

Jianbo Hou, Jing Li, Kyle G. Wilmsmeyer, Zhiyang Zhang, and Louis A. Madsen*

**Department of Chemistry and Macromolecules Interfaces and Institute,
Virginia Tech, Blacksburg, VA 24061
*E-mail: lmadsen@vt.edu; dart270@gmail.com**

Anisotropy, transport and ion associations critically determine the performance of many ionic polymer-based materials and devices, from fuel cells to batteries to ionic transducers. Our group is pursuing a range of NMR studies combined with other structural and morphological information to understand these complex materials. We observe uniformly aligned hydrophilic channels in different perfluorosulfonate ionomers and aromatic-based multi-block copolymers, quantified by ^{2}H NMR spectroscopy and pulsed-field-gradient NMR diffusometry. Nafion 112 exhibits biaxial alignment with its principal and secondary axes along two orthogonal in-plane directions. Both Nafion 212 (NRE212) and block copolymers show uniaxial alignment with the symmetry axis perpendicular to the membrane plane. Our further discovery of the linear coupling between diffusion anisotropy and orientational order parameter for mechanically stretched Nafion 117 membranes strongly indicates that channel dimensions, domain structure, and defect character are unperturbed by the macroscopic mechanical deformation. When combining ionic liquids (ILs) with ionic polymers, ion associations result in up to 4X faster cation than anion diffusion at lower hydration levels and 3X slower cation diffusion at higher hydration levels. Conversely, we use ILs as probes to map local structures in ionic polymers. Ion diffusion coefficients exhibit strong dependencies on diffusion time, signifying the presence of sub-micron domain boundaries. Finally, we will discuss

In NMR Spectroscopy of Polymers: Innovative Strategies for Complex Macromolecules; Cheng, H., et al.;
ACS Symposium Series; American Chemical Society: Washington, DC, 2011.

application of electrophoretic NMR, which renders a promising opportunity to study ion transport and associations under electrochemical cell conditions.

Introduction

Ionic polymers manifest themselves as promising candidates for a series of functional materials and devices, from fuel cells to water reverse osmosis membranes to artificial muscle actuators (*1–5*). Many of these useful ionic polymer membranes consist of hydrophilic and hydrophobic moieties that will nanophase separate to form interconnected hydrophilic channels that allow ion conduction and water transport (*6–9*). As illustrated in figure 1, structural features such as orientation, size and connectivity of ionic domains and channels within the polymer network will strongly impact water and ion transport (*10–15*). Understanding the role of these key factors in the transport process will give insightful guidance on and direct targeted design of new materials.

Our group has endeavored to understand anisotropy, transport and ion associations inside ionic polymers by combining various NMR methods (*15–20*). In general, our strategy relies on probing multi-scale (~10 nm – 10 μm) structural features (domain sizes, periodicity, confinement, defects) in soft materials by tracking the position and reorientation of diffusing species, such as H_2O and ions (*16*, *17*, *21*). Sample modulations, such as hydration level, molecular weight variation and mechanical deformation strongly impact these structural characteristics (*15*, *18*, *22–25*). Through systematic NMR studies on different samples, as well as combining NMR with other techniques like X-ray scattering and TEM (*24*, *26*, *27*), it is our goal to bridge the gap between microscopic and macroscopic worlds to obtain a better understanding of these complex materials. Herein, we summarize our recent work on relevant topics using pulsed-field-gradient NMR diffusometry and ^2H NMR spectroscopy. Diffusion and anisotropy measurements yield quantitative information regarding structural anisotropy and motions of ions and molecules inside ionic polymers. ^2H NMR spectroscopy further provides useful information on the orientational ordering inherited by the probe molecules (D_2O, CD_3OD) through quadrupolar splitting. The combination of these measurements allow quantitative assessment of average alignment and alignment mode of hydrophilic channels inside the polymer. When combining ionic liquids with ionic polymers, ion associations due to strong ionic interactions (molecular packing, electrostatic interactions) will be modulated by variation of hydration levels. The presence of these ionic aggregates results in up to 4X faster cation than anion diffusion inside the ionic polymer at lower hydration levels and 3X slower cation diffusion at higher hydration levels (*28*) Further implementation of electrophoretic NMR (ENMR), which measures ion motions in the presence of an electric field, unfolds a promising prospect for studying and understanding ion transport and ion associations (*29–31*).

Downloaded by STANFORD UNIV GREEN LIBR on June 21, 2012 | http://pubs.acs.org
Publication Date (Web): October 14, 2011 | doi: 10.1021/bk-2011-1077.ch015

Downloaded by STANFORD UNIV GREEN LIBR on June 21, 2012 | http://pubs.acs.org
Publication Date (Web): October 14, 2011 | doi: 10.1021/bk-2011-1077.ch015

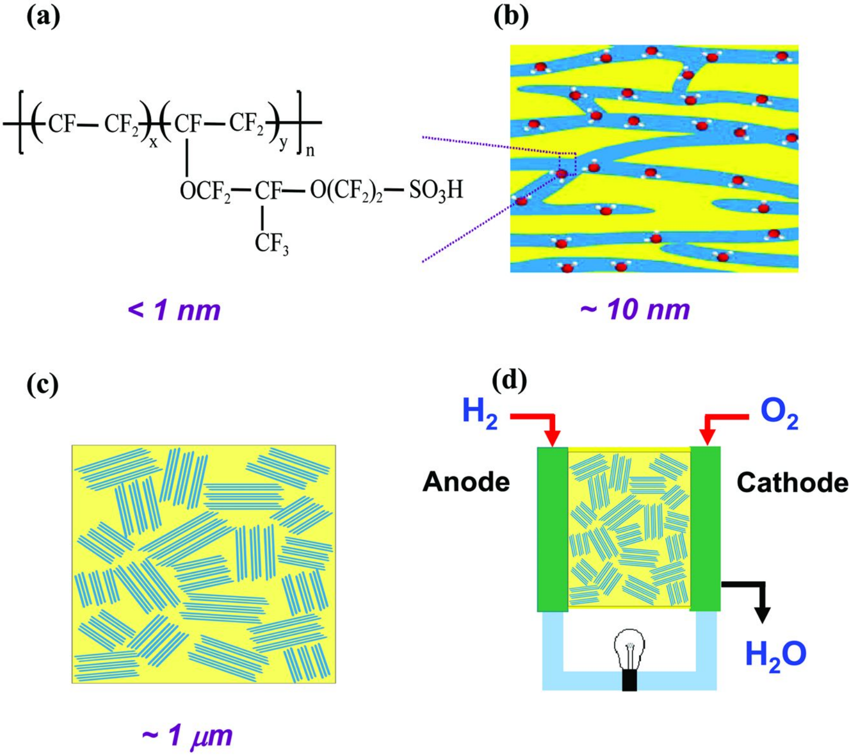

Figure 1. Structural features on different length scales (a-c) inside ionic polymers. (a) Chemical structure of Nafion. x:y represents the ratio of hydrophilic to hydrophobic part. The short side chain is smaller than 1 nm. (b) Ion clusters aggregate and form ion channels that are a few nms in size. (c) Submicron hydrophilic domain bundles (blue part) are distributed within the scaffold of polymer matrix. (d) Distribution of ionic domains impacts proton transport inside ionic polymer membranes for fuel cell applications.

Experimental Methods

Membrane Preparation

Nafion 112, Nafion 117 (extruded) and Nafion 212 (NRE212) (dispersion-cast) membranes, all with equivalent weight of 1100 (grams of dry membrane per mole of sulfonate group), were obtained from E.I. DuPont (Wilmington, Delaware) in acid form. Deuterium oxide was obtained from Cambridge Isotope Laboratories, Inc. (Andover, Massachusetts) at 99.9% purity. The multi-block copolymers named as BPSH-BPS (A: B) were obtained from Prof. James E. McGrath's group and the synthetic procedures have been reported elsewhere (*1*). Similar to Nafion, these multi-block copolymers contain two parts, with A and B representing the block masses of hydrophilic and hydrophobic segments individually, and are coupled with the linkage group of decafluorobiphenyl

(DFBP). For the materials presented in this work, the block masses are equal (A = B). As reported (*1*), all these block copolymers were redissolved in N-methyl-2-pyrrolidinone (NMP, Fisher), followed by solution casting onto a clean glass substrate. The prepared films were then cast under an infrared lamp with temperature controlled between 45-55 °C for 2 days. Membranes were further dried in a vacuum oven at 110 °C for a whole day to remove the residual solvent. For acidification, the membranes were boiled in 0.5 M sulfuric acid for 2h, then rinsed and boiled in deionized water. Dry membrane thicknesses were 30-40 μm. Depending on membrane type and uptake, this value increased to 60-100 μm upon water swelling.

Downloaded by STANFORD UNIV GREEN LIBR on June 21, 2012 | http://pubs.acs.org
Publication Date (Web): October 14, 2011 | doi: 10.1021/bk-2011-1077.ch015

Ionic Liquid and Water Uptake Determination

Water and ion transport in the following four ionic liquids (ILs) were studied: 1-ethyl-3-methyl imidazolium trifluoromethanesulfonate ([C_2mim][TfO]), 1-butyl-3-methyl imidazolium trifluoromethanesulfonate ([C_4mim][TfO]), 1-ethyl-3-methyl imidazolium tetrafluoroborate ([C_2mim][BF_4]) and 1-butyl-3-methyl imidazolium tetrafluoroborate ([C_4mim][BF_4]). All these ILs were purchased from Solvent Innovation GMBH (Cologne, Germany) with purity >99%. ILs were dried in vacuum at 70°C for 48h to remove residual water prior to diffusion measurements, and diffusion coefficients and NMR spectra were checked for stability over time to verify that water absorption was insignificant. Extruded Nafion 117 (N117) membranes were cut into pieces of 5 mm x 5 mm in size, stacked together to a total mass of ~60 mg and dried in a vacuum oven for 12h at room temperature to determine the dry membrane mass ($mass_{dry}$). The membranes were then soaked with IL-D_2O mixtures at different temperatures to achieve different uptakes. The wet membranes were blotted to remove any free surface liquid (ILs and water) and transferred to a sealed Teflon cell to equilibrate for later diffusion measurement. All diffusion measurements were performed at 25°C after sample equilibration. To vary water content, we allowed the samples to dry in open air while the mass of IL plus the mass of the membranes ($mass_{IL}$) remained constant due to its negligible vapor pressure. Masses of wet membranes ($mass_{wet}$) including water and IL were determined gravimetrically after the NMR experiments. IL uptake and water mole ratio (χ_{water}) were calculated respectively using equations (1) and (2):

$$IL\ uptake = \frac{mass_{IL} - mass_{dry}}{mass_{dry}} \times 100\% \qquad (1)$$

$$\chi_{water} = \frac{mass_{wet} - mass_{IL}}{mass_{IL} - mass_{dry}} \times \frac{M_{IL}}{M_{D_2O}} \qquad (2)$$

Diffusion Measured by Pulsed-Field-Gradient NMR

We applied the robust and simple pulsed-gradient stimulated echo (PGSTE) sequence for all diffusion measurements. We measured ^1H and ^{19}F diffusion for

Downloaded by STANFORD UNIV GREEN LIBR on June 21, 2012 | http://pubs.acs.org
Publication Date (Web): October 14, 2011 | doi: 10.1021/bk-2011-1077.ch015

water and ILs using a Bruker Avance III WB 400 MHz (9.4 T) NMR equipped with a Micro5 triple-axis-gradient microimaging probe and 8 mm double resonance (^{1}H/^{2}H) RF coil. The triple axis gradients each having a maximum value of 300 G/cm allowed for measurement of diffusion along three orthogonal directions relative to membranes, denoted as *X, Y* (in-plane) and *Z* (through plane) (*18*). Verification of orientations of the membrane stacks in the magnetic field was via using a *Y-Z* image slice collected with a RARE pulse sequence (Rapid Acquisition with Relaxation Enhancement) (*32*). The PGSTE sequence used a $\pi/2$ pulse time of 32 μs, gradient pulse durations δ ranging from 1 – 5 ms, diffusion times Δ ranging from 10 – 600 ms and 16 gradient steps with appropriate selection of maximum gradient strength to result in 50% - 90% of NMR signal attenuation. Due to differences in signal intensity, the number of scans varied from 4 to 512 to produce sufficient signal-to-noise ratio for each data point. All parameters for the gradient have been calibrated and optimized as reported earlier (*15*, *18*).

^{2}H NMR Spectroscopy

^{2}H NMR experiments were performed additionally to observe orientational ordering in ionic polymers. This method can assist in determining the alignment modes of materials with anisotropic structures (*14–16*). Single pulse experiments ($\pi/2$ = 20 μs) were performed with repetition time of 0.5 s and number of scans ranging from 256-1024, depending on D_2O uptake. The studied materials were soaked in D_2O (99.9%, Cambridge Isotope Labs) with the measured uptake ranging from 6 - 20 wt %. Custom-built Teflon cells with special configurations allowed orientation of membrane stacks either vertically or horizontally with respect to the magnetic field. These cells were placed inside the above described imaging probe and rf coil. Relevant detailed procedures are summarized in our previous report (*15*). Deuterium quadrupole splittings $\Delta\nu_Q$ were obtained by fitting each spectrum with two Lorentzian peaks using NutsPro software (Acorn NMR Inc., Livermore, CA).

Results and Discussion

Diffusion Anisotropy and Channels Alignment in Ionic Polymers

Figure 2a. compares diffusion anisotropy among Nafion 112, NRE212 and BPSH-BPS(10k-10k) multi-block copolymer at a similar water uptake. In general, both Nafion112 and NRE212 show relatively weak diffusion anisotropy as we observe only slightly faster diffusion in plane. In contrast, for the BPSH-BPS(10k-10k) block copolymer, we observe equal in-plane diffusion ($D_x = D_y$) which is much faster than through plane diffusion D_z. This results in substantially larger diffusion anisotropy as compared with Nafion membranes. We further orient the block copolymer membranes in three orthogonal directions along the magnetic field for ^{2}H NMR studies, as shown in Figure 2b. Experimental results suggest uniaxial alignment in the block copolymer membranes. We observe maximum peak splittings when the membrane plane is perpendicular to the magnetic field and half maximum peak splittings when membrane plane is parallel to the magnetic field. This behavior is a result of the $P_2(\cos\theta)$ dependence of the quadrupole splitting, as described in our previous report (*14*, *15*). Both diffusion anisotropy and ^2H NMR results well correlate with the image of lamellar structure revealed by the TEM as shown in Figure 3a. (KD is the microtoming direction and A is the membrane plane normal)

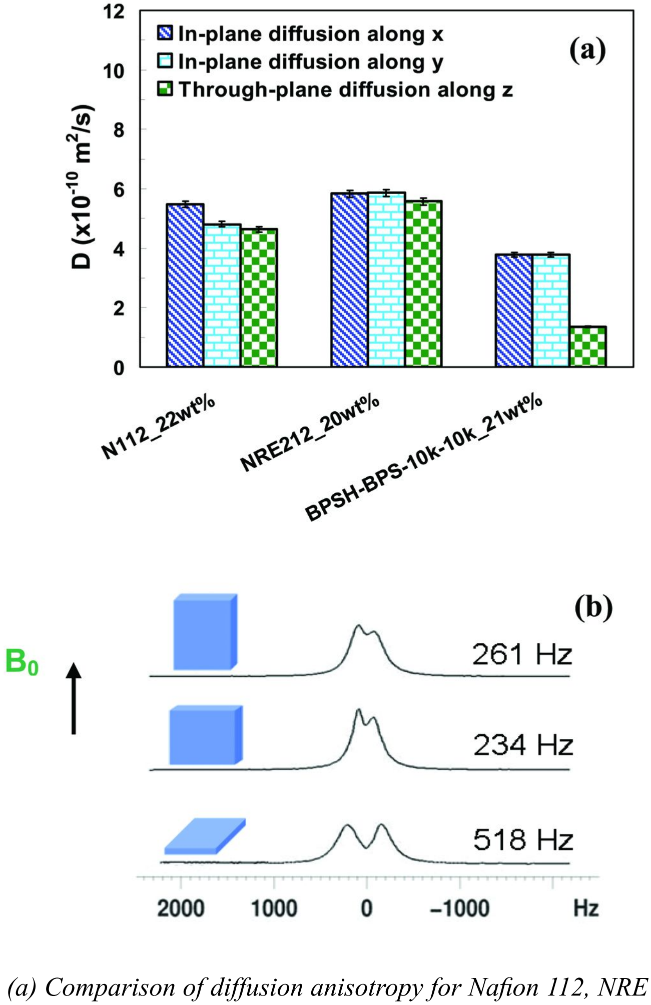

Figure 2. (a) Comparison of diffusion anisotropy for Nafion 112, NRE 212 and BPSH-BPS(10k:10k) block copolymer at a similar water uptake. Both Nafion 112 and NRE212 show weak diffusion anisotropy. In contrast, the block copolymer exhibits large diffusion anisotropy where diffusion in plane is 3X faster than through plane. (b) eExample ^2H NMR spectra for the block copolymer. Membranes are oriented in three orthogonal directions along the magnetic field B_0. Peak splittings show the maximum and half maximum values when membrane plane is perpendicular and parallel to B_0, respectively.

Downloaded by STANFORD UNIV GREEN LIBR on June 21, 2012 | http://pubs.acs.org
Publication Date (Web): October 14, 2011 | doi: 10.1021/bk-2011-1077.ch015

For Nafion112, in-plane diffusion $D_x > D_y$ and D_y is close to through plane diffusion D_z. With regard to NRE212, diffusion along two in-plane directions is similar ($D_x \approx D_y$) and faster than diffusion through plane, D_z. These results, in correlation with ^{2}H NMR measurements (spectra not shown), confirm the biaxial and uniaxial aligned channels inside Nafion 112 and NRE212, respectively. Nafion112 (Figure 3b) exhibits biaxial alignment with its principal axis along the in-plane direction (x direction) and the secondary axis along the other orthogonal in-plane direction (y direction). In contrast, NRE212 (Figure 3c, side view) shows uniaxial alignment. To account for the faster diffusion in plane, the symmetry axis, which represents the average alignment of domain bundle assemblies (blue features), is perpendicular to the membrane plane. Figure 3d is the top view of Figure 3c, where the local domain bundle axes have an average alignment (symmetry) axis coinciding with the membrane plane normal, but the bundle axes are randomly distributed within the plane.

Downloaded by STANFORD UNIV GREEN LIBR on June 21, 2012 | http://pubs.acs.org
Publication Date (Web): October 14, 2011 | doi: 10.1021/bk-2011-1077.ch015

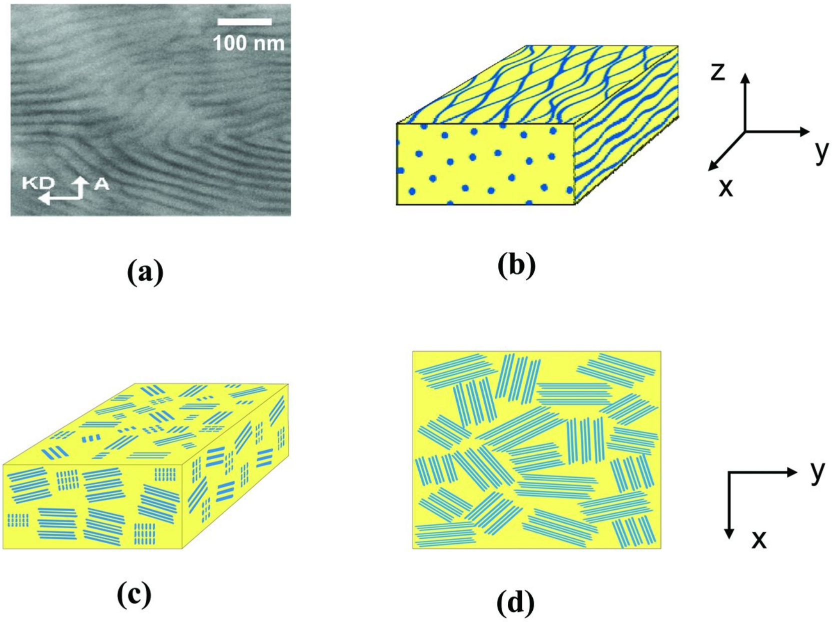

Figure 3. (a) TEM image of BPSH-BPS (10k-10k) multiblock copolymer. "KD" is along the microtoming direction and "A" indicates the air-membrane plane interface normal. (b)Biaxially aligned ion channels (blue cylinders) in (extruded) Nafion112. The principal and the secondary axes are along x and y directions, respectively. (c) Side view of uniaxially aligned domain assemblies inside NRE 212. (d) Top view of figure (c). X-Y plane is perpendicular to the symmetry axis direction which represents the average alignment axis of domain bundles.

We have further investigated the impact of mechanical stretching on channel dimension, domain orientation, and defect structures in ionic polymers. We measure water transport and anisotropy in a series of drawn Nafion 117 membranes, defining the draw ratios as L = final length (l) / initial length (l_0) (*19*). We notice conservation of the diffusion tensor trace (independent of water uptake) and linear coupling between order parameter (by ^{2}H splitting) and diffusion anisotropy. This evidence strongly demonstrates that these domains of channels behave like liquid crystals (*33–36*), simply reorienting along the uniaxial stretching direction without perturbing their dimensions and the nature of defect structures (character, density). Based on the absolute value of order parameter derived from X-ray data, the linear coupling between order parameter and diffusion anisotropy results in a molecular aspect ratio of 1.8, which agrees well with that of the diffusing water molecules (*37*).

Ion Associations of Ionic Liquid Inside Ionic Polymers

Figure 4 summarizes the diffusion ratio of D_{cation}/D_{anion} for ILs inside ionic polymer membranes as a function of hydration level. We observe striking acceleration in anion diffusion than cation diffusion for BF_4-based ILs ([C_2mim][BF_4], [C_4mim][BF_4]) at high hydration level. However, such an effect is relatively smaller for TfO-based ILs ([C_2mim][TfO], [C_4mim] [TfO]). We attribute these results to 1) the interactions of polymer-fixed sulfonate groups and cations 2) difference in basicity and ion pairing between [TfO]$^-$ and [BF^4]$^-$. SO_3^- groups on the polymer side chain can attract cations to hinder their motions. [TfO]$^-$ is more likely to pair up with cations since it is a stronger Lewis base than [BF_4]$^-$. Thus, [BF_4]$^-$ can move relatively free and lead to enhanced anion diffusion for BF^4-based ILs.

On the other side, cations diffuse much faster than anions at low water content for [C_2mim]-based ILs ([C_2mim][TfO], [C_2mim][BF_4]), where D_{cation}/D_{anion} reaches 2.5 and 3.1 for [C_2mim][TfO] and [C_2mim][BF_4], respectively. Such an observation contradicts the general prediction that cation should diffuse slower within the SO_3^-matrix due to the strong coulombic attraction from the side chain. Considering that our measured cation and anion diffusion coefficients are both time independent, we rule out the difference in global viscosity experienced by different ions. In comparison with the diffusion ratio (D_{cation}/D_{anion} ~1.3-1.5) for free state ILs, those novel phenomena strongly suggest the formation of ionic aggregates with specific features. We further propose that anionic aggregates are prevalent inside ionic polymers at low hydration level. Charge neutrality requires charge balance by means of more isolated cations which results in enhanced cation diffusion on average. For the ease of illustration, we use a simple aggregation model as shown in Figure 5 to explain this rationale. We only consider four types of ions: single, dipole, triple and quadrupole. Based on this model, anionic triple ions dominate at low hydration and lead to more isolated (single) cations with enhanced cation diffusion. Dipoles and quadrupoles do not produce imbalanced average D ratios since cations and anions are symmetrically distributed, and cationic triple ions will be less likely to exist as they contribute negatively to the observed $D^+_{Average}$. In other words, we conclude that anionic aggregates with

Downloaded by STANFORD UNIV GREEN LIBR on June 21, 2012 | http://pubs.acs.org
Publication Date (Web): October 14, 2011 | doi: 10.1021/bk-2011-1077.ch015

reduced diffusion are prevalent at low hydration, while the presence of more isolated cations results in faster cation diffusion on average.

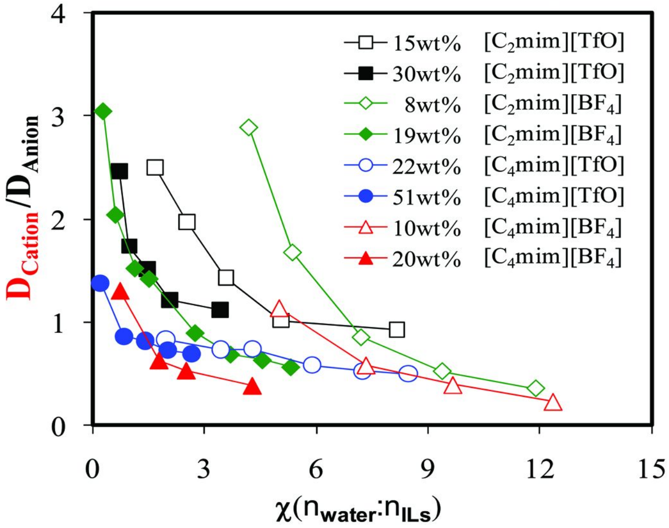

Figure 4. Summary of diffusion ratio D_{cation}/D_{anion} as a function of water content χ_{water} for various types and uptakes of ILs inside Nafion membranes. Anion diffusion dramatically accelerates at higher hydration levels for BF_4-based ILs, and D_{anion}/D_{cation} reaches 3 and 4 for $[C_2mim][BF_4]$ and $[C_4mim][BF_4]$, respectively. At low hydration, cation diffusion becomes substantially faster than anion diffusion for $[C_2mim][TfO]$ and $[C_2mim][BF_4]$, where D_{cation}/D_{anion} reach 2.5 and 3.1 respectively.

Mapping Local Domain Information

In our recent work, we attempt to use ILs to probe structural features such as domain structure and connectivity within the polymer network. Ionic liquids become ideal candidates for such an investigation due to the following reasons: 1) ILs find promising applications in polymer-based materials and devices, like batteries and soft mechanical actuator. 2) topological features strongly impact ion transport inside polymers, thus affecting the performance of materials and devices 3) these ionic "probes" can sense a shorter diffusion length scale on average due to their slow motions (~ 10^{-13} m^2/s) inside polymers. As a result, they will more effectively report on the local structural heterogeneity rather than the average global structural information. Thus, one might obtain more detailed information that correlates ion motions with structural characteristics. Our preliminary results on ion diffusion coefficients (both D_{cation} *and* D_{anion}) exhibit strong dependence on both gradient pulse duration (δ) and diffusion time (Δ), indicating the presence of local barriers sensed by diffusing ions. In agreement with experimental observations, further theoretical analysis and computational results explain the

Downloaded by STANFORD UNIV GREEN LIBR on June 21, 2012 | http://pubs.acs.org
Publication Date (Web): October 14, 2011 | doi: 10.1021/bk-2011-1077.ch015

Downloaded by STANFORD UNIV GREEN LIBR on June 21, 2012 | http://pubs.acs.org
Publication Date (Web): October 14, 2011 | doi: 10.1021/bk-2011-1077.ch015

finite gradient pulse effect and time-dependent diffusion behaviors. We estimate that the relevant length scale that characterizes the ionic domain size is a few hundred nm based on an empirical model for diffusion in a porous network. This study has relevance for fundamental understanding of IL-polymer interactions, ionic polymer morphology, improvement of IL diffusion studies, and the design of IL-polymer composite actuators.

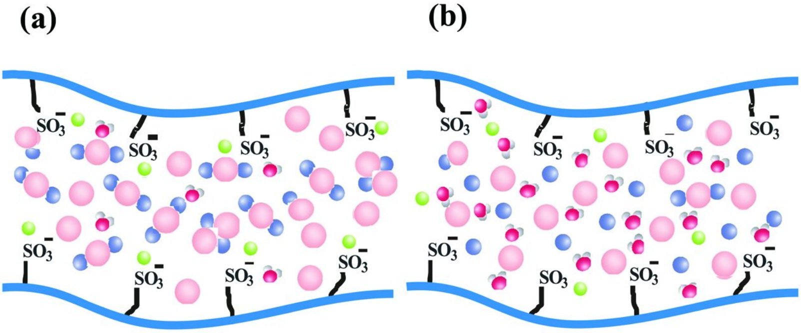

Figure 5. Ion associations of ILs inside the ~ 2 nm hydrophilic channels of Nafion membrane. At low water content, (a) negatively charged triple ions are prevalent due to strong electrostatic attractions among charged species, leaving more isolated cations and resulting in enhanced cation diffusion on average. At high water content (b), water dramatically reduces electrostatic interactions among cations and anions and leads to ion disassociation. Anions (especially $[BF_4]^-$) are released from local electrostatic networks and move relatively freely, while sulfonate groups fixed to polymer side chains attract cations and thus slow their average translational motion.

Probing Ion Motions Using Electrophoretic NMR

We also attempt to study motions of ions under an applied electric field to quantify the degree of ion associations. Electric-field driven, also known as electrophoretic NMR (ENMR), demonstrates to be a powerful tool for studying motions of ions and aggregates in solutions (*38*). In contrast to a normal diffusion spectrum, coherent motion of ions driven by the electric field will result in a net phase shift rather than signal attenuation. The phase shift can be calculated via equation (3):

$$\Delta\Phi = \gamma g \delta \Delta \mu E \qquad (3)$$

Where γ is the nuclei gyromagnetic ratio, g is gradient strength, δ is gradient duration time, Δ is diffusion time, E is electric field strength and μ is ion electrophoretic mobility. For example, Figure 6 shows a series of ^{19}F ENMR spectra for $[BF_4]^-$ in a dilute solution. From the bottom up, spectral phase shift gradually increases with electric current, which also signifies an increment of electric field strength. According to equation (3), for a given set of γ, g, δ, Δ and E values, one can estimate the ion mobility by examing the spectral phase shift. In this case, our measured ion mobility for $[BF4]^-$ is $6x10^{-8}$ $m^2s^{-1}V^{-1}$. In further combination with the Nernst-Einstein equation, which relates molecular diffusion with mobility, these measurements will provide insight into quantifying the degree of ion associations.

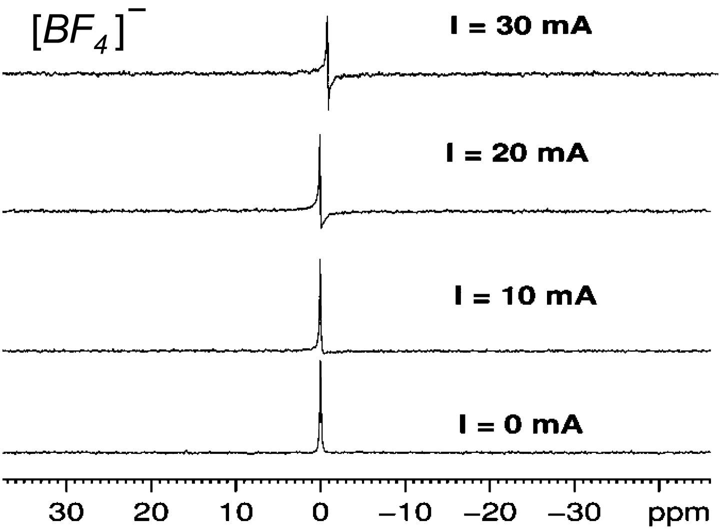

Figure 6. Application of electrophoretic NMR allows measurement of ion mobility. Coherent ion motions result in an NMR spectral phase shift as shown above. From bottom to top, the increment in phase shift is associated with the increment of electric field strength, as indicated by the electric current value. In a dilute solution, the measured ion mobility for $[BF4]^-$ is $6x10^{-8}$ $m^2s^{-1}V^{-1}$.

Conclusion

We have quantified the alignment of hydrophilic channels in a series of ionic polymers, from Nafion 112 to Nafion 212 to aromatic-based multi-block copolymers using ^2H NMR spectroscopy and pulsed-field-gradient NMR diffusometry. We conclude that Nafion 112 exhibits biaxial alignment mode whereas Nafion 212 (NRE212) and block copolymers both uniaxially align along their symmetry axes, which are perpendicular to the membrane plane. We further revealed the linear coupling between diffusion anisotropy and oritentational order parameter for mechanically stretched Nafion 117 membranes. These results strongly demonstrate that macroscopic mechanical deformation has no impact on channel dimensions, domain structure, and defect character. Combining ionic liquids (ILs) with ionic polymers, we observe that ion associations result in up to 4X faster cation than anion diffusion at lower hydration levels and 3X slower cation diffusion at higher hydration levels. When we use ILs as probes to map local structures in ionic polymers, ion diffusion coefficients exhibit strong

Downloaded by STANFORD UNIV GREEN LIBR on June 21, 2012 | http://pubs.acs.org
Publication Date (Web): October 14, 2011 | doi: 10.1021/bk-2011-1077.ch015

dependencies on diffusion time, signifying the presence of sub-micron domain boundaries. Finally, we also show that measurement of coherent ion motions via electrophoretic NMR renders a promising prospect to study ion transport and quantify ion associations.

Acknowledgments

We would like to graciously thank Professor James E. McGrath and Dr. Hae-Seung Lee at Virginia Tech for providing block copolymer samples, Professor Robert B. Moore and Dr. Abhishek Roy for providing N112, NRE212 and N117 membrane samples and Prof. Qiming Zhang at Pennsylvania State University for providing the IL samples and relevant information and discussions. We also thank Dong Wang and Prof. James R. Heflin for helpful discussion on ion associations and actuator bending test. This material is based upon work supported by the National Science Foundation under award number DMR 0844933 and CBET 0756439. Any opinions, findings and conclusions or recommendations expressed in this material are those of the author(s) and do not necessarily reflect the views of the National Science Foundation (NSF). Experiments at PAL were supported in part by the Ministry of Education, Science and Technology of Korea and POSTECH. This material is based upon work supported in part by the U.S. Army Research Office under Grant W911NF-07-1-0452 Ionic Liquids in Electro-Active Devices (ILEAD) MURI. Acknowledgment is made to the Donors of the American Chemical Society Petroleum Research Fund for partial support of this research and to Virginia Tech for startup funds.

References

1. Lee, H. S.; Roy, A.; Lane, O.; Dunn, S.; McGrath, J. E. *Polymer* **2008**, *49*, 715.
2. Duncan, A. J.; Leo, D. J.; Long, T. E. *Macromolecules* **2008**, *41*, 7765.
3. Petersen, R. J. *J. Membrane Sci.* **1993**, *83*, 81.
4. Grot, W. *Chem. Ing. Tech* **.1978**, *50*, 299.
5. Park, J. K.; Moore, R. B. *ACS Appl. Mater. Interfaces* **2009**, *1*, 697.
6. Gierke, T. D.; Munn, G. E.; Wilson, F. C. *J. Polym. Sci., Part B: Polm. Phys.* **1981**, *19*, 1687.
7. Schmidt-Rohr, K.; Chen, Q. *Nat. Mater.* **2008**, *7*, 75.
8. Mauritz, K. A.; Moore, R. B. *Chem. Rev* **.2004**, *104*, 4535.
9. Roy, A.; Lee, H. S.; McGrath, J. E. *Polymer* **2008**, *49*, 5037.
10. Park, M. J.; Balsara, N. P. *Macromolecules* **2010**, *43*, 292.
11. Ohkubo, T.; Kidena, K.; Ohira, A. *Macromolecules* **2008**, *41*, 8688.
12. Rubatat, L.; Rollet, A. L.; Gebel, G.; Diat, O. *Macromolecules* **2002**, *35*, 4050.
13. Li, J.; Wilmsmeyer, K. G.; Hou, J. B.; Madsen, L. A. *Soft Matter* **2009**, *5*, 2596.
14. Li, J.; Wilmsmeyer, K. G.; Madsen, L. A. *Macromolecules* **2008**, *41*, 4555.
15. Li, J.; Wilmsmeyer, K. G.; Madsen, L. A. *Macromolecules* **2009**, *42*, 255.

Downloaded by STANFORD UNIV GREEN LIBR on June 21, 2012 | http://pubs.acs.org
Publication Date (Web): October 14, 2011 | doi: 10.1021/bk-2011-1077.ch015

16. Deloche, B.; Samulski, E. T. *Bull. Am. Phys. Soc.* **1981**, *26*, 327.
17. Stejskal, E. O.; Tanner, J. E. *J. Chem. Phys.* **1965**, *42*, 288.
18. Hou, J. B.; Li, J.; Madsen, L. A. *Macromolecules* **2010**, *43*, 347.
19. Li, J.; Park, J. K.; Moore, R. B.; Madsen, L. A. *Nat. Mater.* **2011** Submitted.
20. Rankothge, M.; Haryadi; Moran, G.; Hook, J.; Vangorkom, L. *Solid State Ionics* **1994**, *67*, 241.
21. Price, W. S. *Concept Magn. Reson.* **1997**, *9*, 299.
22. Zawodzinski, T. A.; Springer, T. E.; Davey, J.; Jestel, R.; Lopez, C.; Valerio, J.; Gottesfeld, S. *J. Electrochem. Soc.* **1993**, *140*, 1981.
23. Lee, M.; Park, J. K.; Lee, H. S.; Lane, O.; Moore, R. B.; McGrath, J. E.; Baird, D. G. *Polymer* **2009**, *50*, 6129.
24. Lin, J.; Wu, P. H.; Wycisk, R.; Pintauro, P. N.; Shi, Z. Q. *Macromolecules* **2008**, *41*, 4284.
25. van der Heijden, P. C.; Rubatat, L.; Diat, O. *Macromolecules* **2004**, *37*, 5327.
26. Cable, K. M.; Maurtiz, K. A.; Moore, R. B. *Chem. Mater.* **1995**, *7*, 1601.
27. Weber, A. Z.; Newman, J. *J. Electrochem. Soc.* **2004**, 151–A311.
28. Hou, J. B.; Zhang, Z. Y.; Madsen, L. A. *J. Phys. Chem. B* **2011**, *115*, 4576.
29. Hallberg, F.; Weise, C. F.; Yushmanov, P. V.; Pettersson, E. T.; Stilbs, P.; Furo, I. *J. Am. Chem. Soc.* **2008**, *130*, 7550.
30. He, Q. H.; Hinton, D. P.; Johnson, C. S. *J. Magn. Reson.* **1991**, *91*, 654.
31. Saarinen, T. R.; Johnson, C. S. *J. Am. Chem. Soc.* **1988**, *110*, 3332.
32. Hennig, J.; Nauerth, A.; Friedburg, H. *Magn. Reson. Med.* **1986**, *3*, 823.
33. Basser, P. J.; Mattiello, J.; Lebihan, D. *J. Magn. Reson., Ser. B* **1994**, *103*, 247.
34. Yin, Y. G.; Zhao, C. H.; Kuroki, S.; Ando, I. *Macromolecules* **2002**, *35*, 2335.
35. Kirkwood, J. G. *J. Polym. Sci.* **1954**, *12*, 1.
36. Doi, M.; Edwards, S. F. *The Theory of Polymer Dynamics*; Oxford University Press: Oxford, U.K., 1988.
37. Hess, S.; Frenkel, D.; Allen, M. P. *Mol. Phys.* **1991**, *74*, 765.
38. Hallberg, F.; Furo, I.; Stilbs, P. *J. Am. Chem. Soc.* **2009**, *131*, 13900.

Downloaded by STANFORD UNIV GREEN LIBR on June 21, 2012 | http://pubs.acs.org
Publication Date (Web): October 14, 2011 | doi: 10.1021/bk-2011-1077.ch015

Downloaded by STANFORD UNIV GREEN LIBR on June 20, 2012 | http://pubs.acs.org
Publication Date (Web): October 14, 2011 | doi: 10.1021/bk-2011-1077.ch016

Chapter 16

^{13}C-NMR Observed Conformations and Motions of Neat Liquid and Crystalline *n*-Hexatriacontane and as a Guest in the Narrow Channels of Its Inclusion Compound Formed with α-Cyclodextrin

M. A. Hunt,[1] S. Villar-Rodil,[2] M. A. Gomez-Fatou,[3] I. D. Shin,[4] F. C. Schilling,[5] and A. E. Tonelli*,[6]

[1]Oak Ridge National Laboratory, Oak Ridge, TN 37831
[2]National Institute of Coal (INCAR), CSIC, Oviedo, Spain
[3]Department of Polymer Physics and Engineering, Institute of Science and Technology of Polymers (ICTP), C.S.I.C., Madrid, Spain
[4]College of Pharmacy & Health Sciences, Campbell University, Buies Creek, NC 27506
[5]37433 South Ocotillo Canyon Dr., Tucson, AZ 85739
[6]Fiber & Polymer Science, North Carolina State University, Campus Box 8301, Raleigh, NC 27695-8301
***E-mail: alan_tonelli@ncsu.edu**

A non-covalently bonded inclusion compound (IC) was formed between a 36 carbon guest *n*-alkane, hexatriacontane (HTC), and the host α-cyclodextrin (α-CD) and observed by solid-state ^{13}C-NMR, as were neat HTC in both its liquid melt and in its crystallline solid. Based on the number and frequencies of observed ^{13}C resonances, HTC in its neat crystals is restricted to the fully extended all *trans* conformation, while in the melt HTC chains are experiencing rapid inter-conversions between all possible conformations containing *trans* and *gauche* bonds. The spin-lattice relax-ation times, $T_1(^{13}C)$, observed for interior CH_2 carbons in crystalline HTC are ~500 s and for the molten liquid are 1-3 s. In the crystal HTC chains experience virtually no ~100 MHz motions, while molten HTC chains are efficiently moving at both this and much higher frequencies, leading to

In NMR Spectroscopy of Polymers: Innovative Strategies for Complex Macromolecules; Cheng, H., et al.;
ACS Symposium Series; American Chemical Society: Washington, DC, 2011.

Downloaded by STANFORD UNIV GREEN LIBR on June 20, 2012 | http://pubs.acs.org
Publication Date (Web): October 14, 2011 | doi: 10.1021/bk-2011-1077.ch016

an over two orders of magnitude decrease in HTC spin-lattice relaxation times. While the narrow channels (~0.5 nm) of its α-CD-IC largely restrict the HTC chains to the all-*trans* conformation, the $T_1(^{13}C)$ relaxation times of its interior CH_2 carbons range from 1-4 s at temperatures from -30 to 85 °C. In other words, even though the conformations of HTC chains in the narrow α-CD-IC channels are severely restricted compared to those of neat molten HTC chains, they are also experiencing efficient ~100 MHz motions that lead to virtually identical $T_1(^{13}C)$s in both environments. Here we attempt to identify similarities and differences between the types, length-scales, and cooperativities of the motions experienced by HTC chains in the neat melt and in the narrow crystalline channels of its α-CD-IC.

Introduction

The conformations and motions experienced by polymer chains in various environments are intimately related to the physical behaviors manifested by the materials made from them. Because NMR spectroscopy can be used to simultaneously probe both the conformations and motions of polymers, their connections to polymer properties can be drawn by NMR examination of samples whose constituent chains reside in distinct and well defined environments, such as those in mobile liquid and rigid crystalline polymers.

In addition, through formation of non-covalently bonded inclusion compounds (ICs) between guest polymer chains and certain small molecule hosts, polymer chains can be separated, extended, and confined to occupy the narrow channels of the resultant IC or clathrate. This is illustrated in Figure 1 with the IC-host α-cyclodextrin (α-CD), a cyclic oligosaccharide containing 6 glucose units and resulting from the enzymatic degradation of starch. The diameter of the α-CD cavity and the resultant channel in its columnar polymer-α-CD-IC crystal is very narrow at ~0.5 nm, similar to the inter-chain separation found in bulk polymer crystals. The extensions and geometrical constraints experienced by individual chains are similar in both of these solid-state environments. However, what may distinguish them are differences between the motional constraints imposed by regularly and closely packed chains in the bulk crystal and the host channels in α-CD-ICs, which are necessarily highly cooperative in the first case and may not be in the second.

Using ^{13}C-NMR, here we probe and compare the conformations and motions of the 36 carbon *n*-alkane hexatriacontane (HTC), in its bulk crystal, in the melt, and as a guest in the narrow channels of its IC formed with α-CD. The observed resonance frequencies, $\delta(^{13}C)$, are used to obtain conformational information, while spin-lattice relaxation times, $T_1(^{13}C)$, are measured to characterize the natures of the ~100 MHz motions experienced by HTC in each of these environments.

Downloaded by STANFORD UNIV GREEN LIBR on June 20, 2012 | http://pubs.acs.org
Publication Date (Web): October 14, 2011 | doi: 10.1021/bk-2011-1077.ch016

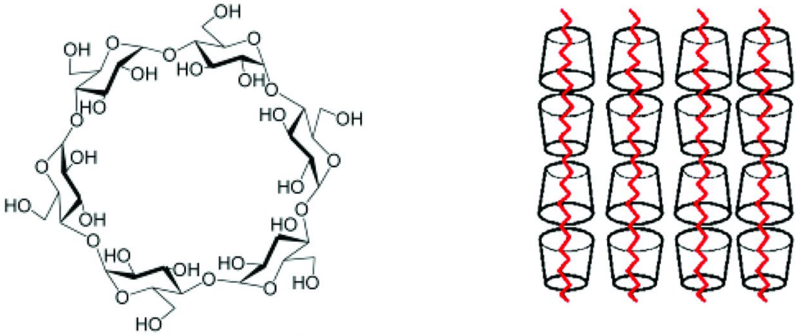

α-CD (cavity diameter ~0.5 nm) **Columnar polymer-α-CD-IC**

Figure 1. Structure of α-CD and a schematic of a polymer-α-CD-IC.

Experimental Section

Materials

α-CD was purchased from Cerestar in powder form. Hexatriacontane (HTC, n-$C_{36}H_{74}$) and a xylene mixture were obtained from Aldrich and used without further purification. Formation of the HTC-α-CD-IC was described previously (*1*) and is schematically illustrated in Figure 2. Approximately 62 mg of HTC was placed in the bottom of a test tube. Then 1 g of α-CD was carefully placed in the test tube above the HTC. Approximately 6 mL of water was poured slowly down the side of the test tube. The test tube was sealed with a rubber septum and placed in an oil bath at 90 °C. The HTC melted and formed a thin layer on top of the water, while the α-CD dissolved in the water. The HTC-α-CD-IC precipitate began to form immediately. After three days at 90 °C, the mixture was slowly cooled to room temperature by turning off the bath heater. The precipitate was then washed with 100 mL of xylenes at 100 °C and water at room temperature and allowed to dry overnight at 50 °C.

Methods

A Bruker AVANCE 500 MHz NMR Spectrometer with an Oxford Narrow Bore Magnet was used to measure ^{13}C T_1s of molten HTC using the inversion recovery pulse sequence. The carbon frequency was 125.77 MHz and DMSO-d_6 was used for spin-locking at approximately 85 °C. Chemical shifts were referenced to DMSO assuming it resonates at 39.51 ppm *vs* TMS.

Downloaded by STANFORD UNIV GREEN LIBR on June 20, 2012 | http://pubs.acs.org
Publication Date (Web): October 14, 2011 | doi: 10.1021/bk-2011-1077.ch016

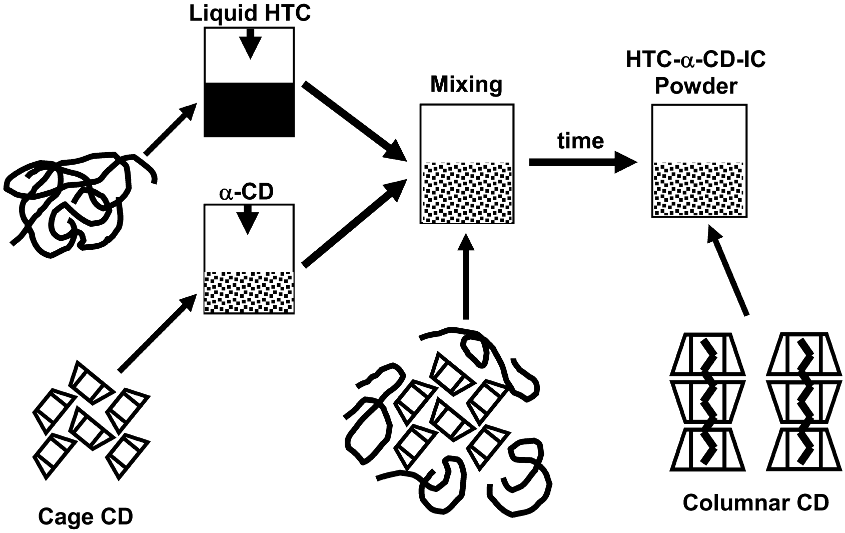

Figure 2. Formation of HTC-α-CD-IC.

High-resolution solid-state ^{13}C-NMR experiments were performed at ICTP (Madrid, Spain) on a Bruker Avance™ 400 spectrometer (Bruker Analytik GmbH Karlsrube, Germany) equipped with a Bruker Ultrashield™ 9.4T (^{13}C frequency of 100.62 MHz), 8.9 cm vertical-bore super-conducting magnet. Cross-polarization and magic angle spinning (CP-MAS) NMR spectra were acquired wth a standard Bruker broad band MAS probe, spinning at 10 KHz. In all cases, high-power proton decoupling was used. The spectra were acquired with 1 ms CP contact time, 5 s recycle delay, and 1920 transients. The NMR spectra were processed and analyzed with the software package XWIN-NMR™ by Bruker. All free-induction decays were subjected to standard Fourier transformation with 10 Hz line broadening and phasing. The chemical shifts were externally referenced to adamantane.

Solid-state spin-lattice relaxation times, $T_1(^{13}C)$, were measured for crystalline HTC and the HTC-α-CD-IC by inversion recovery experiments using the Torchia pulse sequence (*2*). Typically 800 transients were used for each point and 20-30 points were used for each measurement, covering the decay of the signal until it reached 30-40% of its maximum value. The NMR signal intensities of carbon nuclei observed for different time delays were used to calculate the spin-lattice relaxation times by fitting the signal intensity data to a single or double exponential decay function. The criterion for an acceptable fit was set at 95% of residuals within the range ± 0.03.

Results and Discussion

HTC Conformations

Figure 3 presents the 125.8 MHz ^{13}C- NMR spectrum of neat liquid HTC measured at 85 °C, where 5 distinct resonances are observed. Their assignment may be made by reference to Figure 4, which outlines the substituent effects (*3*) experienced by the HTC nuclei. The most intense resonance, at 28.75 ppm *vs* TMS, is produced by the internal methylene carbons $C_{5\text{-}32}$, while the much smaller resonance slightly upfield at 28.37 ppm belongs to the $C_{4,33}$ nuclei. Even though each of the $C_{4\text{-}33}$ carbons have 2α, 2β, and 2γ carbon substituents, carbons C_4 and C_{33} experience increased shielding from one of their γ-substituents (*3*), C_1 or C_{36}, respectively, because the $C_2{-}C_3$ and $C_{34}{-}C_{35}$ bonds are expected (*4*, *5*) to have a slightly higher *gauche* population than the other internal C−C bonds.

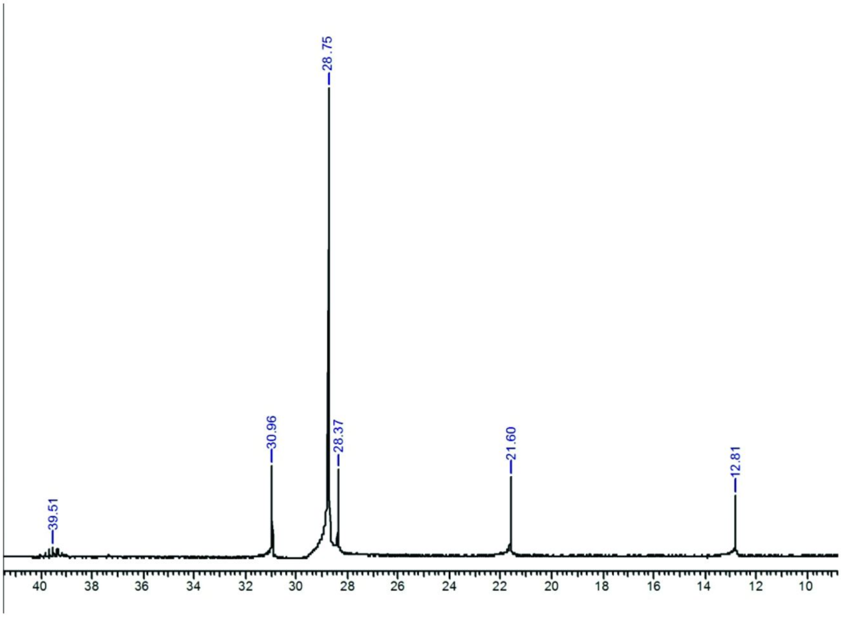

Figure 3. 125.8 MHz ^{13}C- NMR spectrum of neat liquid HTC measured at 85 °C (ppm vs TMS). It should be noted that the chemical shift scale above assumes that δ(DMSO) vs TMS observed at 85 °C remains at 39.51ppm, the value observed at room temperature.

The small resonance ~2.5 ppm downfield from that of the internal $C_{5\text{-}32}$ carbons belongs to $C_{3,34}$, which experience only a single shielding γ-substituent. Finally the two small resonances at 21.60 and 12.81 ppm belong to the $C_{2,35}$ methylene and $C_{1,36}$ methyl carbons, respectively, which have 2α,1β,1γ and 1α,1β,1γ substituents.

$$C_1{-}C_2{-}C_3{-}C_4{-}C_5\ldots\ldots C_{32}{-}C_{33}{-}C_{34}{-}C_{35}{-}C_{36}$$

$C_{1,36}$, $C_{2,35}$, $C_{3,34}$, and $C_{4\text{-}33}$ have α,β,γ; 2α,β,γ; 2α,2β,γ; and 2α,2β,2γ substituents, respectively. α,β-substituents deshield ~ 9-10 ppm, while γ-substituents produce a maximum shielding of ~ -5 ppm (*3*) (See Figure 4).

Downloaded by STANFORD UNIV GREEN LIBR on June 20, 2012 | http://pubs.acs.org
Publication Date (Web): October 14, 2011 | doi: 10.1021/bk-2011-1077.ch016

Downloaded by STANFORD UNIV GREEN LIBR on June 20, 2012 | http://pubs.acs.org
Publication Date (Web): October 14, 2011 | doi: 10.1021/bk-2011-1077.ch016

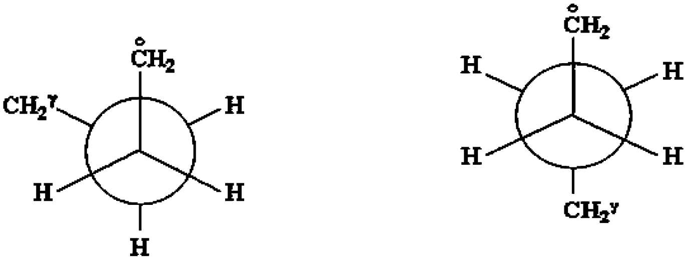

Figure 4. HTC conformations and ^{13}C nuclear shielding. ^{13}C nuclei separated by three bonds in the shielding (~ -5 ppm) gauche (left) and non-shielding (0 ppm) trans (right) conformations.

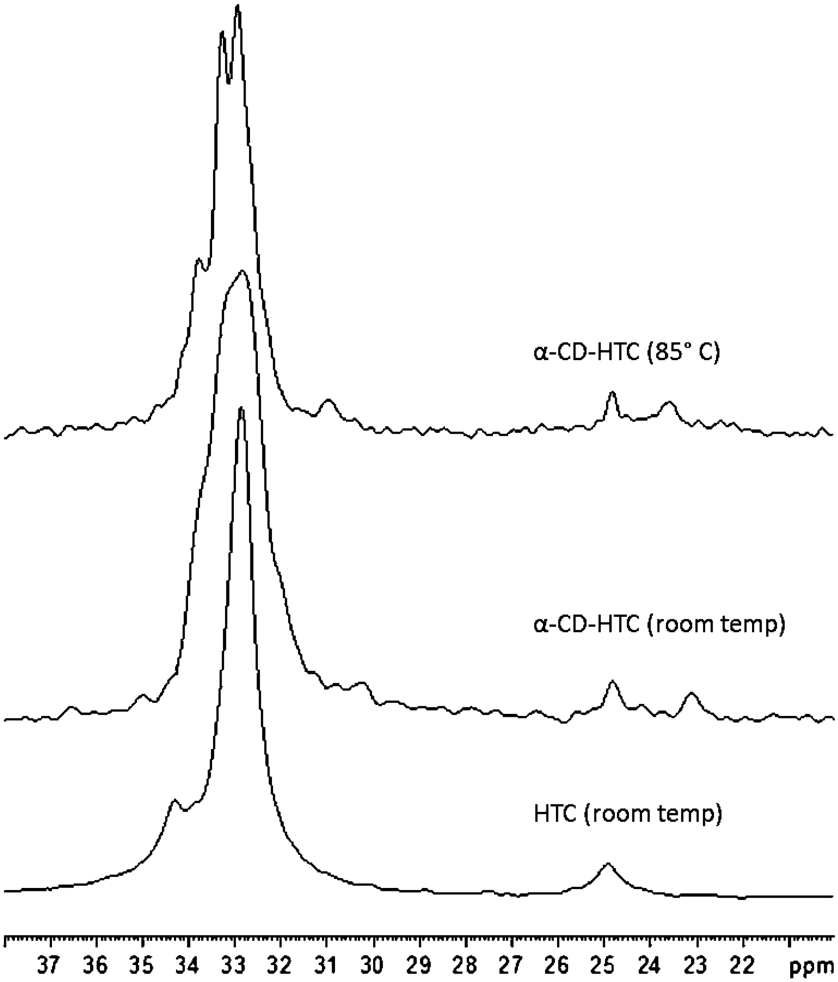

Figure 5. 100.6 MHz CP-MAS/DD ^{13}C- NMR spectra of neat crystalline HTC at 25 °C and HTC-α-CD-IC at 25 and 85 °C.

Downloaded by STANFORD UNIV GREEN LIBR on June 20, 2012 | http://pubs.acs.org
Publication Date (Web): October 14, 2011 | doi: 10.1021/bk-2011-1077.ch016

Figure 5 provides a comparison of the expanded CP-MAS spectra of neat crystalline HTC recorded at 25 and HTC-α-CD-IC recorded at 25 and 85 °C, showing only HTC resonances. All resonances observed in neat crystalline HTC (Figure 5) appear downfield from their positions in the liquid spectrum (Figure 3). The downfield shifts are either ~ 2 or ~ 4 ppm, depending on whether or not a particular carbon has a single ($C_{1,2,3,34,35,36}$) or a pair ($C_{4\text{-}33}$) of γ-substituents, reflecting the fact that the internal C−C bonds in liquid HTC are ~40% *gauche*± (*4*) which provides a shielding of (1 or 2)x0.4x(-5 ppm) ~ -(2 or 4 ppm).

The only notable differences between the CP-MAS spectra of HTC in its neat crystal and in its α-CD-IC is the splitting of the $C_{2,35}$ methylene resonances at 24.8 ppm in crystalline HTC into two resonances at ~24.8 and ~22.8 ppm and the small resonance at 30.5-31.0 ppm, some -2 to -2.5 ppm upfield from the main resonance of the internal methylenes at ~33 ppm in the spectrum of HTC-α-CD-IC. We assign this latter peak to $C_{5,32}$, because they are γ to $C_{2,35}$. In neat crystalline HTC, all internal C−C bonds are *trans*, so the two resonances observed for the $C_{2,35}$ and $C_{5,32}$ methylenes of HTC residing in the narrow α-CD-IC channels strongly suggest two conformational populations for the C_3−C_4 and C_{33}−C_{34} bonds: i) rigidly *trans* (24.8 and 33 ppm) and ii) *trans* and *gauche*± conformations inter-converting rapidly (22.8 and 30.5-31 ppm) on the ~100 MHz frequency scale, like the internal C−C bonds in liquid HTC. This explains the two distinct conformational environments and resultant resonance frequencies for the $C_{2,5,32,35}$ carbons.

It is important to note that the HTC methyl carbon region is absent in all three expanded spectra in Figure 5, but a single methyl resonance at ~15 ppm appears in each full spectrum. This is consistent with C_2−C_3 and C_{34}−C_{35} bonds that are rigidly *trans,* similar to all remaining C−C bonds between C_4 and C_{33}. Apparently, only the C_3−C_4 and C_{33}−C_{34} bonds are exhibiting significant contents of rapidly inter-converting *gauche*± and *trans* conformations, even though the C_2−C_3 and C_{34}−C_{35} bonds might also have been expected to, since they are even closer to the HTC termini.

HTC Dynamics

The spin-lattice relaxation times, $T_1(^{13}C)$, observed for molten HTC are presented in Table 1, and those measured for neat crystalline HTC and HTC residing in the narrow channels of its α-CD-IC are compared in Table 2. The $T_1(^{13}C)$s observed for interior CH_2 carbons in neat crystalline HTC are ~500 s and for the molten liquid HTC are 1-2 s, which are consistent with previous reports (*6*, *7*). The interior CH_2 carbons of HTC chains in the narrow channels (~0.5 nm) of its α-CD-IC exhibit $T_1(^{13}C)$ relaxation times of 1-4 sec. over the temperature range -30 to 85 °C. In the crystal HTC chains experience virtually no ~100 MHz motions, while molten HTC chains are efficiently moving at this frequency, leading to more than a two orders of magnitude decrease in HTC spin-lattice relaxation times. Even though the conformations of HTC chains in the narrow α-CD-IC channels are severely restricted compared to those of neat molten HTC chains, they are also experiencing efficient ~100 MHz motions that lead to virtually identical $T_1(^{13}C)$s in both environments.

Table 1. Spin-lattice relaxation times, $T_1(^{13}C)$, for liquid HTC at 85 °C

HTC Carbon = $\delta(^{13}C)$, ppm	*$T_1(^{13}C)$, s*
$C_{1,36}$ = 12.81	**3.4**
$C_{2,35}$ = 21.60	**2.6**
$C_{4,33}$ = 28.36	**1.7**
$C_{5\text{-}32}$ = 28.75	**1.2**
$C_{3,34}$ = 30.95	**2.1**

Table 2. Spin-lattice relaxation times, $T_1(^{13}C)$, observed for HTC ($C_{5\text{-}32}$) in the neat liquid and crystal and in the channels of its α-CD-IC

Sample	*$T_1(^{13}C)$, s*	*Environment*	*Conformation*
IC (-30 °C)	**1.2**	**α-CD-IC-Channel**	**nearly all trans**
IC (25 °C)	**1,3.6**	**“**	**“ “ “**
IC (85 °C)	**2.6**	**“**	**“ “ “**
Neat (25 °C)	**505**	**Bulk crystal**	**all trans**
Neat (85 °C)	**2.1**	**Bulk liquid**	**random coil**

Thus, we are faced with identifying similarities and differences between the types, length-scales, and cooperativities of HTC chain motions in the very different environments provided by its neat melt and the narrow crystalline channels of its α-CD-IC, as indicated in Figure 6.

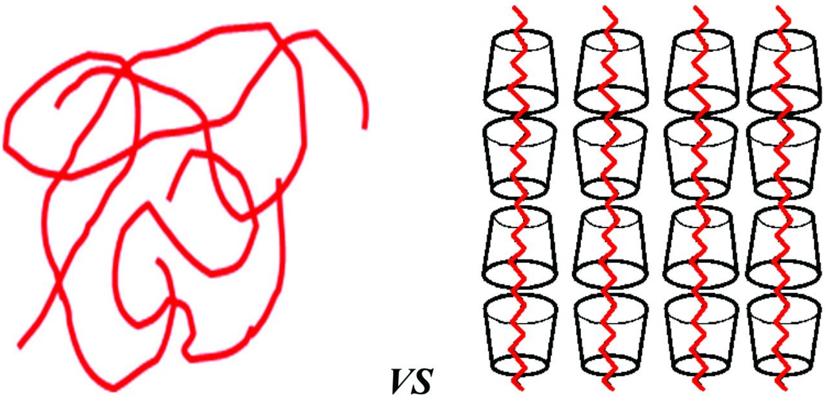

Figure 6. Comparison of conformations and environments of HTC chains in their neat randomly-coiling liquid and confined to the narrow channels of their α-CD-IC.

In Table 3 the spin-lattice relaxation times of neat α-CD and for HTC and α-CD observed in their IC are presented. First, it is obvious that in the cage

Downloaded by STANFORD UNIV GREEN LIBR on June 20, 2012 | http://pubs.acs.org
Publication Date (Web): October 14, 2011 | doi: 10.1021/bk-2011-1077.ch016

crystalline structure of neat α-CD, the constituent carbons in each glucose ring evidence $T_1(^{13}C)$s an order of magnitude longer than those observed in the columnar crystal structure of the HTC-α-CD-IC. It is also clear that the $T_1(^{13}C)$s of the ring carbons (C_{1-5}) in α-CD are also ~ an order of magnitude longer than those of the guest HTC chains residing in the columnar IC channels formed by the stacks of host α-CD. As a result, we cannot attribute the very short $T_1(^{13}C)$s observed for the included guest HTC chains to facile ~100 MHz motions of the host α-CD protons. The near coincidence of $T_1(^{13}C)$s observed for HTC in the melt and in the narrow channels of its α-CD-IC must be a consequence solely of the ability of HTC chains to undergo facile ~100 MHz motions in both of these very disparate environments.

Lyerla et al. (*7*) examined the ^{13}C spin-lattice relaxation times for a series of liquid n-alkanes and a single branched alkane, 2-methylnonadecane. From observations made at 15.08 MHz, they were able to determine the corresponding effective correlation times, τ_{eff}, for rotation of their C−H bond vectors,

$$\tau_{eff} = r_{CH}{}^6/kT_1N_H,$$

where N_H is the number of protons directly attached to a carbon nucleus and r_{CH} is the length of the C−H bond. They noted that *i)* for a particular carbon (C_1, C_2, C_3, etc.) τ_{eff} progressively increases as the chain length increases, *ii)* τ_{eff}s increase from the chain ends toward the interior of each *n*-alkane, and *iii)* the ratio of correlation times for the terminal methyl groups to those of the internal methylene carbons also increases as the length of the *n*-alkane increases. This suggested that the rotational motion of C−H bond vectors in hydrocarbons can be analyzed as a sum of rigid body rotation of the entire *n*-alkane, with a rate of τ_0^{-1}, plus internal motion due to rotations about individual C−C bonds *i*, with a rate τ_i^{-1}.

The methyl branch in 2-methylnonadecane caused its C_{1-5} carbons to have resonances distinct from those of the C_{15-19} carbons at the unsubstituted terminus. However, the $T_1(^{13}C)$ observed and the correlation time derived for C_5 were the same as those observed and derived for the C_{6-15} carbons in 2-methylnonadecane and the C_{5-16} carbons in the linear isomer eicosane. As a consequence, Lyerla et al. (*7*) concluded that "the segmental motion, which determines the correlation time of a carbon in a (liquid) long chain n-alkane, involves *ca.*5-6 carbons on each side of a given carbon." From this we can at least suggest that the efficient ~100 MHz motions responsible for the short $T_1(^{13}C)$s observed for interior HTC carbons in the melt involve somewhat cooperative inter-conversions between the conformations of 10-12 carbon atom chain segments.

Clearly distinguishable from these longer-range cooperative motions are the much faster, more localized, and probably less correlated $t \leftrightarrow g\pm$ conformational inter-conversions occurring about the -C−C- bonds in *n*-alkanes C_n ($n \geq 4$) at frequencies much greater than 100 MHz. These result in the rapid establishment of equilibrium bond conformational populations that are reflected in the resonance frequencies observed in liquid *n*-alkanes, which are described above by the conformationally sensitive γ-*gauche* effect, and are ineffective in the spin-relaxation of their carbon nuclei.

Downloaded by STANFORD UNIV GREEN LIBR on June 20, 2012 | http://pubs.acs.org
Publication Date (Web): October 14, 2011 | doi: 10.1021/bk-2011-1077.ch016

Downloaded by STANFORD UNIV GREEN LIBR on June 20, 2012 | http://pubs.acs.org
Publication Date (Web): October 14, 2011 | doi: 10.1021/bk-2011-1077.ch016

Table 3. Solid-State ^{13}C NMR spin-lattice relaxation times for neat α-CD and HTC and α-CD in HTC-α-CD-IC

T_1, s					
	←	α-CD		→	
Sample	C1	C4	C2,C3,C5	C6	CH_2(HTC)
Cage α-CD (25°C)	200, 13	190, 12	190, 12	103, 7	
HTC/IC (25 °C)	37	27	21	4, 0.4	1, 3.6
HTC/IC (85 °C)	21	17	13	0.6	2.6
HTC (crystal at 25 °C)					505
HTC (melt at 85 °C)					1.2

Turning now to the ~100 MHz motions of HTC chains isolated in the narrow channels of its α-CD-IC, two things are clear from the observed splitting of the $C_{2,35}$ methylene resonance at 24.8 ppm in crystalline HTC into two resonances at ~24.8 and ~22.8 ppm in HTC-α-CD-IC (also $C_{5,32}$ at ~33 and ~31 ppm) and the two distinct T_1s observed for the internal carbons at 25 °C (See Table 3). First, the short T_1s observed for the internal carbons of HTC included in the α-CD-IC channels are not dominated by rigid-body rotation of all-*trans* HTC chains in the host α-CD-IC channels. Second, roughly half the C_3–C_4 and C_{33}–C_{34} bonds are experiencing *t* ↔ *g*± inter-conversions that are much too rapid to cause spin-lattice relaxation of HTC carbon nuclei at the ~100 MHz frequency employed here to observe them, while the other half are rigidly *trans.*

Consistent with the distinct T_1s observed for terminal and interior carbons in crystalline *n*-alkanes (*6*), we observe T_1s of 1.8, 30, and 505 s for $C_{1,36}$, $C_{2,35}$, and $C_{3\text{-}34}$, respectively, in neat crystalline HTC and 3.3 and 1.3 s for the $C_{1,36}$, and $C_{2\text{-}35}$ HTC carbons in the α-CD-IC. When compared to the single T_1s observed for all *n*-alkane carbons in their high temperature rotator phases (*6*), it is clear that neither in the neat crystal or α-CD-IC are the short HTC T_1s a result of rigid body rotation.

In addition, the two T_1s observed at 25 °C for the internal HTC carbons in its α-CD-IC suggest that the HTC chains are moving under the constraints of two distinct channel environments. In Figure 7 note that the difference in diameters of the head and tail portions of α-CDs results in a gradual undulation of their columnar channels that is similar to stacked "hour-glasses". Thus, the motions of those portions of HTC chains in the head-to-head channel regions would not be as constrained as those in the tail-to-tail regions, possibly providing sufficient room for facile ~100 MHz motions important to spin-lattice relaxation. These are likely the regions where C_3–C_4 and C_{33}–C_{34} bonds experience the much more rapid *t* ↔ *g*± conformational inter-conversions that lead to resonance frequencies for some C_2 and C_{35} carbons that are shifted upfield by conformationally averaged γ-*gauche* shielding from those in a rigid *trans* arrangement with C_5 and C_{32}.

To assist our analysis and discussion of the ~100 MHz motions that efficiently relax the HTC carbon nuclei included in the narrow channels of the HTC-α-CD-IC, we briefly summarize a fully atomistic molecular dynamics (MD) modeling of 30 repeat unit (60 carbon) polyethylene (PE-60) chain confined to a single α-CD- IC channel, and conducted by Pozuelo et al. (*8*). Both rigid and flexible α-CD-IC channels were considered during 1ns MD tra-jectories run at 500K. At the end of both trajectories, each -CH_2–CH_2- bond had a *trans* (0 ± 7-11°) population of over 99%. These small torsional fluctuations occured much more rapidly than ~100 MHz, and could not produce efficient $T_1(^{13}C)$ relaxation of the HTC carbons when confined in the narrow α-CD-IC channels. In addition, virtually no rigid-body rotational or translational motions were observed for the included PE-60 chain, consistent with the previously mentioned observation of distinct T_1s for the terminal and interior HTC carbons in its α-CD-IC.

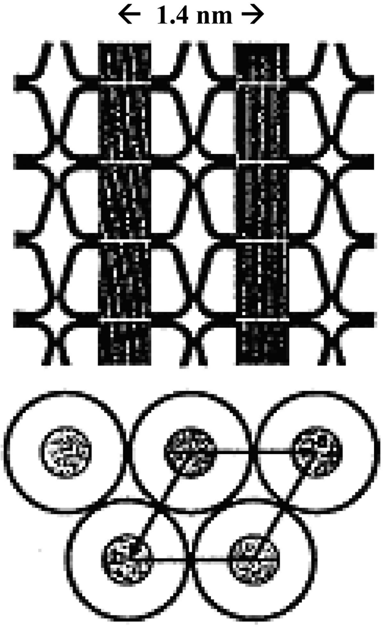

Figure 7. The columnar structure of polymer-α-CD-ICs. The black areas indicate the channels occupied by the included guest polymer chains.

Though an order of magnitude less frequently observed than in a single free PE-60 chain, $t \leftrightarrow g\pm$ conformational inter-conversions were observed about ~ 5 and 0 of the PE-60 bonds when confined to flexible and rigid α-CD-IC channels, respectively. Extrapolation of these PE-60-α-CD-IC MD simulation results, suggests that nearly each of the 59 PE-60 -C–C- bonds [(5 bonds/ns)x 10ns = 50 bonds] would undergo a $t \leftrightarrow g\pm$ conformational inter-conversion over a longer 10ns trajectory, with a corresponding frequency of ~ 100 MHz, while maintaining an overall nearly all *trans* average PE conformation. This might explain the short T_1s observed for the predominantly all *trans* HTC chains in the HTC-α-CD-IC, but do the motions of these highly constrained conformational inter-conversions also explain the similar short T_1s observed for HTC in the melt?

Downloaded by STANFORD UNIV GREEN LIBR on June 20, 2012 | http://pubs.acs.org
Publication Date (Web): October 14, 2011 | doi: 10.1021/bk-2011-1077.ch016

Downloaded by STANFORD UNIV GREEN LIBR on June 20, 2012 | http://pubs.acs.org
Publication Date (Web): October 14, 2011 | doi: 10.1021/bk-2011-1077.ch016

According to the analysis of the spin-lattice relaxations observed in liquid *n*-alkanes by Lyerla et al. (*7*), apparently not, because "the segmental motion, which determines the correlation time of a carbon in a (liquid) long chain *n*-alkane, involves *ca.*5-6 carbons on each side of a given carbon." While the ~100 MHz chain motions effective in relaxing the carbon nuclei in liquid HTC and in its α-CD-IC are both conformational in origin, they likely differ both in their length-scales and cooperativities. In the α-CD-IC, $t \leftrightarrow g^{\pm}$ transitions are likely restricted to shorter-range $ttt \rightarrow g{\pm}tg{\mp}$ (kink) and possibly $ttttt \rightarrow g{\pm}tttg{\mp}$ (jog) transitions in the somewhat flexible α-CD channels (*9*), and, because $t \rightarrow g^{\pm}$ transitions require surmounting a higher intrachain barrier than $g^{\pm} \rightarrow t$ transitions and $g^{\pm}$ conformations are rare there, they are also likely more cooperative. Liquid HTC chains are not, however, constrained by α-CD-IC channels, but must only avoid segmental overlaps during and after their conformational transitions, and so their ~100 MHz motions are likely less cooperative and apparently longer in range.

Before concluding, it should be noted that the conformations and motions of *n*-alkane guests included in the narrow channels of their inclusion compounds or clathrates made with other hosts, such as urea (U), cyclotriphosphazenes (TPP), perhydrotriphenylene (PHTP), etc. generally appear to be distinct (*10–13*) from those discussed here for HTC in its α-CD-IC. This may be due to the unique covalently-bonded cyclic nature of host CDs (See Figure 1). The constraints experienced by guest polymers, that are threaded through host CDs and that are eventually completely included in the channels formed by the uniaxially stacked CDs when they crystallize to form a polymer-CD-IC, are expected to be more severe than those produced by the channels formed from U, TPP, and PHTP hosts, whose constraining channel walls lack the strength of the covalent bonding in individual CDs.

Summary and Conclusions

In the rigid crystals of HTC there are apparently almost no ~100 MHz motions able to relax the HTC ^{13}C nuclei. In the randomly-coiling liquid there are relatively long-range conformational motions, that are able to efficiently relax the HTC ^{13}C nuclei. Though predominantly restricted to the nearly fully extended all trans conformation in the narrow (~5Å) α-CD-IC channels, apparently here there are also facile ~100 MHz conformational (t ↔ g) motions occurring that very efficiently relax the HTC ^{13}C nuclei. However, in the α-CD-IC channels the motions of guest HTC chains are more cooperative in nature and of a shorter-range than in the neat liquid.

References

1. Hunt, M. A.; Tonelli, A. E.; Balik, C. M. *J. Phys. Chem. B* **2007**, *111*, 3853.
2. Torchia, D. A. *J. Magn. Reson.* **1978**, *30*, 613.
3. Tonelli, A. E. *NMR Spectroscopy and Polymer Microstructure:The Conformational Connection*; VCH Publishers: New York, 1989.

4. Flory, P. J. *Statistical Mechanics of Chain Molecules*; Wiley-Interscience: New York, 1969; Chapter 2.
5. Cheng, H. N.; Bovey, F. A. *Org. Magn. Reson.* **1978**, *11*, 457.
6. Russell, K. E.; Wu, G.; Blake, S.; Heyding, R. D. *Polymer* **1992**, *33*, 951.
7. Lyerla, J. R.; McIntyre, H. M.; Torchia, D. A. *Macromolecules* **1974**, *7*, 11.
8. Pozuelo, J.; Mendicutti, F.; Saiz, E. *Polymer* **2002**, *43*, 523.
9. Tonelli, A. E. *Macromolecules* **1990**, *23*, 3134.
10. Sozzani, P.; Bovey, F. A.; Schilling, F. C. *Macromolecules* **1991**, *24*, 6764.
11. Schilling, F. C.; Amundson, K. R.; Sozzani, P. *Macromolecules* **1994**, *27*, 6498.
12. Nakaoki, T.; Nagano, H.; Yangida, T. *J. Mol. Struct.* **2004**, *699*, 1.
13. Becker, J.; Comotti, A.; Simonutti, R.; Sozzani, P.; Saalwachter, K. *J. Phys. Chem. B* **2005**, *109*, 23285.

Downloaded by STANFORD UNIV GREEN LIBR on June 20, 2012 | http://pubs.acs.org
Publication Date (Web): October 14, 2011 | doi: 10.1021/bk-2011-1077.ch016

Downloaded by UNIV OF DELAWARE MORRIS LIB on June 21, 2012 | http://pubs.acs.org
Publication Date (Web): October 14, 2011 | doi: 10.1021/bk-2011-1077.ch017

Chapter 17

NMR Characterization and Product Design of Novel Silk-Based Biomaterials

Aya Nagano,[1] Yu Suzuki,[1] Yasumoto Nakazawa,[2] J. T. Gerig,[3] and Tetsuo Asakura*,[1]

[1]Department of Biotechnology, Tokyo University of Agriculture and Technology, Koganei, Tokyo, 184-8588 Japan
[2]Science Museum, Tokyo University of Agriculture and Technology, Koganei, Tokyo, 184-8588 Japan
[3]Department of Chemistry, University of California, Santa Barbara, CA 93106 U.S.A.
***E-mail: asakura@cc.tuat.ac.jp**

The atomic-level structure of the crystalline region of *B. mori* silk fibroin was studied using solid state NMR and statistical mechanical calculations. Whereas lamellar structures were proposed for both $(AG)_{15}$ and $(AGSGAG)_5$ repetitive sequences of the crystalline region, the β-turn in $(AGSGAG)_5$ was found to be more distorted compared to that in $(AG)_{15}$. In view of this structural information, silk-like mineralized composite materials were designed and characterized by solid state NMR. Furthermore, recombinant proteins were designed and produced in *E. coli* and transgenic silkworm. The films of these recombinant proteins exhibit high calcium binding activity and rapid mineralization.

I. Introduction

Silks are fibrous proteins with properties that have intrigued scientists ranging from polymer chemists to biomedical researchers (*1*). Silkworm (*Bombyx mori or B. mori*) produces silk fibroin filaments with outstanding strength, toughness, and other desirable properties, despite being spun from an aqueous solution at ambient temperature and pressure. In addition, silk fibroin has good biocompatibility, resistance to thermal and enzymatic degradation, and mechanical resilience, and

In NMR Spectroscopy of Polymers: Innovative Strategies for Complex Macromolecules; Cheng, H., et al.;
ACS Symposium Series; American Chemical Society: Washington, DC, 2011.

it can be fashioned into a wide range of forms including nano- and microparticles, films, sponges, and composites. This portfolio of properties suggests its considerable potential for applications in medicine and surgery (*2*).

Silk fibroin is composed of amorphous domains (mainly consisting of hydrophilic amino acids) and crystalline domains (mostly hydrophobic amino acids). The primary structure of crystalline domains contains multiple repetitions of (G-A-G-A-G-S) sequence which make up approximately one-half of the total silk fibroin (*3*). These repetitive sequences are responsible for the formation of antiparallel β-sheets in the spun fibers. The β-sheet formation ultimately contributes to the stability and the remarkable mechanical properties of silk fibers.

The objectives of this work are to investigate the molecular-level conformation of silk fibroin crystalline region and design silk-like biomaterials based on the structural information obtained. In Section II, the conformational analysis of the crystalline region of silk fibroin is described. The design of novel silk-based biomaterials and their characterization are delineated in Section III. The applications of these novel biomaterials are described in Section IV. Finally, in Section V the behavior of silk fibroin in fluorinated alcohols as studied by solution NMR is summarized.

Downloaded by UNIV OF DELAWARE MORRIS LIB on June 21, 2012 | http://pubs.acs.org
Publication Date (Web): October 14, 2011 | doi: 10.1021/bk-2011-1077.ch017

II. Structural Studies

Silk fibroin has two distinct structures in the solid state, silk I (before spinning) and silk II (after spinning). The conformation of silk I has been shown by solid state NMR and X-ray diffraction to have a repeated type II β-turn structure (*4*, *5*). As for the structure of silk II, Marsh et al. (*6*) were the first to propose an antiparallel β-sheet model based on fiber diffraction studies of native *B. mori* silk fiber. Even though the local protein conformation is still the basic β-sheet as proposed by Marsh et al., a *refined* silk II model incorporates stacking of the β-sheet planes in two different arrangements (*7*).

Solid state NMR was used to clarify the silk II structure of both *B. mori* silk fibroin and $(AG)_{15}$ (*8–10*). Broad and asymmetric Ala Cβ peaks were observed in the ^{13}C CP/MAS NMR spectra, indicating a heterogeneous structure. The relative proportions of the various heterogeneous components were determined from the relative peak intensities of the deconvoluted spectra. For example, the deconvoluted Ala Cβ peaks yielded 27% distorted β-turn (16.7 ppm), 46% β-sheet (alternating Ala residues, 19.1 ppm), and 27% β-sheet (parallel Ala residues, 22.4 ppm) (*9*).

In an investigation of the heterogeneous components, the local structure for each Ala residue was determined from ^{13}C CP/MAS NMR spectra for model peptides of the crystalline region of silk fibroin, $(AG)_{15}$ and $(AGSGAG)_5$ (*11*, *12*). Figure 1 shows the difference in Ala Cβ spectra of 10 different $[3\text{-}^{13}C]$Ala-$(AGSGAG)_5$ peptides differing in their ^{13}C labeling positions. It shows that the peak patterns change largely depending on the labeled position of the Ala residue, indicating varying local structures along the peptide chain. The fraction corresponding to the 16.7 ppm component was determined to be 75% for the Cβ carbon of Ala (*1*) in the peptide, indicating that the Ala residue at the start of the sequence has a high probability of forming a random coil. The fraction was markedly lower (26%) at Ala (*5*) but rose to a second maximum (44%) at Ala (*19*).

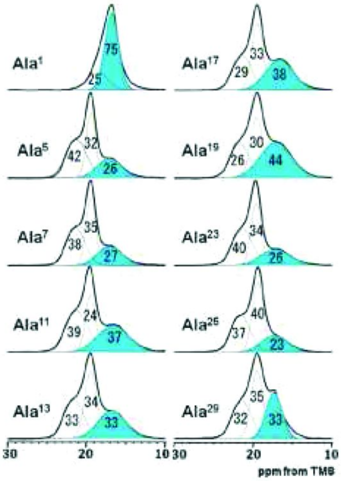

Figure 1. Fraction (%) of the 16.7 ppm peak calculated from the deconvolution of Ala Cβ peaks in the ^{13}C CP/MAS NMR spectra of 10 [3-^{13}C](AGSGAG)$_5$ with different [3-^{13}C]Ala labeling sites as a function of the ^{13}C labeled positions.

For an investigation of the entire conformation of (AGSGAG)$_5$ in silk II form, it is necessary to determine the local conformations of Ser residues as well as Ala residues. In our laboratory the information was obtained from the internuclear distances between [1-^{13}C]Gly and [^{15}N]Gly nuclei in the sequence, [1-^{13}C]Gly-Ser-[^{15}N]Gly, indirectly because the distance reflected the local conformation of the Ser residue between two Gly residues. REDOR (*13*) was used for this purpose.(Figure 2) As a starting point, the theoretical REDOR curve was calculated by assuming the distance between [1-^{13}C]Gly and [^{15}N]Gly nuclei in the sequence, [1-^{13}C]Gly-Ser-[^{15}N]Gly, to be 4.75 Å, similar to the antiparallel β-sheet structure obtained from the crystal structure of *B. mori* silk fibroin determined by Takahashi et al. (*7*) However, the curve could not reproduce the observed REDOR curve, indicating that the conformation of the Ser residue was a mixture of random coil and antiparallel β-sheet structures, as expected. The atomic distance for random coil conformation was calculated to be 3.80 Å by averaging the distances between the carbonyl carbon of the first Gly residue and the amide nitrogen of the third Gly residue in the Gly-Ser-Gly sequences selected from PDB data base. With the assumption of the presence of both antiparallel β-sheets and random coil, the REDOR curve was re-calculated. The theoretical REDOR curve of the mixture, 30% random coil and 70% antiparallel β-sheet, gave the best-fit to the experimental REDOR plot of Ser^{15th}. Thus, the fraction of random coil for Ser^{15th} residue was determined to be 30 % and the same fitting process was performed for the remaining four peptides.

Downloaded by UNIV OF DELAWARE MORRIS LIB on June 21, 2012 | http://pubs.acs.org
Publication Date (Web): October 14, 2011 | doi: 10.1021/bk-2011-1077.ch017

Downloaded by UNIV OF DELAWARE MORRIS LIB on June 21, 2012 | http://pubs.acs.org
Publication Date (Web): October 14, 2011 | doi: 10.1021/bk-2011-1077.ch017

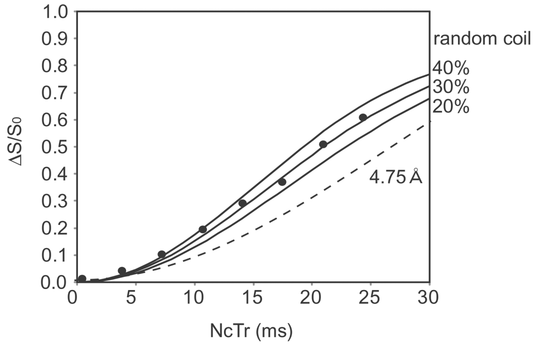

Figure 2. Observed and calculated REDOR plots for the [1-^{13}C]Gly^{14}-Ser^{15}-[^{15}N]Gly^{16}-labeled (AGSGAG)$_5$ peptides (Ser^{15th}). Solid lines represent the REDOR curves calculated by changing the fractions of the random coil (3.80 Å) and β-sheet (4.75 Å) forms. The broken line corresponds to the β-sheet (4.75 Å).

The fractions of the distorted β-turn and/or random coil components were determined from the relative intensities of [3-^{13}C]AlaCβ peaks at 16.7 ppm for Ala residues and for Ser residues from the REDOR curves of the [1-^{13}C]Gly-Ser-[^{15}N]Gly labeled versions. Figure 3 shows these data plotted against the residue position within (AG)$_{15}$ (gray) and (AGSGAG)$_5$ (black). These changes strongly indicate β-sheet – β-turn – β-sheet repeated lamellar structure. A comparison of the plots for (AG)$_{15}$ and (AGSGAG)$_5$ shows that on the whole the fractions of the distorted β-turn and/or random coil component were higher in (AGSGAG)$_5$ except for the two Ala residues at the N-terminal sites. The way the fractions varied with position was slightly different in the two peptides.

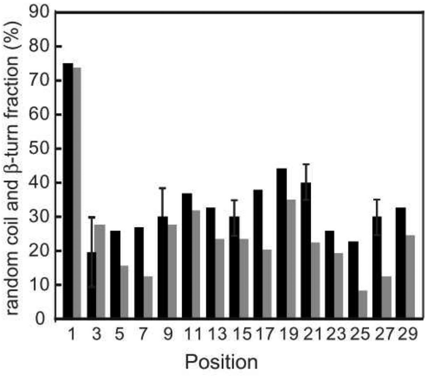

Figure 3. Observed relative intensities (black) of distorted β-turn and/or random coil structural component of (AGSGAG)$_5$ obtained from the peak at 16.7 ppm of Ala Cβ and REDOR bimodal fitting for Ser residues are shown at different position. The observed relative intensities (grey) of distorted β -turn and/or random coil structure component of (AG)$_{15}$ are also shown for comparison.

We used statistical mechanical calculation (*27*) to investigate possible lamellar structures in $(AG)_{15}$ (*14*) and $(AGSGAG)_5$ (*12*). The calculations were initially based on the following assumptions: (1) after β-turn formation along the chain there was at least one pair of intramolecular hydrogen-bonded strands forming a β-sheet structure; (2) the direction of the β-turn formation along the chain was always from the N-terminal to the C-terminal; (3) there was one or two turns in the peptide. The occurrence probability, $p(i)$, of the *i*-th structure for $(AG)_{15}$ and $(AGSGAG)_5$ was calculated as follows:

$$p\,(i) = \exp(-\Delta E(i)\,/\,kT)$$

where $\Delta E(i)$ is the potential energy of the *i*-th structure, *k* is the Boltzmann's constant, and *T* is the absolute temperature. The relative potential energy of the *i*-th structure, $\Delta E(i)$, was estimated from the stabilization energy, ΔE_H (due to the formation of inter-residue hydrogen bonds for each residue with β-sheet structure), ΔE_T (due to the formation of turn structure), and ΔE_S (due to Ser residues incorporated in β-sheet).

$$\Delta E(i) = n_H\,(i)\Delta E_H + n_T\,(i)\Delta E_T + n_S\,(i)\Delta E_S$$

where $n_H(i)$, $n_T(i)$ and $n_S(i)$ are the numbers of hydrogen bonds, turns in the *i*-th structure, and Ser residues incorporated in β-sheet, respectively.

The fraction of non-β-sheet conformations calculated with optimized ΔE_H, ΔE_T, and ΔE_S were plotted against the residue position. The calculated plot agreed well with the observed data for $(AG)_{15}$. However, the agreement between the observed and calculated plots for $(AGSGAG)_5$ was not satisfactory when compared to $(AG)_{15}$ as shown in Figure 4(a). Therefore, the calculations were repeated by changing an assumption slightly for $(AGSGAG)_5$; the residues incorporated in the β-sheet structure next to the β-turn positions were allowed to form one hydrogen bond instead of two. Other assumptions were kept the same. With optimized ΔE_H, ΔE_T and ΔE_S, the fraction of non-β-sheet conformations calculated was plotted against the residue position. A considerably better agreement between the observed and calculated plots was obtained when compared with the first calculation (Figure 4(b)).

The most probable lamellar structure for $(AGSGAG)_5$ is shown in Figure 5. A comparison of the plots for $(AG)_{15}$ and $(AGSGAG)_5$ shows that on the whole the fractions of the distorted β-turn and/or random coil component were higher in $(AGSGAG)_5$ except for the two Ala residues at the N-terminal sites. This result indicates that the presence of repeated Ser residues in the peptide chain may result in some disturbance to the β-sheet distorted β-turn lamella structure. In this connection it is interesting to note that Fraser et al. (*15*, *16*) reported that unit cell dimensions (a, b, c) of $(AG)_n$ and $(AGAGSG)_m$ are 9.42, 6.95, 8.87 Å and 9.39, 6.85, 9.05 Å respectively. In the c-axis, the direction perpendicular to the plane of the pleated sheet, the unit cell dimension in $(AGAGSG)_m$ was 9.05 Å, markedly larger than the 8.87 Å in $(AG)_n$. The data strongly support our hypothesis that the side chains of Ser residues in $(AGSGAG)_5$ stick out perpendicular to the plane of the β-sheet, producing a larger c-spacing compared to $(AG)_{15}$. We suggest that this larger separation allows looser, less regularly located turns in

Downloaded by UNIV OF DELAWARE MORRIS LIB on June 21, 2012 | http://pubs.acs.org
Publication Date (Web): October 14, 2011 | doi: 10.1021/bk-2011-1077.ch017

Downloaded by UNIV OF DELAWARE MORRIS LIB on June 21, 2012 | http://pubs.acs.org
Publication Date (Web): October 14, 2011 | doi: 10.1021/bk-2011-1077.ch017

the lamella structure. Gong et al. (*17*) proposed a tentative structural model for cross-β protofibrils prepared from regenerated *B. mori* silk fibroin solution on the basis of X-ray diffraction, TEM, and AFM images. The nanofibrils were approximately 5 nm in width while the GS or GA at the C-end of a typical segment GAGAGSGAGAGS gave rise to a single turn between a β-strand dimer. The laminated β-sheet length proposed by them is reasonably consistent with our models which consist of turns and β-strand with approximately 8-12 amino acids at the central sequence of the proposed lamella structure with two turns for the peptides, $(AG)_{15}$ and $(AGSGAG)_5$.

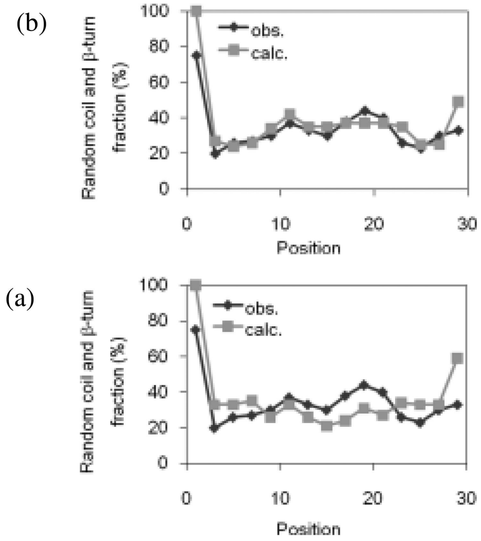

Figure 4. Observed (black) and calculated relative intensities (grey) of the β-turn and/or random coil structure component with different position. (a) this plot represents the first calculation, where the agreement between the observed and calculated plots is not satisfactory compared to the same analysis for $(AG)_{15}$. (b) this plot gives the revised calculation where the assumptions are slightly changed: the residues incorporated into β-sheet structure next to the β-turn positions form only one hydrogen bond instead of two. The agreement between the observed and the calculated plots is satisfactory.

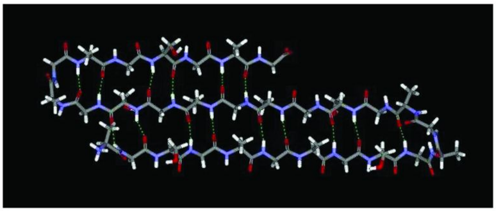

Figure 5. The most probable lamellar structure for $(AGSGAG)_5$, obtained by the combined use of ^{13}C CP/MAS NMR and statistical mechanical calculations.

Downloaded by UNIV OF DELAWARE MORRIS LIB on June 21, 2012 | http://pubs.acs.org
Publication Date (Web): October 14, 2011 | doi: 10.1021/bk-2011-1077.ch017

III. Design and Modifications

The mineralization process is naturally induced in native bone through self-assembly at the charged acidic domains of non-collagenous proteins, which provide adequate conditions for calcium-binding, nucleation and development of ordered hydroxyapatite crystals (*18–21*). Peptide-mediated initiation of nanocrystals offers a new platform for obtaining self-assembling of peptides with tailor-made sequences that promote biomineralization. The concept of molecular self-assembly has become the driving force for the development of new biomaterials (*22–35*). Scientists have identified key parts of molecules (mainly proteins) responsible for the self-assembly process, analyzed them, and developed simpler systems. Earlier research has revealed the tendency of copolypeptides with alternating hydrophilic and hydrophobic residues to form water-soluble β-sheet structures through self-assembly (*36–39*). These studies have shown that alternating amphiphilic-peptide sequences such as poly-(Lys-Phe), poly-(Glu-Ala), poly-(Tyr-Glu), poly-(Val-Lys), and poly-(Lys-Leu) produce β-sheet secondary structures and aggregates, depending on salt concentration and pH (*36–39*).

In our efforts, we sought to design silk-like amphiphilic proteins for bone repair with glutamic acid or aspartic acid components (*40–42*). *B. mori* silk crystalline region has a lamellar structure as indicated in Section II; it seems useful to design biomaterials based on that structure. The design concept also originated from a desire to utilize silk with superior mechanical properties and biocompatibility as bone repair scaffold and to develop the hydrophobic (AGSGAG) region in silk as a part of self-assembling amphiphilic moiety. As mineralization site, we adopted a hydrophilic sequence with contiguous acidic (glutamic and aspartic acids) from non-collagenous proteins. The proteins were then produced with the hydrophobic region of silk and the hydrophilic region with mineralization characteristics.

Thus, we first started with silk-like peptides based on Ala-Gly repeated sequences with a lamellar structure and Asp as a Ca binding site (Figure 6). We further modified the design of the lamellar structure by introducing a Ser residue between $(GlyAla)_3$ and $(AlaGly)_3$ sequences.

1. Structure 41SDSDS - $(GlyAla)_3Ser(AlaGly)_3Asp(GlyAla)_3$ $Ser(AlaGly)_3Asp$ - $(GlyAla)_3Ser(AlaGly)_3$. There are three labeled versions with ^{13}C labeling in different positions.
2. Structure 14DS16 - ThrSer-$[(AlaGly)_3Asp(GlyAla)_3Ser]_{16}$.

The lamellar structures of the two novel artificial silk-like materials (41SDSDS and the much larger 14DS16) were characterized using ^{13}C CP/MAS and spin-diffusion solid-state NMR. The β-sheet fraction in Ala residues increased with increased distance from the Asp residue in the turn part. The Ser residue assumed almost 100% β-sheet structure probably because it formed an extra hydrogen bond that stabilized the stem part of $(AlaGly)_n$. Position-selective and sensitive information useful to characterize the detailed lamellar structure with heterogeneous local conformation was obtained by selective labeling of the peptide with ^{13}C and determining ^{13}C conformation-dependent NMR chemical shifts. If the Asp residue is located at the center of the turn, one-half of these

Ala residues forms β-sheet with intermolecular hydrogen bonding, but the other half takes on a distorted structure under the influence of the adjacent Asp residue. The high fraction of random coils strongly suggested that Asp (*14*) is at the center of the turn as discussed by Wang *et al* (*43*). In contrast, the fraction of β-sheet increased to 67% for Ala (*10*) and 68% for Ala (*8*) residues. Similarly, the β–sheet increased to 70% for Ala (*18*) and 79% for Ala (*20*) residue. Thus, apart from proximity to the turn position (Asp (*14*)) the fraction of β-sheet was high. The fraction of β-sheet was slightly higher for Ala (*16*), Ala (*18*) and Ala (*20*) compared with Ala (*12*), Ala (*10*), and Ala (*8*) indicating that the proportion of β-sheet slightly increased for the Ala residues located in the central parts of the stem region of the lamellar structure (Figure 7). As shown in Figure 7, the Ser Cγ (54.6 ppm) and Cα (63.7 ppm) peaks indicated that the Ser residues in 41SDSDS take on almost solely β-sheet structure (*44*). The deuterium solid-state NMR study of [3,3-$^2H_2$]Ser *B. mori* silk fibroin fiber suggested that the hydroxyl groups of Ser interact with carbonyl groups on adjacent chains and thereby contribute to the intermolecular hydrogen-bonding network of the fiber (*45*). Figures 7(d) and 6(e) show the ^{13}C CP/MAS NMR spectra of nonlabeled 41SDSDS and 14DS16 respectively. The two spectra are very similar; for example, the chemical shifts of the main peaks are identical. Thus, 14DS16 is thought to take on a structure similar to that of 41SDSDS; Asp residues are exposed on the surface of the lamellar structure and are not incorporated into the β-sheet structure. The Ser residues in the 14DS16 may similarly contribute an additional intermolecular hydrogen bond, thereby further stabilizing the β-sheet structure of the stem part of 41SDSDS. Our results from ^{13}C CP/MAS NMR indicated that there are still around 30% distorted β-turn and/or random coil in the Ala residues adjacent to the Ser residues.

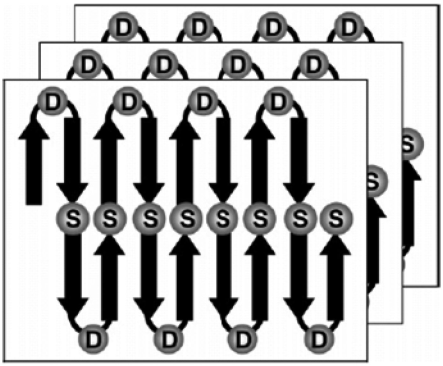

Figure 6. Design of lamellar structure of the silk-like peptide based on Ala-Gly repeated sequences with antiparallel β-sheet structure, where Asp (D) is a Ca binding site in the turn part and a Ser (S) residue is located between (GlyAla)$_3$ and (AlaGly)$_3$ sequences to strengthen the stem part of the lamella.

We designed another silk-like protein, (Glu)$_n$(Ala-Gly-Ser-Gly-Ala-Gly)$_4$; (E)$_n$(AGSGAG)$_4$ where n = 4-8. First, peptides with a combination of hydrophilic and hydrophobic sequences mimicking the primary structure of *Bombyx mori*

Downloaded by UNIV OF DELAWARE MORRIS LIB on June 21, 2012 | http://pubs.acs.org
Publication Date (Web): October 14, 2011 | doi: 10.1021/bk-2011-1077.ch017

silk fibroin were synthesized and studied in the solid state by NMR using ^{13}C selective labeling coupled with ^{13}C conformation-dependent chemical shifts and 2D solid-state spin diffusion NMR (*41*). The hydrophilic sequence was poly(L-glutamic acid) $(E)_n$, and the hydrophobic part was the consensus sequence of the crystalline fraction of *B. mori* silk fibroin, $(AGSGAG)_4$. The balance of hydrophilic and hydrophobic characters of the peptide was controlled by changing the relative length, n, of $(E)_n$ from 4 to 8. When n = 4 and 5, the structure of the hydrophobic sequence is basically Silk I (the structure of *B. mori* silk fibroin before spinning in the solid state), and the polyglutamate sequences take on the random coil form (Figure 8). On the other hand, when n = 6-8, the structure of the polyglutamate sequence changes gradually from random coil to β-sheet, and the hydrophobic sequence adopts a mixture of β-sheet and random coil/distorted β-turn forms, although the fraction of the latter form decreases gradually by increasing the number n from 6 to 8.

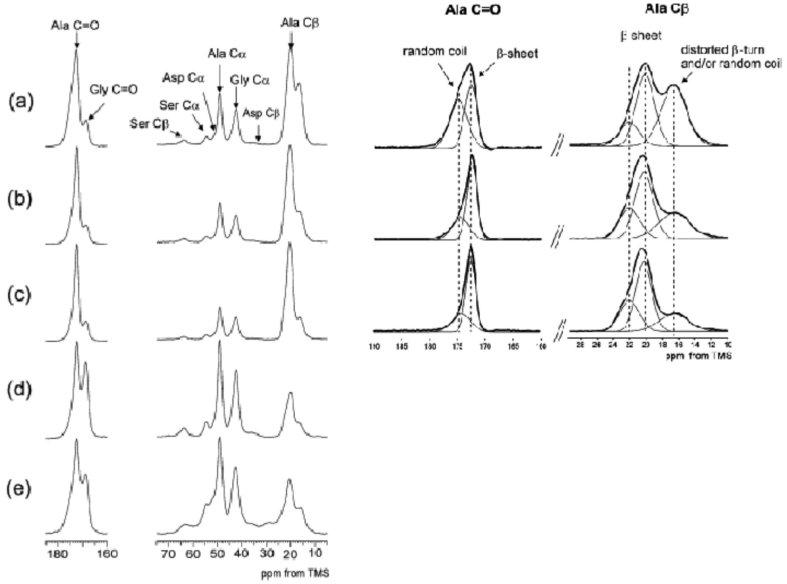

Figure 7. ^{13}C CP/MAS NMR spectra of (a) $[1\text{-}^{13}C]Ala_{12},[3\text{-}^{13}C]\text{-}Ala_{16}$-, (b) $[1\text{-}^{13}C]Ala_{10},[3\text{-}^{13}C]Ala_{18}$-, (c) $[1\text{-}^{13}C]Ala_{8},[3\text{-}^{13}C]Ala_{20}$-labeled 41SDSDS, with expanded spectrum of Ala C=O and Ala Cβ(d) nonlabeled 41SDSDS, and (e) silk-like protein analogue 14DS16.

IV. Applications

The protein 14DS16, analogous to 41SDSDS but considerably larger, was produced by genetic engineering and overexpression in *E. coli* as a possible biomaterial. Mineralization of films of 14DS16 in SBF (simulated body fluid) (*46*) was investigated. Films of this protein treated with SBF were rapidly mineralized with hydroxyapatite (Figure 9). For both Ala residues located closest to the Asp

Downloaded by UNIV OF DELAWARE MORRIS LIB on June 21, 2012 | http://pubs.acs.org
Publication Date (Web): October 14, 2011 | doi: 10.1021/bk-2011-1077.ch017

(*14*) residue, distorted β-turn and/or random coil accounted for one-half of the conformations. Thus, hydroxyapatite formation is promoted by the structure designed through analogy with lamellar silk crystalline region.

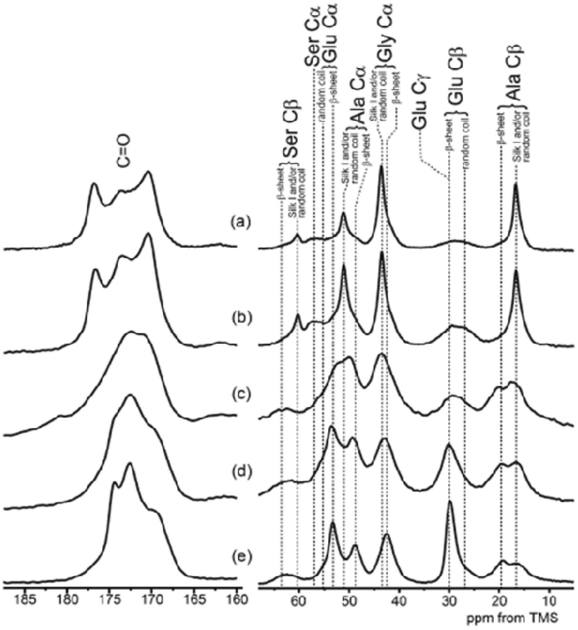

Figure 8. ^{13}C CP/MAS NMR spectra of natural abundance $(E)_n(AGSGAG)_4$ (n = 4-8). The spectra from (a) to (e) correspond to the samples from n = 4 to n = 8, respectively.

Genetically modified silk fibroin containing a poly-glutamic acid site, $[(AGSGAG)_4E_8AS]_4$, for mineralization was produced as fibers by transgenic silkworms through systematic transformation of the silkworms (*42*). The Ca binding activity and mineralization of the transgenic silk fibroin were examined *in vitro*, showing that this transgenic silk fibroin had relatively high Ca binding activity compared with native silk fibroin. Porous silk scaffolds were prepared with the transgenic and native silk fibroins. Healing of femoral epicondyle defects in rabbit femurs treated with the scaffolds was examined by observing changes in images of the defects using micro-computed tomography(Figure 10). Earlier mineralization and bone formation were observed with scaffolds of transgenic silk fibroin compared with those of native silk fibroin. Thus, this study shows the feasibility of using genetically modified silk fibroin from transgenic silkworms as a mineralization-accelerating material for bone repair.

Downloaded by UNIV OF DELAWARE MORRIS LIB on June 21, 2012 | http://pubs.acs.org
Publication Date (Web): October 14, 2011 | doi: 10.1021/bk-2011-1077.ch017

Downloaded by UNIV OF DELAWARE MORRIS LIB on June 21, 2012 | http://pubs.acs.org
Publication Date (Web): October 14, 2011 | doi: 10.1021/bk-2011-1077.ch017

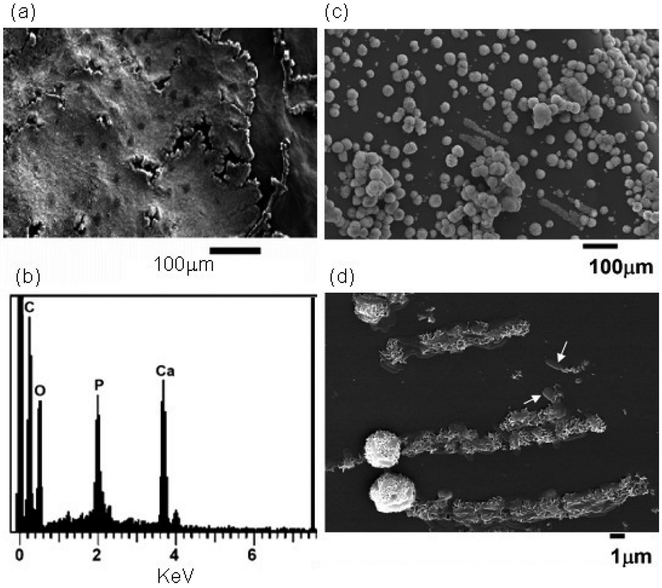

Figure 9. (a) SEM photomicrographs of a film surface of 14DS16 7 days after immersing the films in SBF solution, (b) EDX spectrum of 14DS16 film pretreated with calcium chloride and incubated in SBF for 7 days, (c) High-resolution SEM photomicrographs showing mineralization on the surface of a film of 14DS16 pretreated with calcium chloride and incubated for 7 days in SBF, (d) SEM photomicrographs with arrows indicating small but regular crystals with their flat surfaces in contact with the recombinant protein film.

V. Effects of Fluorinated Solvents

The regenerated silk fibers prepared from aqueous silk solution do not have as good mechanical properties as the native silk fibroin. However, the fluorinated organic solvents 1,1,1,3,3,3-hexafluoro-2-propanol (HFIP) and hexafluoroacetone trihydrate (HFA) have been successfully used to produce silk fibroin fibers with high strength (*47–49*). To understand the reasons for the increased strength of regenerated silk fibers prepared from these two solvents, we analyzed and compared the properties of the native silk fibroin and $(AGSGAG)_2$, a model for the crystalline part of fibroin, in the two solvents by $^1H/^{13}C$ chemical shifts and ^1H-^{19}F intermolecular NOEs (*50*, *51*).

Downloaded by UNIV OF DELAWARE MORRIS LIB on June 21, 2012 | http://pubs.acs.org
Publication Date (Web): October 14, 2011 | doi: 10.1021/bk-2011-1077.ch017

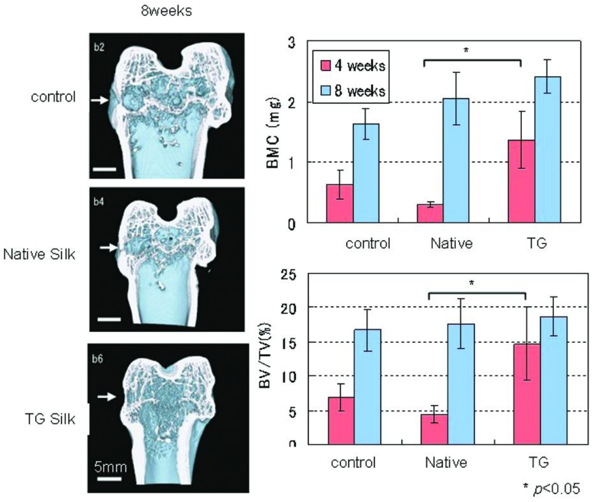

Figure 10. (a) Micro-CT image of rabbit femurs in not-implated group (control), native silk fibroin scaffold-implanted group, and transgenic silk fibroin scaffold with $(E)_8(AGSGAG)_4$ - implanted group, respectively, and quantitative results of (b) bone mineral content and (c) bone volume per total volume.

The ^{13}C and ^{1}H chemical shifts obtained from ^{1}H-^{13}C HSQC spectra of silk fibroin in HFIP, HFA, and water indicated that silk fibroin formed helix-like structures in the fluorinated alcohols. A similar tendency was observed for $(AGSGAG)_2$ although the chemical shift change was smaller. In addition, intramolecular ^{1}H-^{1}H NOE data for $(AGSGAG)_2$ imply the presence of helical structures in the middle part of the peptide in HFIP but not in HFA, although an equilibrating ensemble of conformations are likely present in both solvents.

Nuclear spin dipole-dipole interactions between the spins of $(AGSGAG)_2$ and the fluorines of the solvent can produce relaxation of the protons on the peptide. These solute-solvent interactions lead to intermolecular NOEs and are characterized by a cross relaxation parameter (σ) (*52*). Figure 11 shows the observed ^{1}H-^{19}F NOE spectra of $(AGSGAG)_2$ in HFIP and HFA. All the detectable intermolecular NOEs arising from peptide in HFIP are positive; all NOEs in HFA are negative.

The simplest interpretation of intermolecular NOEs assumes that solute and solvent molecules can be represented by hard spheres and that interactions of the spheres depend only on their mutual translational diffusion (*53*, *54*). A numerical procedure that involves the treatment of Ayant *et al.* (*54*, *55*) can be used to incorporate the shape of the solute molecule into predictions of σ. Input to these calculations includes experimental translational diffusion coefficients, the radius of the sphere that represents a solvent molecule, the effective rotational correlation time that characterizes ^{1}H-^{1}H intramolecular dipolar interactions within the solute and a correlation time for internal rotation of methyl groups. The latter correlation times can be estimated by considering the observed spin-lattice relaxation times of the protons of the solute (*56*).

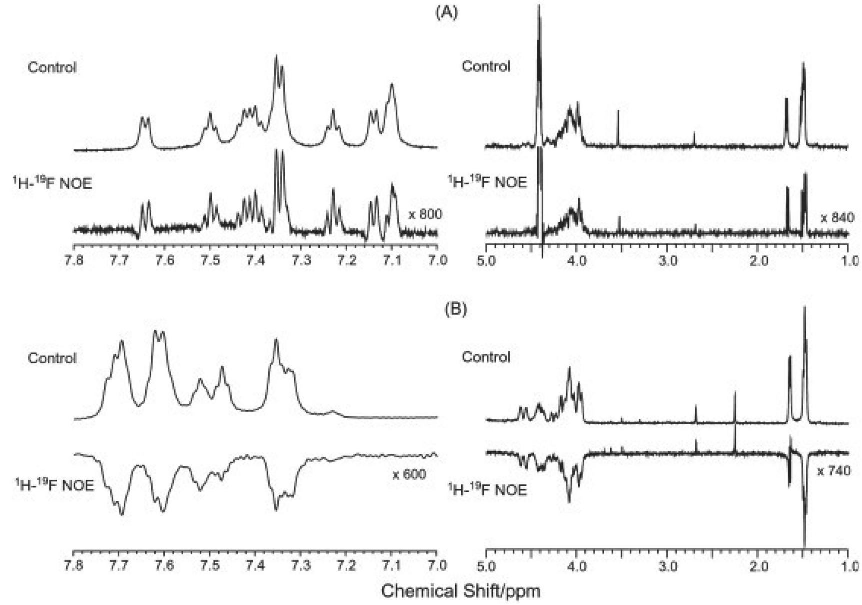

Figure 11. ^{1}H-^{19}F intermolecular NOE spectra of (AGSGAG)$_2$ in HFIP (A) and in HFA(B). Upper spectra in each set are the observed 1D ^{1}H spectrum while the lower spectrum is the ^{1}H-^{19}F NOE spectrum at a mixing time of 500 ms for the HFIP system and 300 ms for the HFA system.

Cross relaxation terms (σ_{HF}) for all conformations of (AGSGAG)$_2$ in HFIP and in HFA developed by our analysis of intramolecular ^{1}H-^{1}H distance constraints were calculated using the diffusion coefficients and the other parameters mentioned. The average of these calculated σ_{HF} values for each proton of the peptide in each solvent is compared to the corresponding experimental value in Figure 12. We find that σ_{HF} predicted in this way for (AGSGAG)$_2$ dissolved in HFIP are in good agreement with experimental data for most protons of the peptide. This result indicates that the model used for these predictions reasonably describes the interactions between HFIP and the peptide. Thus, these interactions can be characterized as random collisions between peptide and HFIP, and the dynamics of these collisions are sufficiently characterized by the experimental bulk diffusion coefficients. In contrast, observed σ_{HF} for (AGSGAG)$_2$ in HFA are negative for all residues while calculated σ_{HF} were positive. Peptide-solvent interactions are thus more complex in HFA than what seems to be the case in HFIP.

In the processes for producing regenerated silk fibers from a silk solution, the solution typically travels through a stainless steel spinneret into methanol to achieve coagulation. Coagulation involves removal of solvents from around the dissolved silk fibroin producing a conformational transition of the crystalline regions of silk fibroin to β-sheet structures. The regenerated fiber prepared from the HFIP solution shows slightly greater tensile strength when the draw ratio is 1:3 than that of native silk fiber, but the strength of the regenerated fiber with

Downloaded by UNIV OF DELAWARE MORRIS LIB on June 21, 2012 | http://pubs.acs.org
Publication Date (Web): October 14, 2011 | doi: 10.1021/bk-2011-1077.ch017

Downloaded by UNIV OF DELAWARE MORRIS LIB on June 21, 2012 | http://pubs.acs.org
Publication Date (Web): October 14, 2011 | doi: 10.1021/bk-2011-1077.ch017

draw ratio 1:3 from the HFA solution is about 40% smaller than that of native silk fiber. The X-ray diffraction patterns and Ala Cβ signals in solid state ^{13}C CP/MAS NMR spectra revealed that this difference in the tensile strength of the regenerated silk fibers between two solvents comes from the difference in the long-range orientation of the crystalline regions (*57*). According to the results, the displacement of HFA molecules during coagulation may be less complete due to the stronger interactions of HFA with silk fibroin. A less extensive β-sheet aggregation during coagulation could result, leading to lower tensile strength of fibers from HFA solutions. Also, the silk model peptide conformation possesses a somewhat helical structure in HFIP compared to that in HFA, implying that silk fibroin with more extensive helical conformations in HFIP tends to align more like native silk solution in silk gland and favor the extensive β-sheet aggregation.

Silk fibroin dissolved in HFIP can be fashioned into a wide range of forms when applied to biomaterials, e.g., sponges and scaffolds for bone tissues, films for wound dressings, and scaffolds for cornia. The knowledge obtained in this work should be useful in the development of better and improved silk-based biomaterials.

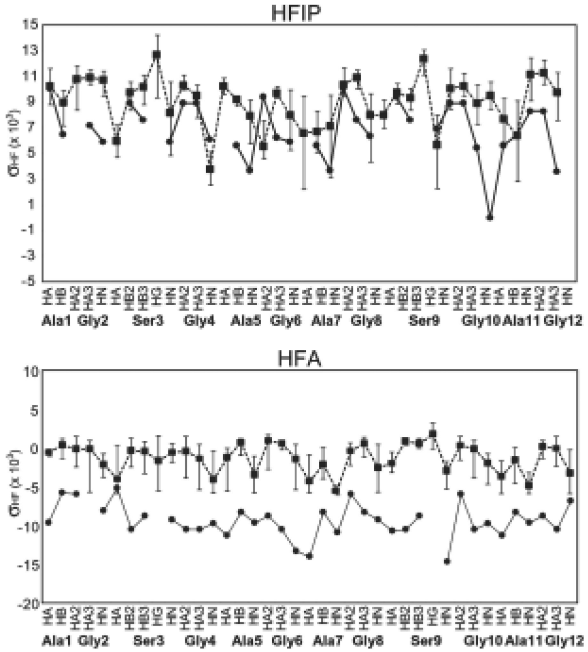

Figure 12. Comparison of observed σ_{HF} (solid line) and calculated σ_{HF} (dotted line). The calculated data are the average of calculations for the conformations obtained by DYANA calculation. Error bars represent standard deviations of calculated data for 10 conformations for HFIP sample and 7 conformations for HFA sample found in the structure determination.

References

1. Asakura, T.; Kaplan, D. *Encylopedia of Agricultural Science*; Academic Press: New York, 1994; p 1.
2. Hakimi, O.; Knight, D. P.; Vollrath, F.; Vadgama, P. *Compos Part B-Eng* **2007**, *38* (3), 324–337.
3. Zhou, C. Z.; Confalonieri, F.; Jacquet, M.; Perasso, R.; Li, Z. G.; Janin, J. *Proteins: Struct., Funct., Genet.* **2001**, *44* (2), 119–122.
4. Asakura, T.; Ohgo, K.; Komatsu, K.; Kanenari, M.; Okuyama, K. *Macromolecules* **2005**, *38* (17), 7397–7403.
5. Asakura, T.; Ashida, J.; Yamane, T.; Kameda, T.; Nakazawa, Y.; Ohgo, K.; Komatsu, K. *J. Mol. Biol.* **2001**, *306* (2), 291–305.
6. Marsh, R. E.; Corey, R. B.; Pauling, L. *Biochim. Biophys. Acta* **1955**, *16* (1), 1–34.
7. Takahashi, Y.; Gehoh, M.; Yuzuriha, K. *Int. J. Biol. Macromol.* **1999**, *24* (2-3), 127–138.
8. Asakura, T.; Yao, J.; Yamane, T.; Umemura, K.; Ulrich, A. S. *J. Am. Chem. Soc.* **2002**, *124* (30), 8794–8795.
9. Yao, J. M.; Ohgo, K.; Sugino, R.; Kishore, R.; Asakura, T. *Biomacromolecules* **2004**, *5* (5), 1763–1769.
10. Asakura, T.; Yao, J. M. *Protein Sci.* **2002**, *11* (11), 2706–2713.
11. Asakura, T.; Nakazawa, Y.; Ohnishi, E.; Moro, F. *Protein Sci.* **2005**, *14* (10), 2654–2657.
12. Suzuki, Y.; Aoki, A.; Nakazawa, Y.; Knight, D. P.; Asakura, T. *Macromolecules* **2010**, *43*, 9434–9440.
13. Gullion, T.; Schaefer, J. *J. Magn. Reson.* **1989**, *81* (1), 196–200.
14. Asakura, T.; Sato, H.; Moro, F.; Nakazawa, Y.; Aoki, A. *J. Am. Chem. Soc.* **2007**, *129* (17), 5703–5709.
15. Fraser, R. D.; MacRae, T. P.; Stewart, F. H. *J. Mol. Biol.* **1966**, *19* (2), 580–582.
16. Fraser, R. D.; Macrae, T. P.; Stewart, F. H.; Suzuki, E. *J. Mol. Biol.* **1965**, *11*, 706–712.
17. Gong, Z. G.; Huang, L.; Yang, Y. H.; Chen, X.; Shao, Z. Z. *Chem. Commun.* **2009** (48), 7506–7508.
18. Tye, C. E.; Rattray, K. R.; Warner, K. J.; Gordon, J. A. R.; Sodek, J.; Hunter, G. K.; Goldberg, H. A. *J. Biol. Chem.* **2003**, *278* (10), 7949–7955.
19. Hunter, G. K.; Goldberg, H. A. *Biochem. J.* **1994**, *302* (Pt 1), 175–179.
20. Harris, N. L.; Rattray, K. R.; Tye, C. E.; Underhill, T. M.; Somerman, M. J.; D'errico, J. A.; Chambers, A. F.; Hunter, G. K.; Goldberg, H. A. *Bone* **2000**, *27* (6), 795–802.
21. Ganss, B.; Kim, R. H.; Sodek, J. *Crit. Rev. Oral Biol. Med.* **1999**, *10* (1), 79–98.
22. Gajjeraman, S.; Narayanan, K.; Hao, J.; Qin, C.; George, A. *J. Biol. Chem.* **2007**, *282* (2), 1193–1204.
23. Palmer, L. C.; Newcomb, C. J.; Kaltz, S. R.; Spoerke, E. D.; Stupp, S. I. *Chem. Rev.* **2008**, *108* (11), 4754–4783.
24. Cui, F. Z.; Li, Y.; Ge, J. *Mater. Sci. Eng., R* **2007**, *57* (1-6), 1–27.

Downloaded by UNIV OF DELAWARE MORRIS LIB on June 21, 2012 | http://pubs.acs.org
Publication Date (Web): October 14, 2011 | doi: 10.1021/bk-2011-1077.ch017

25. Bouligand, Y. *C. R. Palevol* **2004**, *3* (6-7), 617–628.
26. Semino, C. E. *J. Dent. Res.* **2008**, *87* (7), 606–616.
27. Addadi, L.; Weiner, S.; Geva, M. *Z. Kardiol.* **2001**, *90* (3), 92–98.
28. He, G.; Dahl, T.; Veis, A.; George, A. *Nat. Mater.* **2003**, *2* (8), 552–558.
29. Ball, P. *Nature* **1994**, *367*, 323–324.
30. Domurado, D.; Vert, M. *J. Biomater. Sci., Polym. Ed.* **2007**, *18* (3), 287–301.
31. Rijcken, C. J. F.; Soga, O.; Hennink, W. E.; Nostrum, C. F. *J. Controlled Release* **2007**, *120* (3), 131–148.
32. Khokhlov, A. R.; Khalatur, P. G. *Conformation-dependent design of sequences in copolymers*; Springer Verlag: 2006.
33. Firth, A.; Aggeli, A.; Burke, J. L.; Yang, X.; Kirkham, J. *Nanomedicine* **2006**, *1* (2), 189–199.
34. Kirkham, J.; Firth, A.; Vernals, D.; Boden, N.; Robinson, C.; Shore, R. C.; Brookes, S. J.; Aggeli, A. *J. Dent. Res.* **2007**, *86* (5), 426–430.
35. Gajjeraman, S.; He, G.; Narayanan, K.; George, A. *Adv. Funct. Mater.* **2008**, *18* (24), 3972–3980.
36. Peggion, E.; Cosani, A.; Terbojevich, M.; Borin, G. *Pept. Sci.* **1972**, *11* (3), 633–643.
37. Rippon, W. B.; Chen, H. H.; Walton, A. G. *J. Mol. Biol.* **1973**, *75* (2), 369–375.
38. Seipke, G.; Arfmann, H.-A.; Wagner, K. G. *Biopolymers* **1980**, *19* (1), 189–201.
39. Brack, A.; Orgel, L. E. *Nature* **1975**, *256* (5516), 383–387.
40. Asakura, T.; Sato, H.; Moro, F.; Yang, M.; Nakazawa, Y.; Collins, A. M.; Knight, D. *Macromolecules* **2007**, *40* (25), 8983–8990.
41. Nagano, A.; Kikuchi, Y.; Sato, H.; Nakazawa, Y.; Asakura, T. *Macromolecules* **2009**, *42* (22), 8950–8958.
42. Nagano, A.; Tanioka, Y.; Sakurai, N.; Sezutsu, H.; Kuboyama, N.; Kiba, H.; Tanimoto, Y.; Nishiyama, N.; Asakura, T. *Acta Biomater.* **2011**, *7* (3), 1192–1201.
43. Wang, J.; Parkhe, A. D.; Tirrell, D. A.; Thompson, L. K. *Macromolecules* **1996**, *29* (5), 1548–1553.
44. Asakura, T.; Iwadate, M.; Demura, M.; Williamson, M. P. *Int. J. Biol. Macromol.* **1999**, *24* (2-3), 167–171.
45. Kameda, T.; Ohkawa, Y.; Yoshizawa, K.; Naito, J.; Ulrich, A. S.; Asakura, T. *Macromolecules* **1999**, *32* (21), 7166–7171.
46. Kokubo, T.; Kushitani, H.; Sakka, S.; Kitsugi, T.; T. Yamamuro, T. *J. Biomed. Mater. Res.* **1990**, *24*, 721–734.
47. Trabbic, K. A.; Yager, P. *Macromolecules* **1998**, *31* (2), 462–471.
48. Yao, J. M.; Masuda, H.; Zhao, C. H.; Asakura, T. *Macromolecules* **2002**, *35* (1), 6–9.
49. Zhu, Z. H.; Imada, T.; Asakura, T. *Mater. Chem. Phys.* **2009**, *117* (2-3), 430–433.
50. Ha, S. W.; Asakura, T.; Kishore, R. *Biomacromolecules* **2006**, *7* (1), 18–23.
51. Suzuki, Y.; Gerig, I. T.; Asakura, T. *Macromolecules* **2010**, *43* (5), 2364–2370.
52. Gerig, J. T.; Strickler, M. A. *Biopolymers* **2002**, *64*, 227–235.

Downloaded by UNIV OF DELAWARE MORRIS LIB on June 21, 2012 | http://pubs.acs.org
Publication Date (Web): October 14, 2011 | doi: 10.1021/bk-2011-1077.ch017

53. Hennel, J. W.; Klinowski, J. *Fundamentals of Nuclear Magnetic Resonance*; Longman: Essex, U.K., 1993.
54. Ayant, Y.; Belorizky, E.; Fries, P.; Rosset, J. *J. Phys. (Paris)* **1977**, *38* (3), 325–337.
55. Gerig, J. T. *J. Org. Chem.* **2003**, *68* (13), 5244–5248.
56. Neuman, R. C., Jr.; Gerig, J. T. *Magn. Reson. Chem.* **2009**, *47*, 925–931.
57. Zhu, Z.; Kikuchi, Y.; Kojima, K.; Tamura, T.; Kuwabara, N.; Nakamura, T.; Asakura, T. *J. Biomater. Sci., Polym. Ed.* **2010**, *21* (3), 395–411.

Downloaded by UNIV OF DELAWARE MORRIS LIB on June 21, 2012 | http://pubs.acs.org
Publication Date (Web): October 14, 2011 | doi: 10.1021/bk-2011-1077.ch017

Chapter 18

The Interaction of Aβ(1-40) Peptide with Lipid Bilayers and Ganglioside As Studied by Multinuclear Solid-State NMR

Yasumoto Nakazawa,[1] Yu Suzuki,[1] Hazime Saitô,[2] and Tetsuo Asakura*,[1]

[1]Institute of Engineering, Tokyo University of Agriculture and Technology,
2-24-16, Nakacho, Koganei, Tokyo, 184-8588 Japan
[2]Department of Life Science, Himeji Institute of Technology,
University of Hyogo, Kamigori, Hyogo, 678-1297 Japan
***E-mail: asakura@cc.tuat.ac.jp**

Downloaded by DUKE UNIV on June 20, 2012 | http://pubs.acs.org
Publication Date (Web): October 14, 2011 | doi: 10.1021/bk-2011-1077.ch018

Amyloid β-peptide (Aβ) is a major component of plaques in Alzheimer's disease, and formation of senile plaques has been suggested to originate from regions of neuronal membrane rich in gangliosides. We have analyzed the interaction of Aβ with lipid bilayers by multinuclear NMR using ^{15}N, ^{31}P and ^{13}C nuclei. The result of the present study implies that the fibrillogenic seed nucleus involves an interaction of His residues with the sialic acid moiety of GM1. Moreover, Aβ(1-40) with ganglioside GM1 perturbs the bilayer structure to form a non-lamellar structure such as hexagonal H_{11} lipids and also produces single vesicles or micelles, as shown by angular-dependent ^{31}P NMR experiments. In conclusion, the Aβ peptide penetrates into the lipid bilayer, takes on an α-helical form, and produces non-lamellar lipid and micelles.

Introduction

Alzheimer's disease (AD) is a devastating neurodegenerative disease affecting up to 15 million individuals worldwide. The brains of Alzheimer's disease patients are characterized by fibrillar (*1*) amyloid plaques that are associated with progressive deposits (*1*). The principal component of amyloid deposits is a 39-42 amino acid residue peptide, Aβ (*2*, *3*), a product of proteolytic

In NMR Spectroscopy of Polymers: Innovative Strategies for Complex Macromolecules; Cheng, H., et al.;
ACS Symposium Series; American Chemical Society: Washington, DC, 2011.

processing of a much larger amyloid precursor protein (APP) encoded by a gene on chromosome 21 (*4*). Several spectroscopic investigations have clarified the structure of the fibrils, which form a 'cross-β sheet' structure (*5–7*). Moreover, a link between Aβ and AD neuropathological lesions is demonstrated by the toxicity of aggregated Aβ to neuronal cells in culture (*8*) and in aged brain (*9*). However, the molecular mechanisms of the neurotoxic action of Aβ remain unknown. A growing number of observations indicate that Aβ may alter the physicochemical properties of neuronal membranes, including membrane fluidity (*10*) and permeability to ions and nonelectrolytes (*11*). These findings strongly suggest that at least some of the pathophysiological effects of Aβ may be mediated by Aβ-membrane interactions. Indeed, a number of studies have shown that Aβ is able to perturb lipid bilayers (*11–14*). Interest in studies of the interaction between Aβ and constituents of brain membranes has been further stimulated by the identification of an Aβ-GM1 ganglioside-bound form in AD brain (*15–17*).

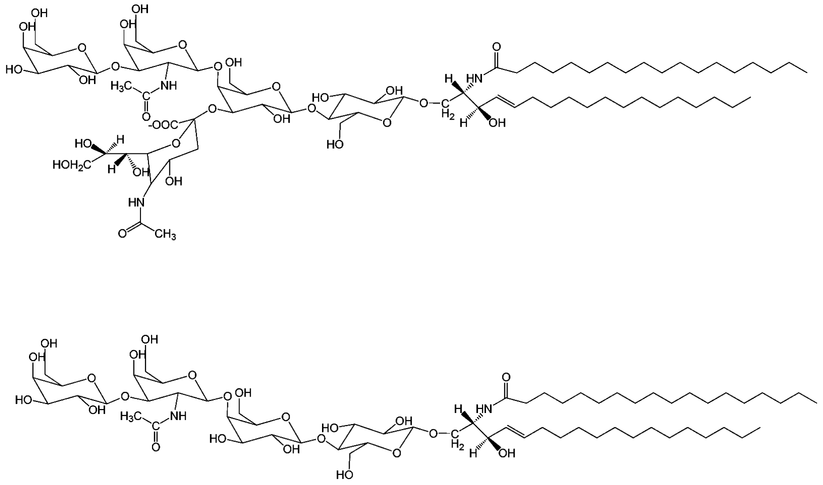

Figure 1. Molecular structure of GM1 ganglioside (top) and asialo-GM1 ganglioside (bottom).

Gangliosides (*18*, *19*) are sialic acid-containing glycosphingolipids and consist of two main components: a hydrophobic ceramide unit, which anchors the ganglioside to the plasma membrane, and a hydrophilic oligosaccharide chain, to which one or more sialic acid groups are attached. Gangliosides are abundant components of neuronal membranes and are involved in important neurobiological events such as neurodifferentiation, synaptogenesis and synaptic transmission (*20*). Aβ permeabilizes ganglioside-containing membranes and thus disturbs ion homeostasis (*21*, *22*). Different research groups have reported extensive studies of Aβ-ganglioside interactions using different methodologies (*16*, *23–26*), but no conclusive results have been obtained. GM1 ganglioside-mediated accumulation of Aβ protein was proposed together with the effect of cholesterol (*26*).

Downloaded by DUKE UNIV on June 20, 2012 | http://pubs.acs.org
Publication Date (Web): October 14, 2011 | doi: 10.1021/bk-2011-1077.ch018

In our efforts to clarify the interaction between β-amyloid peptide and lipid bilayers including ganglioside, we have shown two things. First, we have demonstrated using solution state NMR of ^{15}N-labelled Aβ(1–40) and Aβ(1–42) that ganglioside GM1 and asialo-GM1(Figure 1) contain micelles (*27*). Secondly, we have recorded ^{1}H decoupled ^{31}P solid-state NMR spectra of dimyristoylphospatidylcholine (DMPC) and DMPC/GM1 ganglioside in a mechanically oriented system in the presence of Aβ(1-40) in order to clarify the behavior of Aβ in the presence of GM1 ganglioside. Finally, we have studied ^{13}C-labeled Aβ peptide by CP-MAS, DD-MAS NMR, as well as low-power solution NMR to determine conformational features of the Aβ peptide in the presence of lipid bilayers.

Downloaded by DUKE UNIV on June 20, 2012 | http://pubs.acs.org
Publication Date (Web): October 14, 2011 | doi: 10.1021/bk-2011-1077.ch018

Materials and Methods

Solution NMR Experiments

Uniformly ^{15}N-labelled Aβ(1–40) and Aβ(1–42) were purchased from rPeptide (Athens, GA, U.S.A.), and gangliosides were purchased from Axxora Ltd (Exeter, U.K.). The purity of the gangliosides was quoted as >98% by the manufacturer, but was not checked. All other reagents were from Sigma–Aldrich Co. (St. Louis, MO, USA). The heparin used was the sodium salt (H4784).

Aβ(1–40) solutions were prepared as described earlier (*28*). Briefly, the peptide was dissolved at a concentration of 200 μM in 10 mM NaOH with 1 min of sonication, and immediately frozen if required. Subsequently, the pH was adjusted to 7.2 with a minimal amount of 0.1 M HCl, and $^{2}H_2O$ was added to make an approx. 200 μM peptide solution containing 10% $^{2}H_2O$. Solutions prepared in this way were stable and showed no sign of aggregation for at least 1 week. In contrast, solutions made up in a buffer aggregated much faster, often almost entirely precipitated after 24 h. Aβ(1–42) was pre-treated by dissolution in hexafluoropropan-2-ol and freeze-drying, before dissolving in 10 mM ammonium hydroxide, followed by adjustment of the pH to 7.2. These solutions started to aggregate and form fibrils immediately and were only usable for 2–3 days. Solutions of the commercial material directly into NaOH resulted in no NMR signal, indicating significant aggregation with the use of this method.

Stock solutions of gangliosides or heparin were prepared at high concentrations (approx. 100–200 mM), adjusted to pH 7.2 and added directly to the NMR tube. All NMR experiments were carried out on a Bruker DRX-500 spectrometer equipped with a cryoprobe, and operated at 13°C. ^{15}N HSQC (heteronuclear single-quantum correlation) experiments used gradient selection for water suppression and water flipback pulses to minimize loss of magnetization through exchange and relaxation processes. The three-dimensional TOCSY-HSQC spectrum incorporated solvent suppression using gradients, with a 35 ms spin-lock at 8.3 kHz decoupler power. Processing of NMR data used FELIX (Accelrys, San Diego, CA, U.S.A.), and titration data were analysed using home-written scripts. Cross-peak intensities were measured within FELIX, transferred to a text file, and fitted to an exponential decay using a Marquardt non-linear least-squares fitting based originally on a Numerical Recipes algorithm.

In NMR Spectroscopy of Polymers: Innovative Strategies for Complex Macromolecules; Cheng, H., et al.;
ACS Symposium Series; American Chemical Society: Washington, DC, 2011.

Angular Dependent NMR Experiments

DMPC and GM1 ganglioside were purchased from Sigma (St. Louis, MO, USA). Aβ(1-40) and ^{13}C labeled DAEFRHDSGYEVHHQKL[1-^{13}C]V^{18}FF[3-^{13}C]A^{21}EDVGS-NK[2-^{13}C]G^{29}AIIGLMVGGVV were synthesized in a stepwise fashion on Fmoc-Val-PEG-PS resin (PE Biosystems, Tokyo, Japan) by a Pioneer^{TM} peptide synthesizer (PE Biosystems) using Fmoc chemistry. After synthesis, the peptides were cleaved from the resin by treatment with a mixture of TFA(trifluoroacetic acid), phenol, triisopropylsilane and water (88:5:2:5 vol%) for 2 hours at room temperature. The precipitated peptide was washed repeatedly with cold diethylether. Then, the crude peptide was purified by preparative liquid chromatography.

^{13}C- labeled Aβ peptide in the presence of DMPC bilayer was prepared by drying the DMPC under a stream of nitrogen gas from methanol/chloroform solution, and then in vacuo, followed by hydration with 60% water by weight of lipids wherein the content of DMPC lipids. Repeated freezing and thawing were performed after hydration. For the preparation of oriented samples, DMPC (or DMPC/GM1, 10:1) was dissolved in methanol/chloroform (1:1) and Aβ was dissolved in benzene. These solutions were mixed and spread onto 0.1 mm thin-glass plates (5×9 mm) and then dried under vacuum for 24h. The dry plates and a small amount of water were then stacked in a 10ΦNMR tube (20 mm length). Water was added to achieve 60% hydration. The sample was then sealed with a Teflon cap and epoxy resin and incubated at 45° for 4 days.

High power proton-decoupled ^{31}P NMR spectra were performed on a Chemagnetics CMX 400 spectrometer operating at a resonance frequency of 397.79 MHz for ^{1}H and 161.03 MHz for ^{31}P. A static double-resonance probe equipped with a goniometer was used. ^{31}P NMR spectra were recorded for the oriented samples. ^{31}P NMR spectra of sonicated lipid bilayer were also recorded in a solution NMR spectrometer. For the ^{31}P NMR experiments, typical NMR parameters were 7-8 μs (90°) pulse length, 3 s recycle delay and 1000~2000 scans. The ^{31}P chemical shifts in ppm were referenced to H_3PO_4.

High resolution ^{13}C solid- and liquid-state NMR spectra were recorded on a Chemagnetics CMX-400 and JEOL α-500 NMR spectrometer respectively. For the former, ^{13}C CP-MAS and DD-MAS (dipolar decoupled magic angle spinning) NMR with a single pulse excitation method were recorded. The π/2 pulse for carbon and proton nuclei was 5 μs and a ^{1}H decoupling frequency of 60 kHz was used. Contact time was 2msec and spinning rate was 8kHz. Free induction decays were usually acquired with 512 data points. The ^{13}C chemical shifts were referenced to adamantane [(28.8 ppm from tetramethylsilane (TMS)] and then expressed as relative shifts from the value of TMS.

Results and Discussion

Structural Change of Aβ(1-40)-Ganglioside System with Solution NMR

The HSQC spectrum is shown in Figure 2. Almost all backbone signals are resolved. At 13°C, all signals are found except for the N-terminal residue and His6.

Downloaded by DUKE UNIV on June 20, 2012 | http://pubs.acs.org
Publication Date (Web): October 14, 2011 | doi: 10.1021/bk-2011-1077.ch018

Downloaded by DUKE UNIV on June 20, 2012 | http://pubs.acs.org
Publication Date (Web): October 14, 2011 | doi: 10.1021/bk-2011-1077.ch018

His14 gives a weak signal, as expected because of rapid amide exchange under these conditions (*29*). The reason for the absence of His6 in our HSQC spectra is less clear, but it was also not observable by Hou et al. (*28*). On the basis of the chemical shifts, we concur with other authors (*28*, *30*) that the peptide is a random coil in aqueous solution. The majority of HSQC peaks in Aβ(1–42) has been assigned in the same way, but the assignment is somewhat less complete due to its rapid aggregation, which limits the time available for three-dimensional NMR experiments. The signals from Aβ(1–42) have very similar chemical shifts to those of Aβ(1–40) except at the C-terminus, implying that there are no significant conformational differences between them.

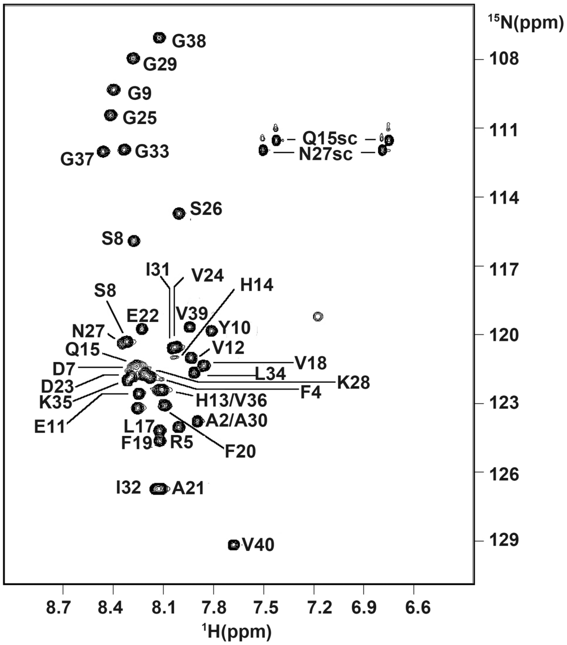

Figure 2. HSQC spectrum of ^{15}N-labelled Aβ-(1–40) in water, pH 7.2, 13°C. The small unlabelled peak at (^{1}H=7.2, ^{15}N=119 p.p.m.) is probably an arginine side chain NH. Single-letter amino acid codes are used.

GM1 forms micelles with a critical micelle concentration in the low micromolar range (*31*). Thus, at concentrations >100 μM, as used here, it is essentially 100% micellar. Upon titration of GM1 micelles into Aβ(1–40), chemical shift changes are seen in the NMR spectrum, as shown in Figure 3 (left). The chemical shift changes are very small, but are reproducible and specific, since many residues have essentially no change in shift. Smaller chemical shift changes have been demonstrated to be biologically relevant on many previous occasions (*32*, *33*). Almost all of the chemical shift changes occur in the N-terminal half of the peptide, and are close to potentially positively charged residues: Glu3–Arg5 (close to Arg5 and His6) and Val12–Leu17 (close to His13, His14 and Lys16). However, the pKa values of the three histidine residues are all approx. 6.5 (*34*). Hence, at the pH of our measurements, 7.2, most of the histidine residues should be unprotonated.

We therefore expect that the only residues significantly positively charged at this pH should be Arg5 and Lys16, together with Lys28. This makes it unlikely that the chemical shift changes are due only to Coulombic interactions with the single negative charge in the GM1 headgroup, the sialic acid.

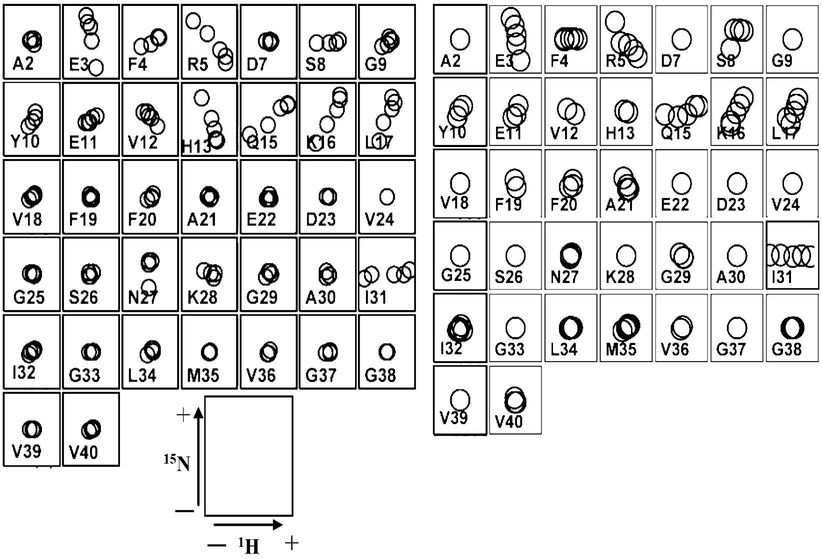

Figure 3. Chemical shift changes in Aβ-(1–40) upon the addition of GM1(Left) and asialo-GM1(Right) to 200 μM peptide in water. Each box shows the results for a different residue, with ^{1}H shifts horizontal (increasing left to right, total range ± 0.02 p.p.m (Left) and 0.015ppm (Right) and ^{15}N shifts vertical [increasing from bottom to top, total range ±0.1 p.p.m (Left) and 0.075ppm (Right)]. This representation therefore resembles the change seen in an HSQC spectrum, except that the directions of the axes are reversed. The start of the titration is indicated with a filled circle, and subsequent titrations contain 1, 2, 4 and 8 equivalents of GM1. The size of the circles approximates the experimental uncertainty. No data are shown for His6 because it could not be observed. Single-letter amino acid codes are used.

In order to confirm this, a further titration has been carried out at an approximate physiological salt concentration (150 mM NaCl), which should markedly reduce purely Coulombic interactions in water. The results show reduced chemical shift changes, indicating a loss of affinity (data not shown). Residues 14–17 still shift, but the changes seen in residues 3–13 are much reduced. This implies that, although some of the binding and the chemical shift

Downloaded by DUKE UNIV on June 20, 2012 | http://pubs.acs.org
Publication Date (Web): October 14, 2011 | doi: 10.1021/bk-2011-1077.ch018

changes are primarily Coulombic in origin, others (and in particular the changes seen in residues 15–17) are much less so. We note that other authors have concluded that binding to GM1 is not primarily Coulombic, although again there are clearly Coulombic interactions (*22*, *35*, *36*).

A further titration of Aβ(1–40) has been carried out, using micelles of asialo-GM1. The results are shown in Figure 3 (right), in which the chemical shift ranges used in the plot are 75% of those used for Figure 3 (left); it can be seen that chemical shift changes with asialo-GM1 are similar to those seen for GM1 but are reduced in magnitude for equivalent concentrations by approx. 25%. A reduction is expected in shift magnitude, because asialo-GM1 is known to bind less tightly than GM1 to Aβ. The extent of the binding has been reported differently before. Choo-Smith et al. (*35*) reported no binding at all to asialo-GM1, while a factor of 2 was also reported (*37*). Our data agree better with the latter result (*37*). The overall similarity of the chemical shift changes for GM1 and asialo-GM1 implies that the binding interactions are similar, although with some differences in the region of His13–Gln15. This result therefore also implies that the interaction is not dominated by Coulombic forces, since asialo-GM1 has no charge in the headgroup.

Downloaded by DUKE UNIV on June 20, 2012 | http://pubs.acs.org
Publication Date (Web): October 14, 2011 | doi: 10.1021/bk-2011-1077.ch018

Interaction between β-Amyloid and Lipid Bilayers

In order to clarify the orientation of lipid bilayers with GM1 ganglioside as a function of Aβ(1-40) peptide concentration, we have recorded the orientational behavior of DMPC lipid bilayers using angular-dependent solid-state ^{31}P NMR experiments. The ^{31}P chemical shift tensors of phospholipids are represented graphically by an ellipsoid. The three main axes of the ellipsoid represent the main tensor elements δ_{11},δ_{22},δ_{33}. The chemical shift that is measured at a certain orientation of the molecule corresponds to the length of a vector parallel to the magnetic field direction. Thus the chemical shifts indicate the tilt of the phospholipids with respect to the magnetic field and/or the mobility of the lipid bilayers. In the case of a completely oriented lipid bilayer, ^{31}P NMR peaks obtained with aligned samples are narrow and there is only a small powder resonance under the aligned signal.

In a first set of experiments, we have obtained ^{31}P solid-state NMR spectra of glass-plate aligned DMPC samples as shown in Figure 4. These results indicate that the DMPC lipid bilayer is completely oriented on the glass plates. The ^{31}P chemical shift values of DMPC move to high field on changing the alignment axis from 0° to 90° relative to the magnetic field B_0. Figure 4(c) and (d) show angular-dependent ^{31}P NMR spectra of a DMPC/GM1 ganglioside system. The behavior of this system is similar to the result in a DMPC lipid bilayer alone, implying that the addition of GM1 ganglioside does not significantly perturb the structure of the DMPC bilayer.

Figure 5 illustrates the ^{31}P NMR spectra of a mechanically oriented DMPC bilayer as a function of the angle (θ) between the applied magnetic field and bilayer normal. The left, central and right traces correspond to the ^{31}P NMR spectra of DMPC/Aβ(1-40) molar ratios of 30:1, 20:1 and 10:1, respectively. Four peaks can be distinguished whose positions vary with the angle, while an isotropic peak remains almost at the same position independent of orientation angle (peak 3 in

Downloaded by DUKE UNIV on June 20, 2012 | http://pubs.acs.org
Publication Date (Web): October 14, 2011 | doi: 10.1021/bk-2011-1077.ch018

Figure 5). In particular, the outermost pairs among the four peaks exhibit an orientation-dependent displacement of peaks (peak 1 and 2 in Figure 5). Peak 4 in Figure 5 represents the edge of the powder pattern of the lipid bilayers. In addition, the separation of the outer and inner peaks varies with orientation, corresponding to the effective chemical shift anisotropies (CSAs) of the phosphodiester moieties ($\Delta = \delta_{//} - \delta_{\perp}$), as summarized in Table 1.

The anisotropy values of the outer and inner pairs decrease from 43.4 and 30.9 ppm, respectively, at a low proportion of Aβ (1-40) to 38.0 and 22.9 ppm at a higher ratio (Table 1). The most anisotropic component (i.e., most ordered) is attributed to a lamellar bilayer, in agreement with the observed CSA values. The component with reduced anisotropy is assigned to a different and therefore non-lamellar structure, most likely the hexagonal H_{II} form (*38*), based on its orientation dependence and the fact that the observed CSA value is approximately one-half the value measured for the bilayer structure (*39*, *40*). The isotropic peak is assigned to a disordered component showing rapid isotropic averaging. The most likely origin of this peak is the micellar components. We note that the chemical shift of the 'isotropic' signal varies with alignment. This is not inconsistent with micellar structure because micelle chemical shifts will still show orientation dependence because of differences in bulk magnetic susceptibility.

Table 1. Chemical shift difference between the parallel and perpendicular components of the ^{31}P shift of DMPC lipid bilayer in the presence of Aβ (1-40)

molar ratio of DMPC/Aβ		Chemical shift difference	
		Outer peak	Inner peak
10/1	Chemical shift Fraction(ppm)	38.0	22.5
20/1	Chemical shift Fraction	41.7	27.0
30/1	Chemical shift Fraction	43.4	30.9

Most significantly, the anisotropies of the ordered components are reduced with increased proportion of Aβ (1-40) (Figure 5, (a) to (b) to (c)). This observation is consistent with insertion of Aβ (1-40) into the membrane, because the observed anisotropies are averages of the large anisotropy arising from free lipids and the smaller anisotropy arising from lipids in direct contact with the peptide.

Downloaded by DUKE UNIV on June 20, 2012 | http://pubs.acs.org
Publication Date (Web): October 14, 2011 | doi: 10.1021/bk-2011-1077.ch018

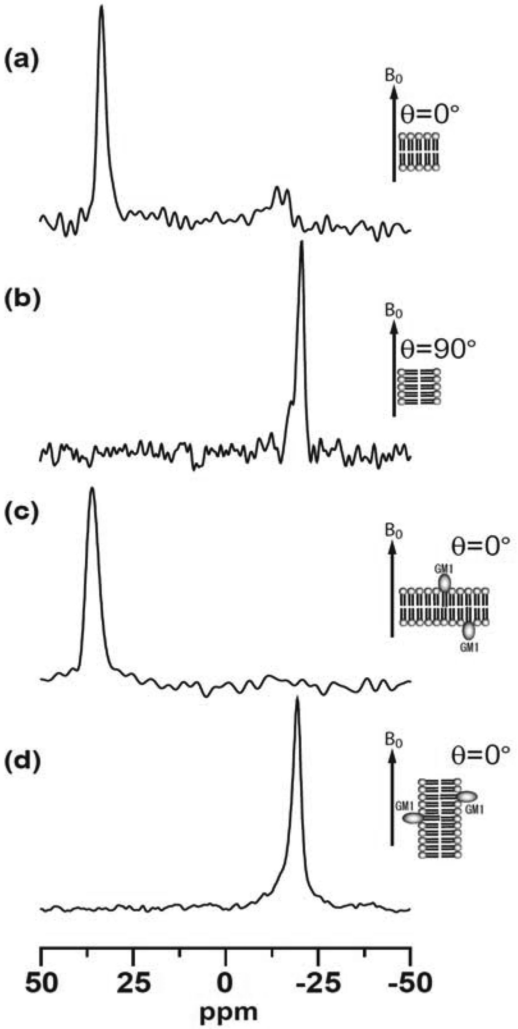

Figure 4. 1D ^{31}P ^{1}H-decoupled solid-state NMR spectra of oriented DMPC samples at 35°C. θ is the angle between the bilayer normal and B_0 (see insert). (a) Oriented DMPC bilayer sample with the order axis parallel to the magnetic field. (b) Oriented DMPC bilayer sample with the order axis perpendicular to the magnetic field. (c) and (d) Oriented bilayers of DMPC:GM1-ganglioside in molar ratio 10:1 in molar ratio, with the order axis respectively parallel and perpendicular to the magnetic field.

Downloaded by DUKE UNIV on June 20, 2012 | http://pubs.acs.org
Publication Date (Web): October 14, 2011 | doi: 10.1021/bk-2011-1077.ch018

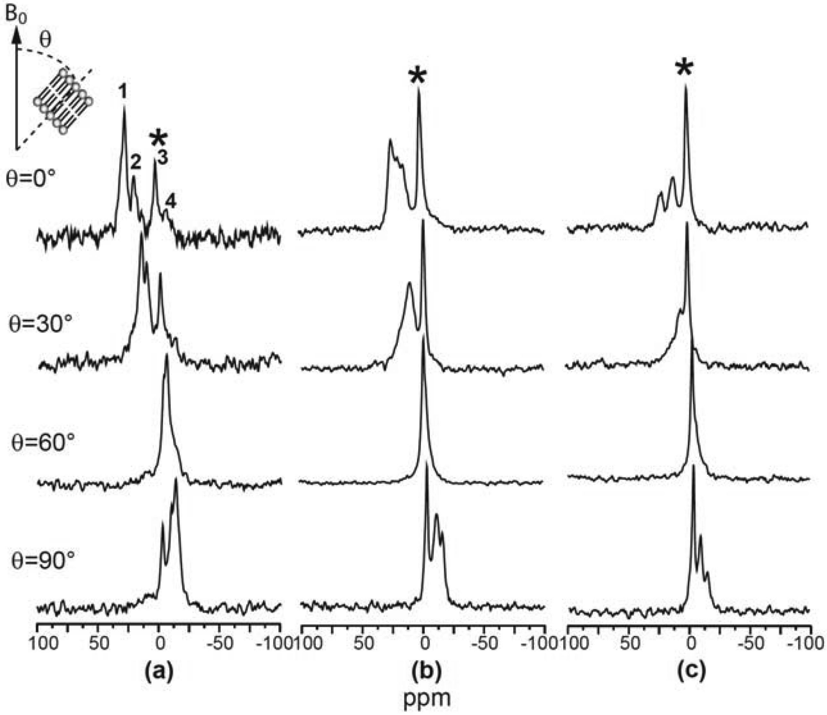

Figure 5. ^{31}P solid-state NMR spectra of macroscopically oriented DMPC samples incorporating varying ratios of Aβ(1-40) at 35°C as a function of the angle between the bilayer and the magnetic field. DMPC/Aβ(1-40) molar ratios were (a) 30:1, (b) 20:1, (c)10:1 respectively. θ is the angle between the bilayer normal and B_0. Asterisk indicates an isotropic peak. From their intensities these are identified as the parallel and perpendicular components, respectively.

Next, we measure the ^{31}P angular-dependent NMR spectra of a range of DMPC/ GM1 ganglioside systems in the presence of Aβ (1-40), as shown in Figure 6. No orientational distribution for DMPC molecules is observed at a DMPC/GM1 ganglioside ratio of 5:1 (data not shown). Therefore, we decide to perform an experiment using a ratio of DMPC to GM1 ganglioside of 10:1. In this case, it is notable that the relative intensity of the isotropic peak is substantially increased. With increasing concentration of Aβ (1-40) peptide, the intensity of the isotropic signal gradually increases further.

This result indicates that the lipid bilayer is gradually disrupted with increasing Aβ (1-40) peptide concentration, again highly suggestive of insertion of Aβ into the membrane.

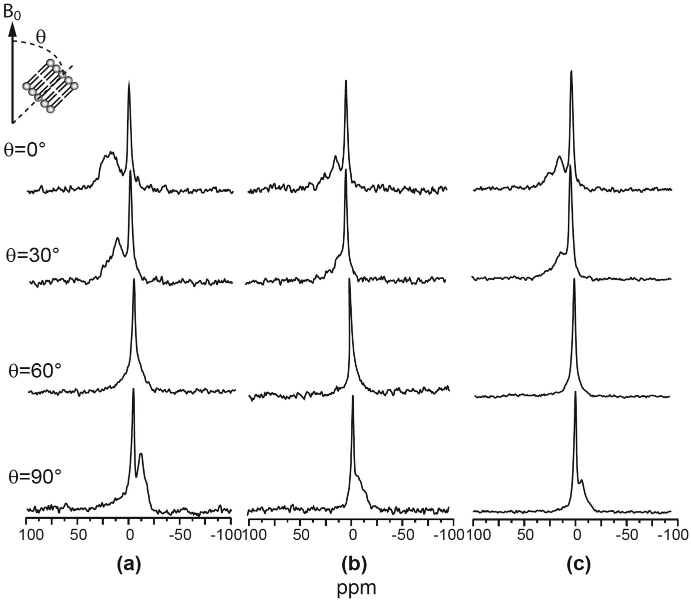

Figure 6. ^{31}P solid-state NMR spectra of macroscopically oriented DMPC/GM1 samples incorporating varying ratios of Aβ(1-40) at 35°C as a function of the angle between the bilayer and the magnetic field. DMPC/GM1/Aβ(1-40) molar ratios were (a) 20:2:1 (b) 10:1:1 (c) 10:1:1.5 respectively. θ is the angle between the bilayer normal and B_0.

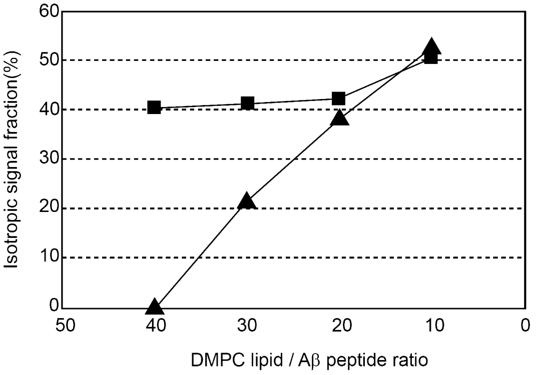

Figure 7. Changes of isotropic signal fraction of DMPC/Aβ and DMPC/GM1/Aβ depend on lipid/Aβ ratio. Triangle is the DMPC/Aβ sample and square is the DMPC/GM1/Aβ sample.

Downloaded by DUKE UNIV on June 20, 2012 | http://pubs.acs.org
Publication Date (Web): October 14, 2011 | doi: 10.1021/bk-2011-1077.ch018

Downloaded by DUKE UNIV on June 20, 2012 | http://pubs.acs.org
Publication Date (Web): October 14, 2011 | doi: 10.1021/bk-2011-1077.ch018

The fraction of the lamellar structure of DMPC decreases with respect to that of DMPC without Aβ(1-40) peptide. A similar decrease in the proportion of oriented phospholipids on glass plates has also been reported in the presence of other membrane-bound peptides (*41*). As expected, the chemical shifts of the two oriented components are dependent on their angle relative to the magnetic field. In the case of the DMPC/GM1/Aβ system, the oriented components make up only about 60% of the observed DMPC signal. It appears that the fraction of isotropic component in DMPC/ Aβ(1-40) peptide samples depends on the amount of Aβ(1-40) peptide present. However, the proportion of the isotropic lipids is almost independent of lipid/peptide ratio when GM1 is present, as shown in Figure 7.

Figure 8 illustrates the ^{13}C CP-MAS ((e) and (f)), DD-MAS ((c) and (d)) and solution NMR (b) spectra of ^{13}C labeled Aβ (1-40), DAEFRHDSGYEVH HQKL[1-^{13}C]V^{18}FF[3-^{13}C]A^{21}EDVGSNK[2-^{13}C]G^{29}AIIGLMVGGVVI, in the presence of DMPC bilayer, recorded both at 38° and 21°C, and also the solution NMR spectrum of sonicated lipid only (a). The ^{13}C NMR spectrum of DMPC in the sonicated single vesicle has very sharp signals and serves as a reference for the peaks arising from lipid itself. The CP-MAS technique emphasizes signals from the more rigidly structured components, whereas DD-MAS tends to emphasise more mobile components (*42*, *43*). It is noted that the ^{13}C NMR signals of fatty acyl chains at 32 and 30 ppm can be very conveniently utilized as a probe to determine the state of the lipid phase as either the gel or liquid crystalline states, respectively (*44*). Therefore, it is clear that the ^{13}C CP-MAS NMR peaks of the fatty acyl chains show the presence of a mixture of gel and liquid crystalline lipids (6:4) at 38 °C but gel phase alone at 21°C.

At least three kinds of different forms can be distinguished for Aβ (1-40) peptide: random coil, β-sheet, and transmembrane-type α-helix structure; they can be characterized by liquid state, CP-MAS and DD-MAS NMR, respectively, in the presence of lipid bilayer as judged from the conformation-dependent displacement of peaks (*45*, *46*) The ^{13}C CP-MAS NMR spectra recorded at 38°C and 21°C clearly exhibit the characteristic peaks of a β-sheet form as judged from the peak-positions of Ala^{21} C$_{\beta}$ at 20.3 ppm, and Val^{18} C=O at 170.1 ppm (Figure 8(e) and (f)). It is therefore concluded that the Aβ peptide is likely to exist in a mixture of monomeric and oligomeric states in the presence of phospholipids: the Aβ peptides which form β-sheet structure are likely to be oligomeric (i.e., the fibrils or protofibrils observed in many other studies), whereas the Aβ peptides which take on a small amount of α-helical structure are most likely to be monomeric. Moreover, it is suggested that these structural differences usually exist in an each domain rather than in single molecules.

It is noteworthy that very sharp isotropic Ala^{21} C$_{\beta}$, Gly^{29} C$_{\alpha}$ and Gly^{18} C=O signals (Figure 8(b)) can be ascribed to Aβ incorporated into micelles, the presence of which is confirmed by an isotropic ^{31}P NMR signal in the presence of this protein (Figure 5). The Ala^{21} C$_{\beta}$ signal at 16.5 ppm is characteristic of α-helical conformation and not random coil (16.7 ppm). Surprisingly, this signal, as well as that from Gly^{29} C$_{\alpha}$, which are clearly visible on liquid-state NMR, is almost completely suppressed when the sample is analyzed with both CP-MAS and DD-MAS NMR. This suppression is ascribed to a well-known phenomenon: the failure of the necessary high-power proton decoupling to produce high-resolution signals when the incoherent fluctuation frequency of peptide chains in liquid crystalline lipids interferes with the coherent frequency of proton decoupling (60 kHz) (*45*, *47*). If so, it is expected that such suppressed peaks can be recovered, at least partially, either by reducing the fluctuation frequency by lowering the temperature, or by reducing the decoupling frequency to some extent, from the original 60 kHz to 37 kHz, for instance. Consistent with this expectation, we found that the peak intensity of Ala C_β is more evident when the decoupling frequency is reduced in the DD-MAS (Figure 7(c)), and the Gly C_α signal is also more visible at low temperature in the gel phase lipid, as viewed from the peak-position of fatty acyl chain (Figure 8(a)).

We have shown in this paper that the bilayer structure is strongly perturbed by the presence of Aβ (1-40) peptide and also GM1, yielding a fraction of anisotropic but non-lamellar structure, suggested to be the hexagonal H_{11} structure. At the same time, the proportion of an isotropic lipid phase such as micelle or single-vesicle increases, as determined from ^{31}P NMR spectra. Such perturbation to the bilayer is significantly more prominent when GM1 is present. The assignment of the non-lamellar phases to H_{11} and micellar structures is based partly on the observation that lipid polymorphic structure is strongly related to the shape of lipids: a cylindrical lipid such as phosphatidylcholine favors bilayer structure, while cone-like lipids such as (unsaturated) phosphatidylethanolamine, cardiolipin and phosphatidic acid-Ca^{2+} prefer to take on a hexagonal H_{11} forms (*38*). Furthermore, an inverted cone such as GM1 favors a micellar structure.

Non-lamellar lipid structures, such as that revealed here by ^{31}P NMR, have been reported for a number of biological membranes containing proteins such as erythrocyte (ghost) (*47*), rat, bovine and rabbit liver microsomal membranes (*48*, *49*), and cytochrome P-450 membrane (*49*). Several peptides including gramicidin, alamethicin, α-helical peptides, and antimicrobial peptides have also been shown to perturb bilayer structure to form non-lamellar hexagonal H_{11} lipids by peptide-induced changes in lipid phases (*50–55*), in addition to the effect of lipid molecules themselves as mentioned above. The hydrophobicity and conformational flexibility of transmembrane peptides in lipid bilayers can affect their propensity to induce the formation of inverted non-lamellar phases by mechanisms not dependent on mainly lipid-peptide hydrophobic mismatch (*54*), although we note that a theoretical interpretation of a mechanism of the lamellar-to-inverted hexagonal phase transition has also been proposed, in relation to the membrane fusion process (*56*, *57*) For this reason, it is likely that the effect of Aβ (1-40) arises from interaction with the lipid bilayer, following an initial penetration into the bilayer. The effect of ganglioside, however, on modulation of lamellar-inverted micelle (H_{11}) phase transition has been examined in relation to biomembranes and shown to vary depending upon the relative concentration of ganglioside to lipids (*56*).

Our ^{13}C NMR study indicates that Aβ (1-40) together with GM1 plays an important role to disrupt bilayer structure to form non-lamellar lipid and micelle by its penetration into bilayer and taking on an α-helical form. As a result, the Ala C_β ^{13}C NMR peak was almost completely suppressed on both CP-MAS and DD-MAS NMR spectra recorded at 38°C but was partially recovered on DD-MAS

Downloaded by DUKE UNIV on June 20, 2012 | http://pubs.acs.org
Publication Date (Web): October 14, 2011 | doi: 10.1021/bk-2011-1077.ch018

NMR spectra utilizing reduced proton decoupling (Figure 5(c)). This means that the features of their ^{13}C NMR spectra are strongly influenced by the fluidity of lipid molecules.

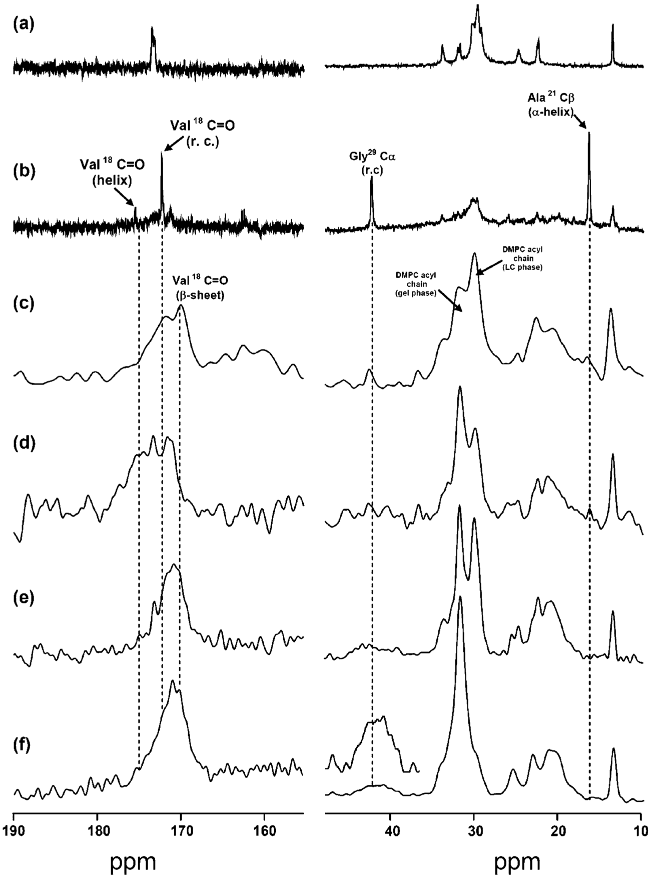

Figure 8. ^{13}C CP-MAS and DD-MAS NMR spectra of selectively ^{13}C-labeled Aβ (1-40) peptide incorporated into lipid bilayers. (a) lipid only, (b) liquid state NMR at 38°C, (c) DD-MAS NMR, using reduced high-power decoupling of 34 kHz at 38°C, (d) DD-MAS NMR at 38°C, (e) CP-MAS NMR at at 38°C, and (f) CP-MAS NMR at 21°C. The molar ratio of DMPC : Aβ peptide is 10:1 in each spectra except of Figure 5(a).

This study is 'non-physiological' in that the lamellar structure is allowed to reform slowly in the presence of Aβ. It may therefore be argued that our observation of interaction of Aβ with lipid tails is not relevant. In response, we note that the current mixed film method is commonly used to incorporate hydrophobic transmembrane peptides in lipid bilayers. Otherwise, such peptides remain outside of the bilayer by forming β-sheet aggregates. Indeed, Separovic and co-workers have been shown that addition of Aβ(1-42) to preformed bilayer

Downloaded by DUKE UNIV on June 20, 2012 | http://pubs.acs.org
Publication Date (Web): October 14, 2011 | doi: 10.1021/bk-2011-1077.ch018

resulted in precipitate on the lipid surface with little effect on the hydrocarbon region of the lipid bilayer and also found that ^{31}P isotropic peak was formed only when the peptide and lipid were co-solubilized for Aβ(1-42) peptides. (*13*). Therefore, the current mixed film method is very important in gaining insight into whether or not the peptide is thermodynamically capable of being incorporated into bilayers. Since the onset of Alzheimer's is a very slow process, it is entirely reasonable to argue that it is the thermodynamically rather than the kinetically preferred product that will eventually prevail.

It is still premature to relate fibrillation of Aβ (1-40) *in vitro* with subsequent neurodegenerative disease. However, it is interesting to note that we observe β-sheet conformation of Aβ, presumably on the lipid surface. GM1 is closely associated with transmembrane signaling, leading to the interesting possibility that aggregation and fibrillisation of Aβ on the membrane surface could interfere with signaling at synaptic junctions. Moreover, we have shown that the interaction with ganglioside GM1 micelles is localized to the N-terminal region of the peptide, particularly residues His^{13} to Leu^{17}, which become more helical when bound as referred to above (*27*). This is consistent with the present data, although here the importance of interaction with fatty acyl chains is emphasized together with formation of non-lamellar structure and micelle formation. This study has shown that GM1 facilitates the membrane disruption caused by Aβ peptide. Indeed, this view is consistent with insertion of Aβ peptide into lipid bilayer to cause disruption of bilayer structure (*17*), although this is in contrast to an alternative view which emphasizes a cholesterol-dependent cluster of GM1 in membranes (*16*).

Conclusion

In order to clarify the interaction between β-amyloid and lipid bilayers including ganglioside, we first demonstrate using solution state NMR on ^{15}N-labelled Aβ(1–40) and Aβ(1–42) that the interaction with ganglioside GM1 micelles is localized to the N-terminal region of the peptide, particularly residues His^{13} to Leu^{17}, which become more helical when bound, leaving the C-terminal region unstructured (*27*). Furthermore, the insertion of Aβ peptide into lipid bilayer to form a micellar structure is proposed on the basis of a monolayer study (*17*). Secondly, we obtain ^{1}H decoupled ^{31}P solid-state NMR spectra of dimyristoylphospatidylcholine (DMPC) and DMPC/GM1 ganglioside in a mechanically oriented system in the presence of Aβ(1-40) in order to clarify the behavior of Aβ in the presence of GM1 ganglioside. Finally, we record the spectra from ^{13}C-labeled Aβ peptide by CP-MAS and DD-MAS NMR, as well as low-power solution NMR to determine conformational features of the Aβ peptide in the presence of lipid bilayers.

In the case of solution NMR experiment, we demonstrate Aβ binding in the low micromolar range to GM1 and asialo-GM1, but no measurable binding to the isolated GM1 headgroup. Several experiments (both ours and those of others (*33*)) demonstrate that although there may be a Coulombic element to the binding, the interactions are not limited to Coulombic ones. Our results are therefore relevant

Downloaded by DUKE UNIV on June 20, 2012 | http://pubs.acs.org
Publication Date (Web): October 14, 2011 | doi: 10.1021/bk-2011-1077.ch018

to the physiological situation where salt concentration is higher and Coulombic interactions are weaker.

The chemical shift changes reported here demonstrate binding of Aβ to GM1 micelles, which is localized to the N-terminal half of the peptide. We confirm that binding to asialo-GM1 is weaker, specifically with differences around residues 12–15 which include His residues. This conclusion is radically different from an earlier NMR study [34]. However, that earlier study was carried out using SDS(Sodium Dodecyl Sulfate) micelles which might explain the discrepancy.

Above all, we find that Aβ (1-40) strongly perturbs the bilayer structure of DMPC to form either a non-lamellar structure or micelles. In particular, GM1 accelerates the effect of Aβ (1-40), as viewed from ^{31}P NMR. Such effect may arise from direct contact with fatty acyl chains of lipids by inserting Aβ (1-40) into the bilayer. The difference of the isotropic peak intensity between DMPC/Aβ and DMPC/GM1/Aβ suggests the presence of a specific interaction between Aβ and GM1 ganglioside. We show that in the DMPC/GM1/Aβ system there are three lipid phases, a completely aligned phase, a hexagonal phase, and non-oriented lipids(or smaller vesicle structures (*13*)). The formation of latter two phases are induced by the presence of the Aβ peptide and facilitated by GM1.

Downloaded by DUKE UNIV on June 20, 2012 | http://pubs.acs.org
Publication Date (Web): October 14, 2011 | doi: 10.1021/bk-2011-1077.ch018

Acknowledgments

This work has been supported by a Grant-in-Aid for Creative Scientific Research of the Japan Society for the Promotion of Science (JSPS)

References

1. Iversen, L. L.; Mortishire-smith, R. J.; Pollack, S. J.; Shearman, M. S. *Biochem. J.* **1995**, *311*, 1–16.
2. Glenner, G. G.; Wong, C. W. *Biochem. Biophys. Res. Commun.* **1984**, *122*, 1131–1135.
3. Masters, C. L.; Multhaup, G.; Simms, G.; Pottgiesser, J.; Martins, R. N.; Beyreuther, K. *EMBO J.* **1985**, *4*, 2757–2763.
4. Kang, J.; Lemaire, H. G.; Unterbeck, A.; Salbaum, J. M.; Masters, C. L.; Grzeschik, K. H.; Multhaup, G.; Beyreuther, K.; Muller-Hill, B. *Nature* **1987**, *325*, 733–736.
5. Kirschner, D. A.; Abraham, C.; Selkoe, D. J. *Proc. Natl. Acad. Sci. U.S.A.* **1986**, *83*, 503–507.
6. Petkova, A. T.; Yau, W. M.; Tycko, R. *Biochemistry* **2006**, *45*, 498–512.
7. Petkova, A. T.; Ishii, Y.; Balbach, J. J.; Antzutkin, O. N.; Leapman, R. D.; Delaglio, F.; Tycko, R. *Proc. Natl. Acad. Sci. U.S.A.* **2002**, *99*, 16742–16747.
8. Lambert, M. P.; Barlow, A. K.; Chromy, B. A.; Edwards, C.; Freed, R.; Liosatos, M.; Morgan, T. E.; Rozovsky, I.; Trommer, B.; Viola, K. L.; Wals, P.; Zhang, C.; Finch, C. E.; Krafft, G. A.; Klein, W. L. *Proc. Natl. Acad. Sci. U.S.A.* **1998**, *95*, 6448–6453.

Downloaded by DUKE UNIV on June 20, 2012 | http://pubs.acs.org
Publication Date (Web): October 14, 2011 | doi: 10.1021/bk-2011-1077.ch018

9. Geula, C.; Wu, C. K.; Saroff, D.; Lorenzo, A.; Yuan, M.; Yankner, B. A. *Nat. Med.* **1998**, *4*, 827–831.
10. Muller, W. E.; Koch, S.; Eckert, A.; Hartmann, H.; Scheuer, K. *Brain Res.* **1995**, *674*, 133–136.
11. Arispe, N.; Rojas, E.; Pollard, H. B. *Proc. Natl. Acad. Sci. U.S.A.* **1993**, *90*, 567–571.
12. Ambroggio, E. E.; Kim, D. H.; Separovic, F.; Barrow, C. J.; Barnham, K. J.; Bagatolli, L. A.; Fidelio, G. D. *Biophys. J.* **2005**, *88*, 2706–2713.
13. Lau, T. L.; Ambroggio, E. E.; Tew, D. J.; Cappai, R.; Masters, C. L.; Fidelio, G. D.; Barnham, K. J.; Separovic, F. *J. Mol. Biol.* **2005**.
14. de Planque, M. R.; Raussens, V.; Contera, S. A.; Rijkers, D. T.; Liskamp, R. M.; Ruysschaert, J. M.; Ryan, J. F.; Separovic, F.; Watts, A. *J. Mol. Biol.* **2007**, *368*, 982–997.
15. Yanagisawa, K.; Odaka, A.; Suzuki, N.; Ihara, Y. *Nat. Med.* **1995**, *1*, 1062–1066.
16. Kakio, A.; Nishimoto, S.; Yanagisawa, K.; Kozutsumi, Y.; Matsuzaki, K. *Biochemistry* **2002**, *41*, 7385–7390.
17. Chi, E. Y.; Frey, S. L.; Lee, K. Y. *Biochemistry* **2007**, *46*, 1913–1924.
18. Brocca, P.; Sonnino, S. *Trends Glycosci. Glycotechnol.* **1997**, *9*, 433–445.
19. Kasahara, K.; Sanai, Y. *Trends Glycosci. Glycotechnol.* **2001**, *74*, 587–594.
20. Nagai, Y. *Behav. Brain Res.* **1995**, *66*, 99–104.
21. McLaurin, J.; Chakrabartty, A. *J. Biol. Chem.* **1996**, *271*, 26482–26489.
22. McLaurin, J.; Franklin, T.; Fraser, P. E.; Chakrabartty, A. *J. Biol. Chem.* **1998**, *273*, 4506–4515.
23. McLaurin, J.; Chakrabartty, A. *J. Biol. Chem.* **1996**, *271*, 26482–26489.
24. Choo-Smith, L. P.; Surewicz, W. K. *FEBS Lett.* **1997**, *402*, 95–98.
25. Yanagisawa, K.; Ihara, Y. *Neurobiol. Aging* **1998**, *19*, S65–67.
26. Kakio, A.; Nishimoto, S.; Kozutsumi, Y.; Matsuzaki, K. *Biochem. Biophys. Res. Commun.* **2003**, *303*, 514–518.
27. Williamson, M. P.; Suzuki, Y.; Bourne, N. T.; Asakura, T. *Biochem. J.* **2006**, *397*, 483–490.
28. Hou, L.; Shao, H.; Zhang, Y.; Li, H.; Menon, N. K.; Neuhaus, E. B.; Brewer, J. M.; Byeon, I. J.; Ray, D. G.; Vitek, M. P.; Iwashita, T.; Makula, R. A.; Przybyla, A. B.; Zagorski, M. G. *J. Am. Chem. Soc.* **2004**, *126*, 1992–2005.
29. Bai, Y.; Milne, J. S.; Mayne, L.; Englander, S. W. *Proteins* **1993**, *17*, 75–86.
30. Zhang, S.; Iwata, K.; Lachenmann, M. J.; Peng, J. W.; Li, S.; Stimson, E. R.; Lu, Y.; Felix, A. M.; Maggio, J. E.; Lee, J. P. *J. Struct. Biol.* **2000**, *130*, 130–141.
31. Basu, A.; Glew, R. H. *J. Biol. Chem.* **1985**, *260*, 13067–13073.
32. Morrison, J.; Yang, J. C.; Stewart, M.; Neuhaus, D. *J. Mol. Biol.* **2003**, *333*, 587–603.
33. Laguri, C.; Phillips-Jones, M. K.; Williamson, M. P. *Nucleic Acids Res* **2003**, *31*, 6778–6787.
34. Ma, K.; Clancy, E. L.; Zhang, Y.; Ray, D. G.; Wollenberg, K.; Zagorski, M. G. *J. Am. Chem. Soc.* **1999**, *121*, 8698–8706.

35. Choo-Smith, L. P.; Garzon-Rodriguez, W.; Glabe, C. G.; Surewicz, W. K. *J. Biol. Chem.* **1997**, *272*, 22987–22990.
36. Bokvist, M.; Lindstrom, F.; Watts, A.; Grobner, G. *J. Mol. Biol.* **2004**, *335*, 1039–1049.
37. Ariga, T.; Kobayashi, K.; Hasegawa, A.; Kiso, M.; Ishida, H.; Miyatake, T. *Arch. Biochem. Biophys.* **2001**, *388*, 225–230.
38. Cullis, P. R.; de Kruijff, B. *Biochim. Biophys. Acta* **1979**, *559*, 399–420.
39. Thayer, A. M.; Kohler, S. J. *Biochemistry* **1981**, *20*, 6831–6834.
40. Smith, I. C. P.; Ekiel, I. H. *Phosphorus-31 NMR*; Academic Press: New York, 1984.
41. Moll, F., 3rd; Cross, T. A. *Biophys. J.* **1990**, *57*, 351–362.
42. Tuzi, S.; Naito, A.; Saito, H. *Eur. J. Biochem.* **1993**, *218*, 837–844.
43. Kamihira, M.; Naito, A.; Tuzi, S.; Nosaka, A. Y.; Saito, H. *Protein Sci.* **2000**, *9*, 867–877.
44. Kimura, S.; Naito, A.; Tuzi, S.; Saito, H. *Biopolymers* **2001**, *58*, 78–88.
45. Saito, H.; Tuji, S.; Tanio, M.; Naito, A. *Annu. Rep. NMR Spectrosc.* **2002**, *47*, 39–108.
46. Saito, H. *Magn. Reson. Chem.* **1986**, *24*, 835–852.
47. Rothwell, W. P.; Waugh, J. S. *J. Chem. Phys.* **1981**, *74*, 2721–2732.
48. Davis, J. H. *Biochim. Biophys. Acta* **1983**, *737*, 117–171.
49. Stier, A.; Finch, S. A.; Bosterling, B. *FEBS Lett.* **1978**, *91*, 109–112.
50. Gasset, M.; Killian, J. A.; Tournois, H.; de Kruijff, B. *Biochim. Biophys. Acta* **1988**, *939*, 79–88.
51. Cornell, B. A.; Separovic, F. *Eur. Biophys. J.* **1988**, *16*, 299–306.
52. Keller, S. L.; Gruner, S. M.; Gawrisch, K. *Biochim. Biophys. Acta* **1996**, *1278*, 241–246.
53. Killian, J. A.; de Kruijff, B. *Biochemistry* **1985**, *24*, 7890–7898.
54. Liu, F.; Lewis, R. N.; Hodges, R. S.; McElhaney, R. N. *Biochemistry* **2001**, *40*, 760–768.
55. Hallock, K. J.; Lee, D. K.; Ramamoorthy, A. *Biophys. J.* **2003**, *84*, 3052–3060.
56. Siegel, D. P. *Biophys. J.* **1986**, *49*, 1155–1170.
57. Siegel, D. P.; Epand, R. M. *Biophys. J.* **1997**, *73*, 3089–3111.

Downloaded by DUKE UNIV on June 20, 2012 | http://pubs.acs.org
Publication Date (Web): October 14, 2011 | doi: 10.1021/bk-2011-1077.ch018

Chapter 19

Characterization of Microbial Poly(ε-L-lysine) and Its Derivatives by Solid-State NMR

Shiro Maeda,*,[1] Chizuru Sasaki,[2] and Ko-Ki Kunimoto[3]

[1]Division of Applied Chemistry and Biotechnology, Graduate School of Engineering, University of Fukui, Japan
[2]Department of Life System, Institute of Technology and Science, The University of Tokushima, Japan
[3]Division of Material Engineering, Graduate School of Natural Science and Technology, Kanazawa University, Japan
***E-mail: smaeda@u-fukui.ac.jp**

Downloaded by DUKE UNIV on June 21, 2012 | http://pubs.acs.org
Publication Date (Web): October 14, 2011 | doi: 10.1021/bk-2011-1077.ch019

The molecular structure and conformation of microbial poly(ε-L-lysine) (ε-PL) and its derivatives in aqueous solution and in the solid-state have been studied with liquid-state ^{1}H and ^{13}C NMR, and solid-state ^{13}C and ^{15}N NMR, together with FT-IR, FT-Raman, and circular dichroism (CD) techniques. CD and vibrational spectroscopic results indicate that ε-PL assumes a β-sheet conformation in aqueous solution and in the solid state. Solid-state ^{13}C NMR spectra of the crystalline and the amorphous components were obtained separately by utilizing difference in ^{13}C spin-lattice relaxation times between the two components. The degree of crystallinity was estimated to be 63%. Conformation models of the crystalline component were also discussed. Chemically modified derivatives of ε-PL, ε-PL/MO and ε-PL/DC were prepared through reactions with methyl orange (MO) and dabsyl chloride (DC), respectively. Characterization of these derivatives was carried out by solid-state ^{13}C and ^{15}N NMR. In ε-PL/MO side chain α-amino groups of ε-PL are involved in ionic bonds with methyl orange (MO) to form poly-ionic complexes, (ε-PL)-NH_3^+ SO_3^--(MO). In contrast, the α-amino groups react with DC in ε-PL/DC to form covalent sulfonamide bonds, (ε-PL)-NH-SO_2-(DC). The ^{15}N NMR data are consistent with these structures.

In NMR Spectroscopy of Polymers: Innovative Strategies for Complex Macromolecules; Cheng, H., et al.;
ACS Symposium Series; American Chemical Society: Washington, DC, 2011.

Downloaded by DUKE UNIV on June 21, 2012 | http://pubs.acs.org
Publication Date (Web): October 14, 2011 | doi: 10.1021/bk-2011-1077.ch019

Introduction

In recent years, there has been considerable interest in biopolymers because of concern over the environmental impacts arising from the disposal of petroleum-based plastics (*1*). Biologically derived polymers have been extensively investigated as biodegradable polymers as a means of reducing environmental impact (*2*). Natural poly(amino acid)s are a class of biodegradable polymers mainly composed of one type of amino acid. Three poly(amino acid)s which are known to occur in nature: poly(ε-L-lysine), Poly(γ-glutamic acid), and cyanophycin (*3*, *4*). Microbial production of ε-PL was first discovered by Shima and Sakai from a culture filtrate of *Streptomyces albulus* (*5*). They studied the detailed fermentation conditions and reported the physicochemical properties of microbial ε-PL (*6–8*). The ε-amino group of L-lysine is linked to the α-carboxyl group to form a peptide bond in a ε-PL molecule. (Scheme 1) Chemical synthesis of ε-PL was also reported by Kushwaha *et al.* (*9*). Owing to antibacterial activities against a broad spectrum of microorganisms, ε-PL has found application as a preservative for various food products (*10*).

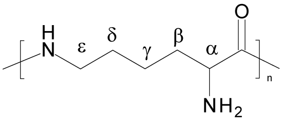

Scheme 1. Repeating units of ε-PL.

ε-PL is water-soluble and biodegradable, in addition to exhibiting antibacterial activities. An understanding of the structure and the conformation is prerequisite for functionalization of ε-PL (*11*). We have studied the molecular structure and the conformation of ε-PL in aqueous solution (*12–14*) and those of dabsylated ε-PL in aqueous DMSO solution (*15*). It is conceivable that the four methylene groups in the backbone of ε-PL endow the polymer with considerable conformational flexibility compared to the case of poly(α-L-lysine). The pH dependent IR and CD spectra have indicated that ε-PL assumes a β-sheet conformation in aqueous solution, the content of which is dependent on the chain length and the pH (*14*). We have characterized the structure and the conformation of ε-PL in the solid-state for the first time by FT-IR, FT-Raman and ^{13}C solid-state NMR (*16*). Since the primary structure of ε-PL is related to nylon 6, the spectral features were compared with those of nylon 6. On the basis of these spectroscopic data, a conformation model was proposed for the crystalline component of ε-PL. We also carried out structural investigation of ε-PL–azo dye derivatives using solid-state ^{13}C and ^{15}N NMR (*17*). Polymers containing azobenzene moieties in a side chain have potential application as an optical materials (*18*, *19*). When methyl orange (MO, 4-dimethylamino-azobenzene-4'-sulfonic acid) is added to an aqueous solution of ε-PL, the ε-PL/dye complex precipitates out of solution. This procedure has been generally utilized for the determination of free amino groups in peptides and proteins (*20*). Likewise, ε-PL also forms a water-insoluble compound in the reaction with an amino labeling reagent, dabsyl chloride (DC, 4-dimethylaminoazobenzene-4'-sulfonyl chloride). ^{13}C and ^{15}N solid-state NMR measurements of ε-PL and its derivatives have been reported, and molecular interaction between ε-PL and the dye discussed.

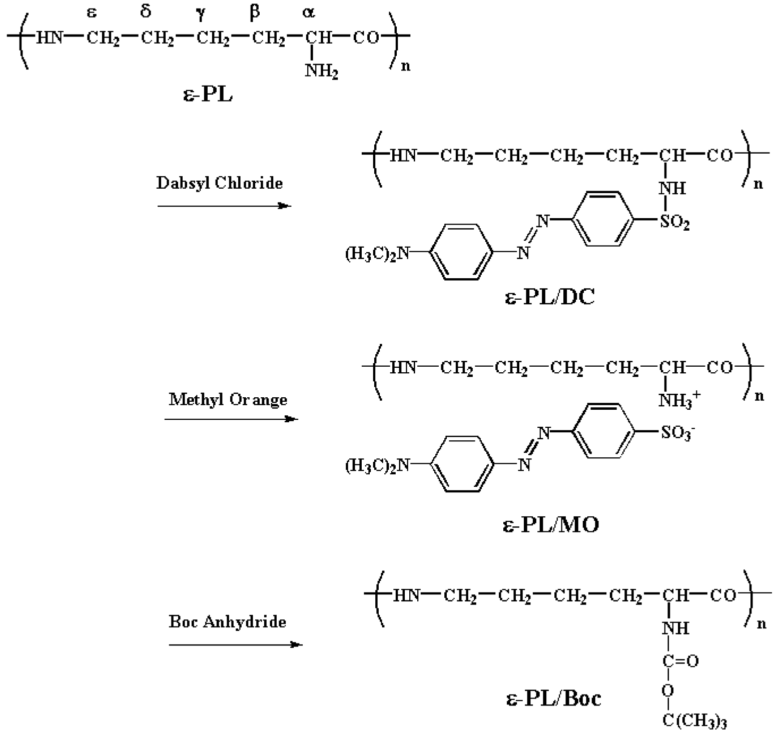

Scheme 2. Preparation of ε-PL derivatives.

Experimental Section

Materials

Microbial ε-PL (free form, ε-PL) was produced from the culture broth of a variant of *Streptomyces albulus* (No. 346) by Chisso Corporation, Japan according to a reported procedure (*21*). Methyl orange (MO), dabsyl chloride (DC) and other reagents were purchased from Tokyo Kasei Kogyo, Japan, and used without further purification. The HCl salt form of ε-PL, ε-PL/HCl was prepared with hydrochloric acid according to a reported procedure (*13*). ε-PL/MO and ε-PL/DC (Scheme 2) were prepared as follows. ε-PL (26 mg, 0.2 mmol) and MO (65.4 mg, 0.2 mmol) were mixed and dissolved in 400 ml of 0.1 M phosphate buffer solution (pH 6.0) and the pH was adjusted to 6.0-7.0 by adding 0.1-1.0 M hydrochloric acid. The molar ratio of [MO]/[lysyl residue] used here corresponds to 1.0. The solution was allowed to react for 4 h at room temperature. When the solution volume was reduced to about 150 ml by evaporation, a precipitate was formed. After centrifugation for 15 min, the orange products were taken out and dried *in vacuo*. ε-PL/DC was prepared according to the conventional Schotten-Baumann

Downloaded by DUKE UNIV on June 21, 2012 | http://pubs.acs.org
Publication Date (Web): October 14, 2011 | doi: 10.1021/bk-2011-1077.ch019

reaction. To a 100 ml MeOH solution of dabsyl chloride (162 mg, 0.5 mmol) containing triethylamine (152 mg, 1.5 mmol), 64 mg of ε-PL (0.5 mmol) was added. The mixture was allowed to stand at room temperature for 20 h. The resulted reddish-orange precipitate was collected by centrifugation. The product was washed with distilled water several times. ε-PL/Boc (*t*-butoxycarbonyl) (Scheme 2) was also prepared through *tert*-butoxycarbonylation using Boc anhydride as a reference compound, which is a completely *N*-substituted ε-PL derivative. The degree of chemical modification was estimated from ^{1}H NMR spectra of DMSO-d_6 solutions, by using integral values obtained from the number of -CH$_2$- protons of ε-PL and appropriate protons of the chemical modifier. The apparent degree of chemical modification was 90 % for ε-PL/MO and 83 % for ε-PL/DC.

Downloaded by DUKE UNIV on June 21, 2012 | http://pubs.acs.org
Publication Date (Web): October 14, 2011 | doi: 10.1021/bk-2011-1077.ch019

Measurements and Instruments

Nuclear Magnetic Resonance (NMR)

High-resolution solid-state ^{13}C and ^{15}N NMR spectra were measured with Chemagnetics CMX Infinity 300 operating at 75.6 MHz and 30.0 MHz, respectively, at room temperature. A 62.6 kHz r.f. field strength was used for a proton 90° pulse, with cross polarization and decoupling. A sample in powder form was contained in a cylindrical rotor of zirconia ceramic. The rotor diameter was 5 mm for ^{13}C and 7.5 mm for ^{15}N, and the rotor was spun at 7.0 kHz and 5.0 kHz, respectively. Contact time was 1ms, and repetition time was 2 sec. The number of scans was about 12,000 for ^{13}C and about 40,000 for ^{15}N. ^{13}C signal of methyl carbon of hexamethylbenzene was externally referenced to 17.35 ppm. ^{15}N signal of glycine was externally referenced to 32.5 ppm from ammonia (liq. NH$_3$, 25°C). ^{1}H, ^{13}C, ^{1}H-^{1}H COSY and ^{1}H-^{13}C COSY NMR spectra of ε-PL were measured either in trifluoroacetic acid-*h* (TFA-*h*), TFA-*d* or D$_2$O solutions with a JEOL JNM-GSX 400 NMR instrument at room temperature. Chemical shifts were calibrated through an internal standard, TMS or sodium 2,2'-dimethyl-2-silapentane-5-sulfonate-d_6 (DSS).

IR, Raman, and Circular Dichroism (CD) Spectroscopies

The IR spectra were recorded on a Perkin Elmer 1650 FT-IR spectrometer by averaging 64 scans with a resolution of 4 cm^{-1}. The spectra were measured as KBr pellets and nujol mulls. The FT-Raman spectra were obtained on a Perkin-Elmer 2000R spectrometer equipped with a quartz beam splitter and InGaAs detector. The 1064 nm line of a Spectron Laser System SL300 Nd: YAG laser was used as the exciting source with an output power of about 200 mW at the sample position. All spectra were accumulated for 60 scans with a resolution of 4 cm^{-1}. CD spectra were measured with a JASCO J-600 spectropolarimeter by courtesy of JASCO Ltd.

Gel Permeation Chromatography (GPC)

Molecular weights and their distributions were determined using the standard set-up of GPC-LALLS (Gel Permeation Chromatography combined with a Low Angle Laser Light Scattering detector, Waters model ALC/GPC 244). Ion-pair chromatography of ε-PL was carried out on a reverse-phase ODS column (L-Column, Chemicals Evaluation and Research Institute, Japan).

Results and Discussion

Physical Properties of ε-PL

ε-PL is a white crystalline powder that shows a glass transition temperature (Tg) at 88°C and a melting point (Tm) at 172.8°C. These values are comparable with the typical values of nylon 6 (Tg 56 °C, Tm 221 °C). Figure 1 shows a HPLC ion-pair chromatogram of ε-PL. The chromatogram is clearly resolved according to the degree of polymerization (n). ε-PL exhibits a train of peaks where the major peak population occurs at retention time around 40 min. Using the pentamer and the decamer as standards for the n value, it is shown that ε-PL has the maximum distribution in the n = 25-32 range. The number-average molecular weight (Mn) of ε-PL was determined to be 4,090, which corresponds to n = 32 based on the unit molecular weight of 128. ε-PL has a relatively narrow molecular weight

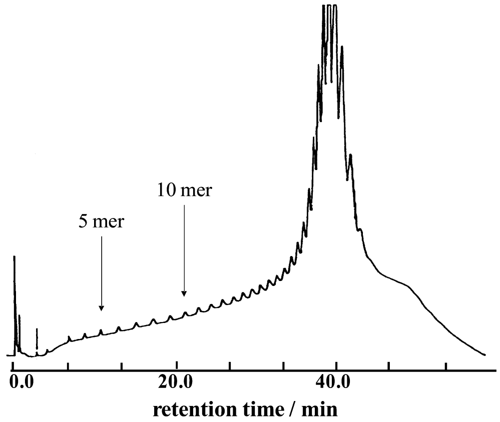

Figure 1. HPLC ion pair chromatogram of ε-PL. (Reproduced with permission from reference (16). Copyright 2003 Elsevier.)

Characterization of ε-PL in Aqueous Solution

Since ε-PL is water-soluble, we examined the molecular structure and the conformation of ε-PL in water (*12–14*). Secondary structure of ε-PL is expected to change with the dissociation state of side chain α-amino groups and end groups. We measured the pH (or pD) dependence of NMR spectra of ε-PL, and a series of ε-PL oligomers in order to investigate molecular structure dependence on the

Downloaded by DUKE UNIV on June 21, 2012 | http://pubs.acs.org
Publication Date (Web): October 14, 2011 | doi: 10.1021/bk-2011-1077.ch019

degree of polymerization. Kushwaha *et al.*(*9*) reported the chemical synthesis of ε-PL and discussed the conformation of the polymer in aqueous solution, although Mn and Mw/Mn of the polymer were not determined. Based mainly on the pH dependence of CD spectra, they concluded that ε-PL took up an electrostatically expanded conformation due to repulsion of protonated α-amino groups at acidic pHs, whereas at basic pHs the conformation changed to something similar to an antiparallel β-sheet. The plots of the $[\theta]_{215}$ *versus* the pH values give sigmoidal curves for all the oligopeptides and the midpoints of the curves coincide with the reported p*K*a values of the α-amino groups (p*K*a=8.5). The spectral similarity between oligo(ε-L-lysine)and ε-PL suggests that the same conformational change occurs with a pH variation for both cases. As shown in Figure 2, the microbial ε-PL exhibited a similar pH dependence in the CD spectra as that reported by Kushwaha *et al.* (*9*).

The result suggests that a similar conformation change occurred in the microbially produced ε-PL with pH changes. We synthesized a series of monodispersed oligo(ε-L-lysine)mers (2-, 4-, 6-, and 8-mers). The pH variation study of the CD spectra suggested that the oligopeptides exhibited a β-sheet conformation in aqueous solution at a pH above the pKa of the α-amino group. The CD band intensity at 215 nm for the high pH solution was dependent on the number of lysine residues in the oligopeptides, indicating an increased interchromophore interaction in the higher oligopeptides. IR spectra measured in D_2O also supported the pH-induced conformational change for the oligopeptides and ε-PL (*14*).

Downloaded by DUKE UNIV on June 21, 2012 | http://pubs.acs.org
Publication Date (Web): October 14, 2011 | doi: 10.1021/bk-2011-1077.ch019

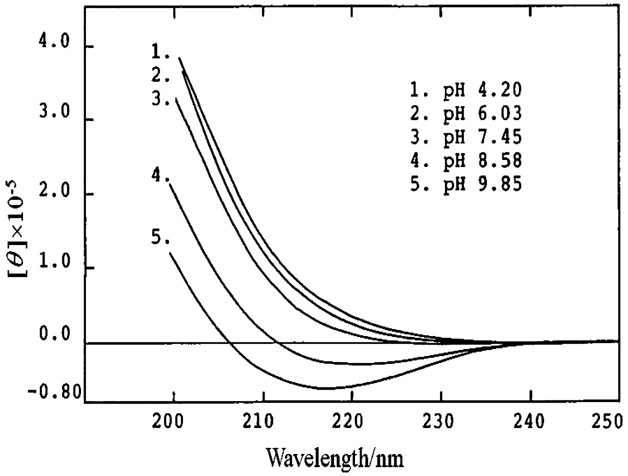

Figure 2. CD curves of ε-PL at various pH. (Reproduced with permission from reference (12). Copyright 1991 Kinki Chemical Society, Japan.)

Downloaded by DUKE UNIV on June 21, 2012 | http://pubs.acs.org
Publication Date (Web): October 14, 2011 | doi: 10.1021/bk-2011-1077.ch019

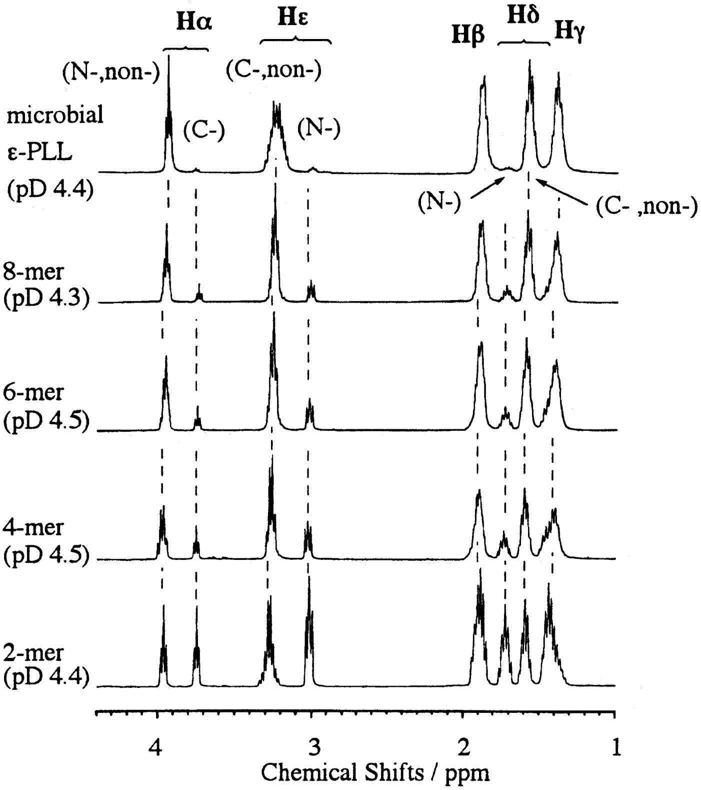

Figure 3. ^{1}H NMR of microbial and fractionated ε-PL in D_2O solution. (N-), (non-) and (C-) designate resonances of the N-, non- and C-terminal L-lysine residues, respectively. (Reproduced with permission from reference (13). Copyright 1993 Kinki Chemical Society, Japan.)

Another evidence for the conformational change comes from the pH titration of ^{1}H and ^{13}C NMR spectra. Figure 3 shows the ^{1}H NMR spectra of the oligomers together with that of microbial ε-PL. All the ^{1}H and ^{13}C resonances can be readily assigned using the off-diagonal peaks in the ^{1}H-^{1}H and ^{1}H-^{13}C COSY spectra: ^{1}H NMR (pD 6.4) δ=1.40(Hγ), 1.59(Hδ), 1.88 (Hβ), 3.25 (Hε), 3.93 (Hα); ^{13}C NMR (pD 6.4) δ=24.5 (Cγ), 30.7 (Cδ), 33.4 (Cβ), 41.9 (Cε), 56.0 (Cα), 172.6 (C=O). Figure 4 shows pD dependence of ^{1}H NMR resonances of the 8-mer. Other oligomers exhibit similar pH dependence. A characteristic feature of the spectra of ε-PL and the oligomers are the signals from N-, C- and non-terminal L-lysine residues. There is only one Hα(C-) per ε-PL molecule which is adjacent to the COOH moiety. This proton appears at slightly upfield position compared with Hα(N-, non-) which is adjacent to the amide linkage. Therefore, the ratio I[Hα (N-, non-)]/I[Hα(C-)] plus 1 should correspond to the degree of polymerization. The ratios of the signal intensities, not only I[Hα (N-, non-)]/I[Hα(C-)], but also I[Hε(C-, non-)]/I[Hε(N-)] and I[Hδ (C-, non-)]/I[Hδ(N-)] are correlated with the degree of polymerization of ε-PL. The p*K*a values of the ionizable groups

Downloaded by DUKE UNIV on June 21, 2012 | http://pubs.acs.org
Publication Date (Web): October 14, 2011 | doi: 10.1021/bk-2011-1077.ch019

can be estimated from these curves; $pKa(COOH)<3$, $pKa(C\alpha\text{-}NH_2)_{N\text{-},non\text{-}term.} \approx 8$, $pKa(C\alpha\text{-}NH_2)_{C\text{-}term.} \approx 10$, $pKa(C\varepsilon\text{-}NH_2)_{N\text{-}term.} > 11$. These results suggest that the dissociation state of the α-NH_2 groups plays an important role in the conformation of the polymer.

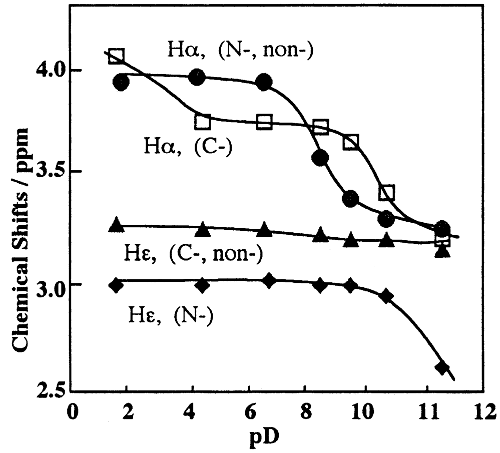

Figure 4. pD dependence of ^1H NMR resonances of 8-mer. (Reproduced with permission from reference (13). Copyright 1993 Kinki Chemical Society, Japan.)

The ^1H resonances of the Hα, Hβ and Hγ protons neighboring the ionizable α-amino group are sensitive to pH change of solution. They showed high-field shifts upon increasing the pD from 7.4 to 10.4. Similarly, ^{13}C resonances of the C=O and the Cβ carbons of ε-PL showed low-field shifts upon the same pD change. Both pD titration curves of ^1H and ^{13}C NMR spectra showed mid points at pD ca. 9.0. Furthermore, ^{13}C spin-lattice relaxation times (T_1) of all carbons rapidly decreased upon increasing the pD from 7.4 to 10.4: T_1 values (sec) at pD.7.4:Cα (0.51), Cβ (0.33), Cγ (0.37), Cδ(0.34), Cε(0.38), C=O (2.93); at pD10.4: Cα (0.42), Cβ (0.26), Cγ (0.29), Cδ (0.31), Cε (0.27), C=O (2.67). Saito and Smith studied the helix-coil transition of poly(α-L-lysine) hydrochloride in aqueous solution by ^{13}C NMR. They found that ^{13}C spin-lattice relaxation times T_1 of the carbonyl and the side-chain carbons decrease sharply at pD 10.2 which is the midpoint of the transition from the random-coil to the α-helix (*22*). The decreases in T_1 values can be interpreted in terms of a conformational change. The NMR results together with the CD data support the pH-induced conformational change when pH exceeds the pKa of α-amino groups.

Characterization of ε-PL in the Solid State

IR and Raman Measurements

ε-PL samples are highly fluorescent due to impurities, and Raman spectra obtained with visible excitation contain an enormous fluorescence background.

FT Raman spectra with near-IR excitation at 1,064 nm were measured in order to eliminate fluorescence problems (*23*). Figure 5 shows IR and FT Raman spectra of ε-PL. Typically α-polyamides exhibit vibrational bands characteristic of the secondary amide group. It is reasonable to assign the IR and Raman bands of ε-PL in comparison with α-polyamino acids. In the IR spectrum of ε-PL, the NH_2 asymmetric stretching is observed at 3382 cm^{-1}. The NH stretching band of the amide group usually appears as a doublet called amide A and amide B bands. These bands originate from Fermi resonance between the first overtone of amide II and the N-H stretching vibration and are observed at 3326 and 3081 cm^{-1}, respectively. Similar frequencies are obtained for the Raman spectra, although the amide B is unobserved. The low frequency $\nu_a(NH_2)$ and the amide A bands indicate that both the NH_2 and the amide NH groups are involved in intra/inter molecular hydrogen bondings. In general, the amide I, II and III modes for α-polypeptides are observed at 1680-1630 cm^{-1}, 1570-1510 cm^{-1} and 1300-1250 cm^{-1}, respectively (*24*). Since the amide bands are affected by the dipole-dipole interaction between neighboring amide groups, their frequencies and intensities are sensitive to the chain conformation (*25*). The amide I and II bands of ε-PL are observed at 1633 and 1534 cm^{-1}, both of which fall within the β-sheet conformation region. If we assume that the spectral region for α-peptides also holds for ω-peptides, ε-PL has a β-sheet conformation in the solid state. Nylon 6, structurally related to ε-PL, is known to assume alpha and gamma crystalline forms where the amide chains participate in the intermolecular hydrogen bonds in either antiparallel or parallel β-sheet form (*26*, *27*). Frequencies and intensities of the amide bands in ε-PL are quite similar to those of nylon 6. This spectral similarity also supports the β-sheet conformation for ε-PL.

Downloaded by DUKE UNIV on June 21, 2012 | http://pubs.acs.org
Publication Date (Web): October 14, 2011 | doi: 10.1021/bk-2011-1077.ch019

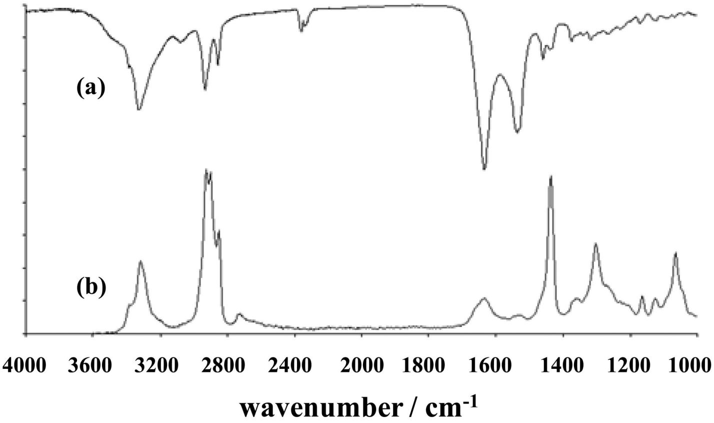

Figure 5. IR (a) and Raman (b) spectra of ε-PL. (Reproduced with permission from reference (16). Copyright 2003 Elsevier.)

Downloaded by DUKE UNIV on June 21, 2012 | http://pubs.acs.org
Publication Date (Web): October 14, 2011 | doi: 10.1021/bk-2011-1077.ch019

Solid-State ^{13}C NMR Measurements

^{13}C CPMAS NMR spectra of ε-PL are shown in Figure 6(a). Peaks are well resolved and assigned based on the ^{1}H-^{1}H COSY and the ^{1}H-^{13}C HETCOR measurements in solution. The chemical shifts and their assignments are summarized in Table 1. The reported data for nylon 6 are also listed.

Table 1. ^{13}C NMR chemical shifts (ppm) of ε-PL. (Reproduced with permission from reference (*16*). Copyright 2003 Elsevier.)

	ε-PL		*nylon 6*[a]	
carbon type	*in D_2O*	*in the solid*[b]	*α-form*	*γ-form*
C=O	180.0	178.6 177.1	173.4	173.0
Cα	57.0	57.9	36.7	37.8
Cβ	36.7	38.0	26.5	30.1
Cγ	25.0	27.9	30.4	30.1
Cδ	30.9	34.0 32.9	30.4	34.1
Cε	41.6	40.5	43.6	39.9

[a] Taken from ref. (*33*). [b] Peak maxima in the T1CP crystalline component discrimination experiment.

We have demonstrated through CD and NMR measurements (*14*) that the amide groups of ε-PL are involved in intermolecular hydrogen bonds with the amide groups of the neighboring molecules, and ε-PL assumes the β-sheet conformation in D_2O solution. Similarity in chemical shifts between the solution and solid ^{13}C NMR spectra implies that ε-PL also takes on the β-sheet conformation in the solid state. The C=O and the Cδ signals of the solid are observed as doublets in contrast with the solution spectrum, which may be attributed to the co-existence of the two crystal forms or the existence of the two magnetically inequivalent sites in the asymmetric cell. Hydrogen bonds between the amide groups in the β-sheet structure lead to down field shift of the C=O carbon signal. There appears to be a small peak at 164 ppm in Figure 6(a). Dos *et al.* found that amino groups of poly(α-L-lysine) can react with atmospheric CO_2 in aqueous and nonaqueous environments to give the carbamates and they assigned a peak at 164 ppm in ^{13}C spectrum to C=O carbon of carbamates (*28*).

Recently, we observed that amino groups of ε-PL also react with CO_2 in aqueous solution to give the carbamates. Detailed discussion will be published elsewhere.

In NMR Spectroscopy of Polymers: Innovative Strategies for Complex Macromolecules; Cheng, H., et al.;
ACS Symposium Series; American Chemical Society: Washington, DC, 2011.

Polymer Morphology of ε-PL

^{13}C spin-lattice relaxation time in the laboratory frame (T_1) can provide information about polymer morphology. The signal intensities of the respective carbon are plotted against the relaxation delay time τ in Figure 7. The decay curves were fitted to a biexponential function decay, $M_{01}\ \exp(-\tau/T_{11}) + M_{02}\ \exp(-\tau/T_{12})$. Table 2 summarizes the observed T_1 values.

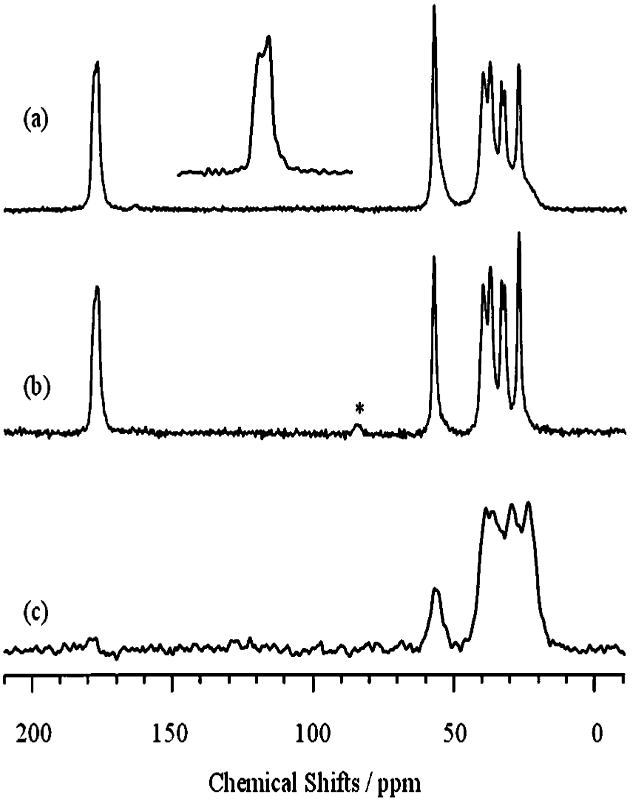

Figure 6. ^{13}C CPMAS NMR spectra of ε-PL. (a) normal spectrum, (b) crystalline component, and (c) amorphous component. Pulse sequences used are normal CPMAS for (a), T1CP with7 s delay time for (b), and saturation recovery with 200 ms delay time for (c). A peak marked with an asterisk is a spining side band. (Reproduced with permission from reference (16). Copyright 2003 Elsevier.)

Downloaded by DUKE UNIV on June 21, 2012 | http://pubs.acs.org
Publication Date (Web): October 14, 2011 | doi: 10.1021/bk-2011-1077.ch019

Downloaded by DUKE UNIV on June 21, 2012 | http://pubs.acs.org
Publication Date (Web): October 14, 2011 | doi: 10.1021/bk-2011-1077.ch019

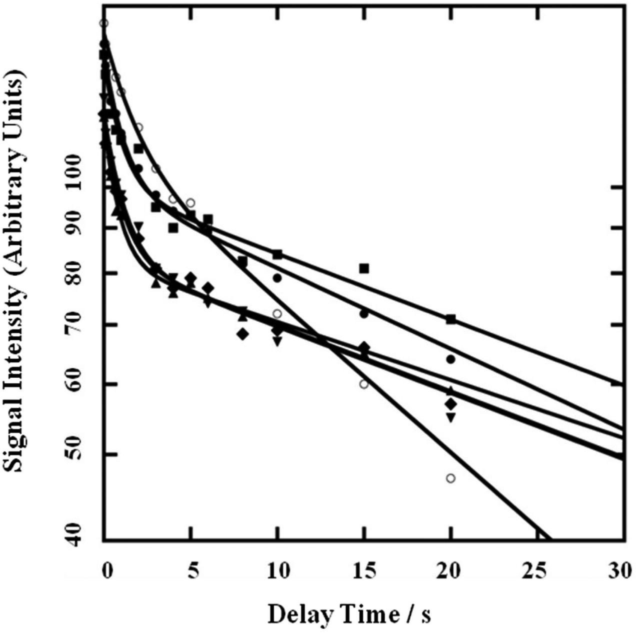

Figure 7. Plots of peak intensities versus delay times in the ^{13}C T1CP experiment for ε-PL. ○ Cα;● Cβ; ■ Cγ; ♦ Cδ (34.0 ppm); ▲ Cδ (32.9 ppm); ▼ Cε. (Reproduced with permission from reference (16). Copyright 2003 Elsevier.)

Table 2. ^{13}C spin-lattice relaxation time in the laboratory frame, T_1 (s) of ε-PL. (Reproduced with permission from reference (*16*). Copyright 2003 Elsevier.)

	carbon type					
Component	*α*	*β*	*γ*	*δ*		*ε*
amorphous	1.81	1.13	1.03	1.07	0.84	1.14
crystalline	25.4	48.8	57.6	57.8	66.1	59.1

Here, shorter relaxation times are those of the amorphous component and longer ones correspond to the crystalline component. The degree of crystallinity of ε-PL was estimated to be 63 % using fit parameters of the decay curve for Cα shown in Figure 7. By using the T1CP experiment with the delay time of 7 s and the saturation recovery experiment (*29*) with the delay time of 200 ms, signals from the crystalline and the amorphous components can be separately obtained as shown in Figure 6(b) and 6(c). The amorphous spectrum has much broader resonances than the crystalline spectrum. This is due to the heterogeneity of the molecular conformations in the amorphous components. Furthermore, chemical shifts of the amorphous component are observed upfield compared to the crystalline one. The upfield shifts and the broadening of the CH_2 resonances are explained by the conformational heterogeneity and the γ-gauche effects in the amorphous components. Recently, Asano *et al.* have investigated the crystallinity and the size of crystalline component of ε-PL in detail (*30*).

Chain Conformation of ε-PL

It is useful to compare the chain conformations of ε-PL and nylon 6. The stable α-form of nylon 6 has trans zigzag conformation, and intermolecular hydrogen bonds are formed in an anti-parallel sense. The less stable γ-form has intermolecular hydrogen bonds in a parallel sense. The principal structural difference between the α- and γ-forms is that the amide-to-methylene dihedral angles are nearly trans in the alpha and nearly perpendicular to the peptide plane in the γ-form. As previously noted, the amide groups of ε-PL are involved in intermolecular hydrogen bonds with those of the neighboring molecules and ε-PL assumes the β-sheet conformation in the solid state. As shown in Table 1, chemical shifts are significantly deshielded for the C=O, α- and β-carbons of ε-PL compared with those of nylon 6. These chemical shifts can be interpreted in terms of the substituent effects of α-NH_2 group. In contrast, the Cγ carbon of ε-PL is shielded due to the through space γ-gauche effect of the α-NH_2 group (*31*). Hydrogen bonds between the amide groups in the β-sheet structure lead to down field shift of the C=O carbon signal. The large down field displacement of the C=O of ε-PL may be due to a combination of the NH_2 substituent effect and the hydrogen bond effect. The chemical shift values of Cδ and Cε are similar and close to those of γ-form nylon 6.

A conformation model for ε-PL described on the basis of the γ-form of nylon 6 is shown in Figure 8. Sasaki *et al.* have carried out X-ray analysis of powder sample of ε-PL using linked-atom Rietveld simulation (*32*). Based on the preliminary simulation, they tentatively assigned the ε-PL chain conformation to the parallel β-sheet similar to the γ-form of nylon 6. Their assignment is consistent with the present solid state ^{13}C NMR results.

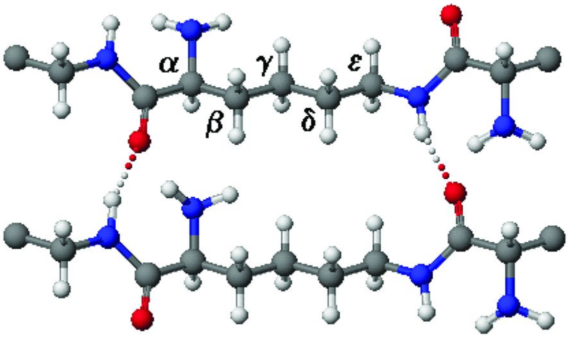

Figure 8. A conformation model of ε-PL based on the parallel β-sheet model of the gamma form of nylon 6. (Reproduced with permission from reference (16). Copyright 2003 Elsevier.)

Downloaded by DUKE UNIV on June 21, 2012 | http://pubs.acs.org
Publication Date (Web): October 14, 2011 | doi: 10.1021/bk-2011-1077.ch019

Downloaded by DUKE UNIV on June 21, 2012 | http://pubs.acs.org
Publication Date (Web): October 14, 2011 | doi: 10.1021/bk-2011-1077.ch019

Characterization of ε-PL Derivatives with Azo Dyes

Solid-State ^{13}C NMR Measurements of ε-PL Derivatives

Figure 9 shows the ^{13}C CPMAS NMR spectra of ε-PL and its azo dye derivatives. ^{13}C chemical shifts are summarized in Table 3 with those for ε-PL and ε-PL/HCl. The C=O carbon signal of ε-PL/HCl shifts to upfield about 6 ppm compared to that of ε-PL. Signals of other chain carbons, except Cγ, also show upfield shift. These chemical shift displacements are interpreted mainly as the substituent effect of the NH_3^+ group upon protonation.

The spectral pattern of ε-PL/MO in the aliphatic carbon region is similar to that of ε-PL/HCl. The Cε peak of ε-PL/MO and the *N*-methyl carbon signal of MO molecule overlap. The peaks in the 112-155 ppm region are due to the aromatic carbons of ε-PL/MO. The signals of the ε-PL/DC in the backbone CH_2 region (20-40ppm) are much less resolved. The broad and unresolved CH_2 peaks suggest that the conformational inhomogeneity of the CH_2 chain is due to the existence of bulky aromatic side chain groups. Since the aromatic carbon signals of ε-PL/MO and ε-PL/DC overlap one another, it is difficult to distinguish covalently bonded sulfonamide linkage from poly-ionic complex formation. An amine-labeling reagent (DC) is expected to be covalently bonded to α-amino group of ε-PL to make sulfonamide bond, (ε-PL)-NH-SO_2-(DC), whereas MO is expected to be negatively ionized to form ionic bond, (ε-PL)-$NH_3^+SO_3^-$-(MO).

Table 3. ^{13}C NMR chemical shifts of ε-PL and its derivatives in the solid state[a]. (Reproduced with permission from reference (*17*). Copyright 2005 Springer.)

sample	ε-PL						dye	
	ε-NHCO	Cα	Cβ	Cγ	Cδ	Cε	α-NHCO	-N(CH_3)$_2$
ε-PL[b]	178.6,177.1	57.0	36.7	25.0	30.9	41.6		
ε-PL/HCl	171.1	54.9	32.5	25.8	25.8	41.4		
ε-PL/Boc[c]	171.8	55.3	-	25.4	25.4	40.6	156.1	
ε-PL/MO[d]	172.2	55.1	33.8	23.1	28.0	40.5		40.5
ε-PL/DC[d]	171.9	57.7	20 - 40			40.5		40.5

a) In ppm with respect to tetramethylsilane.

b) From reference *(16)*.

c) A quaternary carbon signal of Boc appears at 79.4 ppm.

d)Aromatic carbon peaks of azo dyes appear in the region from 112 to 155 ppm.

Downloaded by DUKE UNIV on June 21, 2012 | http://pubs.acs.org
Publication Date (Web): October 14, 2011 | doi: 10.1021/bk-2011-1077.ch019

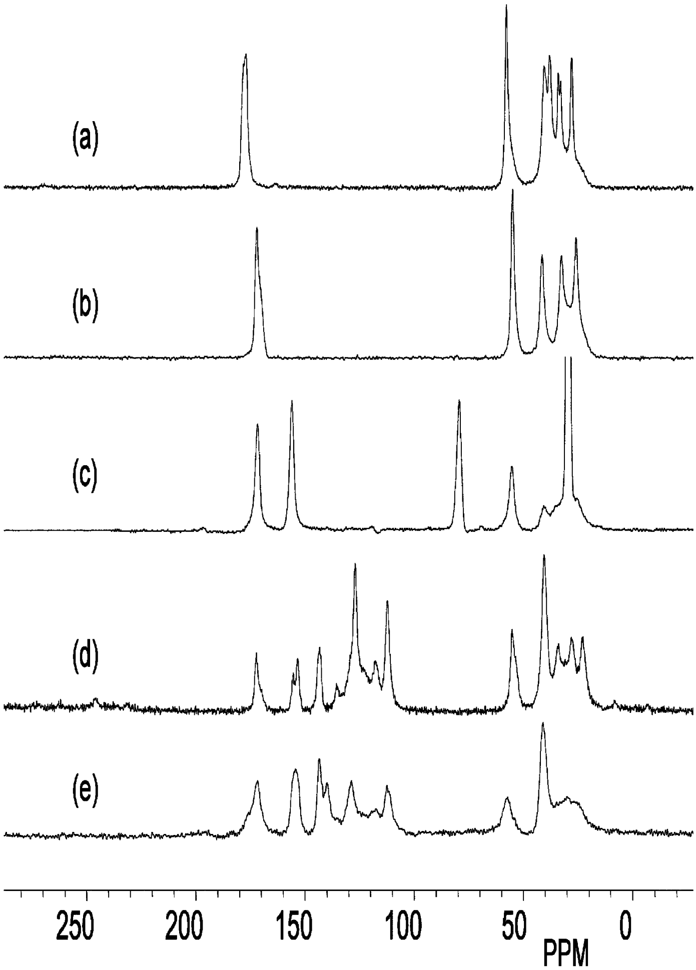

Figure 9. ^{13}C CPMAS NMR spectra of (a) ε-PL, (b) ε-PL/HCl, (c) ε-PL/BocC, (d) ε-PL/MO and (e) ε-PL/DC. (Reproduced with permission from reference (17). Copyright 2005 Springer.)

Solid-State ^{15}N NMR Measurements of ε-PL Derivatives

Figure 10 shows the ^{15}N CPMAS spectra of ε-PL and its azo dye derivatives (*17*). The chemical shifts and their assignments are summarized in Table 4. ε-PL exhibits two distinct ^{15}N peaks at 117 and 26.6 ppm. The former and the latter peaks are assigned to the main chain NHCO and the α-NH_2 groups in comparison with nylon 6 (*33*), and chitosan and chitin (*34–36*). In ε-PL/HCl, the NHCO and the α-NH_2 peaks are observed at 123 and 44 ppm, respectively. These downfield shifts are attributed to protonation of the α-amino group to form α-$NH_3^+Cl^-$ salt in ε-PL/HCl. Similar shift is observed in chitosan blend with poly(acrylic acid) where 2 % formic acid aqueous solution is used as a solvent (*34*, *35*). ε-PL/MO shows three ^{15}N peaks at 115, 34.1 and 59.9 ppm. A peak at 59.9 ppm is assigned to dimethyl amino nitrogen of the dye moiety (*37*, *38*). ^{15}N peaks at 115 and 34.1 are assigned to the main chain CONH and the α-NH_3^+ group, respectively. The ^{15}N chemical shift of the α-NH_3^+ is between those of ε-PL and ε-PL/HCl. Since analogous chemical shift is reported for chitosan/poly(acrylic acid) (*34*, *35*, *39*), the formation of poly-ion complex between ε-PL and MO, (ε-PL)-α-NH_3^+ SO_3^--(MO) is clearly indicated. The azo ^{15}N signals are expected around 510 ppm (*37*, *38*), but no such peaks are observed in this region. ε-PL/DC shows ^{15}N peaks at 121, 102, 61.6 ppm. A peak at 60.6 ppm is assigned to the dimethyl amino group. ^{15}N peaks at 121 and 102 ppm are assigned to the main chain CONH and the sulfonamide groups, suggesting the formation of the covalent (ε-PL)-α-$NHSO_2$-(DC) bond.

Downloaded by DUKE UNIV on June 21, 2012 | http://pubs.acs.org
Publication Date (Web): October 14, 2011 | doi: 10.1021/bk-2011-1077.ch019

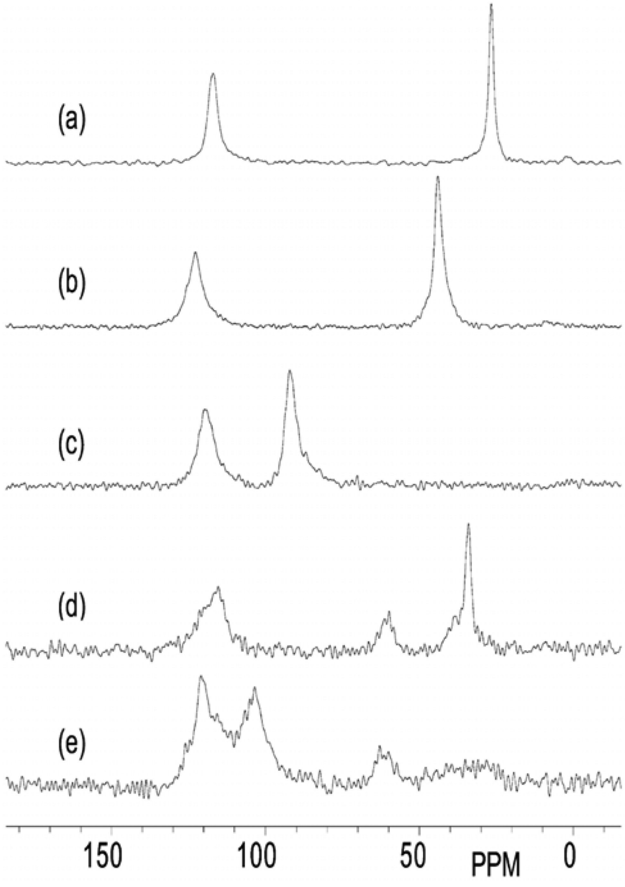

Figure 10. ^{15}N CPMAS NMR spectra of (a) ε-PL, (b) ε-PL/HCl, (c) ε-PL/Boc, (d) ε-PL/MO and (e) ε-PL/DC. (Reproduced with permission from reference (17). Copyright 2005 Springer.)

Table 4. ^{15}N NMR chemical shifts of ε-PL and its derivatives in the solid state[a]. (Reproduced with permission from reference (*17*). Copyright 2005 Springer.)

sample	*ε-NHCO*	*α-NHSO$_2$*	*α-NHCO*	*α-NH$_3^+$*		*α-NH$_2$*	*-N(CH$_3$)$_2$*
				free	*ion-complex*		
Nylon 6 [b]	116.5						
ε-PL	117					26.6	
ε-PL/HCl	123			44.0			
ε-PL/Boc	120		92.2				
ε-PL/MO	115				34.1		59.9
ε-PL/DC	121, 113	102			32.1		61.6
Chitosan [c]						21.2	
CS/PAA [d]					31.6		

[a] In ppm with respect to liquid NH_3 at 25°C. [b] α-crystalline form (*33*). [c] References (*34–36*). [d] Chitosan/poly(acrylic acid) (*34*, *35*, *39*).

A peak at about 32 ppm which corresponds to the α-NH_3^+ group implies that there exists a small amount of ε-PL/MO in ε-PL/DC. Curve fitting for the ε-PL/DC spectrum (Figure 11) reveals a peak at 113 ppm which can be assigned to a signal of main chain amide group, ε-$\underline{N}$HCO-CH(α-NH_3^+) (*40*). We conclude that the ε-PL/DC sample contains a small amount of ion complexes with MO.

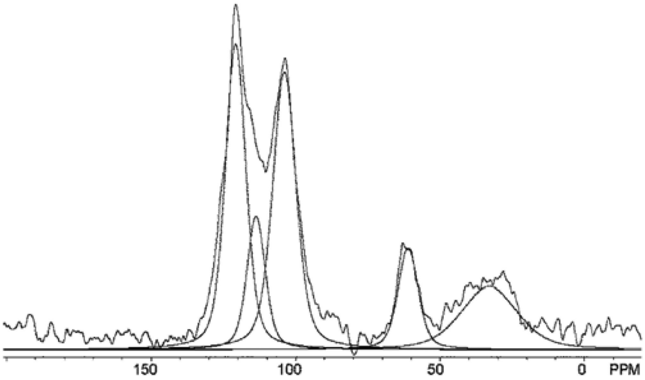

Figure 11. Curve fitting for ^{15}N NMR spectrum of ε-PL/DC. (Reproduced with permission from reference (17). Copyright 2005 Springer.)

Conclusion

In this work characterization of ε-PL was done by using various spectroscopic measurements, e.g., CD, IR, Raman, solution and solid NMR. The pH dependent

Downloaded by DUKE UNIV on June 21, 2012 | http://pubs.acs.org
Publication Date (Web): October 14, 2011 | doi: 10.1021/bk-2011-1077.ch019

IR and CD spectra indicated that ε-PL assumes a β-sheet conformation in aqueous solution, the content of which depends on chain length and pH. ^{13}C spin-lattice relaxation times for solid ε-PL were measured to yield two kinds of T_1s corresponding to the crystalline and amorphous components: the degree of crystallinity was estimated to be 63%. Solid ^{13}C NMR spectra of the crystalline and the amorphous components were observed separately. The amorphous components of the backbone give rise to higher field signals due to the γ-gauche effect. A conformation model for ε-PL was presented where the backbone amide groups participate in inter-chain hydrogen bonds similar to the γ-form nylon 6. The ε-PL derivatives with azo dyes were investigated by using solid ^{13}C and ^{15}N NMR. Side chain α-amino group of ε-PL does not make a covalent bond with methyl orange (MO) but forms poly-ionic complex, (ε-PL)-$NH_3^+SO_3^-$(MO). In comparison, dabsyl chloride (DC) makes covalent bond with ε-PL to form sulfonamide, (ε-PL)-NH-SO_2-(DC). A small amount of DC changes to MO by hydrolysis to form the poly-ion complex, (ε-PL)-NH_3^+ SO_3^- (MO).

Downloaded by DUKE UNIV on June 21, 2012 | http://pubs.acs.org
Publication Date (Web): October 14, 2011 | doi: 10.1021/bk-2011-1077.ch019

Acknowledgments

Microbial poly(ε-L-lysine) was kindly supplied by Chisso Corporation. The authors are grateful to Professors Akio Kuwae and Kazuhiko Hanai for their helpful and valuable cooperation through this work.

References

1. Griffith, L. G. *Acta Mater.* **2000**, *48*, 263–277.
2. Nair, L. S.; Laurencin, C. T. *Prog. Polym. Sci.* **2007**, *32*, 762–798.
3. Shih, I-L.; Shen, M-H.; Van, Y-T. *Bioresour. Technol.* **2006**, *97*, 1148–1159.
4. Oppermann-Sanio, F. B.; Steinbuchel, A. *Naturwissenschaften* **2002**, *89*, 11–22.
5. Shima, S.; Sakai, H. *Agric. Biol. Chem.* **1977**, *41*, 1807–1809.
6. Shima, S.; Sakai, H. *Agric. Biol. Chem.* **1981**, *45*, 2497–2502.
7. Shima, S.; Sakai, H. *Agric. Biol. Chem.* **1981**, *45*, 2503–2508.
8. Shima, S.; Fukuhara, Y.; Sakai, H. *Agric. Biol. Chem.* **1982**, *46*, 1917–1919.
9. Kushwaha, D. R. S.; Mathur, K. B.; Balasubramanian, D. *Biopolymers* **1980**, *19*, 219–229.
10. Ho, Y. T.; Ishizaki, S.; Tanaka, M. *Food Chem.* **2000**, *68*, 449–455.
11. Maeda, S.; Mori, T.; Kunimoto, K.-K.; Sasaki, C. *Kobunshi Kako* **2003**, *52*, 516–522(in Japanese).
12. Lee, H.-H.; Oyama, K.; Hiraki, J.; Hatakeyama, M.; Kurokawa, Y.; Morita, H. *Chem. Express* **1991**, *6*, 683–686.
13. Fukushi, H.; Oyama, K.; Hatakeyama, M.; Hiraki, J.; Fujimori, D.; Lee, H.-H. *Chem. Express* **1993**, *8*, 745–748.
14. Lee, H.-H.; Yamaguchi, H.; Fujimori, D.; Nishida, A.; Yamamoto, H. *Spectrosc. Lett.* **1995**, *28*, 177–190.
15. Sasaki, C.; Hamada, T.; Okumura, H.; Maeda, S.; Muranaka, J.; Kuwae, A.; Hanai, K.; Kunimoto, K.-K. *Polym. Bull.* **2006**, *57*, 747–756.

16. Maeda, S.; Kunimoto, K.-K.; Sasaki, C.; Kuwae, A.; Hanai, K. *J. Mol. Struct.* **2003**, *655*, 149–155.
17. Maeda, S.; Mori, T.; Sasaki, C.; Kunimoto, K.-K.; Kuwae, A.; Hanai, K. *Polym. Bull.* **2005**, *53*, 259–267.
18. Li, N.; Lu, J.; Xu, Q.; Wang, L. *Opt. Mater.* **2006**, *28*, 1412–1416.
19. Smitha, P.; Asha, S. K. *J. Phys. Chem. B* **2007**, *111*, 6364–6373.
20. Chang, J. Y.; Knecht, R.; Braun, D. G. *Methods Enzymol.* **1983**, *91*, 41–48.
21. Hiraki, J., Morita, H. Jpn Patent No. 61-192157, 1986.
22. Saito, J.; Smith, I. C. P. *Arch. Biochem. Biophys.* **1973**, *158*, 154.
23. Hendra, P., Jones, C., Warnes, G., Eds.; *Fourier Transform Raman Spectroscopy: Instrumentation and Chemical Applications*; Ellis Horwood: Chichester, U.K., 1991.
24. Baranska, H.; Labudzinska, A.; Terpinski, J. *Laser Raman Spectroscopy, Analytical Applications*; Ellis Horwood: Chichester, U.K., 1987.
25. Miyazawa, T.; Blout, E. R. *J. Am. Chem. Soc.* **1961**, *83*, 712–719.
26. Arimoto, H. *J. Polym. Sci., Part A-2* **1964**, 2283–2295.
27. Hendra, P. J.; Maddams, W. F.; Royaud, I. A. M.; Wills, H. A.; Zichy, V. *Spectrochim. Acta* **1990**, *46A*, 747–756.
28. Dos, A.; Schimming, V.; Tosoni, S.; Limbach, H.-H. *J. Phys. Chem.* ***B*** **2008**, *112*, 15604–15615.
29. Ernst, R. R.; Bodenhausen, G.; Wokaun, A. *Principles of Nuclear Magnetic Resonance in One and Two Dimensions*; Oxford University Press: Oxford, U.K., 1987.
30. Asano, A.; Tanaka, C.; Murata, Y. *Polymer* **2007**, *48*, 3809–3816.
31. Tonelli A. E. *NMR Spectroscopy and Polymer Microstructure: The Conformational Connection*; VCH: New York, 1989.
32. Sasaki, S.; Hishiyama, T.; Huh, K. M.; Ooya, T.; Yui, N. *Polym. Prep. Jpn.* **2001**, *50*, 2003.
33. Hatfield, G. R.; Glans, J. H.; Hammond, W. B. *Macromolecules* **1990**, *23*, 1654–1658.
34. Maeda, S; Ohshima, T.; Sakurai, K. *Proc. XVIIIth Int. Conference on Magn. Reson. Biological Systems* **1998**, 166.
35. Sakurai, K.; Ohshima, T.; Maeda, S. *Adv. Chitin Sci.* **1998**, 135–140.
36. Yu, G.; Morin, F. G.; Nobes, G. A. R.; Marchessault, R. H. *Macromolecules* **1999**, *32*, 518–520.
37. Levy G. C.; Lichter R. L. *Nitrogen-15 Nuclear Magnetic Resonance Spectroscopy*; John Wiley & Sons, Inc.: New York, 1979; Chapter 3.
38. Berger S.; Braun S.; Kalinowski H.-O. *NMR Spectroscopy of the Non-Metallic Elements*; Wiley & Sons, Inc.: Chichester, U.K., 1997; Chapter 4.
39. Nge, T. T.; Yamaguchi, M.; Hori, N.; Takemura, A.; Ono, H. *J. Appl. Polym. Sci.* **2002**, *83*, 1025–1035.
40. Maeda, S.; Mori, T.; Muto, K; Sasaki, C; Kunimoto, K.-K. *The 42th Annual Meeting Japanese NMR Soc.* **2003**, *1P34*, 188.

Downloaded by DUKE UNIV on June 21, 2012 | http://pubs.acs.org
Publication Date (Web): October 14, 2011 | doi: 10.1021/bk-2011-1077.ch019

Downloaded by STANFORD UNIV GREEN LIBR on June 20, 2012 | http://pubs.acs.org
Publication Date (Web): October 14, 2011 | doi: 10.1021/bk-2011-1077.ch020

Chapter 20

NMR, NIR, and Infrared Spectroscopy of Carbohydrate−Protein Interactions and Glycoproteins

I. C. Baianu* **and V. Prisecaru**

AFC-NMR & NIR Microspectroscopy Facility, College of ACES, FSHN and NPRE Departments, University of Illinois at Urbana, 350 Burnsides Research Laboratory, 1208 W. Pennsylvania Ave., Urbana, IL 61801
***E-mail: ibaianu@illinois.edu**

A review of selected data sets for carbohydrate−proteins interactions and glycoproteins is presented together with authors' results from nuclear magnetic resonance (NMR) and infrared (NIR and mid-IR) spectroscopy, as well as chemical imaging (micro-spectroscopy) experiments. Previous reports by X-ray, neutron and electron diffraction are also considered in this context, and are combined with high-resolution NMR spectroscopy and relaxation data for glycoproteins in solution and in biomembranes. High-resolution NMR and transverse relaxation results are then presented for wheat gliadin interactions with sucrose in aqueous solutions, as well as wheat gluten--glucomannan interactions in hydrated gels that are relevant to food physical chemistry and novel food formulations for products with increased stability and shelf-life. NMRI and FT-NIR microspectroscopy data are reported also for intact, hydrated seeds that contain proteins and carbohydrates as their major components.

Introduction

Protein−carbohydrate interactions are important for glycoprotein structure, dynamics and function. They play key roles in physiology, medicine, biochemistry and biophysical chemistry. Moreover, protein *glycosylation* is ubiquitous in living cells as a post-translational modification. Many proteins that play key structural

In NMR Spectroscopy of Polymers: Innovative Strategies for Complex Macromolecules; Cheng, H., et al.;
ACS Symposium Series; American Chemical Society: Washington, DC, 2011.

and functional biological roles are glycosylated; such cell-surface or extracellular glycoproteins are involved in immunity and cell-cell recognition (*1–3*). Protein glycosylation is also of great significance in pharmacology and medicine because more than one-third of the approved protein therapeutics are glycoproteins (*4*). Protein−carbohydrate interactions play important roles in protein stability and function, and are also involved in complex molecular and cellular processes such as cell adhesion and aggregation, oncogenesis and lectin biology. Thus, protein glycosylation is a structural variation of both biological/physiological and pharmaceutical importance because of its major effects on protein stability, cell adhesion and aggregation.

On the other hand, carbohydrate−protein interactions are also important in industrial applications and in several, related applied sciences such as food chemistry/food science, pharmacology and medicinal chemistry. In food chemistry they are important for several reasons, such as their role in determining food properties containing both proteins and carbohydrates, and the correct formulation and engineering of foods. In pharmacology and medicinal chemistry such interactions are important for the design of novel drugs with increased effectiveness and very high selectivity.

Protein residues, or side chains, can form a variety of non-covalent bonds with carbohydrates, and this may occur with different sugar interface propensity for different amino acid residues. Thus, hydrogen bonds may be formed between the hydroxyl groups of sugars and the charged R-groups of amino acid residues in a protein such as those of Asp, Glu, Lys, Arg and His. Another case is that of a hexose in a conformation in which several of its carbon atoms are in a cluster that allows for energetically favorable CH-π interactions to occur with the parallel aligned aromatic rings of Phe, Trp or Tyr (*5*, *6*), when the sugar and aromatic rings are within 0.4nm from each other. For example, CH-pi interactions can form between sugars and the aromatic amino acids Tyr296, Phe241, Phe243 on each of the two chains of the Fc antibody, whereas Phe243 forms an actual contact with GlcNAc as found from crystal structures of human IgG—Fc (*7*). The N-glycolsylation of the conserved residue Asn297 in an IgG antibody is an example of both types of such interactions.

The first step in carrying out detailed physicochemical studies of glycosylated proteins, and glycoconjugates in general, is their separation with a high degree of purity for elucidation of structure and function (*8*). Highly effective methods for the separation of naturally derived glycoconjugates are various forms of high-performance liquid chromatography (HPLC) that can also be effectively combined with their analysis by isoelectric focusing . On the other hand, structurally well-defined glycoconjugates can also be synthesized and then separated by HPLC.

Conformational studies of highly-purified, both natural and synthetic glycoconjugates can be then carried out on such highly purified fractions by high-resolution NMR, including various 2D-FT NMR techniques and/or triple resonance, $^{1}H \rightarrow {}^{13}C \rightarrow {}^{15}N$, or by FT-IR, including polarized spectroscopy. Such interesting studies were reported, for example, in the case of the human glycophorin ***A***, an important structural protein in the erythrocyte membrane (*9*, *10*).

Downloaded by STANFORD UNIV GREEN LIBR on June 20, 2012 | http://pubs.acs.org
Publication Date (Web): October 14, 2011 | doi: 10.1021/bk-2011-1077.ch020

Whereas NMR spectroscopy allows the elucidation of the 3D molecular structure in solutions, X-ray diffraction (XRD) - also combined sometimes with neutron diffraction and scattering techniques) - allows the determination of structure only in crystalline solids such as hydrated protein crystals. On the other hand, flexibility is essential to the physiological function(s) of many proteins (*11*), including glycoproteins. However, XRD cannot distinguish between structural and dynamic disorder (p.439 of Ch. 12 in ref. (*12*)), whereas NMR spectra and relaxation (*11*, *12*) are quite sensitive to both main-chain and side-chain dynamics (*13*, *14*). NMR spectroscopy has been employed to study the flexibility of both protein segments and domains; combined X-ray and resolution-enhanced NMR spectroscopy studies were also reported as in the case of the *lac*-repressor low-resolution structure (see Figure **XII-7** on p. 459 in (*12*)). Quantitative studies of internal motions in proteins are also possible by NMR relaxation (p. 465 in (*12*)); especially useful are ^{13}C T_1 measurements that were reported for resolved aromatic amino acid residues of proteins in aqueous electrolyte solutions (p.475, *loc. cit.* and (*14*)).

Both NMR and neutron techniques are also available for the study of isotope exchanges, such as the $^{1}H \rightarrow {}^{2}H$ *isotope exchange* of the amide protons in any protein peptide groups (p. 461 in ref. (*12*)), or the proton exchange of Tyrosine-OH, Threonine-OH, SerineOH and Cystine SH groups, or for liquid water protons in carbohydrate solutions or gels (*15*, *16*); the chemical exchange of protons between water molecules and proteins also affects the ^{17}O NMR relaxation of water (ref. (*17*) and references cited therein).

In the special case of a highly ordered array of bacteriorhodopsin molecules in the 'purple' membrane of *Halobacterium halobium* a high-resolution structural determination was reported from electron diffraction (ED) studies (*18*, *19*). However, this is not generally possible in either bacterial or mammalian cell membranes, unless highly-ordered membrane arrays can be formed, and also if the proteins themselves preserve a definite orientation relative to the membrane surfaces; this was indeed observed for oriented arrays of both human and porcine erythrocyte membranes that had a lamellar periodicity of 12.1 nm, as determined from the XRD low-angle patterns in the fully hydrated state (*20*). In such oriented membrane systems, the glycophorin *A* dimers exhibited discrete, sharp X-ray reflections (Figure 1) corresponding to an orientation of glycophorin *A* chains normal to the erythrocyte membrane surface, as shown in *Figure 78c* on page 191 for porcine red cell membrane arrays, and in *Figure 81b* on page 197 for human erythrocyte membranes in ref. (*20*).

The transmembrane helix of glycophorin A contains a seven-hydrophobic residue motif, **LIxxGVxxGVxxT**, that was proposed to mediate protein dimerization (*9*). Then, magic angle spinning (MAS) NMR allowed the determination of the helix-to-helix contacts in the glycophorin ***A*** transmembrane domain by showing that the methyl groups of Val-80 and Val-84 are close-packed, respectively, with the Gly-79 and Gly-83 (*10*). On the other hand, threonines and serines are the most common polar residues found in the transmembrane domains of proteins such as glycophorin ***A*** because they are able to readily to form hydrogen bonds back to the carbonyls on the same helix. Polarized Fourier transform infrared spectroscopy was employed to study the orientation

Downloaded by STANFORD UNIV GREEN LIBR on June 20, 2012 | http://pubs.acs.org
Publication Date (Web): October 14, 2011 | doi: 10.1021/bk-2011-1077.ch020

of glycophorin *A* in reconstituted membranes and the analysis of the dichroic ration of the 1655 cm^{-1} amide I vibration band yielded a value of 35° for the helix crossing angle (*9*) for the transmembrane orientation. Rotational-echo double-resonance (NMR) measurements also showed the close packing of the Thr-87 γ-methyl group with the backbone nitrogen of Ile-88 across the dimer interface, at ~0.4nm distance; such a short inter-helical distance makes it possible for the β-hydroxyl of Thr-87 to hydrogen-bond to the backbone carbonyl of Val-84 on the opposing glycophorin *A* transmembrane helix (*9*, *21*).

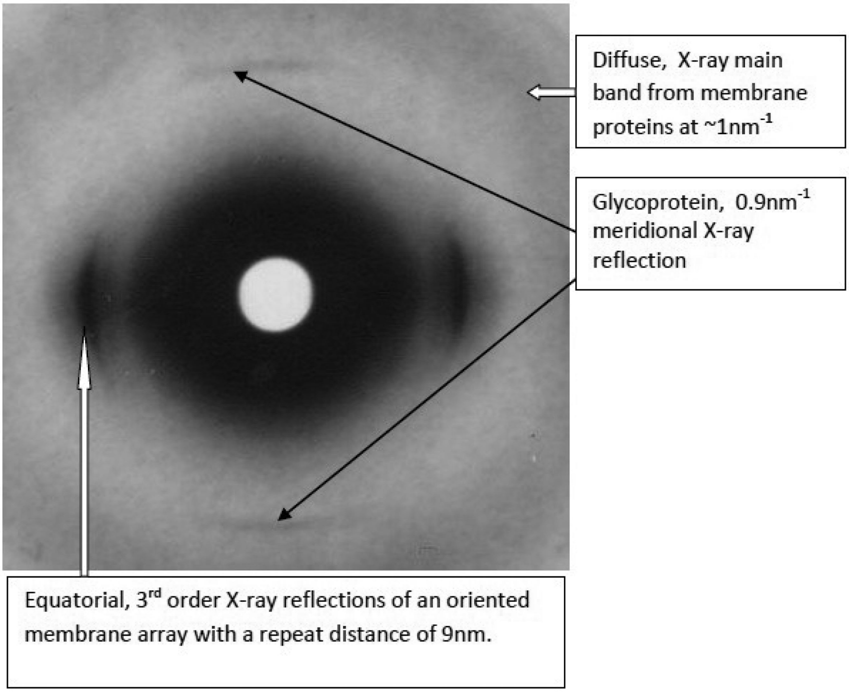

*Figure 1. XRD pattern of oriented, human erythrocyte membrane arrays showing meridional **0.9 nm^{-1}** X-ray reflection of glycophorin **A** chains oriented normally to the membrane surface (20), corresponding to a repeat distance of ~1.2 nm along the transmembrane helix axis of human glycophorin.*

In this concise review, several NMR and NIR/mid-IR results are also presented that are pertinent to practical applications in the formulation of novel food formulations with proteins and complex polysaccharides as major components.

Our results are also relevant to several other industrial applications such as wheat grain conditioning, soybean processing and corn milling, as well as biomedical and biotechnology applications, such as the early detection/ prevention

Downloaded by STANFORD UNIV GREEN LIBR on June 20, 2012 | http://pubs.acs.org
Publication Date (Web): October 14, 2011 | doi: 10.1021/bk-2011-1077.ch020

of disease, and the development of novel, individualized therapies with highly effective and selective medicines or vaccines.

Experimental Section

Materials and Measurements

Analytical grade sucrose was a product of ER Industries, Inc, (Addison, IL 60101). Analytical grade fructose was a gift from General Mills Inc. (Minneapolis, MN). Amylopectin purified from corn starch was obtained from Sigma Chemical Co. (St. Louis, MO). Amaizo Polar Gel 5 and Fro-Dex-55L were gifts from the American Maize Products Co. (Hammomd, IN). Moisture contents of fructose, glucose and sucrose samples were determined in triplicate by a vacuum oven method to be less than 0.2%.

^{1}H NMRI microscopy was carried out at 17MHz with a laboratory-built instrument (Taylor and Baianu, 1978:(*23*)) .

^{1}H NMR relaxation measurements were carried out in triplicate at 10MHz on a PC-10, and also on a PC-20 Multispec NMR relaxometer (Bruker- IBM Instr., Danbury, CT). The inversion recovery sequence, 180^o- τ- 90^o, was employed for T_1 measurements of aqueous solutions, gels and hydrated solids. The Carr-Purcell multi-pulse sequence was employed with the Meiboom-Gill modification (CPMG) for transverse relaxation times, T_2, measurements in solutions and hydrated gels. For low moisture solid proteins, small carbohydrates, polysaccharides and gels the multi-pulse Ostroff-Waugh (O-W) NMR pulse sequence was employed for recording spin-echo spectra with up to 10,000 pulses in the O-W sequence, as further detailed in (*22*, *29*).

^{1}H NMR high-resolution spectra for protein and carbohydrate solutions in D_2O were recorded in a 1mm capillary on a Varian UNITY-500 spectrometer operating at 500MHz as detailed in ref. (*23*).

^{13}C NMR spectra were recorded at 125MHz on a GE 500 spectrometer with multi-pulse proton decoupling at 500MHz using WALTZ and WAHUHA pulse sequences in the decoupling channel.

^{17}O and ^{2}H NMR measurements were carried out with a Bruker multi-nuclear CXP-200 spectrometer operating with a 98mm bore magnet at 4.7 Tesla (*23*). Other NMR techniques employed were as specified in (*24*).

FT-NIR spectra of glycoproteins, carbohydrates and intact, fully hydrated whole soybean seeds were recorded with a Perkin-Elmer spectrometer model SpectrumOne NTS (soybean seeds moisture contents were varied between 6 and 24% by dry weight). FT-NIR chemical/hyperspectral images were recorded with the same spectrometer attached to the NIR Microspectroscopy AutoImage system which was optimized for 1 micron spatial resolution and nanogram sensitivity. High-resolution FT-NIR images of selected sample areas of 4 mm^2 were recorded under PC control in less than 1 hour.

Downloaded by STANFORD UNIV GREEN LIBR on June 20, 2012 | http://pubs.acs.org
Publication Date (Web): October 14, 2011 | doi: 10.1021/bk-2011-1077.ch020

Downloaded by STANFORD UNIV GREEN LIBR on June 20, 2012 | http://pubs.acs.org
Publication Date (Web): October 14, 2011 | doi: 10.1021/bk-2011-1077.ch020

Results and Discussion

NMR Spectroscopy and Relaxation Studies of Carbohydrate−Protein Interactions

Wheat Gliadin Interactions with Sucrose in Acidic Aqueous Solutions

Wheat storage proteins are of prime importance to the US food industry because of their use in large amounts for making human foods. Such proteins, not unlike membrane proteins have a high proportion of hydrophobic amino acid residues and are not soluble in water at neutral phi A relatively small fraction of wheat proteins—the gliadins, is soluble at pH values lower than about 3.5. The ^{13}C NMR spectra of wheat gliadins in solution are compared in Figure 2 with those of corn zeins in a similar solvent mixture, and both were recorded at room temperature. The observed ^{13}C NMR peaks of wheat gliadins are overall considerably sharper than those of corn zeins even though the average molecular weights of such two selected samples of cereal proteins are very close - 35,000 for wheat gliadins vs. 32,000 for the corn zeins. The higher mobility of the aromatic amino acid residues of wheat gliadins in comparison with those of corn zeins, which is reflected in the sharper peaks in the spectral range from 100 to 150 ppm, for example, is suggestive of either more compact, folded structures of corn zeins than those of wheat gliadins or a significant degree of corn zein aggregation in solution even at low zein concentrations. A similar observation regarding the sharpness of the ^{13}C NMR peaks holds for the aliphatic and carbonyl and carboxyl regions in Figure 2. Specific assignments of the resolved ^{13}C peaks were previously reported (*36*, *37*) for 21 amino acid residues although considerable overlap did occur between the resonance peaks arising from several amino acid residue groups.

Their hydration behavior and weak interactions with small carbohydrate molecules was investigated by ^{1}H NMR transverse relaxation measurements at low magnetic fields in the presence of a Mn^{+2} paramagnetic ion probe. Both atlow (<1.4 T) and high magnetic fields (> 4.69 T) the water proton transverse magnetization decay of wheat gliadin solutions with/without carbohydrates was a single exponential up to 5mM gliadin concentrations at pH 3.4. At low concentrations of the paramagnetic ion probe, e.g. < 0.6 mM as in ref. (*22*), one can therefore assume a *fast-exchange model* with bulk water for the bound water protons surrounding the Mn^{+2} ion probe which is attached to the wheat gliadin negatively charged surface residues, Glu and Asp, in solution at pH 3.2. With this model, one can derive a slow correlation time τ_s for isotropic tumbling of water bound to such divalent cations of ~18 ns, consistent with the calculated value from the tumbling rate of globular wheat gliadins of an average molecular weight of 37,000 using the Stokes-Einstein equation, as explained on p. 475 in (*12*). Moreover, the sucrose concentration dependence of the 10 MHz relaxation rate of water protons in 3 mM gliadin solutions in the presence of a constant concentration of 0.5 mm Mn^{+2} exhibited a linear decrease with sucrose up to 0.4 M sucrose, as shown in *Figure 8* on p. 372 in (*22*). A nonlinear regression analysis of such data was carried out with a thermodynamic linkage model that yields the coefficients of non-ideal protein-protein interactions that indicate attraction rather than repelling between the wheat gliadin and sucrose molecules in solution, whereas the second order virial coefficient of gliadin-gliadin interactions in these solutions are characteristic of repulsion between the protein molecules. Such observations can be also considered as evidence for *a preferential hydration* of wheat gliadins in the presence of sucrose (*25*). In other words, there is a carbohydrate competition for water with the residues present in the protein hydration domain, as proposed by Arakawa and Timasheff in ref. (*25*). Moreover, using a spin probe, Pearce et al. found that spin label binding to wheat gliadins in solution decreased significantly upon heating (*26*). After heating to 50 ° C, and then cooling to 20 ° C, the ^{13}C NMR peaks of wheat gliadins in solution were significantly sharper than those before heating suggesting a partial, irreversible denaturation through loss of hydrogen bonds (*37*).

Downloaded by STANFORD UNIV GREEN LIBR on June 20, 2012 | http://pubs.acs.org
Publication Date (Web): October 14, 2011 | doi: 10.1021/bk-2011-1077.ch020

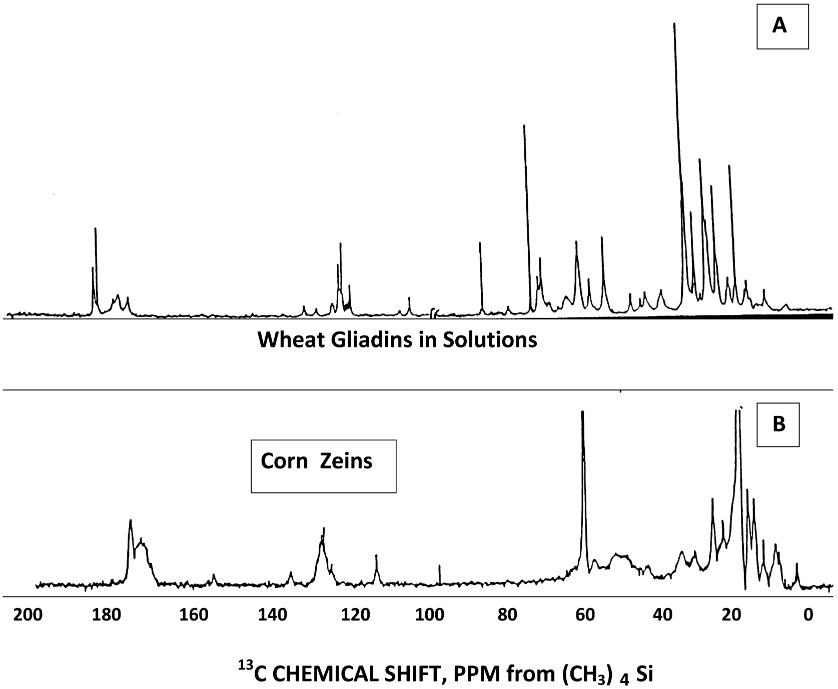

Figure 2. Multi-pulse, proton decoupled ^{13}C NMR spectra of cereal proteins recorded at 125 MHz with a GE500 spectrometer: ***A****. Wheat gliadins, and* ***B****. Corn zeins in aqueous solutions at pD 3.4.*

Proton broadband decoupled ^{13}C NMR spectra were previously reported both for wheat gluten ((*23*) and references cited therein) and various polysaccharides from wheat (*23*), or other plant sources ((*27–30*), and references cited therein). ^{13}C chemical shift assignments were made for wheat gluten CP-MAS spectra by comparison with those of wheat gliadins in acidic aqueous solutions at pD 3.4 (*23*). In the interesting, but very complex, case of branched glucomannan polysaccharides (GP) purified from *Amorphophalus konjac K. Kock* tuber powders, partial ^{13}C NMR chemical shift assignments were made by comparison with glucomannan oligosaccharides derived from GP by partial hydrolysis (*27*, *28*). Such GP carbohydrates that are relatively hydrophobic form very readily gels at GP concentrations in water as low as 0.1%, which become quite firm or rigid at GP concentrations higher than ~ 2%. In spite of the complexity of both GP and wheat gluten, their mixture in a system of two partially hydrated, branched hydrophobic materials-- which independently form stable gels-- may have considerable potential for increasing the shelf-life of wheat bread by the addition of as little as 0.1% GP to the hydrated gluten. The FT-NIR spectra of very low moisture GP's were quite similar to those of carbohydrates in the soybean seed (Figure 3) with the exception of several relatively sharp bands below 5,500 cm^{-1} that are present only in the GP spectra; such sharp NIR bands may correspond to a crystalline fraction of GP's that has been also detected previously by XRD studies of GP films (as described in previous studies cited in (*27*)). ^{1}H NMR transverse relaxation data with varying GP concentration in wheat gluten gels were previously interpreted in terms of the formation of cross-linked GP gels with the cross-links or junctions being formed with divalent cations such as Ca^{+2}. Such studies could also be carried with the Mn^{+2} ion probe in a manner similar to the experiments described in the previous section with wheat gliadins interacting with sucrose in aqueous solutions. As in the case of wheat gliadin solutions it was found from low-field ^{1}H NMR transverse relaxation measurements that water protons exchange rapidly between the water bound to GP in gels and bulk water trapped in the GP gel. One can therefore predict that in the hydrated wheat gluten--GP gel system doped with low concentrations of the paramagnetic Mn^{+2} ion probe one would observe a marked increase in the transverse relaxation rates of water protons as the concentration of GP is increased and becomes cross-linked, thereby resulting in tough, rubber-like, textured gels. Further ^{13}C NMR observations carried out in parallel with such ^{1}H NMR transverse relaxation studies may also allow one to identify the cross-linking sites in GP—wheat gluten gels.

On the other hand, in soybean protein gels cross-linking occur more frequently than in the case of wheat gluten--GP gels and additional ionic interactions are also present. In spite of the high molecular weights of the soy proteins one notes in the WALTZ ^{1}H-decoupled ^{13}C NMR spectra of such gels highly resolved peaks throughout the entire spectrum (Figure 3). Thus, relatively rapid molecular motions of the amino acid residues are occurring in the highly hydrated soybean protein gels whose high resolution ^{13}C NMR spectra are shown in Figure 3.

Downloaded by STANFORD UNIV GREEN LIBR on June 20, 2012 | http://pubs.acs.org
Publication Date (Web): October 14, 2011 | doi: 10.1021/bk-2011-1077.ch020

Downloaded by STANFORD UNIV GREEN LIBR on June 20, 2012 | http://pubs.acs.org
Publication Date (Web): October 14, 2011 | doi: 10.1021/bk-2011-1077.ch020

In Vivo Microscopy and Microspectroscopy of Proteins and Carbohydrates in Complex Hydrated Systems

NMR Imaging and Relaxation of Hydrated Wheat Grains

One of the earliest *in vivo* microscopic images reported for wheat proteins, polysaccharides, starch, water and oils was obtained with 50 micron resolution in hydrated wheat grains by ^{1}H NMRI at 17 MHz in 1978 (*22*, *23*); at the time, the spatial resolution was mostly limited by the available computer FFT/imaging speed and digitization capabilities. However, T_1 --contrast enhancement allowed the specific visualization of germ oil in the intact, fully hydrated wheat grain (*22*, *23*). For higher ^{1}H resonance frequencies in the higher magnetic fields currently available, it has been hypothesized that the spatial image resolution obtainable by 2D-FT NMRI might be on the order of 1 to 5 microns, and does obviously depend on the size of the imaged object. However, technological NMR advances may very well push even further this spatial resolution limit of NMRI microscopy, as it has already happened with FT-NIR hyperspectral imaging (*29*); an example of such recent developments is presented next.

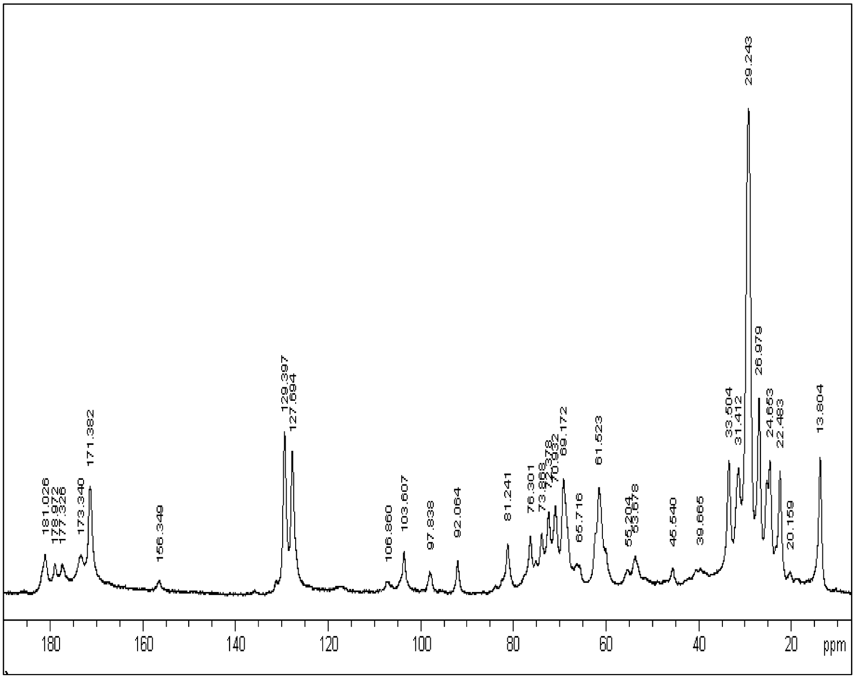

Figure 3. WALTZ-16 ^{1}H Decoupled ^{13}C Liquid-State NMR of a soy flour gel sample of 38.7% protein content. Spectrum recorded with 10,000 transients on a Varian UI600 NMR spectrometer, in a 14.1T external magnetic field. (Source: ref. (38).)

Downloaded by STANFORD UNIV GREEN LIBR on June 20, 2012 | http://pubs.acs.org
Publication Date (Web): October 14, 2011 | doi: 10.1021/bk-2011-1077.ch020

Even though the spectral resolution in FT-NIR spectra of proteins and carbohydrates is quite limited as a result of overlapping NIR bands from these components it is possible to quantitate these components in hydrated complex systems, such as wheat grains or whole soybean seeds and embryos. Moreover, unlike the case of FT-IR, the presence of thick samples and high levels of either water or oils does not prevent the investigation of proteins and carbohydrates in intact hydrated seeds. An example is presented here in Figure 4 for intact whole soybeans at hydration levels as high as 16% (by dry weight), even though such studies can be carried out even at higher hydration levels with appropriate multiple scattering and reflectivity corrections. Furthermore, the NIR sensitivity is sufficiently high to carry out both micro-spectroscopic and microimaging studies with state-of-the-art instrumentation.

FT-IR Chemical Imaging can be carried out with very high sensitivity but is limited in spatial resolution primarily because of the longer wavelength and focal-point-array (FPA) detector design limitations. An example was presented in *Figure 2.1.14* of ref (*29*) for the *in vivo* detection of protein bodies (Figure 5) in fully hydrated somatic soybean embryos grown in culture from single cells (*29*). On the other hand, FT-NIR hyperspectral imaging has lower sensitivity than the FT-IR microspectroscopy but is capable of ten times higher spatial resolution in hyperspectral images and does not have the FPA detector design limitations of the FT-IR microspectrometers. The latest developments discussed in ref. (*29*) indicate that the sensitivity range of FT-NIR microspectroscopy observations can be extended to the *femtogram* level, with submicron spatial resolution. Such FT-NIR/IR microspectroscopy instrumentation developments are potentially very important for agricultural and food biotechnology-as well as biomedical and pharmacological applications-- that require rapid and sensitive analyses, such as the screening of high-content microarrays in Genomics and Proteomics research.

Novel, two-photon NIR excitation fluorescence correlation microspectroscopy results were obtained with submicron resolution for concentrated suspensions of plant cells and membranes. With advanced super-resolution microscopy designs, a further, tenfold resolution increase is attainable, at least in principle, along the optical (**z**) axis of the microspectrometer. Especially promising are current developments that employ multi-photon NIR excitation which could lead, for example, to novel cancer prevention methodology and the early detection of cancers using NIR-excited fluorescence. Other related developments are the applications of Fluorescence Cross-Correlation Spectroscopy (FCCS) detection to monitoring DNA hybridization kinetics, DNA binding and ligand-receptor interactions--such as glycoprotein recognition of individual receptors on cell surfaces (*31*, *33*), as well as HIV, or HBV (viral) single--particle detection (*29*, *30*) and potential treatments for Alzheimer's disease (*32*, *33*).

Downloaded by STANFORD UNIV GREEN LIBR on June 20, 2012 | http://pubs.acs.org
Publication Date (Web): October 14, 2011 | doi: 10.1021/bk-2011-1077.ch020

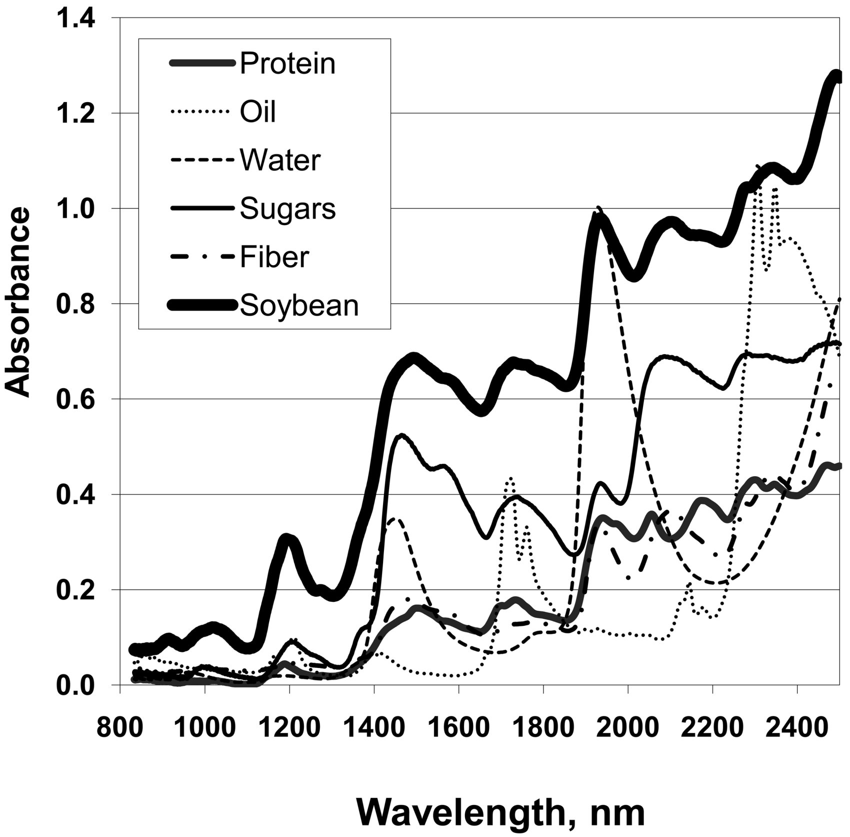

Figure 4. FT-NIR spectroscopy of the soybean major components, including protein, soluble and insoluble carbohydrates (fiber), water, and oils.

Molecular Interactions and Solute Activity Determination from NMR Relaxation Measurements on Hydrated Proteins, Carbohydrates, and Protein−Carbohydrate Systems

In a ternary system such as proteins, carbohydrates and water, one has to consider protein−water, protein−protein, protein−carbohydrate, as well as carbohydrate−water and carbohydrate−carbohydrate interactions. For solutions the problem is readily solved, at least in principle, by an equilibrium thermodynamic approach in terms of solute and solvent activitities by employing

Downloaded by STANFORD UNIV GREEN LIBR on June 20, 2012 | http://pubs.acs.org
Publication Date (Web): October 14, 2011 | doi: 10.1021/bk-2011-1077.ch020

the well-known Gibbs-Duhem equation. On the one hand, there are several experimental approaches to determining water activity for both solutions and crystalline solids. On the other hand, the determination of protein-protein interactions or protein activity in solutions, as well as protein−carbohydrate interactions has been traditionally difficult to measure except for solutions at very low concentrations. The approach presented above in Sections **II**.a and **II**.b by employing NMR relaxation measurements for water nuclei in concentrated protein solutions has allowed the quantitative determination of the virial coefficients of protein activity in such aqueous solutions, as well as in hydrated gels. This was possible for small proteins---such as lysozyme (*17*), corn zeins (*22*) and caseins—and for very large proteins, such as soy glycinins (*14*) and intact myosin (*22*). The most reliable protein activity determinations were made from water ^{17}O NMR measurements in protein solutions with or without added salt; the addition of salt ions to protein solutions has marked effects on ^{17}O, ^{2}H and ^{1}H NMR transverse relaxation rates of water that vary in a strongly nonlinear manner with the concentration of salt added to solutions of the same protein concentration, for salts such as NaCl, NaBr, KCl, KBr, LiCl or ammonium sulfate. As expected from the thermodynamic theory of solutions, the protein virial coefficients determined from the protein concentration dependence of water ^{17}O NMR are also dependent upon the type of both the added cation and anion, following the lyotropic series (*22*). A thermodynamic linkage approach also becomes necessary for the correct treatment of protein solutions in water with added salt ions (*34*). This approach has also been tested for amino acids in aqueous solutions with or without added salt, and in the case of carbohydrates the prerequisite NMR relaxation studies were carried out for several polysaccharides of practical importance (*15*, *16*, *22*). Although, protein−carbohydrate interactions can be investigated by NMR relaxation measurements even in complex systems, such as those discussed above in **Section II.b,** and in the next section**,** the question of the direct determination of protein and carbohydrate activities in such complex ternary systems remains a difficult one unless coupled with a thermodynamic linkage approach (*34*), as well as a careful consideration of irreversible systems that are far from equilibrium (*35*). However, it would be possible to estimate the sum of protein and carbohydrate activities in such ternary systems by subtracting the measured water activity, in accordance with the Gibbs-Duhem equation. For solid gels and powders of non-crystalline, or glassy, protein and protein−carbohydrate systems the equilibrium thermodynamics approach is no longer valid and alternate, nonequilibrium thermodynamic models are currently being investigated, as indicated above.

Conclusions

The study of protein−carbohydrate interactions and glycoproteins has significant potential for both biological and practical applications, such as the development of foods with improved shelf-life, better pharmaceuticals and ‘nutraceuticals’.

Downloaded by STANFORD UNIV GREEN LIBR on June 20, 2012 | http://pubs.acs.org
Publication Date (Web): October 14, 2011 | doi: 10.1021/bk-2011-1077.ch020

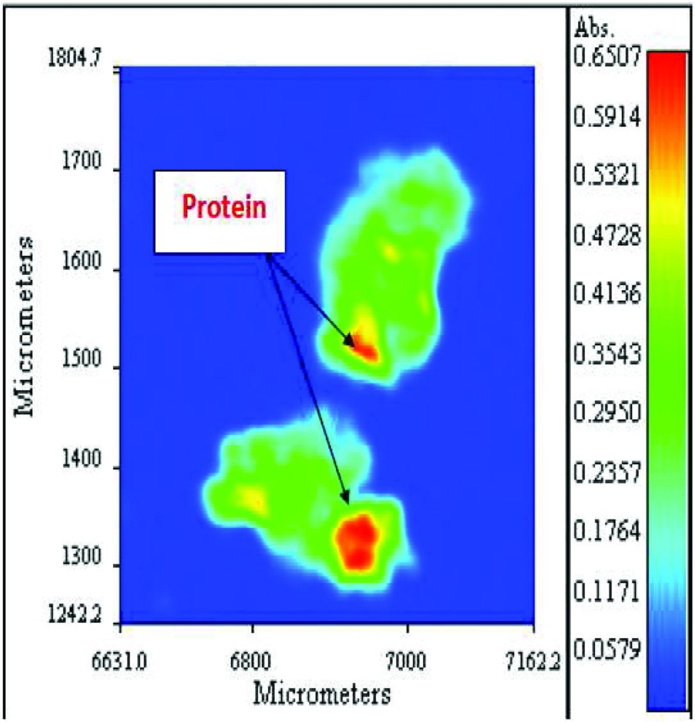

Figure 5. Transmission FT-IR Chemical Image of a fully hydrated, live soybean somatic embryo (i.e., cloned): shown in red is the high intensity (~0.65) of the protein amide II absorption band. The image was recorded in 20 minutes with a spectral IR resolution of 0.2 cm^{-1}*, and a spatial image resolution of ~10 µm. (Image adapted from ref. (29).)*

A wide range of NMR techniques, when combined with FT-NIR/IR, CCS, XRD and neutron scattering offer very substantial advantages for physico-chemical studies of important protein–carbohydrate interactions both *in vitro* and *in vivo*.

Some of the expected novel therapeutics may include safer biomaterials and also highly-selective and effective, non-toxic drugs (*31*) or drug-delivery systems.

Acknowledgments

The first author would like to thank the various researchers who contributed through fruitful discussions to this work, including: Dr. David G. Taylor of the University of Surrey, Dr. Eiichi M. Ozu of the University of Osaka, Japan, Dr. M. Balyuzzi and Prof. Ronald E. Burge, F.Inst.P. of the Cavendish Laboratory at the University of Cambridge, U.K.

The partial financial support for this research by Renessen Co. is gratefully acknowledged.

References

1. Arnold, J. N.; Wormald, M. R.; Sim, R. B.; Rudd, P. M.; Dwek, R. A. The impact of glycosylation on the biological function and structure of human immunoglobulins. *Annu, Rev. Immunol.* **2007**, *25*, 21–50.
2. Kaneko, Y.; Nimmerjahn, F.; Ravetch, J. V. Anti-inflammatory activity of immunoglobulin G resulting from **Fc** sialylation. *Science* **2006**, *313*, 670–673.
3. Bucior, I.; et al. Carbohydrate-carbohydrate interaction provides adhesion force and specificity for cellular recognition. *J. Cell Biol.* **2004**, *165*, 529–537.
4. Lee, J. C. Biochemistry of carbohydrate-protein interaction—Review. *FASEB J.* **1992**, *6*, 3193–3200.
5. Quiocho, F. A. Protein-Carbohydrate Interactions—Basic Molecular Features. *Pure Appl. Chem.* **1989**, *61*, 1293–1306.
6. Spiwok, V.; et al. Modelling of carbohydrate-aromatic interactions: *ab initio* energetics and force field performance. *J. Comput.-Aided Mol. Des.* **2005**, *19*, 887–901.
7. Krapp, S.; et al. Structural analysis of human IgG-Fc glycoforms reveals a correlation between glycosylation and structural integrity. *J. Mol. Biol.* **2003**, *325*, 979–989.
8. Karnoup, A.; et al. A novel HPLC–UV–MS method for quantitative analysis of protein glycosylation. *J. Chromatogr., B* **2007**, *859*, 178–191.
9. Smith, S. O.; et al. Implications of Threonine Hydrogen Bonding in the Glycophorin ***A*** Transmembrane Helix Dimer. *Biophys. J.* **2002**, *82*, 2476–2486.
10. Smith, S. O.; Bormann, B. J. Determination of helix– helix interactions in membranes by rotational resonance NMR. *Proc. Natl. Acad. Sci. U.S.A.* **1995**, *92*, 488–491.
11. Baianu, I. C. Structural Order and Partial Disorder in Biological Systems. *Bull. Math. Biol.* **1980**, *42*, 110–112.
12. Jardetsky, O.; and Roberts, G. C. K. *NMR in Molecular Biology*; Academic Press: New York, 1981.
13. Deslaurier, R.; Smith, I. C. P.; Walter, R. *J. Am. Chem. Soc.* **1974**, *96*, 2289.
14. (a) Baianu, I. C.; Kakalis, L. Carbon-13 NMR of Soy Glycinins and Conglycinins. *J. Agric. Food Chem.* **1989**, *37*, 1222-1228. (b) Baianu, I. C.; Kakalis, L. Carbon-13 NMR of Soy Glycinins and Conglycinins. *J. Agric. Food Chem.* 1990, *37*, 1479−1486.
15. Mora-Gutierrez, A.; Baianu, I. C. *J. Agric. Food Chem.* **1989**, *37*, 1459–1465.
16. Mora-Gutierrez, A.; Baianu, I. C. Hydration Studies of Maltodextrins by Proton, Deuterium and Oxygen-17 Nuclear Magnetic Resonance. *J. Food Sci.* **1990**, *55*, 462–467.
17. Kakalis, L. T.; Baianu, I. C. Oxygen-17 and Deuterium Nuclear Magnetic Relaxation Studies of Lysozyme Hydration in Solution: Field dispersion, concentration, pH/pD and protein activity dependences. *Arch. Biochem. Biophy.* **1988**, *267*, 829–841.

Downloaded by STANFORD UNIV GREEN LIBR on June 20, 2012 | http://pubs.acs.org
Publication Date (Web): October 14, 2011 | doi: 10.1021/bk-2011-1077.ch020

18. Henderson, R.; Unwin, P. N. T. *Nature (London)* **1975**, *257*, 28–32.
19. Hayward, S. B.; et al. Molecular orientation of bacteriorhodopsin within the purple membrane of *Halobacterium halobium*. *Proc. Natl. Acad. Sci. U.S.A.* **1978**, *75* (9), 4320–4324.
20. Baianu, I. C. *Structural Studies of Erythrocyte and Bacterial Cytoplasmic Membranes by X-ray Diffraction and Electron Microscopy*. Ph.D. Thesis, University of London, U.K., 1974.
21. McKenzie, K. R.; Prestegard, J. H.; Engelman, D. M. A Trans- membrane helix dimer structure and implications. *Science* **1997**, *276*, 131–133.
22. Baianu, I. C. Multinuclear Spin Relaxation and High-resolution NMR Studies of Food Proteins, Agriculturally Important Materials and Related Systems. In *NMR Applications in Biopoloymers*; Finley, J. W. et al., Eds.; Plenum Press: New York, 1980; pp 361−389.
23. Baianu, I. C.; Taylor, D. G. NMRI microscopy and T_1 experiments on the hydration of single variety wheat grains at 50 μm resolution. *Phys. Medicine Dept. Report*; University of Surrey, U.K., 1978; p 4.
24. Ferentz, A. E.; Wagner, G. NMR spectroscopy: a multifaceted approach to macromolecular structure. *Q. Rev. Biophys.* **2000**, *33* (1), 29–65.
25. Arakawa, T.; Timasheff, S. N. *Biochemistry* **1982**, *21*, 6543–6546.
26. Pearce, L. F.; et al. *J. Food Microstruct.* **1987**, *6*, 121–126.
27. Ozu, M. E.; Baianu, I. C.; Wei, L. S. *Physical Chemistry of Food Processes*; Baianu, I. C., Eds.; Intl. Thompson Pubs.: New York, 1992; Vol. 2, Chapter 14.
28. Baianu, I. C.; Ozu, M. E. Gelling Mechanisms of Glucomannans and Polysaccharide Interactions with Wheat Gluten Proteins. *NMR Spectroscopy of Polymers in Solution and in the Solid State*; Cheng, H. N., English, A. D., Eds.; ACS Symposium Ser. 834; American Chemical Society: Washington, DC, 2003; Chapter 23, pp 298−305.
29. Baianu, I. C. Near Infrared Microspectroscopy, Fluorescence Microspectroscopy, Infrared Chemical Imaging and High-resolution NMR Analysis of Soybean Seeds, Somatic Embryos and Single Cancer Cells. In *Analysis of Oil Seeds*; Luthria, D., Ed.; AOCS Pubs.: Champaign, IL, 2004; pp 241−273.
30. Baianu, I. C.; You, T. High-resolution Near-Infrared and Nuclear Magnetic Resonance Analysis of Food and Grain Composition. In *Handbook of Food Analysis Instruments*; Otish, S., Ed.; CRC Press: Boca Raton, FL, 2009; Chapter 12, pp 247−280, ISBN: 978-1-4200- 4566-6.
31. Baianu, I . C. Complex Systems Analysis of Cell Cycling Models in Carcinogenesis: Cell Genome and Interactome, Neoplastic Non-random Transformation Models. *Quantitative Biology*; Urbana, Illinois, 2008; Update of *abstract q-bio.EXT-2004-065*.
32. Charles, M.; Baianu, I. C.; Prisecaru, V. Visual Molecular Dynamics (VMD) and the Possible Impact of Lectins on Alzheimer's Disease Treatment. *Internal UIUC Report*; 2007.
33. Baianu, I. C. Applications of Novel Techniques to Health Foods, Medical and Agricultural Biotechnology. *Quant. Biol. arXiv*, 2005. Available from: http://arxiv.org/abs/q-bio/0406047.

Downloaded by STANFORD UNIV GREEN LIBR on June 20, 2012 | http://pubs.acs.org
Publication Date (Web): October 14, 2011 | doi: 10.1021/bk-2011-1077.ch020

34. Kakalis, L. T.; Kumosinki, T. F.; Baianu, I. C. Nonideal Effects of Protein Aggregation and Protein Activity on the Sorption of Water Vapor by Proteins: A Thermodynamic Linkage Study. *J. Agric. Food Chem.* **1992**, *40*, 2063–2071.
35. Prigogine, I.; Nicolis, G. *Self-Organization in Non-Equilibrium Systems: From Dissipative Structures to Order through Fluctuations*; J. Wiley & Sons: New York, 1977.
36. Baianu, I. C. Carbon-13 and Proton NMR studies of Wheat Proteins in Solution. *J. Sci. Food Agric.* **1981**, *32*, 309–313.
37. Baianu, I. C.; Johnson, L. F.; Waddell, D. K. High-field, high- resolution Proton, Carbon-13 and Nitrogen-15 NMR of Wheat Proteins in Solution. *J. Sci. Food Agric.* **1982**, *33*, 373–383.
38. Baianu, I. C. et al. High-Resolution Nuclear Magnetic Resonance and Near Infrared Determination of Soybean Oil, Protein and Amino Acid Residues in Soybean Seeds. *94th AOCS Symp. Proceed.*; Kansas, MO, 2003; AOCS: Champaign, 2004; Chapter 11.

Downloaded by STANFORD UNIV GREEN LIBR on June 20, 2012 | http://pubs.acs.org
Publication Date (Web): October 14, 2011 | doi: 10.1021/bk-2011-1077.ch020

Downloaded by CORNELL UNIV on June 21, 2012 | http://pubs.acs.org
Publication Date (Web): October 14, 2011 | doi: 10.1021/bk-2011-1077.ch021

Chapter 21

Advanced Solution 2D-NMR of Fluoropolymers

**Peter L. Rinaldi,[*,a] Silapong Baiagern,[a] Peter Fox,[b] Jon L. Howell,[b]
Linlin Li,[a] Xiaohong Li,[a] Donald F. Lyons,[b] Elizabeth F. McCord,[b]
Sangrama K. Sahoo,[a] Eric B. Twum,[a] and Faith J. Wyzgoski[c]**

**[a]Department of Chemistry, The University of Akron,
Akron, Ohio 44325-3601
[b]E. I. Dupont de Nemours and Co, Experimental Station Laboratory,
Wilmington, DE 19880-0402
[c]Department of Chemistry, The Ohio State University Mansfield,
Mansfield, Ohio 44906
[*]E-mail: peterrinaldi@uakron.edu**

In this paper, new methodology is described for characterizing the structures of fluoropolymers. The methods are based on $^{19}F/^{1}HH/^{13}C$ multiple resonance and 2D NMR experiments, taking advantage of the unique ranges of ^{19}F-^{19}F and ^{19}F-^{13}C couplings. ^{19}F-^{13}C heteronuclear single quantum correlation (HSQC) 2D-NMR experiments based on $^{1}J_{CF}$ and $^{2}J_{CF}$ experiments provide short range correlations within monomer units and in many cases help to distinguish between structure fragments identified using $^{3}J_{FF}$, $^{4}J_{FF}$ and $^{5}J_{FF}$ correlations. COSY and especially selective COSY experiments provide high resolution 2D-NMR experiments with correlations based on $^{3}J_{FF}$, $^{4}J_{FF}$ and $^{5}J_{FF}$ couplings. These permit identification of long-range structure correlations between monomer units. Examples using poly(hexafluoropropylene oxide) and poly(vinylidene fluoride) are shown.

Introduction

In recent years, there has been renewed interest in the synthesis and study of fluoropolymers. This interest is derived in part from the unique stability of the C-F bond to chemical, thermal and radiation degradation compared to hydrocarbon-based structures. The presence of a high level of fluorination in

In NMR Spectroscopy of Polymers: Innovative Strategies for Complex Macromolecules; Cheng, H., et al.;
ACS Symposium Series; American Chemical Society: Washington, DC, 2011.

polymers also imparts desireable physical and mechanical properties such as excellent lubrication characteristics, high boiling properties, and desirable optical properties such as transparency in regions of the spectrum where hydrocarbons usually absorb. Because of the strength of the C-F bond (relative to the C-H bond) and the fact that fluorine on the surface of the molecule can shield the carbon skeleton from chemical attack, fluoropolymers usually have long lifetimes. They can be used in applications where replacement or replenishment is not possible and/or desirable.

The properties of ^{19}F make NMR an interesting and useful method for studying fluoropolymer structure and composition. ^{19}F has many characterististic similar to that of ^{1}H including 100% natural abundance, nuclear spin I=1/2, and a large magnetic moment (such that it's signal strength is similar to that of ^{1}H). In addition, ^{19}F has a large chemical shift range (over 200 ppm) compared to ^{1}H (10 ppm); its chemical shift is extremely sensitive to variations in chemical structure; and it exhibits a large range of J-couplings (couplings over 2 to 6 bonds are commonly observed which range from 0-300 Hz). Finally, in many polymers, the presence of ^{1}H, ^{13}C and ^{19}F provides many structure-dependent NMR parameters to measure.

NMR, especially ^{19}F NMR, has always been a useful tool for characterizing fluoropolymers, especially PHFPO and PVDF. In a series of papers, Howell et al. (*1–3*) used NMR to characterize PHFPO polymers and short chain oligomers. Kostjuk et al. (*4*) used ^{19}F 1D-NMR to study the mechanism of HFPO polymerization using alkali metal fluorides as initiators. Durand et al. (*5*) reported NMR data on PHFPO telomers.

Murasheva et al. (*6*) used ^{19}F NMR to study PVDF, PVDF/TFE and PVDF/TFE/HFP copolymers. In their seminal work, Cais and Sloane (*7*) used ^{19}F 1D-NMR spectra to study inverse addition of monomer units in PVDF, and made use of additivity relationships to assign resonances from the various triad sequences formed by normal and inverse addition. Ovenall and Uschold (*8*) used ^{19}F NMR to detect signals attributed to chain-ends and branches. Pianca et al. (*9*) used 1D- and COSY 2D-NMR methods to study the chain-end structures in a series of fluoropolymers, including PVDF. The branched structures in PVDF were characterized by Hedhli et al. (*10*), using 1D- and 2D- NMR methods. Gulot et al. (*11*) used ^{1}H and ^{19}F NMR to investigate the microstructure of PVDF; and Ameduri et al. (*12*) used NMR and MALDI-TOF mass spectrometry to study the structures of a range of VDF telomers. Wormald et al. (*13*) used 1D-NMR methods, aided by solid state high power decoupling techniques, to get high resolution spectra of a VDF telomere; and Durand et al. (*14*) reported NMR data on PVDF telomers.

Most of the previously published NMR work involved simple 1D-NMR experiments, however, a few notable papers on 2D-NMR characterization of the fluoropolymers which are the subject of this work have been published. Katoh et al. (*15*) first showed how ^{1}H/^{19}F/^{13}C triple resonance and 2D-NMR methods could be used to simplify the spectra of fluoropolymers using data from PVDF as an example. Takasaki et al. (*16*) used low resolution ^{19}F-^{19}F COSY, and ^{19}F-^{13}C HSQC- and HMBC-based 2D-NMR experiments to study PHFPO segments in perfluorinated ionomers. Macheteau et al. (*17*) have used selective versions of

Downloaded by CORNELL UNIV on June 21, 2012 | http://pubs.acs.org
Publication Date (Web): October 14, 2011 | doi: 10.1021/bk-2011-1077.ch021

Downloaded by CORNELL UNIV on June 21, 2012 | http://pubs.acs.org
Publication Date (Web): October 14, 2011 | doi: 10.1021/bk-2011-1077.ch021

^1H-^{19}F heteronuclear shift correlation experiments to study low molecular weight oligomers of PVDF. It is amazing how much useful characterization has been accomplished using low field instruments and limited instrumental capabilities.

In the past few decades multidimensional NMR techniques have become routine. Instruments with three or more rf channels have become commonplace. In addition, the Rf and pulse programming capabilities of modern instruments (past 5 years) have become tremendously flexible. These factors make it useful to reconsider the nature of NMR methods for studying fluoropolymer structures.

This paper illustrates some NMR capabilities for studying fluoropolymer structures. While some of these methods have been around for a decade or more, their proper execution has required recent improvements in the NMR instruments' rf performance. These methods will be illustrated with applications to the study of poly(hexafluoropropylene oxide) (PHFPO) and low molecular weight oligomers, and poly(vinylidene fluoride) (PVDF).

Fluorine NMR

The ^{19}F NMR spectrum of PHFPO in Figure 1 exhibits the NMR characteristics of ^{19}F that make it both powerful for solving structure problems and challenging to execute. The resonances are spread over a large spectral window, in this case over 60 ppm, and their chemical shifts are very sensitive to variations in the chemical and stereochemical environments.

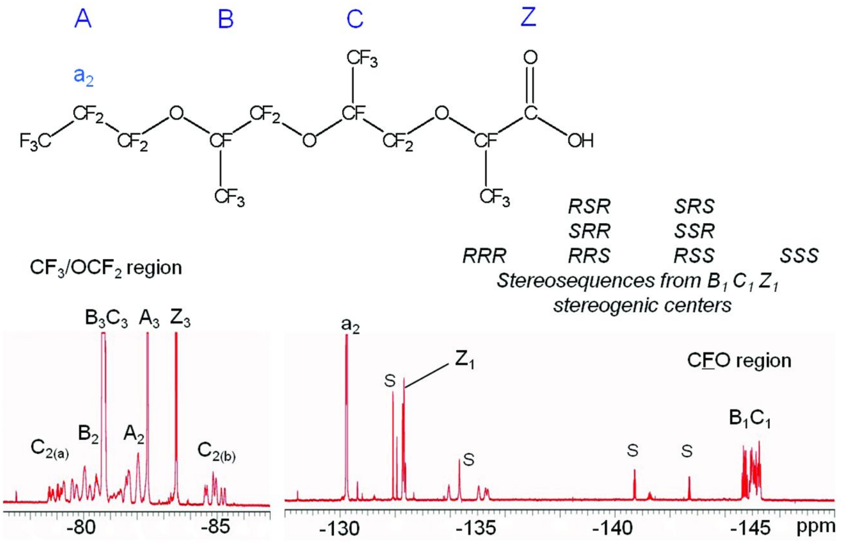

Figure 1. Peak containing regions from the 470 MHz ^{19}F 1D-NMR spectrum of PHFPO; s are signals from identified impurities in C_6F_6 solvent.

Several sets of multiplets are observed near -145 ppm for the CF fluorines in the B and C units of the structure in the Figure 1. The multiplets are not resolved from one another because there are four structures for each CF group (4 diastereomers and their mirror images). Furthermore, the multiplets are broad and complex due to 3-bond couplings to the CF_2 and CF_3 groups on the same monomer unit, and 4-bond couplings to the CF_2 groups on the other side of the ether linkage.

The nomenclature adopted in this paper to identify atoms in PHFPO/THFPO is illustrated using the structure of THFPO in Figure 1, where the monomer units are labeled A, B, C and Z starting from the initiation end (left) and proceeding to the termination end of the chain. Subscripts are used to refer to the number of fluorines on the groups within each monomer; for example, B_1, B_2 and B_3 refer to the CF, CF_2 and CF_3 groups, respectively, in monomer unit B.

2D-NMR experiments generally provide the solution to resolving overlapping signals, and also provide correlations between resonances to identify structure fragments. While the large spectral window makes it more likely to resolve many resonances in complex molecules, it also creates problems because short pulse widths are required for uniform excitation of resonances in standard NMR experiments. In 1D-NMR experiments narrow pulses that produce small tip angles can be used without severe consequences, but it is generally not possible to use arbitrary flip angles in 2D-NMR experiments

Furthermore, if ^{19}F chemical shift is to be used in the indirectly detected dimension of a 2D-NMR experiment, a significantly long experiment time is needed to collect the many t_1 increments needed to produce good digitial resolution in the indirectly detected dimension. In this case, a simple COSY experiment could provide correlations that prove structure, but excellent digital resolution is needed to resolve the multiplets in the -145 ppm region and this same digital resolution must be maintained in the 50 ppm peak-free region in the middle of the spectral window. A weekend-long experiment was needed to provide a 2D-COSY spectrum with relatively poor digital resolution in the f_1 dimension, even though sufficient signal-to-noise was obtained in only 15 min.

Selective excitation experiments offer a solution to these problems (*18*). Most of the needed information exists in relatively small areas of the 2D-NMR spectra. If experiments are performed to select only these areas, a few short experiments can be performed in a few hours to provide all the needed structural information. Selective ^1H-^1H COSY experiments using shaped pulses were described some time ago (*19*). While the large ^{19}F spectral window should facilitate the use of selective excitation, the large frequency offsets compared to ^1H places excessive demands for fast frequency/phase shifting requirements during the rf pulses and are beyond the capabilities of older NMR instruments.

The rf circuitry on modern NMR aspectrometers is very flexible and permits the rapid amplitude, frequency and phase switching to generate arbitrary pulse shapes. Figure 2 shows the full ^{19}F 1D-NMR spectrum of PHFPO (bottom) along with several selective spectra. To generate the selective spectra, selective/shaped rf pulses were sliced into small increments (1-5 us) and the phase was progressively shifted to track the precession of the magnetization from a group of spins using shifted laminar pulses (SLP) (*20*). The selective pulses were designed to excite (from bottom to top) the CF, CF_2 and CF_3/OCF_2 regions.

Modern hardware is capable not only of selective excitation with large (100 kHz) offsets from the transmitter, but also of arbitrarily combining two or more

Downloaded by CORNELL UNIV on June 21, 2012 | http://pubs.acs.org
Publication Date (Web): October 14, 2011 | doi: 10.1021/bk-2011-1077.ch021

offset pulses to excite/flip the nuclear spins of atoms whose resonances occur in two or more such regions.

NMR Methods

Typical ranges of couplings in fluoropolymers are shown on structure **1**, which shows a segment from PHFPO. One- and two-bond ^{19}F-^{13}C couplings in fluorinated materials are large compared to their hydrocarbon counterparts. This makes them ideal for characterization of fluoropolymers which give broad lines and suffer from difficulty in detecting 2D-NMR correlations which rely on weaker couplings. Because $^{1}J_{CF}$ and $^{2}J_{CF}$ differ by almost a factor of ten, it is easy to implement experiments that produce correlations that are selective for one or the other interaction. Two- and four-bond ^{19}F-^{19}F homonuclear couplings are usually large, while other homonuclear couplings are much smaller.

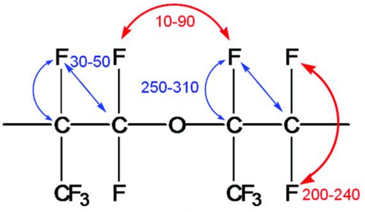

1

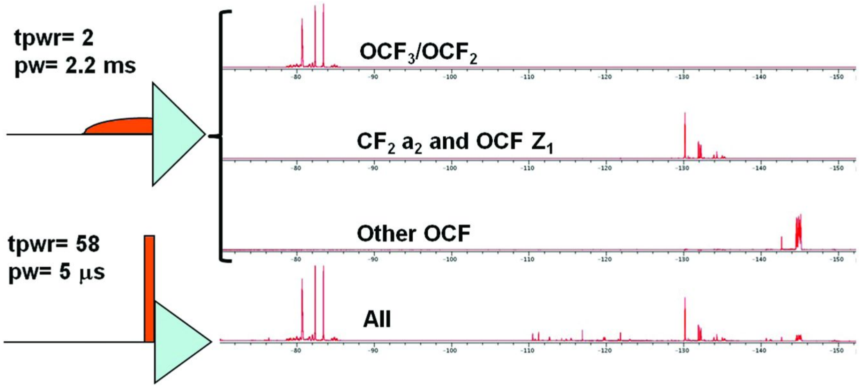

Figure 2. 470 MHz ^{19}F 1D-NMR spectra of PHFPO going from bottom to top: with broadband excitation of all the resonances in the spectra, and with selective excitation of the CF, CF_2 and CF_3/OCF_2 regions.

In PHFPO, it is possible to use two different ^{19}F-^{13}C HSQC (*21*, *22*) (heteronuclear single quantum) 2D-NMR experiments, one tuned for $^{1}J_{CF}$ and a second tune for $^{2}J_{CF}$, to obtain the atomic connectivities highlighted by the blue arrows in **1**. In this way, all of the monomer fragments can be identified. A COSY experiment would then primarily contain correlations between fluorines on either side of the ether linkage, coupled by the large $^{4}J_{FF}$.

Downloaded by CORNELL UNIV on June 21, 2012 | http://pubs.acs.org
Publication Date (Web): October 14, 2011 | doi: 10.1021/bk-2011-1077.ch021

Figure 3 shows the modified version of the HSQC pulse sequence used to study the fluoropolymers which are the subject of this work. Details regarding the implementation of this experiment can be found in reference (*23*), however, there are several unique and noteworthy features. ^{1}H decoupling is performed on a third rf channel throughout the experiment, especially with materials such as PVDF, which have high hydrogen content. Even the HSQC spectra of perfluorinated PHFPO's benefit from continuous ^{1}H decoupling as there are sometimes residual protons present (identified by ^{1}H 1D-NMR spectra and ^{13}C 1D-NMR spectra obtained with and without ^{1}H decoupling). Several spectra are collected with different ^{19}F spectral windows (CF, CF_2 and CF_3 regions). To accomplish this, all of the ^{19}F pulses, with the exception of the composite inversion pulse in the middle of t_1, are low power region-selective pulses. The composite pulse in the middle of t_1 has high power, and is performed with the transmitter moved to the center of the peak-containing regions of the ^{19}F spectrum for maximum effectiveness at decoupling ^{19}F in the f_1 (^{13}C chemical shift) dimension. The delays (Δ_1) during the TANGO (Testing for Adjacent Nuclei with a Gyration Operator) (*24*) period are set based on $^{1}J_{CF}$; and the phase of the last (135°) pulse is set based on whether ^{19}F-^{13}C or ^{19}F-C-^{13}C correlations are to be detected. The delays Δ during the rest of the pulse sequence are set to $1/(4x^{n}J_{CF})$, where the appropriate one-bond or two-bond correlation is to be detected.

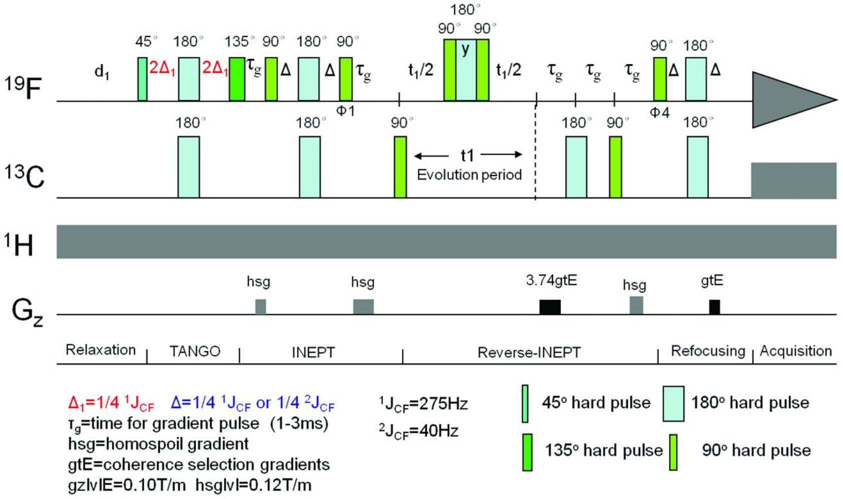
^{19}F
^{13}C
^{1}H
G_z
d_1
45°
$2\Delta_1$
180°
$2\Delta_1$
135°
τ_g
90°
Δ
180°
Δ
90°
τ_g
Φ1
$t_1/2$
180°
90° 90°
y
$t_1/2$
τ_g τ_g τ_g
90°
Δ
180°
Δ
Φ4
180°
180°
90°
t1
Evolution period
180° 90°
180°
hsg
hsg
3.74gtE
hsg
gtE
Relaxation
TANGO
INEPT
Reverse-INEPT
Refocusing
Acquisition
Δ_1=1/4 $^1J_{CF}$ Δ=1/4 $^1J_{CF}$ or 1/4 $^2J_{CF}$
τ_g=time for gradient pulse (1-3ms)
hsg=homospoil gradient
gtE=coherence selection gradients
gzlvlE=0.10T/m hsglvl=0.12T/m
$^1J_{CF}$=275Hz
$^2J_{CF}$=40Hz
45° hard pulse
180° hard pulse
135° hard pulse
90° hard pulse

Figure 3. Pulse sequence for selective HSQC; see text for details.

Figure 4 shows schematic illustrations of various options used for perfoming selective COSY experiments. In all cases, the schematic illustrations of the standard COSY spectra are illustrated by the full boxes with diagonal in Figure 4a-c, while the gray areas represent the detected spectrum obtained with each variation of the selective COSY. If the pulse scheme in Figure 4d is used with the blue pulse shaped and selective, and the yellow pulse as a standard high power pulse, then the strip COSY spectrum illustrated by the gray area in Figure 4a is obtained. If both blue and yellow pulses are selective for the same region, then the endo-COSY spectrum in Figure 4b is obtained. If the pulse scheme shown in

Downloaded by CORNELL UNIV on June 21, 2012 | http://pubs.acs.org
Publication Date (Web): October 14, 2011 | doi: 10.1021/bk-2011-1077.ch021

Downloaded by CORNELL UNIV on June 21, 2012 | http://pubs.acs.org
Publication Date (Web): October 14, 2011 | doi: 10.1021/bk-2011-1077.ch021

Figure 4e is used with blue and yellow pulses selective for the indicated region of the f_1 dimension if Figure 4c and the orange pulse selective for the indicated region in the f_2 dimension, then the exo-COSY (ECOSY) spectrum in Figure 4c is obtained. This spectrum will contain a cross-peak pattern with couplings in all dimensions. By inserting an inversion pulse (green) in the middle of t_1 then selective coupling can be removed in the f_1 dimension. On modern NMR instruments, this green pulse can be the sum of two or more arbitrary pulse shapes, to remove multiple couplings to fluorines in different regions of the spectrum.

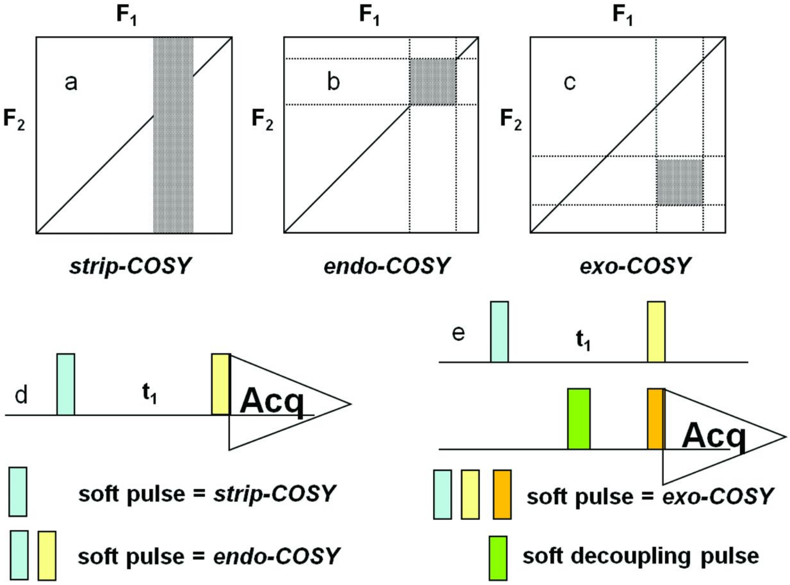

Figure 4. Schematic illustration of selective COSY experiments; see text for details.

Characterization of PHFPO

Structure

The first material chosen to illustrate the NMR methodology was PHFPO because it was relatively simple to prepare NMR samples, and had well-defined ^{19}F spectral regions which were well separated from one another. Here we show results from tetrameric(hexafluoropropylene oxide) (tHFPO) shown in Figure 1. This material was readily available from the commercially available acid fluoride, readily dissolves in many solvents, and exhibits many of the NMR characteristics of the PHFPO backbone and selected chain-end resonances found in the spectrum of the polymer. As illustrated in Figure 1, four sets of stereoisomers (and their mirror images) are present due to the three stereogenic centers present in the structure.

Downloaded by CORNELL UNIV on June 21, 2012 | http://pubs.acs.org
Publication Date (Web): October 14, 2011 | doi: 10.1021/bk-2011-1077.ch021

2D-NMR

Figure 5 shows selected data from the one-bond (top highlighted in red), and two-bond (bottom highlighted in blue) ^{19}F-^{13}C HSQC spectra; showing the correlations that prove the CF_3 one-bond attachments at the chain-end and two-bond correlations between the same CF_3 fluorine and adjoining CF_2 carbon. The experiments were optimized using the couplings indicated in the figure. Note that the ^{19}F bound to ^{13}C (top) is shifted by ca. 0.1ppm upfield compared the the ^{19}F bound to ^{12}C as a result of the well-known isotope shift (*25*). Many regions such as this were identified in the HSQC spectra, in order to identify resonances from each of the unique structure fragments in tHFPO.

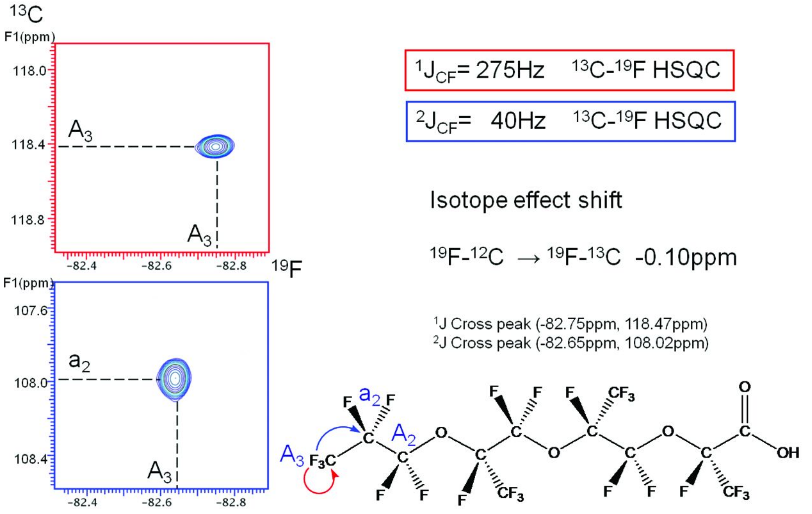

Figure 5. Selected regions from the region selective $^{19}F^{13}C$ HSQC spectra of tHFPO showing the correlations indicated on the structure; the region from the one-bond HSQC spectrum is shown in red and the corresponding region from the two-bond HSQC spectrum is shown in blue.

With the four structure elements circled in blue on the structure in Figure 6 identified by HSQC experiments, the methodology then relies on COSY correlations to prove how they are attached to one another. An expansion from the standard COSY spectrum (ca. 1% of the total area from this 2D-NMR spectrum) showing the correlations indicated on the structure is shown in Figure 6a. Two groups of cross peaks are seen correlating B_2-C_1 and A_2-B_1 fragments. Poor digital resolution hides an enormous amount of detail in this region despite the fact that thousands of t_1 increments were collected over the course of a weekend-long experiment.

Downloaded by CORNELL UNIV on June 21, 2012 | http://pubs.acs.org
Publication Date (Web): October 14, 2011 | doi: 10.1021/bk-2011-1077.ch021

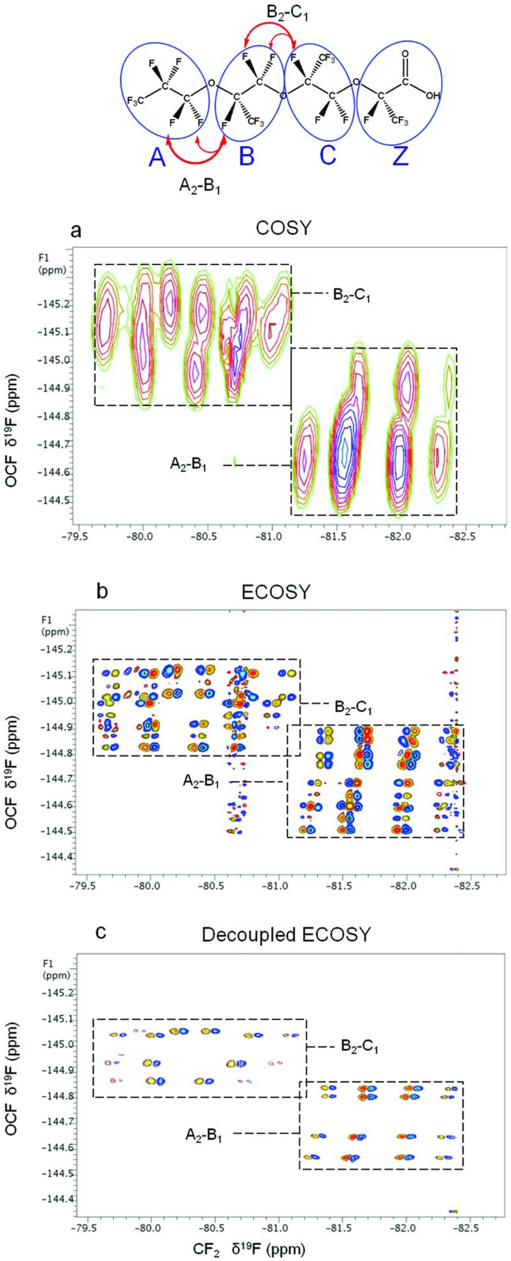

Figure 6. Selected regions from the COSY (a), and ECOSY (b) and decoupled ECOSY (c) showing the region containing four-bond correlations between the structure fragments shown on the included structure.

Downloaded by CORNELL UNIV on June 21, 2012 | http://pubs.acs.org
Publication Date (Web): October 14, 2011 | doi: 10.1021/bk-2011-1077.ch021

Using selective COSY 2D-NMR experiments the spectrum in Figure 6b was collected. Even though only 2x256 t_1 increments were collected, considerably better digital resolution is evident in this spectrum. From the data in the figure, it is clear that there are many overlapping cross-peak patterns. All of the homonuclear couplings can be removed in the f'_1 dimension by insertion of shaped inversion pulses (at the chemical shifts of those ^{19}F atoms to be decoupled) in the middle of the evolution time. As a result, the spectrum in Figure 6c was obtained. Four sets of multiplet are observed in each of the regions, from the four sets of diastereomers. All of the couplings are retained in the f_2 dimension where there is good digital resolution, at little cost of instrument time to produce this digital resolution. At each slice, AB patterns ($^2J_{FF}$=150-160 Hz) are observed for each of the unique CF_2 groups; these are further split by doublet couplings to the CF group on the other side of the ether linkage. Three-bond couplings are too small, and are not resolved.

The shaped decoupling pulse during t_1 was actually a combination of shapes at several shifts, for those ^{19}F's that produce the couplings in f_1. An additional delay was required at the end of the evolution period to allow creation of the antiphase magnetization from coupling between the nuclei creating the cross-peaks. The original paper should be consulted for details (*23*).

Characterization of PVDF

Structure

The primary structure components of the main-chain repeat units in PVDF are illustrated by those shown in Figure 7. The nomenclature to describe these structures is based on that first described by Cais et al. (*7*), where 0 and 2 (number of fluorine in backbone methylene groups) represent CH_2 and CF_2 groups along the chain. Normal addition produces -0202- carbon sequences, however, occasionally an inversion occurs to produce tail-to-tail (-2002-) and head-to-tail (-0220-) sequences.

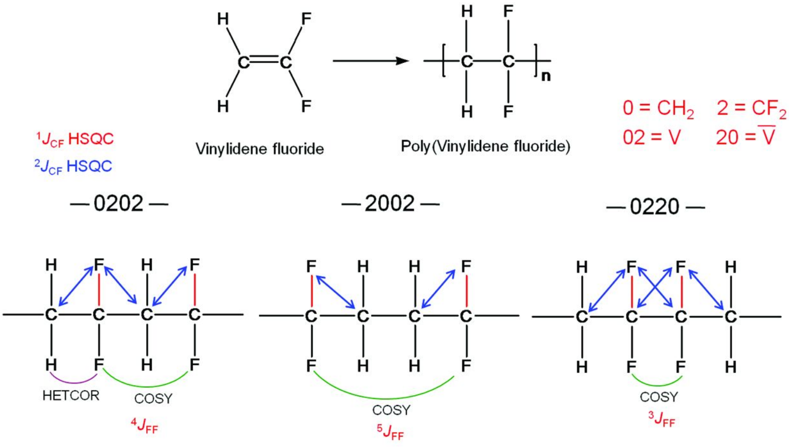

Figure 7. Structures and nomenclature used to define PVDF.

As with tHFPO above, HSQC experiments provide one-bond and two-bond C-F correlations illustrated by the blue arrows on the structures across the bottom of Figure 7. These experiments can be used to identify the immediate neighbors (0 or 2) of each 2 unit. COSY spectra exhibit three-, four- and five bond correlations between 2 carbons on sequential monomer units in all threes types of structures (-0202-, -2002- and -0220-), however, from these data it is not always possible to identify which units produce which cross-peaks. Two-bond ^{19}F-^{13}C HSQC experiments help to distinguish among these: F-C correlation in -0202- will show correlations to the ^{13}C shifts of the same 0 units; F-C correlations in -2002- units will not show correlations to the ^{13}C shifts of the same 0 units; and -0220- units will show correlations to the ^{13}C shifts of each other's two resonances.

Downloaded by CORNELL UNIV on June 21, 2012 | http://pubs.acs.org
Publication Date (Web): October 14, 2011 | doi: 10.1021/bk-2011-1077.ch021

2D-NMR

The one-bond and two-bond ^{19}F-^{13}C HSQC 2D-NMR spectra of a PVDF sample are shown in Figure 8a and b, along with the ^{19}F and ^{13}C 1D-NMR spectra, which are plotted along the corresponding axes of the 2D-NMR spectra. The ^{19}F signals of 020 and 022/220 carbon sequences occur in distinct regions (red and yellow) as indicated by the labels on the figure. These ^{19}F resonances have been assigned based on empirical shift additivity rules and the γ substituent effect (*7*). Distinction between the ^{13}C resonances of 0 and 2 carbons is straightforward based on the power of electronegative fluorine to shift the ^{13}C resonances downfield.

These assignments of resonances from three-carbon sequences are confirmed by the HSQC data. ^{19}F resonances of 020 sequences only show two-bond F-C correlation to 0 carbons (red circles in Figure 8b). However, ^{19}F resonances of 022/220 sequences show correlations to carbons in both the 2 and 0 carbon resonance region (yellow circles in Figure 8b). Note that 222 sequences are not possible in PVDF.

The double quantum filtered (dq) COSY spectrum of PVDF is shown in Figure 9. The ^{19}F spectral window for PVDF is relatively narrow compared to that for PHFPO, so that it is not essential to use the selective versions of this experiment. The correlations shown on the dqCOSY spectrum permit identification of attachments between fragments of three carbon sequences: A (020) to E (022), E (022) to F (220), F (220) to D (020), and D (020) to C (020). The ^{19}F resonances are correlated with each other via 3-, 4- and 5-bond J_{FF} couplings through 22, 202 and 2002 attachements, respectively. As mentioned above, HSQC data permits distinction between these connectvities (i.e. whether 2-2 linkages occur through one-bond, -0-, or -00-).

Through combined use of HSQC and COSY based 2D-NMR experiments, this 13 carbon sequence has been identified and its resonances assigned. Similar interpretation of the spectra easily permits identification of 9-carbon sequences needed to identify pentad sequences in the polymer.

Downloaded by CORNELL UNIV on June 21, 2012 | http://pubs.acs.org
Publication Date (Web): October 14, 2011 | doi: 10.1021/bk-2011-1077.ch021

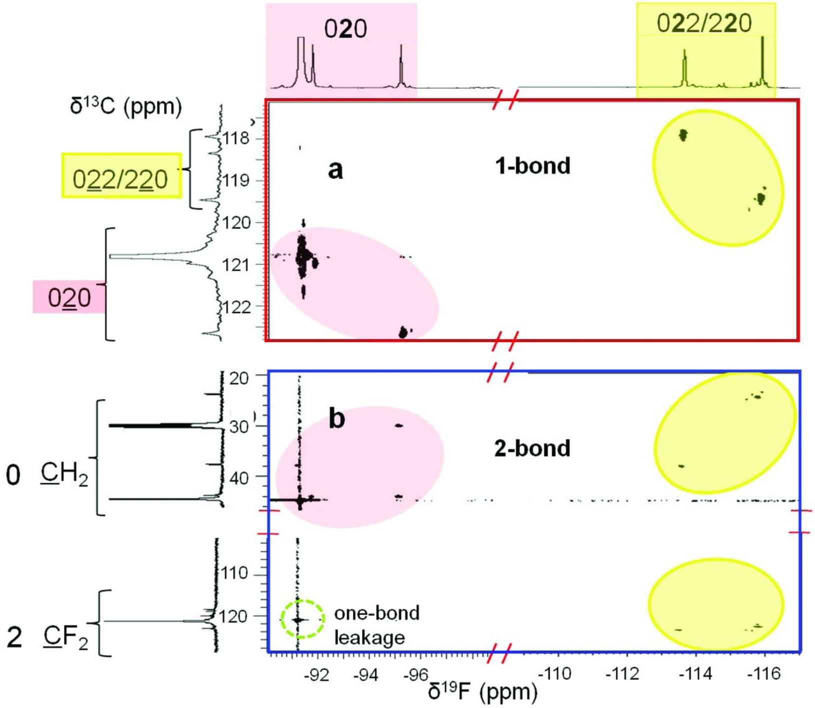

Figure 8. Selected regions from the one-bond (a) and two-bond (b) ^{19}F-^{13}C HSQC 2D-NMR spectra of PVDF.

Experimental Section

Materials

Solvents were purchased from Aldrich Chemical Co and Cambridge Isotope Laboratories and used as received; THFPO was purchased as the acid fluoride from Alfa Aesar and converted to the carboxylic acid as previously described (*23*). PVDF was provided by E. I. Dupont de Nemours and Co.

Instrumentation

NMR measurements were made with a Varian direct drive 500 MHz NMR spectrometer with five rf channels. Channels 1 and 3 were designed for high frequency (^1H/^{19}F) and channel 2 was designed and used for low frequency band operation (^{31}P-^{15}N). All channels were equipped with waveform generators for pulse shaping. The probe used was a 5mm four channel (^1H/^{19}F/^{13}C/^2H) design with a single high-band input for the ^1H and ^{19}F signals, and pulsed field gradient coils (capable of up to 0.7 T/m gradients). A duplexer was used with internal filters to combine ^1H and ^{19}F rf transmitter signals, direct them to the high band channel of the probe, take the NMR signal from the probe, isolate the ^1H and ^{19}F signals from the sample, and direct the desired signal to the instrument receiver.

Complete details describing the pulse programs used have been summarized in reference (*23*).

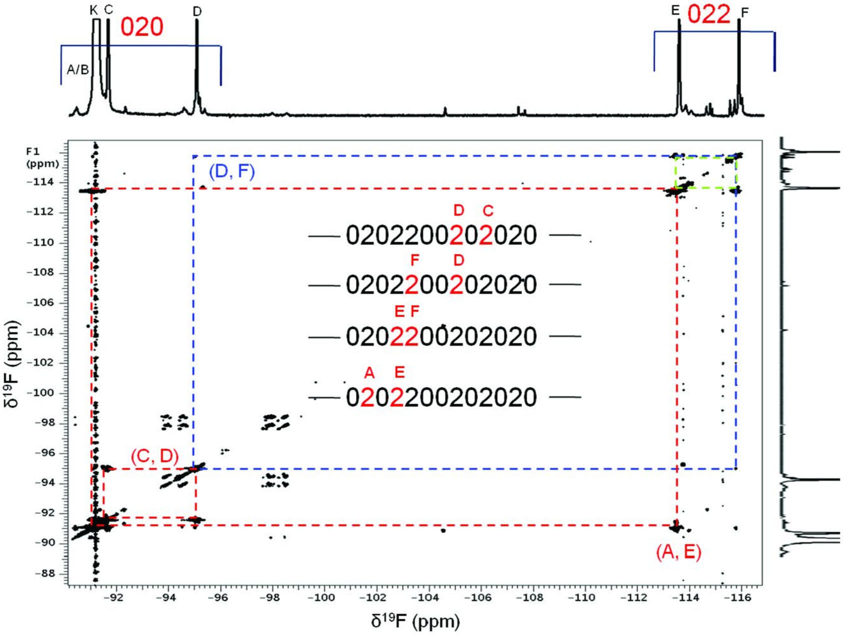

Figure 9. ^{19}F-^{19}F double quantum filtered COSY spectrum of PVDF.

Summary

Recent advances in the capabilities of NMR instrument hardware and the software used to control that hardware warrants a reevaluation of older NMR techniques and their utility in solution NMR studies of polymer structures. NMR studies of fluoropolymers can particularly benefit from application of selective excitation techniques. The unique characteristics of ^{19}F (compared to ^{1}H) create difficulities in applications of 2D-NMR method of structure elucidation. These same characteristics contribute to the successful applications of selective excitation NMR experiments. In this paper, examples of these applications are presented involving the characterization of PHFPO and PVDF. Unprecendented detail is resolved in the selective 2D-COSY and HSQC spectra. These data permit the assignment of resonances from monomer- and stereo-sequences in the polymer backbone.

These experiments can and are being used to study polymer chain-end structures, in order to shed light on the inititiation and termination processes in polymerization. Similar analyses are also underway to characterize poly(vinylidene fluoride-co-tetrafluoroethylene) (PVDF/TFE), poly(vinylidene fluoride-co-hexafluoropropene) (PVDF/HFP) and poly(vinylidene fluoride-co-tetrafluoroethylene- co-hexafluoropropene) (pCDF/TFE/HFP)

Downloaded by CORNELL UNIV on June 21, 2012 | http://pubs.acs.org
Publication Date (Web): October 14, 2011 | doi: 10.1021/bk-2011-1077.ch021

Acknowledgments

The authors wish to thank the National Science Foundation (DMR-0905120) and E. I. Dupont de Nemours and Co. for financial support during the preparation of this work. We thank The Ohio Board of Regents and The National Science Foundation (CHE-0341701 and DMR-0414599) for funds used to purchase the NMR instrument used in this work. We wish to thank the staff of the Magnetic Resonance Center at The University of Akron for maintaining the equipment used in this work.

References

1. Howell, J. L.; Hofmann, M. A.; Waterfeld, A.; Sipyagin, A. M.; Friesen, C. M.; Thrasher, J. S. *J. Fluorinie Chem.* **1998**, *89*, 131–135.
2. Howell, J. L.; Lu, N.; Perez, E. W.; Friesen, C. M.; Novak, I.; Waterfeld, A.; Thrasher, J. S. *J. Fluorine Chem.* **2004**, *125*, 1513–1518.
3. Howell, J. L.; Lu, N.; Friesen, C. M. *J. Fluorine Chem.* **2005**, *126*, 281–288.
4. Kostjuk, S. V.; Ortega, E.; Ganachaud, F.; Ameduri, B.; Boutevin, B. *Macromolecules* **2009**, *42*, 612–619.
5. Durand, N.; Mariot, D.; Ameduri, B.; Boutevin, B.; Ganachaud, F. *Langmuir* **2011**, *27*, 4057–4067.
6. Murasheva, Y. M.; Shashkov, A. S.; Dontsove, A. A. *Polym. Sci. U.S.S.R.* **1981**, *23*, 711–720.
7. Cais, R. E.; Sloane, N. J. A. *Polymer* **1983**, *24*, 179–187.
8. Ovenall, D. W.; Uschold, R. E. *Macromolecules* **1991**, *24*, 3235–3237.
9. Pianca, M.; Barchiesi, E.; Esposto, G.; Radice, S. *J. Fluorine Chem.* **1999**, *95*, 71–84.
10. Hedhli, L.; Mekhilef, N.; Moyses, S.; Lewis, R. H. *Macromolecules* **2008**, *41*, 2011–2021.
11. Guiot, J.; Ameduri, B.; Boutevin, B. *Macromolecules* **2002**, *35*, 8694–8707.
12. Ameduri, B.; Ladeaviere, C.; Delolme, F.; Boutevin, B. *Macromolecules* **2004**, *37*, 7602–7609.
13. Wormald, P.; Ameduri, B.; Harris, R. K.; Hazendonk, P. *Polymer* **2008**, *49*, 3629–3638.
14. Durand, N.; Ameduri, B.; Boutevin, B. *J. Polym. Sci., Part A: Polym. Chem.* **2011**, *49*, 82–92.
15. Katoh, E.; Ogura, K.; Ando, I. *Polym J.* **1994**, *26*, 1352–1359.
16. Takasaki, M.; Kimura, K.; Kawaguchi, K.; Abe, A.; Katagiri, G. *Macromolecules* **2005**, *38*, 6031–6037.
17. Macheteau, J.-P.; Oulyadi, H; van Hemelryck, B.; Bourdonneau, M.; Davoust, D. *J. Fluorine Chem.* **2000**, *104*, 149–154.
18. Morris, G. A.; Freeman, R. *J. Magn. Reson.* **1978**, *29*, 433–462.
19. Huth, J.; Kurur, N.; Bodenhausen, G. *J. Magn. Reson., Ser. A* **1996**, *118*, 286–290.
20. Patt, S. L. *J. Magn. Reson.* **1992**, *95*, 94–102.
21. Bodenhausen, G.; Ruben, D. J. *Chem. Phys. Lett.* **1980**, *69*, 185–188.

Downloaded by CORNELL UNIV on June 21, 2012 | http://pubs.acs.org
Publication Date (Web): October 14, 2011 | doi: 10.1021/bk-2011-1077.ch021

22. Vuister, G. W.; Boelens, R.; Kaptein, R.; Hurd, R. E.; John, B.; Zijl, P. C. M. V. *J. Am. Chem. Soc.* **1991**, *113*, 9688–9690.
23. Li, X.; McCord, E. F.; Baiagern, S.; Fox, P.; Howell, J. L.; Sahoo, S. K.; Rinaldi, P. L. *Magn. Reson. Chem.* **2011**in press.
24. Wimperis, S.; Freeman, R. *J. Magn. Reson.* **1984**, *58*, 348–353.
25. Tordeux, M.; Magnier, E.; Guidotti, J.; Diter, P.; Wakselman, C. *Magn. Reson. Chem.* **2004**, *42*, 700–703.

Downloaded by CORNELL UNIV on June 21, 2012 | http://pubs.acs.org
Publication Date (Web): October 14, 2011 | doi: 10.1021/bk-2011-1077.ch021

Chapter 22

Statistical Models and NMR Analysis of Polymer Microstructure

H. N. Cheng*[,1] **and Massoud J. Miri**[2]

[1]**Southern Regional Research Center, USDA Agricultural Research Service,**
1100 Robert E. Lee Blvd., New Orleans, LA 70124, U.S.A.
[2]**Department of Chemistry, Rochester Institute of Technology, Rochester,**
NY 14623, U.S.A.
***E-mail: hncheng100@gmail.com**

Downloaded by UNIV OF DELAWARE MORRIS LIB on June 20, 2012 | http://pubs.acs.org
Publication Date (Web): October 14, 2011 | doi: 10.1021/bk-2011-1077.ch022

Statistical models can be used in conjunction with NMR spectroscopy to study polymer microstructure and polymerization mechanisms. Thus, Bernoullian, Markovian, and enantiomorphic-site models are well known. Many additional models have been formulated over the years for additional situations. Typically spectral interpretation and data treatment can be done through either "analytical" or "simulation" approaches. These can be combined into "integrated" approaches for specific situations. An alternative (and more general) approach considers the kinetics of the polymerization process and carries out predictions of polymer microstructures and NMR spectra. These various methodologies are briefly reviewed here. Also reviewed is a recent effort in the simulation category involving a user-friendly Excel program ("Polytact") that can simulate the tacticities of a large number of statistical models, particularly those that pertain to polyolefins made with single-site catalysts.

Introduction

High-resolution solution NMR is now a routine technique for polymer analysis (*1–5*). It is fairly straightforward to dissolve a polymer in a solvent and obtain a ^{1}H or ^{13}C spectrum. Analyses of a polymer NMR spectrum can be carried out at different levels (Figure 1). At the simplest level, one can use the gross

In NMR Spectroscopy of Polymers: Innovative Strategies for Complex Macromolecules; Cheng, H., et al.;
ACS Symposium Series; American Chemical Society: Washington, DC, 2011.

NMR spectral features to search the spectral libraries for routine identification or pattern recognition. At a more involved level, one can interpret the spectrum (in whole or in part), using a variety of techniques, and assigning the observed peaks to specific structures. From the assignments, it may then be possible to derive detailed information on polymer microstructure, such as homopolymer tacticity, copolymer composition and sequence, branching, defect structures, and chain ends. With additional work, it may be possible to infer information on monomer reactivity and polymerization mechanisms. In general, the amount and the quality of information that can be extracted from the NMR data depend on the methodologies used and the efforts expended.

Downloaded by UNIV OF DELAWARE MORRIS LIB on June 20, 2012 | http://pubs.acs.org
Publication Date (Web): October 14, 2011 | doi: 10.1021/bk-2011-1077.ch022

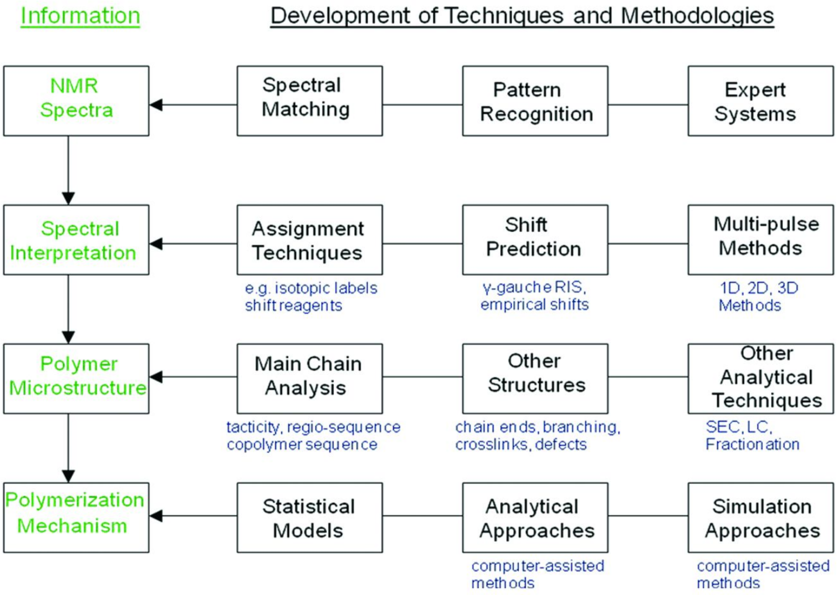
Information
Development of Techniques and Methodologies
NMR Spectra
Spectral Matching
Pattern Recognition
Expert Systems
Spectral Interpretation
Assignment Techniques
e.g. isotopic labels shift reagents
Shift Prediction
γ-gauche RIS, empirical shifts
Multi-pulse Methods
1D, 2D, 3D Methods
Polymer Microstructure
Main Chain Analysis
tacticity, regio-sequence copolymer sequence
Other Structures
chain ends, branching, crosslinks, defects
Other Analytical Techniques
SEC, LC, Fractionation
Polymerization Mechanism
Statistical Models
Analytical Approaches
computer-assisted methods
Simulation Approaches
computer-assisted methods

Figure 1. Information content available in the NMR data together with methods and techniques used to extract the information.

Statistical models (also known as reaction probability models) have been used extensively in polymer studies (*3–7*). They provide fundamental understanding of polymerization processes and serve as a theoretical framework whereby NMR, molecular weight, fractionation, and polymerization kinetics data can be analyzed in a rational manner. In many cases the models can assist in NMR spectral assignments and help interpret the spectral intensities. Sometimes they provide information on the mechanisms of initiation and propagation. Suitably applied, they may permit maximum amount of information to be obtained from each spectrum.

In this work a brief review is made of common statistical models being used and selected methodologies being applied in the NMR analysis of polymers, with a particular emphasis placed on the work done in the authors' laboratories.

Statistical Models

Over the years, many statistical models have been used to depict polymerization. New models have been devised for specific situations. The interrelationships of some of these models are shown in Figure 2.

One-State Models

The simple one-state models, such as Bernoullian (B), first-order Markovian (M1), second-order Markovian (M2), and enantiomorphic-site models (E) are well-known and have been previously described (*6*, *8*, *9*). It is important to note that with B, M1 and M2 models, the polymerization are chain-end controlled, whereas with E model, the polymerization is catalytic-site controlled (*8*, *10–12*). Models that provide dual control (both chain-end and catalytic-site) are also known and used (*7*, *11–13*). Other useful models include Markovian with reversible propagation (*14–16*), complex participation (*17*, *18*), and bootstrap models (*19*).

Two-State Models

These models are used when two separate states are involved in polymerization. The two states can be consecutive or concurrent (*20*). The consecutive two-state model can be applied to a polymerization where the catalytic site switches back and forth between two states as it polymerizes; the result may be a block copolymer consisting of blocks that conform to different statistics. The consecutive two-state model can also be used for other block copolymers or for a polymerization where the reaction condition changes during polymerization (e.g., changes in monomer feed, pressure, or temperature). The concurrent two-state model is basically a mixture model. It can be used for a polymerization where two separate active sites are present, each site making its own polymer according to its propagation statistics; in effect, a blend of two polymers is formed. The concurrent two-state model can also be used if a catalytic site switches back and forth between two states but the rate of switching is low relative to chain propagation and chain termination, and separate chains are formed that can be attributed to each of the two states (*20*).

Each of the two states can be Bernoullian (B) or enantiomorphic-site (E), giving rise to two-state B/B, B/E, or E/E models. The first two-state B/B model has been formulated by Coleman and Fox (*21*) and included both consecutive and concurrent features. The concurrent B/B model has been used to analyze NMR data of olefin copolymers (*22–25*). Similarly, the concurrent B/E model has been used to analyze the tacticity of polypropylene (*26*, *27*). Yet another two-state model has been reported by Ewen, et al (*13*, *28*) and used to analyze the NMR data of syndiotactic polypropylene made with metallocene catalysts; the model includes dual catalytic-site and chain-end control. In addition, a general treatment of the two-state consecutive models has been formulated (*20*); this is a structural approach that is different from the Coleman-Fox treatment and is applicable to two-state B/B, B/E, and E/E models These models have been used for the analysis

Downloaded by UNIV OF DELAWARE MORRIS LIB on June 20, 2012 | http://pubs.acs.org
Publication Date (Web): October 14, 2011 | doi: 10.1021/bk-2011-1077.ch022

of NMR tacticity data of elastomeric polypropylene (*29*, *30*). Variant models have also been proposed (*31*).

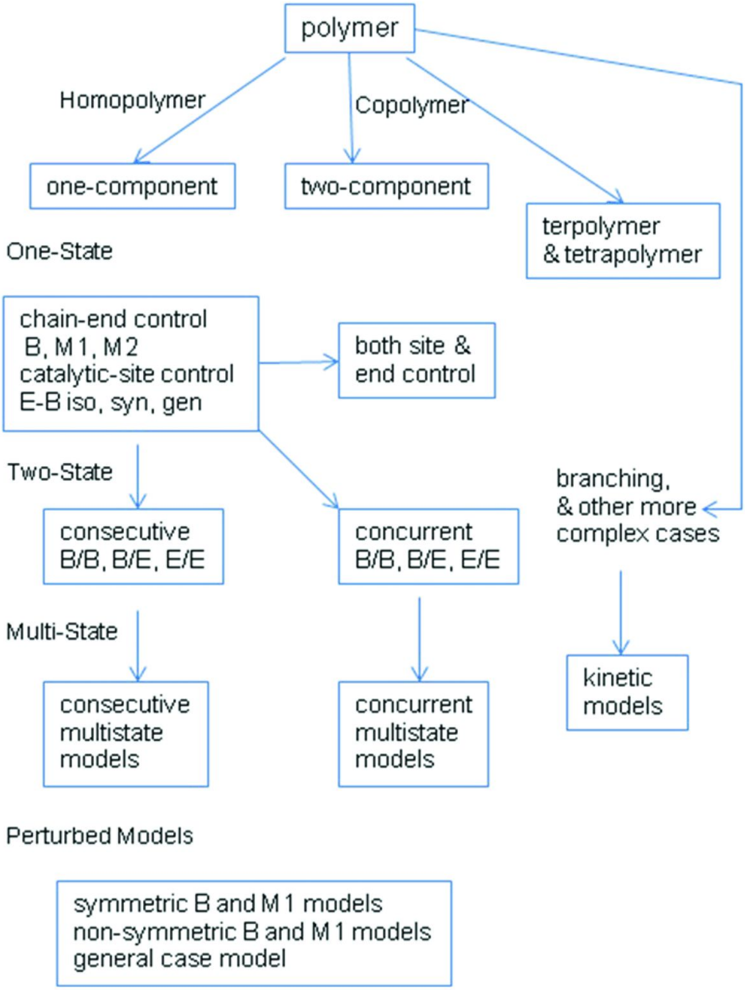
polymer
Homopolymer
Copolymer
one-component
two-component
terpolymer & tetrapolymer
One-State
chain-end control B, M1, M2 catalytic-site control E-B iso, syn, gen
both site & end control
Two-State
branching, & other more complex cases
consecutive B/B, B/E, E/E
concurrent B/B, B/E, E/E
Multi-State
kinetic models
consecutive multistate models
concurrent multistate models
Perturbed Models
symmetric B and M1 models
non-symmetric B and M1 models
general case model

Figure 2. A general scheme for selected statistical models commonly used for NMR characterization.

Multistate Models

Many polymers are found to have multiple polymeric components due to polymerization made at different catalytic sites, at different phases, or (in programmed monomer addition) at different times. The multistate models are useful for the analysis of these polymers. A general methodology involving multistate models has been reported (*25*, *32*). The analysis is facilitated when NMR data of polymer fractions (from fractionation or chromatographic

Downloaded by UNIV OF DELAWARE MORRIS LIB on June 20, 2012 | http://pubs.acs.org
Publication Date (Web): October 14, 2011 | doi: 10.1021/bk-2011-1077.ch022

separation) are available. The methodology has been applied to a large number of synthetic polymers, particularly those made from Ziegler-Natta catalysts which may contain more than two active sites, e.g., for the analysis of copolymer sequences (*25*, *32–39*) and homopolymer tacticity (*25*, *33*, *38*). In addition, it has been used on natural polymers, e.g., pectin (*40*, *41*) and alginate (*41–43*).

Perturbed Models

Many industrial (and some lab-made) polymers exhibit varying degrees of compositional heterogeneity. Compositional heterogeneity may also influence polymer microstructure, such as tacticity, composition, and sequence distribution. Perturbed Markovian (*44*, *45*) and enantiomorphic-site (*46*) models have been designed as convenient tools for the interpretation of compositional and tacticity data. In general, compositional heterogeneity can arise from many sources (*47–50*). Depending on the source(s) of heterogeneity, the chemical composition distribution (CCD) curve may take on a symmetric or non-symmetric appearance (Table 1) (*48*).

For the analysis of CCD or NMR data, multistate heterogeneity can usually be treated with multistate models. Perturbed models can be used for the treatment of the other three types of heterogeneities. Computations can be done via either analytical (*44–48*) or simulation approaches (*47–50*).

Downloaded by UNIV OF DELAWARE MORRIS LIB on June 20, 2012 | http://pubs.acs.org
Publication Date (Web): October 14, 2011 | doi: 10.1021/bk-2011-1077.ch022

Table 1. Different types of compositional heterogeneity. (adapted from (*45*))

type	*possible source(s) of heterogeneity*	*CCD curve*
statistical	statistical fluctuations in copolymer composition	symmetric
conversion	different comonomer reactivities	skewed or tent-shaped
multistate	1. different polymers made at different initiator sites or phases 2. programmed comonomer feeds 3. polymer blending 4. polymers from biological sources	variable (skewed to multimodal)
process	fluctuations in polymerization process conditions	symmetric or slightly skewed

Kinetic Models

Instead of reaction probabilities, an alternative treatment (*51*) uses the actual reactions taking place during polymerization. The resulting kinetic scheme can then be used to generate all requisite information corresponding to the observed NMR data, e.g., composition, sequence, branching, defect structure, and chain ends. These kinetic models are especially useful for the treatment of complex NMR data. For example, the kinetic model of a simple binary copolymerization

In NMR Spectroscopy of Polymers: Innovative Strategies for Complex Macromolecules; Cheng, H., et al.;
ACS Symposium Series; American Chemical Society: Washington, DC, 2011.

Downloaded by UNIV OF DELAWARE MORRIS LIB on June 20, 2012 | http://pubs.acs.org
Publication Date (Web): October 14, 2011 | doi: 10.1021/bk-2011-1077.ch022

has been reported (*51*). A detailed study of short- and long-chain branching in low-density polyethylene using kinetic modeling has also appeared (*52*).

Other Models

Most of the preceding discussion deals with homopolymer tacticity or sequence distribution of binary copolymers. The first-order Markovian model for ternary copolymerization (terpolymerization) is also known (*53*); an excellent example of its utility has been shown by Carman et al (*54*) for the analysis of NMR spectra of ethylene-propylene rubbers. The first-order Markovian model for quaternary copolymerization (tetrapolymerization) has also been formulated (*55*) with mathematical expressions for all relevant sequences. It has been used successfully for styrene-butadiene copolymers (*56*), where 1,2-, 1,4-trans, and 1,4-cis additions of butadiene to the propagating chain are regarded as three separate comonomers. The same model has been used for stereoirregular and regioirregular polypropylene (*57*), where primary and secondary insertions of propylene in two configurations are considered the four comonomers. The mathematical expressions for a pentapolymerization (involving 5 comonomers) would be very complex (*55*). A simulation approach for a pentapolymerization has been published for ethylene-propylene rubber (*48*, *58*); in that case, the five "comonomers" are ethylene, propylene in the primary insertion (up and down configuration), and propylene in the secondary insertion (up and down configuration).

The versatility of metallocene catalysts gives rise to new statistical models. Some of these have been recently reviewed (*59*). A new model ("E-B gen") will be described in the last section of this article.

Application Methodologies

Analytical Approaches

Whereas the models are useful for an understanding of polymerization mechanism and statistics, an appropriate methodology is needed to apply these models to the treatment of NMR data. Many methods and techniques have been developed for this purpose (*1–9*). Most of the methods can be grouped under the category of "analytical" approaches (*5*, *6*, *60*):

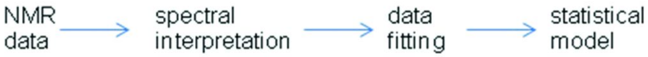

Thus, the NMR data of a polymer are first acquired and the spectral features assigned to pertinent polymer microstructures. Spectral intensities are then obtained, and calculations made to give copolymer composition and sequence distribution. A more refined treatment takes all assignable intensities in a spectrum and fits them to an appropriate statistical model, from which reaction probabilities can be derived (*54*, *60–62*). This approach has also been extensively

Downloaded by UNIV OF DELAWARE MORRIS LIB on June 20, 2012 | http://pubs.acs.org
Publication Date (Web): October 14, 2011 | doi: 10.1021/bk-2011-1077.ch022

used for many statistical models (*5–7*, *11*, *12*, *25*, *32*, *48*), often with some variations in methodologies (*63*, *64*).

Simulation Approaches

The second category of approaches can be called “simulation” (or "synthetic") approaches. The starting point here is an appropriate statistical model, from which composition and sequence distribution for a set of model parameters can be calculated through theory or computer simulation. The observed and the calculated sequence distribution can be compared and adjustments in the model parameters made until a satisfactory fit is obtained. A number of people have utilized this approach over the years (*59*, *60*, *62*, *65–68*). The advantage of this approach is that it is often easier to calculate the sequence distribution or to simulate the polymerization than to engage in a direct data fitting procedure for many polymeric systems.

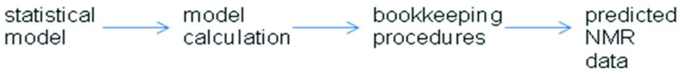

In one variation of this approach, one can take the reaction probabilities of a model and use Monte Carlo method to generate an ensemble of polymer chains, from which composition and sequence (and their heterogeneities) can be gathered (*49*, *50*, *66–68*). When good correlations between microstructures and chemical shifts are known, one can produce a predicted NMR spectrum. As an example, a general computer program has been written that can be used to calculate the copolymer sequences and to simulate the ^{13}C NMR spectra of vinyl and vinylidene copolymers and terpolymers (*67*, *68*). For polymers exhibiting stereoisomerism and regioisomerism, detailed ^{13}C shift rules incorporating tacticity, head-to-tail, head-to-head, and tail-to-tail structures are needed to produce simulated shifts or spectra. For example, such ^{13}C rules for polypropylene and ethylene/propylene copolymer have been obtained (*69*). For these two polymer systems, it is possible to simulate a range of polymer microstructures, including tacticity, regiosequences, and chain ends (*58*, *70*).

Integrated Approaches

A third category of methods incorporates elements of analytical and simulation approaches. The use of both approaches in suitable cases provides more detailed understanding of polymer microstructure and NMR shift/structure correlations. For example, for copolymers obtained at high conversion, the direct use of a statistical model can lead to wrong results; an integrated approach permits more correct results to be obtained (*71*). Other examples of integrated approaches have also been published (*48*, *72*).

Downloaded by UNIV OF DELAWARE MORRIS LIB on June 20, 2012 | http://pubs.acs.org
Publication Date (Web): October 14, 2011 | doi: 10.1021/bk-2011-1077.ch022

Kinetic Simulation Approaches

These approaches can be used with kinetic models (above). A schematic of this type of approaches is shown below.

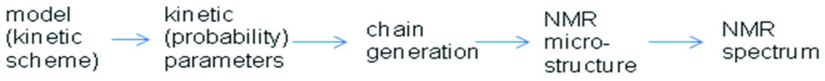

If we can formulate a realistic kinetic scheme of a polymerization under consideration, the scheme can then be used for simulation of polymer chain growth and NMR spectral prediction. Of course, rate constants need to be known either *a priori* or through model-fitting. Detailed descriptions of this approach have been reported earlier (*51*, *52*).

Program Polytact

Recently a convenient and pragmatic program, called Polytact, was reported by Miri, et al (*59*). It was written on the Excel software with the objective to calculate all relevant characteristics of the polymer tacticity and to present them in graphical form in a user-friendly manner using macros. Six types of tacticities can be produced with the program: isotactic, syndiotactic, atactic, hemiisotactic, stereoblock, and heterotactic (the latter meaning that ideally two adjacent substituents point in one direction followed by two substituents pointing in the other direction). Seven one-state statistical models were built into the program: B, M1, M2, E-B iso, E-B syn, E-B gen, and the E-M1 combination.

The "E-B gen" model is introduced for the first time in this program (*59*). It enables a user to model and simulate four different types of enantiomorphically controlled tacticities with one single model: isotactic, syndiotactic, atactic and hemiisotactic polymer. It is based on a simplified scheme, in which it is only relevant what the probabilities are for each of the two types of enantiofaces of the monomer to coordinate with each of the catalyst's two lateral, enantiotopic sites. Specific types of catalyst symmetry groups need not be explicitly considered in this model. Also, the equations for the pentads for the E-M1 model have been published for the first time in the article cited (*59*). The "E-B iso" and "E-B syn" models are to be used for isotactic and syndiotactic polyolefins, respectively. The model simulations have been applied to twenty polymers with different tacticities found in the literature (*59*).

A screen shot of the summary sheet of the program is shown in Figure 3. The program's user can select each of these models on an input window, and enter the corresponding numerical probabilities, e.g., P_{mm} and P_{rr} in case of the M1 model. The program then produces the following output: (1) the numerical dyad, triad, tetrad and pentad values for the specific input probability(ies), (2) bar diagrams for the triad and pentad values, (3) 2D or 3D graphs for the triad and pentad distribution over the entire probability range(s), depending on the model, (4) the average sequence lengths for the meso and racemic dyads, (5) a sequence length distribution graph, and (6) a graph for the simulation of 50 units in the polymer.

In addition, a tab can be selected on the input window to use short-cuts for the models (with stored ideal probabilities) to produce the six types of tacticities mentioned above. These are intended to help the beginning user to get familiar with the concepts more easily. Furthermore, a third tab can be selected to choose from different metallocene symmetries that cause certain tacticities; for example, by clicking the icon with the figure representing a metallocene with a C1 chirality, the program will produce data for a hemiisotactic polymer as output.

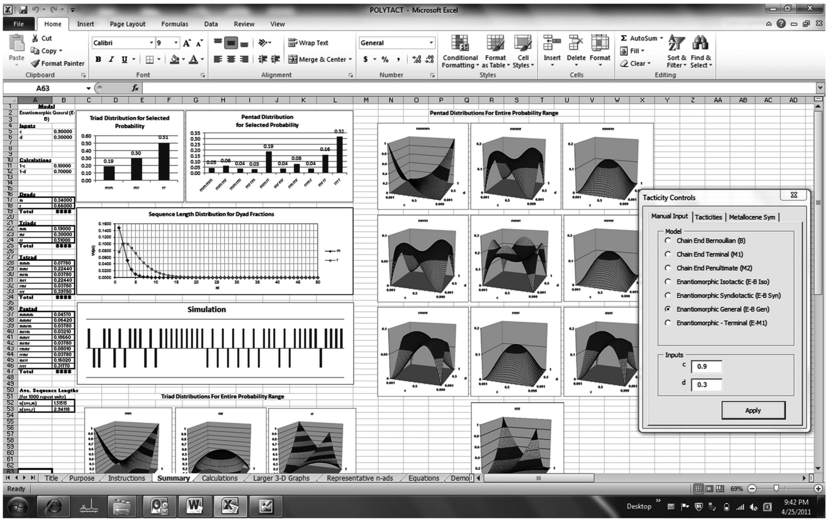
POLYTACT - Microsoft Excel
File
Home
Insert
Page Layout
Formulas
Data
Review
View
A63
Triad Distribution for Selected Probability
Pentad Distribution for Selected Probability
Pentad Distributions For Entire Probability Range
Sequence Length Distribution for Dyad Fractions
Simulation
Triad Distributions For Entire Probability Range
Title
Purpose
Instructions
Summary
Calculations
Larger 3-D Graphs
Representative n-ads
Equations
Ready
69%
9:42 PM
4/25/2011

A	B
Model	
Enantiomorphic General (E-B)	
Inputs	
c	0.90000
d	0.30000
Calculations	
1-c	0.10000
1-d	0.70000
Dyads	
m	0.34000
r	0.66000
Total	####
Triads	
mm	0.19000
mr	0.30000
rr	0.51000
Total	####
Tetrad	
mmm	0.07780
mmr	0.22440
mrm	0.03780
mrr	0.22440
rmr	0.03780
rrr	0.39780
Total	####
Pentad	
mmmm	0.04570
mmmr	0.06420
mmrm	0.03780
mrrm	0.03210
mmrr	0.18660
mrmr	0.03780
rmmr	0.08010
rrmr	0.03780
mrrr	0.16020
rrrr	0.31770
Total	####
Ave. Sequence Lengths	
(for 1000 repeat units)	
n(ave,m)	1.51515
n(ave,r)	2.94118

Tacticity Controls

Manual Input | Tacticities | Metallocene Sym

Model
- ○ Chain End Bernoullian (B)
- ○ Chain End Terminal (M1)
- ○ Chain End Penultimate (M2)
- ○ Enantiomorphic Isotactic (E-B Iso)
- ○ Enantiomorphic Syndiotactic (E-B Syn)
- ● Enantiomorphic General (E-B Gen)
- ○ Enantiomorphic - Terminal (E-M1)

Inputs
- c: 0.9
- d: 0.3

Apply

Figure 3. Screenview of the summary sheet of program Polytact with the movable input window on the right (applying the "E-B gen" model).

More detailed views of the 2D and 3D plots of the triad and pentad distributions are available on a separate spreadsheet in Polytact. These can be used to determine quickly which types of triads or pentads cannot be produced with certain models or what their maximum or minimum value is. For example, the [mmmm] pentad reaches a maximum 6.25% for a syndiotactic polymer (with a = 0.5), which is also the minimum value of [mmmm] for an isotactic polymer (with b = 0.5) using the E-B syn and E-B iso models, respectively. However, the [mmmm] pentad can become zero using the E-B gen model (when either both of its probabilities c and d approach zero or both probabilities approach 1).

A major use of the program Polytact is to compare experimental n-ad sequences, which can be obtained from NMR spectroscopy, with those calculated by the program. To test if the experimental data are in agreement with one of the seven models, one needs to take a set of n-ads and decide on the particular probabilities associated with a model. These probabilities then need to be entered into the program, and the resulting n-ad sequences can be compared to the corresponding experimental sequences. If the differences between the experimental n-ads and those calculated by the program lie within a reasonable

In NMR Spectroscopy of Polymers: Innovative Strategies for Complex Macromolecules; Cheng, H., et al.;
ACS Symposium Series; American Chemical Society: Washington, DC, 2011.

Downloaded by UNIV OF DELAWARE MORRIS LIB on June 20, 2012 | http://pubs.acs.org
Publication Date (Web): October 14, 2011 | doi: 10.1021/bk-2011-1077.ch022

margin of error, the actual polymerization is considered compatible with the particular model within the limit of experimental error.

The sequence distributions obtained can also be used to make predictions about the degree of order and crystallinity of a polymer or its other physical properties. If a polymer with a certain tacticity is to be grafted or modified during post-polymerization, predictions can be made about the polymer's reactivity as well.

The limitation of the program is that it currently includes only the seven given statistical models. Thus, it does not include tactictities which are based on two-state or multi-state models.. It may also be noted that the program represents a simulation approach; thus, optimization of reaction parameters can be done manually, but there is currently no provision for automated iteration.

The program will be made available by the authors upon request (e-mail: mjmsch@rit.edu, or hncheng100@gmail.com).

Downloaded by UNIV OF DELAWARE MORRIS LIB on June 20, 2012 | http://pubs.acs.org
Publication Date (Web): October 14, 2011 | doi: 10.1021/bk-2011-1077.ch022

Acknowledgments

Thanks are due to the many collaborators over the years. These include (in alphabetical order) G. N. Babu, Mark A. Bennett, J. C. W. Chien, John A. Ewen, Leo J. Kasehagen, R. A. Newmark, Michael T. Roland, and Stanley B. Tam. G. H. Lee, Thomas G. Neiss, and David A. Smith contributed to the applications of some of the models to several polymer systems. Moreover, B. P. Pritchard at RIT contributed to the writing of Program Polytact.

Mention of trade names or commercial products in this publication is solely for the purpose of providing specific information and does not imply recommendation or endorsement by the U.S. Department of Agriculture. USDA is an equal opportunity provider and employer.

References

1. Cheng, H. N., English, A. D., Eds.; *NMR spectroscopy of polymers in solution and in the solid state*; ACS Symposium Series No. 834; American Chemical Society: Washington, DC, 2002.
2. Brandolini, A. J.; Hills, D. D. *NMR spectra of polymers and polymer additives*; M. Dekker: New York, 2000.
3. Mirau, P. A. *A practical guide to understanding the NMR of polymers*; Wiley: Hoboken, NJ, 2004.
4. Kitayama, T.; Hatada, K. *NMR spectroscopy of polymers*; Springer: New York, 2004.
5. Cheng, H. N. *Structural studies of polymers by solution NMR*; RAPRA Review Reports, Vol. 11, Number 5; Rapra: Shewsbury, U.K., 2001.
6. Cheng, H. N. In *Encyclopedia of NMR*; Grant, D. M., Harris, R. K., Eds.; Wiley: New York, 1996; pp 3713−3721.
7. Cheng, H. N. In *New advances in polyolefins*; Chung, T. C., Ed.; Plenum Press: New York, 1993; pp 15−30.

8. Bovey, F. A. *High Resolution NMR of Macromolecules*; Academic Press: New York, 1972.
9. Koenig, J. L. *Chemical Microstructure of Polymer Chains*; Wiley: New York, 1980.
10. Price, F. P. In *Markov Chains and Monte Carlo Calculations in Polymer Science*; Lowry, G. G., Ed.; Marcel Dekker: New York, 1970; Chapter 7.
11. Cheng, H. N. In *Transition Metal Catalyzed Polymerizations: Ziegler Natta and Metathesis Polymerizations*; Quirk, R. P., Ed.; Cambridge Univ. Press: Cambridge, 1988, p 599.
12. Cheng, H. N. *J. Appl. Polym. Sci.* **1988**, *36*, 229.
13. Ewen, J. A.; Elder, M. J.; Jones, R. L.; Curtis, S.; Cheng, H. N. In *Catalytic Olefin Polymerizations*; Keii, T., Soga, K., Eds.; Kodansha: Tokyo, 1990, p. 439.
14. Izu, M.; O'Driscoll, K. F.; Hill, R. J.; Quinn, M. J.; Harwood, H. J. *Macromolecules* **1972**, *5*, 90.
15. Cais, R. E.; Hill, D. J. T.; O'Donnell, J. H. *J. Macromol. Sci., Chem. A* **1982**, *17*, 1437.
16. Szwarc, M.; Perrin, C. L. *Macromolecules* **1985**, *18*, 528.
17. Seiner, J. A.; Litt, M. *Macromolecules* **1971**, *4*, 308.
18. Hill, D. J. T.; O'Donnell, J. H.; O'Sullivan, P. W. *Prog. Polym. Sci.* **1982**, *8*, 215.
19. Harwood, H. J. *Makromol. Chem., Makromol. Symp.* **1987**, *10/11*, 331.
20. Cheng, H. N.; Babu, G. N.; Newmark, R. A.; Chien, J. C. W. *Macromolecules* **1992**, *25*, 6980.
21. Coleman, B. D.; Fox, T. G. *J. Chem. Phys.* **1963**, *38*, 1065.
22. Ross, J. F. In *Transition Metal Catalyzed Polymerizations, Alkenes and Dienes*; Quirk, R. P., Ed.; Harwood Academic: New York, 1983; p 799.
23. Cozewith, C. *Macromolecules* **1987**, *20*, 1237.
24. Floyd, S. *J. Appl. Polym. Sci.* **1987**, *34*, 2559.
25. Cheng, H. N. *J. Appl. Polym. Sci.* **1988**, *35*, 1639.
26. Zambelli, A; Locatelli, P.; Provasoli, A.; Ferro, D. R. *Macromolecules* **1980**, *13*, 267.
27. Zhu, S.-N.; Yang, X-Z.; Chujo, R. *Polym. J. (Tokyo)* **1983**, *12*, 859.
28. Ewen, J. A. In *Catalytic Polymerization of Olefins*; Keii, T., Soga, K., Eds.; Kodansha-Elsevier: Tokyo, 1986; p 271.
29. Babu, G. N.; Newmark, R. A.; Cheng, H. N.; Llinas, G. H.; Chien, J. C. W. *Macromolecules* **1992**, *25*, 7400.
30. Kravchenko, R.; Masood, A.; Waymouth, R. M.; Myers, C. L. *J. Am. Chem. Soc.* **1998**, *120*, 2039.
31. Gauthier, W. J.; Collins, S. *Macromolecules* **1995**, *28*, 3779.
32. Cheng, H. N. In *New Advances in Polyolefins*; Chung, T. C., Ed.; Plenum: New York, 1993; pp 159−174.
33. Cheng, H. N. *ACS Symp. Ser.* **1989**, *404*, 174.
34. Cheng, H. N.; Kakugo, M. *Macromolecules* **1991**, *24*, 1724.
35. Cheng, H. N. *Polym. Bull.* **1990**, *23*, 589.
36. Cheng, H. N. *Macromolecules* **1991**, *24*, 4813.
37. Cheng, H. N. *Polym. Bull.* **1991**, *26*, 325.

Downloaded by UNIV OF DELAWARE MORRIS LIB on June 20, 2012 | http://pubs.acs.org
Publication Date (Web): October 14, 2011 | doi: 10.1021/bk-2011-1077.ch022

38. Cheng, H. N. *Makromol. Chem., Theor. Simul.* **1992**, *1*, 415.
39. Masson, P.; Llauro-Darricades, M.-F.; Spitz, R.; Cheng, H. N. *Int. J. Polym. Anal. Charact.* **1996**, *2*, 379.
40. Neiss, T. G.; Cheng, H. N.; Daas, P. J. H.; Schols, H. A. *Macromol. Symp.* **1999**, *140*, 165.
41. Neiss, T. G.; Cheng, H. N. *ACS Polym. Prepr.* **2000**, *41* (2), 76.
42. Cheng, H. N. *Polym. Bull.* **1999**, *43*, 247.
43. Neiss, T. G.; Cheng, H. N. *ACS Symp. Ser.* **2002**, *834*, 382.
44. Cheng, H. N. *Macromolecules* **1992**, *25*, 2351.
45. Cheng, H. N. *Macromolecules* **1997**, *30*, 4117.
46. Cheng, H. N. *Makromol. Chem., Theor. Simul.* **1993**, *1*, 561.
47. Cheng, H. N. *J. Appl. Polym. Sci.: Appl. Polym. Symp.* **1992**, *11*, 21.
48. Cheng, H. N. *Polym. News* **2000**, *25*, 114.
49. Cheng, H. N.; Tam, S. B.; Kasehagen, L. J. *Macromolecules* **1992**, *25*, 3779.
50. Cheng, H. N.; Kasehagen, L. J. *Macromolecules* **1993**, *26*, 4774.
51. Cheng, H. N.; Kasehagen, L. J. *ACS Polym. Prepr.* **2003**, *44* (1), 381.
52. Cheng, H. N.; Kasehagen, L. J. *ACS Polym. Prepr.* **1997**, *38* (1), 863.
53. Ham, G. E. *Copolymerization*; Interscience Publishers: New York, 1964.
54. Carman, C. J.; Harrington, R. A.; Wilkes, C. E. *Macromolecules* **1977**, *10*, 536.
55. Roland, M. T.; Cheng, H. N. *Macromolecules* **1991**, *24*, 2015.
56. Cheng, H. N.; Roland, M. T. *ACS Polym. Prepr.* **1991**, *32* (1), 549.
57. Cheng, H. N. *Macromol. Theory Simul.* **1994**, *3*, 979.
58. Cheng, H. N.; Bennett, M. A. *Makromol. Chem.* **1987**, *188*, 2665.
59. Miri, M. J.; Pritchard, B. P.; Cheng, H. N. *J. Molecular Modeling*, 2010, published online: DOI 10.1007/s00894-010-0880-8.
60. Cheng, H. N. *J. Appl. Polym. Sci.: Appl. Polym. Symp.* **1989**, *43*, 129.
61. Cheng, H. N. *J. Chem. Inf. Computer Sci.* **1987**, *17*, 8.
62. Crowther, M. W.; Begemann, J. H.; Levy, G. C. *ACS Symp. Ser.* **1989**, *404*, 161.
63. Cheng, H. N. *ACS Polym. Prepr.* **2003**, *44* (1), 381.
64. Cheng, H. N.; Gillette, P. C *Polym. Bull.* **1997**, *38*, 555.
65. Harwood, H. J. *J. Polym. Sci.: Part C* **1968**, *25*, 37.
66. Harwood, H. J.; Chen, T.-K.; Lin, F.-T. *ACS Symp. Ser.* **1984**, *247*, 197.
67. Cheng, H. N.; Bennett, M. A. *Anal. Chem.* **1984**, *56*, 2320.
68. Cheng, H. N. *Trends Anal. Chem.* **1994**, *13*, 95 and references therein.
69. Cheng, H. N.; Bennett, M. A. *Makromol. Chem.* **1987**, *188*, 135 and references therein.
70. Cheng, H. N. *Macromol. Symp.* **1994**, *86*, 77.
71. Cheng, H. N. *Int. J. Polym. Anal. Charact.* **1997**, *4*, 71.
72. Cheng, H. N. *Int. J. Polym. Anal. Charact.* **1996**, *2*, 439.

Downloaded by UNIV OF DELAWARE MORRIS LIB on June 20, 2012 | http://pubs.acs.org
Publication Date (Web): October 14, 2011 | doi: 10.1021/bk-2011-1077.ch022

Downloaded by OHIO STATE UNIV LIBRARIES on June 21, 2012 | http://pubs.acs.org
Publication Date (Web): October 14, 2011 | doi: 10.1021/bk-2011-1077.ch023

Chapter 23

Composition and Phase Morphology of Hard/Soft Acrylic Latex Polymers: NMR and AFM Study

Kebede Beshah* **and Robert F. Antrim**

The Dow Chemical Company, 727 Norristown Road,
Spring House, PA 19477
***E-mail: KBeshah@dow.com**

Butyl Acrylate (BA) and Methyl Methacryate (MMA) copolymers with different molar ratios in latex particles lead to segregated hard and soft nanodomains. The presence of both monomers in the hard and soft nanodomains is challenging for traditional techniques for morphology studies such as Transmission Electron Microscopy (TEM) due to lack of atomic contrast. We have used NMR experiments together with statistical analysis of comonomer sequences to determine the composition of the monomers in each phase coupled with Atomic Force microscopy (AFM) to probe the phase morphology and particle sizes. The synergy of the two techniques provides the opportunity to probe interface mixing between the continuous soft phase and the segregated hard phase that has some impact on the final size of the hard and soft phases after film formation.

Introduction

Emulsion polymer particles for coatings applications (about 100 nm in size) need to coalesce during film formation in order to form transparent and crack free films that provide hardness for better scrub and dirt pickup resistance of paints (*1–3*). Such opposing properties of softness for coalescence and hardness after film formation have been circumvented by applying coalescing agents such as Texanol (2,2,4-trimethyl-1, 3- pentanediol monoisobutyrate) that help with plasticization of the polymer during film formation and later evaporates to leave a

In NMR Spectroscopy of Polymers: Innovative Strategies for Complex Macromolecules; Cheng, H., et al.;
ACS Symposium Series; American Chemical Society: Washington, DC, 2011.

relatively hard film. With the drive to reduce and even eliminate volatile organic compounds (VOC) from the environment, formulators are looking for ways to achieve film formation at ambient temperature while maintaining certain degree of hardness. One of the approaches involve designing a hard and soft morphology within the same latex particle of the binder (*4*). The soft component delivers the film formation property at ambient temperatures while the hard components provide the mechanical strength and aids in dirt pick-up resistance. In some designs the soft phase forms the continuous phase while the hard phases could be as low as 10% and with nanodomain sizes below 20 nm. Such designs make it very difficult for the standard analytical methods such as DSC, DMA, and TEM to study phase segregation (*5*).

The challenge is exacerbated by the design of the hard and soft components from the same pair of monomers, methyl methacrylate (MMA) and butyl acrylate (BA). MMA rich BA/MMA copolymer provides the hard phase while a BA rich BA/MMA copolymer forms the soft phase. A lack of atomic mass differentiation and the similarities in components makes it difficult to image by TEM. In addition, the lack of specific stains to differentiate MMA from BA is a limitation of TEM. The widely dispersed nanodomains of less than 20 nm sizes provide challenges to detect a glass transition temperature of the hard phase by DSC and DMA.

In this study we have used a combination of solution and solid state NMR together with Scanning Probe Microscopy (SPM) to determine the phase behaviors and obtain quantitative information on the phase segregated latex particles. SPM is sensitive to hard and soft components and the technique is capable of differentiating these in a film. In some instances, the similarities in chemical composition could also lead to phase mixing that has significant effect on detecting less that 5 nm domain sizes even by Scanning Probe Microscopy (SPM). NMR permits the study of such systems as solid films by solid state NMR or in solution where the comonomer sequence reveals the heterogeneity of the polymer and the possible phase segregation.

Downloaded by OHIO STATE UNIV LIBRARIES on June 21, 2012 | http://pubs.acs.org
Publication Date (Web): October 14, 2011 | doi: 10.1021/bk-2011-1077.ch023

Experimental Section

Materials

The emulsion polymers for this study were made using standard emulsion polymerization techniques (*6*). The model ladder statistical emulsion polymers of varying BA/MMA mole ratios are synthesized using standard procedures with thermal initiation and a gradual monomer feed time of about 2 hours for the polymerization. This provides for uniform composition of the copolymers even for monomers with varying reactivity ratios compared to batch polymerization that invariably leads to heterogeneous polymer chains as dictated by reactivity ratios of the monomers than by intentional design. The complex polymers (Samples 2, 3 and 4) require a staged feed protocol in order to achieve the desired hard and soft components.

Downloaded by OHIO STATE UNIV LIBRARIES on June 21, 2012 | http://pubs.acs.org
Publication Date (Web): October 14, 2011 | doi: 10.1021/bk-2011-1077.ch023

Nuclear Magnetic Resonance Spectroscopy

The solution and solid state NMR experiments were all done on a Bruker AVANCEIII 400 MHz spectrometer. The solution NMR experiments were done on latex polymers that were dissolved in tetrahydrofuran (THF-d_8) at room temperature. For the solid state experiments, circular disks of about 6 mm in diameter were punched out of the films and stacked in a 7 mm sample rotor for cross polarization and magic angle spinning (CPMAS) experiment. We have also used 4 mm sample rotors where the film is introduced after a strip had been rolled to fit the inner diameter of the rotor. The Cross Polarization mix times for the high temperature experiments were chosen to be 1 ms in order to optimize the discrimination of the hard and soft components.

We have used the well established Bernoullian distribution (*7*, *8*) for a binary radical copolymerization of BA and MMA, the statistical comonomer sequence is well approximated by:

$$\mathbf{P(m,n,f)} = \binom{m}{n}(f_{BA})^{n}(1-f_{BA})^{m-n}$$

$$= \frac{m!}{(n!)(m-n)!}(f_{BA})^{n}(1-f_{BA})^{m-n}$$

Where: m = number of sites; for our triads, $m = 3$.
n = 0,1,2,…,m
f_{BA} = the fraction of one of the components; in this case, mole ratio of BA.

Scanning Probe Microscopy (SPM), a.k.a. AFM

Characterization of these emulsions consisted of evaluating the dried films and faces cut tangential to the surface of the film. All AFM images have been obtained using Bruker's D 5000 scanning probe microscope, Santa Barbara, CA. The tapping mode was used to obtain the images and operated under ambient conditions. A FESP tip (Bruker) was chosen for imaging and operated at a frequency 5% lower than its harmonic frequency. The engage set point was 0.8, gains and scan speed were adjusted to allow good tracking of the tip with the surface. Both phase and height images were collected simultaneously.

The dried films were prepared using 8 mil gauge bar to draw the emulsion along Mylar substrate. The film was then air dried. Small samples were placed into the instrument for imaging. All cryo faces were prepared by air drying a puddle of material. A small piece was cut out and glued onto a bulls eye pin mount (Electron Microscopy Sciences, Hatfield, Pa) and cryo faced on a Reichert FCS Cryo Ultramicrotome using a diamond knife (Diatome, Hatfield, Pa) , at -60°C. Image analysis was carried out using either Scanning Probe Image Processor (SPIP) or image analysis on version 6 software.

Downloaded by OHIO STATE UNIV LIBRARIES on June 21, 2012 | http://pubs.acs.org
Publication Date (Web): October 14, 2011 | doi: 10.1021/bk-2011-1077.ch023

Results and Discussion

Solution State NMR: Quantitative Analysis with Standards

The solution state ^1H NMR lineshapes of BA/MMA statistical copolymers have characteristic signals due to the comonomer sequence structures (*9–11*). Model samples with a composition ladder provide a vivid illustration of the effects of nearest and next nearest neighbors in the chemical shifts of species of interest. As mentioned above, these copolymers were made with a standard radical polymerization of emulsion polymers. Hence, they illustrate close to a random distribution of near neighbors distribution since the reactivity ratio differences are compensated for by slow feed rates of monomers during polymerization.

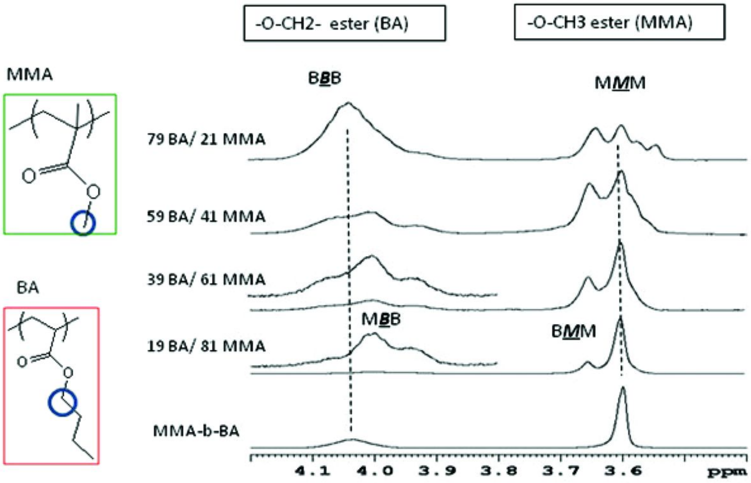

Figure 1. Partial ^1H NMR spectrum of BA/MMA statistical copolymers and a block copolymer to illustrate the effect of near neighbors on the spectra.

Figure 1 shows an expanded region of interest of the ^1H spectrum from 3.4 to 4.3 ppm of the ladder composition of BA/MMA copolymers. The signals centered at 3.6 ppm are due to $–OCH_3$ (methyl ester) of MMA and the signals centered at 4 ppm are due to $–OCH_2$- (methylene ester) of BA as shown by the circles in the figure. These signals are particularly sensitive to nearest and next nearest neighbor monomers in the polymer sequence. For example, the $–OCH_2$- signal of BA is sensitive to whether it is in a triad sequence between two other BAs (*B**B**B*), or a BA and MMA unit (*B**B**M*), or *M**B**M* triad. Similarly, the MMA signal gives rise to a variety of peaks compared to a poly methyl methacrylate homopolymer, which has just one peak centered at 3.6 ppm, due to sequencing effects (*B**M**M* and *B**M**B*). We are not going to go into details of sequence distribution analysis in this report. Extensive studies of Bernoullian distribution in copolymers have been reported by other workers (*7*, *8*). We will focus only on the part of the sequence analysis relevant to our morphology study.

As illustrated in the figure, the relative intensities of the fine structures for BA and MMA change as the molar ratio of BA and MMA changes in the sample. We have only shown the effect of triad sequences, but one can envision that in some favorable cases we could also have well resolved signals from tetrad and pentad sequence effects on the spectra giving us rich information on copolymer sequences as discussed by many authors in a variety of polymers including heterogeneity effect studied by perturbed first-order Markovian distribution (*7–20*).

Since these lineshapes of random distributions are characteristic of radical polymerization, we can use them to determine if we have any heterogeneous composition that would lead to hard and soft morphologies.

The glass transition temperature (Tg) of poly methyl methacrylate homopolymer is greater than 110ºC depending upon the tacticity while poly butyl acrylate has Tg about -60ºC. There is a linear relationship between Tg and MMA or BA fraction in the copolymer as shown in Figure 2 below. Heterogeneous polymers with segregated BA rich and MMA rich components would lead to a SOFT (low Tg component from the BA rich composition) and a HARD (high Tg component from the MMA rich composition). In some instances it is difficult to register the presence of segregated hard and soft phases due to the total amount and the particle size of the dispersed phase.

Downloaded by OHIO STATE UNIV LIBRARIES on June 21, 2012 | http://pubs.acs.org
Publication Date (Web): October 14, 2011 | doi: 10.1021/bk-2011-1077.ch023

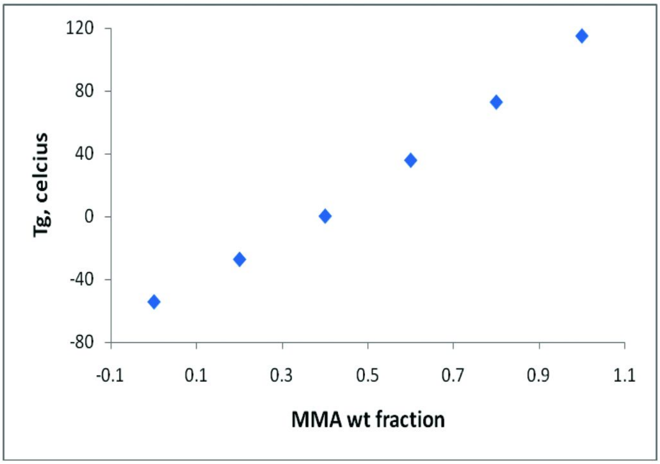

Figure 2. Tg of BA/MMA copolymers as a function of mole fractions.

Heterogeneous Polymer of Known Composition

Figure 3 shows the high resolution ^{1}H NMR spectrum of a heterogeneous polymer, Sample 2. We have also plotted model polymers of known composition to assess the composition of the hard and soft phases. As indicated above, the MMA signals of Sample 2 show fine structures due to triad monomer sequences ($B\underline{M}M$ and $M\underline{M}M$) similar to copolymer composition in the range of 20BA/80MMA to 40BA/60MMA. Based on the integration of the $B\underline{M}M$ and $M\underline{M}M$ triad sequences as discussed below, we estimate the composition of the polymer that is responsible for the MMA signal pattern in Sample 2 is 34BA/66MMA which is essentially the similar to the synthesis ratio of 35%BA and 65%MMA.

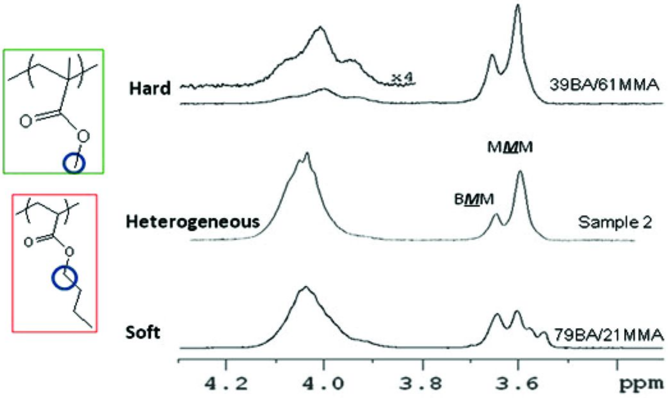

Figure 3. Solution NMR of heterogeneous polymer (Sample 2) and reference homogeneous statistical copolymers.

On the other hand, the BA signal at 4 ppm for Sample 2 resembles that of 100% BA. In the model sample with about 80% BA we note that the MMA signals have strong features at 3.5 ppm due to neighboring BA. These signals are not detected in the heterogeneous Sample 2 spectrum, which indicates that the BA component of the SOFT phase of Sample 4 is close to 100%.

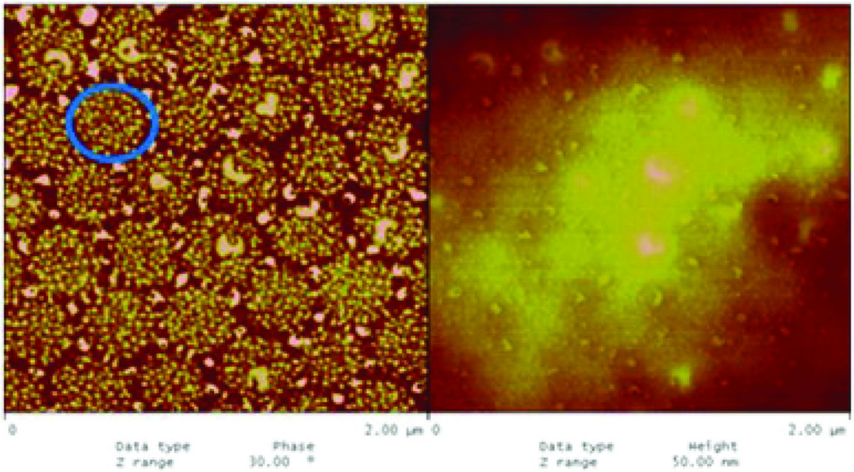

Figure 4. 2µm AFM image of Sample 2, phase image (left) and height image (right). A circle is drawn to aid visualization of the individual particles.

Using the Bernoullian distribution equation (experimental section) and the intensities of the signals of the triad sequences, we estimate the MMA rich

Downloaded by OHIO STATE UNIV LIBRARIES on June 21, 2012 | http://pubs.acs.org
Publication Date (Web): October 14, 2011 | doi: 10.1021/bk-2011-1077.ch023

Downloaded by OHIO STATE UNIV LIBRARIES on June 21, 2012 | http://pubs.acs.org
Publication Date (Web): October 14, 2011 | doi: 10.1021/bk-2011-1077.ch023

component to be 24% of the total polymer with composition of 65MMA/35BA and the BA rich component to be 76% of the total polymer with composition of greater than 90% BA. These values agree well with the synthesis composition of 25% (64MMA/34BA/2AA) and 75% (92BA/7AN/1AA).

From DSC measurement we could only detect one phase transition at -26ºC that is attributed to the BA rich component of the heterogeneous polymer. The lack of a clear transition for the MMA rich phase in spite of the 25% hard phase components could indicate the presence of dispersed nanodomains of the MMA rich phase. We used Scanning Probe Microscopy (SPM), sometimes referred to as Atomic Force Microscopy (AFM), which excels in the imaging of hard/soft polymer domains.

In Figure 4, the 2 µm phase image, on the left, shows greater details of the particles surface. Here we can start to see the individual spherical particles centered at 400 nm in diameter, and the well distributed smaller hard component (bright spots) on the surface. In addition, bright non-spheroid features are also seen on top of the particles, which are tentatively assigned to surfactant migration to the surface. The hard components of the particles are readily observed on the surface, which are well controlled in particle size and spacing.

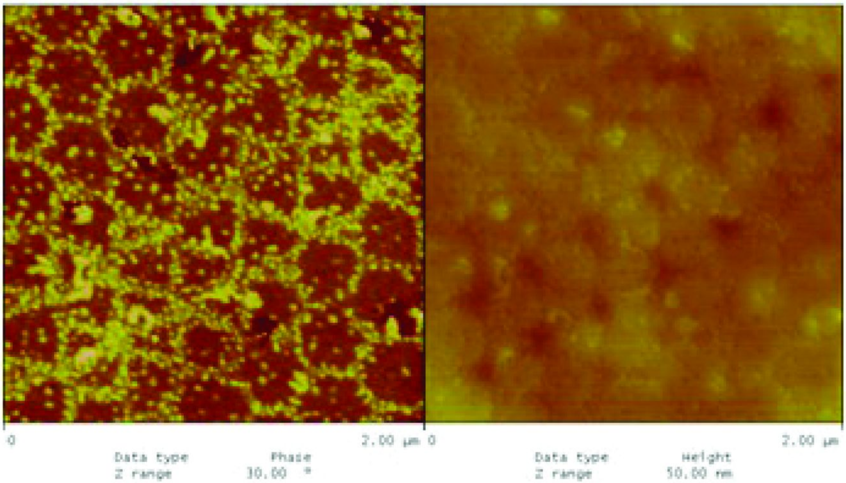

Figure 5. 2 µm AFM of cryo faced Sample 2; phase image on left and height image on right.

To determine if the hard component is found only on the outer surface of the particle or within the particle, a cryo microtomy with perpendicular incision was used to reveal the interior of the film and particles. The phase image of the cryo surface in Figure 5 with higher magnification (2µm x 2µm) shows more clearly the edges of the particles and the distribution of the harder component. It is seen that the hard phase is predominately found on the outer edge of the particles. The emulsion particles after film formation no longer look as spherical as they did on the surface. The deformation of the particle is commonly seen during film formation. Deformation of the particles to form the film increases the contact

Downloaded by OHIO STATE UNIV LIBRARIES on June 21, 2012 | http://pubs.acs.org
Publication Date (Web): October 14, 2011 | doi: 10.1021/bk-2011-1077.ch023

surface area between the particles forming a more rigid structure. From image analysis, we obtained that 20% of the polymer is from the hard component in good agreement with 25% obtained by NMR.

Heterogeneous Polymer with Unknown Composition

In some instances, the polymerization process could lead to compositional heterogeneity that is not readily deduced from the synthesis process. These are probably the best conditions for the application of NMR and SPM techniques where NMR provides the compositional information and SPM the phase morphology as we saw above for a known system.

In Figure 6, we have solution state ^1H NMR spectra of three samples. For better visual comparison, the spectrum of Sample 1 is also overlaid on the spectrum of Sample 3 and the Sample 3 spectrum on Sample 4 with dashed lines. Note that the –O-**CH$_2$**- ester signal of BA (at about 4 ppm) is essentially identical for the three copolymers, while there is a difference in the MMA ester (-O-CH$_3$) signal.

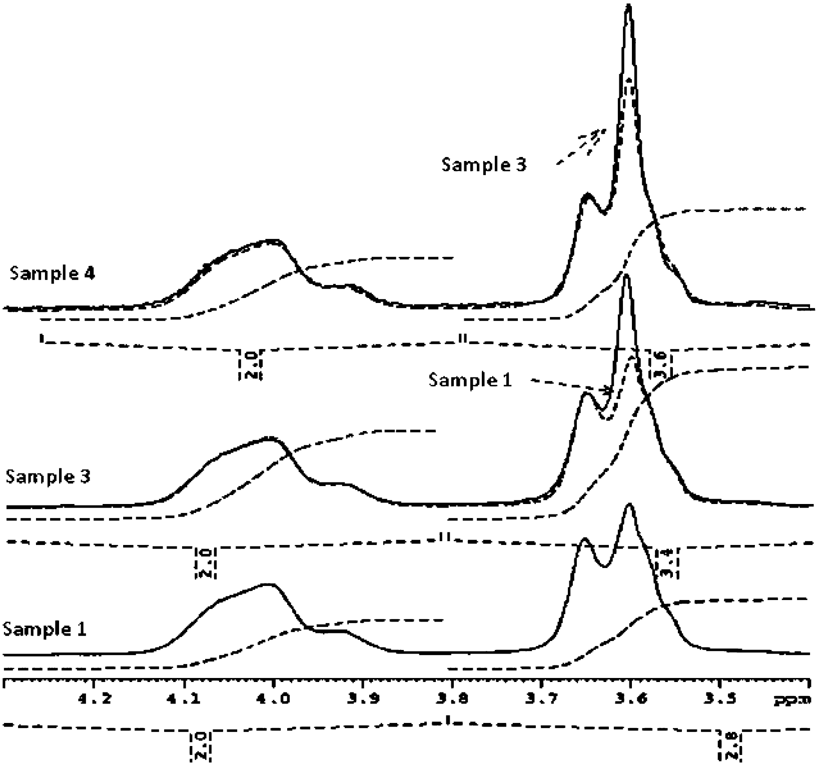

Figure 6. Solution state ^1H NMR of Samples 1 (statistical 58BA/42MMA copolymer) and heterogeneous polymers, Samples 3 and 4.

Downloaded by OHIO STATE UNIV LIBRARIES on June 21, 2012 | http://pubs.acs.org
Publication Date (Web): October 14, 2011 | doi: 10.1021/bk-2011-1077.ch023

From the integrals of MMA and BA signals as well as the triad sequence structures, we can readily determine that the signal for Sample 1 is from a homogeneous random polymerization of 58BA/42MMA copolymer as we have observed in the ladder compositions in Figure 1. On the other hand, the spectrum for Sample 3 shows similar lineshape as that of Sample 1 except for higher intensity of one of the multiplicity at 3.6 ppm , the *MMM* triad; compare this signal with the spectral patterns in the model ladder compositions in Figure 1. A random copolymer of BA and MMA in Sample 3 could not explain this higher intensity at 3.6 ppm. Note that the 3.6 ppm signal is characteristic of MMA rich copolymer (bottom of Figure 1) or from a blocky poly methyl methacrylate sequence. So, this additional intensity at *MMM* has to arise from another heterogeneous sequence distribution of the polymer that is mainly due to MMA rich phase.

The signal for Sample 4 shows even higher MMA block (*MMM*) signal at 3.6 ppm compared to Sample 1 and Sample 3, while the rest of the spectral pattern fits a similar 58BA/42MMA random copolymer lineshape. Hence, Sample 3 and 4 are heterogeneous polymers with one phase comprised of BA rich copolymer (58BA/42MMA) and another that is predominantly MMA. We can now assess the relative composition of the heterogeneous phases based on the precedent qualitative analysis since we know the actual composition of Sample 1. The BA signal in Samples 3 and 4 is from a BA rich polymer matrix (phase) similar to Sample 1, hence the BA ratio in the soft phase has to be 58%, the same as Sample 1. At this stage we can assume that almost all of BA is derived from the soft phase of the 58% BA copolymer and we can rewrite the relative integration we obtained from the figure to reflect that we have a 58% BA containing copolymer. Hence, the proportional amounts of all BA and MMA in Sample 3 copolymer is rewritten from 53BA/47MMA to 58BA/51MMA, a simple proportional adjustment. Knowing that we have now a 58%BA/42%MMA component, we further rewrite the total composition as; 58BA/51MMA = 58BA/42MMA//9MMA = 53.2BA/38.5MMA//8.3MMA, to normalize the total composition to 100%. Given that we do not observe lineshape difference between Sample 1 and Sample 3 and 4 except for the *MMM* triad sequence, we conclude that there might be only a small amount of BA, if any, in the MMA rich component of the heterogeneous polymer. Similarly, we determine that Sample 4 is 51.8BA/37.5MMA//10.7MMA. Hence, Sample 3 and 4 are heterogeneous polymers with about 90% BA rich soft phase and about 10% predominantly poly methyl methacrylate polymers.

Quantitative Analysis without a Standard

In the previous analysis we used a standard copolymer that has essentially identical BA rich copolymer which helped with a visual comparison of the heterogeneous polymer. It is not always possible to obtain a copolymer with exactly the same composition as one of the components of the heterogeneous polymer. So, we need an approach that would not require a standard sample to match the compositions until we find the one that fits, which could lead to a tedious trial and error task in synthesis. Even though the ^{1}H NMR lineshape is sensitive to comonomer compositions, accurate integration of the triad signals

Downloaded by OHIO STATE UNIV LIBRARIES on June 21, 2012 | http://pubs.acs.org
Publication Date (Web): October 14, 2011 | doi: 10.1021/bk-2011-1077.ch023

($B\underline{\boldsymbol{B}}B$, $B\underline{\boldsymbol{B}}M$, $M\underline{\boldsymbol{B}}M$) is difficult due to peak overlap. So, we turn to ^{13}C NMR spectroscopy where one of the side chain methylene signals (-O-CH_2-$\underline{\mathbf{C^{*}H_2}}$ -CH_2-CH_3) at about 30.1 – 30.8 ppm is also sensitive to comonomer sequences. One of the triad segments ($M\underline{\boldsymbol{B}}M$) for -O-$CH_2$-$\underline{\mathbf{C^{*}H_2}}$ -CH_2-CH_3 is uniquely resolved from the rest of the signals at 30.28 ppm permitting an integration of this signal as shown in Figure 7. In the Figure, we have included four random copolymers with known compositions of random distribution for the validation of the approach and the two heterogeneous Samples 3 and 4. Since we can only resolve the $M\underline{B}M$ triad sequence signal, we will just determine its ratio with respect to all the triads ($M\underline{B}M$, $B\underline{B}B$, $M\underline{B}B$) intensities.

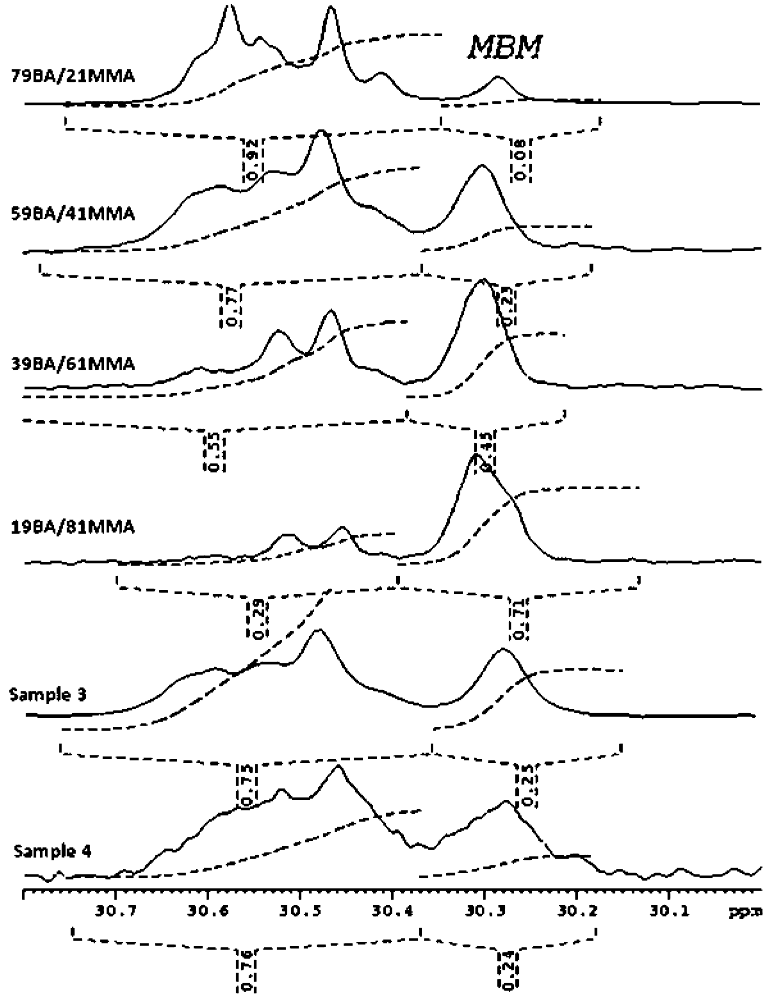

Figure 7. A partial ^{13}C solution NMR of statistical homogeneous copolymers (top 4) and heterogeneous polymers (bottom 2). Only the highlighted -O-CH_2-$\underline{C^{*}H_2}$ -CH_2-CH_3 signal is shown.

We can now calculate the probability of the $M\underline{\mathbf{B}}M$ occurrence for any composition of BA/MMA using Equation 1. For example, for a 39BA/61MMA copolymer with mole ratio of 33.3BA/66.7MMA; for triads, m=3 and $f_{BA} = 0.333$, the various relevant probabilities (P) are given by:

$P_{B\underline{B}B} = (f_{BA})^3 = (0.333)^3 = 0.037$

$P_{M\underline{B}B} = P_{B\underline{B}M} = 2/3\ (P_{B\underline{B}M,\ M\underline{B}B,\ BMB}) = 2(f_{BA})^2(1\text{-}f_{BA})^1 = 2(0.333)^2(0.667)^1 = 0.148$

$P_{M\underline{B}M} = 1/3\ (P_{M\underline{B}M,\ MMB,\ BMM}) = (f_{BA})^1(1\text{-}f_{BA})^2 = (0.333)^1(0.667)^2 = 0.148$

The probability, $P_{M\underline{B}B}$, is the placement of two BAs and one MMA in a triad sequence; *BBM, MBB, BMB*. For our BA signal analysis, we are only interested in those triads with BA at the center. So, we are only interested with 2/3 of the $P_{M\underline{B}B}$ probability. Similarly, only 1/3 of the probability of two MMAs and one BA give us BA at the center of the triad sequence ($M\underline{\mathbf{B}}M$, *MMB, BMM*). Hence, converting the wt% composition of 0.39BA/0.61MMA to mole%, we obtain 0.333BA/0.667MMA , the sum of these probabilities is ($P_{B\underline{B}B} + P_{M\underline{B}B} + P_{M\underline{B}M}$) = 0.037 + 0.148 + 0.148 = 0.333 = f_{BA}, where f_{BA} = mole fraction of BA in comonomer

Hence the relative amount of $M\underline{\mathbf{B}}M$ from the Bernoullian distribution is given by: $P_{M\underline{B}M}/(P_{B\underline{B}B} + P_{M\underline{B}B} + P_{M\underline{B}M}) = P_{M\underline{B}M}/f_{BA} = (0.148/0.333) = 0.444 = I_{M\underline{B}M}$ compared to 0.45 from integration of the experimental data in Figure 3, where I_{MBM} is the fractional experimental integral of $M\underline{\mathbf{B}}M$ triad.

This approach does not require any standard and the composition of the soft component is readily determined by comparing the experimental integral and the calculated probability. The conversion from experimental integral of the $M\underline{\mathbf{B}}M$ signal to that of the composition is straight forward using the above relations; i.e., P_{MBM}/f_{BA} = the *MBM* fractional integral in Figure 7.

We can rewrite $P_{MBM}/f_{BA} = f_{BA}(1\text{-}f_{BA})^2/f_{BA}$, using Equation 1 to define $P_{MBM} = f_{BA}(1\text{-}f_{BA})^2$. Hence, the experimental integral, I_{MBM}, and the probability, P_{MBM}, are correlated as: $P_{MBM}/f_{BA} = f_{BA}(1\text{-}f_{BA})^2/f_{BA} = I_{MBM}$, where I_{MBM} is the fractional, experimental integral of *MBM*, and after simplification, $(1\text{-}f_{BA})^2 = f_{MMA}{}^2 = I_{MBM}$, since $(1\text{-}f_{BA}) = f_{MMA}$. $f_{MMA} = \sqrt{}(I_{MBM})$, remember that f_{MMA} is mole fraction of MMA in the BA rich component. This relationship enables us to determine the mole fraction of MMA directly from the integrals of the experimental spectra such as Figure 5. For example, for Sample 4, this integral is given by 0.24. Using the relation, $f_{MMA} = \sqrt{}(I_{MBM})$, f_{MMA} is determined from $\sqrt{}(0.24) = 0.4899$, $f_{BA} = (1\text{-}f_{MMA}) = 0.5101$. We can thus convert it to weight ratio of 57BA/43MMA. Note that we obtained 58BA/42MMA for this component with a comparison to a known standard, Sample 1.

Below is a table of experimental and calculated values of the *MBM* fractional amount among the triads. For the heterogeneous polymers, the table also provides the weight ratios calculated from the experimental data using the equation derived above.

Downloaded by OHIO STATE UNIV LIBRARIES on June 21, 2012 | http://pubs.acs.org
Publication Date (Web): October 14, 2011 | doi: 10.1021/bk-2011-1077.ch023

Downloaded by OHIO STATE UNIV LIBRARIES on June 21, 2012 | http://pubs.acs.org
Publication Date (Web): October 14, 2011 | doi: 10.1021/bk-2011-1077.ch023

Table 1. Experimental and calculated molar ratio of MBM on model copolymers and soft phase composition of segregated copolymer

SAMPLE (wt. ratio)	$\frac{MBM}{(M\underline{B}M+MBB+BBB)}$ *Experimental*	$\frac{P(MBM)}{P(M\underline{B}M+MBB+BBB)}$ *Calculated*	*Weight ratio calculated* $f_{MMA} = \sqrt{(I_{M\underline{B}M})}$
79BA/21MMA	0.08	0.07	
59BA/41MMA	0.23	0.23	
39BA/61MMA	0.45	0.44	
19BA/81MMA	0.71	0.71	
Sample 3	0.25		56.2BA/43.8MMA
Sample 4	0.24		57BA/43MMA

Clearly, we have a very good match of the BA rich composition. In this case, however, we did it without any need for a standard sample. Matching the spectral features of the unknown with a known standard that happen to have the same composition is a daunting task. One should remember that in the presence of crosslinking and interphase diffusion, the Tg would not be a reliable source for the use of the Fox equation to obtain the composition of each phase. In the case of Sample 3 and 4, we do not have any indication of the presence of a heterogeneous polymer by DSC or DMA measurements.

The use of this approach will require high signal to noise and resolution spectrum in order to calculate the composition accurately. Otherwise, we will get erroneous results due to poor integrals of the spectra. We are also assuming that the contribution of the BA from the hard phase is minimal and we need to have any of the independent checks we have in this report such solid state NMR and solution state ^{1}H NMR lineshapes to ascertain the presence of phase segregation. Whenever possible use of integration from other regions of the spectrum, such as carbonyl region, will enhance the accuracy of the results in Table 1.

In the preceding discussion we have determined that we do have heterogeneous composition of the copolymers in Sample 3 and 4 with a BA rich BA/MMA copolymer and another predominantly MMA composition in the complex. Since all the compositional calculation was done in solution, we do not have any indication if these heterogeneous polymers segregate to provide a hard and soft phase in the polymer film. For that we need to study the films by solid state NMR and AFM.

Solid State NMR

In Figure 8, the solid state CPMAS NMR spectra of Samples 1, 3 and 4, taken at ambient temperature are shown. The signal of Sample 1, the homogeneous 58BA/42MMA, is also overlaid (dashed lines) on the other two heterogeneous polymers for better visual comparison. Note that we have excluded the carbonyl

Downloaded by OHIO STATE UNIV LIBRARIES on June 21, 2012 | http://pubs.acs.org
Publication Date (Web): October 14, 2011 | doi: 10.1021/bk-2011-1077.ch023

carbon signal at about 176 ppm from these spectra in order to expand and display the more informative section.

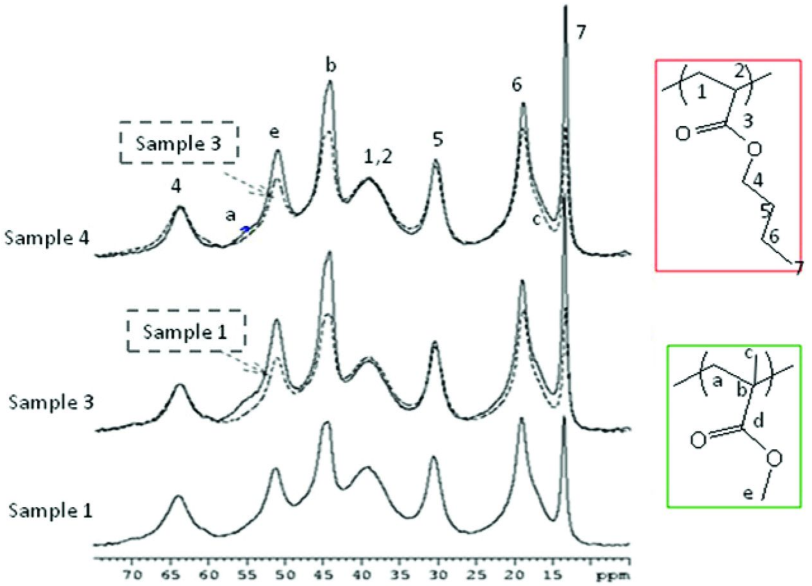

Figure 8. Room temperature 13C CPMAS spectra of Samples 1, 3, and 4.

The resonance assignments are shown in the spectrum for the various moieties of the copolymers. Some of the backbone methylene signals of the nearest neighbor BA/MMA sequences (BBM, MBM, BMM, BMB) are shifted downfield and upfield respectively from the homopolymer resonances and are spread between 40 and 50 ppm resulting in the broad signal close to the baseline. The intensity of the ester –O**CH$_2$**- signal of BA at 64 ppm is normalized for this comparison. We readily observe that while the BA signals are similar in intensity except for peaks 3 and 4 of the butyl group that will be addressed later, the MMA signals at 51, 45, 15-20 ppm for Samples 3 and 4 are higher than those for sample 1. This is consistent with what we have seen from solution spectra where Samples 3 and 4 have similar BA rich component as Sample 1 and, in addition, they both have a predominantly poly methyl methacryate component in the complex. As shown from the plot of Tg as a function of MMA composition of the complex, if there is phase segregation, the predominantly MMA segment of the complex is expected to have Tg as high as 100°C. So raising the sample temperature during CPMAS experiment to about 90°C will increase the mobility of the BA rich segment of the polymer that has Tg close to 0°C, hence reducing the efficiency of the cross polarization transfer for the BA rich component while retaining the CP efficiency of the predominantly MMA component of the polymer.

In Figure 9 a set of solid state NMR spectra are shown for Sample 3 at 90°C. The top spectrum is a standard direct polarization (DP) ^{13}C spectrum with quantitative representation of all species irrespective of their mobility (phase). The middle spectrum is obtained by CP and the intensity of the backbone signals at about 40 ppm is normalized to the DP spectrum in the top plot; the backbone signals being less mobile even at 90ºC will have comparable intensities with both DP and CP experiments. The DP spectrum (top) has signals of the butyl side chains of BA as the most intense peaks due to their highly mobile domain as they are almost 100 degrees above their Tg. In contrast, and as expected, we observe that the methyl group signal of BA is the least intense with the cross polarization experiment. This is because the -CH_3 group in the soft, low Tg, phase of the copolymer is the most mobile with weak dipolar coupling, hence the least efficient to cross-polarize.

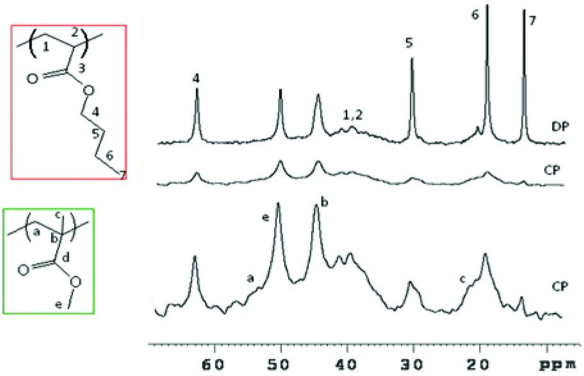

Figure 9. DP and CP experiments of Sample 4 at 90ºC. The bottom spectrum is a vertical expansion of the middle spectrum for better visualization.

The CP signals that are most intense at 90ºC are those of MMA indicating a higher CP efficiency which is consistent with a strong dipolar coupling environment for MMA that one would expect from a hard phase. We acknowledge that we lost a good portion of the MMA signal with CP compared to DP (top spectrum) even if we detect mainly MMA signals with CP at 90ºC. This is because most of MMA of the total heterogeneous polymer is in the BA rich phase copolymerized with BA, which constitute the soft phase, hence with poor CP efficiency.

We do indeed observe weak BA signals after cross polarization at 90ºC and we attribute these signals partly due to small BA components in the hard phase MMA rich composition. More likely, it could be from some soft phase polymer segments that interdiffuse into the isolated hard phases leading to a restricted motion that in turn leads to CP signal.

Figure 10 shows the ^{13}C CPMAS experiment taken at about 90ºC for all three samples. We notice that the signal to noise is poor in general for all samples. This is an indication that the sample is predominantly of 'softer' material at 90ºC.

Even though we have significantly reduced the signals by CP experiment at 90ºC for Sample 1 (the homogeneously low Tg polymer), we do indeed observe some residual signals from mainly the backbone and the species close to the backbone, namely the ester methylene (BA) and α-methyl (MMA). There is

Downloaded by OHIO STATE UNIV LIBRARIES on June 21, 2012 | http://pubs.acs.org
Publication Date (Web): October 14, 2011 | doi: 10.1021/bk-2011-1077.ch023

Downloaded by OHIO STATE UNIV LIBRARIES on June 21, 2012 | http://pubs.acs.org
Publication Date (Web): October 14, 2011 | doi: 10.1021/bk-2011-1077.ch023

one exception to this observation, the relatively restricted backbone species, the quaternary carbon signal of MMA at 45 ppm, is barely detected in this experiment. A quaternary carbon with no directly bonded proton and in a soft domain will have the least efficiency in cross polarization transfer since it is the farthest from protons; one of the two necessary conditions for efficient cross-polarization as discussed in the experimental section above – rigidity and proximity to ^{1}H are missing for the 45 ppm signal of MMA (peak b in the figure) in a soft polymer matrix (Sample 1).

We still observe some signals from the backbone protonated carbons and those very close to the backbone (-OCH2- for BA at 64 ppm and –OCH3 for MMA at 51 ppm) since these moieties still have some restricted motions even at 90ºC and owing to the proximity of ^{1}H rich environment. Unlike DSC and DMA, where we observe the dynamics for the bulk polymer as a whole, NMR, as a powerful molecular probe, discriminates between the dynamics of the backbone and sidechain groups. As one would expect, the side chains are more mobile than the backbone groups hence their signals diminish the most with CP at higher temperatures.

Sample 3 and 4 also show diminished signals for the BA sidechains similar to Sample 1 indicating a similar dynamics or copolymer environment and the presence of a soft phase in these films. On the other hand, some of the MMA signals at 54, 51, 45, 15-23 ppm remain the most intense in the spectra due to their rigid environment within the polymer. In other words, we have two segregated phases in Samples 3 and 4; a SOFT phase, consisting of BA/MMA copolymers that behaved the same as Sample 1 under CP and a hard phase consisting of a predominantly MMA component with much higher CP efficiency.

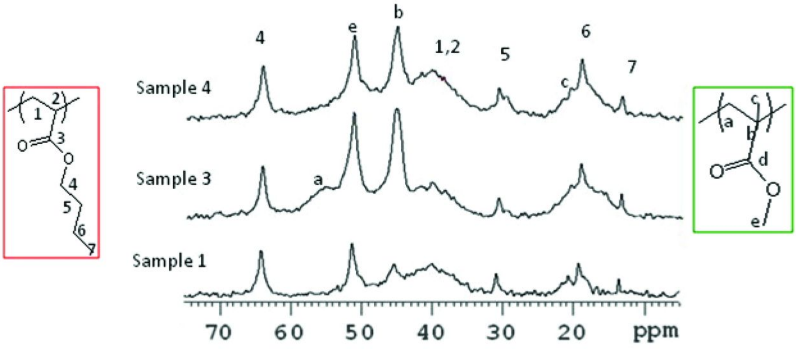

Figure 10. CPMAS spectra of Samples 1, 3, and 4 at 90ºC.

The MMA signals in Sample 3 are slightly stronger than those of Sample 4, especially the 54 ppm broad peak that is due to the backbone –CH$_2$- signal of MMA. The diminished 54 ppm signal in Sample 4 is an indication that the hard phase MMA in Sample 4 is probably copolymerized with more BA than the corresponding hard phase in Sample 3. Even a slightly higher level of BA in the hard phase will have an effect of shifting some of the backbone –CH$_2$- signal of

MMA in Sample 4 from 54 ppm towards 40-50 ppm. A closer look at about 40 ppm region of the spectra indicates that sample 4 has higher intensity consistent with having more BA in the hard phase compared to sample 3. Hence, Sample 4 is likely to contain more BA in the hard phase that could lower its Tg more than that of the hard phase of Sample 3. This could lead to a relatively more miscible hard and soft phases of Sample 4 compared to Sample 3.

Figure 11 shows the 2 micron images obtained from the cryo face of Sample 4. Unlike the images in Figure 4 and 5, the particle morphology is not well defined and appears to be well distributed throughout the polymer film. This type of distribution is indicative of a different type of polymerization. In addition, the contrast in brightness of the phase appears to differ. There is a gradual change of the brightness of the "harder" component.

From image analysis of the AFM data, we determined that about 26% of the polymer constitutes the bright spots that are attributed to the hard phase of the polymer. This is in contrast to 11% hard composition from the NMR analysis. Note that the NMR analysis is based only on the heterogeneous composition of the polymer and could not account for any interdiffusion that might occur resulting in different amount of hard/soft domains of the film except some qualitative indication we saw from CP intensities at 90°C.

Downloaded by OHIO STATE UNIV LIBRARIES on June 21, 2012 | http://pubs.acs.org
Publication Date (Web): October 14, 2011 | doi: 10.1021/bk-2011-1077.ch023

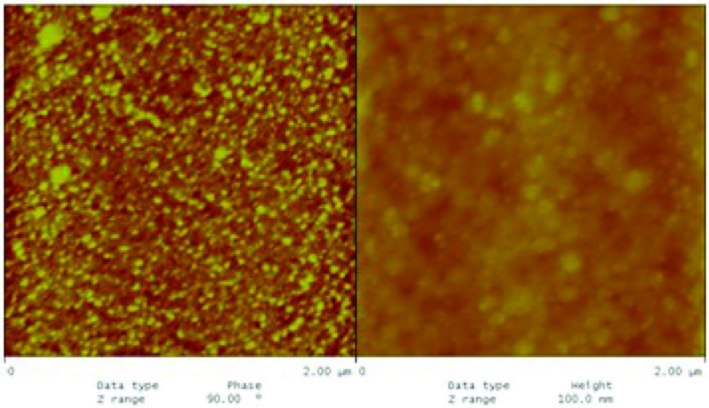

Figure 11. AFM image of Sample 4, 2um image. Phase image on left; height image on right.

Such interdiffusion between (meth)acrylic heterogeneous polymers has been studied earlier (*21*) where an interface structure showed a gradient (gradual) composition change from BA rich to MMA rich component. Such interface structures could bring more BA rich component close to the MMA rich phases leading to an increase in the rigidity of some of the BA rich (soft phase) components. In other words, we have more material in the hard phase of the polymer than the 11% we calculated based on the composition from the analysis of the solution phase spectra. Such gradient mixed phase may also be responsible for the lack of DSC and DMA phase transitions as we also expect to have a Tg

In NMR Spectroscopy of Polymers: Innovative Strategies for Complex Macromolecules; Cheng, H., et al.;
ACS Symposium Series; American Chemical Society: Washington, DC, 2011.

gradient which does not permit a clear phase transition by the two methods. We note that in some favorable cases, for example involving styrene, DSC, DMA and TEM could also indicate interphase mixing of latex polymers (*22*).

Summary

We have employed a combined NMR and AFM methods to probe challenging phase morphology where we have similar types of monomers in both hard and soft phases. In addition, the MMA rich hard phase is well dispersed in the soft BA rich phase with particle sizes below 20 nm. The NMR data provided us with composition in each phase with solid state NMR experiment providing the existent of a segregated hard and soft phase with the chemical composition information.

Unlike TEM, AFM does not require any atomic contrast between the two phases. It is based on the modulus of the various phases, hence ideal for hard and soft phase characterization. AFM data provided us with the distribution of the various phases including particle sizes of the dispersed phase.

The synergy between the two methodologies goes beyond just determining chemical composition in each phase by NMR and morphology by AFM. We were able to obtain the effect of interdiffusion between the two phases where the amount of hard and soft phases is determined to be different from that of the synthesis composition.

References

1. Steward, P. A.; Hearn, J.; Wilkinson, M. C. *Adv. Colloid Interface Sci.* **2000**, *86*, 195–267.
2. Sperry, P. R.; Snyder, B. S.; O'Dowd, M. L.; Lesko, P. M *Langmuir* **1994**, *10*, 2619–2628.
3. Blandin, H. P.; David, J. C.; Vergnaud, J. M.; Illien, J. P.; Malizewicz, M. *J. Coat. Technol.* **1987**, *59* (746), 27–32.
4. Eckersley, S. T.; Helmer, B. J. *J. Coat. Technol.*, *69* (864), 97–107.
5. Stubbs, J. M.; Sundberg, D. C. *J. Coat. Technol. Res.* **2008**, *5* (2), 169–180.
6. Athley R. D., Jr. *Emulsion Polymer Technology*; Marcel Dekker Inc.: New York, 1991.
7. Bovey, F. A. *High Resolution NMR of Macromolecules*; Academic Press: New York, 1972
8. Koenig, J. L. *Chemical Microstructure of Polymer Chains*; Wiley: New York, 1980.
9. Kim, Y.; Harwood, H. J. *Polymer* **2002**, *43*, 3229–323.
10. Candau, F.; Zekhnini, Z.; Heatley, F. *Macromolecules* **1986**, *19* (7), 1895–1902.
11. Anders, M.; Smulders, W.; Acrdts, A. M.; van Herk, A. M. *Macromolecules* **1997**, *30*, 322–323.
12. Cheng, H. N.; Tam, S. B.; Kasehagen, L. J. *Macromolecules***1992**, *25*, 3779. Cheng, H. N. *J. Appl. Polym. Sci.***1992**, *51*, 21.
13. Cheng, H. N. *Macromolecules* **1992**, *25*, 2351.

Downloaded by OHIO STATE UNIV LIBRARIES on June 21, 2012 | http://pubs.acs.org
Publication Date (Web): October 14, 2011 | doi: 10.1021/bk-2011-1077.ch023

14. Cheng, H. N. *Macromolecules* **1997**, *30*, 4117.
15. Bujak, P.; Henzel, N.; Matlengiewicz, M. *J. Polym. Anal. Charact.* **2008**, *13* (3), 149–162.
16. Brar, A. S.; Kaur, S. *J. Polym. Chem.* **2005**, *43*, 1100–1118.
17. Aerdts, A. M.; German, A. L.; van der Velden, G. P. M. *Magn. Resonance Chem.* **1994**, *32*, S80–S88.
18. Beshah, K. *Macromol. Chem.* **1993**, *194*, 3311–3321.
19. Beshah, K. *Macromol. Symp.* **1994**, *86*, 35–46.
20. Randall, J. C. *Polymer Sequence Determination, Carbon13 NMR Method*; Academic Press: New York, 1977.
21. Beshah, K.; Molnar, L. K. *Macromoleules* **2000**, *33* (2), 1036.
22. Colombini, D.; Ljungberg, N.; Hassander, H.; Karlson, O. J. *Polymer* **2005**, *46*, 1295.

Downloaded by OHIO STATE UNIV LIBRARIES on June 21, 2012 | http://pubs.acs.org
Publication Date (Web): October 14, 2011 | doi: 10.1021/bk-2011-1077.ch023

Downloaded by CORNELL UNIV on June 20, 2012 | http://pubs.acs.org
Publication Date (Web): October 14, 2011 | doi: 10.1021/bk-2011-1077.ch024

Chapter 24

Application of Melt-State NMR Spectroscopy for Polyolefin Characterization in Industry

Gerhard Hubner, Isa Fonseca, and Matthew Parkinson[*]

Borealis Polyolefine GmbH, St-Peters-Strasse 25, Linz, Austria
[*]E-mail: matt.parkinson@borealisgroup.com

Melt-state ^{13}C NMR spectroscopy of polyolefins has been shown to be sensitive, quantitative and allow rapid sample throughput. The method was implemented in an industrial research and development environment and has proved to be both highly sensitive and versatile. For general problem solving melt-state MAS NMR was found to complement standard high-temperature solution state NMR. The main strength of the technique was found to be the possibility of high throughput, due to the combination of high sensitivity and rapid sample preparation. This was most clearly demonstrated for materials of low solubility. A broad scope of application of melt-state MAS NMR is demonstrated through the study of the whole family of polyolefins including HDPE homopolymers, HDPE copolymers, LLDPE, LDPE, LDPE copolymers, PP homopolymers and PP copolymers. The application of the techniques to the study of fractionated materials and filled materials is also demonstrated. Some key advantages as compared to standard solution-state NMR spectroscopy are emphasized and recent research on decoupling in the molten-state is presented.

Introduction

The macroscopic properties of polyolefins are strongly dependant on their polymer chain microstructure. Through a variety of modern analytical techniques a clear understanding of the microstructure of polyethylene (PE) and polypropylene (PP) may be gained. The application of such analytics has

In NMR Spectroscopy of Polymers: Innovative Strategies for Complex Macromolecules; Cheng, H., et al.;
ACS Symposium Series; American Chemical Society: Washington, DC, 2011.

allowed a better understanding of the various polymerization processes and in-turn facilitates greater synthetic control over polyolefin chain microstructure. Polymerization of olefins is commonly undertaken using either a low pressure processes using heterogeneous catalysis (PE and PP) or a high-pressure radical process (PE).

The physical properties of PEs produced by heterogeneous catalysis in a low-pressure process can be tuned by the presence of branches of various lengths in the polymer backbone. Through copolymerization of ethylene with α-olefins, short chain branches (SCB) can be introduced in a controlled way (*1–12*). Such branches form structural defects during crystallization and thus strongly affect crystallization rates, ultimate crystallinity, melting point, glass transition and other bulk mechanical properties (*13*). In contrast, macromonomer incorporation during polymerization leads to long-chain branches (LCB). With these branches typically being longer than the entanglement molecular weight their presence strongly affects the processability of the bulk polymer (*14*, *15*). The nature of the process allows for the production of high-density polyethylene (HDPE) and linear low-density polyethylene (LLDPE). In contrast, if produced by radical polymerization in a high-pressure process, polyethylene typically has a wider variety of branch types (*16*, *17*). The possible high content of structural defects results in low-density polyethylene (LDPE). Although a very large number of reactions are possible, in practice only a limited number of key structures are observed in significant concentration, due to differences in stability of reactive intermediates and associated rearrangement reactions (*16*). The radical nature of the high-pressure process also allows the copolymerization of polar commoners, facilitating for further tuning of physical properties. In general SCB content and distribution as well as comonomer sequence distribution are the defining properties of PE microstructure.

The physical properties of PPs produced by heterogeneous catalysis in a low-pressure process are also strongly dictated by their chain microstructure (*18–22*). For homopolymers stereo- and regio-regularity play a key role in crystallization, whereas for propene based copolymers chain defects derived from comonomer incorporation also play an important role. As such tacticity, regio-regularity, comonomer content, commoner sequence distribution, total defect content and various sequence lengths are the defining properties of PP microstructure.

A variety of analytical techniques are sensitive to polyolefin microstructure, these include infrared (IR) spectroscopy, differential scanning calorimetry (DSC) (*13*, *15*), triple-detection gel permeation chromatography (GPC) (*21*, *23*) and rheology (*14*, *24–32*). The analytical technique that has provided the most direct insight into polyolefin microstructure however is NMR spectroscopy, and in particular quantitative ^{13}C NMR spectroscopy (*26*, *27*). When applied to polyolefins this method allows direct access to quantitative information about, tacticity, comonomer content, SCB distribution and monomer sequence distribution (*17*, *19*).

The typical implementation of NMR spectroscopy undertakes analysis of the sample in the solution-state, however when applied to polyolefins a number of problems arise (*26*, *33*, *34*). The most important being low solubility

Downloaded by CORNELL UNIV on June 20, 2012 | http://pubs.acs.org
Publication Date (Web): October 14, 2011 | doi: 10.1021/bk-2011-1077.ch024

Downloaded by CORNELL UNIV on June 20, 2012 | http://pubs.acs.org
Publication Date (Web): October 14, 2011 | doi: 10.1021/bk-2011-1077.ch024

of polyolefins, even at high temperatures (*35*, *36*) and in solvents such as trichlorobenzene (TCB) or tetrachloroethane (TCE). The low concentration of ^{13}C nuclei results in extended measurement times, especially for the quantification of very low levels of branching. Typically between 6-12 hours are needed for a single high quality spectrum suitable for further spectral analysis. Despite these limitations considerable effort is still made to optimize both the sample preparation and acquisition of quantitative ^{13}C solution-state NMR spectra of polyolefins.

Recently, the alternative implementation of quantitative ^{13}C melt-state NMR spectroscopy has been shown to address some of the limitation of the standard solution-state approach, while still providing high quality results (*37–42*). Through the combination of high spin concentrations and motional averaging of line broadening interactions (*43–48*) by the application of common solid-state NMR resolution enhancing methodologies, resolution and sensitivity is considerably increased. In practice the use of magic-angle spinning (MAS) and high-power dipolar decoupling allow high-resolution spectra to be obtained from polymers in the bulk molten state. When approximations are made with respect to key acquisition parameters, further considerable timesaving may also be made with respect to standard quantitative ^{13}C NMR spectroscopy (*38–42*). In addition to time saving during acquisition further time saving is also made due to the removal of the solution-state sample preparation stage. The latter also has important safety advantages, as toxic solvents no longer need to be handled. In addition to the investigation of chain branching in polyolefins this implementation has also been used to investigate sparse branching in other polymer systems, which have proven problematic for quantitative solution-state ^{13}C NMR analysis (*49*).

Experimental Section

Materials

All material presented were selected to demonstrate the wide application possibilities of melt-state NMR spectroscopy. Materials were produced from a variety of catalysts and polymerization conditions and range from full plant scale products, through pilot scale lots to materials produced at bench-scale. As such all material can be considered to be typical commercial polyolefin grades suitable for a variety of applications with standard microstructures, molecular weights, molecular weight distributions and rheological behavior.

Hardware Setup

All melt-state NMR spectra were obtained on a Bruker Avance III 500 solid-state NMR spectrometer with a 11.4 T wide-bore magnet. All spectra were obtained using a custom Bruker high-temperature (WVT) 7 mm MAS probehead with the double-resonance coil optimized for ^{13}C detection and compensated for operation under a pure nitrogen atmosphere. Standard 7 mm zirconia rotors zirconia rotor caps were also used (*39*). Sample temperature for all PEs were

Downloaded by CORNELL UNIV on June 20, 2012 | http://pubs.acs.org
Publication Date (Web): October 14, 2011 | doi: 10.1021/bk-2011-1077.ch024

150°C, whereas for PP based systems typically 180°C was used. Temperature calibration of the MAS probehead was carried out using $Pb(NO_3)_2$ in the standard manner. Samples were spun between 3 and 5 kHz using a standard MAS controller using a custom spin-up procedure, to ensure no overlap of MAS spinning side bands with spectral signals. Shimming was undertaken on the ^1H line-shape; and all quantitative ^{13}C spectra were acquired using standard single-pulse excitation (SPE) with ^1H dipolar decoupling (DD). Excitation was achieved using a 10 us 90° pulse. Due to the long spin-spin relaxation times (T_2) encountered for molten polyolefins low-load dipolar decoupling sequences were employed (*38*, *39*). For decoupling 20 us 180° pulses and associated delays were used. To ensure optimum time efficiency shorter than true quantitative pulse repetitions delays were used ($< 5\ T_1$) e.g. 3 s for PE copolymers. However, close attention was paid to ensure signals used during spectral analysis were quantitative with respect to each other (*38–40*). For all experiments a dwell time of 15 us was used for a spectral window of 265 ppm (33.3 kHz). An acquisition time of 571 ms was used based upon a duty cycle of 8 % which resulted in the digitization of 38056 complex data points. The FID was zero-filled to 64k data points prior to Fourier-transformation and Lorentz-to-Gauss apodization used.

Spectral Analysis Setup

To ensure repeatable analysis of quantitative ^{13}C NMR spectra a set of fully automated module spectral analysis programs was implemented. Such an approach was necessary due to the rapid rate at which spectra were produced. Such programs assess the presence of key substructures, integrate the spectrum, calculate primary quantitative results, calculate secondary result from the primary results, fit the results to models and report all quantitative results with the spectra as PDF and CSV files.

Results and Discussion

Comparison of Melt-State and Solution-State NMR

When standard solution-state and melt-state ^{13}C NMR spectra of a PE are compared it is clear that high-resolution has been achieved in the molten-state (Figure 1). All sites needed for further quantification are resolved and limited significant differences are seen between the two spectra. Upon closer inspection of the bulk CH_2 signals it can be seen that the line widths in the melt-state spectra are broader. However, as most spectral analysis methods tend to integrate groups of signals, quantitative analysis is not hindered. The broader line widths are mostly due to residual dipolar coupling, which is more problematic to remove in the molten state due to the long spin-spin relaxation times (*37–40*). With respect to sensitivity, both spectra have the same signal to noise ratio, however higher quantification accuracy is achieved for melt-state due to the broader lines observed resulting in larger integrals. Although 200 mg of PE was used for both implementations and the same signal-to-noise was achieved the solution-state spectra required 6.5 h of measuring time whereas only a 1 h measurement was needed for the melt-state. When combined with sample preparation the total time for the solution-state setup was 8 h whereas only 1.5 h was needed to obtain a melt-state spectrum. In practice a compromise between sensitivity and resolution is made with less sample preparation and measurement time needed for the melt-state implementation (*39*).

Scalar Coupling Mediated Method in the Molten State

With melt-state NMR considered to be closer to solid-state NMR than solution state NMR, the possibility of applying spectral editing with multidimensional pulse-sequences to molten polyolefins was assessed. The melt-state techniques were found to be amenable to such methods with only minor modifications to the pulse sequences to account for slow MAS. The spectral editing methods of DEPT and INEPT were both applicable with INEPT found to be more robust in the molten-state (*39*). As to why DEPT was more susceptible to pulse mis-adjustment remains unclear, however the influence of residual dipolar couplings or rotor synchronization issues is suspected. The use of INEPT has been found to particularly useful for assignment, especially when comparing to chemical shifts encountered in the solution-state e.g. when solvent effects exchange the location of CH and CH_2 signals. More advanced multi-dimensional techniques were also found to be possible such as INADEQUATE which benefited from the enhanced sensitivity and has proved useful for the conformation of assignments (*39*).

Advanced Low-Load Dipolar Decoupling

With strong residual heteronuclear dipolar couplings present in the molten-state high-power dipolar decoupling methods commonly applied in solid-state NMR need to be employed. Whereas in the solid-state the dipolar network remains fixed during the rotor period in the molten state the dipolar network is constantly changing. In practice this means that the advances in heteronuclear dipolar decoupling commonly used in solid-state NMR based on phase modulation during the decoupling block e.g. TPPM are not applicable in the molten state. Thus continuous wave (CW) decoupling still provided the best performance. The alternative approach of composite pulse based low power decoupling, common in solution state ^{13}C NMR, has previously been shown to not be beneficial in the molten-state (*39*). Although CW decoupling provides the best performance, hardware constraints based on amplifier duty cycle limits its application to a few tens of milliseconds. For true solids this is not a problem as T_2 are short and FID truncation is limited. In contrast, for molten samples T_2 are long and FID truncation is severe. Such FID truncation strongly influences the quality and repeatability of the spectra following strong line broadening. To address this issue low-load decoupling is used based on a sequences π pulses and delays of equal length (*38*, *39*). Recently this has also successfully been applied in solid-state NMR as Hahn-echo pulse train (HEPT) decoupling (*50*, *51*). Such HEPT decoupling allows acquisition of the whole molten polyolefin FID and thus improved quantitative results.

Downloaded by CORNELL UNIV on June 20, 2012 | http://pubs.acs.org
Publication Date (Web): October 14, 2011 | doi: 10.1021/bk-2011-1077.ch024

Downloaded by CORNELL UNIV on June 20, 2012 | http://pubs.acs.org
Publication Date (Web): October 14, 2011 | doi: 10.1021/bk-2011-1077.ch024

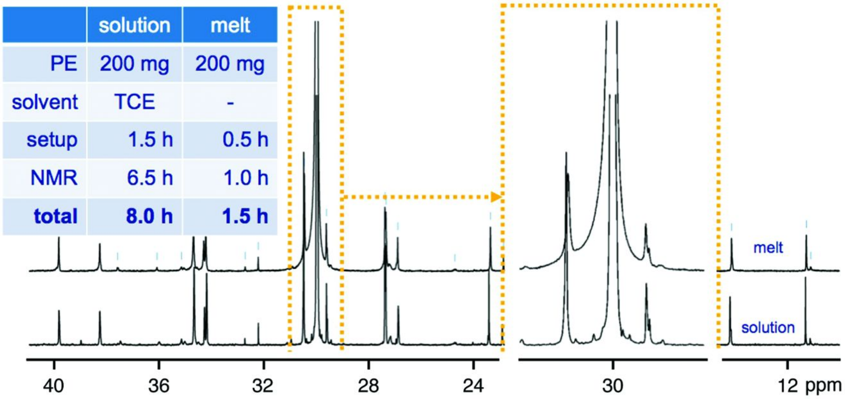

	solution	melt
PE	200 mg	200 mg
solvent	TCE	-
setup	1.5 h	0.5 h
NMR	6.5 h	1.0 h
total	**8.0 h**	**1.5 h**

Figure 1. Comparison of solution-state and melt-state 125 MHz ^{13}C NMR spectra of a polyethylene-co-butene-co-hexene terpolymer.

It should be stated that if CW and HEPT decoupling are applied for the same time HEPT does not provide better resolution i.e. it does not have higher decoupling efficiency (*38*). However, as HEPT can be applied for longer times then less truncation and thus less artificial line broadening is needed. Further improvements are made if standard duty cycle rules are broken and HEPT is applied at 6 or 8 % duty cycle.

Recently, methods for heteronuclear decoupling of polyolefins in the solution-state have been improved by using alternative super cycles of the standard WALTZ approach (*52*). Further improvement has also been gained both in efficiently and decoupling sideband suppression through the use of bi-level composite pulse based decoupling (*52*). In such as approach, decoupling is started in a high power CW mode, most needed at start of the FID, and then as the signal decays, decoupling is switched to the lower power WALTZ modulation. With clear advantages seen in solution-state NMR this approach was modified for melt-state NMR with an initial CW block < 50 ms followed by the low load HEPT decoupling of > 200 ms. This so called CW-HEPT approach can also be implemented with the initial CW part being higher in power than the remaining HEPT part i.e. bi-level CW-HEPT (Figure 2). For such implementation, the duty cycle was further extended to 9 % with no decernable issues.

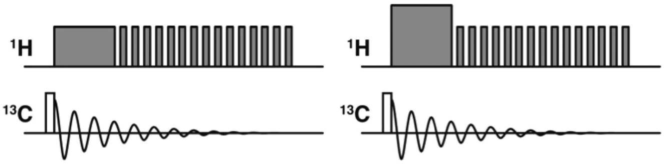

Figure 2. The CW-HEPT (left) and bi-CW-HEPT (right) decoupling schemes.

When line widths are compared, it is clear that the CW-HEPT approach provides improved resolution as compared to standard HEPT (Figure 3). Surprisingly, limited influence was seen when raising the power of the CW block in the bi-level-CW-HEPT manner. Even more surprisingly, similar decoupling efficiency was achieved with the CW block having a lower power than the HEPT block. In practice this means that the bi-CW-HEPT approach with lower initial CW power, has more promise as it places less strain on the hardware, especially at 9 % duty cycle. Such decoupling, however, strongly heats the sample and the temperature instabilities need to be compensated for as a part of the temperature regulation. As such this decoupling method is probably only applicable for elevated temperature measurements.

Applications of Melt-State NMR in Industry

In general, the melt-state NMR approach has been found to be applicable to all polyolefins. It has proved most successful for rapid identification and microstructure quantification. No major differences have been found between the setup needed for the measurement of ethylene or propylene based systems. The de-facto standard spectral analysis method used for polyolefins microstructure quantification have been found to be easily adapted for use on melt-state spectra with only minor widening or shifting of some key integral regions. Importantly, comparable results are achieved when comparing results obtained by high-temperature solution-state NMR spectroscopy with those obtained by melt-state NMR spectroscopy. With respect to resonance assignments, the majority of resonances have been found to be comparable to those observed in solution-state. However some ’solvent’ effects have been observed which means some caution needs to be exercised before results can be used.

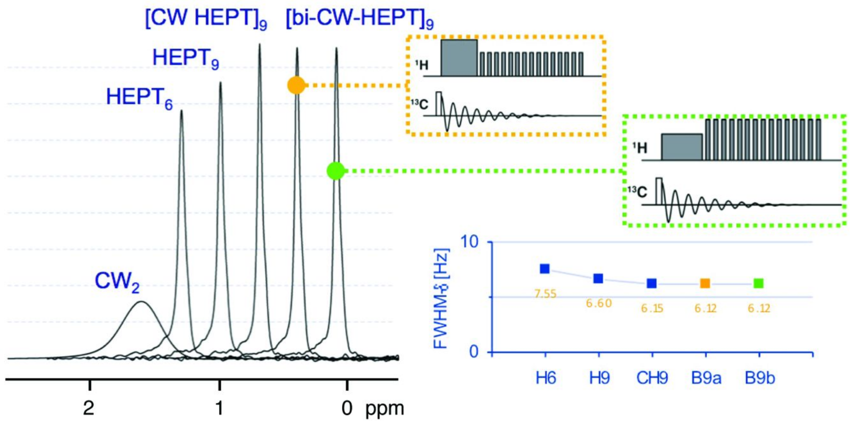

Figure 3. Comparison of resolution achieved for different decoupling schemes illustrating the enhanced decoupling efficiency of CW-HEPT at high duty cycle.

Downloaded by CORNELL UNIV on June 20, 2012 | http://pubs.acs.org
Publication Date (Web): October 14, 2011 | doi: 10.1021/bk-2011-1077.ch024

Polyethylene-co-α-olefin Microstructure

Standard spectral analysis methods for the quantification of comonomer sequence distributions at the triad level were found to be equally applicable to spectra recorded in the melt-state. Only minor modifications to the integral regions were needed. The simultaneous equations used in these approaches need to be modified to exclude signals know to be non quantitative (e.g. methyl groups). Triad comonomer sequence distributions were shown to be comparable between solution-state and melt-state within an acceptable error (±0.2%). More importantly, the properties derived from the triad distribution, such as sequence lengths, run numbers and cluster indices showed very high agreement between the two implementations. Due to the higher sensitivity, quantities derived from melt-state spectra were also found to be highly reproducible and showed less variance as compared to solution-state results. Polyethylene based terpolymers were also studied and again melt-state NMR provided comparable results to solution-state NMR in considerably less time.

Difficult to Dissolve Polyolefins

The melt-state techniques is particularly useful when considering materials that are very difficult to dissolve. One such class of material is HDPE homopolymers. In such materials considerable sample preparation time is needed to ensure a homogenous solution for standard solution-state NMR analysis. Even after dissolution, the extremely low content of branches in such materials often makes the measurement of quantitative spectra for branch quantification unfeasibly long. In contrast, such materials are easily studied by melt-state NMR, with limited reduction of spectral resolution as compared to standard LLDPEs. In such cases the sensitivity of the melt-state technique allows quantification of branching produced by alternative catalytic reactivity or feed stock impurity.

Rapid LCB Quantification

With respect to the quantification of long-chain branching, extreme measures have been applied to achieve the desired sensitivity. In such cases levels of the order of a few branches per 100,000 backbone carbons have been quantified using weeks of measuring time at high field (*14*). In contrast, the sensitivity of the melt-state techniques allows for the quantification of similar levels of sparse branching in less than one day. In one such example, 4 branches per 100,000 backbone carbons were quantified in a single 13 h overnight measurement (*38*). Such quantification opens up new opportunities for understanding LCB in PE. Similar sensitivity has been seen for measuring LCB in PP, although this is more difficult and requires assumptions concerning the structure of the branch site.

Downloaded by CORNELL UNIV on June 20, 2012 | http://pubs.acs.org
Publication Date (Web): October 14, 2011 | doi: 10.1021/bk-2011-1077.ch024

Downloaded by CORNELL UNIV on June 20, 2012 | http://pubs.acs.org
Publication Date (Web): October 14, 2011 | doi: 10.1021/bk-2011-1077.ch024

Application to Isotactic Polypropylene

With respect to PP, the analysis of isotactic PP (iPP) produced by Zeigler-Natta catalysis is also readily accomplished by melt-state NMR (*53*). However, for polypropylenes resolution is limited to measurement of pentad isotacticity and triad stereo sequence distribution. Resolution is not sufficient to measure the pentad stereo sequence distribution or higher orders of tacticity (Figure 4). For such systems, resolution is very important and solution-state NMR is needed as a complementary technique. Melt-state NMR, however, does have a role to play with respect to rapid screening of materials before solution-state analysis or for the quantification of regio-irregularity. Through the application of fitting to standard polymerization models similar results are obtained to those calculated from solution-state spectra of the same material.

Application to Polypropylene-co-α-olefins

As with ethylene-based copolymers the melt-state techniques was found to be extremely useful for the analysis of propylene-based copolymers with α-olefins. Comonomer incorporation, commoner sequence analysis, tacticity of propene sequences and degree of regio-irregularity could all be measured with melt-state ^{13}C NMR spectra (*39*). In addition to propylene-based copolymers, propylene-based terpolymers have also been studied using this technique.

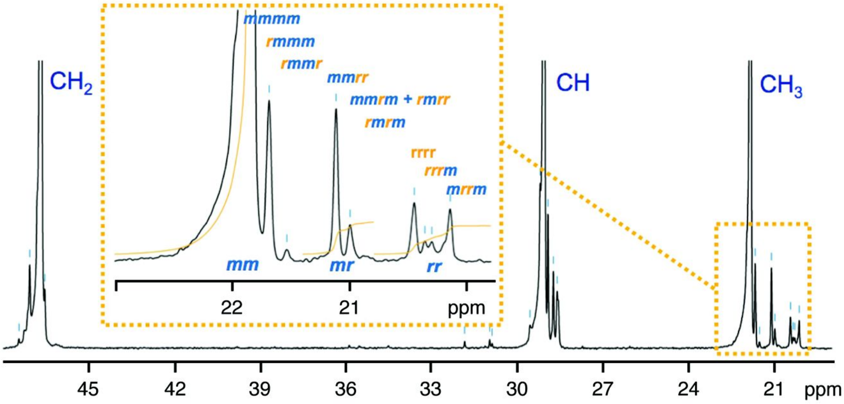

Figure 4. Typical melt-state 125 MHz ^{13}C NMR spectrum of a regio-regular isotactic polypropylene illustrating resolution necessary for both pentad isotacticy and triad tacticity distribution quantification.

Application to Filled and Pigmented Materials

Unlike IR spectroscopy or solution-state NMR spectroscopy direct analysis of filled or pigmented material was found to possible by melt-state NMR, without the time-consuming step of hot filtration. Such a process not only increases the throughput of such analyses but has been found to play an important role in general problem solving. With the high amount of information provided by a single quantitative ^{13}C NMR spectrum often many answers can be provided after one quick measurement. Through the use of MAS the anisotropic NMR interactions are address and averaged to their isotropic values, similarly MAS also averages any sample anisotropy caused by filler or pigment and thus limits its influence on the final spectrum. Very good agreement has was seen between the analysis of original and hot filtered materials (Figure 5).

Application to the Analysis of Fractionated HDPE

A common analysis strategy for comonomer containing PE is preparative fraction followed by commoner quantification. Commonly, such analysis of PE fractions by NMR is limited to special cases, due to the time consuming nature of the NMR analysis. Not only is less material available per fraction but also the commoner content in some of the fraction may be very low. Although time consuming, the information provided about comonomer distribution with respect to molecular weight is highly valuable. The higher sensitivity of the melt-state NMR approach has reduced the time of such analyses from almost a week to only 15 h. This has allowed us to offer such analysis to a wider community. With often only 50 mg or less provided for each fraction, the question was raised what is the smallest quantity of material from which meaningful quantitative results can be obtained? To study this, a series of spectra were recorded using different amount of material from 200 mg down to 5 mg (Figure 6). As expected sensitivity and signal-to-noise ratio decreased will lower sample amounts, however, the determined quantities remained relatively constant. Although the actual determined quantity remained constant as the signal-to-noise ratio decreased, the error, as judged by the reciprocal of the signal-to-noise, increased (*38*, *39*, *49*). The advantage of NMR spectroscopy, however, is that such a loss in signal can be compensated for through the acquisition of more transients. Thus for such systems longer measurement can be undertaken to compensate for the lower than usual sample quantities. Another major advantage of the melt-state NMR approach is that the sample is not consumed during analysis. It is thus possible for melt-state NMR spectroscopy to be the first analytical step for a material. The rotor can then be unpacked and the sample used for further analysis. This has key advantages when very small amounts of material are produced and a series of tests are needed.

Downloaded by CORNELL UNIV on June 20, 2012 | http://pubs.acs.org
Publication Date (Web): October 14, 2011 | doi: 10.1021/bk-2011-1077.ch024

Downloaded by CORNELL UNIV on June 20, 2012 | http://pubs.acs.org
Publication Date (Web): October 14, 2011 | doi: 10.1021/bk-2011-1077.ch024

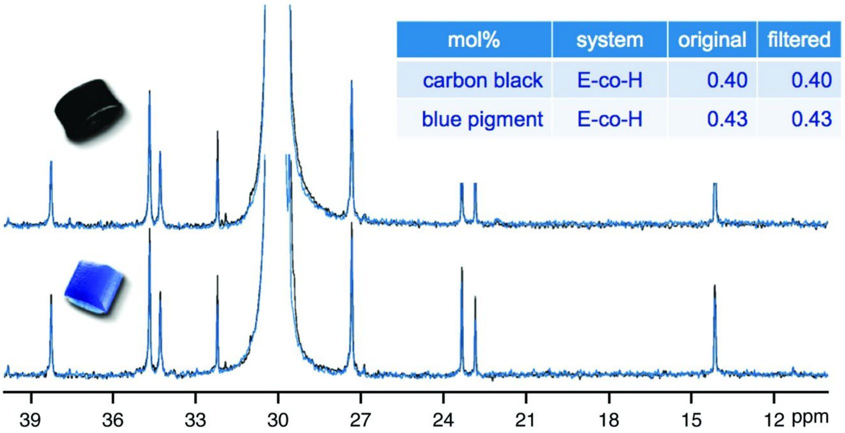

mol%	system	original	filtered
carbon black	E-co-H	0.40	0.40
blue pigment	E-co-H	0.43	0.43

Figure 5. Comparison of melt-state 125 MHz ^{13}C NMR spectra of two polyethylene-co-hexene copolymers containing carbon black and blue pigment illustrating access to comparable hexene contents without hot filtration.

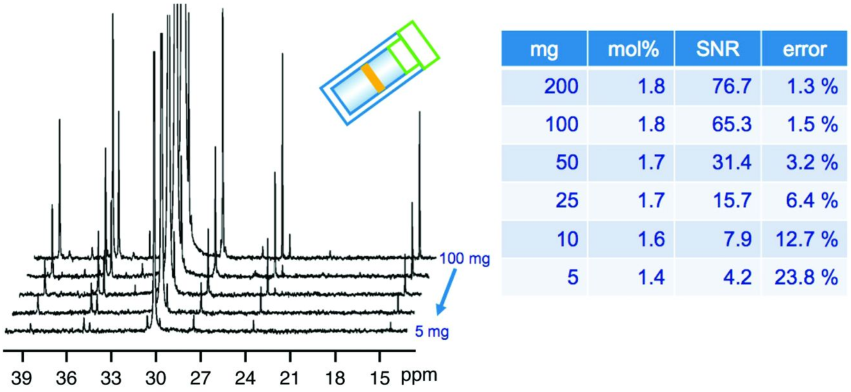

mg	mol%	SNR	error
200	1.8	76.7	1.3 %
100	1.8	65.3	1.5 %
50	1.7	31.4	3.2 %
25	1.7	15.7	6.4 %
10	1.6	7.9	12.7 %
5	1.4	4.2	23.8 %

Figure 6. Comparison of melt-state 125 MHz ^{13}C NMR spectra of a polyethylene-co-hexene. Illustrating constant hexene content with decreasing signal-to-noise ratios of the CH branch site and associated quantification error.

Downloaded by CORNELL UNIV on June 20, 2012 | http://pubs.acs.org
Publication Date (Web): October 14, 2011 | doi: 10.1021/bk-2011-1077.ch024

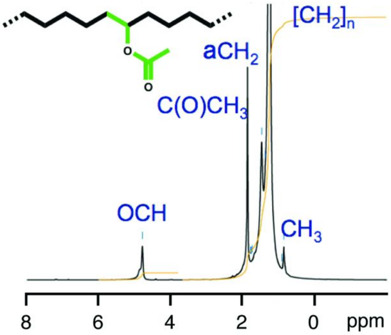

Figure 7. Typical melt-state 500 MHz ^1H NMR spectrum of a polyethylene-co-vinylacetate copolymer.

Quantitative ^1H Melt-State NMR Spectroscopy

As expected ^1H melt-state NMR spectra show much lower resolution, as compared to solution-state, due to the inherent strength of the ^1H-^1H homonuclear dipolar interactions. However, unlike solid-state ^1H NMR of polyolefins, where very limited microstructure information can be gained, for some copolymers the combination of motional averaging and MAS provided sufficient resolution for basic microstructure quantification. As such for standard HDPEs, LLDPEs and PP ^1H melt-state NMR spectroscopy is of limited use except for ^{13}C NMR setup. However, for heteroatom containing copolymers, such as ethylene-methylacrylate (EMA) or ethylene-vinylacetate (EVA), the presence of polar functionality provides sufficient chemical shift dispersion to allow simple quantification (Figure 7). Such measurements have been found to be highly reproducible and experimentally robust due to the shorter ^1H spin-lattice relaxation times. The only major factor that need be considered is if the MAS spinning-sidebands for all peaks are used in the quantitative analysis.

Conclusion

Quantitative melt-state ^{13}C NMR was successfully integrated into an industrial research and development laboratory environment. The technique was found to be applicable for the analysis of a wide range of industrial polyolefins and their copolymers. Importantly, quantitative results were found to be highly comparable to those obtained by standard high-temperature solution-state NMR. Results obtained by melt-state NMR were also found to be considerably more reproducible due to the high sensitivity of the technique.

Although the melt-state NMR technique does addresses some of the main issues encountered with the more standard solution-state NMR approach it does not completely replace the need for access to solution-state NMR. Although sensitivity is important, some problems will always need to be addressed with the higher resolution obtained using solution-state NMR. As such melt-state NMR does not replace the need for solution-state NMR, however the two experimental methods strongly complement one another when both are used to emphasize their particular strengths.

The main advantage found for melt-state NMR has been for rapid microstructure screening and for the analysis of difficult to dissolve polyolefins (e.g. highly-isotactic PP, HDPEs with very-low comonomer contents, preparative fractions of low comonomer content systems and filled systems).

In general, the implementation of the melt-state NMR approach has allowed much wider access to the wealth of knowledge provided by quantitative ^{13}C NMR spectroscopy of polyolefins. Consequently, quantitative ^{13}C NMR results may now be offered at a much earlier stage of problem solving or general research activities. By the implementation of such an approach we have gained better insight into polyolefins and facilitated new research and development opportunities.

Downloaded by CORNELL UNIV on June 20, 2012 | http://pubs.acs.org
Publication Date (Web): October 14, 2011 | doi: 10.1021/bk-2011-1077.ch024

Acknowledgments

The authors of the paper would like to thank the numerous researchers who contributed samples or problems presented in this work. The authors would also like to acknowledge the continued support of IOS management, and specifically Jens Reussner, concerning the development and implementation of advanced polyolefin characterization methods within Borealis.

References

1. Brintzinger, H. H.; Fischer, D.; Mülhaupt, R.; Rieger, B.; Waymouth, R. *Angew. Chem., Int. Ed. Engl.* **1995**, *34*, 1143.
2. Kokko, E.; Malmberg, A.; Lehmus, P.; Löfgren, B.; Seppälä, J. *J. Polym. Sci., Part A: Polym. Chem.* **2000**, *38*, 376.
3. Wang, W.; Zhu, S.; Park, S. *Macromolecules* **2000**, *33*, 5770.
4. Kaminsky, W. *Adv. Catal.* **2001**, *46*, 89.
5. Kokko, E.; Lehmus, P.; Malmberg, A.; Löfgren, B.; Seppälä, J. Long-Chain Branched Polyethene via Metallocene-Catalysis: Comparison of Catalysts. In *Organometallic Catalyst and Olefin Polymerization, Catalysts for a New Millennium*; Springer: New York, 2001; pp 335–345.
6. Galland, G. B.; Quijada, R.; Rojas, R.; Bazan, G.; Komon, Z. J. A. *Macromolecules* **2002**, *35*, 339.
7. Capacchione, C.; Proto, A.; Okuda, J. *J. Polym. Sci., Part A: Polym. Chem.* **2004**, *42*, 2815.
8. Furlan, L. G.; Kunrath, F. A.; Mauler, R. S.; de Souza, R. F.; Casagrande, O. L., Jr *J. Mol. Catal. A: Chem.* **2004**, *214*, 207.
9. Izzo, L.; Caporaso, L.; Senatore, G.; Oliva, L. *Macromolecules* **1999**, *32*, 6913.
10. Lehmus, P.; Kokko, E.; Leino, R.; Luttikhedde, H. J. G.; Rieger, B.; Seppälä, J. V. *Macromolecules* **2000**, *33*, 8534.
11. Prosenc, M. H.; Brintzinger, H. H. *Organometallics* **1997**, *16*, 3889. 29.

12. Thorshaug, K.; Stovneng, J. A.; Rytter, E.; Ystenes, M. *Macromolecules* **1998**, *31*, 7149.
13. Zhang, M.; Wanke, S. E. *Polym. Eng. Sci.* **2003**, *43*, 1878.
14. Wood-Adams, P. M.; Dealy, J. M.; deGroot, A. W.; Redwine, O. D. *Macromolecules* **2000**, *33*, 7489.
15. Shroff, R. N.; Mavridis, H. *Macromolecules* **2001**, *34*, 7362.
16. Axelson, D. E.; Levy, G. C.; Mandelkern, L. *Macromolecules* **1979**, *12*, 41.
17. Randall, J. C. *J. Macromol. Sci., Rev. Macromol. Chem. Phys.* **1989**, *C29*, 201.
18. Resconi, L.; Cavallo, L.; Fait, A.; Piemontesi, F. *Chem. Rev.* **2000**, *100*, 1253.
19. Busico, V.; Cipullo, R. *Prog. Polym. Sci.* **2001**, *26*, 443.
20. Busico, V.; Cipullo, R.; Segre, A. L. *Macromol. Chem. Phys.* **2002**, *203*, 1403.
21. Bovey, F. A.; Schilling, F. C.; McCrackin, F. L.; Wagner, H. L. *Macromolecules* **1976**, *9*, 76.
22. Vestberg, T.; Denifl, P.; Parkinson, M.; Wilen, C-E. *J. Polym. Sci., Part A: Polym. Chem* **2010**, *48*, 351.
23. Bugada, D. C.; Rudin, A. *Eur. Polym. J.* **1987**, *23*, 847.
24. Striegel, A. M.; Krejsa, M. R. *J. Polym. Sci., Part B: Polym. Phys.* **2000**, *38*, 3120.
25. Vega, J. F.; Santamaria, A.; Munoz-Escalona, A.; Lafuente, P. *Macromolecules* **1998**, *31*, 3639.
26. Shroff, R. N.; Mavridis, H. *Macromolecules* **1999**, *32*, 8454.
27. Wood-Adams, P. M. *J. Rheol.* **2001**, *45*, 203.
28. Lohse, D. J.; Milner, S. T.; Fetters, L. J.; Xenidou, M.; Hadjichristidis, N.; Mendelson, R. A.; Garcia-Franco, C. A.; Lyon, M. K. *Macromolecules* **2002**, *35*, 3066.
29. Gabriel, C.; Münstedt, H. *Rheol. Acta* **2002**, *41*, 232.
30. Gabriel, C.; Kaschta, J.; Münstedt, H. *Rheol. Acta* **1998**, *37*, 7.
31. Crosby, B. J.; Mangnus, M.; de Groot, W.; Daniels, R.; McLeish, T. C. B. *J. Rheol.* **2002**, *46*, 401. 30.
32. Trinkle, S.; Walter, P.; Friedrich, C. *Rheol. Acta* **2002**, *41*, 103.
33. Bovey, F. A.; Mirau, P. A. *NMR of Polymers*; Academic Press: San Diego, 1996.
34. Morris, G. A. *Magn. Reson. Chem.* **1986**, *24*, 371.
35. Liu, W.; Ray, D. G.; Rinaldi, P. *Macromolecules* **1999**, *32*, 3817.
36. Seger, M. R.; Maciel, G. E. *Anal. Chem.* **2004**, *76*, 5734.
37. Pollard, M.; Klimke, K.; Graf, R.; Spiess, H. W.; Wilhelm, M.; Sperber, O.; Piel, C.; Kaminsky, W. *Macromolecules* **2004**, *37*, 813.
38. Klimke, K.; Parkinson, M.; Piel, C.; Kaminsky, W.; Spiess, H. W.; Wilhelm, M. *Macromol. Chem. Phys.* **2006**, *207*, 382–395.
39. Klimke, K. Optimisation of Polyolefin Branch Quantification by ^{13}C NMR Spectroscopy. Ph.D. Thesis, Universität Mainz, Germany 2006, http://ubm.opus.hbz-nrw.de/volltexte/2006/1077/pdf/diss.pdf.
40. Parkinson, M.; Klimke, K.; Spiess, H. W.; Wilhelm, M. *Macromol. Chem. Phys.* **2007**, *208*, 2128.

Downloaded by CORNELL UNIV on June 20, 2012 | http://pubs.acs.org
Publication Date (Web): October 14, 2011 | doi: 10.1021/bk-2011-1077.ch024

Downloaded by CORNELL UNIV on June 20, 2012 | http://pubs.acs.org
Publication Date (Web): October 14, 2011 | doi: 10.1021/bk-2011-1077.ch024

41. Stadler, F. J.; Piel, C.; Klimke, K.; Kaschta, J.; Parkinson, M.; Wilhelm, M.; Kaminsky, W.; Münstedt, H. *Macromolecules* **2006**, *39*, 1474.
42. Vittorias, I.; Parkinson, M.; Klimke, K.; Debbaut, B.; Wilhelm, M. *Rheol. Acta* **2007**, *46*, 321.
43. Dechter, J.; Komoroski, R.; Axelson, D.; Mandelkern, L. *J. Polym. Sci., Part B: Polym. Phys.* **1981**, *19*, 631.
44. Hatfield, G.; Killinger, W.; Zeigler, R. *Anal. Chem.* **1995**, *67*, 3082.
45. Litvinov, V. M.; Mathot, V. B. F. *Solid State Nucl. Magn. Reson.* **2002**, *22*, 218.
46. Thakur, K. High-Temperature Solid-State NMR of Cross-Linked, Insoluble, and Unswellable Polymers. In *NMR Spectroscopy of Polymers in Solution and in the Solid State*; ACS Symposium Book Series 834; American Chemical Society: Washington, DC, 2003; p 32.
47. Zeigler, R. C. *Macromol. Symp.* **1994**, *86*, 213.
48. Guo, M.; Cheng, S. Z. D.; Quirk, R. P. Variable temperature, solid-state ^{13}C NMR study of linear low-density polyethylene. In *Olefin Polymerization, Emerging Frontiers*; Symposium Book Series 749; American Chemical Society: Washington, DC, 2000, p 163.
49. Castignolles, P.; Graf, R.; Parkinson, M.; Wilhelm, M.; Gaborieau, M. *Polymer* **2009**, *50*, 2373.
50. Filip, X.; et al. *J. Magn. Reson.* **2005**, *176*, 239.
51. Griffin, J.; et al. *Magn. Reson. Chem.* **2007**, *45*, S1–S198.
52. Zhou, Z.; Kümmerle, R.; Qiu, X.; Redwine, D.; Cong, R.; Taha, A.; Baugh, D.; Winniford, B. *J. Magn. Reson.* **2007**, *187*, 225.
53. Hu, W.; et al. *Macromolecules* **2007**, *40* (9), 3505.

Downloaded by UNIV OF GUELPH LIBRARY on June 21, 2012 | http://pubs.acs.org
Publication Date (Web): October 14, 2011 | doi: 10.1021/bk-2011-1077.ch025

Chapter 25

NMR Rescaling Revisited

M. E. Ries,[*] A. Bansal, and M. G. Brereton

**School of Physics and Astronomy, University of Leeds,
Leeds, LS2 9JT, United Kingdom
[*]E-mail: m.e.ries@leeds.ac.uk**

The purpose of this work is to examine the approximation known as NMR rescaling, in which a polymer chain is replaced by a series of NMR submolecules. This coarse graining of the atomistic details makes various NMR calculations analytically possible. To test the accuracy of this approach a computer simulation of network chains consisting of freely jointed rigid rods has been carried out. The time dependence of the orientation of these rods relative to their network chain end-to-end vector has been recorded. From this the NMR Hahn spin echo sampled transverse relaxation and double quantum build-up and subsequent decay have been calculated. The simulated NMR signals are then compared with theoretical results derived from a rescaling approach. In this work we also test the Anderson-Weiss second moment approximation by using it to derive analytical expressions for the NMR signals for the simulated chains, which can then be directly compared with the simulated results. From this work it is shown that for a polymer melt above its glass transition temperature both rescaling and the second moment approximations are valid.

Introduction

It is well-known that pulsed nuclear magnetic resonance (NMR) is a useful tool for the study of dynamics and orientation in polymer melts and networks (*1–11*). For the NMR measurements to be meaningful though there needs to be a theoretical link connecting the NMR signal to the microscopic properties of interest, such as entanglement / crosslink density, chain persistence length,

In NMR Spectroscopy of Polymers: Innovative Strategies for Complex Macromolecules; Cheng, H., et al.;
ACS Symposium Series; American Chemical Society: Washington, DC, 2011.

dynamic correlation times and order parameters. To make these connections quantitative has proved very challenging.

The classical starting point for the quantitative analysis of stress optical anisotropy in strained polymer networks is the Kuhn and Grün theory of 1942 (*12*). The true molecular network is replaced by an idealized network of identical chains each of which consists of *n* freely jointed rods of length *l*. The motivation for using a replacement chain comes from the fact that it is generally not possible to derive the material properties if all the atomistic details are included. For example, a representative or coarse grained chain such as the Rouse bead and spring model (*13*) enables the rheological properties of a polymer melt to be theoretically calculated.

In the 1970s and 80s J. P. Cohen-Addad introduced and pioneered the idea of the NMR submolecule (*14–19*); a coarse grained unit comprising of several monomers. In this approach the real polymer chains are replaced by a series of these NMR submolecules connected together. For the Kuhn and Grün model the parameters (*n, l*) of the replacement chain are chosen such that both the maximum end-to-end length and root mean square end-to-end length of the rigid rod chain have the same values as that of the real chain it is replacing (*20*). For the case of the NMR submolecule it must generate an effective $P_2(\cos\theta)$ for the part of the polymer chain it represents, where $P_2(...)$ is the second-order Legendre polynomial and θ is the angle between an inter nuclear vector and the applied static magnetic field. The NMR properties of the polymer chain are then *rescaled* onto the NMR submolecule.

Motional averaging of the NMR properties for a polymer chain is considered to take place in two steps (*21*). The first involves local, monomer length scale, fast reorientations. These fluctuations take place within the NMR submolecule and partially average the NMR properties such that they become dependent on the end-to-end vector coordinates of their containing submolecule. The second step is the slower reorientation of the submolecule itself. This submolecule can be, for example, a Rouse unit, an entanglement vector or a network chain. The key point being that the submolecule coordinates can be handled analytically, which enables the calculation of the NMR signal in terms of these variables. The pre-averaging of the NMR properties so that they depend on the NMR submolecule coordinates is termed *rescaling* (*20*).

The motivation for this piece of work is that, to the best of our knowledge, this approach has never before been verified. It has of course been used in many publications, where it has been assumed to be true, but the rescaling approximation itself has not been directly tested. Rescaling is just an approximation used to make the NMR problem analytically solvable, but its accuracy and limits of applicability are not known. For experiments such as the transverse relaxation, as sampled by a spin-echo experiment, or the double quantum build-up and decay signal to be quantitatively interpreted in terms of polymeric material microscopic properties, rescaling must be valid. Otherwise the connection between these properties and the NMR response becomes broken. It is the purpose of this work to determine if and when rescaling is valid.

Downloaded by UNIV OF GUELPH LIBRARY on June 21, 2012 | http://pubs.acs.org
Publication Date (Web): October 14, 2011 | doi: 10.1021/bk-2011-1077.ch025

Downloaded by UNIV OF GUELPH LIBRARY on June 21, 2012 | http://pubs.acs.org
Publication Date (Web): October 14, 2011 | doi: 10.1021/bk-2011-1077.ch025

Simulation Procedure

Freely Jointed Rigid Rod Chain

To test rescaling we simulated a pseudo-atomic chain. For this we used the freely jointed rigid rod chain where each rod was taken to have unit length. The rods are connected together to form a polymer chain via hinges that allow complete free rotation, so that consecutive rods can freely take up any orientation with respect to each other. In Figure 1 a freely jointed chain is shown forming an end-to-end vector, or network vector, ***R*** with one of the rigid rods making an angle θ with the external reference direction ***B***.

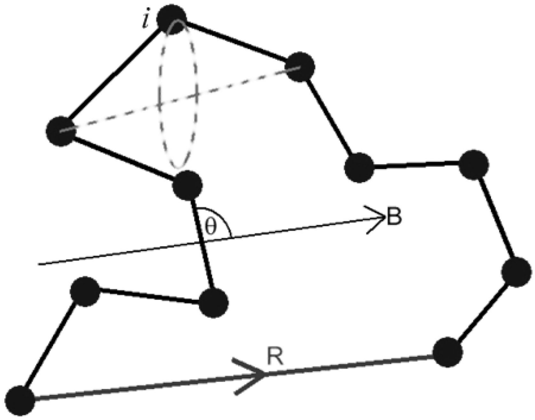

*Figure 1. Freely jointed chain showing the end-to-end vector **R**, reference direction **B** and the instantaneous angle θ that a rod makes with the reference direction. The dashed ellipse and straight line are explained in the text.*

A C++ program was written that simulates a chain of n freely jointed rigid rods. Initially the rods were connected together so that they formed a pre-chosen network vector ***R***. In each time step a hinge i was chosen, see Figure 1, and the line that links the previous $(i\text{-}1)$ and next hinge $(i+1)$ was determined from the coordinates of the hinges, which is the dashed line in Figure 1. Then a circle, seen in perspective in Figure 1 as a dashed ellipse, was determined such that the plane of the circle is at right angles to the dashed line, the centre of the circle is where this plane and line meet and the radius of the circle is such that the i^{th} hinge is on this circle. This circle indicates all the possible positions available to hinge i that both keeps hinges $i\text{-}1$ and $i+1$ fixed and all the rod lengths unchanged. A random location on this circle was chosen as the new position of hinge i. In each time step each hinge, except for the first and last, were moved in this manner, such that the chain adopted a new configuration without altering the set up network vector ***R***. After each time step the orientation θ for each rod relative to the reference direction ***B*** was recorded. In all this work we have kept ***B*** parallel to ***R***. The chain was always allowed to undergo 1000 time steps to equilibrate before recording the orientations of the rods. How this data were then used to calculate the NMR response for our simulated chains will be described in the sections below.

To confirm that our simulated chain was behaving as a freely jointed rigid rod chain we determined the time averaged orientation $\langle P_2(\cos\theta)\rangle$ for each rod as a function of network vector length *R*. Each rod in the chain was found to have the same time averaged value, as expected, and followed the classical Treloar results (*22*). This states that

$$\langle P_2(\cos\theta)\rangle = \frac{1}{5}\left\{3\left(\frac{R}{R_{\max}}\right)^2 + \left(\frac{R}{R_{\max}}\right)^4 + \left(\frac{R}{R_{\max}}\right)^6\right\} \qquad (1)$$

where R_{max} is the fully extended length of the chain, which for our *n* rods of unit length is *n*. Figure 2 shows the simulated values of $\langle P_2(\cos\theta)\rangle$ versus R/R_{max}, where the solid line is a no parameter fit given by eq 1. In this simulation *n* was 10.

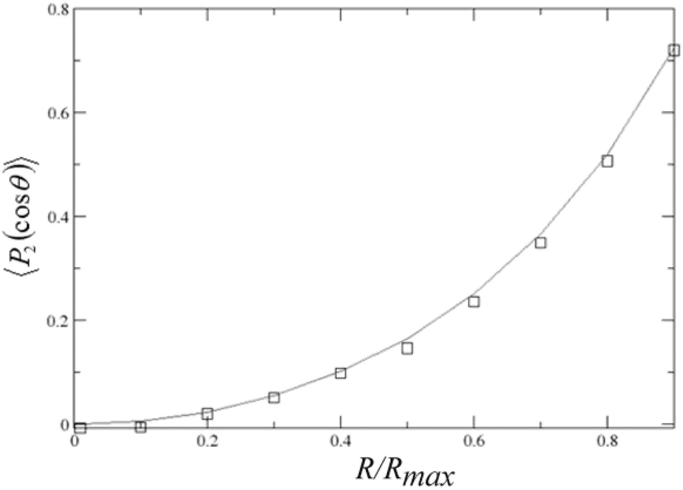

Figure 2. The time average orientation $\langle P_2(\cos\theta)\rangle$ of the rigid rods relative to their end-to-end vector as a function of the ratio of the chains end-to-end length R to the maximum end-to-end length R_{max}. The solid line is given by eq 1.

Background Theory

NMR Signals

The experimental pulse sequences used to measure the Hahn echo sampled transverse relaxation function (*23*, *24*) and the double quantum (DQ) build-up and decay curve (*25*, *26*) can be found in the literature. Both these techniques can be thought of as measuring an intensity *I* as a function of experimental time *t*. The time evolution of these signals depends on the time dependent relative orientation of an inter-nuclear vector relative to the external magnetic field. In this work we will consider chains comprising $n=11$ rigid rods and the central one will be taken to be this inter-nuclear vector giving rise to the NMR signal.

The Hahn echo sampled transverse relaxation function I_H is given by (*27*)

Downloaded by UNIV OF GUELPH LIBRARY on June 21, 2012 | http://pubs.acs.org
Publication Date (Web): October 14, 2011 | doi: 10.1021/bk-2011-1077.ch025

$$I_H(t) = \overline{\cos\phi(0,t)} \qquad (2)$$

and the DQ signal I_{DQ} by (*27*)

$$I_{DQ}(t) = \overline{\sin\frac{2}{3}\phi\left(0,\frac{t}{2}\right)\times\sin\frac{2}{3}\phi\left(\frac{t}{2},t\right)} \qquad (3)$$

where

$$\phi(t_1,t_2) = \frac{3}{2}D\int_{t_1}^{t_2} P_2\left[\cos\theta(t')\right]dt' \qquad (4)$$

and D is an NMR interaction constant that in this work was set to 0.01 and the solid lines in eq 2 and eq 3 indicates an averaging over all the chains in the system. The size of D determines the timescale for the NMR signal and a value of 0.01 was chosen simply to give NMR signals that lasted many time steps (~1000) in our simulation. In this work the simulations are repeated 1000 times, meaning that effectively there are 1000 chains to average the NMR signal over. Finally, the integrals in the above equations are actually discrete summations over each time step when used to calculate the NMR signals from the simulation data.

Results and Discussions

NMR Rescaling and the NMR Submolecule Approach

It is the aim of this work to test the NMR submolecule approximation approach, known as rescaling. To do this we need to compare the theoretical results from applying the method of NMR rescaling with the simulation results calculated from the simulation data. In the following work the NMR submolecule is taken to be the network vector ***R***. Next the rescaled NMR signal for the transverse relaxation function is calculated after which the same is repeated for the DQ build-up and decay function.

Transverse Relaxation Function

The rigid rod reorientations that take place within the submolecule ***R*** result in an average orientation of these rods and therefore our inter-nuclear vector, which in this simulation is the central rigid rod in each submolecule. Rescaling means that just this time averaged value is needed to calculate the NMR signal. The atomistic submolecule details, such as their fluctuations about this average orientation are not used. In this way the NMR response becomes dependent only on the submolecule coordinates, as it is these that determine this average orientation, recall eq 1. To find an analytic expression for eq 2 we first replace the integral in eq 4 with the time averaged value. This result is then substituted into eq 2. In this simulation every chain has the same network vector and therefore all

Downloaded by UNIV OF GUELPH LIBRARY on June 21, 2012 | http://pubs.acs.org
Publication Date (Web): October 14, 2011 | doi: 10.1021/bk-2011-1077.ch025

the rigid rods have the same average orientation. This makes the averaging over all chains implied by the solid line in eq 2 trivial, giving

$$I_H(t) = \cos\left[\frac{3}{2} D\langle P_2[\cos\theta]\rangle \times t\right] \tag{5}$$

In Figure 3 the simulated transverse relaxation function for network chains with $R/R_{max} = 0.6$ is shown.

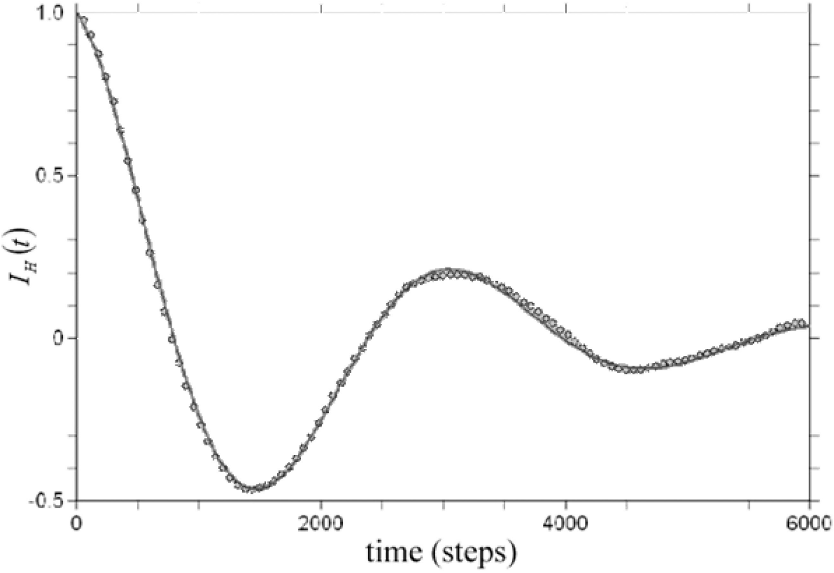

Figure 3. The simulated transverse relaxation function eq 2 for network chains with $R/R_{max} = 0.6$. The circles are simulation data points and the solid line is eq 15.

The NMR rescaled result eq 5 predicts an oscillation with a time period that is dependent on the average orientation of the rigid rods within the NMR submolecule. In Figure 3 this oscillation, with the correct time period (within 5%), is seen but of key importance is that the signal also decays away. This is not predicted from the rescaling approximation and therefore rescaling for our simulation is not sufficiently accurate.

To understand the origin of the decaying part of the signal seen in Figure 3 it is necessary to look more closely at the time dependence of the orientation of the rigid rods. To do this we write the instantaneous orientation of a rigid rod in terms of its time average orientation, as

$$P_2(\cos\theta(t')) = \langle P_2(\cos\theta)\rangle + \varepsilon(t') \tag{6}$$

where all the time dependence is contained within the *ε(t')* term that represents the instantaneous difference between the orientation of the rigid rod and the time averaged value. We now substitute eq 6 into eq 4 and eq 2 to obtain

Downloaded by UNIV OF GUELPH LIBRARY on June 21, 2012 | http://pubs.acs.org
Publication Date (Web): October 14, 2011 | doi: 10.1021/bk-2011-1077.ch025

$$I_H(t) = \overline{\cos\left[\frac{3}{2}D\langle P_2(\cos\theta)\rangle t + \frac{3}{2}D\int_0^t \varepsilon(t')dt'\right]} \tag{7}$$

The cosine term can be written as the real part of a complex exponential and recalling that all our network chains have the same time average orientation enables this to be more clearly written as

$$I_H(t) = \mathrm{Re}\left\{\exp\left[i\frac{3}{2}D\langle P_2(\cos\theta)\rangle t\right] \times \overline{\exp\left[i\frac{3}{2}D\int_0^t \varepsilon(t')dt'\right]}\right\} \tag{8}$$

Eq 8 is the product of two terms, the first is the rescaling result eq 5 and the second term is an extra relaxation term that is the origin of the decay seen in Figure 3. The time dependent departures from the average orientation causes the NMR response from each network chain to go out of phase with each other, resulting in a signal that decays away.

The first term in eq 8 represents the solid-like contribution to the signal that gives rise to a coherent, or reversible time evolution, which can be refocused by appropriate pulse sequences (*28*). The second term in eq 8 is related to the fluctuating part or liquid like contribution and corresponds to a homogenous broadening of the signal (*28*). Saalwächter et al have pioneered the use of normalised experimental DQ build up data, which removes the influence of relaxation processes on the double quantum intensity (*26*). This allows the determination of absolute values for the residual dipolar couplings (*8*).

Next we use the Anderson-Weiss second moment approximation (*29*) to quantify the extra relaxation caused by the second term in eq 8. The extra relaxation is given by

$$g(t) = \overline{\exp\left[i\frac{3}{2}D\int_0^t \varepsilon(t')dt'\right]} \tag{9}$$

The second moment approximation uses a result that is exact for a variable *X* when it has Gaussian statistics,

$$\overline{\exp(\mathrm{X})} = \exp\left[\overline{X} + \frac{1}{2}\left(\overline{\mathrm{X}^2} - \overline{\mathrm{X}}^2\right)\right] \tag{10}$$

A comparison of eq 9 with eq 10 gives

$$X = i\frac{3}{2}D\int_0^t \varepsilon(t')dt' \tag{11}$$

From the definition of *ε(t')* in eq 6 the average value of *X* is zero. Therefore substituting eq 11 into eq 10 gives

Downloaded by UNIV OF GUELPH LIBRARY on June 21, 2012 | http://pubs.acs.org
Publication Date (Web): October 14, 2011 | doi: 10.1021/bk-2011-1077.ch025

$$g(t) = \exp\left[-\frac{1}{2}\left(\frac{3D}{2}\right)^2 \int_0^t \int_0^t \overline{\varepsilon(t')\varepsilon(t'')} dt'dt'' \right] \qquad (12)$$

To calculate eq 12 we need to assume a form for the correlations of the fluctuations of the orientation about their average value. For simplicity we take this to have the following form

$$\overline{\varepsilon(t')\varepsilon(t'')} = \overline{\varepsilon^2} \exp\left(\frac{-|t' - t''|}{\tau} \right) \qquad (13)$$

where τ is the correlation time of these fluctuations and $\overline{\varepsilon^2}$ represents the size of these fluctuations.

It should be noted that polymer chains display a spectrum of relaxation times, such as Rouse modes (*13*). Our chains consist of only 11 freely jointed rigid rods and for such short chains and our calculations eq 13 is found to adequately describe the auto-correlation function of the fluctuations ε. For an interesting discussion on the relationship between a polymer's spectrum of relaxation times and its NMR relaxation times the reader is pointed to the work by Gubaidullin et al (*30*).

The integrals in eq 12 can now be evaluated and in the limit where the experimental time is longer than the fluctuation correlation time we obtain

$$g(t) = \exp\left[-\tau \left(\frac{3D}{2}\right)^2 \overline{\varepsilon^2} \times t \right] \qquad (14)$$

Substituting this result into eq 8 gives

$$I_H(t) = \cos\left[\frac{3}{2} D \langle P_2[\cos\theta] \rangle \times t \right] \times \exp\left[-\tau \left(\frac{3D}{2}\right)^2 \overline{\varepsilon^2} \times t \right] \qquad (15)$$

The final result is the original rescaling result multiplied by an exponential decay envelope. We can now turn to our simulation data to obtain the τ and $\overline{\varepsilon^2}$.

It follows directly from eq 6 and 13 that

$$\overline{P_2[\cos\theta(0)] \cdot P_2[\cos\theta(t)]} = \overline{\varepsilon^2} \exp(-t/\tau) + \langle P_2(\cos\theta) \rangle^2 \qquad (16)$$

This correlation between the orientation at one moment with the orientation at a later time can be directly calculated from the simulation data. In Figure 4 $\overline{P_2[\cos\theta(0)] \cdot P_2[\cos\theta(t)]}$ is shown as a function of time with a fit to eq 16.

Downloaded by UNIV OF GUELPH LIBRARY on June 21, 2012 | http://pubs.acs.org
Publication Date (Web): October 14, 2011 | doi: 10.1021/bk-2011-1077.ch025

Downloaded by UNIV OF GUELPH LIBRARY on June 21, 2012 | http://pubs.acs.org
Publication Date (Web): October 14, 2011 | doi: 10.1021/bk-2011-1077.ch025

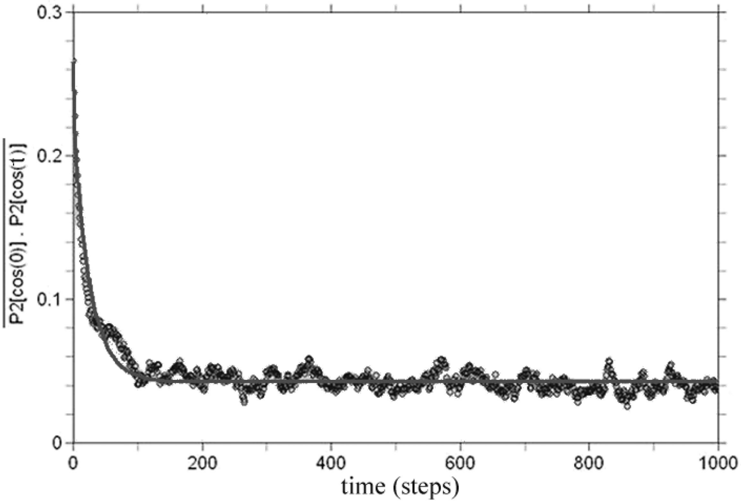

Figure 4. Correlation function of the orientation at one moment with the orientation at a later time as a function of time. The circles are simulation data points and the solid line is eq 16.

In Figure 4 the data has been fitted to eq 16 giving a correlation time τ of 27 time steps, size of fluctuations $\overline{\varepsilon^2}$ of 0.18 and an average orientation $P_2(\cos\theta)$ equal to 0.21. This is all the information that is needed to predict the NMR signal in Figure 3 using eq 15. From eq 15 we determine an oscillation with period 3050 time steps and exponential decay envelope with a *1/e* time of 2100 time steps. A free fit of eq 15 to the data in Figure 3 shown as the solid line gives an oscillation period of 3200 time steps and a *1/e* time for the single exponential relaxation of 2000 time steps. The agreement is therefore excellent, showing that the second moment approximation is working for this system. Next we develop similar arguments for the DQ build-up and decay signal.

Double Quantum Build-up and Decay function

The starting point for the DQ build-up and decay function is eq 3. Again we make the rescaling assumption and replace the integrals in eq 3 with the time average values and recalling that our network vectors are fixed, we obtain

$$I_{DQ}(t) = \sin^2\left[D\langle P_2[\cos\theta]\rangle \times \frac{t}{2}\right] \tag{17}$$

As before, an oscillating signal with a period that depends on the average orientation of the rigid rods within the NMR submolecule or network vector is predicted. In Figure 5 is the DQ signal calculated from the simulation data for $R/R_{max} = 0.5$.

Downloaded by UNIV OF GUELPH LIBRARY on June 21, 2012 | http://pubs.acs.org
Publication Date (Web): October 14, 2011 | doi: 10.1021/bk-2011-1077.ch025

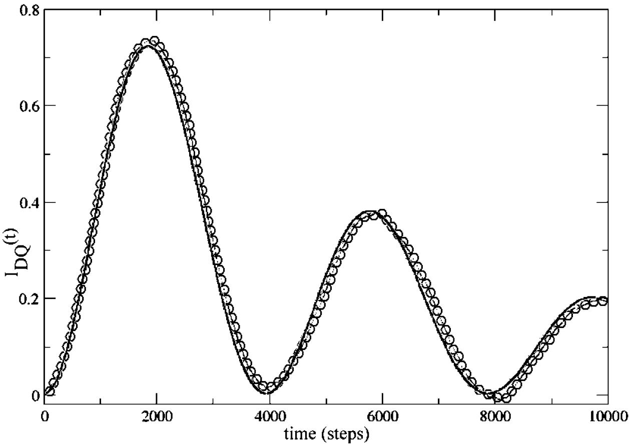

Figure 5. Simulated double quantum build-up and decay function eq 3 for network chains with R/R_{max} = 0.5. The circles are the simulation data points and the solid line is eq 19.

In Figure 5 the oscillation predicted by eq 17 is seen with the correct time period (within 5%) but similarly to the previously calculated transverse relaxation function, recall Figure 3, the signal decays away. To understand the origin of this decaying part we again look at the effect of the time dependence of the orientation of the rigid rods using eq 6. To carry out this calculation we first rewrite eq 3 using the mathematical identity *sinA.sinB = ½ (cos(A-B) – cos (A+B))*, to give

$$I_{DQ}(t)=\frac{1}{2}\left\{\overline{\cos\frac{2}{3}\left[\phi\left(0,\frac{t}{2}\right)-\phi\left(\frac{t}{2},t\right)\right]}-\overline{\cos\frac{2}{3}\phi(0,t)}\right\} \tag{18}$$

Now that the problem is written in terms of cosine functions the derivation for each term in eq 18 follows exactly the same steps as those for the transverse relaxation calculation, see eq 7 to eq 15. This gives

$$I_{DQ}(t)=\sin^2\left[D\langle P_2[\cos\theta]\rangle\times\frac{t}{2}\right]\times\exp\left[-\tau\times D^2\overline{\varepsilon^2}\times t\right] \tag{19}$$

which has the form of an oscillation multiplied by a single exponential. Analyzing data from the simulation as was done before in Figure 4 using eq 16 we can generate a no free parameter fit to the DQ signal. This is the solid line in Figure 5. The DQ simulation data in Figure 5 has an oscillation period and decay time both within 5% of the predictions from eq 19. Therefore for both the transverse relaxation function and DQ build-up and decay signal the Anderson-Weiss approximation, eq 10, is generating excellent agreement.

In NMR Spectroscopy of Polymers: Innovative Strategies for Complex Macromolecules; Cheng, H., et al.;
ACS Symposium Series; American Chemical Society: Washington, DC, 2011.

Downloaded by UNIV OF GUELPH LIBRARY on June 21, 2012 | http://pubs.acs.org
Publication Date (Web): October 14, 2011 | doi: 10.1021/bk-2011-1077.ch025

Applicability of Rescaling

In the above section it was shown that rescaling for our system of network vectors, which were our NMR submolecules, does not quite work. The time dependent fluctuations of the rigid rods about their average orientation causes an extra relaxation in the generated NMR signal. For rescaling to work only the average orientation of the rigid rods should be needed to calculate the NMR signal. Here we find that this approach does not obtain the correct answer to the integrals in equations 2 and 3. Each NMR submolecule due to its own particular time dependent path for the rigid rod orientations has a different result for the phase angle given by eq 4. This loss of phase coherence between the NMR submolecules is the origin of the decays seen in Figures 3 and 5. Through application of the Anderson-Weiss second moment approximation (*29*), given by eq 10, it is possible to quantify this extra relaxation. This result connects the atomistic details, such as the rigid rod orientation correlation time τ to the NMR response, recall equations 15 and 19. It is therefore now possible to estimate for real polymer melts when rescaling will be applicable. To do this we will consider the transverse relaxation signal given by eq 15.

For rescaling to work such that we can replace the real atomistic details with NMR submolecules and re-write the NMR problem more simply in terms of pre-averaged orientations eq 5 needs to hold. For this result to be a good approximation we need the time period of the oscillations in the first term of eq 15 to be much shorter than the relaxation time of the second term in eq 15, i.e.

$$\frac{2\pi}{\frac{3}{2}D\langle P_2[\cos\theta]\rangle} << \frac{1}{\tau\left(\frac{3D}{2}\right)^2\overline{\varepsilon^2}} \tag{20}$$

If this holds in a real system, one that contains numerous NMR submolecules each with a different orientation, the NMR signal would relax principally due to each NMR submolecule having a different oscillation frequency. These different frequencies would result in the NMR submolecules going out of phase with each other. The resultant NMR signal would therefore relax and of key importance this relaxation would not be due to the second term in eq 15. Simply put, when eq 20 holds then eq 15 becomes eq 5 and rescaling is valid. It would then be possible to correctly calculate the NMR signal using only the rescaling result represented by eq 5.

For polymer chains in a polymer melt $<P_2(\cos\theta)>$ ~1/n, for proton and deuterium NMR D ~ 100 kHz, atomic bond reorientations take place on timescales shorter than $\tau \sim 10^{-10}$s and $\overline{\varepsilon^2}$ ~1/5, which can be seen from its definition in eq 16 and remembering that the value of $\overline{(P_2\cos\theta)^2}$ averaged over all orientations is 1/5. Putting these values into eq 20 gives that n << 2000 for rescaling to be valid. Therefore, as long as the NMR submolecule is not too large in terms of the number of monomers it replaces, so that it produces a significantly large average orientation on its constituent atomic units, then the NMR submolecule description is valid.

Conclusions

A simulation of network chains comprising of freely jointed rigid rods with fixed end-to-end vectors has been carried out. By monitoring the orientation of the central rod and taking this to be the NMR relevant inter nuclear vector the transverse relaxation function and double quantum build-up and decay have been explicitly calculated. These simulated NMR signals were then compared with analytical predictions made using the approximation known as rescaling. For these simulated chains an extra relaxation was observed arising from the time dependent fluctuations of the orientation of the rods about their average value. To calculate theoretically this extra relaxation the Anderson-Weiss second moment approximation (*29*) was employed. Excellent agreement was found between these theoretical predictions and the simulated data, see the solid lines in Figures 3 and 5. Using these results it was then possible to calculate if rescaling in polymer melts well above their glass transition temperature was valid. It was determined that, as long as the NMR submolecules used to coarse grain the atomistic details of the real polymer chains are not too large (n<<2000), rescaling is indeed valid.

Acknowledgments

Many years ago Michael Rubinstein first brought this potential problem with rescaling to our attention and showed MER the method used in this work of simulating freely jointed rigid rods. Several undergraduate students have been involved in different parts of this work. They are Ian Waterman, Rachel Moody, Adam Royles and Robert Ramsay.

Downloaded by UNIV OF GUELPH LIBRARY on June 21, 2012 | http://pubs.acs.org
Publication Date (Web): October 14, 2011 | doi: 10.1021/bk-2011-1077.ch025

References

1. Ball, R. C.; Callaghan, P. T.; Samulski, E. T. *J. Chem. Phys.* **1997**, *106* (17), 7352–7361.
2. Brereton, M. G. *Macromolecules* **1989**, *22* (9), 3667–3674.
3. Brereton, M. G.; Ward, I. M.; Boden, N.; Wright, P. *Macromolecules* **1991**, *24* (8), 2068–2074.
4. Deloche, B.; Dubault, A.; Durand, D. *J. Polym. Sci., Part B: Polym. Phys.* **1992**, *30* (12), 1419–1421.
5. Kimmich, R.; Kopf, M.; Callaghan, P. *J. Polym. Sci., Part B: Polym. Phys.* **1991**, *29* (8), 1025–1030.
6. Klein, P. G.; Ries, M. E. *Progr. Nucl. Magn. Reson. Spectrosc.* **2003**, *42* (1-2), 31–52.
7. Saalwachter, K.; Herrero, B.; Lopez-Manchado, M. A. *Macromolecules* **2005**, *38* (23), 9650–9660.
8. Saalwachter, K.; Heuer, A. *Macromolecules* **2006**, *39* (9), 3291–3303.
9. Saalwachter, K.; Kleinschmidt, F.; Sommer, J. U. *Macromolecules* **2004**, *37* (23), 8556–8568.
10. Saalwachter, K.; Sommer, J. U. *Macromol. Rapid Commun.* **2007**, *28* (14), 1455–1465.

11. Sotta, P.; Deloche, B. *Makromol. Chem., Macromol. Symp.* **1989**, *23* (Eur. Symp. Polym. Mater., 1987, Pt. 2), 183−90.
12. Kuhn, W.; Grün, F. *Kolloid-Z* **1942**, *101*, 248.
13. Rouse, P. E. *J. Chem. Phys.* **1953**, *21*, 1272.
14. Cohen Addad, J. P. *J. Chem. Phys.* **1974**, *60* (6), 2440–2453.
15. Cohen Addad, J. P. *J. Chem. Phys.* **1976**, *64* (8), 3438–3445.
16. Cohen Addad, J. P. *J. Chem. Phys.* **1979**, *71* (9), 3689–3696.
17. Cohen Addad, J. P. *Polymer* **1983**, *24* (9), 1128–1138.
18. Cohen Addad, J. P.; Dupeyre, R. *Polymer* **1983**, *24* (4), 400–408.
19. Cohen Addad, J. P.; Feio, G. *J. Polym. Sci., Part B: Polym. Phys.* **1984**, *22* (6), 957–978.
20. Ries, M. E.; Brereton, M. G.; Ward, I. M.; Cail, J. I.; Stepto, R. F. T. *Macromolecules* **2002**, *35* (14), 5665–5669.
21. Cohen Addad, J. P.; Guillermo, A. *J. Polym. Sci., Part B: Polym. Phys.* **1984**, *22* (6), 931–955.
22. Treloar, L. R. G. *Trans. Faraday Soc.* **1954**, *50*, 881.
23. Carr, H. Y.; Purcell, E. M. *Phys. Rev.* **1954**, *94* (3), 630–638.
24. Levitt, M. H.; Freeman, R. J. *Magn. Reson.* **1981**, *43*, 65.
25. Baum, J.; Pines, A. *J. Am. Chem. Soc.* **1986**, *108* (24), 7447–7454.
26. Saalwachter, K. *Progr. Nucl. Magn. Reson. Spectrosc.* **2007**, *51* (1), 1–35.
27. Ries, M. E.; Brereton, M. G. *Phys. Chem. Chem. Phys* **.2009**, *11* (32), 6918–6924.
28. Sotta, P.; Fulber, C.; Demco, D. E.; Blumich, B.; Spiess, H. W. *Macromolecules* **1996**, *29* (19), 6222–6230.
29. Anderson, P. W.; Weiss, P. R. *Rev. Mod. Phys.* **1953**, *25* (1), 269–276.
30. Gubaidullin, A.; Shakirov, T.; Fatkullin, N.; Kimmich, R. *Solid State Nucl. Magn. Reson.* **2009**, *35* (3), 147–51.

Downloaded by UNIV OF GUELPH LIBRARY on June 21, 2012 | http://pubs.acs.org
Publication Date (Web): October 14, 2011 | doi: 10.1021/bk-2011-1077.ch025

Downloaded by OHIO STATE UNIV LIBRARIES on June 20, 2012 | http://pubs.acs.org
Publication Date (Web): October 14, 2011 | doi: 10.1021/bk-2011-1077.ch026

Chapter 26

An NMR Investigation of a Polymer Melt under Shear

Ute Böhme and Ulrich Scheler[*]

**Leibniz-Institut für Polymerforschung Dresden e.V.,
Hohe Str. 6, 01069 Dresden, Germany
[*]E-mail: scheler@ipfdd.de**

Mechanical shear is part of processing steps of polymers in the melt. Shear influences polymer dynamics and chain order in the melt. The effect of mechanical shear on the NMR relaxation behaviour of polymer melts has been studied. A dedicated probehead capable for high-temperature rheo NMR has been developed and applied. Both the transverse and the longitudinal relaxation time exhibit a strong temperature dependence. The prolongation of the longitudinal relaxation time T_1 with increasing temperature is attributed to slowed down spin diffusion as a function of the enhanced motion. The enhanced mobility of polymer segments between the entanglements is directly reflected in the prolongation of the transverse relaxation time T_2. Shearing the polymer sample results in an increase of the transverse relaxation time, indicating enhanced molecular mobility which implies, that as an effect of the shear a fraction of entanglements in the polymer have been lost, resulting in longer chain segments, these in turn exhibit an increased molecular mobility as manifested in a prolongated T_2.

Introduction

The flow behaviour of polymer melts is critical for various steps of the processing and defines the materials properties in a wide range of applications. Therefore rheological measurements are an important source of information on the behaviour of polymer materials (*1–3*). For a further understanding molecular insight into the origin of materials properties is desirable. The combination of

In NMR Spectroscopy of Polymers: Innovative Strategies for Complex Macromolecules; Cheng, H., et al.;
ACS Symposium Series; American Chemical Society: Washington, DC, 2011.

rheology with X-Ray scattering (rheo SAXS) has proven to be a valuable tool for the investigation of molecular order resulting from shear of the material (*4–6*).

The combination of rheology with nuclear magnetic resonance (NMR) as rheo NMR permits to link macroscopic properties as measured in rheology with molecular parameters and thus yields insight in the rheological behaviour of materials (*7*) with all the information content of NMR on structure, order and mobility. Applications to liquid crystalline materials show shear-induced orientation and the competition between orientation in the shear field to magnetically-induced orientation (*8*, *9*). The formation of multilamellar vesicles has been followed as well (*10*). Applications to polymer melts sofar have been limited to the room temperature range. Callaghan and coworkers showed, that the NMR relaxation of all protons in the polymer is affected by the shear. Results are complicated by the formation of shear bands (*11*). Other studies showed, that shearing a polymer melt may result in loosening of entanglements (*12*).

Especially the transverse relaxation time T_2 is sensitive to slow motions (*13*) as they are present in the polymer chain segments between chemical or physical crosslinks (*14*, *15*). Another efficient measure of the polymer dynamics is the evaluation of the residual dipolar coupling between protons via the generation of double quantum coherences (*16–18*). A major advantage of the double quantum experiments is the fact, that a buildup of the double quantum signal is observed as opposed to the different kinds of decays like in the relaxation time experiments. The data may directly be converted into a dynamic order parameter. Relaxation experiments are feasible, even whan the residual dipolar couplings are too weak, i.e. in liquid-like systems, they can often be performed much faster.

Experimental Section

For the rheo NMR experiments an in-house built high-temperature rheo NMR probe head with an integrated Couette cell has been used. The probe head fits in the micro 2.5 gradient system of a Bruker Avance 300 WB NMR spectrometer operating at a Larmor frequency of 300 MHz for protons. The micro 2.5 gradient system generates magnetic field gradients of up to 1 T/m in three axis. The Couette cell is composed of a 10 mm NMR tube as the outer cylinder with an inner diameter of 8.6 mm and exchangeable rotating inner cylinders with a diameter of 6 mm, generating a gap of 1.3 mm. The rotor is made of PEEK with a structured surface to minimize slip. Shear is applied by driving the rotor with an external servo motor located on the top of the magnet and controlled by the spectrometer. The sample is heated by hot air. The gradient system, the shims and the superconducting magnet are protected by a cooling gas flow. Between the sample and the gradient coils a temperature gradient of 10 K/mm has to be maintained. A dedicated temperature control system is in place to protect the probehead, the gradient system and the superconducting magnet monitoring the entire experiment. Initially temperatures have been calibrated in a an off-line experimente, because temperature sensors would detoriate the sensitivity of the NMR experiment. Gas flow and gas temperatures have been monitored to adjust the sample temperature.

Downloaded by OHIO STATE UNIV LIBRARIES on June 20, 2012 | http://pubs.acs.org
Publication Date (Web): October 14, 2011 | doi: 10.1021/bk-2011-1077.ch026

The sample has been molten in the outer cylinder outside of the magnet. Subsequent the components of the rheo cell were assembled in a dedicated holder centering the rotor in the melt and placed into the probehead.

Imaging and velocity profiles, derived from a combination of NMR imaging with PFG NMR, have been used to view the melt in the gap and to monitor the steady shear. Due to the visco-elasticity, increasing rotational velocity causes the polymer melt to climb up the rotor (Weissenberg effect) and thus disrupting the shear in the gap. The used rotor frequencies were 0.5, 1, 2 and 5 rps, yielding shear rates at the wall of the inner cylinder between 12 and 122 s^{-1}.

Downloaded by OHIO STATE UNIV LIBRARIES on June 20, 2012 | http://pubs.acs.org
Publication Date (Web): October 14, 2011 | doi: 10.1021/bk-2011-1077.ch026

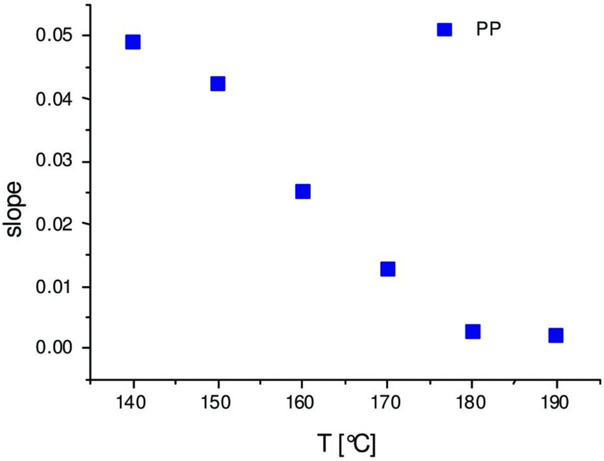

Figure 1. Intensities of the double quantum signal of poly(propylene) as a function of the sample temperature.

The influence of different temperatures and shear rates of the melt has been investigated by relaxation and DQ measurements without spatial resolution. CPMG, spin echo and inversion recovery sequences have been used for T_2 and T_1 experiments, for the double quantum experiments a pulse sequence based on (*16*, *17*) has been applied. The 90° pulse length was 28 µs and a repetition delay of 3 s was employed. The number of points has been restricted to limit the time duration for which the sample is exposed to high temperatures in order to avoid sample degradation.

The sample used in this study was isotactic poly(propylene) (i-PP), blended with 3% PP-g-maleic anhydride (M_w = 250 kg/mol, M_w/M_n = 4.1), which is often used as an additive in composite materials. The melt temperature of 163.5 °C and the crystallinity of 50 % (based on the melting enthalpy of 207 J/g of 100% crystalline i-PP (*19*)), were analyzed by DSC.

Results and Discussion

Homonuclear double quantum spectra have been recorded as a measure of the residual dipoar coupling during the melting process of the polymers. As is depicted in Fig. 1 the intensity of the double quantum signal diminishes, when the polymer melts. The mobility in the polymer becomes sufficiently high, that the dipolar coupling is averaged to a degree, that no double quantum intensity is observable. Unexpectedly no double qunatum signals have been observed under the shear rates applied in the present study, indicating, that only limited order of the polymer chains has been induced by the shear.

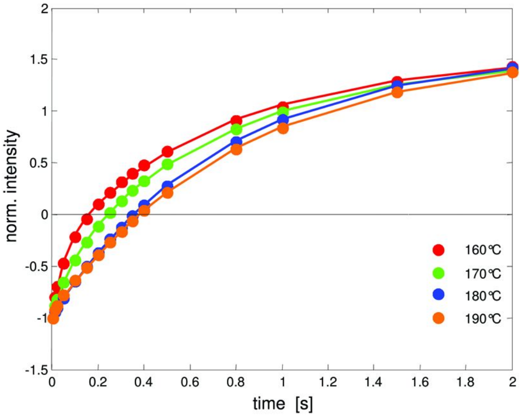

Figure 2. Longitudinal relaxation time (T_1) experiments by inversion recovery of poly(propylene) as a function of the sample temperature.

Fig. 2 shows the temperature dependence of the longitudinal relaxation time, the lines show the fitted curves with the values shown in Table 1. At temperatures below the nomimal melting point (160 °C) biexponential decay is observed. Above 170 °C T_1 can be described by a single exponential. The increase of T_1 with increasing temperature is attributed to slowing down spin diffusion due to the enhanced molecular mobility. The small difference of the two components below the melting point and the fact that above the melting point a single component is observed, show that spin diffusion is important for T_1. The major relaxation mechanism is the methyl rotation and thus the efficiency of the spin diffusion from CH and CH_2 protons is important for the longitudinal relaxation. The parameters used to fit the experimental data of all T_1 experiments a summarized in Table 1.

The temperature dependence of the transverse relaxation time T_2 is depicted in Fig. 3 showing a strong increase of T_2 upon melting. T_2 increases further with increasing temperature showing the enhanced mobility of polymer chain segments between entanglements as expected. T_2 shows a multiexponential behaviour as for most polymers, and can sufficiently be described by a biexponential fit. The results from the fit are shown in Table 2. A short component in the order of 20 to 80 ms

Downloaded by OHIO STATE UNIV LIBRARIES on June 20, 2012 | http://pubs.acs.org
Publication Date (Web): October 14, 2011 | doi: 10.1021/bk-2011-1077.ch026

and the longer component raises from 200 ms to 300 ms. The parameters used to fit the experimental data of all T_2 experiments a summarized in Table 2.

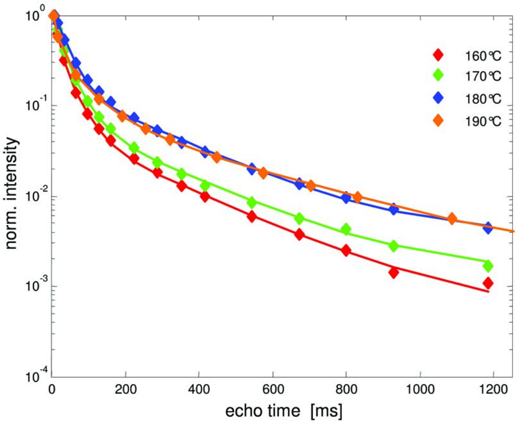

Figure 3. Decay curves from CPMG experiments as a function of the sample temperature.

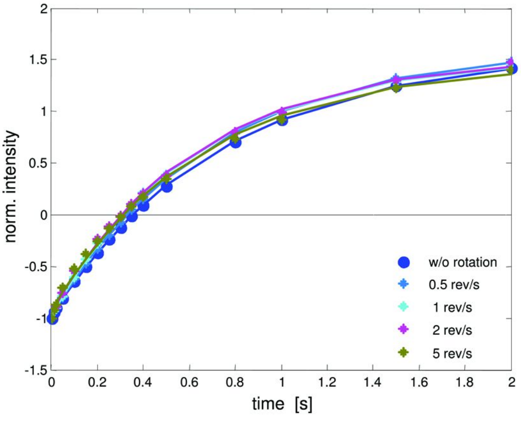

Figure 4. T_1 as a function of the shear rate of poly(propylene) at 180 °C.

If the inner cylinder is rotated with a torque applied from the servo motor, the poymer melt in the gap between the two cylinders is sheared. The melt sticks to both cylinders, thus the polymer is at rest on the outer wall and rotates with the inner cylinder.

Downloaded by OHIO STATE UNIV LIBRARIES on June 20, 2012 | http://pubs.acs.org
Publication Date (Web): October 14, 2011 | doi: 10.1021/bk-2011-1077.ch026

Downloaded by OHIO STATE UNIV LIBRARIES on June 20, 2012 | http://pubs.acs.org
Publication Date (Web): October 14, 2011 | doi: 10.1021/bk-2011-1077.ch026

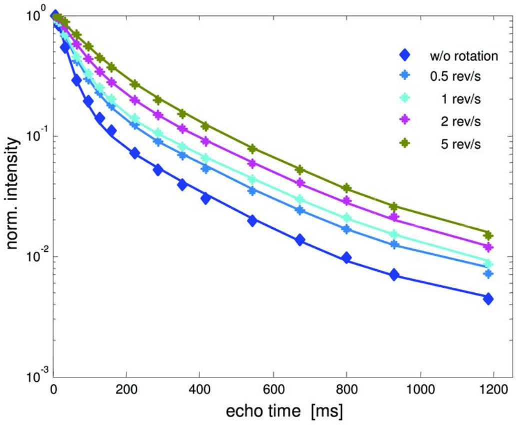

Figure 5. Decay curves from CPMG experiments at 180 °C as a function of the shear rate.

Shearing the polymer at a constant sample temperature of 180 °C does not result in a significant change of T_1 as depicted in Fig. 4. Comparing to the strong temperature dependence of the longitudinal relaxation seen in Fig. 2 one can conclude, that the sample temperature has not been increased by shearing the highly viscous polymer melt. From the viscosity a temperature increase of up to 30 K would have been anticipated. Because the sample is heated by an air flow of 17 l/min, the additional heat is taken away from the sample by convection.

Table 1. Results from the fits for the longitudinal relaxation time T_1

T [°C]	*rotation* [rev/s]	T_1 [s] component 1	T_1 [s] component 2
160	0	0.73	0.06
170	0	0.73	0.10
180	0	0.74	
190	0	0.83	
180	0.5	0.70	
180	1	0.63	
180	2	0.64	
180	5	0.64	

Downloaded by OHIO STATE UNIV LIBRARIES on June 20, 2012 | http://pubs.acs.org
Publication Date (Web): October 14, 2011 | doi: 10.1021/bk-2011-1077.ch026

Table 2. Results from the fits for the transverse relaxation time T_2

T *[°C]*	*rotation* *[rev/s]*	*T_2 [ms]* *component 1*	*T_2 [ms]* *component 2*
160	0	19	224
170	0	25	227
180	0	34	242
190	0	53	375
180	0.5	47	258
180	1	50	281
180	2	65	285
180	5	83	269

The effect of shearing on T_2 is shown in Fig. 5, showing an increase in T_2 as a function of the shear. The signal decay curves under shear are well-described by a double exponential decay. Both components increase from 40 ms to 60 ms and 150 ms to about 300 ms respectively. The fraction of the component with a larger T_2 increases with the shear rate.

The increase in T_2 implies an increase in the mobility of chain segments as a result of the shear. A decrease in T_2 would have been indicative for possible chain ordering, which has not been observed. The increase of T_2 and thus of chain mobility is explained by loosing some of the entanglements of the polymer chains as a result of the shear-induced motion of the polymer chains.

Conclusions

Rheo NMR of polymer melts at high temperatures has been demonstrated. Both the longitudinal and the transverse relaxation times exhibit a strong temperature dependence in the temperature range of the melting point. The observed temperature dependence of the longitudinal relaxation time has been utilized to exclude a shear-induced rise in the sample temperature in the present study.

The transverse relaxation time T_2, which is sensitive to slow molecular motions typical for polymer chain segments between crosslinks or entanglements, is becoming longer. The polymer network looses entanglements as a result of the shear. The absence of a significant double quantum signal together with the increase in T_2 indicate, that chain ordering, which would be anticipated, is not the dominating effect. The effect of orientation of the polymer chains is negligible. The most reasonable explaination for the prolongation of T_2 is the partial loss of entanglements resulting in longer chain segments between entanglements.

Acknowledgments

This work has been supported by the Deutsche Forschungsgemeinschaft (DFG) under grant SCHE 524/9 in the Materials World Network. The sample has been provided by Dr. Harkin-Jones (Queen's University Belfast).

References

1. Gogos, C. C.; Tadmor, Z.; Kim, M. H. *Advances in Polymer Technology*; John Wiley & Sons, Inc.: New York, 1998; Vol. 17, No. 4, pp 285–305.
2. Dealy, J. M.; Wissbrun K. F. *Melt Rheology and Its Role in Plastics Processing*; Chapman and Hall: London, 1996.
3. Chenoy, A. V.; Saini, D. R. *Thermoplastic Melt Rheology and Processing*; Marcel Dekker: New York, 1996.
4. Phillips, A. W.; Bhatia, A.; Zhu, P.-w.; Edward, G. *Macromolecules* **2011**, *44*, 3517.
5. Somani, R. H.; Yang, L.; Hsiao, B. S. *Polymer* **2006**, *47*, 5657.
6. Xu, J.-Z.; Chen, C.; Wang, Y.; Tang, H.; Li, Z.-M.; Hsiao, B. S. *Macromolecules* **2010**, *44*, 2808.
7. Callaghan, P. T. In *Encyclopedia of NMR*; Grant, D. M., Harris, R. K., Ed.; Wiley: Chichester, 2002; Vol. 9, p 737.
8. Grabowski, D. A.; Schmidt, C. *Macromolecules* **1994**, *27*, 2632.
9. Lukaschek, M.; Grabowski, D. A.; Schmidt, C. *Langmuir* **1995**, *11*, 3590.
10. Medronho, B.; Schmidt, C.; Olsson, U.; Miguel, M. G. *Langmuir* **2010**, *26*, 1477.
11. Callaghan, P. T.; Gil, A. M. *Macromolecules* **2000**, *33*, 4116.
12. Badiger, M. V.; Rajamohanan, P. R.; Suryavanshi, P. M.; Ganapathy, S.; Mashelkar, R. A. *Macromolecules* **2002**, *35*, 126.
13. Fedotov, V. D; Schneider, H. *NMR Basic Principles and Progress*; Springer: Heidelberg, 1989; Vol. 21.
14. Hiller, W.; Schneider, H. *Acta Polym.* **1988**, *39*, 276.
15. Knörgen, M.; Menge, H.; Hempel, G.; Schneider, H.; Reis, M. E. *Polymer* **2002**, *43*, 4091.
16. Saalwächter, K. *Prog. Nucl. Magn. Reson. Spec.* **2007**, *51*, 1–35.
17. Graf, R.; Heuer, A.; Spiess, H. W. *Phys. Rev. Lett.* **1998**, *80*, 5738.
18. Schneider, M.; Gasper, L.; Demco, D. E.; Blümich, B. *J. Chem. Phys.* **1999**, *111*, 402–415.
19. Bu, H. S.; Cheng, S. Z. D.; Wunderlich, B. *Makromol. Chem., Rapid Commun.* **1988**, *9*, 75.

Downloaded by OHIO STATE UNIV LIBRARIES on June 20, 2012 | http://pubs.acs.org
Publication Date (Web): October 14, 2011 | doi: 10.1021/bk-2011-1077.ch026

Chapter 27

NMR Imaging and Its Application in the Study of Pharmaceutical Tablets

H. Thérien-Aubin, Y. J. Wang, and X. X. Zhu*

**Département de Chimie, Université de Montréal, C.P. 6128, succursale
Centre-ville, Montréal, QC H3C 3J7, Canada
*E-mail: julian.zhu@umontreal.ca**

NMR imaging is a non-destructive and non-invasive technique especially well suited to investigate the kinetics of water uptake, swelling and erosion of pharmaceutical tablets used for drug delivery. Polysaccharides such as high amylose starch, cellulose derivatives and chitosan have been used as excipients in the tablets for the controlled release of drugs. NMR imaging may be used to quantitatively study the swelling of the compressed polymer tablets and the penetration of water in the polymer matrices. These results help to elucidate the effects of temperature, tablet size and drug loading on the properties and drug release process of the tablets. The new physicochemical understanding gained with NMR imaging techniques may help in the design and development of new oral tablets for more efficient drug delivery.

Introduction

Nuclear magnetic resonance (NMR) imaging, because of its non-destructive and non-invasive nature, requires no physical slicing of the sample to observe the interior of an object and has grown to be a technique of choice not only for biomedical imaging, but also in a myriad of other applications in material sciences and engineering (*1*). NMR imaging has become an interesting technique in the study of the dynamics of diffusion in polymer systems (*2–8*), and has been adapted to characterize the behavior of pharmaceutical tablets after immersion (*9–18*). A better understanding of the process of controlled release of drugs from the pharmaceutical tablets is essential to design and prepare more efficient

In NMR Spectroscopy of Polymers: Innovative Strategies for Complex Macromolecules; Cheng, H., et al.;
ACS Symposium Series; American Chemical Society: Washington, DC, 2011.

drug delivery systems. Therefore, it is essential to study the diffusion of small molecules, especially water and drugs, and the swelling and the dissolution of the tablets. NMR imaging may provide unique information on such phenomena.

The diffusion process in pharmaceutical tablets is usually studied by gravimetric methods for solvent uptake and by high performance liquid chromatography (HPLC) or UV spectrophotometry for the kinetics of drug release. These techniques, and others such as optical methods (*19–21*), allow an efficient overall general characterization of the system, while NMR imaging provides both general and spatially-localized information on the distribution of the compounds of interest inside and outside the polymeric matrix. NMR imaging is used to provide the spatial mapping of proton signals. The contrast of the images can be adjusted by the use of a range of physicochemical properties such as the difference in concentration, relaxation times, self-diffusion coefficients or flow rates. NMR imaging of pharmaceutical tablets has been mainly used to image the protons of mobile water molecules inside the system during the kinetic analysis of water uptake (*9*, *11*, *15*, *16*, *22–27*) as well as the diffusion of drugs from the tablets (*22*).

NMR Imaging Techniques

Basic Principles of NMR Imaging

In 1973, Lauterbur obtained the first image of the interior of an object (*23*) using magnetic field gradient to spatially encode information on both frequency and phase. Lauterbur (*23*) used frequency-encoding to map his sample, two tubes of water in a larger D_2O tube (Figure 1), by the conversion of spectral information into spatial information. A linear gradient of magnetic field with different orientation was applied to obtain multiple profiles of the object. With different projection acquired at different angle, it was possible to reconstruct the 2D image of the original object using the backprojection technique and algorithms used in X-ray tomography. Frequency-encoding is based on the fact that the resonance frequency of a nucleus changes with the strength of the magnetic field. If a gradient of magnetic field (G) is overlaid to the magnetic field of the NMR magnet (B_0), a variation in frequency is observed. The application of the gradient during the signal acquisition (Figure 2A) will encode the space in frequency leading to the recording of the sample's profile, the spin density distribution, i.e., the projection of the sample along the axe where the gradient is applied.

Subsequently, in 1974, Mansfield introduced a technique to add a third dimension to the NMR images using selective irradiation (*24*). As for the frequency-encoding, the slice selection is based on the fact that the presence of a gradient of magnetic field changes the Larmor frequency of the nucleus under observation according to its position in space. To selectively excite a given slice of the sample, a RF pulse should be applied simultaneously with the gradient pulse (Figure 2B). A sinc-shaped RF pulse was used to selectively excite a given Larmor frequency. When a short rectangular RF pulse is generated at a frequency ν_x, a broad distribution of RF with an average frequency centered at ν_x is generated, the broadness of the distribution being inversely proportional to the length of the pulse. RF pulses of lower intensity and longer duration could be used to contain only one frequency, or at least a narrower range of frequencies (*24*).

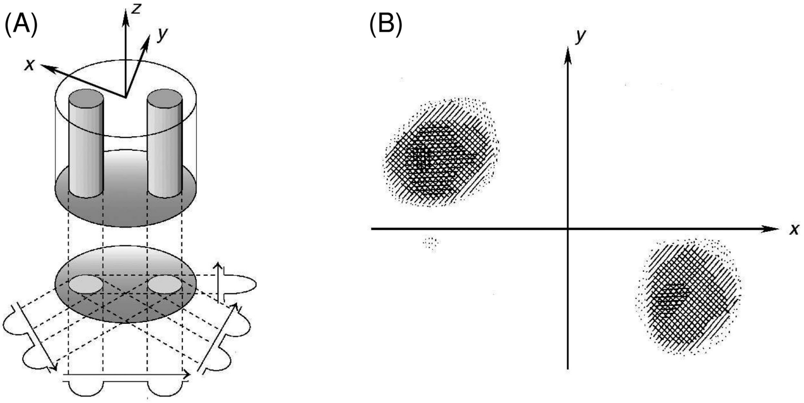

Figure 1. Lauterbur's experiment. (A) Acquisition of 4 profiles where the gradient axis is rotated by 45 increments. (B) Image obtained after the backprojection of the 4 profiles. Adapted by permission from Macmillan Publishers Ltd: Nature 242, 190-191, copyright 1973 (23).

An important development to NMR imaging, allowing faster image acquisition, was the concept of phase-encoding (*25*), which permits the construction of 2D images much faster than with the Lauterbur projection method. When a gradient of magnetic field is applied to the sample between the excitation and the signal acquisition, the precession speed of the nucleus spins is modified and spatially encoded (Figure 2C). The application of a linear gradient (G_x) causes a dephasing of the spin leading to reduction in the signal intensity. The 2D image is obtained by the frequency-encoding to provide a profile, and phase-encoding to relate the position of the nucleus to the spin phase by the application of N gradients of the magnetic field applied in the orthogonal direction to the slice and frequency-encoding gradients.

Signal Acquisition

NMR images are usually obtained using pulse sequences based either on a spin-echo (Figure 3A) or gradient-echo (Figure 3B) technique (*26*). The gradient-echo permits faster imaging caused by small flip angles needed for the excitation and the absence of a second RF impulsion which allows for shorter repetition time (TR) leading to the faster acquisition of similar S/N ratio in comparison to the spin-echo sequence. However, since gradient-echo is also more sensitive to small variation in the magnetic field, artifacts could be observed in region of variable magnetic susceptibility.

The intensity of the signal measured by NMR imaging varies according to Equations 1 and 2 for the spin-echo and gradient-echo experiments, respectively. The equations show that the intensity of the signal (S) varies with sample-specific factors such as spin density (ρ), longitudinal relaxation time (T_1) and transverse relaxation time (T_2), and with experiment-specific factors such as the echo time (TE) and the repetition time (TR) and the flip angle (α) in the gradient-echo experiment.

$$S = \rho(1 - e^{-TR/T_1})e^{-TE/T_2} \tag{1}$$

$$S = \rho\left(\sin\alpha\right)e^{-TE/T_2}\,\frac{1 - e^{-TR/T_1}}{1 - \left(\cos\alpha\right)e^{-TR/T_1}} \tag{2}$$

In the study of drug release from pharmaceutical tablets, a crucial factor is the diffusion coefficient or the velocity of the molecule in the presence of flow at different positions inside the tablet (*9*, *11*, *15*, *16*, *27*). The self-diffusion coefficients can be easily measured with NMR spectroscopy using the pulsed gradient spin-echo (*28*) or stimulated echo sequence (*29*). A first magnetic field gradient pulse is used to spatially encode the spin with their phase angle, while a second gradient pulse of the same amplitude and intensity applied after a given diffusion time is used to cancel the phase difference created by the first gradient pulse if the nucleus has not diffused to a new position; otherwise the signal measured will be attenuated. The NMR signal decreases with the amplitude of the gradient pulses and the diffusion coefficient following the equation

$$S\left(G\right) = S_0 \exp\left[\frac{-2\tau}{T_2} - \left(\gamma\delta G\right)^2 D\left(\Delta - \delta/3\right)\right] \tag{3}$$

where S(G) is the intensity of the NMR signal in presence of a gradient of amplitude G, S_0 the signal intensity in the absence of any gradient, γ the gyromagnetic ratio of the nucleus, δ the duration of the two gradients pulses, Δ the delay between the two gradients pulses and τ the interval between the 90° and 180° pulses of the spin-echo sequence. It is possible to obtain a diffusion coefficient map by merging the pulsed gradient spin-echo with the imaging spin-echo pulse sequences; one could then acquire a series of spin density images with different amplitudes of diffusion gradient and build the diffusion coefficient image (*30*, *31*).

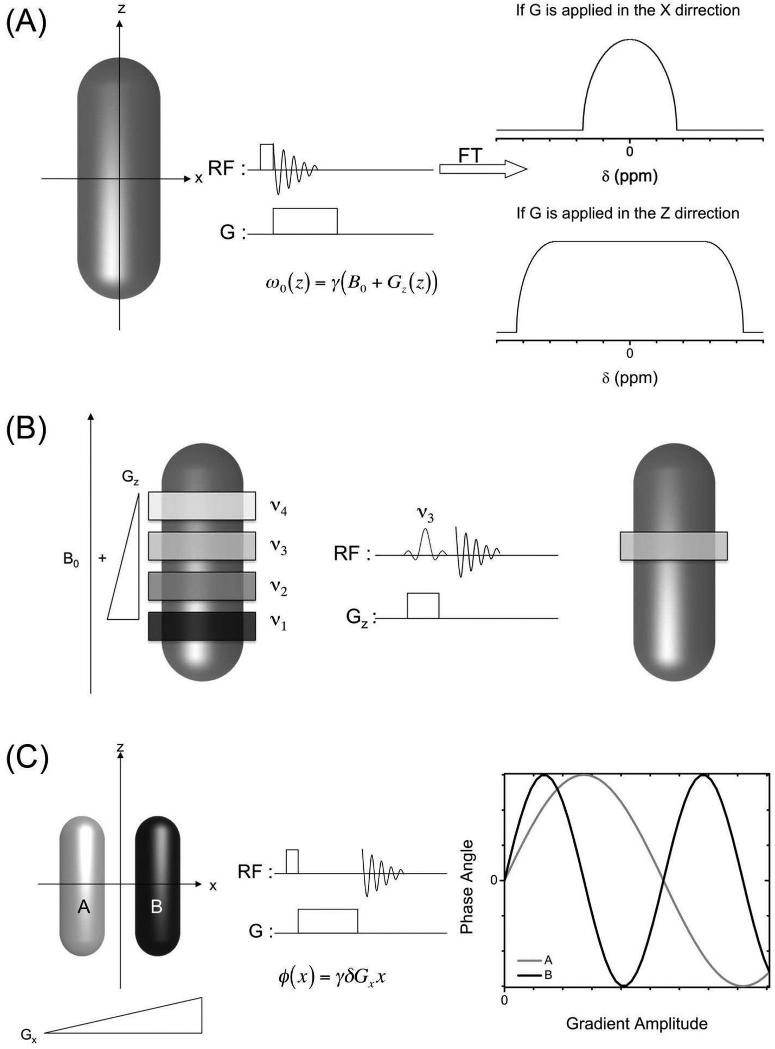
(A)
z
x
RF :
G :
FT
$\omega_0(z) = \gamma(B_0 + G_z(z))$
If G is applied in the X dirrection
0
δ (ppm)
If G is applied in the Z dirrection
0
δ (ppm)
(B)
B_0
+
G_z
ν_4
ν_3
ν_2
ν_1
ν_3
RF :
G_z :
(C)
z
x
A
B
G_x
RF :
G :
$\phi(x) = \gamma\delta G_x x$
Phase Angle
0
0
Gradient Amplitude
A
B

Figure 2. Basic principles of NMR imaging. (A) Frequency encoding of a cylindrical object, generated by the application of a magnetic field gradient during signal acquisition. (B) Slice selection with selective excitation pulse in presence of a magnetic field gradient. (C) Phase encoding generated by the application of a magnetic field gradient between the initial RF perturbation and signal recording.

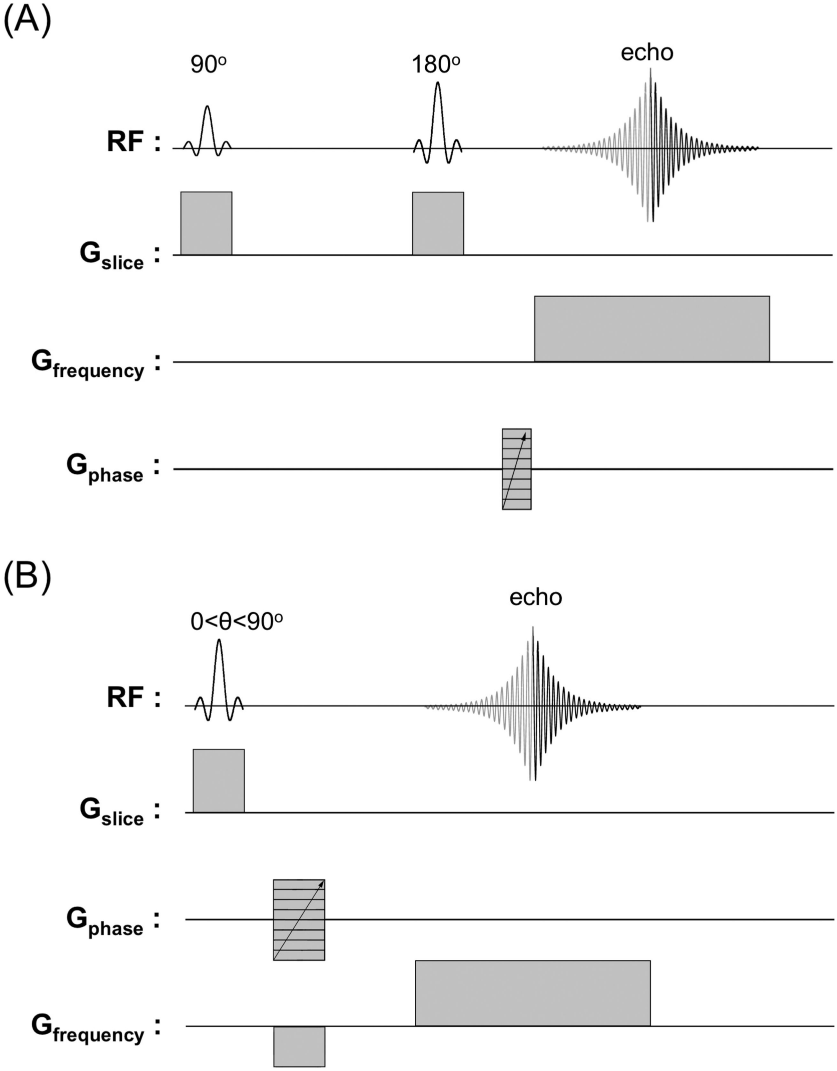

Figure 3. Simplified NMR imaging pulse sequences. (A) Spin-echo imaging; (B) Gradient-echo imaging.

It is also possible to obtain images where the signal is proportional to the relaxation times, by the acquisition of multiple images at different echo times, which could be used to reconstruct a T_2 map. A T_1 map could be obtained by the introduction of an inversion recovery segment in the pulse sequence and the acquisition of a series of images at different inversion times. With these relaxation time imaging techniques, it is possible to obtain useful results on the local dynamics of the water molecules in the tablets, which help to gain a better understanding of the swelling and drug release since the relaxation times vary with the local molecular environment as shown in Figure 4 (*11*, *12*, *32*, *33*).

Technical Considerations

Equations 1 and 2 show that if the echo time TE is kept short in comparison with T_2 and if the repetition time TR is long in comparison with T_1, the mapping will be only proportional to the spin density, i.e., the concentration of the nucleus under observation. If TR is kept short or TE is long, it is possible to obtained T_1- or T_2-weighted images, respectively. By choosing the repetition and echo times, one can change the signal intensity of different species of the image for a better contrast; this is particularly interesting for whole body imaging since relatively large variation of relaxation times may be observed for different types of tissues (*34*).

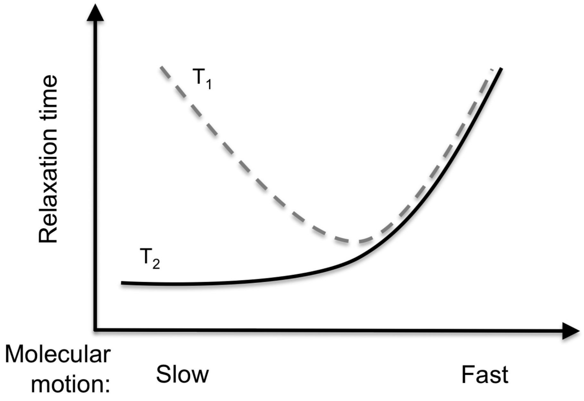

Figure 4. Variation of the relaxation times according to the molecular motion velocity of the sample.

In the study of diffusion in pharmaceutical tablets, the results obtained by NMR imaging are usually maps of water concentration inside the tablets. Figure 5 shows examples of the spin density images of the water uptake of a polysaccharide-based tablet. One can observe a receding dry part of the tablet (purple) and an increase in the overall dimension of the tablet with the immersion time. At the water-tablet interface in Figure 5, a red area is observed, giving the impression that the spin density is higher in this region than in free water (*14*, *35*, *36*). This effect is created to facilitate the identification of the water-tablet interface by setting the TR shorter than the T_1 of free water but longer than the T_1 of the water inside the tablet, leading to the attenuation of the signal of free water because the TR does not allow the full relaxation of the free water protons, while allowing full relaxation of the water inside the tablet between two repetitions.

The spin-spin relaxation is so fast in the dry part of the tablet that even with very short TE it is difficult to observe the signal from this part. When the echo time used is short enough, only the mobile protons are observed selectively. In this case the water protons are the only ones contributing to the NMR signal. As water diffuses in the tablet, the proton signal (or spin density) increases, which is also partly due to an increase in the T_2 of water (Figure 4).

The maximal resolution that could be achieved by NMR imaging varies with a number of factors, including the concentration and relaxation time of the sample and also the spectrometer frequency and gradient strength. In whole body imaging, a resolution of 1-2 mm is typical, but in microimaging, which operate usually at a much higher frequency, a resolution of 100 μm is standard and resolutions of 10 μm are possible.

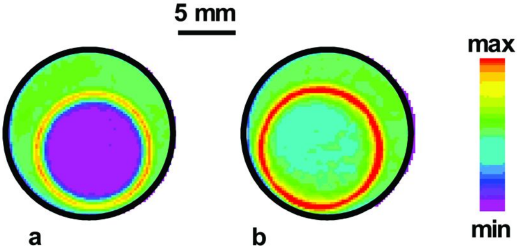

Figure 5. Radial section of the crosslinked high amylose starch (CHAS) tablet after immersion in water at 37 °C for (a) 45 minutes and (b) 50 hours. Color gradient scale represents the ^{1}H spin density. (see color insert)

NMR Imaging of Pharmaceutical Tablets

Experimental Setup

NMR imaging is an ideal method to record *in situ* the swelling behavior of solid oral dosage forms. It can be used to evaluate the polymer concentration profile in the tablets (*37*, *38*), quantify dimensional changes (thickness, area and volume) during the swelling (*14–16*, *35*, *36*), and define the diffusion front of the sample (*14*, *35*). Furthermore, the NMR imaging studies can provide the diffusion coefficient of a liquid component (*15*, *16*), and T_1 and T_2 values which are related to the environment of the penetrant and its interaction with the polymer excipients (*12*).

The NMR imaging experiments are normally carried out at 37.0 °C. We used a Bruker Avance-400 NMR spectrometer operating at a frequency of 400.27 MHz for protons and equipped with a microimaging probe with a 20 mm inner diameter. A standard spin-echo pulse sequence was used to obtain spin density images of each tablet in a 20 mm o.d. NMR tube containing 20 mL of the media (distilled water, buffer solutions or simulated physiological fluids). A slice of 0.5 mm in thickness was selected either perpendicular or parallel to the main magnetic field using a sinc-shaped pulse. Eight scans were accumulated to obtain 128 × 128 pixel images for a field of view of 2.0 cm, leading to an in-plane resolution of 156 μm. An echo time of 3 ms and a repetition time of 1 s were fixed, leading to an acquisition time of about 17 min for each image. The tablets were placed on a home-made Teflon support, which allowed three-dimensional liquid penetration (Figure 6).

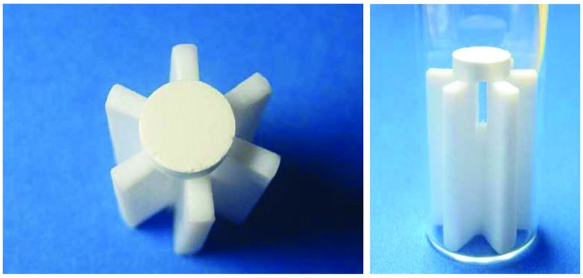

Figure 6. A tablet on a Teflon support placed in a 20 mm o.d. NMR tube.

Diffusion-weighted images were acquired by combining the spin-echo pulse sequence with the pulsed gradient spin-echo (PGSE) pulse sequence developed by Stejskal and Tanner (*28*). The diffusion time (Δ) and the length of the gradient pulse (δ) were set at 10 ms and 2 ms, respectively. The gradient strength varied from 5 to 100 G/cm.

When the simulated physiological fluids were used, some defects might be observed due to the high ionic strengths of the fluids, as shown by the bright spots above the tablets in SGF in Figure 7. ^{1}H tuning and matching strongly depend on the ionic strength of the sample. A buffer solution may cause de-tuning of the probe and the appearance of artifacts in the NMR images (*39*, *40*).

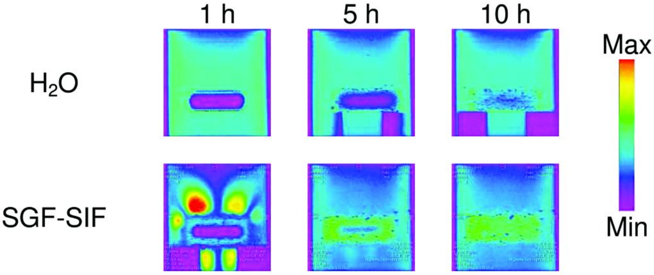

Figure 7. The NMR images of the carboxymethylated starch (CMS)-chitosan complex tablets immersed in water and simulated physiological fluids at 37 °C for 1, 5, and 10 h. (see color insert)

Swelling and Water Diffusion of Polysaccharide Tablets

Cross-linked high amylose starch (CHAS) (*41*, *42*) was used to prepare selected tablets. The starch of a high content of amylose yields a stronger gel (*43*). Covalent cross-links and hydroxypropyl side chains of the final product allow greater stability by hindering retrogradation over time (*43*). Retrogradation of starch is used to define the changes from amorphous state to a more ordered or crystalline state.

CHAS can provide sustained drug release as an excipient of oral drug dosage form by the formation of a membrane at the outer layer of the tablets upon hydration and maintaining the tablet integrity in water for days. The absence of erosion and limited swelling allow for further explorations of the applications in drug delivery (*44*). Review articles on the NMR imaging of starch-based tablets were published previously (*45*, *46*). We summarize here the NMR imaging results obtained for selected polysaccharide tablets (*14–16*, *35*, *36*, *45–47*) in an effort to illustrate the usefulness of NMR imaging in such studies.

Gel Formation and Water Gradient

NMR imaging could be used to spatially map the proton signals, and thus to follow water uptake by starch tablets. In Figure 5, the tablet is immerged in water inside a NMR tube and a 2D NMR image of a slice inside the sample could be obtained using a slice selective pulse sequence. The NMR images show the formation of a hydrated membrane at the water-tablet interface. Figure 8 shows that the membrane thickness increases rapidly at first then remains constant at ca. 0.4 mm until 50 h. This membrane regulates the diffusion of water into the tablet (*48*). The water concentration in the core of the tablet increases slowly after the initial swelling of the tablet until a constant water concentration is reached. After 80 h, the membrane thickness increases drastically to reach ca. 2 mm and then the gelation of the whole tablet is observed (*14*, *22*, *35*, *36*, *48*).

The NMR images provide access to water concentration profile inside the tablet, which can be used to calculate the water diffusion coefficient (*15*, *16*, *36*). If the diffusion is Fickian, and that the shape of the tablet is assumed to be an infinite cylinder (to disregard the edge effects). At the initial stage of the diffusion process in water at 37 °C, these assumptions are considered to be fulfilled for the CHAS tablet, at longer immersion times the edge effects will not be negligible. The solution of Fick's law of diffusion for an infinite cylinder can be used for the calculation of the diffusion coefficients (*49*). The diffusion coefficient measured decreases by a factor of 10 during the first 10 h following the immersion (Figure 9), the period during which the outer gel membrane was formed. The formation of a gel layer with a low porosity resulting from the reorganization of the starch chains accounts for the reduced diffusivity observed after the immersion. While Figure 9 provides a general trend for the changes in water diffusion coefficient values, it should be noted, however, that the *D* values at longer immersion times have larger errors since the contribution of the edge effects becomes important and, strictly speaking, the assumptions made are no longer appropriate.

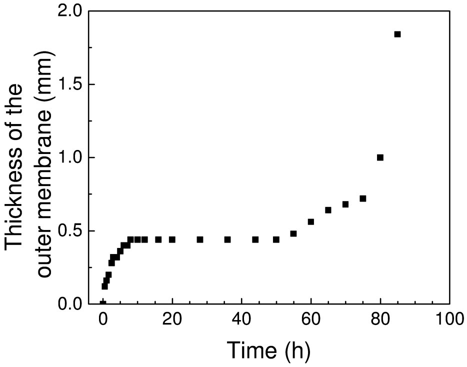

Figure 8. Thickness of the hydrated membrane shell of the CHAS tablet at 37 °C after its immersion in water.

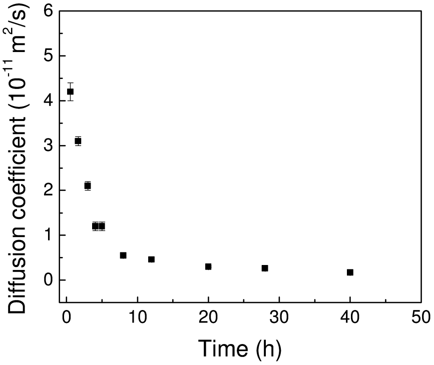

Figure 9. The decrease of the self-diffusion coefficient of water at 37 °C in the CHAS tablet during the formation of the outer gel membrane.

When a CHAS tablet is immersed into water, water penetrates into the hydrophilic polymer matrix to form a hydrogel, leading to a steep water gradient. The formation of the membrane at the liquid/tablet interface is essential to the tablet integrity and to the sustained drug release (*15*, *50*). X-ray tomography experiments of the membrane showed the significant difference between the porosity of the outer layer and dry core (*50*). The formation of the membrane can be followed with the NMR images adjusted with either proton density or self-diffusion coefficient contrast (*15*). The different regions of the tablets are more obvious on the self-diffusion coefficient profile extracted at the center of the tablet (Figure 10) than in the water concentration profile (*15*). The membrane is mainly composed of a region where the self-diffusion coefficient of liquid is stable.

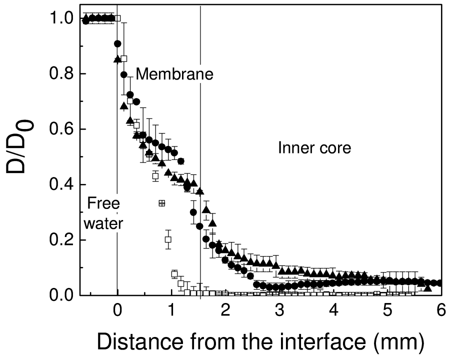

Figure 10. Self-diffusion coefficient profile in the center of the tablet for CHAS tablet (□) without drug, (•) loaded with 10% acetaminophen, and (▴) loaded with 10% ciprofloxacin after 15 h of immersion. Adapted from ref. (15).

Anisotropic Swelling

The swelling is anisotropic with the axial swelling being much more significant than the radial swelling for all the tablets of different sizes and within the temperature range from 25 to 60 °C (Figure 11) (*14*, *35*, *36*). The more pronounced axial swelling is related to the relief of the stresses induced during compaction of the tablets (*51*). However, the thicknesses of the gel layer along both directions are similar (*52*). The glassy-rubbery transition is based on the lowering of the glass-transition temperature (T_g) of the polymer, which is controlled by the water concentration and depends on temperature and thermodynamic interactions of the polymer-water system. The swelling of the CHAS tablets approaches its maximum at around 10 h at 37 °C but 60% of swelling can be achieved within the first 4 h (*36*). The water uptake and the tablet swelling strongly depend on the size of the tablets (*35*). The swelling rate is faster for small tablets along both swelling directions due to their larger surface/volume ratio.

Effect of Temperature

The water diffusion in the CHAS tablets was studied at four different temperatures (25, 37, 45, and 60 °C) (*14*, *36*). The diffusion process is Fickian between 25 and 45 °C and Case II at 60 °C (*36*). The tablets manifested a faster swelling with increasing temperature up to 60 °C (Figure 11). The difference is caused by the different degrees of the transformation from V-type single helix polymorph to B-type double helices during water uptake (*35*, *36*). The double helical conformation acts as physical cross-links which in turn limit the swelling and is thus essential for the sustained drug release, which is verified by CP-MAS ^{13}C NMR spectroscopy (*44*, *53*). Water penetrating into a tablet to acts as a plasticizing agent. This plasticizing effect increases the intermolecular spaces and thus allows greater mobility to starch molecules which rapidly reorganize into the thermodynamically more stable B-type double helix conformation (*43*).

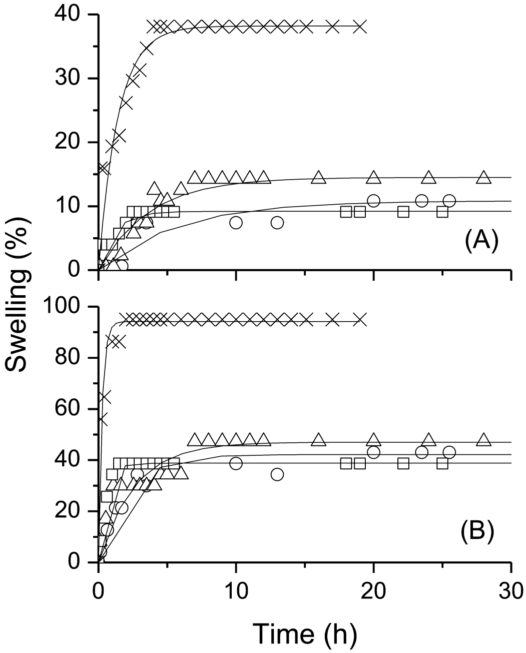

Figure 11. Swelling kinetics of the CHAS tablets along (A) radial direction and (B) axial direction at various temperatures. □, *25 °C;* ○, *37 °C;* △, *45 °C; and* ×, *60 °C. Adapted from ref. (36).*

Effect of Drug Loading

The drug loading effect was studied first by comparing tablets loaded with 10 wt% soluble drugs (ciprofloxacin and acetaminophen) and tablets without the drugs (*15*). The extent of the swelling of the tablets was not noticeably influenced by a 10 wt% drug-loading, since the presence of drugs at this content did not interfere with the formation of double helices which limited the overall swelling of the CHAS tablets (*15*). However, the presence of drug molecules caused a faster water uptake, as reflected by the higher diffusion coefficients of water.

The swelling of the CHAS tablets loaded with different amounts of acetaminophen (10, 20 and 40 wt%) were studied by NMR imaging (Figure 12) (*16*). The presence of drug molecules accelerated water uptake due to the changes in the chemical potential gradient. The higher drug loading led to a faster water diffusion into the tablet. The drug solubility and the degree of drug loading have little influence on the diffusion coefficient of water in the outer membrane formed. Water diffuses faster for tablets with higher drug loading and increases gradually with time (Figure 13).

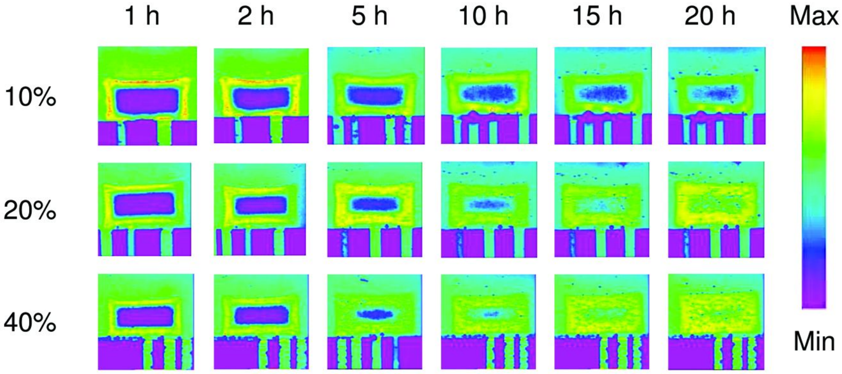

Figure 12. NMR images of CHAS tablets of different drug loading levels (10 – 40 wt %) immersed in water at 37 °C for 1, 2, 5, 10, 15, and 20 h. The purple part at the bottom of the images is the Teflon support. Reproduced with permission from NRC Research Press (16). (see color insert)

Despite the different rates of water uptake and diffusion in the tablets, the percentage of the drug released remained similar for all the CHAS tablets. The outer membrane ensured a controlled release of acetaminophen, regardless of the amount of drug in the tablet (*16*).

The changes of the water diffusion coefficient and the tablet swelling strongly depend on the solubility of the drug and the loading level. The drug releasing rate merely undergoes a minor change with increasing drug loading amount. Compared to the CHAS tablets without loaded drugs, the tablets loaded with 10 – 40 wt % acetaminophen swell substantially faster. The matrix is able to keep the integrity of all the tablets after their immersion in water for a long time up to 50 hours.

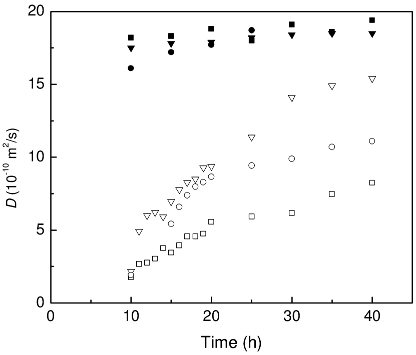

Figure 13. Self-diffusion coefficients of water in the inner core of the tablets loaded with 10% (□), 20% (○), and 40% acetaminophen (▿) obtained by diffusion-weighted imaging. The D values of water in the hydrated gel membrane of the tablets are shown by closed symbols. Reproduced with permission from NRC Research Press (16).

The Study of Various Polymer Matrices

The swelling of the CHAS tablets were compared with the tablets made of polyelectrolyte matrices including chitosan, carboxymethylated starch (CMS) and CMS-chitosan complex in both acidic and neutral media. Simulated gastric and intestinal liquids (SGF and SIF) were used for the *in vitro* study of the swelling and drug dissolution of the tablets (Figure 7). In the case of SGF, some artifacts appeared on the NMR images.

The tablets made of chitosan, CMS, and the CMS-chitosan complex showed pH-sensitive swelling due to the presence of –COONa and/or $–NH_2$ functional groups. The CMS-chitosan polyelectrolyte complex tablets have similar swellings to those of CHAS tablets in neutral media. However, the complex tablets in SGF showed a greater extent of swelling. The remarkable dimensional change in SGF was mainly contributed by chitosan that was dissociated from its complex with CMS.

The effect of pH is more pronounced than that of the ionic strength for the tablets without drug loading. The swelling at different pH values depends on the pK_a of the matrix. In the case of drug-loaded tablets, the drug release rate is affected by the pK_a values of both the matrix and the drug rather than the drug loading level.

Conclusion

NMR imaging is an effective method that can provide information on the diffusion and swelling processes of tablets useful in the development and formulation of new drug delivery vehicles for pharmaceutical applications. The contrast of the images may be adjusted by the choice of the experiment parameters such as gradient strength, repetition time, echo time and flip angle. The self-diffusion coefficients of the diffusing fluid may also be obtained and correlated with the swelling of the tablets. The formation of the gel membrane, the disappearance of the dry core and the drug dissolution can be visualized. The membrane is crucial in obtaining the controlled release of drugs from the tablets. The effects of tablet size, temperature, drug loading level and different polymer matrices on the tablet swelling and liquid diffusion in the tablets have been studied. These studies show that the use of NMR imaging techniques provides results that facilitate the development and optimization of polymeric excipients for controlled drug delivery.

Acknowledgments

The authors acknowledge the financial support from the Natural Science and Engeneering Research Consil of Canada (NSERC), le Fond Québécois de Recherche sur la Nature et les Technologie (FQRNT), and the Canada Research Chair program.

References

1. Blumich, B. *NMR Imaging of Materials*; Oxford University Press: Oxford, 2003.
2. Rothwell, W. P.; Holecek, D. R.; Kershaw, J. A. *J. Polym. Sci., Part C: Polym. Lett.* **1984**, *22*, 241–247.
3. Blackband, S.; Mansfield, P. *J. Phys. C: Solid State Phys.* **1986**, *19*, L49–L52.
4. Weisenberger, L. A.; Koenig, J. L. *Appl. Spectrosc.* **1989**, *43*, 1117–1126.
5. Malveau, C.; Beaume, F.; Germain, Y.; Canet, D. *J. Polym. Sci., Part B: Polym. Phys.* **2001**, *39*, 2781–2792.
6. Mayele, M.; Oellrick, L. R. *Appl. Spectrosc.* **2004**, *58*, 338–343.
7. Zainuddin; Strounina, E. V.; Hill, D. J. T.; Whittaker, A. K. *Polym. Int.* **2010**, *59*, 1520–1525.
8. Hill, D. J. T.; Whittaker, A. K. *Radiat. Phys. Chem.* **2011**, *80*, 213–218.
9. Bowtell, R.; Sharp, J. C.; Peters, A.; Mansfield, P.; Rajabi-Siahboomi, A. R.; Davies, M. C.; Melia, C. D. *Magn. Reson. Imaging* **1994**, *12*, 361–364.
10. Rajabi-Siahboomi, A. R.; Bowtell, R. W.; Mansfield, P.; Henderson, A.; Davies, M. C.; Melia, C. D. *J. Controlled Release* **1994**, *31*, 121–128.
11. Rajabi-Siahboomi, A. R.; Bowtell, R. W.; Mansfield, P.; Davies, M. C.; Melia, C. D. *Pharm. Res.* **1996**, *13*, 376–380.
12. Fyfe, C. A.; Blazek, A. I. *Macromolecules* **1997**, *30*, 6230–6237.
13. Fyfe, C. A.; Blazek-Welsh, A. I. *J. Controlled Release* **2000**, *68*, 313–333.
14. Baille, W. E.; Malveau, C.; Zhu, X. X.; Marchessault, R. H. *Biomacromolecules* **2002**, *3*, 214–218.
15. Thérien-Aubin, H.; Zhu, X. X.; Ravenelle, F.; Marchessault, R. H. *Biomacromolecules* **2008**, *9*, 1248–1254.
16. Wang, Y. J.; Ravenelle, F.; Zhu, X. X. *Can. J. Chem.* **2010**, *88*, 202–207.
17. Mikac, U.; Sepe, A.; Kristl, J.; Baumgartner, S. *J. Controlled Release* **2010**, *145*, 247–256.
18. Tajiri, T.; Morita, S.; Sakamoto, R.; Suzuki, M.; Yamanashi, S.; Ozaki, Y.; Kitamura, S. *Int. J. Pharm.* **2010**, *395*, 147–153.
19. Bussemer, T.; Peppas, N. A.; Bodmeier, R. *Eur. J. Pharm. Biopharm.* **2003**, *56*, 261–270.
20. Gao, P.; Meury, R. H. *J. Pharm. Sci.* **1996**, *85*, 725–731.
21. Moussa, I. S.; Cartilier, L. H. *J. Controlled Release* **1996**, *42*, 47–55.
22. Fyfe, C. A.; Grondey, H.; Blazek-Welsh, A. I.; Chopra, S. K.; Fahie, B. J. *J. Controlled Release* **2000**, *68*, 73–83.
23. Lauterbur, P. C. *Nature* **1973**, *242*, 190–191.
24. Mansfield, P.; Grannel, P. K. *J. Phys. C: Solid State Phys.* **1973**, *6*, L422–L426.
25. Kumar, A.; Welti, D.; Ernst, R. R. *J. Magn. Reson.* **1975**, *18*, 69–83.
26. Callaghan, P. T. *Principles of Nuclear Magnetic Resonance Microsocopy*; Oxford University Press: Oxford, 1991.
27. Tritt-Goc, J.; Kowalczuk, J.; Pislewski, N. *J. Pharm. Pharmacol.* **2003**, *55*, 1487–1493.
28. Stejskal, E. O.; Tanner, J. E. *J. Chem. Phys* **1965**, *42*, 288–292.

29. Tanner, J. E. *J. Chem. Phys.* **1970**, *52*, 2523–2526.
30. Callaghan, P. T.; Eccles, C. D.; Xia, Y. *J. Phys. E: Sci. Instrum.* **1988**, *21*, 820–822.
31. Callaghan, P. T.; Xia, Y. *J. Magn. Reson.* **1991**, *91*, 326–352.
32. Kowalczuk, J.; Tritt-Goc, J. *Carbohydr. Polym.* **2011**, *83*, 166–170.
33. Chowdhury, M. A.; Hill, D. J. T.; Whittaker, A. K.; Braden, M.; Patel, M. P. *Biomacromolecules* **2004**, *5*, 1405–1411.
34. Rinck, P. A. *Magnetic Resonance in Medicine*, 5th ed.; Blackwell: Berlin, 2003.
35. Malveau, C.; Baille, W. E.; Zhu, X. X.; Marchessault, R. H. *Biomacromolecules* **2002**, *3*, 1249–1254.
36. Thérien-Aubin, H.; Baille, W. E.; Zhu, X. X.; Marchessault, R. H. *Biomacromolecules* **2005**, *6*, 3367–3372.
37. Djemai, A.; Sinka, I. C. *Int. J. Pharm.* **2006**, *319*, 55–62.
38. Baumgartner, S.; Lahajnar, G.; Sepe, A.; Kristl, J. *Eur. J. Pharm. Biopharm.* **2005**, *59*, 299–306.
39. Bock, C.; Frederich, M.; Wittig, R.-M.; Pörtner, H.-O. *Magn. Reson. Imaging* **2001**, *19*, 1113–1124.
40. Bock, C.; Sartoris, F.-J.; Pörtner, H.-O. *Magn. Reson. Imaging* **2002**, *20*, 165–172.
41. Lenaerts, V.; Beck, R. H. F.; Van Bogaert, E.; Chouinard, F.; Hopcke, R.; Desevaux, C. U.S. Patent 6,607,748, August 19, 2003.
42. Mateescu, M. A.; Lenaerts, V.; Dumoulin, Y. U. S. Patent 5,456,921, Oct.10, 1995.
43. Ravenelle, F.; Rahmouni, M. In *Polysaccharides for Drug Delivery and Pharmaceutical Applications*; Marchessault, R. H., Ravenelle, F., Zhu, X. X., Eds.; American Chemical Society: Washington, DC, 2006; pp 79−104.
44. Lenaerts, V.; Moussa, I.; Dumoulin, Y.; Mebsout, F.; Chouinard, F.; Szabo, P.; Mateescu, M. A.; Cartilier, L.; Marchessault, R. *J. Controlled Release* **1998**, *53*, 225–234.
45. Thérien-Aubin, H.; Zhu, X. X. *Carbohydr. Polym.* **2009**, *75*, 369–379.
46. Thérien-Aubin, H.; Zhu, X. X. In *Polysaccharides For Drug Delivery And Pharmaceutical Applications*; Marchessault, R. H., Ravenelle, F., Zhu, X. X., Eds.; American Chemical Society: Washington, DC, 2006; pp 105−120.
47. Wang, Y. J. Master's thesis, Université de Montréal, Montréal, Canada, 2011.
48. Kowalczuk, J.; Tritt-Goc, J.; Pislewski, N. *Solid State Nucl. Magn. Reson.* **2004**, *25*, 35–41.
49. Crank, J. *The Mathematics of Diffusion*, 2nd ed.; Oxford University Press: Oxford, 1975.
50. Chauve, G.; Ravenelle, F.; Marchessault, R. H. *Carbohydr. Polym.* **2007**, *70*, 61–67.
51. Papadimitriou, E.; Buckton, G.; Efentakis, M. *Int. J. Pharm.* **1993**, *98*, 57–62.
52. Moussa, I. S.; Lenaerts, V.; Cartilier, L. H. *J. Controlled Release* **1998**, *52*, 63–70.
53. Shiftan, D.; Ravenelle, F.; Mateescu, M. A.; Marchessault, R. H. *Starch/ Stärke* **2000**, *52*, 186–195.

Downloaded by STANFORD UNIV GREEN LIBR on June 20, 2012 | http://pubs.acs.org
Publication Date (Web): October 14, 2011 | doi: 10.1021/bk-2011-1077.ch028

Chapter 28

Effect of Molecular Architecture on the Performance of ^{19}F NMR Imaging Agents

**Hui Peng, Kristofer Thurecht, Steven Hsu, Idriss Blakey,
Oliver Squires, Nyoman Kurniawan, Stephen Rose,
and Andrew K Whittaker***

**Australian Institute for Bioengineering and Nanotechnology and
Centre for Advanced Imaging, University of Queensland,
Brisbane, QLD 4072, Australia
*E-mail: a.whittaker@uq.edu.au**

Traditional magnetic resonance medical imaging agents based on paramagnetic ions or particles have a number of critical limitations, namely image contrast is often limited at low concentrations and sensitivity of the agents becomes diminished at higher magnetic field strengths. In this chapter we describe the development of a new class of polymeric imaging agent which relies on direct detection of the NMR signal of fluorine nuclei and hence circumvents these potential problems. The imaging performance of the new materials relies on the maintenance of librational motion of the fluorinated segments, necessary for partial averaging of the otherwise strong dipole-dipole interactions and large chemical shift interactions of the ^{19}F nuclei. The performance of partially-fluorinated block copolymers assembled into particles is described and related to the interactions of the polymer chains with the surrounding solvent medium. A second generation of materials based on a hyperbranched structure was developed based on the learning obtained from the earlier experiments and these demonstrated excellent *in vitro* and *in vivo* imaging performance.

In NMR Spectroscopy of Polymers: Innovative Strategies for Complex Macromolecules; Cheng, H., et al.;
ACS Symposium Series; American Chemical Society: Washington, DC, 2011.

Downloaded by STANFORD UNIV GREEN LIBR on June 20, 2012 | http://pubs.acs.org
Publication Date (Web): October 14, 2011 | doi: 10.1021/bk-2011-1077.ch028

Introduction

Over the past several years the field of *in vivo* ^{19}F NMR imaging has started to receive renewed attention. This is a result of particular advantages of the ^{19}F imaging experiment, since unlike in ^{1}H NMR imaging, the body does not contain a significant concentration of fluorine to provide a background signal. The signal from injected fluorine-containing molecules will therefore appear bright against a dark background, and furthermore if the image is superimposed on a proton density image the location of the probe molecules in the body can be readily discerned. If probe molecule has included a targeting functionality, the text above describes the field of ^{19}F molecular imaging.

The fluorine nucleus possesses several attractive features for NMR imaging. The NMR-sensitive isotope,^{19}F, is present in high natural abundance, possesses a spin of I=1/2 and has the second-highest gyromagnetic ratio (40.03 MHz/T) of the commonly-encountered nuclei (*1*). This last property provides high sensitivity in the ^{19}F NMR experiment, however in the absence of fast, large amplitude motion may lead to substantial dipolar couplings to near-neighbor nuclei (^{1}H and ^{19}F). This is compounded by the large static chemical shift anisotropy of fluorine. Despite this, the promise of high sensitivity imaging of mobile fluorinated species has lead to a growing body of work.

Initial studies of the potential of ^{19}F for medical imaging were performed by Holland and co-workers who reported images of solutions of sodium fluoride and perfluorotributylamine within phantoms (*2*). The first *in vivo* ^{19}F images were reported by McFarland et al. (*3*) on rats injected with fluorocarbons. The ^{19}F longitudinal relaxation time is known to depend on the oxygen tension in the blood stream (*4*), and this was exploited by several workers in small animal models (*5*, *6*). These early studies did not progress beyond pre-clinical examination, due primarily to the lack of clinical scale scanners suitable for ^{19}F observation. This commercial bottleneck has now been removed.

The field therefore has been reinvigorated, as reflected by the work from groups in Carnegie Mellon University (*7–9*) and Washington University in St. Louis (*10–15*) who have advanced work on nanoparticles agents based on linear and cyclic perfluoroethers, and on branched polymers. The former molecules have the advantage of being able to be labelled covalently in a facile manner with fluorescent dyes, while the Wickline group incorporates a fluorescently-labelled phospholipid into an emulsion particle (*10–13*). The principal application proposed for these agents is cell tracking (*16*), and these workers and others have demonstrated *in vivo* imaging of dendritic cells labelled appropriately with the fluorinated particles. In more recent work, Higuchi et al. (*17*) have reported the imaging of amyloidophilic compounds containing fluorine as potential markers for the early stages of Alzheimer's disease. The potential use of fluorinated markers for non-invasive studies of physiology is abundantly clear and has been reviewed by Yu and others (*18*). In addition Ruiz-Cabello and colleagues have recently published an excellent review of the application of ^{19}F spectroscopy and MRI to medicine (*19*).

Examination of the literature reveals that there remain a number of fundamental challenges to be overcome for this technology to become widely

Downloaded by STANFORD UNIV GREEN LIBR on June 20, 2012 | http://pubs.acs.org
Publication Date (Web): October 14, 2011 | doi: 10.1021/bk-2011-1077.ch028

accepted. These are principally the low sensitivity resulting from the low fluorine content of many potential marker molecules, the large (isotropic) chemical shift dispersion of the ^{19}F nucleus, and the short T_2 relaxation times observed for potential structures arising from the large shift anisotropy and strong dipole-dipole couplings to near-neighbor fluorine and proton nuclei. This chapter describes two generations of polymeric molecules developed to address these issues, firstly self-assembled particles consisting of partially-fluorinated amphiphilic block, and secondly hyperbranched polymers consisting of similar building blocks. Polymeric agents have been chosen because of their potential for high fluorine content, and the possibility of attachment of multiple targeting agents to the end groups and side chains. Excretion of the polymers was confirmed as described below. The *in vitro* and *in vivo* performance is related in this chapter to the molecular structure of the polymeric agents.

Materials and Methods

Materials

Tert-butyl acrylate(*t*BA), 2,2,2-trifluoroethyl acrylate (TFEA), 2,2,2-trifluoroethyl methacrylate (TFEMA), hexafluoroisopropyl acrylate (HFPA), hexafluoroisopropyl methacrylate (HFPMA) and *n*-butyl acrylate (BA) were purchased from Aldrich, dried over CaH_2 and distilled under reduced pressure before use. CuBr was obtained from Aldrich and purified by washing with glacial acetic acid followed by absolute ethanol and ethyl ether, and then dried under vacuum. Ethyl 2-bromopropionate (EBrP), *N*,*N*,*N'*,*N''*,*N''*-pentamethyl diethylenetriamine (PMDETA) and trifluoroacetic acid (TFA) were purchased from Aldrich and used as received. Acetone was refluxed over CaH_2 and distilled under nitrogen before use. 2-dodecylsulfanyl thiocarbonyl sulfanyl-2-methyl propionic acid (*20*) and the alkyne analogue (*21*) were synthesized as previously reported. AIBN was recrystallized from methanol three times before use.

Dried toluene, dichloromethane (DCM) and dimethylformamide (DMF) were obtained oxygen- and moisture-free using a purification unit under an inert nitrogen environment (MBraun Solvent Purification System Auto-5).

Characterization

^{1}H NMR spectra of the polymers and intermediates were measured on a Bruker Avance 500MHz or 300 MHz spectrometer equipped with a TXI probe and operating at room temperature.

Gel permeation chromatography (GPC) measurements were performed using a Waters Alliance 2690 Separations Module equipped with an auto-sampler, column heater, differential refractive index detector, and a Photodiode Array (PDA) connected in series. HPLC-grade tetrahydrofuran was used as eluent at a flow rate of 1 mL/min. The columns consisted of three 7.8 × 300 mm Waters Styragel GPC columns connected in series, comprising two linear UltraStyragel and one Styragel HR3 columns. Polystyrene standards ranging from 517 to 2×10^6 g mol^{-1} were used for calibration.

Downloaded by STANFORD UNIV GREEN LIBR on June 20, 2012 | http://pubs.acs.org
Publication Date (Web): October 14, 2011 | doi: 10.1021/bk-2011-1077.ch028

Differential Scanning Calorimetry (DSC) analyses were performed using a Mettler Toledo DSC1 Star System calorimeter with a sub-ambient temperature attachment. The glass transition temperature (T_g) was determined as the centre of the change in heat capacity measured at a heating rate of 10 °C/min.

Dynamic light scattering (DLS) measurement was performed on a Nanoseries (Malvern, UK) zetasizer. The scattering angle used was 90° and the temperature was fixed at 298 K.

^{19}F NMR spectroscopy was performed on an AMX300 spectrometer interfaced to a 7 T vertical super-wide bore magnet. The system is equipped with a Bruker microimaging gradient set and the probe used was a Bruker 5 mm ^{19}F single-tuned bird-cage resonator probe tuned to 282.404 MHz for fluorine detection. The 90° pulse time was 5.5 μs. Samples of the fluorinated block copolymers were prepared as described below, and either maintained in mixed DMF-water solvent (or DMSO-water) or examined after dialysis in water. The concentration of the solutions prepared in 5 mm NMR tubes was approximately 2.5 wt. % of polymer. All measurements were performed at 310 K.

^{19}F NMR spectra of the solutions were recorded using a 90° pulse of 5.5 μs and a repetition delay of 10 seconds. The spectrum width was 50 kHz, and 4 k data points were collected. Typically 16 FIDs were co-added to improve the signal-to-noise ratio.

^{19}F T_2 relaxation times were measured using the CPMG pulse sequence, with from 2 to 256 180° pulses in the echo train. A total of 12 data points were collected. Spin-lattice relaxation times were measured using the standard inversion-recovery pulse sequence, with 16 value of inversion time used. A single T_1 relaxation time was observed for all samples.

^{19}F MRI Experiments

^{19}F images were collected on the AMX 300 spectrometer using the 3D spin-echo pulse sequence (*22*). Typical experimental details are as follows. The field of view was 20×20 mm^2, and the slice thickness was 2.5 mm in a 128×128×8 matrix. The echo time was 4.8 ms and the repetition time equal to three seconds. The images presented here were all acquired by co-adding two acquisitions resulting in a constant imaging time of one hour and 20 minutes.

In vivo ^{19}F MRI images were collected on a Bruker 700 MHz wide-bore microimaging system. Proton images were taken using a standard gradient echo sequence. The ^{19}F images were collected using a spin-echo 3D pulse sequence with a repetition time of 1 s and echo time of 6.4 ms. A total of 32 scans were averaged to improve the signal-to-noise and 8 slices were generally taken with a field of view of 3 cm. The total scan time for the *in vivo* experiments was approximately 8 minutes.

Ethical clearance for testing of the polymers on live mice was obtained from the University of Queensland (AIBN/076/08). The respiration rate of the mouse was monitored at all times during the imaging.

Downloaded by STANFORD UNIV GREEN LIBR on June 20, 2012 | http://pubs.acs.org
Publication Date (Web): October 14, 2011 | doi: 10.1021/bk-2011-1077.ch028

Preparation of Block Copolymer Assemblies

Example Synthesis of Amphiphilic Block Copolymer

Monobromo-terminated p(*t*BA) (*Mn*=6800, *Mw*/*Mn* = 1.09), prepared by ATRP, and CuBr were added to a 50 mL round-bottom flask which was sealed with a rubber septum, then degassed with argon. Deoxygenated toluene was added, after which *n*BA and the fluoroacrylate (FA, here FA refers to TFEA, TFEMA, HFPA and HFPMA monomer) were added, both via syringes, then PMDETA was introduced. The molar ratio of p(*t*BA) : CuBr : PMDETA : *n*BA : FA=1:1:1:30:100. The solution was stirred for approximately 10 minutes until the Cu complex had formed, as judged by the complete dissolution of the CuBr powder particles and the formation of a deep green solution. After complex formation, the flask was placed in an oil bath at 90 °C. After certain times, the polymer was dissolved in THF and passed through an alumina column to remove the copper catalyst. The THF was removed by evaporation and the polymer was then dried under vacuum at 40 °C. For further purification, the polymer was dissolved in THF, precipitated into a 10-fold excess of hexane, and then washed with hexane twice. The polymer was dried under vacuum at 40 °C for two days.

Hydrolysis of the tert-butyl groups was achieved by addition to the solution of the block copolymer a quantity of trifluoroacetic acid. A clean, 100 mL, round-bottom flask fitted with a stirrer bar was charged with p(*t*BA)-*b*-p(*n*BA-*co*-FA), followed by dried dichloromethane. The mixture was stirred for 10 min to dissolve the polymer. Trifluoroacetic acid (TFA, 5.0 equiv to the *tert*-butyl ester) was then added. After the mixture was allowed to stir at room temperature for 10 h, the dichloromethane and excess TFA were removed at room temperature with dry nitrogen gently flowing through the flask. The resulting light-brown polymer solid was dried under vacuum for 3 days under room temperature. For further purification, the polymer was redissolved in THF, precipitated into a 10-fold excess of water, and then washed with water twice. The polymer was dried under vacuum at room temperature for three days to give to a white product which was pAA-*b*-p(*n*BA-*co*-FA).

Spherical micelles were obtained by the dissolution of the purified amphiphilic copolymer pAA-*b*-p(*n*BA-*co*-FA) (20 mg/mL) in DMF, a good solvent for both blocks, followed by the gradual addition (10.0 mL/h) of an equal volume of non-solvent for the hydrophobic polyfluoroacrylate to induce micellization. The micelles were allowed to stir for 24 h before being transferred to pre-soaked and rinsed dialysis bags (molecular weight cut off, M_W=3500) and dialyzed against ultrapure water (18.2 mΩ.cm) for three days for removal of the remaining organic solvent. The particle sizes of the micelles were determined by DLS.

Synthesis of Hyperbranched Copolymers

One gram of dimethylaminoethyl methacrylate (DMAEA) (1.06 mL, 6.98 x 10^{-3} mol), 269 mg TFEA (221 μL, 1.74 x 10^{-3} mol), 157 mg 2-dodecylsulfanyl thiocarbonyl sulfanyl-2-methyl propionic acid (4.34 x 10^{-4} mol), 7 mg AIBN

(4.34×10^{-5} mol) and 101 mg EGDMA (96 μL, 5.1×10^{-4} mol) were dissolved in 5 mL toluene and sealed in a round-bottom flask fitted with a septum. The mixture was purged with argon for 15 minutes then heated to 65 °C for 48 hours. Upon completion of the reaction, the polymer was precipitated in hexane and the viscous oil dried under vacuum. The polymer was characterized by gel permeation chromatography couple with multi-angle laser light scattering (GPC-MALLS) and ^{1}H NMR. The alkyne-terminated PDMAEA-stat-TFEA was prepared as above using an alkyne-terminated RAFT agent (174 mg, 4.34×10^{-4} mol) in place of the 2-dodecylsulfanyl thiocarbonyl sulfanyl-2-methyl propionic acid.

The hyperbranched polymer was chain extended with poly(ethylene glycol) methacrylate (PEGMA) in the following manner. 0.5 g of the hyperbranched polymer (~ 1.5×10^{-4} mol, ~ 6×10^{-4} mol RAFT units) and 2 g PEGMA-475 was dissolved in 5 mL THF containing 2.5 mg AIBN. The solution was degassed with argon and then reacted for 24 hours at 65 °C. The polymer was precipitated in hexane and dialyzed against water for 5 days to remove unreacted monomer. The polymer was freeze-dried yielding a slightly yellow, viscous oil.

Folic acid was attached to the hyperbranched polymer via standard DCC coupling of acid group on folic acid to the amine group on the polymer. Typically, the alkyne-terminated hyperbranched polymer was chain extended with 11-azido-3,6,9-trioxaundecane-1-amine via standard azide-alkyne click chemistry. The terminal amine group was then exploited for DCC coupling. The concentration of folic acid attached to the polymer was determined by UV-vis spectrophotometry by measuring absorbance at 363 nm. Typically, 2-3 folic acid moieties were attached per polymer chain.

Results and Discussion

Synthesis and Evaluation of Diblock Copolymers

A series of amphiphilic block copolymers containing partially-fluorinated segments were prepared using controlled radical polymerization (ATRP), subsequent removal of t-butyl groups to produce a hydrophilic polyacid block. Solutions of assemblies were prepared by addition of water to the polymers in DMF solution followed by dialysis. The overall synthetic scheme is illustrated below (Scheme 1) and described in the Experimental section above. Polymers of low molar mass dispersity and of high structural fidelity were produced and characterized as described in more detail elsewhere.

The NMR imaging performance of the diblock copolymer assemblies after dialysis into pure water was poor, however, good images were obtainable for solutions of the particles in mixed solvent systems, for example a 1:1 mixture of water and DMF. The ^{19}F NMR images of dilute solutions (2.5 wt%) in the mixed solvents were measured at 7 T using a standard three-dimensional spin echo pulse sequence with an echo time of 4.8 ms, and a repetition time of 3 seconds. The imaging time was restricted to 80 minutes, and comparisons were made of the signal-to-noise ratio of the images under identical conditions. For a spin-echo imaging sequence the image intensity is a function of the fluorine

Downloaded by STANFORD UNIV GREEN LIBR on June 20, 2012 | http://pubs.acs.org
Publication Date (Web): October 14, 2011 | doi: 10.1021/bk-2011-1077.ch028

content, the spin-spin and spin-lattice relaxation times, and the imaging echo and repetition times, as described in equation 1 (*23*). The fluorine content is known from the structure of the polymer which was determined by careful chemical characterization, as described in the Experimental section. The spin-lattice (T_1) relaxation times were measured for all of the samples and were of the order of 500 ms. On the other hand, the spin-spin (T_2) relaxation times did vary appreciably across the materials prepared (from < 0.5 ms to > 300 ms depending on the structure) (*24*), and showed at least two components when measured by the CPMG sequence. Using these parameters, and assuming that all fluorine nuclei could be measured under high-resolution NMR condition, it was possible to predict the relative imaging intensities of all of the polymers prepared in this study. A comparison of the predicted relative intensities and the observed MRI intensities is provided in Figure 1.

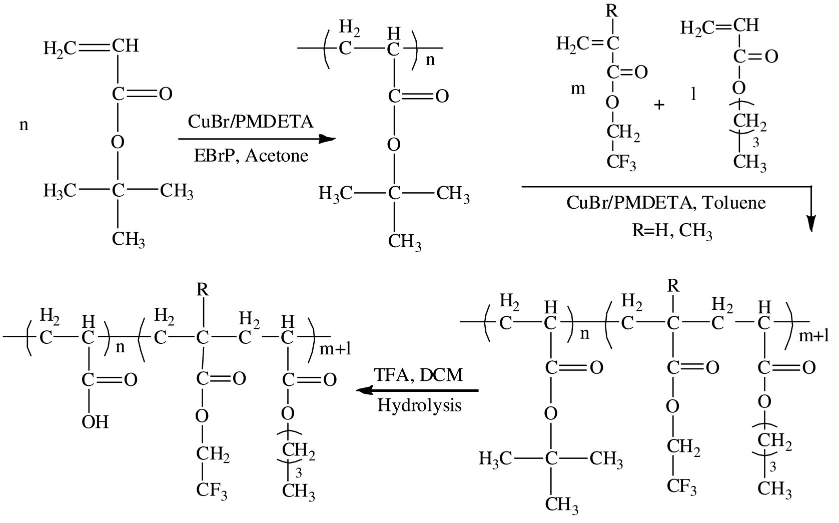

Scheme 1. The synthetic route and structure of the amphiphilic copolymer PAA-b-P (nBA-co-TFE (M)A).

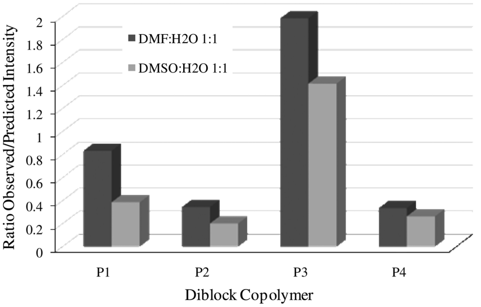

P1	PAA_{50}-*b*-P(nBA_{39}-*co*-$TFEA_{115}$)
P2	PAA_{53}-*b*-P(nBA_{28}-*co*-$TFEMA_{126}$)
P3	PAA_{53}-*b*-P(nBA_{4}-*co*-$HFPA_{3}$)
P4	PAA_{53}-*b*-P(nBA_{2}-*co*-$HFPMA_{11}$)

Figure 1. Bar plot showing the ratio of the measured NMR image intensity (arbitrary units) divided by the relative intensity predicted from the observed molecular parameters and using equation 1.

Downloaded by STANFORD UNIV GREEN LIBR on June 20, 2012 | http://pubs.acs.org
Publication Date (Web): October 14, 2011 | doi: 10.1021/bk-2011-1077.ch028

$$Intensity = N(F)e^{-T_{echo}/T_2}\left[1-2e^{-(T_{rep}-T_{echo}/2)/T_1}+e^{-T_{rep}/T_1}\right] \tag{1}$$

As can be seen in Figure 1, the NMR imaging performance of the diblock copolymer assemblies depends strongly on the chemical structure of the partially-fluorinated monomer and the identity of the organic solvent in the mixed solvent system. Several important rules can be obtained from this simple comparison. Firstly, for an equivalent fluorine content the acrylate polymers (P1, P3) perform significantly better that the methacrylate polymers (P2, P4). Secondly, polymers in water:DMF (dark gray bars) consistently have a higher image intensity compared with the polymers in water:DMSO (light gray bars). Finally the hexafluoroisopropyl-containing acrylate polymer (P3) provided the best performance relative to the predicted behaviour, however it must be noted that the relatively low reactivity of the HFPA to free radical polymerization lead to low levels of incorporation of this monomer and hence overall low image intensities.

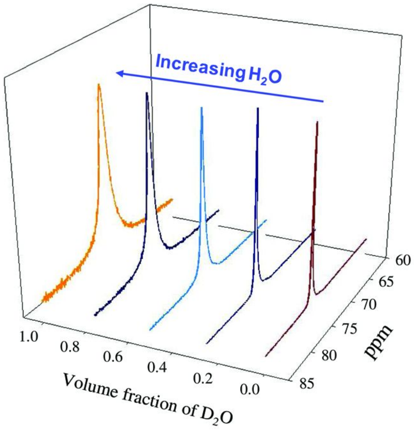

Figure 2. Stack plot of the ^{19}F NMR spectra of the diblock copolymer PAA_{50}-b-P(nBA_{39}-co-$TFEA_{115}$) in mixtures of DMF-d_7 and D_2O as a function of volume fraction of D_2O.

A detailed examination of the effect of polymer and solvent on the imaging performance has been reported elsewhere (*24*, *25*), however an additional important piece of information can be obtained from the ^{19}F NMR spectra collected under high-resolution NMR conditions (receiver dead time of 15 μs) as a function of solvent composition. In Figure 2 above we have plotted the ^{19}F spectra of PAA_{50}-*b*-P(*n*BA_{39}-*co*-$TFEA_{115}$) in the different solvents. It can be clearly seen that the linewidth of the observed NMR signal increases as the solvent becomes more polar. On passing from DMF to D_2O the block copolymers are forced to assemble into particles with most-likely a shell of polar poly(acrylic acid) chains. The increasing line width is evidence that the mobility of the fluorine-containing side-chains becomes progressively more restricted on addition of water. Of more relevance to the imaging performance, the integrated intensities of the ^{19}F signal of the trifluoroethyl side-chains decreases appreciably as solvent polarity

Downloaded by STANFORD UNIV GREEN LIBR on June 20, 2012 | http://pubs.acs.org
Publication Date (Web): October 14, 2011 | doi: 10.1021/bk-2011-1077.ch028

increases (data not shown here). We observed an approximately 30% decrease in intensity for the TFEA-containing block copolymers in D_2O. The intensity of the spectra of the TFEMA-containing materials decreased by 55% in 1:1 DMF:D_2O and approximately 90% in pure D_2O. This observation accounts for the lower MRI imaging intensity observed for the methacrylate polymers. Remarkably there is a population of nuclear spins with very short T_2 relaxation times, of the order of several microseconds or less, which do not contribute to the high-resolution NMR experiments (Figure 4) and of course the spin-echo-based MRI experiment. This population of fluorine atoms is behaving much like a rigid solid polymer and is due to fluorinated segments associating strongly in the hydrophilic environment.

Based on these observations, we proposed a set of design criteria for successful, i.e. high sensitivity ^{19}F MRI agents. Clearly the agents must have a high volume/weight fraction of fluorine atoms so as to maximize the potential signal amplitude. The hexafluoroisopropyl acrylate monomer gave the best imaging performance, however its use is restricted by the low reactivity to radical addition as discussed above. The comparison between the performance of the acrylate and the methacrylate polymers demonstrates that the flexibility of polymeric main chain is of importance. It is well known that methacrylate polymers are relatively conformationally-restricted compared with acrylate chains, as reflected in the systematically lower glass-to-rubber transitions in bulk acrylate polymers. Chain flexibility is important in these application because of the role chain motion plays in motion of the side chains (*26*, *27*). The importance of maintaining flexibility of the fluorinated segments was demonstrated by the effects of the solvent on the NMR properties and the imaging intensities. Thus it is necessary to design materials in which association of the fluorinated moieties, driven here by unfavorable polymer-solvent interactions, is frustrated. This can be achieved for example by including a branched structure. These design considerations have the overall effect of increasing the amplitude of motion of the trifluoroethyl groups, which in turn partially averages the dipolar and anisotropic chemical shift interactions of the fluorine nuclei. Finally we may desire to attach to the imaging agent a suitable targeting group, to direct the molecules *in vivo* to a particular tissue type, for example cancer cells.

Hyperbranched Polymeric ^{19}F Imaging Agents

To overcome the problems encountered with particles self-assembled from diblock copolymers, we proposed the synthesis of hyperbranched polymers which demonstrate high segmental molecular mobility while maintaining relatively high fluorine contents. A degree of control over the structure of the hyperbranched polymers can be achieved using the controlled radical polymerization method dubbed reversible addition fragmentation chain transfer (or RAFT). Molecular mobility is maintained in these molecules by using acrylate (i.e. low-T_g) and polar repeat units that are well hydrated under aqueous conditions. A difunctional monomer is incorporated to introduce branching placed in a statistical manner; this has the effect of frustrating the aggregation of the fluorinated segments present in the diblock copolymer assemblies, allowing incorporation of up to 20 mol. % of the fluoro-monomer. Hyperbranched polymers possess a degree of

Downloaded by STANFORD UNIV GREEN LIBR on June 20, 2012 | http://pubs.acs.org
Publication Date (Web): October 14, 2011 | doi: 10.1021/bk-2011-1077.ch028

Downloaded by STANFORD UNIV GREEN LIBR on June 20, 2012 | http://pubs.acs.org
Publication Date (Web): October 14, 2011 | doi: 10.1021/bk-2011-1077.ch028

"shape-persistence" which means that the disadvantages of polymer assemblies, such as disassociation under dilute conditions, do not arise. The highly branched structure and hence high content of chain ends enables the fictionalization of the polymers with a high concentration of targeting ligands. Finally use of RAFT polymerization allows one to incorporate chemically-different end groups suitable for labeling with multiple functional groups via orthogonal chemistries.

The hyperbranched polymers reported here were synthesized using the method first published by Perrier and his colleagues (*28*); the reaction scheme is reproduced in Scheme 2. An alkyne-terminated derivative of 2-dodecylsulfanyl thiocarbonyl sulfanyl-2-methylpropionic acid was employed as the RAFT agent. For example, a statistical hyperbranched copolymer of dimethylaminoethyl acrylate (DMAEA - 77 mol. %) and trifluoroethyl acrylate (TFEA – 19 mol. %) was synthesized using ethyleneglycol dimethacrylate (EGDMA – 4 mol. %) as branching agent. Chain-extension of the resultant hyperbranched polymer with polyethyleneglycol monomethylether methacrylate (PEGMA) was performed resulting in a highly-branched polymers having a polycationic core with pendant PEGMA arms which because of their pronounced hydrophilicity are likely to surround the partially-fluorinated core. As reported by us elsewhere (*29*) we examined the cytotoxicity of the various generations of hyperbranched polymers using the MTS cell viability assay (*30*). These tests demonstrated that chain-extension with the PEG-containing monomers reduced the toxicity of the polycationic core to levels comparable to the non-toxic control, PEG(400). This suggests that the PEGMA chains are able to shield the hyperbranched core.

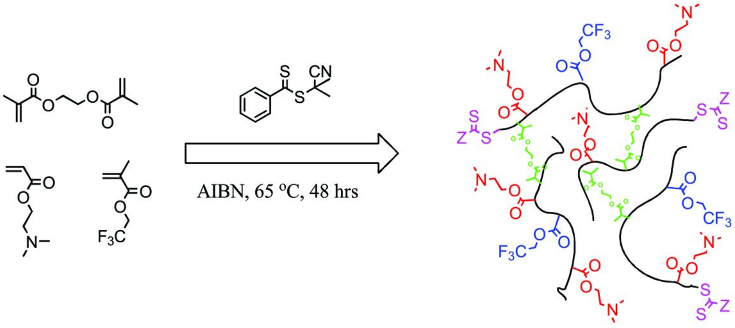

Scheme 2. Generic scheme for synthesis of hyperbranched polymers using RAFT polymerization. The intact RAFT end groups are available for extension with PEGMA.

The ^{19}F NMR imaging performance of this series of hyperbranched polymers is outstanding, with excellent images being obtained *in vitro* over short imaging times. In Figure 3 below we show the cross-sectional images of four plastic tubes containing solutions of the hyperbranched polymer at various concentrations. The right hand part of the figure demonstrates the good linear relationship between polymer concentration and image intensity.

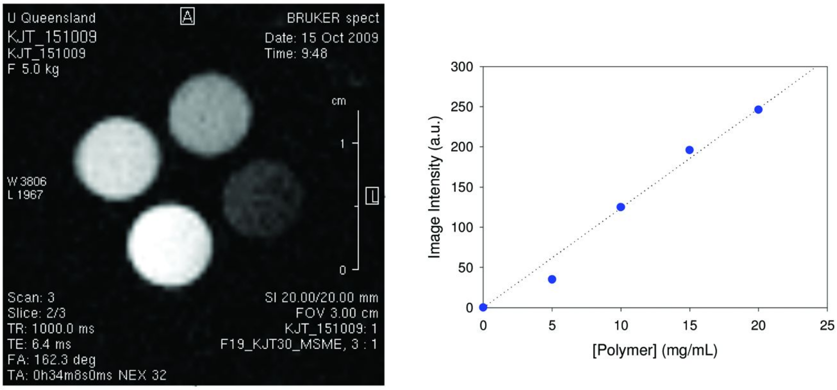

Figure 3. The left-hand side of this figure shows the ^{19}F image of four solutions of the hyperbranched polymer (Scheme 2) in water at concentrations of 5, 10, 15, 20 mg/mL, shown as areas of increasing brightness with increasing concentration. On the right is a plot showing the linear relationship between ^{19}F image intensity and solution concentration.

Excellent *in vivo* imaging has also been demonstrated (*29*). In the absence of a targetting ligand the polymer was rapidly excreted, being observed in the bladder two hours after injection into the tail vein of the mouse. Clearly the compact hyperbranched polymerics are able to be pass through the tight membranes within the kidney. To demonstrate the ability of these molecules to target specific cell types the alkyne-functionalised hyperbanched polymers were conjugated via the Huisgen's cycloaddition reaction with azide-functionalised folate. It is well known that cancer cells over-express the folate receptors. The animal model for this experiment was a mouse with approximately 10^6 B16 melanoma cells (a mouse cell line) injected sub-cutaneaously. One week following implantation of the cells, 20 μL of a 20 mg/mL solution of the folate-functionalised hyperbranched polymer was injected into the tail-vein of the mouse. After waiting one hour the ^{19}F image of the anaesetised mouse shown in Figure 4 was acquired on a vertical-bore 16.4 T system. The total imaging time was just over eight minutes. In Figure 4 the ^{19}F image in orange/orange shades has been superimposed onto the ^1H density image, and demonstrates clearly that there is localisation of the targetting agent in the centre of the tumour. We have also demonstrated that in the absence of the folate ligand no accumulation of the polymer was observed in the tumour mass. There is clear evidence that the hyperbranched imaging agent can provide high-quality images within short time periods, and that the incorporation of folate groups results in localisation of the imaging agent in the tumour mass. Further experiments are in progress to extend the number of animal targets, and to for example examine the limits of sensitivity of the agents especially in non-solid tumours.

Downloaded by STANFORD UNIV GREEN LIBR on June 20, 2012 | http://pubs.acs.org
Publication Date (Web): October 14, 2011 | doi: 10.1021/bk-2011-1077.ch028

Downloaded by STANFORD UNIV GREEN LIBR on June 20, 2012 | http://pubs.acs.org
Publication Date (Web): October 14, 2011 | doi: 10.1021/bk-2011-1077.ch028

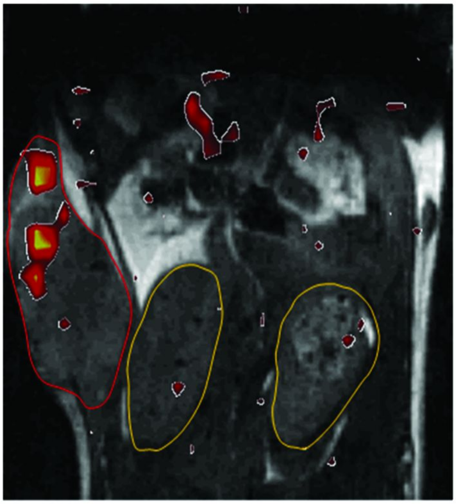

Figure 4. Targeted imaging of B16 melanoma cells. The proton density of the image of the torso of the mouse shows the kidneys (yellow curve) and the tumor mass (red curve) highlighted. Superimposed on this image in color is the ^{19}F image, demonstrating ^{19}F intensity within the mass of the tumors. A threshold has been applied to the ^{19}F image so that regions of low intensity have no color, those with a moderate intensity appear red, and high intensity regions appear yellow. The fluorine imaging time was 8 minutes. (see color insert)

Conclusions

In this chapter we have described the development and testing of two generations of ^{19}F MRI agents with potential application in so-called "molecular imaging". Extensive learning was gained from the preparation of a large series of partially-fluorinated amphiphilic diblock copolymers, which when transferred to aqueous solution formed nanometer-scaled assemblies. The ^{19}F imaging intensity was found to be profoundly influenced by the details of molecular structure and the tendency of the fluorinated segments to self-associate. This behaviour of the diblock copolymers was determined by the interactions of the chain segments with each other, and with the surrounding medium. Without control the lowest-energy structures were also those in which solid-like structures were present. Ultimately the reduction in molecular motion resulted in a decrease in the spin-spin relaxation times and a pronounced deterioration in the imaging performance.

The learning gained from these self-assembled systems lead to the design and synthesis of a series of uni-molecular "particles" of hyperbranched polymers. A degree of control of the branching could be achieved using RAFT polymerization methods. The presence of branched resulting from the inclusion into the polymerizing mixture of a di-functional monomer lead to a shape-persistent structure, and which in combination with the proximity of hydrophilic monomeric units lead to a "frustration" of the association of the fluorinated monomers, as demonstrated by the extended spin-spin relaxation times, and the excellent imaging performance. The molecules were tested both in test tubes, and in animals, and performed exceptionally well, with only relatively short imaging times required in the *in vivo* experiments. In the absence of targeting moieties the polymers are excreted rapidly, however, when conjugated with the folate ligand, the molecules were directed to a mass of melanoma cells previously seeded under the skin of the mouse. The excellent imaging performance demonstrates the potential of this class of agents, and this potential is being actively explored by our group.

Downloaded by STANFORD UNIV GREEN LIBR on June 20, 2012 | http://pubs.acs.org
Publication Date (Web): October 14, 2011 | doi: 10.1021/bk-2011-1077.ch028

References

1. Ulrich, A. S. *Prog. Nucl. Magn. Reson. Spectrosc.* **2005**, *46*, 1.
2. Holland, G. N.; Bottomley, P. A.; Hinshaw, W. S. *J. Magn. Reson.* **1977**, *28*, 133.
3. McFarland, E.; Koutcher, J. A.; Rosen, B. R.; Teicher, B.; Brady, T. J. *J. Comput. Assist. Tomogr.* **1985**, *9*, 8.
4. Parhami, P.; Fung, B. M. *J. Phys. Chem.* **1983**, *87*, 1928.
5. Eidelberg, D.; Johnson, G.; Barnes, D.; Tofts, P. S.; Delpy, D.; Plummer, D.; McDonald, W. I. *Magn. Reson. Med.* **1988**, *6*, 344.
6. Longmaid, H. E., 3rd; Adams, D. F.; Neirinckx, R. D.; Harrison, C. G.; Brunner, P.; Seltzer, S. E.; Davis, M. A.; Neuringer, L.; Geyer, R. P. *Invest. Radiol.* **1985**, *20*, 141.
7. Ahrens, E. T.; Flores, R.; Xu, H.; Morel, P. A. *Nat. Biotechnol.* **2005**, *23*, 983.
8. Srinivas, M.; Morel, P. A.; Ernst, L. A.; Laidlaw, D. H.; Ahrens, E. T. *Magn. Reson. Med.* **2007**, *58*, 725.
9. Janjic, J. M.; Srinivas, M.; Kadayakkara, D. K. K.; Ahrens, E. T. *J. Am. Chem. Soc.* **2008**, *130*, 2832.
10. Lanza, G. M.; Winter, P. M.; Neubauer, A. M.; Caruthers, S. D.; Hockett, F. D.; Wickline, S. A. *Curr. Top. Dev. Biol.* **2005**, *70*, 57.
11. Lanza, G. M.; Yu, X.; Winter, P. M.; Abendschein, D. R.; Karukstis, K. K.; Scott, M. J.; Chinen, L. K.; Fuhrhop, R. W.; Scherrer, D. E.; Wickline, S. A. *Circulation* **2002**, *106*, 2842.
12. Morawski, A. M.; Winter, P. M.; Yu, X.; Fuhrhop, R. W.; Scott, M. J.; Hockett, F.; Robertson, J. D.; Gaffney, P. J.; Lanza, G. M.; Wickline, S. A. *Magn. Reson. Med.* **2004**, *52*, 1255.
13. Partlow, K. C.; Chen, J.; Brant, J. A.; Neubauer, A. M.; Meyerrose, T. E.; Creer, M. H.; Nolta, J. A.; Caruthers, S. D.; Lanza, G. M.; Wickline, S. A. *FASEB J.* **2007**, *21*, 1647.
14. Becker, M. L.; Remsen, E. E.; Wooley, K. L. *J. Polym. Sci., Part A* **2001**, *39*, 4152.
15. Du, W. J.; Xu, Z. Q.; Nystrom, A. M.; Zhang, K.; Leonard, J. R.; Wooley, K. L. *Bioconjugate Chem.* **2008**, *19*, 2492.
16. Srinivas, M.; Heerschap, A.; Ahrens, E. T.; Figdor, C. G.; de Vries, I. J. M. *Trends Biotech.* **2010**, *28*, 363.

In NMR Spectroscopy of Polymers: Innovative Strategies for Complex Macromolecules; Cheng, H., et al.;
ACS Symposium Series; American Chemical Society: Washington, DC, 2011.

17. Higuchi, M.; Iwata, N.; Matsuba, Y.; Sato, K.; Sasamoto, K.; Saido, T. C. *Nat. Neurosci.* **2005**, *8*, 527.
18. Yu, J.-x.; Kodibagkar, V. D.; Cui, W.; Mason, R. P. *Curr. Med. Chem.* **2005**, *12*, 819.
19. Ruiz-Cabello, J.; Barnett, B. P.; Bottomley, P. A.; Bulte, J. W. M. *NMR Biomed.* **2011**, *24*, 114.
20. Lai, J. T.; Filla, D.; Shea, R. *Macromolecules* **2002**, *35*, 6754.
21. Quemener, D.; Davis, T. P.; Barner-Kowollik, C.; Stenzel, M. H. *Chem. Comm.* **2006**, 5051.
22. Callaghan, P. *Principles of Nuclear Magnetic Resonance Microscopy*; Clarendon Press: Oxford, 1994.
23. Hendrick, R. E. *Magn. Reson. Imaging* **1987**, *5*, 31.
24. Peng, H.; Blakey, I.; Dargaville, B.; Rasoul, F.; Rose, S.; Whittaker, A. K. *Biomacromolecules* **2009**, *10*, 374.
25. Nurmi, L.; Peng, H.; Seppala, J.; Haddleton, D. M.; Blakey, I.; Whittaker, A. K. *Polym. Chem.* **2010**, *1*, 1039.
26. Kuebler, S. C.; Heuer, A.; Spiess, H. W. *Macromolecules* **1996**, *29*, 7089.
27. Kuebler, S. C.; Schaefer, D. J.; Boeffel, C.; Pawelzik, U.; Spiess, H. W. *Macromolecules* **1997**, *30*, 6597.
28. Liu, B. L.; Kazlauciunas, A.; Guthrie, J. T.; Perrier, S. *Macromolecules* **2005**, *38*, 2131.
29. Thurecht, K. J.; Blakey, I.; Peng, H.; Squires, O.; Hsu, S.; Alexander, C.; Whittaker, A. K. *J. Am. Chem. Soc.* **2010**, *132*, 5336.
30. Cory, A. H.; Owen, T. C.; Barltrop, J. A.; Cory, J. G. *Cancer Commun.* **1991**, *3*, 207.

Downloaded by STANFORD UNIV GREEN LIBR on June 20, 2012 | http://pubs.acs.org
Publication Date (Web): October 14, 2011 | doi: 10.1021/bk-2011-1077.ch028

Downloaded by UNIV OF GUELPH LIBRARY on June 20, 2012 | http://pubs.acs.org
Publication Date (Web): October 14, 2011 | doi: 10.1021/bk-2011-1077.ch029

Chapter 29

Latex State and Solid-State NMR Spectroscopy of Elastomers

Seiichi Kawahara[*]

**Department of Materials Science and Technology, Faculty of Engineering,
Nagaoka University of Technology, Nagaoka, Niigata 940-2188, Japan
[*]E-mail: kawahara@mst.nagaokaut.ac.jp**

Latex state NMR spectroscopy and field gradient fast magic angle spinning solid-state NMR spectroscopy were utilized for structural characterization of rubbery polymers and crosslinked rubbery materials. High resolution NMR spectra for elastomers were achieved either through Brownian motion of a latex dispersion or fast magic angle spinning for a solid. Sequence distribution of *cis*-1,4-, *trans*-1,4- and 1,2-butadiene units was investigated for polybutadiene through latex state NMR spectroscopy because the polybutadiene used in this work was prepared by emulsion polymerization. Crosslinking junctions of vulcanized natural rubber were analyzed by field gradient fast magic angle spinning solid-state NMR spectroscopy. The vulcanized natural rubber with quaternary carbons linking to sulfur as the crosslinking junction was found to be superior in mechanical properties compared to the rubber samples with tertiary carbons linking to sulfur.

1. Introduction

Rubbery polymers and polymer gels hold a unique place in polymer science because they exhibit both liquid and solid behavior in terms of molecular motion. They are usually crosslinked in practical use to maintain their physical dimension. This crosslinking makes it difficult to apply solution NMR for structural characterization. Moreover, the molecular motions present in them also pose difficulties for solid-state NMR spectroscopy of the crosslinked rubbers; e.g., two-dimensional NMR measurements cannot be easily performed on them

In NMR Spectroscopy of Polymers: Innovative Strategies for Complex Macromolecules; Cheng, H., et al.;
ACS Symposium Series; American Chemical Society: Washington, DC, 2011.

in the solid state. This is explained to be due to very low concentration of the crosslinking junctions and their unsatisfied molecular motions, compared with repeating units. It is necessary to develop a special NMR technique for the rubbery polymers and polymer gels in order to perform two-dimensional NMR measurements for their structural characterization.

Two-dimensional NMR measurements for the rubbery polymers and polymer gels may be performed by eliminating dipole-dipole interactions. However, in the case of the crosslinked rubbers, which consist of the mobile main chain and the constrained crosslinking junctions, motionary inhomogeneity prevent the efficient elimination of the dipole-dipole interactions. One way to eliminate the interactions is a superposition of another motions onto molecular motions. Thus, the rotational movement of latex particles in a dispersion may be superposed onto molecular motions. An alternative way is to carry out fast magic angle spinning (FMAS) in solid-state NMR (*1*, *2*); in this case, at least 20 kHz spinning is required to obtain a high resolution NMR spectrum (*3*), and a large amount of sample is needed for an analysis of crosslinking junctions. In order to carry out the analysis of the crosslinking junctions as extremely small amount of building block through two-dimensional NMR, it is necessary to develop latex state NMR spectroscopy (*1*, *2*) and use a solid-state NMR spectrometer equipped with a field gradient-fast magic angle spinning (FG-FMAS) probe (*4*). Using the FG-FMAS probe, particulary, we may achieve large increase in sensitivity for the measurement.

Thus far, only several preliminary studies of the latex state NMR spectroscopy have been reported: an observation of hydrolysis on the surface of PMMA dispersoid in latex by Tarcha (*5*) and determination of dried rubber content for natural rubber latex by Ang (*6*) and Gambhir (*7*). In my opinion, latex state NMR spectroscopy has not been studied systematically in the previous articles, and the conditions for getting a high resolution spectrum via latex state NMR spectroscopy have not been determined. Moreover, fast MAS (more than 20 kHz) has not been achieved for solid-state NMR measurement equipped with FG-FMAS probe, even though some results of structural characterizations of soft materials have been reported earlier (*8–10*).

In a series of earlier studies, we have conducted two-dimensional NMR measurements of rubbery polymers and polymer gels through latex state NMR spectroscopy, using a solid-state NMR spectrometer equipped with a FG-FMAS probe. In this article, I shall attempt to summarize the work we have done so far.

Downloaded by UNIV OF GUELPH LIBRARY on June 20, 2012 | http://pubs.acs.org
Publication Date (Web): October 14, 2011 | doi: 10.1021/bk-2011-1077.ch029

2. Latex State NMR Spectroscopy

2.1. Effect of Crosslinking

Aliphatic carbon signals obtained for polybutadiene (PB) by latex state ^{13}C-NMR spectroscopy are shown in Figures 1 and 2, and they are compared with those obtained for solution and solid samples, in which the solid-state measurement was performed with gated high power decoupling at magic angle spnning of 5 kHz. Characteristics of the PB latices are tabulated in Table 1.The chemical shifts of these signals were shown in Table 2 together with the assignment reported thus far

(*11–13*), where the number of the carbon atoms in 1,4 and 1,2 units of PB belongs to IUPAC nomenclature.

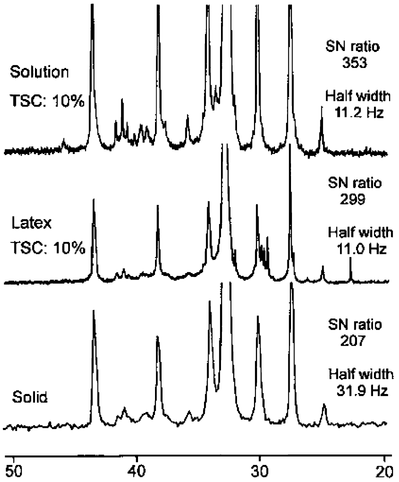

Figure 1. ^{13}C-NMR spectra for PBD-S.

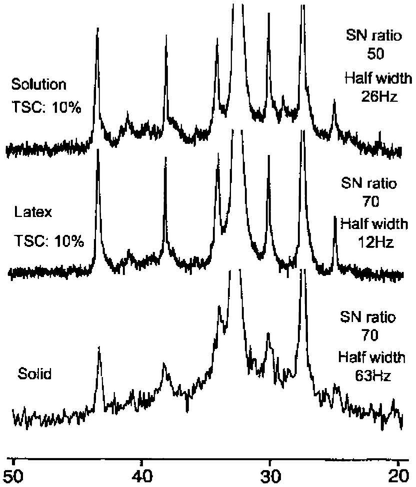

Figure 2. ^{13}C-NMR spectra for PBD-G.

Downloaded by UNIV OF GUELPH LIBRARY on June 20, 2012 | http://pubs.acs.org
Publication Date (Web): October 14, 2011 | doi: 10.1021/bk-2011-1077.ch029

Downloaded by UNIV OF GUELPH LIBRARY on June 20, 2012 | http://pubs.acs.org
Publication Date (Web): October 14, 2011 | doi: 10.1021/bk-2011-1077.ch029

Table 1. Glass transition temperature, melting temperature, gel content, molecular weight, polydispersity, volume mean particle diameter of PBD latex

Specimen	T_g /°C	T_m /°C	*gel content /w/w%*	M_w /10 ^{6}	M_w/M_n	<D>[1] /μm
PBD-S	-75.8	-6.7	0	3.2	4.9	0.111
PBD-G	-76.0		80			0.106

[1] <D> : volume mean particle diameter

Table 2. ^{13}C-NMR chemical shifts for solution, latex and solid samples of PBD-S and PBD-G

		Chemical Shift / ppm						
		Sato et. al.[9]	*PBD-S*			*PBD-G*		
Sequence	*C*		*Solution*	*Latex*	*Solid*	*Solution*	*Latex*	*Solid*
C-v	4	24.98-25.10	24.93	25.06	24.95	24.93	25.00	24.85
C-1,4 1,4-C	4 1	27.42-27.57	27.47	27.64	27.47	27.45	27.58	27.47
T-v	4	30.16	30.10	30.76	30.19	30.14	30.22	30.19
v-v-C (m)	1	31.60-32.13	32.19	32.12				
1,4-v-C T-1,4 1,4-T	1 4 1	32.72	32.72	32.89	32.72	32.73	32.79	32.72
v-v-C (r)	1	33.35-33.53	33.60		33.21			
1,4-V-1,4	1	33.99-34.16	34.05	34.17	34.06	34.05	34.13	33.98
1,4-V-v(m)	1	34.31						
1,4-V-v(r)	1	35.63-36.00	35.74	35.90	36.00	35.72	35.84	35.67
v-v-T(m)	1	37.24-37.48	37.60	37.62	37.58	37.53	37.71	37.40
1,4-v-T	1	38.18	38.13	38.39	38.26	38.17	38.30	38.26

Continued on next page.

Downloaded by UNIV OF GUELPH LIBRARY on June 20, 2012 | http://pubs.acs.org
Publication Date (Web): October 14, 2011 | doi: 10.1021/bk-2011-1077.ch029

Table 2. (Continued). ^{13}C-NMR chemical shifts for solution, latex and solid samples of PBD-S and PBD-G

		Chemical Shift / ppm						
		Sato et. al.[9]	*PBD-S*			*PBD-G*		
Sequence	*C*		*Solution*	*Latex*	*Solid*	*Solution*	*Latex*	*Solid*
v-V-v	2	38.57-39.13	39.05	39.30	39.13	39.06	39.23	
v-v-T(r)	1	38.96-39.13	39.58	39.59	39.62	39.44	39.52	39.61
v-V	1	39.43-41.72	40.60	40.75	40.59	40.68	40.75	
1,4-V-v	2	40.55-41.00	41.08	41.22	41.08	41.11	41.21	41.08
v-V-1,4	2	41.13-41.73	41.57	41.70	41.56	41.59	41.66	
1,4-V-1,4	2	43.47-43.70	43.45	43.60	43.48	43.53	43.51	43.50

C, *cis*-1,4 unit; T, *trans*-1,4 unit; V, 1,2 unit; 1,4, *cis*- and *trans*-1,4 units m, meso; r, racemic

As shown in Figure 1, for PB-S solution sample containing no gel fraction, all of the expected signals appeared in the spectrum, but several signals were invisible due to line broadening for latex and solid samples. The invisible signals are explained by the constraint of molecular movement of the polymer in the solid phase. The data demonstrate the important role that active molecular movement of polymer plays in the latex state ^{13}C-NMR spectroscopy. For latex, solution and solid samples of PB-G, some diad and triad signals were invisible in the spectrum. Since the gel content of PB-G was more than 80 w/w% while PB-S did not contain any gels, the invisible signals in PB-G was due to inhomogeneity in the molecular movement due to the presence of crosslinking junctions.

The values of T_1 for most carbon atoms of latex sample were smaller than those of the solution sample but were actually similar to those of the solid sample. Thus, the movement of PB molecules in the latex dispersion is similar to that in the solid sample. Since a value of glass transition temperature, T_g, for PB is about –76 °C, segmental motions are expected to occur at the observed temperature for the polymers even in the solid state.

2.2. Effect of Dry Rubber Content (DRC)

The signal-to-noise (S/N) ratio and half-width are well-defined parameters, which express the resolution of NMR spectrum, where high resolution are characterized by high S/N ratio or narrow half-width. Thus, the resolution of latex state ^{13}C-NMR measurement was expressed via S/N ratio and half-width.

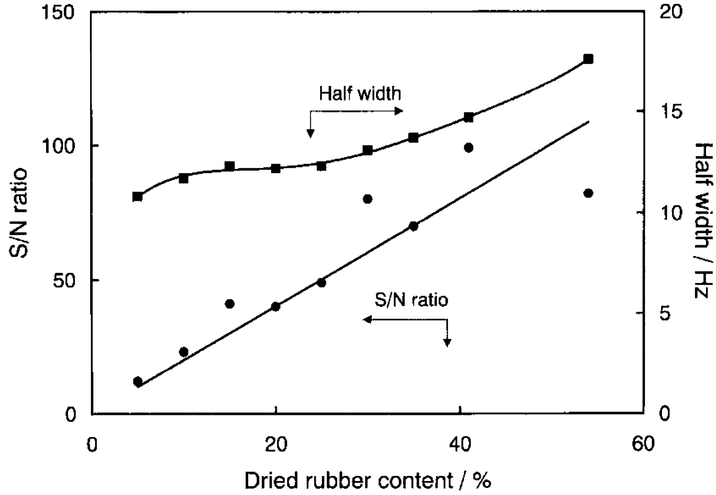

Figure 3. Dependence of S/N ratio (○) and half-width (●) on dried rubber content of PBD-G latex.

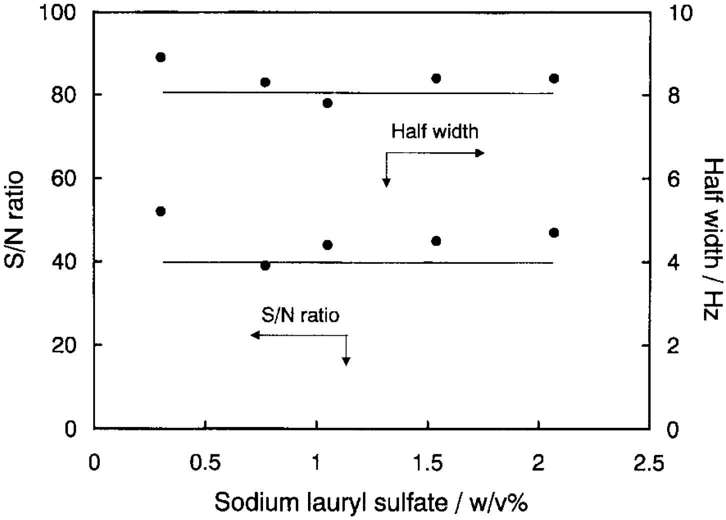

Figure 4. S/N ratio (○) and half-width (●) of PBD-G latex versus surfactant concentration.

Downloaded by UNIV OF GUELPH LIBRARY on June 20, 2012 | http://pubs.acs.org
Publication Date (Web): October 14, 2011 | doi: 10.1021/bk-2011-1077.ch029

Table 3. S/N ratio and half-width of PBD-S and PBD-G

Experimental condition	*S/N ratio / 10^2*	*Half-width / Hz*
PBD-S		
Complete decoupling		
Solution [b]	6.6	11
Latex [c]	2.2	10
Gated dcoupling [a]		
Solution [b]	3.5	11
Latex [c]	3.0	11
Solid	2.1	32
PBD-G		
Complete decoupling		
Solution [b]	0.7	26
Latex [c]	1.0	11
Gated dcoupling [a]		
Solution [b]	0.5	26
Latex [c]	0.7	12
Solid	0.7	63

[a] Gated decoupling without nuclear Overhauser effect . [b] 10w/v% $CDCl_3$ solution of PBD. [c] Dried rubber content of the latex was 10%.

As shown in Figure 3, the S/N ratio for PB-G latex sample increased linearly up to 60 w/w% in DRC, while the half-width increased abruptly at about 20 w/w% in DRC. This implies that an appropriate DRC necessary for high resolution latex state ^{13}C-NMR measurement hovered around 10 w/w%. Yet, the S/N ratio and half-width were independent of surfactant concentration as shown in Figure 4. Thus, the surfactant concentration was kept at 1 w/v% for future experiments.

Table 3 shows the values of S/N ratio and half-width determined for the signal at 32.7 ppm, for latex, solution and solid samples of PB-S and PB-G, obtained under the experimental conditions of complete decoupling (COM) and gated decoupling without nuclear Overhauser effect (NNE). In the absence of gel fraction, the S/N ratio for PB-S solution sample, measured with a COM pulse sequence, was higher than that measured with a NNE pulse sequence by a factor of about 2. This is due to the influence of nuclear Overhauser effect, as reported in the previous work (*11*). For PB-S latex sample, the S/N ratio estimated by COM measurement was similar to that estimated by NNE measurement, being comparable to the S/N ratio determined by the solid-state ^{13}C-NMR measurement. This may be due to either the absence of nuclear Overhause effect or other

Downloaded by UNIV OF GUELPH LIBRARY on June 20, 2012 | http://pubs.acs.org
Publication Date (Web): October 14, 2011 | doi: 10.1021/bk-2011-1077.ch029

unknown effects in the latex state ^{13}C-NMR spectroscopy. The value of half-width for PB-S latex sample was nearly equal to that of the solution sample, and smaller than the solid sample by a factor of about three. These results demonstrate that the resolution of ^{13}C-NMR measurement for PB latex without the gel fraction was identical to that for the solution sample, even though the latex is heterogeneous, consisting of a polymer dispersion in water.

In the presence of the gel fraction, as shown in Figures 1 and 2, the S/N ratio for PB-G swollen with $CDCl_3$ was smaller than that for the latex sample by about one-half under observation conditions of both COM and NNE, despite the fact that the polymer content in solution was the same as that in the latex. Here, the solution measurement of swollen PB-G containing about 80 w/w% gel fraction was carried out for the sake of comparison with the latex state measurement. The half-width for latex sample was about one-half of that for the swollen sample and one-sixth of that for the solid sample. Several signals for the solution and solid samples of PB-G were influenced by drifting baseline due to the crosslinks present in the gel fraction, as shown in Figures 1 and 2. Thus, highly crosslinked rubber samples may be quantitatively characterized by ^{13}C-NMR spectroscopy, when they are dispersed in water as small particles.

Downloaded by UNIV OF GUELPH LIBRARY on June 20, 2012 | http://pubs.acs.org
Publication Date (Web): October 14, 2011 | doi: 10.1021/bk-2011-1077.ch029

2.3. Effect of Particle Size

Deproteinized natural rubber (DPNR) latex was fractionated by centrifugation into four fractions with narrow, Gaussian, and nearly unimodal distributions in particle size. The volume mean particle diameter distribution of the four isolated fractions of DPNR is shown in Figure 5. At least three fractions were completely separated from each other, and two larger fractions were somewhat overlapped.

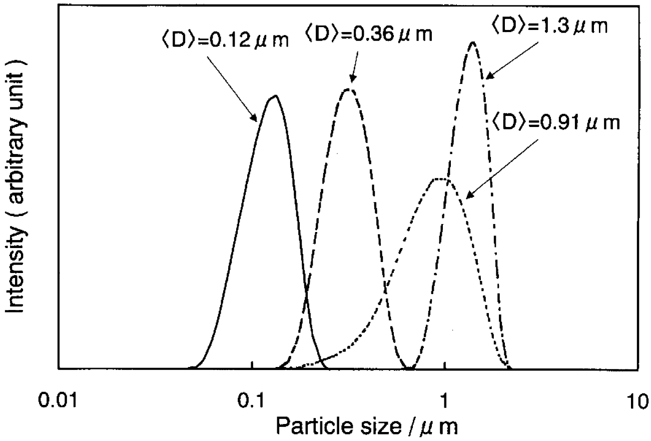

Figure 5. Volume weighted particle size distribution for DPNR fractionated by centrifugation: (A) DPNR-1, (B) DPNR-2, (C) DPNR-3 and (D) DPNR-4.

Downloaded by UNIV OF GUELPH LIBRARY on June 20, 2012 | http://pubs.acs.org
Publication Date (Web): October 14, 2011 | doi: 10.1021/bk-2011-1077.ch029

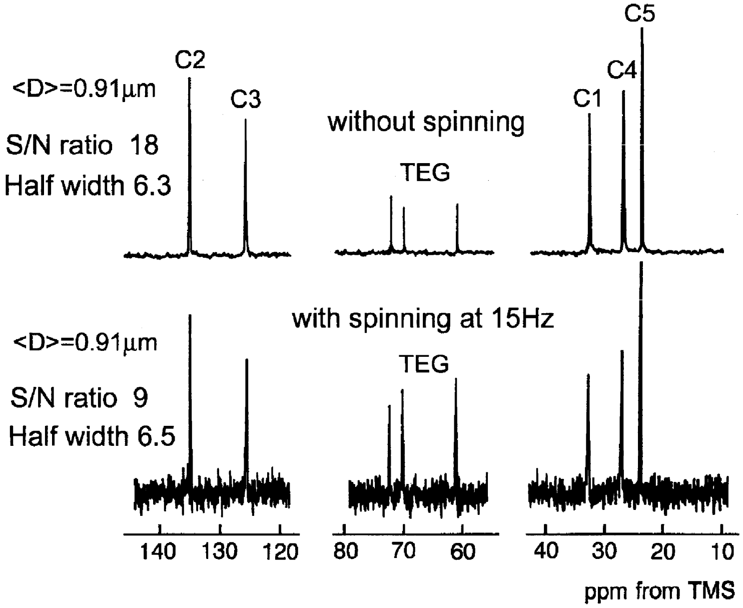

Figure 6. Latex state ^{13}C-NMR spectra for DPNR-3 obtained (A) with spinning of the sample tube and (B) without spinning.

The latex state ^{13}C-NMR measurements were made under two conditions: one with the sample tube spinning at a rate of 15 Hz and the other without spinning. A typical ^{13}C-NMR spectrum for DPNR-3 latex with a volume mean particle diameter of 0.901 µm is shown in Figure 6. The spectrum with spinning was distinguishable from that without spinning. The S/N ratio decreased to one-half and half-width increased a little, as the sample tube was spun at 15 Hz. This is explained to be due to segregation of the dispersed natural rubber particles (ρ=0.91 g/cm^3) onto the upper layer of the latex as a supernatant after spinning the NMR tube. The concentration of natural rubber at the pulse-irradiated region may, thus, be too low to obtain a sufficient S/N ratio. In Table 6, the values of S/N ratio and half-width for the other latex fractions are also shown. For DPNR-1 and DPNR-2 latexes with the volume mean particle diameters of 0.12 and 0.36 µm, respectively, the S/N ratio and half-width were independent of sample spinning. For these two fractions with the small particle diameter, the particles were homogeneously dispersed in water after NMR measurement. In contrast, as for DPNR-4, no signals were seen in the NMR spectrum when the sample tube was spun at 15 Hz. This demonstrates that the latex state ^{13}C-NMR measurement is significantly dependent upon the homogeneity in the latex particle distribution.

The diffusion coefficient of the Brownian motion (*14*) was measured by light scattering technique, since the diffusion coefficient is proportional to the rotational motion of the particles, which may perhaps be related to the rotational correlation time. We postulate that the molecular order rotational correlation time is interfered by the rotational motion of the particles of about 1 µm in the average diameter.

The motions of the particles in the latex were expected to play an important role in eliminating the effect of dipole-dipole interactions.

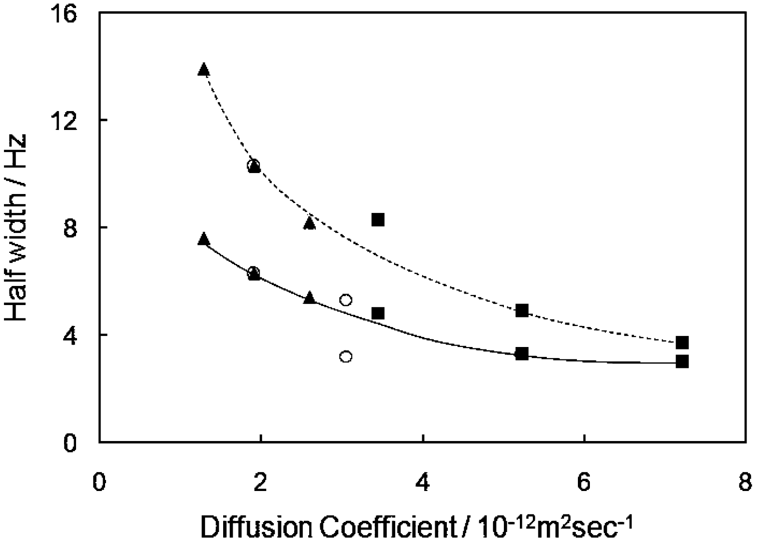

Figure 7. Dependence of half-width on diffusion coefficient of Brownian motion for methyl carbon (solid line) and methine carbon (dotted line) : DPNR-1–DPNR-4 latex at 50 °C (○), DPNR1 at 30–70 °C (●) and DPNR4 at 30–70 °C (▵).

In order to confirm the relationship between Brownian motion and resolution of ^{13}C-NMR spectroscopy that is associated with dipole-dipole interactions, the half width was plotted against diffusion coefficient of the Brownian motion. Figure 7 shows a typical plot of the half width of methyl signal at 24 ppm and methine at 124 ppm *versus* the diffusion coefficient. The half width for the latex decreased with increasing diffusion coefficient and was close to that for the corresponding solution. This is strong evidence showing that the Brownian motion of the latex particles (or its related motions) eliminates the effect of dipole-dipole interactions on the latex-state ^{13}C-NMR measurement.

3. Solid-State NMR with FG-FMAS Probe

3.1. Effect of Crosslinking

Solid-state ^{13}C-NMR spectrum for the vulcanized natural rubber, measured with a FG-FMAS probe, is shown in Figure 8, together with a solution ^{13}C-NMR spectrum for unvulcanized natural rubber. Five major signals in the spectrum were assigned to C nuclei of *cis*-1,4-isoprene units, according to the previous paper (*15*). Half width of the signals and signal to noise (S/N) ratio of the solid-state ^{13}C-NMR spectrum for the vulcanized natural rubber were quite similar to those

Downloaded by UNIV OF GUELPH LIBRARY on June 20, 2012 | http://pubs.acs.org
Publication Date (Web): October 14, 2011 | doi: 10.1021/bk-2011-1077.ch029

in the solution ^{13}C-NMR spectrum for unvulcanized natural rubber. The narrow half width and the ample S/N ratio of the solid-state ^{13}C-NMR spectrum for the vulcanized natural rubber may imply that high resolution was maintained for the solid-state ^{13}C-NMR spectroscopy, even after vulcanization, since heteronuclear dipole-dipole interactions was eliminated by FMAS. This is distinguished from low resolution solid-state NMR spectrum for the vulcanized natural rubber reported by Klüppel (*16*) and Köenig (*17–22*).

3.2. Spectral Assignments

In Figure 8, small signals appeared at 40, 44, 50 and 58 ppm in the solid-state ^{13}C-NMR spectrum for the vulcanized natural rubber, which were not shown in the solution ^{13}C-NMR spectrum for the unvulcanized natural rubber. To assign the signals, we applied DEPT measurement at 45 ° (DEPT45), 90 ° (DEPT90) and 135 ° (DEPT135) pulses and APT measurement to the solid-state ^{13}C-NMR spectroscopy. Figure 9 shows DEPT45, DEPT90 and DEPT135 spectra for the vulcanized natural rubber. The signals at 24, 26 and 32 ppm characteristic of methyl, methylene and methine carbons of *cis*-1,4-isoprene unit were shown to be up, up, and up in the DEPT45 spectrum and almost null in the DEPT90 spectrum. On the other hand, in the DEPT135 spectrum, the signals were up, down, and down. Thus, the pulse width determined for DEPT measurements was confirmed to be correct.

The small signals at 40 and 44 ppm were shown to be up in the DEPT45 spectrum, null in the DEPT90 spectrum, and down in the DEPT135 spectrum; hence, they were assigned to secondary carbons. The signal at 50.5 ppm was assigned to quaternary carbon due to null signal in the spectra, while the signal at 50 ppm was assigned to tertiary carbon due to up signals in the spectra. In contrast, the signal at 58 ppm was assigned to tertiary and quaternary carbons due to the very small up signals in the DEPT45, DEPT90 and DEPT135 spectra and null signals; in fact, almost all signals disappeared. In Figure 9, the APT spectrum is also shown for the vulcanized natural rubber. The APT spectrum showed up signals at 40 and 44 ppm, up and down signals at 50 ppm, and up and down signals at about 58 ppm. Thus, we assigned the signals at 40 and 44 ppm to the secondary carbons and the signals at 50 and 58 ppm to the tertiary and quaternary carbons.

Figure 10 shows solid-state ^{1}H-NMR spectrum for the vulcanized natural rubber and solution ^{1}H-NMR spectrum for the unvulcanized natural rubber. Major signals at 1.7, 2.1 and 5.1 ppm in the spectra were assigned to methyl, methylene and unsaturated methine protons of *cis*-1,4-isoprene units, respectively. Values of half width and signal to noise (S/N) ratio of the signals in the solid-state ^{1}H-NMR spectrum for the vulcanized natural rubber were a little bit larger and smaller, respectively, than the values of the half width and the S/N ratio of the signals in the solution ^{1}H-NMR spectrum for the unvulcanized natural rubber. For instance, the value of half width of the signals in the solid-state spectrum was about 1.5 times as large as that in the solution spectrum. This may be explained to be due to a reduced effect of the homonuclear dipole-dipole interactions in the solid-state ^{1}H-NMR spectrum; i.e., a major portion of the homonuclear dipole-dipole interactions are eliminated by FMAS. (The homonuclear dipole-dipole interaction

Downloaded by UNIV OF GUELPH LIBRARY on June 20, 2012 | http://pubs.acs.org
Publication Date (Web): October 14, 2011 | doi: 10.1021/bk-2011-1077.ch029

may be completely eliminated by extremely fast MAS with smaller sample tube, but this is not the focus of this work.) In Figure 10, small signals at 3.4 and 4.2 ppm appeared in the solid-state ^{1}H-NMR spectrum for the vulcanized natural rubber, but not in the solution ^{1}H-NMR spectrum for the unvulcanized natural rubber. The signal at 3.4 ppm was assigned to aliphatic ^{1}H linking to –C-CH-Sx group and the signal at 4.2 ppm to unsaturated aliphatic ^{1}H linking to =C-CH-Sx group, according to literatures (*23*), where x represents the number of S atoms.

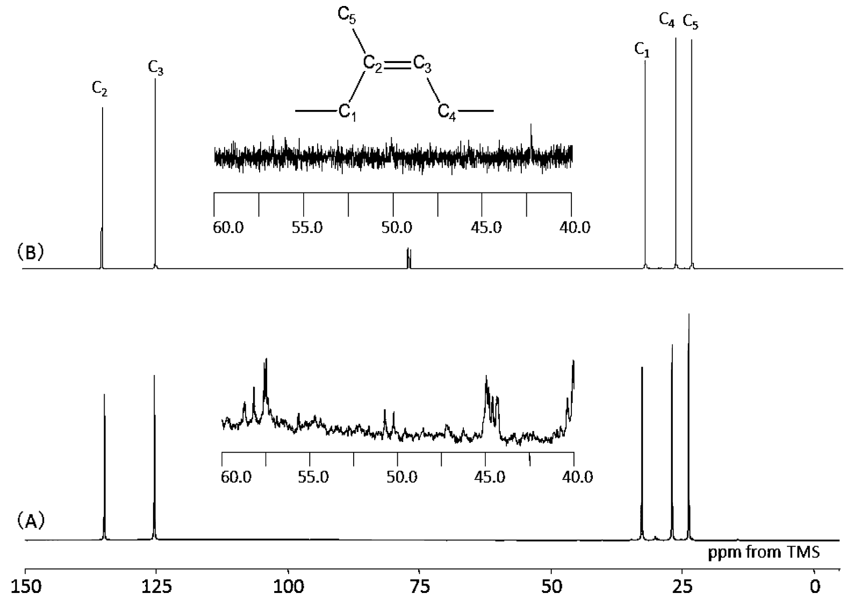

Figure 8. Typical ^{13}C-NMR spectra: (A) solid-state ^{13}C-NMR spectrum for the vulcanized natural rubber, (B) solution-state ^{13}C-NMR spectrum for unvulcanized natural rubber. The solid-state ^{13}C-NMR measurement was performed with a 4 mm FG-FMAS probe at 18 kHz in spinning rate. The solution state ^{13}C-NMR measurement was performed with a NM-40TH5AT/FG2SL probe at 12 Hz in spinning rate.

3.3. 2D NMR Measurement

Figure 11 shows HSQC spectra obtained through solid-state NMR spectroscopy equipped with the FG-FMAS probe. The signals at 1.7, 2.1 and 5.1 ppm in the ^{1}H-NMR spectrum were correlated with the signals in the ^{13}C-NMR spectrum; e.g., the signal at 1.7 ppm was correlated with the signal at 23 ppm, the signal at 2.1 ppm with the signals at 26 and 32 ppm, and the signal at 5.1 ppm with the signal at 135 ppm. However, no heteronuclear correlation between the small signals was detected in HSQC spectra due to inadequate accumulation time for HSQC measurement.

Downloaded by UNIV OF GUELPH LIBRARY on June 20, 2012 | http://pubs.acs.org
Publication Date (Web): October 14, 2011 | doi: 10.1021/bk-2011-1077.ch029

Downloaded by UNIV OF GUELPH LIBRARY on June 20, 2012 | http://pubs.acs.org
Publication Date (Web): October 14, 2011 | doi: 10.1021/bk-2011-1077.ch029

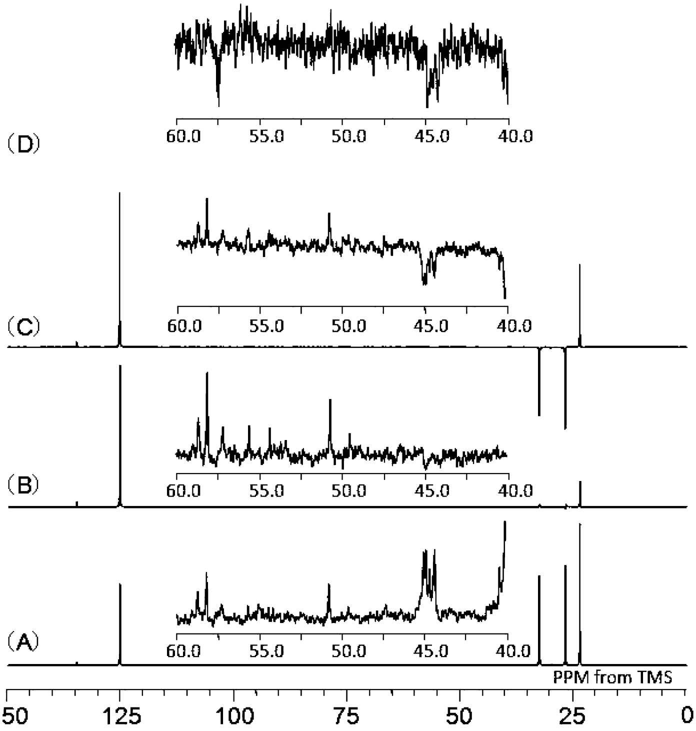

Figure 9. Solid-state ^{13}C-NMR spectra with pulse sequences of distortionless enhancement by polarization transfer (DEPT) and attached proton test for the vulcanized natural rubber: (A) DEPT45, (B) DEPT90, (C) DEPT135, (D) APT.

To detect heteronuclear correlation between the small signals, HMQC measurement was performed in a selective region of chemical shift: 2–4 ppm in ^{1}H domain and 35–70 ppm in ^{13}C domain. Figure 12 shows HMQC spectra obtained by the selective experiment. The ^{13}C-signals at 40, 44, 50 and 58 ppm were well correlated to the ^{1}H-signals at 2.1, 1.7, 2.8 and >3.6 ppm. In the previous works (*15*, *24*), the signals at 40, 44 and 58 ppm of the vulcanized liquid *cis*-1,4-polyisoprene as a model were assigned through solution NMR spectroscopy with various pulse sequences, viz., DEPT, APT, HETCOR, HSQC and HMBC. The signal at 40 ppm was assigned to C4 of *trans*-1,4-isoprene units, obtained by isomerization of *cis*-1,4-isoprene units. In contrast, the signals at 44 ppm in the ^{13}C-NMR spectrum were assigned to the secondary carbons adjacent to carbons linking to S atoms. The signals at 58 ppm in ^{13}C-NMR spectrum were assigned to the tertiary and quaternary carbons linking to S atoms. In the present work, the same results were obtained by the solid-state NMR spectroscopy equipped with the FG-FMAS probe. Furthermore, the ^{13}C-signals at 58 ppm were correlated to the ^{1}H-signals at 3.4 and 4.2 ppm, which were assigned to the –C-CH-Sx group and =C-CH-Sx group.

Downloaded by UNIV OF GUELPH LIBRARY on June 20, 2012 | http://pubs.acs.org
Publication Date (Web): October 14, 2011 | doi: 10.1021/bk-2011-1077.ch029

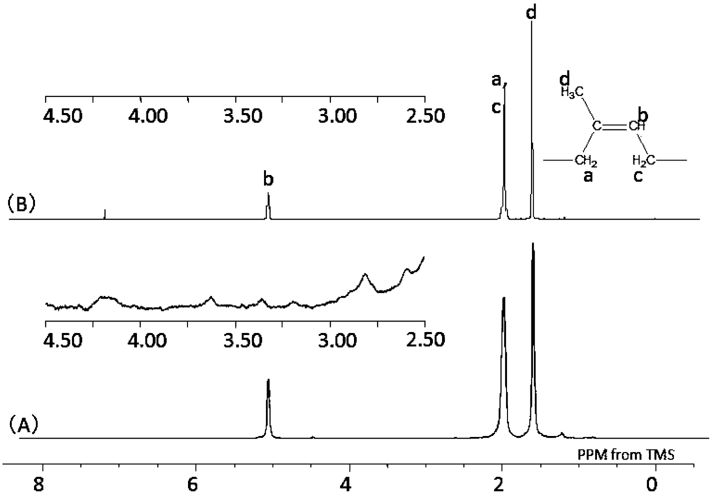

Figure 10. Typical ^{1}H-NMR spectra: (A) solid-state 1H-NMR spectrum for the vulcanized natural rubber, (B) solution-state ^{1}H-NMR spectrum for the unvulcanized natural rubber. The solid-state ^{1}H-NMR measurement was performed with a 4 mm FG-FMAS probe at 18 kHz in spinning rate. The solution state ^{1}H-NMR measurement was performed with a NM-40TH5AT/FG2SL probe at 12Hz in spinning rate.

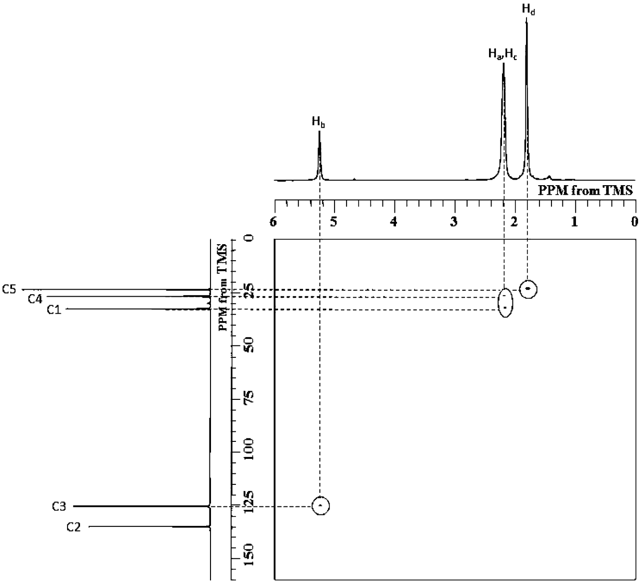

Figure 11. HSQC spectra for the vulcanized natural rubber, obtained through solid-state NMR spectroscopy equipped with a 4 mm FG-FMAS probe at 18 kHz in spinning rate for 1 h 2 min.

Downloaded by UNIV OF GUELPH LIBRARY on June 20, 2012 | http://pubs.acs.org
Publication Date (Web): October 14, 2011 | doi: 10.1021/bk-2011-1077.ch029

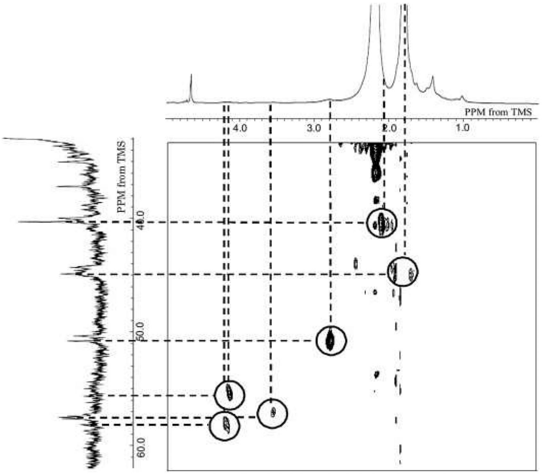

Figure 12. HMQC spectra for the vulcanized natural rubber, obtained through solid-state NMR spectroscopy equipped with a 4 mm FG-FMAS probe at 18 kHz in spinning rate for 71.5 h. HMQC measurement was performed in a selective region of chemical shift: 2–4 ppm in ^{1}H domain and 35–70 ppm in ^{13}C domain.

3.4. Application of FG-FMAS Solid-State NMR Spectroscopy

The crosslinking junctions of three rubbers (CV, EV and SemiEV crosslinked rubbers) were analyzed by solid-state ^{1}H-NMR and ^{13}C-NMR spectroscopy. Table 4 shows crosslink density of these three rubbers. Values of crosslink density of the crosslinked rubbers were similar, implying that the crosslink density is adjustable, as long as we prepare the samples under the optimum condition for crosslinking. The slight difference in the value of crosslink density may be due to the comparatively short time for crosslinking and it is difficult to use exactly the same optimum time for crosslinking.

Figure 13 shows solid-state ^{1}H-NMR spectra for the three rubbers. Major signals at 1.7, 2.1 and 5.1 ppm in the spectra were assigned to methyl, methylene and unsaturated methine protons of *cis*-1,4-isoprene units, respectively. In Figure 13, small signals at 3.4 ppm and 4.2 ppm were found for the three crosslinked rubbers. The signal at 3.4 ppm was assigned to aliphatic ^{1}H linking to –C-CH-Sx group and the signal at 4.2 ppm to unsaturated aliphatic ^{1}H linking to =C-CH-Sx group, according to our work (*4*). The intensity of the aliphatic ^{1}H linking to –C-CH-Sx group (3.4 ppm) and the unsaturated aliphatic ^{1}H linking to =C-CH-Sx group (4.2 ppm) was estimated from intensity ratio of the signals to the methyl proton signal at 1.7 ppm. The estimated value of the intensity ratio is tabulated in Table 5. It was found that the intensity of the aliphatic ^{1}H linking to –C-CH-Sx group at 3.4 ppm was 0.02 % for CV, EV and SemiEV crosslinked rubbers, whereas that of the unsaturated aliphatic ^{1}H linking to =C-CH-Sx group at 4.2 ppm was 0.03 % for CV and SemiEV crosslinked rubbers and 0.02 % for EV crosslinked rubber. From these results, it is concluded that the content of the small signals of the aliphatic ^{1}H linking to –C-CH-Sx group and unsaturated aliphatic ^{1}H linking to

=C-CH-Sx group for CV, EV and SemiEV crosslinked rubbers was almost similar to each other.

Table 4. Vulcanization characteristics of HANR and DPNR compounds

Sample	*Crosslink density ($x10^{-4}$, mol/cm^3)*		
	CV system	*EV system*	*SemiEV system*
HANR	1.86	1.45	1.67

Table 5. Intensity ratio of the signal at 3.4 ppm (aliphatic ^1H linking to –C-CH-S_x group signal) and the signal at 4.2 ppm (unsaturated aliphatic ^1H linking to =C-CH-S_x group signal) to the signal at 1.7 ppm

Crosslinked rubber	*Intensity of signals (%)*	
	3.4 ppm (aliphatic ^1H linking to –C-CH-S_x group)	*4.2 ppm (unsaturated aliphatic ^1H linking to =C-CH-S_x group)*
CV	0.02	0.03
EV	0.02	0.02
SemiEV	0.02	0.03

Table 6. Intensity ratio of the signals at 40, 44 and 58 ppm to the signal at 24 ppm

Crosslinked rubber	*Intensity of crosslinking junction signals (%)*		
	40 ppm	*44 ppm*	*58 ppm*
CV	0.010	0.005	0.005
EV	0.010	0.000	0.000
SemiEV	0.009	0.001	0.001

Downloaded by UNIV OF GUELPH LIBRARY on June 20, 2012 | http://pubs.acs.org
Publication Date (Web): October 14, 2011 | doi: 10.1021/bk-2011-1077.ch029

Downloaded by UNIV OF GUELPH LIBRARY on June 20, 2012 | http://pubs.acs.org
Publication Date (Web): October 14, 2011 | doi: 10.1021/bk-2011-1077.ch029

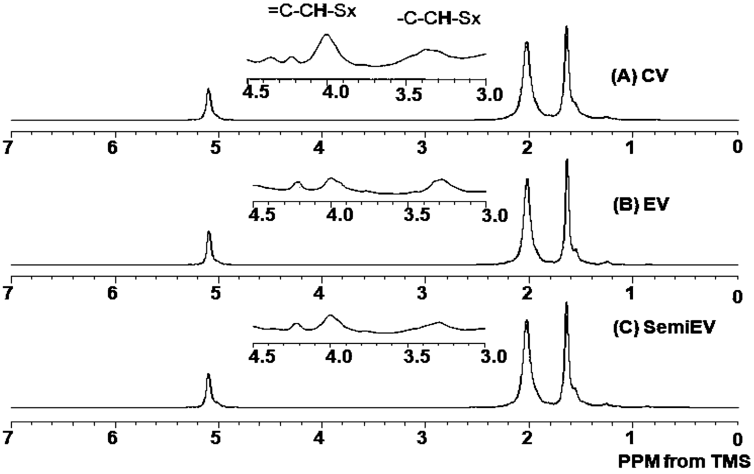

Figure 13. Solid-state ^{1}H-NMR spectra for the crosslinked natural rubbers prepare by (A) CV, (B) EV and (C) SemiEV.

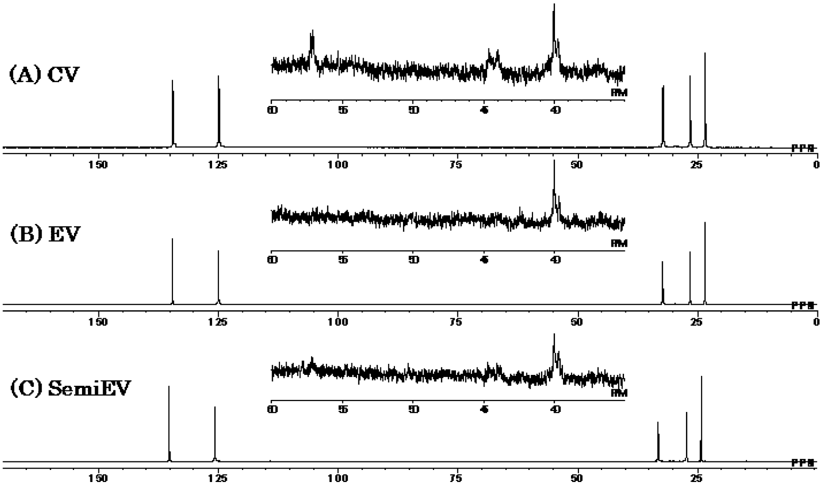

Figure 14. Solid-state ^{13}C-NMR spectra for the crosslinked natural rubbers prepared by (A) CV, (B) EV and (C) SemiEV.

In NMR Spectroscopy of Polymers: Innovative Strategies for Complex Macromolecules; Cheng, H., et al.;
ACS Symposium Series; American Chemical Society: Washington, DC, 2011.

Downloaded by UNIV OF GUELPH LIBRARY on June 20, 2012 | http://pubs.acs.org
Publication Date (Web): October 14, 2011 | doi: 10.1021/bk-2011-1077.ch029

Solid-state ^{13}C-NMR spectra for the same samples are shown in Figure 14. Small signals at 40, 44 and 58 ppm appeared in the solid-state ^{13}C-NMR spectra for the CV and SemiEV crosslinked rubber, whereas only signal at 40 ppm appeared in the solid-state ^{13}C-NMR spectrum for the EV crosslinked rubber. The signals at 40 and 44 ppm were assigned to C4 of *trans*-1,4-isoprene units (*25*, *26*) and secondary carbons adjacent to carbons linking to S atom, respectively, and the signals at 58 ppm were assigned to the tertiary and quaternary carbons linking to S atoms, according to our work (*4*). This may imply that the crosslinking junctions of the CV and SemiEV crosslinked rubbers were not only secondary carbon but also tertiary and quaternary carbons whereas that of the EV crosslinked rubber may contain small amount of quaternary carbon. The intensity of the small signals at 40 ppm, 44 ppm, and 58 ppm was estimated from intensity ratio of the signals to the methyl carbon signal at 24 ppm. The estimated values of the intensity ratio of the small signals at 40, 44 and 58 ppm to the methyl carbon signal at 24 ppm were tabulated in Table 6. The intensity of the signal at 40 ppm was similar to each other (0.010 %) for CV, EV and SemiEV crosslinked rubbers. This indicates that cis-trans isomerization occurs similarly for CV, EV and SemiEV crosslinked rubbers in spite of differences in formulation. In contrast, the intensity of the signals at 44 ppm and 58 ppm in the solid-state ^{13}C-NMR spectrum decreased in the order of CV, SemiEV and EV crosslinked rubbers. The intensity of the secondary carbon (44 ppm), the tertiary and quaternary carbon (58 ppm) for CV crosslinked rubber was the highest among the three. They decreased for SemiEV crosslinked rubber and disappeared for EV crosslinked rubber. This implies that the amount of the quaternary carbon of the CV crosslinked rubber is larger than that of the SemiEV crosslinked rubber. The EV crosslinked rubber may contain a small amount of quaternary carbon as a crosslinking junction.

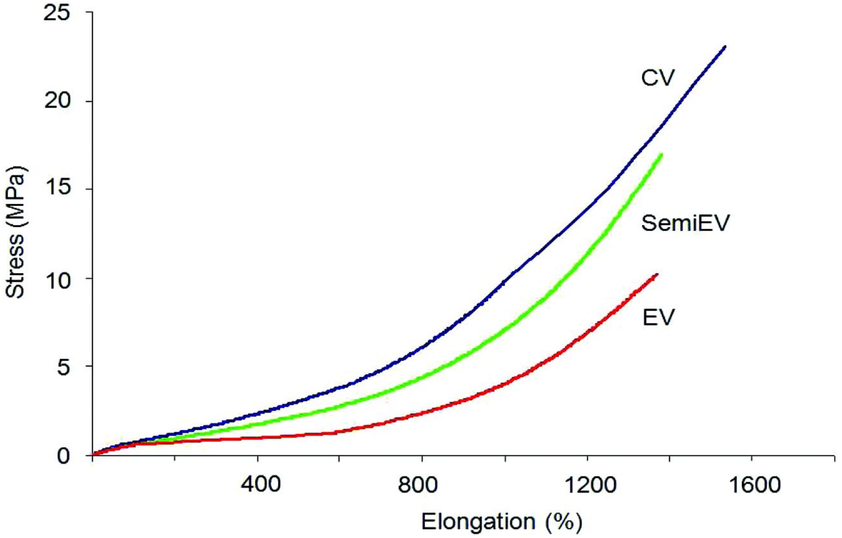

Figure 15. Stress-strain curves for CV, EV and Semi-EV crosslinked rubbers.

Downloaded by UNIV OF GUELPH LIBRARY on June 20, 2012 | http://pubs.acs.org
Publication Date (Web): October 14, 2011 | doi: 10.1021/bk-2011-1077.ch029

The stress-strain curves for the CV, EV and SemiEV crosslinked rubbers are shown in Figure 15. Modulus at 100% strain of the CV crosslinked rubber is almost similar with that of EV and SemiEV crosslinked rubbers. This is consistent with the fact that the values of the crosslink density of the CV, EV and SemiEV crosslinked rubbers were similar to each other, as shown in Table 4. In contrast, tensile strength of the three crosslinked rubbers was different; that is, the value of stress at break of the CV crosslinked rubber (22.5 MPa) was the highest among the three crosslinked rubbers and was reduced for the SemiEV (17.0 MPa) and EV (9.2 MPa), in that order. In the previous work (*27*), Suchiva and co-workers reported that better mechanical properties of the CV crosslinked rubber was due to higher concentrations of the polysulfidic crosslinks compared to those of the EV crosslinked rubber. Moreover, the superior mechanical properties of CV crosslinking system may be explained to be due to differences in the vulcanization mechanism of the crosslinking systems. It may be noted that the conventional crosslinking system produces a homogeneous network. Yet, an efficient crosslinking system results in significant polymerization of double bonds of adjacent chains leading to a network of unevenly distributed crosslinks and in impediment to NR crystallization and stress concentration that anticipates compound failure (*28*). In the present work, it was found that the excellent mechanical properties of the CV crosslinked rubber could be attributed to the quaternary carbon of crosslinking junctions.

Acknowledgments

This work was supported in part by a Grant-in-Aid (21655080) for Challenging Exploratory Research and Grant-in-Aid (22350100) for Scientific Research (B) from Japan Society for the Promotion of Science and JST-JICA SATREPS.

References

1. Kawahara, S.; Bushimata, S.; Sugiyama, T.; Hashimoto, C.; Tanaka, Y. *Rubber Chem. Technol.* **1999**, *72*, 844–853.
2. Kawahara, S.; Washino, K.; Morita, T.; Tanaka, Y.; Isono, Y. *Rubber Chem. Technol.* **2001**, *74*, 295–302.
3. Duer, M. J. *Introduction to Solid-State NMR Spectroscopy*; Blackwell Publishing: Cambridge, MA, 2004.
4. Kawahara, S.; Chaikumpollert, O.; Sakurai, S.; Yamamoto, Y.; Akabori, K. *Polymer* **2009**, *50*, 1626–1631.
5. Fitch, R. M.; Gajria, C.; Tarcha, P. J. *J. Colloid Interface Sci.* **1979**, *71*, 108–109.
6. Ang, T. T.; Roberts, J. D. *Plast. Rubber: Mater. Appl.* **1979**, *August 4*, 138–139.
7. Gambhir, P. N.; Joshi, D. K.; Tiwari, P. N.; Mani, J. *J. Nat. Rubber Res.* **1993**, *8*, 208–212.

8. Romanova, E. E.; Grinberg, F.; Pampel, A.; Kaerger, J.; Freude, D. *J. Magn. Reson.* **2009**, *196*, 110–114.
9. Viel, S.; Ziarelli, F.; Pages, G.; Carrara, C.; Caldarelli, S. *J. Magn. Reson.* **2008**, *190*, 113–123.
10. Pampel, A.; Fernandez, M.; Freude, D.; Kaerger, J. *Chem. Phys. Lett.* **2005**, *407*, 53–57.
11. Sato, H.; Takebayashi, K.; Tanaka, Y. *Macromolecules* **1987**, *20*, 2418–2423.
12. Bywater, S. *Polym. Commun.* **1983**, *24*, 203–205.
13. Tanaka, Y.; Takeuchi, Y.; Kobayashi, M.; Tadokoro, H. *J. Polym. Sci.* **1971**, *A-2* (9), 43–57.
14. Einstein, A. *Ann. Phys.* **1905**, *17*, 549–560.
15. Kawahara, S.; Jinta, U.; Sakai, J.; Yamamoto, Y.; Isono, Y. *Rubber Chem. Technol.* **2007**, *80*, 751–761.
16. Klüppel, M.; Menge, H.; Schmidt, H.; Schneider, H.; Shuster, R. H. *Macromolecules* **2001**, *34*, 8107–8116.
17. Zaper, A. M.; Köenig, J. L. *Rubber Chem. Technol.* **1987**, *60*, 252–277.
18. Mori, M.; Köenig, J. L. *Rubber Chem. Technol.* **1995**, *68*, 551–562.
19. Mori, M.; Köenig, J. L. *Rubber Chem. Technol.* **1997**, *70*, 671–680.
20. Mori, M. *Rubber Chem. Technol.* **2003**, *76*, 1259–1275.
21. Mori, M.; Köenigh, J. L. *J. Appl. Polym. Sci.* **1998**, *70*, 1391–1399.
22. Patterson, D. J.; Köenigh, J. L.; Shelton, J. R. *Rubber Chem. Technol.* **1983**, *56*, 971–994.
23. Frust, A.; Pretsch, E. *Anal. Chem. Acta.* **1990**, *229*, 17–25.
24. Ukawa, J.; Kawahara, S.; Sakai, J. *J. Polym. Sci., Part B: Polym. Phys.* **2007**, *45*, 1003–1009.
25. Tanaka, Y. *Rubber Chem. Technol.* **1991**, *64*, 325–385.
26. Buzare, J. Y.; Silly, G.; Emery, J.; Boccaccio, G.; Rouault, E. *Eur. Polym. J.* **2001**, *37*, 85–91.
27. Suchiva, K.; Kowitterawut, T.; Srichantamit, L. *J. Appl. Polym. Sci.* **2000**, *78*, 1495–1504.
28. Gonzalez, L.; Rodriguez, A.; Valentin, J. L.; Marcos-Fernandez, A.; Posadas, P. *Kautsch. Gummi Kunstst.* **2005**, *67*, 638–643.

Downloaded by UNIV OF GUELPH LIBRARY on June 20, 2012 | http://pubs.acs.org
Publication Date (Web): October 14, 2011 | doi: 10.1021/bk-2011-1077.ch029

Downloaded by CORNELL UNIV on June 19, 2012 | http://pubs.acs.org
Publication Date (Web): October 14, 2011 | doi: 10.1021/bk-2011-1077.ch030

Chapter 30

Proton MAS NMR Analysis of Phenyl Silane Functionalized Silica Nanoparticles

Khalid A. M. Thakur,*,1 Mark McCormick,1b Wendy L. Thompson,2 Chuntao Cao,2 and William J. Schultz2

**[1]3M Corporate Research Analytical Laboratory, 6801 River Place Blvd,
142-4N-01, Austin, TX 78726
[1b]3M Corporate Research Analytical Laboratory, 3M Center, 201-BS-08,
St. Paul, MN 55144
[2]3M Corporate Research Materials Laboratory, 3M Center, 201-1W-28,
St. Paul, MN 55144
*E-mail: kathakur@mmm.com**

High temperature magic-angle-spinning (MAS) ^{1}H NMR was used to identify organic components on the surface of functionalized silica nanoparticles. The high temperature data acquisition, by preferential narrowing of resonances, enabled differentiation between species that were adsorbed or weakly bound versus those that were covalently bound to the surface. MAS NMR of a sample as a slurry with appropriate solvent provided information similar to that obtained at higher temperatures. With increasing temperature, gradual separation and up-field shift of silanol proton and water resonances at different rates was observed, possibly a result of diminished hydrogen bonding at increasingly higher temperatures.

Introduction

Functionalized or surface modified silica nanoparticles are used in numerous applications including biomedicine, biotechnology, foam generation and polymer modification (*1–12*). They are prepared by reacting the silanol (-Si-OH) groups that are on silica nanoparticle surface with an appropriately reactive organic molecule. The reactive organic molecules most commonly used for functionalization have the following general formula – $R'Si(-OR)_3$, where R may

In NMR Spectroscopy of Polymers: Innovative Strategies for Complex Macromolecules; Cheng, H., et al.;
ACS Symposium Series; American Chemical Society: Washington, DC, 2011.

be methyl or ethyl group, and R′ has the desired terminal functional group. The wish list for characterization of the functionalized nanoparticles includes: (1) Extent of reaction of the surface silanols; (2) Confirmation of desired functional group on molecules that are covalently bound to the surface; (3) Identification of any self-condensed oligomeric silane; (4) Identification of inaccessible cavities in the silica particles; and (5) Identification of adsorbed water or solvent molecules that may be present after the drying process. FT-IR is the most common spectroscopic analytical tool used for the molecular structure characterization of functionalized or modified silica particles (*13–17*). Solution NMR, though well known for molecular structure characterization, has found limited applications in study of functionalized nanoparticles. There may be a number of possible reasons for it including poor solubility and broad NMR resonance linewidths.

A variety of solid-state NMR techniques have been used for analysis of silica particles including ^{1}H MAS 1D/2D and ^{29}Si CP-MAS NMR (*18–30*). In functionalized nanoparticles, the surface chemistry is of most interest. Because of the surface area to volume ratio, the NMR sensitivity is inversely proportional to the silica particle size. ^{1}H MAS NMR spectra are significantly more sensitive than ^{13}C or ^{29}Si CP-MAS NMR. However, the normal single pulse ^{1}H NMR spectra of rigid materials acquired at nominal MAS speeds are usually too broad to be useful. Fast spinning (>15 kHz) ^{1}H MAS NMR has been shown to improve the resolution of the resonances and enable analysis of the silica particle surfaces (*18*, *19*).

Here, we describe some of the capabilities of high temperature magic-angle-spinning (MAS) single pulse ^{1}H NMR for the characterization of functionalized nanoparticles. MAS NMR as a slurry after addition of a small fraction of solvent also provided similar information. Interpretations were made based on changes in proton NMR resonance linewidths as a function of temperature.

Downloaded by CORNELL UNIV on June 19, 2012 | http://pubs.acs.org
Publication Date (Web): October 14, 2011 | doi: 10.1021/bk-2011-1077.ch030

Experimental Section

Materials and Measurements

MAS NMR spectra were acquired by spinning the sample in Chemagnetics™ probes at speeds of up to 23 kHz in a 3.2 mm rotor. Data were acquired at temperatures between 22 ºC and 250 ºC on a Varian INOVA 400 MHz NMR spectrometer. The temperature values reported were not corrected for possible frictional heating. Custom made fluoropolymer (PTFE) end-caps for the MAS rotors were utilized to enable high temperature data acquisition and reduce background resonance. Unless specifically mentioned, pulse sequences employing single pulse Bloch decay measurements were used. Most of the ^{1}H MAS NMR spectra were acquired with less than a 25° tip angle and 64 scans were averaged with recycle time of 3 seconds. The ^{1}H NMR chemical shift was externally calibrated using methyl resonance of cured poly(dimethyl siloxane) gel at δ 0.2 ppm. MAS NMR spectra of AD and HMB were collected on a Varian NMRS 400 MHz NMR Spectrometer equipped with a Varian HXY 3.2 mm probe at speeds of 22 kHz.

Downloaded by CORNELL UNIV on June 19, 2012 | http://pubs.acs.org
Publication Date (Web): October 14, 2011 | doi: 10.1021/bk-2011-1077.ch030

Materials: Hexamethylbenzene (HMB) and Adamantane (AD) were purchased from Aldrich and Avocado respectively and used without further purification. Silica nanoparticles with nominal 20 nm particle size distribution were obtained from Nalco as a 40 weight% aqueous colloidal silica solution (Nalco 2327). Trimethoxy phenyl silane (TPS) and 1,1,1,3,3,3-Hexamethyldisilazane (HDMS) were purchased from Aldrich.

The procedure for surface functionalization has been described in patent US 5,648,407 (*31*). All samples were dried for the analysis.

Sample **I**: 24.8 mmol of TPS in 150g of methoxyl-2-propanol was added dropwise to 100g of Nalco 2327 while stirring. After stirring for another 30 minutes, the mixture was kept in an oven at 90 °C for 24 hours. This was then air-dried in a heated Aluminum pan.

Sample **II**: The dried Sample I solid was re-dispersed in 75g of acetone. 5g of HDMS was added, and the mixture was stirred for four hours. The dispersion was dried at 100 °C for 30 minutes in an oven.

Sample **III**: 24.8 mmol of TPS in 150g of Diglyme was added dropwise to 100g of Nalco 2327 while stirring. After stirring for another 30 minutes, the mixture was kept in an oven at 90 °C for 24 hours. Upon cooling to room temperature, an additional 100g of Diglyme was added and the mixture was put on a Buchi rota-vapor to remove water. Subsequently, 10g of HDMS was added, and the mixture was stirred for four hours. The solution was then dried at 100 °C for 30 minutes in an oven.

In Sample **III** the two functionalized steps in Sample **I** and Sample **II** were combined in to a pseudo one step process.

Overview of Resonance Linewidth Broadening Mechanisms in NMR

In order to facilitate discussions in subsequent sections, this sub-section attempts to provide a non-mathematical description of mechanisms that govern linewidths of NMR resonances and related key concepts and commonly used acronyms.

Chemical shifts of resonances (δ) obtained in dilute solution NMR spectra have been routinely used for molecular structure identification and characterization of organic solutes (*32–35*). The narrow resonances in solution at their isotropic chemical shifts are a result of (1) molecular motion averaging orientation effects with respect to the magnetic field direction; and (2) isolation of the solutes in deuterated (or non-protonated) solvent. Each resonance peak is often representative of a specific three dimensional chemical structure vibrating and rotating in isolation. Any change in the molecular structure or its electronic environment shifts the NMR resonance, the magnitude of which is typically related to the distance of the change from the observed nuclei.

During NMR measurements of rigid and semi-rigid materials, the rotational and translational motions are not rapid enough to average out the orientation dependent effects leading to broader resonances than in dilute solution. Typically, all possible orientations of molecules are present in a randomly distributed "isotropic" sampling. The orientation dependent shielding from electronic environment results in a range of observed chemical shift that is referred to as the

In NMR Spectroscopy of Polymers: Innovative Strategies for Complex Macromolecules; Cheng, H., et al.; ACS Symposium Series; American Chemical Society: Washington, DC, 2011.

Chemical Shift Anisotropy (CSA). Nuclei spins also have orientation dependent dipolar interactions that can lead to resonance broadening up to several kHz. In isotropic samples, solid-state NMR spectrometers use magic-angle-spinning (MAS) to mechanically average CSA and dipolar broadening, leading to narrower resonances.

Anisotropic properties, however, are not completely averaged by MAS. Consider two contrasting examples: (1) Hexamethylbenzene (HMB) that has significant orientation dependent shielding and (2) Adamantane (AD) which has a more symmetric environment. In HMB powder, the asymmetric shielding from each crystallite will also interact with asymmetric shielding from randomly oriented HMB crystallites in the environment. Even in the first shell of nearest-neighbor HMB crystallites, there are infinite numbers of possible combinations of orientations, each with a distinct net shielding effect on the central HMB. Furthermore, as the sample rotates, the shielding effect of the neighboring crystallites changes due to its dependence on relative orientation of static magnetic field. Such Anisotropic Bulk Magnetic Susceptibility (ABMS) broadening effect is significantly smaller than the CSA, but is not averaged by MAS, and manifests as residual broadening of the resonance (*36–41*). This effect is demonstrated in the Figures 1(a) and 1(b) for ^{1}H decoupled ^{13}C 22 kHz MAS NMR of AD and HMB, respectively. The AD resonances had Full-Width-at-Half-Maximum (FWHM) linewidth of 8 Hz, while HMB Methyl resonance had FWHM of 100 Hz. Furthermore, in a physical mixture of HMB and AD, the AD crystallites experience the ABMS broadening from the asymmetric environment of HMB crystallites around it. This effect can be observed in Figure 1(c). In this case the HMB Methyl groups still have a FWHM of about 100 Hz, but the AD peaks broadened to about 80 Hz at FWHM.

Downloaded by CORNELL UNIV on June 19, 2012 | http://pubs.acs.org
Publication Date (Web): October 14, 2011 | doi: 10.1021/bk-2011-1077.ch030

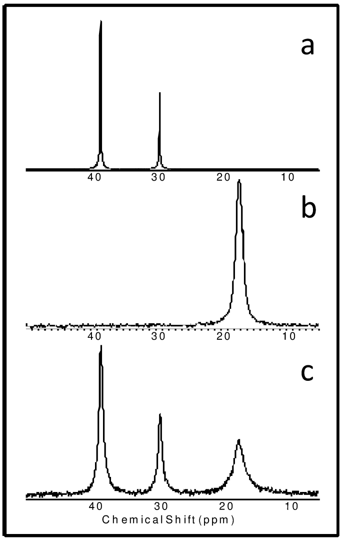

Figure 1. ^{13}C Direct Polarization proton decoupled 22 kHz MAS NMR Spectra of (a) Adamantane powder; (b) Hexamethylbenzene powder (Methyl resonance); (c) Mixture of AD and HMB.

Downloaded by CORNELL UNIV on June 19, 2012 | http://pubs.acs.org
Publication Date (Web): October 14, 2011 | doi: 10.1021/bk-2011-1077.ch030

Spin-diffusion is another source of residual broadening, especially for abundant nuclei such as ^{1}H and ^{19}F whose dipolar broadening has been averaged by MAS in an isotropic sampling (*18*, *42–46*). In Fourier Transform NMR (FT-NMR), a Radio-Frequency pulse generates a coherence of nuclei spins that oscillate in phase at their characteristic Larmor frequency, and are recorded as Free Induction Decay (FID). Fourier transforms of the FID results in the normally reported NMR spectrum. Longer phase coherence translates to narrower peaks in the NMR spectrum. Spin diffusion or adiabatic spin exchange among dipolar coupled nuclei in close proximity scrambles the encoded phase information and hence destroys the coherence, leading to broader NMR resonances. This broadening effect can be reduced by increased motion such that neighboring interacting/coupled nuclei positions fluctuate more rapidly and to a larger degree. The higher the frequency of fluctuations, the lower is the efficiency of spin diffusion, and narrower are the observed ^{1}H NMR resonances (*42–45*). Ultra fast MAS speeds also reduce spin-diffusion and the related spectral broadening (*18*, *42–47*). However, obtaining ^{1}H MAS spectra of non-spin-isolated molecules with resonance linewidths comparable to those found in solution NMR is difficult, except in some favorable cases where ABMS broadening is negligible (*42–45*).

Results and Discussion

^{1}H MAS NMR spectrum of (**I**) acquired at 22 kHz spinning speed and 200 °C temperature is shown in Figure 2. Broad phenyl silane resonances between δ 6.5-8.2 ppm, narrow residual 2-methoxy-1-propanol solvent resonances at δ 1.1/ 3.3/3.4/3.9 ppm, water resonance at δ 5 ppm, and silanol resonance at δ 3 ppm were observed in this MAS NMR spectrum (*vide infra*).

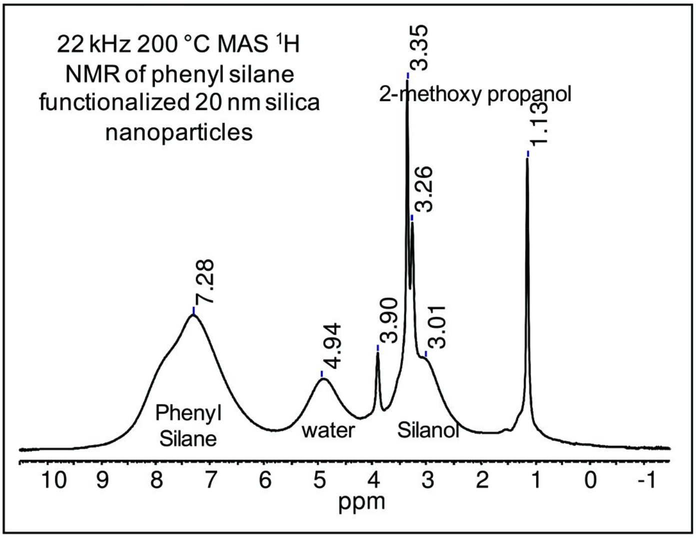

*Figure 2. Proton 22 kHz MAS 200 °C NMR spectrum of (**I**).*

Figure 3 shows a progression of proton NMR spectra at increasing MAS speeds for (**I**). At lower MAS speeds, significant fractions of the intensity of the functionalized phenyl silane and silanol resonances were spread in to its spinning side bands, primarily due to ^{1}H-^{1}H dipolar broadening. Resonances from these molecular species covalently bound to the silica surface were better represented in the center bands of spectrum only at higher spinning speeds. The resonance intensity of the solvent adsorbed on the silica surface did not appear to spread into the spinning side bands at nominal speeds (~ 8 kHz), suggesting motional averaging and mobility of the adsorbed species at room temperature.

Figure 4 shows a progression of spectra of sample (**I**) acquired at increasing temperatures and 22 kHz MAS speed. At ambient temperature (24 °C), the fast spinning proton NMR resonance linewidths of all molecules at the surface whether covalently bound, hydrogen bonded, or adsorbed, were comparable. At increasingly higher temperatures, the resonances of adsorbed 1-methoxy-2-propanol narrowed significantly. In comparison, the line width of phenyl silane resonances changed marginally with increase in temperature.

Downloaded by CORNELL UNIV on June 19, 2012 | http://pubs.acs.org
Publication Date (Web): October 14, 2011 | doi: 10.1021/bk-2011-1077.ch030

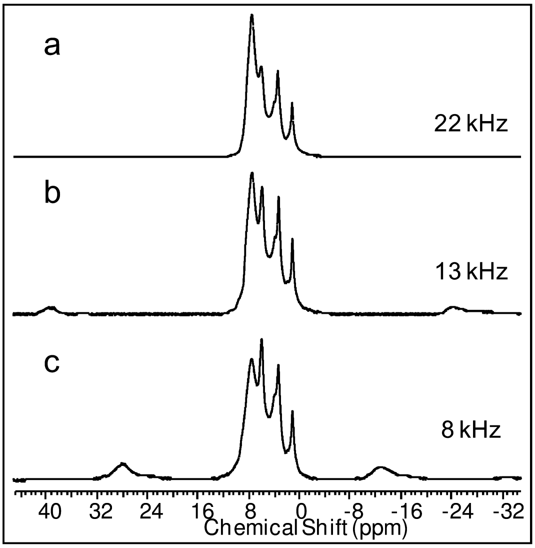

*Figure 3. ^{1}H MAS 24 °C NMR spectra of (**I**) at MAS speeds of (a) 8 kHz, (b) 13 kHz, and (c) 22 kHz. Note absence of spinning side bands from the narrower resonances representing weakly bound species. A broad underlying probe background signal was subjectively removed as part of baseline correction.*

At higher temperatures, weakly attached or adsorbed species are expected to hop sites and reoriented frequently, possibly by being in vapor phase for increasing durations, and resulting in isotropic averaging of its immediate environment and reduction in spin diffusion. In comparison, the strongly attached covalently bound species would have fewer degrees of freedom and minimal change in environment with increasing temperature since the silica particles would not be expected to be mobile. The observed marginal variance in phenyl silane resonance linewidth with

MAS speed and temperature could be due to a combination of ABMS, molecular structure variations, and spin diffusion. However, no further experiments were carried out in order to explore the contributions of each to the broadening.

The resonance around δ 6 ppm in 24 °C spectrum was assigned in other reports to combination of silanol and water (*14*, *18*). In the 100 °C spectrum, part of its intensity appears as a smaller upfield resonance around δ 4.5 ppm. Hydrogen bonded silanol has been reported at this proton chemical shift (*14*). The 150 °C spectrum indicated a more intense resonance shifted upfield to δ 4 ppm. With increasing temperature, this resonance shifted further upfield reaching δ 2.5 ppm in the 225 °C spectrum. The chemical shift of isolated silanol on silica in the limit of no hydrogen bonding has been reported at δ 1.8-2.1 ppm (*14*, *18*). Hence, the upfield shifting resonance can be assigned to unreacted silanol on the silica nanoparticle surface whose silanol-silanol and silanol-water hydrogen bonding reduces with increasing temperature.

Downloaded by CORNELL UNIV on June 19, 2012 | http://pubs.acs.org
Publication Date (Web): October 14, 2011 | doi: 10.1021/bk-2011-1077.ch030

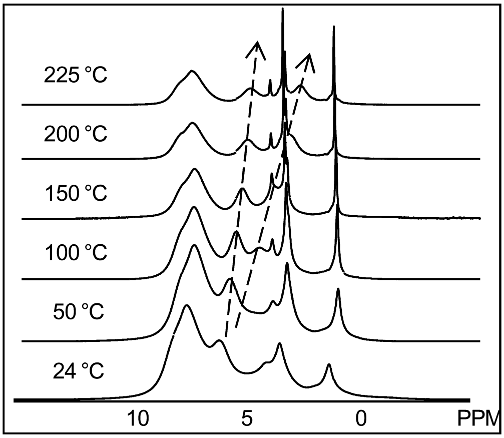

*Figure 4. ^{1}H 22 kHz MAS NMR spectra of (**I**) at increasing temperatures up to 225 °C. Note the shift of resonances marked by arrows.*

The other part of the δ 6 ppm resonance in the 24 °C spectrum shifted up field at a slower rate to δ 4.9 ppm in the 225 °C spectrum. This behavior is consistent with that of water whose hydrogen bonding interactions are reduced. However, the broad width of the water resonance compared to that of the methoxy propanol solvent suggests that the water molecules do not experience motional averaging similar to that done by solvent at increasing temperature. The binding strength of water hydrogen bonded to surface silanols is expected to be stronger compared to the weak surface interactions of adsorbed solvent, but if the water were to hop sites increasingly rapidly or be in vapor phase for longer durations at temperatures above 100 °C, the resulting isotropic environmental averaging would have resulted in narrower resonances with increasing temperature. As explored later, this resonance represents water trapped within cavities of the nanoparticles that is hydrogen bonded with other water molecules and silanols in the cavities.

The identity of the resonance assigned to residual silanols on the particle surfaces was confirmed by additional functionalization reactions.

1,1,1,3,3,3-Hexamethyldisilazane (HMDS) reacts aggressively with silanol groups to form “M” siloxane groups, viz. –O-Si$(CH_3)_3$ (*14*, *15*, *48*). Silanol groups on the surface that could not react with the trimethoxy phenyl silane due to conformational incompatibilities were expected to react with HMDS, even though at least one report suggests that presence of hydrogen bonding among the silanol groups can reduce the reactivity (*14*).

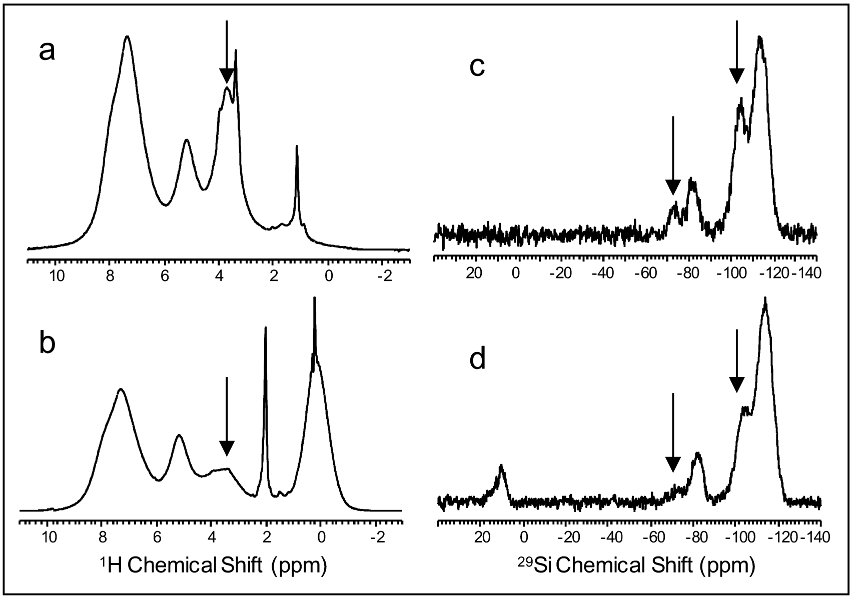

*Figure 5. (a) ^{1}H 22kHz MAS 150 °C NMR of (**I**). Narrow resonances are residual solvent; (b) ^{1}H 22 kHz MAS 150 °C NMR of (**II**). Resonance at δ 2 ppm is residual acetone; (c) ^{29}Si CP-MAS NMR of (**I**); (d) ^{29}Si CP-MAS NMR of (**II**). The arrows mark silanol resonances that react with HMDS.*

In Figure 5, the ^{1}H 22 kHz MAS 150 °C NMR and ^{29}Si CP-MAS 24 °C NMR spectra of (**I**) and (**II**) are compared. Upon HMDS treatment in (**II**) shown in Figure 5(b), compared to (**I**) shown in Figure 5(a), a reduction in intensity of the resonance assigned to silanol (^{1}H δ 3.6 ppm marked with arrow) was detected along with appearance of a broad “M” siloxane group resonance. In Figures 5(a) and 5(b) the narrow resonances represent methoxy propanol in (**I**) and acetone in (**II**), respectively. Comparison of ^{29}Si CP-MAS NMR spectra of (**I**) and (**II**) shown in Figures 5(c) and 5(d), respectively, confirm that the silanols at the silica surface (δ -100 ppm) and on the phenyl silane (δ -72 ppm) , both marked by arrows in the figure, had reacted while “M” groups had formed (δ ~ 10 ppm). Due to the long data acquisition time requirements of the ^{29}Si CP-MAS NMR spectra, no attempt was made to acquire multiple spectra with varying cross-polarization contact times that could enable a quantitative comparison of integral intensities from the various ^{29}Si resonances. The water resonance intensity in proton NMR did not appear to significantly reduce upon HMDS functionalization. The small fraction of silica

Downloaded by CORNELL UNIV on June 19, 2012 | http://pubs.acs.org
Publication Date (Web): October 14, 2011 | doi: 10.1021/bk-2011-1077.ch030

silanols that remained unreacted in (**II**) are most likely in cavities of the silica particles along with water, and are probably not accessible to the solvents used in the functionalization reactions. In Figure 5(b), the width of the methyl siloxane group resonance is likely a result of ABMS broadening since the methyl groups are expected to be freely rotating at this temperature (*38*, *40*).

^{1}H MAS NMR spectra of (**I**) and (**II**) acquired at lower MAS speeds after addition of a small fraction of tetrachloroethane-d2 (TCE-d_2) are shown in Figures 6(a) and 6(b), respectively. Solvent was added in order to increase the mobility of adsorbed species. In Figure 6(b), the width and spinning sideband intensity of the "M" siloxane resonance was comparable to that of the phenyl resonance, and hence is consistent with the "M" groups being covalently attached to the silica surface. The silanol proton resonances on the other hand (marked by arrow in Figure 6), though attached to the silica surface did not indicate similar spinning side-band intensity distribution. We speculate that the combination of broad resonance and lack of spinning side-band intensity, compared to the methyl "M" groups on the surface, may indicate rapid proton hopping and exchange among the silanols at the silica surface.

Downloaded by CORNELL UNIV on June 19, 2012 | http://pubs.acs.org
Publication Date (Web): October 14, 2011 | doi: 10.1021/bk-2011-1077.ch030

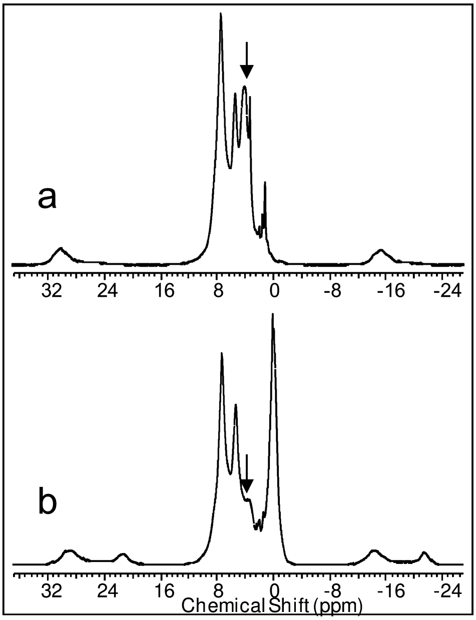

*Figure 6. (a) Proton 9 kHz MAS 100 °C NMR of (**I**) with addition of deuterated tetrachloro ethane (TCE-d_2); (b) Proton 9 kHz MAS 100 °C NMR of (**II**) with addition of TCE-d_2. The arrows mark silanol resonances that do not have spinning side band intensity.*

In order to further probe whether the water resonances observed in the ^{1}H MAS NMR spectra were from the molecules at the surface or in cavities within the nanoparticles, NMR spectra were acquired after dispersion in a solvent. Depending on the size of the particles, type, and coverage of functional groups at the surface, the nanoparticles can form non-precipitating dispersions. Presence of solvable pendant oligomeric chains from the nanoparticles allows the relatively large (on average) 20 nm particles to form clear dispersed solutions (in absence of charged species on its surfaces to prevent aggregations). In its solution, the water on the surface of the nanoparticles was expected to be solvated by the solvent (THF-d_8) and appear as resonance at its characteristic solvated chemical shift (^{1}H δ 2.5 ppm) in the NMR spectra. Water within inaccessible cavities of nanoparticles would not be solvated by the solvent and should appear as resonance around ^{1}H δ ppm. Presence of non-solvated (δ 5.3 ppm) water resonance in the ^{1}H NMR of (**III**) in THF-d_8 shown in Figure 7 confirms that the water observed in the ^{1}H MAS NMR spectra as a resonance around δ 5 ppm is trapped within cavities of the nano-particles and is not accessible to the solvent. The ^{1}H δ 1.7 and 3.6 ppm are residual THF-d_8 solvent resonances while the ^{1}H δ 2.6 ppm resonance is water solvated by THF. The resonances between δ 3.3-3.6 ppm represent diglyme that was present on nanoparticle surface.

Downloaded by CORNELL UNIV on June 19, 2012 | http://pubs.acs.org
Publication Date (Web): October 14, 2011 | doi: 10.1021/bk-2011-1077.ch030

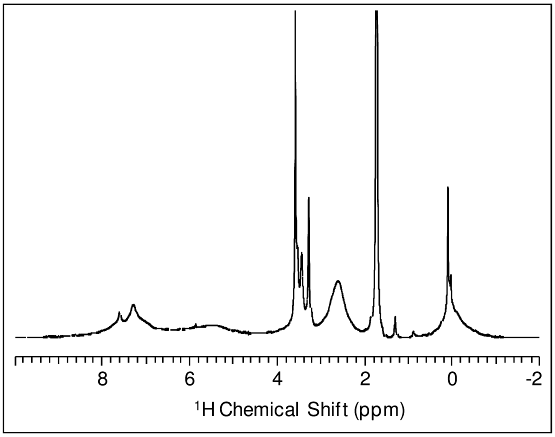

*Figure 7. ^{1}H NMR of (**III**) in THF-d_8 solution.*

In Figure 7, the phenyl silane and methyl “M” siloxane resonances have varying linewidths – from the two split narrow ones to the broad underlying resonance. As mentioned earlier, long molecular chain extensions from the surface, e.g. self-condensed silanes, are solvated and mobile leading to narrower resonances. These pendant chain extensions can also be identified in their ^{1}H MAS NMR spectra at high temperature and fast MAS as narrower resonances, as shown in Figure 8(a). Here again, the narrow resonances between δ 3.3-3.6 riding on top of a broad silanol resonance are from residual diglyme. Other researchers have also used double-quantum ^{1}H MAS NMR techniques to probe the surface interactions and pendant oligomers (*49*).

Another method to distinguish the mobile pendant phenyl silane groups from those closer to the surface is by MAS ^{1}H NMR analysis of the functionalized nanoparticles as a “slurry”. The slurry can be formed by adding only a small fraction of solvent and mixing well. The solvent molecules solvate the pendant

Downloaded by CORNELL UNIV on June 19, 2012 | http://pubs.acs.org
Publication Date (Web): October 14, 2011 | doi: 10.1021/bk-2011-1077.ch030

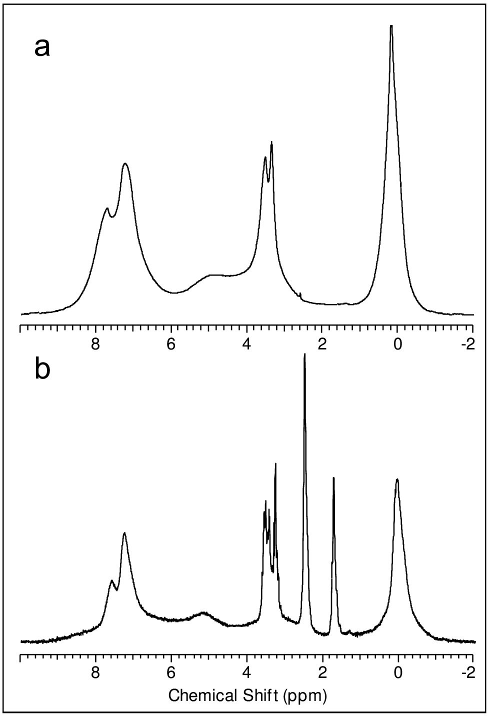

*Figure 8. (a) ^{1}H 17 kHz MAS 150 °C NMR spectrum of (**III**) as dried powder. (b) ^{1}H 8.7 kHz MAS 50 °C NMR spectrum of (**III**) as slurry in THF-d$_8$.*

and adsorbed components more than those covalently bound to the surface, mimicking the influence of high temperature. As a result, similar mobility based differentiation can be obtained at a lower temperature and lower MAS speeds. Figure 8(b) shows the ^{1}H 8.7 kHz MAS NMR of the same sample as 8(a), but in a slurry in THF-d$_8$ at 50 °C. Here again, the narrow phenyl silane and methyl siloxane resonances from more mobile fractions are riding on top of broad resonances representing rigid groups on the silica surface. The narrow 2.5 ppm is solvated water in THF while the 5 ppm resonance is water in inaccessible cavities of the nanoparticles. The rest of the narrow resonances represent THF and diglyme. ^{1}H MAS spectra in Figure 6 were also acquired as a slurry and indicated presence of non-solvated water resonances. It may be noted that due to the lower MAS speeds used with the slurry, the relative intensity of the rigid components in the central band is often lower than expected.

Figures 7 and 8 demonstrate that depending on the solubility of the functionalized nanoparticles, a number of methods can be used to obtain information about binding strengths of the various species at the surface.

Conclusion

Single pulse high temperature ^{1}H MAS NMR was used to characterize functionalized nanoparticles. The high temperature helped accentuate the difference in resonance linewidths of the various species based on mobility and surface binding strength. In these nanoparticles based on colloidal silica, water molecules trapped in inaccessible cavities were identified. Gradual reduction of hydrogen bonding among silanol groups on silica surface with increasing temperature and rapid exchange of the silanol protons was inferred from the NMR data. Oligomeric pendant chains attached to the nanoparticles were readily distinguished from those covalently attached directly to the surface. For nanoparticles that are soluble in an appropriate solvent, a number of alternative methods can also be used.

Acknowledgments

Strong support from Dr. Dale Perry and Dr. Rebecca Dittmar at 3M enabled a significant portion of this work.

Downloaded by CORNELL UNIV on June 19, 2012 | http://pubs.acs.org
Publication Date (Web): October 14, 2011 | doi: 10.1021/bk-2011-1077.ch030

References

1. Giri, S.; Trewyn, B. G.; Lin, V. S. Y. *Nanomedicine* **2007**, *2*, 99–111.
2. Du, M.; Zheng, Y. *Polym. Compos.* **2007**, *28*, 198–207.
3. Trewyn, B. G.; Slowing, I. I.; Giri, S.; Chen, H.-T.; Lin, V. S.-Y. *Acc. Chem. Res.* **2007**, *40*, 846–853.
4. Schulz, H.; Pratsinis, S. E.; Rüegger, H.; Zimmermann, J.; Klapdohr, S.; Salz, U. *Colloids Surf., A* **2008**, *315*, 79–88.
5. Roy, I.; Ohulchanskyy, T. Y.; Bharali, D. J.; Pudavar, H. E.; Mistretta, R. A.; Kaur, N.; Prasad, P. N. *Proc. Natl. Acad. Sci. U.S.A.* **2005**, *102*, 279–284.
6. Blute, I.; Pugh, R. J.; van de Pas, J.; Callaghan, I. *J. Colloid Interface Sci.* **2007**, *313*, 645–655.
7. Ahn, S. H.; Kim, S. H.; Lee, S. G. *J. Appl. Poly. Sci.* **2004**, *94*, 812–818.
8. Hong, R. Y.; Fu, H. P.; Zhang, Y. J.; Liu, L.; Wang, J.; Li, H. Z.; Zheng, Y. *J. Appl. Poly. Sci.* **2007**, *105*, 2176–2184.
9. Xu, X.; Li, B.; Lu, H.; Zhang, Z.; Wang, H. *J. Appl. Poly. Sci.* **2008**, *107*, 2007–2014.
10. Xu, X.; Li, B.; Lu, H.; Zhang, Z.; Wang, H. *Appl. Surface Sci.* **2007**, *254*, 1456–1462.
11. Giraldo, L. F.; Echeverri, M.; López, B. L. *Macromol. Symp.* **2007**, *258*, 119–128.
12. Song, R.; Yang, D.; He, L. *J. Mater. Sci.* **2007**, *42*, 8408–8417.
13. Almeida, R. M.; Pantano, C. G. *J. Appl. Phys.* **1990**, *68*, 4225–4232.
14. Haukka, S.; Root, A. *J. Phys. Chem.* **1994**, *98*, 1695–1703.
15. Kytokivi, A.; Haukka, S. *J. Phys. Chem. B* **1997**, *101*, 10365–10372.
16. Bruni, S.; Cariati, F.; Casu, M.; Lai, A; Musinu, A.; Piccaluga, G.; Solinas, S. *Nanostruct. Mater.* **1999**, *11*, 573–586.
17. Jana, N. R.; Earhart, C.; Ying, J. Y. *Chem. Mater.* **2007**, *19*, 5074–5082.
18. Trebosc, J; Wiench, J. W.; Huh, S; Lin, V. S. Y.; Pruski, M. *J. Am. Chem. Soc.* **2005**, *127*, 3057–3068.
19. Brus, J.; Dybal, J. *Polymer* **2000**, *41*, 5269–5282.

20. Hartmeyer, G.; Marichal, C.; Lebeau, B.; Rigolet, S.; Caullet, P.; Hernandez, J. *J. Phys. Chem. C* **2007**, *111*, 9066–9071.
21. Kumar, R.; Chen, H. T.; Escoto, J. L. V.; Lin, V. S. Y.; Pruski, M. *Chem. Mater.* **2006**, *18*, 4319–4327.
22. Bronnimann, C. E.; Ziegler, R. C.; Maciel, G. E. *J. Am. Chem. Soc.* **1988**, *110*, 2023–2026.
23. Liu, C. C.; Maciel, G. E. *J. Am. Chem. Soc.* **1996**, *118*, 5103–5119.
24. Alam, T. M.; Fan, H. *Macromol. Chem. Phys.* **2003**, *204*, 2023–2030.
25. d’Espinose de la Caillerie, J.-B.; Aimeur, M. R.; El Kortobi, Y.; Legrand, A. P. *J. Colloid Interface Sci.* **1997**, *194*, 434–439.
26. Ek, S.; Root, A.; Peussa, M.; Niinisto, L. *Thermochim. Acta* **2001**, *379*, 201–212.
27. Turov, V. V.; Leboda, R. *Adv. Colloid Interface Sci.* **1999**, *79*, 173–211.
28. Christiansen, S. C.; Zhao, D.; Janicke, M. T.; Landry, C. C.; Stucky, G. D.; Chmelka, B. F. *J. Am. Chem. Soc.* **2001**, *123*, 4519–4529.
29. Bronnimann, C. E.; Chuang, I.-S.; Hawkins, B. L.; Maciel, G. E. *J. Am. Chem. Soc.* **1987**, *109*, 1562–1564.
30. Shenderovich, I. G.; Buntkowsky, G.; Schreiber, A.; Gedat, E.; Sharif, S.; Albrecht, J.; Golubev, N. S.; Findenegg, G. H.; Limbach, H.-H. *J. Phys. Chem. B* **2003**, *107*, 11924–11939.
31. Goetz, D. P.; Hine, A. M.; Schultz, W. J.; Thompson, W. L. Patent U.S. 5,648,407.
32. Becker, E. D. *High Resolution NMR: Theory and Chemical Applications*, 2nd ed.; Academic Press: New York, 1980.
33. Harris, R. K. *Nuclear Magnetic Resonance Spectroscopy*; Pittman: London, 1983.
34. Sternhell, S.; Kalman, J. R. *Organic Structures from Spectra*; John Wiley and Sons: New York, 1986.
35. Sanders, J. K. M.; Hunter, B. K. *Modern NMR Spectroscopy: A Guide for Chemists*, 2nd ed.; Oxford University Press: New York, 1993.
36. VanderHart, D. L.; Earl, W. L.; Garroway, A. N. *J. Magn. Reson.* **1981**, *44*, 361–401.
37. Thakur, K. A. M.; Kean, R. T.; Zupfer, J. M.; Buehler, N. U. *Macromolecules* **1996**, *29*, 8844–8851.
38. Elbayed, K.; Bourdonneau, M.; Furrer, J.; Richert, T.; Raya, J.; Hirschinger, J.; Piotto, M. *J. Magn. Reson.* **1999**, *136*, 127–129.
39. Alla, M.; Lippmaa, E. *Chem. Phys. Lett.* **1982**, *87*, 30–33.
40. Zorin, V. E.; Brown, S. P.; Hodgkinson, P. *J. Chem. Phys.* **2006**, *125*, 144508.
41. Schwerk, U.; Michel, D.; Pruski, M. *J. Magn. Reson., Ser. A* **1996**, *119*, 157–164.
42. Thakur, K. A. M. *Polym. News* **2002**, *27*, 237–242.
43. Thakur, K. A. *NMR Spectroscopy of Polymers in Solution and in the Solid-State*; Cheng, H. N., English, A. D., Eds.; ACS Symposium Series 834; American Chemical Society: Washington DC, 2002; Chapter 3, 32-42.
44. Thakur, K. A. M.; Newmark, R. A.; Kuehn, N. K.; Gregar, T. Q. *Macromecules* **2003**, *36*, 719–723.

Downloaded by CORNELL UNIV on June 19, 2012 | http://pubs.acs.org
Publication Date (Web): October 14, 2011 | doi: 10.1021/bk-2011-1077.ch030

45. Thakur, K. A. *Presentation at 221st ACS National Meeting*, San Diego, CA, April 2001; Thakur, K.A. *Polym. Prepr.* **2001**, *42*, 57−58.
46. Ando, S.; Harris, R. K.; Scheler, U. Fluorine-19 NMR of Solids Containing Both Fluorine and Hydrogen. In *Encyclopedia of Nuclear Magnetic Resonance*; Grant, D. M., Harris, R. K., Ed.; John Wiley & Sons, Ltd: Chichester, 2002; Volume 9, 531−550.
47. Isbester, P. K.; Brandt, J. L.; Kestner, T. A.; Munson, E. J. *Macromolecules* **1998**, *31*, 8192–8200.
48. Slavov, S. V.; Sanger, A. R.; Chuang, K. T. *J. Phys. Chem. B* **2000**, *104*, 983–989.
49. Saalwachter, K; Krause, M.; Wolfram Gronski, W. *Chem. Mater.* **2004**, *16*, 4071–4079.

Downloaded by CORNELL UNIV on June 19, 2012 | http://pubs.acs.org
Publication Date (Web): October 14, 2011 | doi: 10.1021/bk-2011-1077.ch030

Chapter 31

Dependence of the Amount of Xe Sorption on the ^{129}Xe NMR Chemical Shift in Glassy Polymers

H. Yoshimizu*

Graduate School of Engineering, Nagoya Institute of Technology,
Gokiso-cho, Showa-ku, Nagoya 466-8555, Japan
***E-mail: yoshimizu.hiroaki@nitech.ac.jp**

Microvoids in glassy polymers are considered to be correlated with unrelaxed volume (so-called “excess free volume”). In this article, the microvoids were investigated by Xe sorption and ^{129}Xe NMR measurements. The Xe sorption isotherms of glassy polymers were successfully interpreted by the dual-mode sorption model composed of Henry and Langmuir sorption sites. ^{129}Xe NMR chemical shifts of ^{129}Xe in glassy polymers showed a non-linear low-field shift with increasing amount of Xe sorption because of fast exchange of Xe atoms between the two sites. From the ^{129}Xe NMR chemical shift, we could determine the mean size of the microvoids. In several polymers, this methodology was examined from three perspectives of free volume, viz., thermal expansion, miscibility with reduced free volume in a polymer blend, and specific crystalline structure. From these findings, ^{129}Xe NMR spectroscopy is shown to be a powerful technique to determine the mean size of microvoids in glassy polymers.

Introduction

A complete understanding of a solid amorphous polymer at molecular level is very difficult because of the complex static, dynamic, and steric structures present. Yet, it is important to understand the detailed structures of glassy polymers, such as the amount, the size and the shape of inter-spaces between polymer chains, and connectivity among them. These are not only important from an academic point

In NMR Spectroscopy of Polymers: Innovative Strategies for Complex Macromolecules; Cheng, H., et al.;
ACS Symposium Series; American Chemical Society: Washington, DC, 2011.

of view but also relevant to many applications. For example, the design and the development of gas barriers or polymeric separation membranes both need the information on the qualities and the quantities of the inter-space.

It is often thought that computational chemistry (such as MD simulations) (*1*) and positron annihilation lifetime spectroscopy (*2*) are good approaches for the detailed characterization of the polymeric inter-space. In this article, another method is described, which should be complementary to the above approaches. Xenon is an inert gas and some of its isotopes are NMR active. Through the use of Xe as a gaseous penetrant and an NMR probe, the micro-interspaces within a polymeric material can be characterized from the observed NMR signals. Thus, it is demonstrated here that ^{129}Xe NMR spectroscopy is a powerful technique for the characterization of glassy polymers.

Background of ^{129}Xe NMR

^{129}Xe is an isotope of xenon with spin number $I = 1/2$ and a natural abundance of 26.4 %. The relative sensitivity for NMR observation of ^{129}Xe is larger than that of ^{13}C; thus, ^{129}Xe NMR of Xe gas at relatively low pressures can be easily observed with good sensitivity. The gyromagnetic ratio of ^{129}Xe is about 1.1 times larger than that of ^{13}C, indicating that the resonant frequency for ^{129}Xe is close to that for ^{13}C, i.e., easily tunable using standard multinuclear NMR probes in commercial spectrometers. In addition, Xe atom is slightly larger than methane, so it is a suitable probe for the sorption environment experienced by typical gases in polymer membranes. The most attractive aspect of ^{129}Xe NMR is the sensitivity of the shielding to the sorption environment. The shift range of sorbed xenon relative to the resonance of the free gas is well over 200 ppm. Since the Xe atom has a very large polarizability, it is expected that ^{129}Xe NMR signal is sensitive to its environments. Indeed, the induced ^{129}Xe NMR chemical shifts are strongly correlated with the size and the nature of micro-pores, because the interactions with the host system can disturb the Xe electron density. In the case of microporous materials like zeolites, ^{129}Xe NMR chemical shift (δ) of adsorbed ^{129}Xe obeys the following equation (*3–7*);

$$\delta = \delta_{(S)} + \delta_{(Xe)} + \delta_{(E)} + \delta_{(SAS)} + \delta_{(M)} \qquad [1]$$

where $\delta_{(S)}$ is due to the interactions between Xe and porous inner walls; $\delta_{(Xe)}$ corresponds to the interactions among Xe atoms; $\delta_{(E)}$, $\delta_{(SAS)}$, and $\delta_{(M)}$ are the contribution of electric field created by multivalent cations, the interaction of Xe with the strong adsorption site, and the contribution of the magnetic field created by the paramagnetic compensation cations, respectively. Figure 1 shows schematically the relationships between δ and density of Xe. The $\delta_{(E)}$, $\delta_{(SAS)}$, and $\delta_{(M)}$ terms can be ignored for glassy polymers because most of them have no strong charge groups. Therefore, ^{129}Xe NMR chemical shifts of ^{129}Xe sorbed in glassy polymers can be interpreted by only two terms: $\delta_{(S)}$ and $\delta_{(Xe)}$. As shown in Figure 1, for common polymers the observed δ increases linearly with Xe density. The value of $\delta_{(S)}$ can be experimentally determined through linear extrapolation of the data obtained at various pressures of Xe. For zeolites, there are many

In NMR Spectroscopy of Polymers: Innovative Strategies for Complex Macromolecules; Cheng, H., et al.;
ACS Symposium Series; American Chemical Society: Washington, DC, 2011.

reports that $\delta_{(S)}$ values of adsorbed ^{129}Xe are strongly correlated with the sizes of micro-cage (*3–10*). Similarly it is possible to characterize the mean sizes of micro-interspaces between polymer chains using $\delta_{(S)}$ values.

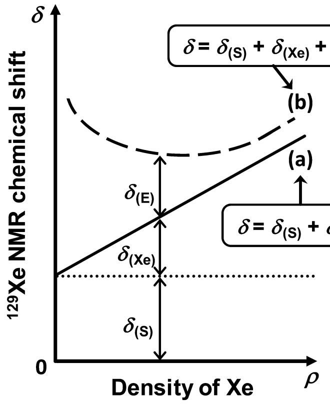
δ
$\delta = \delta_{(S)} + \delta_{(Xe)} + \delta_{(E)}$
(b)
(a)
$\delta_{(E)}$
$\delta = \delta_{(S)} + \delta_{(Xe)}$
$\delta_{(Xe)}$
$\delta_{(S)}$
^{129}Xe NMR chemical shift
0
Density of Xe
ρ

Figure 1. Schematic representation of the relationships between ^{129}Xe NMR chemical shift and density of Xe.

According to Fraissard *et.al.*, when the NMR chemical shift of ^{129}Xe in zeolites is only determined by the collisions with the walls, where disturbances due to paramagnetic species or electric fields ($\delta_{(E)}$, $\delta_{(SAS)}$, or $\delta_{(M)}$) are absent or negligible, the mean free path λ is linked to $\delta_{(S)}$ in equation [1]. Hence $\delta_{(S)}$ can be related to the mean size of the micro cage by the following equation (*3*, *5*).

$$\delta_{(S)} = 243 \times \frac{2.054}{2.054 + \lambda} \qquad [2]$$

λ is a function of both the shape and dimension of micro cage. In the case of a sphere, the following relationship has been derived,

$$\lambda = \frac{(D_S - D_{Xe})}{2} \qquad [3]$$

where D_S is the diameter of the sphere and D_{Xe} is the diameter of Xe = 4.4 Å. When the shape of the cage is cylindrical, the diameter of crosssection, λ is related to D_C as follows,

$$\lambda = D_C - D_{Xe} \qquad [4]$$

Usually, the average shape of micro inter-spaces in the glassy polymer is assumed to be spherical because of random coil conformations. However, in the crystalline structures of helical rigid rod chains, the shape of inter space in chain bundles should be closer to cylindrical.

It is of interest that some researchers have published many articles on polymeric systems, but they have rarely paid any attention to the density dependence of ^{129}Xe NMR chemical shift (*11–16*). In order to obtain $\delta_{(S)}$ which reflects the micropore size in glassy polymer, it is important to evaluate density dependence of Xe chemical shift together with the sorptive properties of Xe. In view of the considerations mentioned above, we have tried to investigate the relationship between the ^{129}Xe NMR chemical shift and Xe sorptive properties for glassy polymers in this work.

Gas Sorption Properties of Glassy Polymers

In general, gas sorption of glassy polymers can be rationalized by the dual-mode sorption model (*17–20*), which is represented by the following equation,

$$C = C_D + C_H = k_D p + \frac{C_H' bp}{1 + bp} \qquad [5]$$

where C is the equilibrium sorption amount at pressure p; C was defined as the molar concentration of a gas per unit volume in the polymer, usually expressed in unit of cm^3 (STP) / cm$^3_{\text{polym}}$, which corresponds to the density of the gas in the polymer. C_D is the concentration due to Henry's law contribution, C_H is the concentration due to Langmuir mode contribution, k_D is the Henry's law coefficient, b is the affinity constant of the Langmuir site, and C_H' is the hole saturation constant in the Langmuir sorption mode. The value of C_H' generally corresponds to the unrelaxed volume (so-called "excess free volume") of glassy polymer as mentioned below. Figure 2 shows a schematic representation of specific volume–temperature (*V–T)* curve of a typical amorphous polymer together with its occupied volume. In the temperature region for the glassy state, the apparent slope of *V–T* curve is almost similar as the curve of occupied volume. Thus, the volume of non-equilibrium state (i.e., the unrelaxed volume) linearly increases with decreasing temperature. The polymer free volume has also been discussed by other researchers from the viewpoints of gas sorption properties (*19–23*). The mechanisms of gas sorption below and above the glass transition temperature, T_g, are different, reflecting the differences in physical structures and thermodynamic states, viz., the non-equilibrium nature of the glassy state and the equilibrium liquid–like nature of the rubbery state. In general, the sorption isotherms for gases in glassy polymers are interpreted in terms of a dual–mode sorption model, based on the assumption that the gas is sorbed both by Henry and Langmuir sorption mechanisms. The former sorption behavior is similar to the gas sorption in rubbery polymers (*20*), whereas in the latter mechanism, the gas sorbs into the microvoids that exist in the glassy polymer and gets saturated at high pressures.

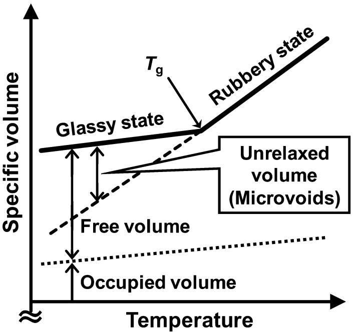

Figure 2. Schematic representation of specific volume–temperature (V–T) curve of typical amorphous polymer together with its occupied volume.

Therefore, it is possible to understand the behavior of unrelaxed volume by examining the Langmuir sorption mechanism. The presence of unrelaxed volume in glassy polymers plays an important role in the gas sorption as microvoids. As shown in Figure 2, the unrelaxed volume depends on the difference between measurement temperature and T_g. The aim of utilization of ^{129}Xe NMR for glassy polymer is to clarify the relationship between the unrelaxed volume and microvoid size. As another technique, positron annihilation lifetime spectroscopy (PALS) is also useful in investigating size and distribution of free volume in polymers (*2*, *24–27*). PALS can estimate the micro-space whose size is larger than that determined by ^{129}Xe NMR, because positron is smaller than Xe atom. However, PALS technique probably cannot estimate the microvoids in glassy polymers independently, due to the fact that PALS data rely on the very short lifetime of *o*-positronium and are not affected by molecular motions. This means PALS cannot distinguish between rubbery and glassy states.

Figure 3 shows Xe sorption isotherms of polystyrene (PS), polycarbonate (PC), tetramethyl polycarbonate (TMPC), and polyphenyleneoxide (PPO) at 25 °C (*28*, *29*). All sorption isotherms obtained here are concave toward the pressure axis, which is commonly observed in glassy polymers. The solid curves show the results of curve fitting by a non-linear least-square method based on equation [5]. These isotherms can be explained successfully on the basis of the dual-mode sorption model. The calculated parameters are summarized in Table I. The value of C_H' is followed by the fact that the orders of C_H' and temperature difference between T_g and observing temperatures show a similar trend with one another (see Table I). C_H' of PS is the minimum of all samples. It indicates that the total amount of microvoid in PS is the smallest.

In NMR Spectroscopy of Polymers: Innovative Strategies for Complex Macromolecules; Cheng, H., et al.;
ACS Symposium Series; American Chemical Society: Washington, DC, 2011.

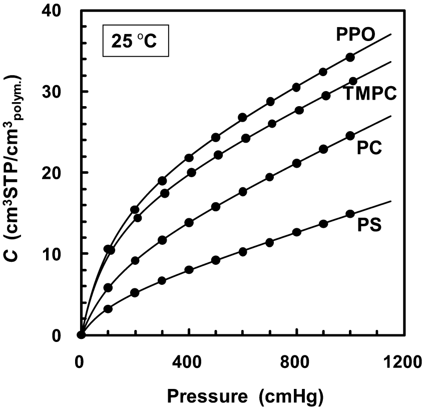

Figure 3. Xe sorption isotherms of polystyrene (PS), polycarbonate (PC), tetramethyl polycarbonate (TMPC), and polyphenyleneoxide (PPO) at 25 °C.

Table I. Dual-mode sorption parameters of Xe and glass transition temperature of selected glassy polymers

Sample	$k_D \times 10^2$	C_H'	$b \times 10^3$	T_g*
PS	1.1	4.8	8.8	98
PC	1.8	13.3	6.0	160
TMPC	1.5	17.4	6.0	196
PPO	1.7	20.6	7.8	216

k_D : [cm^3 (STP)/cm$^3_{polym.}$ cmHg], C_H': [cm^3 (STP)/cm$^3_{polym.}$], b : [1/cmHg], T_g : [°C]. * T_g was determined by DSC.

Determination of Microvoid Size through ^{129}Xe NMR

^{129}Xe NMR spectrum obtained for the PS film in a NMR sample tube with thick wall at 25 °C and 760 cmHg of Xe (with natural abundance of ^{129}Xe) by single pulse method is shown in Figure 4 as an example. Internal pressure can be determined from the Xe sorption amount and weight change of the NMR sample tube, and/or the chemical shift value of gaseous ^{129}Xe signal. All ^{129}Xe NMR chemical shifts are referenced to an external standard of zero-pressure of Xe gas. The peak width of the ^{129}Xe in PS is broad compared with that of gaseous xenon, showing considerably restricted motion of Xe atom in PS. It may be emphasized that the peak shape of ^{129}Xe in PS is almost Gaussian, completely symmetric, although two sorption sites in PS are clearly confirmed from Xe sorption isotherm measurements as mentioned above. Similar results are obtained for the other samples and pressure conditions. In view of this interpretation, the pressure dependence of ^{129}Xe NMR chemical shift will be described below.

In NMR Spectroscopy of Polymers: Innovative Strategies for Complex Macromolecules; Cheng, H., et al.;
ACS Symposium Series; American Chemical Society: Washington, DC, 2011.

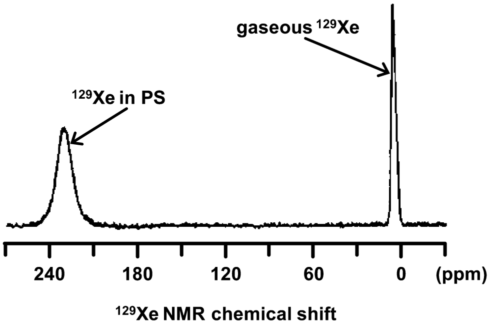

Figure 4. ^{129}Xe NMR spectrum obtained for the PS film in a NMR sample tube with thick wall at 25 °C and 760 cmHg of Xe (with natural abundance of ^{129}Xe) by single pulse method at 110 MHz.

Figure 5 shows the plots of ^{129}Xe NMR chemical shift against total Xe sorption amounts of C for four glassy polymers (*28*, *29*). These downfield shifts with increasing C are caused by increasing of interactions among Xe atoms, i.e., the contribution of term $\delta_{(Xe)}$ in equation [1]. The symmetric peak at about 230 ppm as shown in Figure 4 indicates that the Xe atoms that dissolve in glassy polymer diffuse quickly, and exchange rapidly between the Henry and Langmuir sites in the time scale of NMR observation. When contributions of $\delta_{(E)}$, $\delta_{(SAS)}$, and $\delta_{(M)}$ in equation [1] can be ignored, the ^{129}Xe NMR chemical shift shows linear low-field shift with Xe density. Actually, the chemical shift of gaseous ^{129}Xe shifts to low-field linearly with increasing pressure. Thus, it is expected that ^{129}Xe NMR chemical shifts in the glassy polymers shift linearly with total Xe sorption amounts (C) because Xe density can correspond to C. As shown in Figure 5, however, the shift is non-linear. This finding indicates that the density of Xe in glassy polymer is not proportional to C. Since the value of C for glassy polymer is composed of C_D and C_H (see equation [5]), which is different from the case of gaseous Xe, it is necessary to evaluate the dependence of ^{129}Xe chemical shifts in glassy polymers on C_D and C_H.

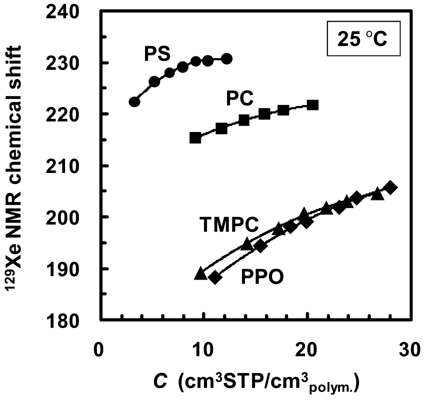

Figure 5. Plots of ^{129}Xe NMR chemical shift against total Xe sorption amounts (C) for four glassy polymers.

Assuming fast exchange of Xe atoms between Henry and Langmuir sites, the pressure-dependence of NMR chemical shifts for each site can be described via C_D and C_H at each pressure and calculated using the dual-mode sorption parameters. Thus, the observed NMR chemical shift, $\delta_{obs.}$ is expressed in the following equations,

$$\delta_{obs.} = \phi_D \delta_D + \phi_H \delta_H \qquad [6]$$

$$\phi_D + \phi_H = 1 \qquad [7]$$

where φ_D and φ_H are fractional concentrations of Xe for the Henry and Langmuir sites at each pressure, and δ_D and δ_D are NMR chemical shifts for the Henry and Langmuir sites, respectively. In subsequent equations, subscripts D and H correspond to the Henry and Langmuir sites, respectively. From the equation [1], NMR chemical shift for each site is explained by following equations,

$$\delta_D = \delta_{(Xe)D} + \delta_{(S)D} = A_D C_D + \delta_{(S)D} \qquad [8]$$

$$\delta_H = \delta_{(Xe)H} + \delta_{(S)H} = A_H C_H + \delta_{(S)H} \qquad [9]$$

where A_D and A_H are constants proportional to Xe concentration for each site, and $\delta_{(S)D,H}$ and $\delta_{(Xe)D,H}$ are NMR chemical shifts due to the interactions among Xe and porous inner walls, respectively. Using these equations, Xe concentration dependence of NMR chemical shifts for the Henry and the Langmuir sites can be calculated. Figure 6 illustrates the result for PS, and it is noted that the unit of the x axis is the pressure (cm Hg).

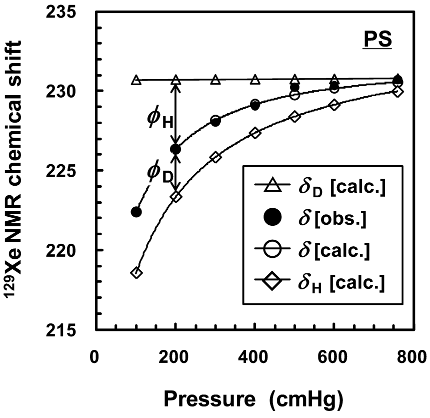

Figure 6. The plots of ^{129}Xe NMR chemical shift against pressure of Xe for PS at 25 °C.

Table II. ^{129}Xe NMR parameters of glassy polymers

Sample	A_D	$\delta_{(S)D}$	A_H	$\delta_{(S)H}$
PS	0.012	230.8	5.82	205.4
PC	0.18	225.0	1.59	200.7
TMPC	0.18	210.5	1.88	169.7
PPO	0.67	210.1	1.90	166.4

$A_{D,H}$: [ppm cm$^3_{polym.}$/cm^3 (STP)], $\delta_{(S)D,H}$: [ppm].

δ_D is shifted more downfield than $\delta_{obs.}$, and δ_H is more upfield. The parameters for each polymer are summarized in Table II. It can be seen from Table II that A_H is larger than A_D by about one order of magnitude for each polymer. It indicates that Xe density dependence of the ^{129}Xe NMR chemical shift of ^{129}Xe in the Langmuir site is larger than that in the Henry site. In practice, for rubbery polymer that contains “only” the Henry site, ^{129}Xe NMR chemical shift of sorbed ^{129}Xe rarely reveals Xe density dependence. Moreover, the proportion of Xe in the Langmuir site is larger than that in the Henry site at low-pressure region, while this is opposite at high-pressure region. From these facts, ^{129}Xe NMR chemical shift of ^{129}Xe sorbed in glassy polymer apparently shows non-linear low-field shift against total sorption amount of C. Additionally A_H corresponds to total amount of microvoids in the glassy polymer; it becomes small with increasing amount of microvoids. For example, the A_H value for PS is larger than that for PPO.

It may be said that the NMR chemical shift extrapolated to $C_H = 0$, i.e., $\delta_{(S)H}$, reflects the mean size of microvoids in the glassy polymer. The value of $\delta_{(S)H}$ can be substituted in equation [2] and then the diameter of spherical space, D_S can be calculated. The results are summarized in Table III together with literature data of PALS (*25*, *26*). It appears that the spherical spaces correlated to microvoids in glassy polymers are on the order of angstroms. The order of mean size of microvoid in four glassy polymers, PPO > TMPC > PC > PS, is consistent with that of T_g and C_H' for Xe as shown in Table I. In addition, D_S value is close to the corresponding PALS data, suggesting that the ^{129}Xe NMR spectroscopy is a good method for characterizing microvoids in glassy polymers.

Table III. Mean size of microvoid and/or micro-pore in glassy polymers determined by ^{129}Xe NMR ($D_{S,\ NMR}$) and PALS ($D_{S,\ PALS}$)

Sample	$D_{S,\ NMR}$ / [Å]	$D_{S,\ PALS}$ / [Å]*
PS	5.15	5.76
PC	5.27	5.88
TMPC	6.17	6.40
PPO	6.29	6.56

* from references (*25*) and (*26*).

Reliability of Microvoid Size Determination by ^{129}Xe NMR

This section examines the reliability of microvoid size determination by using the ^{129}Xe NMR chemical shift from three perspectives of free volume, viz., thermal expansion (*30*), miscibility with reduced free volume in polymer blends (*31*, *32*), and specific crystalline structures (*33*).

First, we show the Xe sorption properties and ^{129}Xe NMR spectra of PPO measured at various temperatures. All the sorption isotherms obtained in temperature range of –60 to +80 °C can be analyzed based on the dual–mode sorption model. The Langmuir saturation constant C_H', which corresponds to unrelaxed volume, is then determined. C_H' increases linearly with decreasing temperature. When this straight line is extrapolated to $C_H' = 0$, the temperature obtained is almost the same as T_g of PPO as shown in Figure 7(a). Yet, the mean diameter of the microvoids (assuming spheres) of PPO which are determined from the analyses of the pressure-dependence ^{129}Xe NMR chemical shift of the ^{129}Xe in PPO, also increases with decreasing temperature. The straight line drawn in Figure 7(b) is a rough estimation because only a few data points are available, but this suggests that the extrapolated value at T_g is close to 4.4 Å, which is the diameter of Xe atom. These findings support the interpretation of unrelaxed volume as shown above in Figure 2.

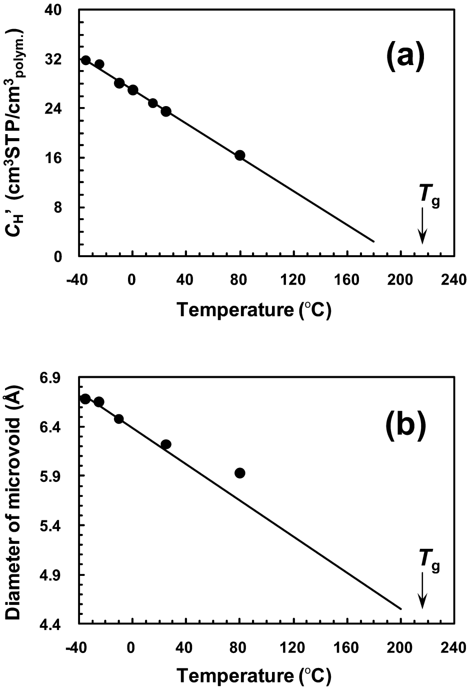

Figure 7. Langmuir saturation constant of Xe (C_H') (a) and the mean diameter of individual microvoids (b) of PPO plotted against temperature.

The next topic is the relationship between the variations of microvoids and gas sorption properties for miscible PPO / PS blend in the glassy state (*31*, *32*).

This has been investigated by Xe sorption and ^{129}Xe NMR measurements. The composition dependence of the specific volume (V_{sp}) has been determined from the density measurement. It has been shown that V_{sp} values of the blends are lower than those calculated by the simple additive rule. Thus, a volume contraction has taken place when blending PPO and PS, and this may be attributed to an attractive interaction between the methyl groups of PPO and the phenyl rings of PS (*34*). Xe sorption isotherms of this blend system can be interpreted successfully on the basis of the dual-mode sorption model, indicating that both polymers are in the glassy state. In Figure 8(a), C_H' is plotted against the volume fraction of PPO in the blend. It appears that C_H' is smaller than that expected from a simple additive rule drawn as dashed line, whereas k_D and b follow additive rules. The data indicate that the decrease in the total amount of microvoids in the blends has occurred by blending, which is consistent with the result of the density measurement. ^{129}Xe NMR spectra of ^{129}Xe in the blends show a non-linear low-field shift with increasing sorption amount of Xe because of fast exchange of Xe atoms between Henry and Langmuir sites. From the analysis of ^{129}Xe NMR chemical shifts, it has been found that the mean volume of individual microvoids (v) varies with a negative deviation versus volume fraction of PPO in the blend as well as versus V_{sp} and C_H' (Figure 8(b)). For PPO / PS blend system, it is confirmed that the contraction of individual microvoids occurs by blending.

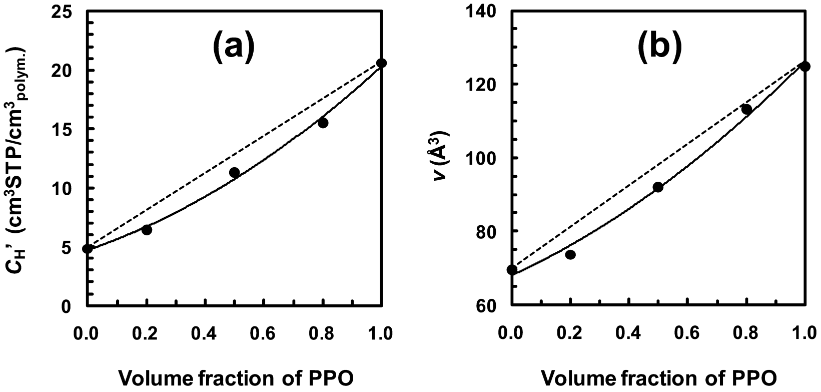

Figure 8. Langmuir saturation constant of Xe (C_H') (a) and the mean volume of individual microvoids (v) (b) plotted against volume fraction of PPO in the PPO / PS blend system at 25 °C.

Additional data on microvoid size determined by means of ^{129}Xe NMR chemical shift are summarized here. Figure 9 shows the plots of the mean volume of individual microvoids (v) against C_H' (*35*). A good linear relationship between v and C_H' is obtained. This relationship can be seen as a result of an equation ($v = 3.8 \times C_H' + 48.8$), indicating that the minimum microvoid volume is 48.8 Å^3, which is close to that of Xe atom (44.6 Å^3). In other words, if the microvoid size is smaller than Xe atom, sorption is impossible. These results make it clear that unrelaxed volume (total amount of microvoids) takes on its value in response to the changing size of individual microvoids, and C_H' is a parameter which indicates the total amount of microvoids. Also, it is possible that microvoid size can be predicted from C_H'.

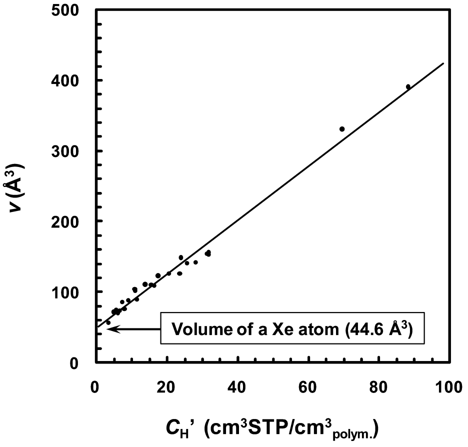

Figure 9. Plot of the mean volume of individual microvoids (v) against Langmuir saturation constant of Xe (C_H') for many glassy polymers at various temperatures.

The final topic in this section is the characteristic cavity in a crystalline part of poly(4-methyl-1-pentene), (PMP) investigated by gas permeation and ^{129}Xe NMR measurements on PMP membranes with various degrees of crystallinity (*33*).

PMP is one of the semi-crystalline polymers and is widely used in industry because of its good transparency, heat stabilty, and solvent-resistance. It is one of the significant properties of PMP that the density of the crystalline region is lower than that of amorphous region at around room temperature. Kusanagi *et.al.* have investigated the crystalline structure of PMP, which is characterized by molecular chains in 7/2 helical conformation packed in a tetragonal unit cell and concluded that the lower density of crystal region is attributed to a coarse packing of the chains; as a result, the cylindrical cavity with a diameter of about 4 Å is formed in the crystalline phase (*36*). This fact means that transport of gas and vapor molecules occurs not only in amorphous but also in crystalline regions. Figure 10 presents a schematic model of crystalline PMP as a cross-section of four 7/2 helical chain bundle. It can be expected that small gases can diffuse in the center circle of about 4 Å diameter drawn in the figure. The permeability coefficient extrapolated to 100 % crystallinity, i.e., the permeability coefficient for the cylindrical cavity along the helical PMP chains can be determined from the permeation data of PMP membranes with various degrees of crystallinity. For the cavity, permeability coefficients of He, N_2, O_2, CH_4, and CO_2 have shown finite values, whereas those of C_3H_8 and *tert*-C_4H_{10} are zero. Xe sorption measurements of PMP membranes lead to the conclusion that Xe with a diameter of 4.4 Å is able to penetrate the cylindrical cavity of crystalline PMP. From the analysis of ^{129}Xe NMR chemical shifts of ^{129}Xe in PMP membranes with various degrees of crystallinity by using equations [2] and [4], it has been able to evaluate the size of the cavity in PMP crystal as about 4.5 Å. This value is consistent with the results of not only crystallographical analysis but also gas permeation and Xe sorption

In NMR Spectroscopy of Polymers: Innovative Strategies for Complex Macromolecules; Cheng, H., et al.;
ACS Symposium Series; American Chemical Society: Washington, DC, 2011.

measurements mentioned above. From the present study, it is concluded that the width of the cylindrical cavity in PMP crystal is about 4.5 Å.

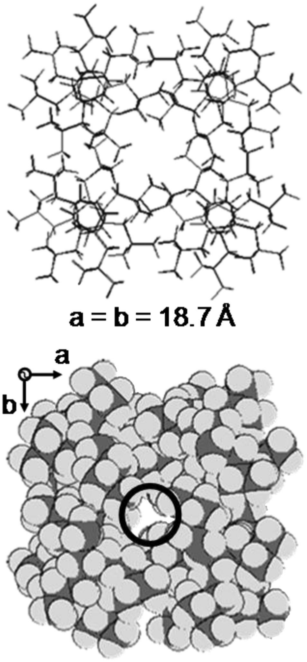

Figure 10. Schematic model of PMP crystal as a cross-section of four 7/2 helical chain bundle: stick (upper) and CPK (lower) models. The circle with a diameter of ~ 4 Å has been drawn in the center of the CPK model.

Concluding Remarks

In this article, the potential of ^{129}Xe NMR spectroscopy for the characterization of glassy polymers is demonstrated through the pressure dependence of ^{129}Xe NMR chemical shift. Previously it has been reported that the size of molecular cavity in the crystalline form of syndiotactic polystyrene can be determined by means of ^{129}Xe NMR spectroscopy (*37*). In our work, ^{129}Xe NMR chemical shift of the ^{129}Xe in rubbery polymers and liquids is shown to depend on Xe concentration, δ_D, and A_D, as mentioned above (Table II and Figure 6). The relationships between ^{129}Xe NMR chemical shift ($\delta_{(S)}$) of ^{129}Xe in *n*-alkane liquid (*38*), and its fractional free volume (V_f) are very useful in predicting the density of organic and polymeric materials in the liquid and rubbery states. In addition, we successfully reported the estimation of the density of side chain regions in low-density liquid-crystalline polyester with n-alkyl side chain (*39*, *40*). We have also demonstrated that the linewidth of ^{129}Xe NMR signal of the ^{129}Xe in this polyester corresponds to its mobility and (therefore) diffusivity. It is anticipated that ^{129}Xe NMR spectroscopy will be increasingly used in the near future as a sophisticated technique for the characterization of diffusive properties of polymeric materials and for the determination of microvoid size in glassy polymers.

Acknowledgments

We gratefully acknowledge partial financial support by a Grant-in-Aid for Scientific Research (C), No. 20550186 (2008) from the Japan Society for the Promotion of Science.

References

1. Koyama, A.; Yamamoto, T.; Fukao, K.; Miyamoto, Y. *J. Chem. Phys.* **2001**, *115*, 560–566.
2. Hill, A. J.; Jones, P. L.; Lind, J. H.; Pearsall, G. W. *J. Polym. Sci., Part: A Polym. Chem.* **1988**, *26*, 1541–1552.
3. Demarquay, J.; Fraisaard, J. *Chem. Phys. Lett.* **1987**, *136*, 314–318.
4. Ripmeester, J. A.; Ratcliffe, C. I.; Tse, J. S. *J. Chem. Soc., Faraday Trans. 1* **1988**, *84*, 3731–3745.
5. Fraisaard, J.; Ito, T. *Zeolites* **1988**, *8*, 350–361.
6. Ito, T.; Springuel-Huet, M. A.; Fraisaard, J. *Zeolites* **1989**, *9*, 68–73.
7. Ripmeester, J. A.; Ratcliffe, C. I. *J. Phys. Chem.* **1990**, *94*, 7652–7656.
8. Fetter, G.; Tichit, D.; De Ménorval, L. C.; Fraisaard, J. *Appl. Catal.* **1990**, *65*, L1–4.
9. Dybowski, C.; Bansal, N. *Annu. Rev. Phys. Chem.* **1991**, *42*, 433–464.
10. Barrie, P. J.; Klinowski, J. *Prog. Nucl. Magn. Reson. Spectrosc.* **1992**, *24*, 91–108.
11. Walton, J. H.; Miller, J. B.; Roland, M. *J. Polym. Sci., Part B: Polym. Phys.* **1992**, *30*, 527–532.
12. Miller, J. B. *Rubber Chem. Technol.* **1993**, *66*, 455.
13. Miyoshi, T.; Takegoshi, K.; Terao, T. *Polymer* **1997**, *38*, 5475–5479.
14. Walton, J. H.; Miller, J. B.; Roland, C. M.; Nagode, J. B. *Macromolecules* **1993**, *26*, 4052–4054.
15. Mansfeld, M.; Flohr, A.; Veeman, W. S. *Appl. Magn. Reson.* **1995**, *8*, 573–586.
16. Morgan, D. R.; Stejskal, E. O.; Andrady, A. L. *Macromolecules* **1999**, *32*, 1897–1903.
17. Koros, W. J.; Paul, D. R.; Huvard, G. S. *Polymer* **1979**, *20*, 956–960.
18. Hachisuka, H.; Tsujita, Y.; Takizawa, A.; Kinoshita, T. *Polymer* **1991**, *32*, 2382–2386.
19. Merkel, T. C.; Bonder, V.; Nagai, K.; Freeman, B. D. *Macromolecules* **1999**, *32*, 370–374.
20. Kesting, R. E.; Fritzsche, A. K. *Polymeric Gas Separation Membranes*; John Wiley & Sons, Inc.: New York, 1993; pp 19−59.
21. Kamiya, Y.; Mizoguchi, K.; Naito, Y.; Hirose, T. *J. Polym. Sci., Part B: Polym. Phys.* **1986**, *24*, 535–547.
22. Fleming, G. K.; Koros, W. J. *Macromolecules* **1986**, *19*, 2285–2291.

23. Yampolskii, Yu. P.; Kaliuzhnyi, N. E.; Durgarjan, S. G. *Macromolecules* **1986**, *19*, 846–850.
24. Ruan, M. Y.; Moaddel, H.; Jamieson, A. M.; Simha, R.; McGervey, J. D. *Macromolecules* **1992**, *25*, 2407–2411.
25. Li, H. L.; Ujihira, Y.; Nanasawa, A.; Jean, Y. C. *Polymer* **1999**, *40*, 349–355.
26. Liu, J.; Jean, Y. C.; Yang, H. *Macromolecules* **1995**, *28*, 5774–2779.
27. Bohlen, J.; Kirchheim, R. *Macromolecules* **2001**, *34*, 4210–4215.
28. Suzuki, T.; Miyauchi, M.; Takekawa, M.; Yoshimizu, H.; Tsujita, Y.; Kinoshita, T. *Macromolecules* **2001**, *34*, 3805–3807.
29. Suzuki, T.; Miyauchi, M.; Yoshimizu, H.; Tsujita, Y. *Polymer J.* **2001**, *33*, 934–938.
30. Yoshimizu, H.; Ohta, S.; Asano, T.; Tsujita, Y. *Polymer J.* 2011, submitted.
31. Suzuki, T.; Yoshimizu, H.; Tsujita, Y. *Desalination* **2002**, *148*, 359–361.
32. Suzuki, T.; Yoshimizu, H.; Tsujita, Y. *Polymer* **2003**, *44*, 2975–2982.
33. Suzuki, T.; Tanaka, T.; Nakajima, M.; Yoshimizu, H.; Tsujita, Y. *Polymer J.* **2002**, *34*, 891–896.
34. Djordjevic, M. B.; Porter, R. S. *Polym. Eng. Sci.* **1983**, *23*, 650–657.
35. Yoshimizu, H.; Asano, T.; Saji, J.; Ogawa, Y.; Ohta, S.; Suzuki, T.; Tsujita, Y. *Sen'i Gakkaishi*. 2011, submitted.
36. Kusanagi, H.; Takase, M.; Chatani, Y.; Tadokoro, H. *J. Polym. Sci., Polym. Phys. Ed.* **1978**, *16*, 131–142.
37. Sivakumar, M.; Suzuki, T.; Yamamoto, Y.; Mahesh, K. P. O.; Yoshimizu, H.; Tsujita, Y. *J. Membr. Sci.* **2004**, *238*, 75–81.
38. Stengle, T. R.; Williamson, K. L. *Macromolecules* **1987**, *20*, 1428–1438.
39. Tsukahara, M.; Tsujita, Y.; Yoshimizu, H.; Kinoshita, T. *ACS Symposium Series 876*; Pinnau, I., Freeman, B., Eds.; American Chemical Society, Washington, DC, 2004; pp 129−138.
40. Yoshimizu, H.; Tsukahara, M.; Suzuki, T.; Toida, J.; Ando, A.; Watanabe, J.; Tsujita, Y. *J. Mol. Struct.* **2005**, *739*, 19–26.

Epilogue: An Addiction to NMR

What do people think about NMR?
To some it's an instrument with a quirk;
To others it's boring or just bizarre;
Yet to a chosen few, it's our life's work.

Liquid NMR is a chemist's dream,
That can determine structures yet unknown.
Solid techniques are held in high esteem;
Their elegance has never been outshone.

Whether liquid or solid, we fiddle
With polymers, composites, and resins.
We struggle to unravel the riddle,
Seeking the mysteries of nuclear spins.

We play with pulses, probes, and smart gadgets,
Tuning them like a banjo or a bass.
We use magic angle in large magnets
And relish spinning in a special space.

Thus, spurred by fun and curiosity,
We labor willingly into the night.
We revel in our creativity,
Be it a new technique or an insight.

Why are we so delighted with our lot,
Forever working, not willing to change?
Yes, we have *an addiction* that, once caught,
We cannot shake off, nor want to shortchange!

H. N. Cheng
July 4, 2011

Downloaded by UNIV OF GUELPH LIBRARY on June 19, 2012 | http://pubs.acs.org
Publication Date (Web): October 14, 2011 | doi: 10.1021/bk-2011-1077.ot001

In NMR Spectroscopy of Polymers: Innovative Strategies for Complex Macromolecules; Cheng, H., et al.;
ACS Symposium Series; American Chemical Society: Washington, DC, 2011.

Editor's Biographies

H. N. Cheng

H. N. Cheng (Ph.D., University of Illinois) is currently a research chemist at Southern Regional Research Center of the U.S. Department of Agriculture in New Orleans, where he works on projects involving improved utilization of commodity agricultural materials, green chemistry, and polymer reactions. Over the years, his research interests have included NMR spectroscopy, polymer characterization, biocatalysis and enzymatic reactions, functional foods, and pulp & paper technology. He is an ACS and a POLY Fellow and has authored or co-authored 148 papers, 24 patent publications, co-edited 7 books, and organized or co-organized 20 symposia at national meetings since 1997.

Tetsuo Asakura

Tetsuo Asakura (Ph.D., Tokyo Institute of Technology) has been Associate Professor and Professor in the Department of Biotechnology of Tokyo University of Agriculture and Technology since 1981. He was Assistant Professor of Nihon University School of Dentistry at Matsudo in 1980–81 and Visiting Professor in the Department of Chemistry at Florida State University in 1990–91. He has produced approximately 300 publications. His research specialties include structural analysis of polymers using NMR, NMR chemical shift calculation, characterization of silk and transgenic silk, and applications of silk to biomaterials. He received Awards of Polymer Society in Japan and Fiber Society in Japan

Alan D. English

Alan D. English Ph.D. is a DuPont Fellow in DuPont Central Research and Development at the Experimental Station in Wilmington, DE. His interests include solid state NMR spectroscopy of polymers and development of polymer structure/property/processing relationships. He is both an APS Fellow and an ACS Fellow and has been the recipient of a number of awards including the ACS Award in Applied Polymer Science and the International Award of the Society of Polymer Science Japan. He is the author of nearly 100 papers/patents/books and has organized or co-organized 15 symposia at national meetings/workshops since 1981. He is also an Associate Editor of *Macromolecules*.

In NMR Spectroscopy of Polymers: Innovative Strategies for Complex Macromolecules; Cheng, H., et al.;
ACS Symposium Series; American Chemical Society: Washington, DC, 2011.

Subject Index

A

Aβ. *See* Amyloid β-peptide (Aβ)
α-CD. *See* α-cyclodextrin (α-CD)
Acidic aqueous solutions, 342
Acrylic latex polymers
  emulsion polymerization techniques, 384
  heterogeneous polymer, 387
  nuclear magnetic resonance spectroscopy, 385
  overview, 383
  quantitative analysis, 391
  scanning probe microscopy, 385
  solid state NMR, 394
  solution state NMR, 386
α-cyclodextrin (α-CD)
  AVANCE 500 MHz NMR Spectrometer, 267
  HTC conformations, 268
  HTC dynamics, 271
  overview, 265
  structure, 267*f*
Advanced low-load dipolar decoupling, 405
$(AGSGAG)_5$, 286*f*
Alternative lock channel, 60, 61*f*
Amorphous macromolecules, advanced NMR experiments
  molecular weights, 69
  overview, 67
  representative structures, 69
Amphiphilic block copolymer, 463, 465*s*, 466*f*
Amyloid β-peptide (Aβ)
  angular dependent NMR experiments, 302
  chemical shift changes, 304*f*
  lipid bilayers, 305
  overview, 299
  solution NMR experiments, 301
  structural change, 302
Anisotropic spin interactions, 19
Anisotropic swelling, 452
Application-driven polymer designs, 9
Arrhenius plot, iPP, 202*f*
Atactic polypropylene (aPP), 69*s*, 75*f*, 76*f*, 77*f*, 80*f*

B

BA/MMA copolymers, 386*f*, 387*f*, 390*f*
Bicellar pore size probing, 239
Bicellar self-assemblies, 223*f*
Bicelle disk versus perforated lamellae, 234
Bicelle morphology, 231
  bicellar pore size probing, 239
  DHPC, 234
  membrane crowding, 233
  PEG diffusion, 237
  PEGylated lipid diffusion, 232
Bicelles, magnetic alignment, 225*f*
Bi-Gaussian RDC distributions, 218*f*
Block copolymer assembly preparation, 463
^{11}B MAS spectra
  borax, 136*f*
  boric acid/PVA film, 135*f*
  PVA film, 140*f*
B16 melanoma cells, 470*f*
Borax
  ^{11}B MAS spectra, 136*f*
  signal intensities, 138*f*
  stationary NMR spectra, 137*f*
^{11}B 3QMQMAS spectrum
  boric acid/PVA film, 141*f*
^{11}B stationary NMR spectra
  boric acid/PVA film, 141*f*
Bulk polymers
  anisotropic spin interactions, 19
  chain microstructure, defects and dynamics, 26
  double quantum NMR, 23
  empty helical nano-channels, 31
  hydrogen bonding, 29
  manipulation of spin interactions, 22
  overview, 17
  packing in polymers, 30
  polymeric proton conductor dynamics, 27
  side chain conformation, 29
  two-dimensional NMR spectroscopy, 24

C

Canopy
  D_2O, 155*t*
  NIM diagram, 152*f*

Downloaded by 89.163.35.42 on June 19, 2012 | http://pubs.acs.org
Publication Date (Web): October 14, 2011 | doi: 10.1021/bk-2011-1077.ix002

Downloaded by 89.163.35.42 on June 19, 2012 | http://pubs.acs.org
Publication Date (Web): October 14, 2011 | doi: 10.1021/bk-2011-1077.ix002

Carbon T_1 versus temperature, 154*f*
Carboxylic acid-carboxylic acid ester structure, 120*s*
Carboxylic acid dimer structure, 120*s*
Carboxylic acid – Li$^+$ neutralized dimer structure, 126*s*
Carboxylic acid – Li$^+$ neutralized tetramer structure, 126*s*
Carboxymethylated starch (CMS)-chitosan complex tablets, 449*f*
^{13}C CPMAS NMR spectra, 283*f*, 289*f*, 290*f*
  CαH carbon, 91*f*
  ε-PL, 327*f*, 331*f*, 332*f*
  PVIBE, 89*f*
^{13}C CPMAS spectra, 395*f*
^{13}C CPMAS SSNMR spectra, 98*f*
CD curves, ε-PL, 322*f*
^{13}C direct polarization proton, 498*f*
CDT-PTZ copolymer, 31*f*
Centerband-only detection of exchange (CODEX), 70*f*
Chain diffusions, 196*f*
Chain- ends, polymer structure, 38
Chain microstructure, 26
Channels alignment, 255
Chemical shift ranges, organic compounds, 21*f*
^{13}C liquid-state NMR, soy flour gel, 345*f*
^{13}C NMR chemical shifts, ε-PL, 326*t*, 330*t*
^{13}C NMR observed conformations, 265
^{13}C NMR spectra, 269*f*, 270*f*
  poly(propylene-co-1-octene), 58*f*
  proteins, 343*f*
^{13}C NMR spin-lattice relaxation, 274*t*
^{13}C nuclear shielding, 270*f*
CH^2 resonances, 129*f*
Coefficient of thermal expansion, 110*t*
Collective motion, precise polyethylene, 28*f*
Compositional heterogeneity, 375*t*
Confinement effect, 105
Conformational transition, 196*f*
  side-chain, 197*f*
COOH, signal intensity, 129*f*
COOH proton chemical shift, 124*f*
Core, NIM diagram, 152*f*
Corona, NIM diagram, 152*f*
Correlation spectroscopy (COSY), 46, 46*f*, 361*f*, 363*f*
Correlation time distribution widths, temperature dependence, 77*f*
COSY. *See* Correlation spectroscopy (COSY)
CPMAS spectra, 397*f*
CPMG, decay curves, 435*f*, 436*f*
CP-OH angle distribution, 29*f*
Crosslinked EPDM rubbers, chain mobility
  ^{1}H NMR, 210
  ^{1}H NMR transverse relaxometry, 210
  multiple-quantum ^{1}H NMR, 211
  overview, 207
  systematic T_2 relaxometry study, 209
Crosslinked high amylose starch (CHAS), 448*f*
Crystallinity determination methods, 180
^{13}C spin-lattice relaxation time, 169*f*, 175*f*, 328*t*
Curves, 209
CW-HEPT, 406*f*, 407*f*

D

2D contour plot, 1H-1H DQ NMR spectrum, 31*f*
2D-COSY spectra, hexafluoropropylene oxide tetramer, 55*f*
Decay analysis, transverse magnetization relaxation, 182
Decay curves, CPMG, 435*f*, 436*f*
2D exchange NMR, 26*f*
1D ^{1}H MAS NMR line shape, 129*f*
1D ^{1}H MAS NMR spectra, 129*f*
2D ^{1}H MAS NOESY, 128*f*
DHPC. *See* Dihexanoylphosphatidylcholine (DHPC)
2D-HSQC NMR spectra poly(ethylene-co-octene), 53*f*
Diblock copolymer synthesis, 464
Differential scanning calorimetry, regioregulated P3AT, 165*f*
Diffusion anisotropy, 255
Diffusion NMR, 52
Diffusion NMR, polymers
  bicelle fundamentals, 222
  bicelle morphology, 231
    bicellar pore size probing, 239
    bicelle disk versuss perforated lamellae, 234
    DHPC, 234
    membrane crowding, 233
    PEG diffusion, 237
    PEGylated lipid diffusion, 232
  lipid bilayer membranes, 229
  overview, 221
Diffusion tensor, membrane frame, 227*f*
Dihexanoylphosphatidylcholine (DHPC), 222, 234
Dimyristoylphosphatidylcholine (DMPC), 222
  schematic cross-section, 238*f*

Downloaded by 89.163.35.42 on June 19, 2012 | http://pubs.acs.org
Publication Date (Web): October 14, 2011 | doi: 10.1021/bk-2011-1077.ix002

Disordered structure, π-conjugated polymers, 161
Distortionless enhancement by polarization transfer, 487*f*
2D MAS NMR correlation experiments, 126
DMPC. *See* Dimyristoylphosphatidylcholine (DMPC)
DMPC lipid bilayer, Aβ, 306*t*
2D-NMR methodologies
  heteronuclear, 48
  homonuclear, 46, 46*f*
Domain size determination, NMR spin-diffusion experiments, 185
Donor-acceptor group
  local packing, 31*f*
  organization, 31*f*
Double quantum build-up, 425, 426*f*
  curves, 213*f*
  intensity, 212*f*
  rates, 215*f*
Double quantum filtered COSY (DQCOSY), 46*f*, 47
Double quantum NMR, 23, 24*f*
1D ^{31}P ^{1}H-decoupled solid-state NMR spectra, Ab, 307*f*
DPNR, vulcanization characteristics, 490*t*
DQCOSY. *See* Double quantum filtered COSY (DQCOSY)
Drawing rate effect, 188
Drawing ratio effect, 188
Drawing temperature effect, 188
Drug loading effect, 453
DSC curves
  PVIBE/e-PL, 92*f*
  PVIBE/e-PL/saponite-clay nanocomposites, 91
Dynamic heterogeneity, 128

E

ECOSY, 363*f*
Elastomers
  latex state NMR spectroscopy
    crosslinking effect, 476
    dry rubber content effect, 479
    particle size effect, 482
  overview, 475
  solid state NMR
    crosslinking effect, 484
    2D NMR measurement, 486
    FG-FMAS, 489
    spectral assignments, 485
Electrophoretic NMR, 261*f*
Elevated temperatures, long term aging, 186
Empty helical nano-channels, spectroscopic fingerprints, 32*f*
EPDM. *See* Ethylenepropylene-diene terpolymers (EPDM)
ε-PL. *See* Microbial poly(ε-L-lysine) (ε-PL)
EPM. *See* Ethylene-propylene copolymers (EPM)
Estimated repeat lengths, 95*t*
Ethylene copolymers, 187
Ethylene-octene copolymer (m-PE), 183
Ethylene-propylene copolymers (EPM), 207
Ethylenepropylene-diene terpolymers (EPDM), 207
  thermoplastic vulcanizates, 184
Exchange time constants, 80*f*

F

^{19}F detected HSQC spectra, 60*f*
^{19}F 1D-NMR spectrum
  hexafluoropropylene oxide tetramer, 56*f*
  poly(hexafluoropropylene oxide), 44*f*
Field-effect transistors, 30
Filler-matrix interactions, 105
Fluorinated solvent effects, 191
Fluorine NMR, 357
Fluoropolymers
  fluorine NMR, 357
  instrumentation, 366
  materials, 366
  NMR methods, 359
  overview, 355
  PHFPO characterization
    2D-NMR, 362
    structure, 361
  PVDF characterization
    2D-NMR, 365
    structure, 364
^{19}F NMR imaging agents
  block copolymer assembly preparation, 463
  characterization, 461
  diblock copolymer synthesis, 464
  hyperbranched copolymers synthesis, 463
  hyperbranched polymeric ^{19}F imaging agents, 467
  materials, 461
  MRI experiments, 462
  overview, 459

Fractionated HDPE analysis, 410
Freely jointed rigid rod chain, 419, 419*f*
  time average orientation, 420*f*
Frequency encoding, NMR imaging, 445*f*
FT-IR chemical image, soybean, 349*f*
FT-NIR spectroscopy, soybean, 347*f*
Functionalized silica nanoparticles
  overview, 495
  resonance linewidth broadening mechanisms, 497
FWHM, isotropic resonance, 129*f*

G

Ganglioside, 299, 300*f*
Gas sorption properties, glassy polymers, 512
Gel formation, 450
Gibbs-Thomson relationship, 88
Glassy polymers, gas sorption properties, 512
Glycoprotein, 337
Glycosylation, 337
Graphene oxide, 108, 108*f*
Graphite, 105, 108*f*

H

HANR, vulcanization characteristics, 490*t*
H2BC, 49*f*
^{1}H-^{11}B CP profiles, boric acid/PVA films, 144*f*
^{1}H-^{11}B HETCOR spectrum, boric acid doped in PVA, 144*f*
^{1}H-^{13}C WISE NMR spectra, 195*f*, 198*f*
HDPE, 183
Head-to-head polypropylene (hhPP), 69*s*, 80*f*
Helical packing arrangement, macrocyclic channel, 33*f*
Heterogeneous polymer, 388*f*
Heteronuclear 2D-NMR, 48, 49*f*
Heteronuclear multiple bond correlation (HMBC), 48, 49*f*, 61*f*
Heteronuclear multiple quantum coherence (HMQC), 48, 49*f*
Heteronuclear single quantum coherence (HSQC), 48, 49*f*, 360*f*
  nested pulse sequences, 60*f*
Hexafluoropropylene oxide tetramer, 55*f*, 56*f*
Hexatriacontane (HTC), 265
^{1}H-^{19}F intermolecular NOE spectra, 293*f*
^{1}H MAS NMR chemical shifts, 122*t*
^{1}H MAS NMR spectra, 125*f*, 195*f*, 198*f*
^{1}H MAS NMR spectroscopy
  ab initio calculations, 118
  2D MAS NMR correlation experiments, 126
  dynamic heterogeneity, 128
  ^{1}H MAS NMR, 119
  material preparation, 116
  solid-state ^{1}H NMR spectroscopy, 117
HMBC. *See* Heteronuclear multiple bond correlation (HMBC)
HMQC. *See* Heteronuclear multiple quantum coherence (HMQC)
^{1}H NMR, e-PL, 323*f*, 324*f*
^{2}H NMR spectroscopy, 255
^{1}H NMR transverse relaxation rates, EPDM, 211*f*
^{1}H NMR transverse relaxometry, 210
Homogeneous copolymers, 392*f*
Homonuclear decoupling, 54
Homonuclear 2D-NMR, 46, 46*f*
HPLC ion pair chromatogram, ε-PL, 321*f*
^{1}H spin-diffusion rates, 95*t*
HSQC. *See* Heteronuclear single quantum coherence (HSQC)
HSQC spectrum, 303*f*
HSQC-TOCSY, 49*f*
^{1}H SS NMR fit data, 110*t*
^{1}H SS NMR spectra, 109*f*
HTC. *See* Hexatriacontane (HTC)
HTC-α-CD-IC, 268*f*
HTC chains, 272*f*
HTC conformations, 268
HTC dynamics, 271
Human erythrocyte membrane arrays, 340*f*
^{1}H wPMLG NMR spectra, PVA films, 143*f*
Hydrated gels, 344
Hydrated membrane shell, CHAS tablet, 451*f*
Hydrated wheat grains, 345
Hydrogen bonding, 29
Hydrostatic pressure, 186
Hyperbranched copolymers synthesis, 463
Hyperbranched polymeric ^{19}F imaging agents, 467
Hyperbranched polymers, 468*s*, 469*f*

I

Information content, NMR data, 372*f*
Intensity, 212*f*
Ion associations, 251, 258, 260*f*
Ionic liquid, 254, 258

Downloaded by 89.163.35.42 on June 19, 2012 | http://pubs.acs.org
Publication Date (Web): October 14, 2011 | doi: 10.1021/bk-2011-1077.ix002

- Ionic polymers
  - channels alignment, 255
  - diffusion anisotropy, 255
  - ^{2}H NMR Spectroscopy, 255
  - ion associations, 258
  - ion motions, 260
  - ionic liquid, 254, 258
  - mapping local domain information, 259
  - membrane preparation, 253
  - overview, 252
  - pulsed-field-gradient NMR, 254
  - structures, 253*f*
  - water uptake determination, 254
- Ion motions, 260
- Ionomers, 115
- IPB1. *See* Isotactic poly(1-butene) (iPB1)
- IPP. *See* Isotactic polypropylene (iPP)
- I-PP, 183
  - aging, 186
  - thermoplastic vulcanizates, 184
- IR, ε-PL, 325*f*
- Isotactic poly(1-butene) (iPB1), 191, 194
  - ^{13}C CODEX reference, 199*f*
- Isotactic-polyolefins
  - iPB1, 194
  - iPP, 200
  - measurements, 193
  - overview, 191
  - samples, 192
- Isotactic polypropylene (iPP), 187, 191, 200, 409
  - arrhenius plot, 202*f*
  - *l* versus f_{order}, 203*f*
  - polymer chain trajectory, 204*f*
  - unit cell structure, 201*f*
- Isotropic signal fraction, Aβ, 309*f*

L

- Langevin dynamics simulation, 164*f*
- Lauterbur's experiment, 443*f*
- Lipid bilayer membranes, 229
- Lipid bilayers, 299
- Local motion, precise polyethylene, 28*f*
- Local packing, donor-acceptor groups, 31*f*
- Low branch content quantification, 28*f*
- Low-symmetry macrocycles, 31

M

- Macrocycles, helical packing arrangement, 33*f*
- Mapping local domain information, 259
- Melt-crystallized PE, temperature effect, 182*f*
- Melt-state NMR applications, 407
- Melt-state NMR spectroscopy, polyolefins
  - advanced low-load dipolar decoupling, 405
  - hardware setup, 403
  - materials, 403
  - melt-state NMR applications, 407
  - melt-state versus solution-state, 404
  - overview, 401
  - scalar coupling mediated method, 405
  - spectral analysis setup, 404
- Melt-state versus solution-state, 404
- Membrane crowding, 233
- Membrane preparation, 253
- Methine carbon, 484*f*
- Methyl carbon, 484*f*
- Microbial poly(e-L-lysine) (e-PL)
  - aqueous solution, 321
  - azo dyes, 330
  - chain conformation, 329
  - conformation model, 329*f*
  - derivative preparation, 319*s*
  - instruments, 320
  - materials, 319
  - measurements, 320
  - overview, 318
  - physical properties, 321
  - polymer morphology, 327
  - repeating units, 318*s*
  - solid state, 324
- Micro-CT image, rabbit femurs, 292*f*
- Molecular dynamics, regioregulated P3AT, 163
- Molecular mobility, 179
- Monomer sequence, polymer structure, 39
- MR T_2 relaxometry, phase composition analysis, 181
- Multiblock copolymer, 257*f*
- Multinuclear solid state NMR, 299
- Multiple-quantum ^{1}H NMR, 211
- Multiple receiver systems, 59

N

- Nafion 112, 251, 256*f*
- Nanoscale ionic materials (NIM), 150
  - materials, 150
  - NMR characterization, 151
  - overview, 150
  - preparation, 150
- ^{15}N CPMAS NMR spectra, PK60PA40, 99*f*
- Nested HSQC pulse sequences, 60*f*

Downloaded by 89.163.35.42 on June 19, 2012 | http://pubs.acs.org
Publication Date (Web): October 14, 2011 | doi: 10.1021/bk-2011-1077.ix002

N-Hexatriacontane, 265
NIM. *See* Nanoscale ionic materials (NIM)
NIM, D_2O, 155*t*
NIM diagram, 152*f*
NIM preparation, 150
NMR. *See* Nuclear magnetic resonance (NMR)
NMR characterization, 151
  statistical models, 374*f*
NMR imaging
  frequency encoding, 445*f*
  magnetic field gradient, 445*f*
  overview, 441
  pharmaceutical tablets
    experimental set-up, 448
    swelling, 449
    water diffusion, 449
  phase encoding, 445*f*
  pulse sequence, 446*f*
  techniques
    principles, 442
    signal acquisition, 443
    technical considerations, 447
NMR rescaling, 421
  NMR signals, 420
  overview, 417
  simulation, freely jointed rigid rod chain, 419
NMR spin-diffusion experiments, domain size determination, 185
NMR submolecule, 421
^{15}N NMR chemical shifts, e-PL, 333*t*
^{15}N NMR spectrum, e-PL, 333*f*
NOESY, 46*f*
Normalized diffusive intensity decays, STE PFG ^{1}H NMR spectra, 241*f*
Normalized exchange intensities, 72*f*, 74*f*, 79*f*
Normalized quantum build-up curves, 214*f*, 215*f*
N1s XPS fit data, 110*t*
Nuclear magnetic resonance (NMR)
  advanced experiments, 67
  application-driven polymer designs, 9
  biopolymers, biochemistry, and bio-inspired chemistry, 9
  blends, composites, and nanostructures, 8
  bulk polymers
    applications, 25
    background, 18
    overview, 17
  confinement effect, 105
  filler-matrix interactions, 105
  ^{1}H MAS NMR spectroscopy, 115
  methodologies, 5
  micelles, interfaces, and confined environments, 8
  nanoscale ionic materials (NIM), 149
  overview, 3
  polymers in melt, 7
  polymers in solution, 7
  polymers with precise control of structure, 8
  solid state ^{13}C NMR, 85
  solid-state, boric acid, 133
  solution NMR methods, 37
  strategies, 5
  structure-dynamics-properties relationships, 7
Nuclei interaction, NMR, 20*t*

O

Optimum analysis temperature, 181

P

Packing, polymers, 30
Paraffinic oil, thermoplastic vulcanizates, 184
P3AT. *See* Poly(alkylthiophene) (P3AT)
P3BT. *See* Poly(3-butylthiophene) (P3BT)
P3BT versus P3HT, 174
π-conjugated polymers, disordered structure, 161
PEB66, 72*f*, 74*f*, 76*f*, 77*f*
PEG diffusion, 237
PEG diffusion coefficient versus degree of polymerization N, 240*f*
PEGylated lipid diffusion, 232
PFG. *See* Pulsed-field gradient (PFG) diffusion
PFG diffusion, NaCl, 156*f*
PFG NMR diffusion, 155*f*
Phase composition, 179
Phase composition analysis, NMR T_2 relaxometry, 181
Phase encoding, NMR imaging, 445*f*
PHFPO, 357*f*, 359*f*
Phospholipids, reduced transbilayer water diffusion coefficient, 236*f*
P3HT. *See* Poly(3-hexylthiophene) (P3HT)
Pigmented materials, 410
PK10PA90, 97*f*
PK60PA40, 97*f*
  ^{15}N CPMAS NMR spectra, 99*f*
PK80PA20, 97*f*
PK90PA10, 97*f*

Downloaded by 89.163.35.42 on June 19, 2012 | http://pubs.acs.org
Publication Date (Web): October 14, 2011 | doi: 10.1021/bk-2011-1077.ix002

Downloaded by 89.163.35.42 on June 19, 2012 | http://pubs.acs.org
Publication Date (Web): October 14, 2011 | doi: 10.1021/bk-2011-1077.ix002

PLGA-PEG-folate, 50*f*
^{31}P NMR spectra, bicelles, 235*f*
Poly(alkylthiophene) (P3AT), 163
Poly(3-butylthiophene) (P3BT), 163
Polyethylene acrylic acid copolymers, 115, 117*s*
Polyethylene-co-α-olefin microstructure, 408
Polyethylene-co-butene-co-hexene terpolymer, 406*f*
Polyethylene-co-butene (PEB), 69*s*
Polyethylene-co-hexene, 411*f*
Polyethylene-co-hexene copolymers, 411*f*
Polyethylene-co-vinylacetate copolymer, 412*f*
Poly(hexafluoropropylene oxide), 44*f*
Poly(3-hexylthiophene) (P3HT), 163
Polyimide composites, 107
Polyimides, 106
Polyisobutylene (PIB), 69, 79*f*, 80*f*
Polyisoprene (PI), 69*s*
Polyketone/nylon 6 (PK/PA), solid state ^{13}C NMR, 85
  See also Poly(vinyl isobutyl ether) (PVIBE)/e-PL, solid state ^{13}C NMR
Polymer-α-CD-IC, 275*f*
Polymer chain crowding, 157*f*
Polymer chain trajectory, iPP, 204*f*
Polymeric proton conductor dynamics, 27
Polymer melt, shear, 431
Polymer microstructure
  application methodologies
    analytical approaches, 376
    integrated approaches, 377
    kinetic simulation approaches, 378
    simulation approaches, 377
  overview, 371
  Polytact, 378
  statistical models
    kinetic models, 375
    one state models, 373
    perturbed models, 375
    two state models, 373
Polymer nanocomposites
  characterization, 107
  overview, 105
  polyimide composites, 107
Polymers
  bicelles, 221
  diffusion NMR, 221
  melt, 7
  nanocomposites, 105
  packing, 30
  precise control of structure, with, 8
  solution, 7
  solution NMR methods, 37
Polymer structure
  chain- ends, 38
  defects, 41
  monomer sequence, 39
  stereosequence, 40
Polyolefins, 408
  annealing effects, 185
  crystallinity determination methods, 180
  deformation effects, 186
  domain size determination, NMR spin-diffusion experiments, 185
  overview, 179
  phase composition analysis, NMR T_2 relaxometry, 181
Poly(propylene)
  double quantum signal, 433*f*
  longitudinal relaxation time experiments, 434*f*
  shear rate, 435*f*
Polypropylene-co-α-olefin applications, 409
Poly(propylene-co-1-octene), 58*f*
Polysaccharides, 344
Polytact, 378, 379*f*
Polyvinylethylene (PVE), 69*s*, 80*f*
Poly(vinylidene fluoride) (PVDF)
  COSY spectrum, 367*f*
  19F-13C HSQC 2D-NMR spectra, 366*f*
  structure, 364*f*
Poly(vinyl isobutyl ether) (PVIBE)/ε-PL, solid state ^{13}C NMR
  crystallinity and crystal size, 88
  Gibbs-Thomson relationship, 88
  impact resistence, 96
  instruments, 320
  measurements, 320
  morphology, 96
  overview, 85
  See also Polyketone/nylon 6 (PK/PA), solid state ^{13}C NMR
Precise polyethylene, 28*f*
Protein-carbohydrate interactions
  carbohydrate-protein interactions, 342
  hydrated systems, 345
  materials, 341
  measurements, 341
  overview, 337
^{31}P solid-state NMR spectra, Aβ, 308*f*, 309*f*
Pulsed-field-gradient NMR, 254
Pulsed-field gradient (PFG) diffusion, 151
Pulse sequence, 45
  direct polarization, 139*f*
  double quantum NMR, 24*f*
PVA film
  ^{11}B MAS spectra, 140*f*
  ^{1}H wPMLG NMR spectra, 143*f*

Downloaded by 89.163.35.42 on June 19, 2012 | http://pubs.acs.org
Publication Date (Web): October 14, 2011 | doi: 10.1021/bk-2011-1077.ix002

PVDF. *See* Poly(vinylidene fluoride) (PVDF)

Q

Quantitative ^{1}H melt-state NMR spectroscopy, 412
Quantitative NMR, 2D-NMR, 51
Quantitative one-dimensional NMR, 41
  data acquisition, 41
  data processing, 43

R

Raman spectra, ε-PL, 325*f*
Random coil structural component, 284*f*
Random poly(ethylene-co- propylene), 184
Rapid LCB quantification, 408
Rates, 215*f*
REDOR plots, 284*f*
Reduced transbilayer diffusion coefficients, 242*f*
Reduced transbilayer water diffusion coefficient, phospholipids, 236*f*
Regio-regular isotactic polypropylene, 409*f*
Regioregulated P3AT
  differential scanning calorimetry, 165*f*
  FTIR spectra, 166*f*
  molecular dynamics, 163
Regioregulated P3BT
  ^{13}C CPMAS NMR measurements, 166
  ^{13}C CPMAS NMR spectra, 167*f*
  ^{13}C spin-lattice relaxation time measurements, 168
  DSC, 163
  FTIR measurements, 165
  FTIR spectra, 166*f*
  phase diagram, 176*f*
Regioregulated P3HT
  ^{13}C CPMAS NMR, 170, 172*f*
  ^{13}C spin-lattice relaxation time measurements, 173
  DSC, 163
  FTIR measurements, 165
  FTIR spectra, 166*f*
  phase diagram, 176*f*
Rescaling applicability, 427
Resonance linewidth broadening mechanisms, 497
Rf signal control
  alternative lock channel, 60
  homonuclear decoupling, 54
  multiple receiver systems, 59
  selective excitation, 52
  sensitive detection, 57
Rigid-rod copolymers, 29
Rod-coil copolymers, scheme packing, 30*f*
Rubbers
  ^{13}C-NMR spectra, 486*f*
  HMQC spectra, 488*f*, 489*f*
  ^{1}H-NMR spectra, 488*f*
  latex state ^{13}C-NMR spectra, 483*f*
  solid-state ^{13}C-NMR spectra, 491*f*
  solid-state ^{1}H-NMR spectra, 491*f*
  stress-strain curves, 492*f*

S

Scalar coupling mediated method, 405
Scattering versus NMR, 34*t*
Schematic cross-section through, DMPC, 238*f*
Scheme packing, rod-coil copolymers, 30*f*
Segregated copolymer, 394*t*
Selective excitation, 52
Self-diffusion coefficient, 155*t*, 156*t*
  CHAS tablet, 451*f*, 452*f*
SEM photomicrographs, 291*f*
Sensitive detection, 57
Sideband patterns, double quantum NMR, 24*f*
Side-chain conformation, 29
Side-chain conformational transition, 197*f*
Signal intensity, pulse length, 139*f*
Silk-based biomaterials
  applications, 289
  design, 287
  fluorinated solvent effects, 291
  modifications, 287
  overview, 281
  structural studies, 282
Silk-like peptide, 288*f*
Single-Gaussian RDC distributions, 218*f*
Small angle neutron scattering, 34*t*
Small angle X-ray scattering, 34*t*
Sodium nitride, stationary NMR spectra, 137*f*
Solid-state NMR, boric acid doped in PVA
  ^{11}B MAS NMR, 135
  interactions between boric acid and polymer chains, 142
  overview, 133
  possible conformation, 145
  quantitative analysis, 139
Solid-state NMR spectra, 22*f*
  disordered structure, π-conjugated polymers, 161

  - ^{1}H, 117, 118*f*
  - ^{1}H MAS, 120*s*
  - isotactic-polyolefins, 191

- Solution NMR methods, 37
  - hardware, 52
    - rf signal control, 52
  - new experiments
    - diffusion, 52
    - 2D-NMR methodologies, 46
    - quantitative NMR, 51
  - polymer structure, 38
  - pulse sequences, 45
  - quantitative one-dimensional NMR, 41
    - data acquisition, 41
    - data processing, 43
- Soybean seeds, 346
- Spin interaction manipulation, 22
- SSB spectral region, 129*f*
- Static solid state NMR spectra, 22*f*
- Stationary NMR spectra
  - borax, 137*f*
  - sodium nitride, 137*f*
- Statistical models, NMR characterization, 374*f*
- STE intensity decays, DMPE-PEG 2000 concentration, 233*f*
- STE PFG ^{1}H NMR spectra, normalized diffusive intensity decays, 241*f*
- STE PFG ^{1}H NMR spectral series, 232*f*
- Stereosequence, polymer structure, 40
- Stimulated echo pulsed field gradient NMR pulse sequence, 229*f*
- Storage modulus, 110*t*
- Structure-dynamics-properties relationships, 7
- Subject analysis, NMR, 4*t*
- Swelling kinetics, CHAS tablet, 453*f*

T

- Temperature dependence
  - correlation time distribution widths, 77*f*
  - polyolefins, 183
- Temperature effect, melt-crystallized PE, 182*f*
- T_1H decay curves, 101*f*
- Thermoplastic vulcanizates, i-PP, 184
- tHFPO, 362*f*
- T_1H relaxation curves, PVIBE, 94*f*
- TOCSY. *See* Total correlation spectroscopy (TOCSY)
- Total configurational entropy, 82*f*
- Total correlation spectroscopy (TOCSY), 46*f*, 47
- Transverse magnetization relaxation, decay analysis, 182
- Transverse relaxation function, 421
- Two-dimensional NMR spectroscopy, 24

U

- Ultrahigh charge carrier mobility, 30
- Unit cell structure, iPP, 201*f*

W

- Water uptake determination, 254
- Wheat gliadin interactions, 342
- Wide angle X-ray scattering, 34*t*

X

- ^{129}Xe NMR, 510, 511*f*
  - glassy polymers, 517*t*
  - PS films, 515*f*
- Xenon sorption
  - gas sorption properties, glassy polymers, 512
  - isotherms, 513
  - langmuir saturation constant, 518*f*, 519*f*, 520*f*
  - microvoid size determination, 514
  - overview, 509
  - ^{129}Xe NMR, 510

Downloaded by 89.163.35.42 on June 19, 2012 | http://pubs.acs.org
Publication Date (Web): October 14, 2011 | doi: 10.1021/bk-2011-1077.ix002